UNIVERSIDAD
DE GRANADA

Departamento de Química Inorgánica

Estudio y preparación de nanomateriales moleculares basados en híbridos metal-ADN

Tesis doctoral con mención internacional

Programa de Doctorado en Química

Director: Miguel Ángel Galindo Cuesta

Antonio Pérez Romero

Granada, Julio de 2024

Editor: Universidad de Granada. Tesis Doctorales
Autor: Antonio Pérez Romero
ISBN: 978-84-1195-430-3
URI: https://hdl.handle.net/10481/94828

UNIVERSIDAD
DE GRANADA

Department of Inorganic Chemistry

Study and preparation of molecular nanomaterials based on metal-DNA hybrids

PhD Tesis with international mention

PhD Programme in Chemistry

Director: Miguel Ángel Galindo Cuesta

Antonio Pérez Romero

Granada, July 2024

ÍNDICE

Resumen – Abstract……**15**

Objetivos – Objetives……**22**

Abreviaciones-Abbreviations……..**25**

Capítulo 1. Introducción……..…..**31**

1.1. El ADN como biomolécula que condensa la vida……..….31

1.2. El ADN como nanomaterial tecnológico…….……...35

1.3. Las interacciones metal-ADN en la naturaleza y en la nanotecnología……..……...41

1.4. Bibliografía……..……....56

Capítulo 2. Estudios de Interacción de las Nucleobases con Complejos Metálicos Complementarios. Formación de Híbridos Supramoleculares ADN-Pd Altamente Organizados…….…...…**65**

2.1. Estudios con derivados de adenina……..…..….67

2.1.a. Síntesis y caracterización del compuesto de coordinación [Pd(Cheld)(CH_3CN)] (**CH_3CN-Pd-Cheld**)……...…...**69**

2.1.b. Síntesis y caracterización de compuestos de coordinación con derivados de la adenina; [Pd(Cheld)(eA)] (**eA-Pd-Cheld**) y [Pd(Cheld)(pX)] (**pX-Pd-Cheld**)……..……...…**70**

2.1.c. Formación y caracterización de los híbridos supramoleculares [{Pd(Cheld)}$_{15}$(dA_{15})] (**dA_{15}-Pd-Cheld**) y [{Pd(Cheld)}$_{15}$(dX_{15})] (**dX_{15}-Pd-Cheld**)……..…...**77**

2.2. Estudios con derivados de citosina……..……...……90

2.2.a. Síntesis y caracterización del compuesto de coordinación [Pd(Aqa)(DMSO)] (**DMSO-Pd-Aqa**)……...……...…**91**

2.2.b. Síntesis y caracterización del compuesto de coordinación con derivados de la citosina; [Pd(Aqa)(mC)] (**mC-Pd-Aqa**)…….…...**93**

2.2.c. Formación y caracterización del híbrido supramolecular [{Pd(Aqa)}$_{15}$(dC$_{15}$)] (**dC$_{15}$-Pd-Aqa**)……...**101**

2.3. Estudios con derivados de timina……..……...107

2.3.a. Síntesis y caracterización del compuesto de coordinación con derivados de la timina; [Pd(dPy)(DMSO)] (**DMSO-Pd-dPy**)……..……..**108**

2.3.b. Síntesis y caracterización del compuesto de coordinación [Pd(dPy)(eT)] (**eT-Pd-dPy**)……....**109**

2.3.c. Formación y caracterización del híbrido supramolecular [{Pd(dPy)}$_{15}$(dT$_{15}$)] (**dT$_{15}$-Pd-dPy**)……**113**

2.4. Conclusiones……..116

2.5. Materiales y métodos…….……..……..117

2.6. Bibliografía……..……..129

2.7. Anexo……..131

Capítulo 3. Estudios de Competitividad Entre Fragmentos Metálicos de Pd^{II} y Moléculas de ADN……..……..**145**

3.1. Estudios de competitividad metal-nucleobase...……146

3.1.a. Estudios de competitividad entre los fragmentos metálicos [Pd(Cheld)] (**Pd-Cheld**) y [Pd(Aqa)] (**Pd-Aqa**) con las nucleobases adenina y citosina……**146**

3.2. Formación de sistemas ADN-Pd heterolépticos……..155

3.2.a. Estudios de competitividad entre los fragmentos metálicos [Pd(Cheld)] (**Pd-Cheld**) y [Pd(Aqa)] (**Pd-Aqa**) con monohebras de **dC_{15}**……....**156**

3.2.b. Estudios de competitividad entre los fragmentos metálicos [Pd(Cheld)] (**Pd-Cheld**) y [Pd(Aqa)] (**Pd-Aqa**) con monohebras de **dA_{15}** …….**167**

3.2.c. Formación de sistemas heterolépticos de tipo ADN-Pd……...…**169**

3.3. Conclusiones……..……172

3.4. Materiales y métodos…….173

3.5. Bibliografía……..……..……179

3.6. Anexo……..……181

Chapter 4. Supramolecular DNA-Pd Hybrids Integrated with Conducting Polymers…….....189

4.1. Synthesis and characterization of 4-hydroxypyridine-2,6-dicarboxylic acid (Cheld) functionalized with 2-(2-thienyl)pyrrole (TP)…….……...192

4.2. Synthesis and characterization of metal complex [Pd(CheldTP)(DMSO)] (DMSO-Pd-CheldTP)……...…….....…...194

4.3. Synthesis and characterization of metal complex with adenine derivative: [Pd(CheldTP)(eA)] (eA-Pd-CheldTP)……197

4.4. Synthesis and characterization of supramolecular hybrid [{Pd(CheldTP)}$_{15}$(dA$_{15}$)] (dA$_{15}$-Pd-CheldTP)…..…...……..199

4.5. Studies of the conducting properties of the polymerized dA$_{15}$-Pd-CheldTP^{polym} supramolecular system...……..……...……..……...214

4.6. Conclusions……..……..223

4.7. Materials and methods ……..…...224

4.8. Bibliography…….....233

4.9. Appendix…….....237

Chapter 5. Crystallization of DNA-metal hybrids…..……**245**

5.1. Crystallization of Biomolecules…….……...245

5.2 Crystallization of silver-modified Watson-Crick-Franklin base pairs complexes…….…….....246

5.3 Crystallization of ADN-Ag and ADN-Pd supramolecular structures…….…….251

5.3.a. Crystallization and characterization of the supramolecular hybrid [{Ag}$_{12}$(dY$_4$C$_4$T$_2$X$_2$)] (**ODN1-Ag**)…….…….…….…...**251**

5.3.a.1. Capillary Crystallization methods…….……..…….…..**252**

5.3.a.2 Sitting drop crystallization…..…….....**255**

5.3.b. Crystallization and characterization of the supramolecular hybrid [{Pd(Cheld)}$_{12}$(dA$_{15}$)] (**dA$_{15}$-Pd-Cheld**)…….…….…...**258**

5.4. Conclusions……262

5.5. Materiales y métodos……...……..……263

5.6. Bibliografía……..……..……265

RESUMEN

En esta tesis doctoral se describen los procesos para desarrollar nanomateriales tecnológicos basados en híbridos ADN-Pd.

En primer lugar, se han estudiado las interacciones entre complejos de Pd^{II} y las nucleobases modelo del ADN aisladas, derivadas de la adenina (A), citosina (C) y timina (T), para comprobar que es posible formar pares de bases mediados por paladio del tipo **A-Pd^{II}-L**, **C-Pd^{II}-L** o **T-Pd^{II}-L** (L = ácido 4-hidroxipiridín-2,6-dicarboxílico (Cheld); 8-amino-4-hidroxiquinolina-2-carboxílico (Aqa); 2,6-piridina-dimetanamina (dPy)). Con este objetivo, los fragmentos metálicos Pd-L han sido diseñados de manera racional para que sean capaces de reconocer nucleobases a través de la formación de un enlace de coordinación y enlaces de hidrógeno intramoleculares complementarios. Para dilucidar la formación de los pares de bases mediados por paladio se han empleado distintas técnicas de caracterización, entre las que se incluyen; Resonancia Magnética Nuclear (^{1}H-RMN, COSY, DOSY, NH-HSQC), Difracción de Rayos X en polvo (XRPD) y monocristal (XR), Espectrometría de Masas (ESI-MS), Cálculos Computacionales (DFT) y Calorimetría de Titulación Isotérmica (ITC).

A continuación, se presenta una metodología para estudiar la formación de estructuras supramoleculares mediante la interacción de los fragmentos metálicos de Pd-L y hebras simples de ADN formadas por homopolímeros de 2'-deoxi-adenosina, 2'-deoxicitidina o 2'-deoxi-timidina. Esta metodología permite organizar los iones de Pd^{II} a lo largo del eje central de la hebra simple de ADN, mediante la formación de una estructura que se asemeja a una doble hebra de ADN natural. Una de las hebras estará formada por un homopolímero (adenosina, citidina o timidina) y la otra por el apilamiento de complejos metálicos unidos a las nucleobases mediante enlaces de coordinación. La formación de enlaces de hidrógenos intramoleculares y fuerzas de apilamiento a lo largo de la estructura resultarán fundamentales para la estabilización del

sistema supramolecular híbrido ADN-Pd. El estudio de la formación de estas estructuras supramoleculares ADN-Pd se ha llevado a cabo empleando técnicas de caracterización, entre las que se incluyen; Dicroísmo Circular (CD), Espectrometría de Masas (ESI-MS), Cálculos Computacionales (DFT), Espectroscopía UV-Vis (UV-Vis), Difracción de Rayos X de Ángulo Bajo (SAXS) y Calorimetría de Titulación Isotérmica (ITC).

En tercer lugar, en esta tesis doctoral se ha estudiado la selectividad de los fragmentos metálicos de Pd-L con respecto a sus nucleobases complementarias. Para esto, se han realizado estudios de competitividad aislados entre los fragmentos metálicos **Pd-Cheld** y **Pd-Aqa** con respecto a sus nucleobases complementarias modificadas 9-etil-adenina (**eA**) y 1-metil-citosina (**mC**), respectivamente. Estos estudios han revelado una preferencia a la hora de formar los complejos complementarios **[Pd(Cheld)(eA)]** y **[Pd(Aqa)(mC)]**. A continuación, se han realizado estudios de competitividad y especificidad entre los fragmentos **Pd-Cheld** y **Pd-Aqa** y hebras simples de ADN formadas por homopolímeros de 2'-deoxiadenosina y 2'-deoxicitidina. Se ha demostrado que los complejos metálicos son capaces de discriminar entre las nucleobases del ADN para unirse de manera específica a su nucleobases complementaria. Estos estudios han permitido sentar las bases para el desarrollo de una metodología que nos permite desarrollar estructuras supramoleculares heterolépticas mediante la formación de pares de bases complementarios mediados por iones de Pd^{II}. Para estos estudios se han empleado las siguientes técnicas de caracterización; Resonancia Magnética Nuclear (^{1}H-RMN), Difracción de Rayos X en monocristal (XR), Espectrometría de Masas (ESI-MS), Dicroísmo Circular (CD), Espectroscopía UV-Vis (UV-Vis) y Calorimetría de Titulación Isotérmica (ITC).

En cuarto lugar, se ha explorado la posibilidad de dotar a los sistemas ADN-Pd con propiedades no inherentes, como un aumento de su conductividad. Con este objetivo, se ha dotado al fragmento metálico **Pd-Cheld** con un grupo 2-(2-tienil)pirrol (**TP**). El monómero **TP** tienen la capacidad de

polimerizar para formar polímeros conductores conjugados capaces de conducir carga eléctrica. Para esto estudios se han sintetizado y caracterizado estructuras supramoleculares híbridas **[Pd(CheldTP)(poly(A))]**, donde es posible organizar a los monómeros de **TP** a lo largo de la hebra simple de ARN, promoviendo su polimerización de forma controlada. Mediante técnicas de caracterización de microscopía de sonda de barrido (AFM y EFM), se ha comprobado que los polímeros obtenidos son potencialmente conductores y además que su formación sigue la disposición helicoidal de doble hebra.

Finalmente, se han investigado procesos de cristalización para obtener estructuras de los sistemas híbridos ADN-metal. Por un lado, se presenta la metodología empleada para intentar obtener cristales de pares de bases canónicas y aisladas del tipo A-Ag^{I}-T y G-Ag^{I}-C. Por otro lado, se presenta la metodología para obtener cristales de un sistema de ADN-Ag modificado. Para esto, se han empleado secuencias de nucleobases modificadas donde el grupo N7 de adenina y guanina ha sido sustituido por un grupo CH. Esto permite a los iones Ag^{I} unirse por la cara Watson-Crick-Franklin de las nucleobases y obtener sistemas DNA-Ag que se asemejan a una doble hebra natural donde los puentes de hidrógenos entre las bases han sido sustituidos por enlaces de coordinación. Además, se ha investigado una metodología para intentar obtener estructuras cristalinas de los híbridos ADN-Pd descritos en este trabajo de tesis. Para la resolución de las estructuras cristalinas de los pares de bases aislados se se realizaron medidas de Difracción de Rayos X en monocristal (XR), aunque los resultados no fueron los esperados. Para intentar resolver los cristales obtenidos de los sistemas híbridos ADN-Ag y ADN-Pd se realizaron medidas de Difracción de Rayos X, también sin el éxito esperado, en el *European Synchrotron Radiation Facility* (**ESRF**), de Grenoble (Francia), y en el *National Synchrotron Light Source II, beamline 17-ID-2*, de New York (Estados Unidos).

ABSTRACT

This thesis describes the processes for developing technological nanomaterials bases on DNA-Pd supramolecular hybrids.

Firstly, interactions between Pd^{II} complexes and isolated DNA model nucleobases derived from adenine (A), cytosine (C) and thymine (T) have been studied to verify the possibility of forming palladium-mediated base pairs such as **A-Pd^{II}-L**, **C-Pd^{II}-L** o **T-Pd^{II}-L** (**L** = 4-hydroxypyridin-2,6-dicarboxilic acid (**Cheld**); 8-amino-4-hydroxyquinoline-2-carboxylic acid (**Aqa**); 2,6-pyridin-dimethanamide (**dPy**)). Towards this aim, the Pd-L metal complexes have been rationally designed to recognize their complementary nucleobases and bind through a coordination bond and complementary intramolecular hydrogen bonds. Various characterization techniques have been employed to elucidate the formation of palladium-mediated base pairs, including; Nuclear Magnetic Resonance (^{1}H-RMN, COSY, DOSY, NH-HSQC), Powder X-Ray Diffraction (XRPD) and single crystal X-Ray (XR), Mass Spectrometry (ESI-MS), Computational Calculations (DFT) and Isothermal Titration Calorimetry (ITC).

Secondly, a protocol is presented to study the formation of supramolecular structures through the interaction of Pd-L metal fragments with single strands of DNA formed by homopolymers of 2'-deoxyadenosine, 2'-deoxycytidine or 2'-deoxythymidine. This methodology allows for the organization of Pd^{II} ions along the central axis of DNA-Pd systems, by forming a structure resembling a natural double strand DNA. One of the strands will consist of a homopolymer (adenosine, cytidine, thymidine), while the other will consists of stacked metal complexes bound to the nucleobases through a coordination bonds. The formation of complementary intramolecular hydrogen bonds between the metal fragments and the DNA, along with the stacking interactions along the structure, will be crucial for stabilizing DNA-Pd supramolecular hybrids. The formation of supramolecular DNA-Pd structures, has been carried out using various characterization techniques, including Circular Dichroism (CD), Mass

Spectrometry (ESI-MS), Computational Calculations (DFT), UV-Vis Spectrometry, Small Agle X-ray Diffraction (SAXS) and Isothermal Titration Calorimetry (ITC).

Thirdly, this doctoral thesis has investigated the selectivity of Pd^{II} metal fragments towards their complementary nucleobases. For this purpose, isolated competitive studies have been conducted between the **Pd-Cheld** and **Pd-Aqa** metal fragments regarding their complementary nucleobases 9-ethyl-adenine (**eA**) and 1-methyl-cytosine (**mC**), respectively. These studies have revealed a preference in forming complementary complexes **[Pd(Cheld)(eA)]** and **[Pd(Aqa)(mC)]**. Subsequently, competitive and specificity studies have been conducted between the **Pd-Cheld** and **Pd-Aqa** metal fragments and two homopolymers of 2'-deoxyadenosine and 2'-deoxycytidine. It has been demonstrated that metal complexes are capable of discriminating between DNA nucleobases to selectively bind to their complementary nucleobase. These studies have laid the groundwork for the development of a methodology allowing the construction of heteroleptic supramolecular structures. For this studies, the following characterization techniques have been employed; Nuclear Magnetic Resonance (^{1}H-RMN), Single Crystal X-Ray (XR), Mass Spectrometry (ESI-MS), Circular Dichroism (CD), UV-Vis Spectrometry and Isothermal Titration Calorimetry (ITC).

Fourthly, the possibility of endowing DNA strands with non-inherent properties, such as conductivity, has been explored. To achieve this goal, the Pd-Cheld metal fragment has been modified with a 2-(2-thienyl)pyrrole (**TP**) group. **TP** monomer has the ability to polymerize to form conjugated conductive polymers capable of carrying electrical charge. For this studies, supramolecular **[Pd(CheldTP)(poly(A))]** hybrids have been synthetized and characterized, where it is possible to organize the **TP** monomers along the single strand RNA, promoting their controlled polymerization. Using scanning probe microscopy characterization techniques (AFM and EFM), it has been

confirmed that the obtained polymers are potentially conductive and their formation nicely follow a double helical arrangement.

Finally, processes of crystallization have been investigated to obtain structures of DNA-metal hybrids systems. On one hand, the methodology employed to attempt obtaining crystals of canonical and isolated base pairs, such as A-Ag^{I}-T and G-Ag^{I}-C, is presented. On the other hand, the methodology to obtain crystals of modified DNA-Ag hybrids is also presented. To this end, sequences of modified nucleobases have been used where the N7 group in adenine and guanine has been substituted by a CH group. This allows Ag^{I} ions to bind to the Watson-Crick-Franklin face of the nucleobases, resulting in DNA-Ag systems resembling a natural double helix where hydrogen bonds between the bases have been replaced by coordination bonds. Furthermore, a methodology to obtain crystalline structures of DNA-Pd hybrids has been investigated. For the resolution of the crystalline structures of the isolated meta-base pairs, Single Crystal X-Ray Diffraction (XR) measurements were performed, although these results were not as expected. To resolve the crystals obtained from the DNA-Ag and DNA-Pd hybrids, X-Ray Diffraction measurements were conducted, but without the expected success, at the *European Synchrotron Radiation Facility* (**ESRF**) of Grenoble (France), and at the *National Synchrotron Light Source II, beamline 17-ID-2*, de New York (United States).

OBJETIVOS

Objetivo 1: Estudios de reacción entre las nucleobases modelo libres con complejos de Pd^{II} para la obtención de pares de bases medidadas por iones de Pd^{II}, de tipo nucleobase-Pd^{II}-ligando. Formación de híbridos supramoleculares de tipo ADN-Pd a partir de una reacción de autoensamble en la que participan los complejos de Pd^{II} estudiados y oligonucleótidos de cadena simple.

a. Estudios de reacción entre el complejo **[Pd(Cheld)(CH_3CN)]** con las nucleobases modificadas 9-etil-adenina, 9-propil-7-deaza-adenina y cadenas homopolimérica de 2'-deoxiadenosina, **poly(dA),** y cadenas de 2'-deoxi-7-deazaadenosina, **poly(dX)**.
b. Estudios de reacción entre el complejo **[Pd(Aqa)(DMSO)]** con la nucleobase modificada 1-metil-citosina y cadenas homopolimérica de 2'-deoxicitidina, **poly(dC).**
c. Estudios de interacción entre el complejo **[Pd(dPy)(DMSO)]** con la nucleobase modificada 1-etil-timina y cadenas homopolimérica de 2'-deoxitimidina, **poly(dT).**

Objetivo 2: Síntesis y caracterización de estructuras ADN-metal heterolépticas a partir de reacciones de autoensamblaje entre los fragmentos metálicos **[Pd(Cheld)]** y **[Pd(Aqa)]** y oligonucleótidos de cadena homotópica y heterotópica.

a. Estudios de competitividad entre los fragmentos metálicos de Pd^{II} y las nucleobases modificadas 9-etil-adenina y 1-metil-citosina.
b. Estudios de competitividad entre los fragementos metálicos de Pd^{II} y homopolímeros de 2'-deoxi-citidina y 2'-deoxi-adenosina.

Objetivo 3: Funcionalización de los sistemas híbridos ADN-metal mediante el uso del empleo del fragmento metálico **[Pd(CheldTP)]**, diseñado para

transportar un monómero precursor de polímeros conductores, y capaz de autoensamblarse a oligonucleótidos de cadena simple.

a. Modificación del ligando **Cheld** con monómeros de 2-(2-tienil)pirrolo (**TP**), para obtener el complejo **[Pd(CheldTP)(DMSO)]**.
b. Estudios de interacción entre el complejo modificado **[Pd(CheldTP)(DMSO)]** con la nucleobase modificada 9-etil-adenina y cadena homopolimérica de 2'-deoxi-adenosin.
c. Estudios del proceso de polimerización y estudios de conductividad de los sistemas polimerizados **[Pd(CheldTP)(poly(A))]^{polym}** .

Objetivo 4: Cristalización de los híbridos ADN-metal para su posterior resolución estructural.

a. Cristalización de los pares de bases WCF de tipo A-Ag^{I}-C y C-Ag^{I}-G modificadas por iones de Ag^{I}.
b. Cristalización del cadenas de ADN de doble hebra con pares de bases WCF modificadas por iones Ag^{I}
c. Cristalización de los híbridos ADN-Pd descritos en el objetivo 1.

OBJETIVES

Objective 1: Reaction studies between model nucleobases with Pd^{II} complexes to obtain palladium-mediated base pairs, of the nucleobase-Pd^{II}-L type. Formation of supramolecular DNA-Pd hybrids through a self-assembly reaction involving Pd^{II} complexes and single strand oligonucleotides.

a. Reaction studies between **[Pd(Cheld)(CH_3CN)]** complex and the modified nucleobases 9-ethyl-adenine, 9-propyl-7-deaza-adenine, and homopolymers of 2'-deoxy-adenosine, **poly(dA)**, and 2'-deoxy-7-deaza-adenosine, **poly(dX)**.
a. Reaction studies between **[Pd(Aqa)(DMSO)]** complex and the modified nucleobases 1-methyl-cytosine and the homopolymer 2'-deoxy-cytidine, **poly(dC)**.
b. Reaction studies between **[Pd(dPy)(DMSO)]** complex and the modified nucleobases 1-ethyl-Thymine and the homopolymer 2'-deoxy-thymidine, **poly(dT)**.

Objective 2: Synthesis and characterization of heteroleptic DNA-metal structures through self-assembly reactions between **[Pd(Cheld)]** and **[Pd(Aqa)]** metal fragments and homotopic and heterotopic oligonucleotides.

a. Competitiveness studies between Pd^{II} metal fragments and modified nucleobases 9-ethyl-adenine and 1-methyl-cytosine.
b. Competitive studies between Pd^{II} metal fragments homopolymers of 2'-deoxy-adenosine and 2'-deoxycytidine.

Objective 3: Functionalization of DNA-metal hybrids using the modified **[Pd(CheldTP)]** metal fragment, designed to transport a precursor monomer of conductive polymer, capable of self-assembling with single strand oligonucleotides.

a. Modification of **Cheld** ligand with 2-(2-thienyl)pyrrole (**TP**) monomers, to obtain the **[Pd(CheldTP)(DMSO)]** complex.
b. Reaction studies between the modified [**Pd(CheldTp)(DMSO)]** complex with the modified nucleobase 9-ethyl-adenine and homopolymers of 2'-deoxyadenosine, **poly(A)**.
c. Polymerization process studies and conductivity studies of the polymerized Conductivity studies of the polymeric **[Pd(CheldTP)(poly(A))]^{polym}** system

Objective 4: Crystallization of metal-DNA hybrids for their structural resolution.

a. Crystallization of isolated silver-modified A-Ag^{I}-C y C-Ag^{I}-G base pairs.
b. Crystallization of doubled stranded DNA molecules with silver-modified WCF base pairs.
c. Crystallization of DNA-Pd hybrids described in objective 1.

ABREVIATURAS Y ACRÓNIMOS

ABBREVIATIONS AND ACRONYMS

A	Adenina
ABTS	2,2'-azino-bis(3-etillbentotiazolina-6-sulfonato)
AE	Análisis Elemental
AFM	Microscopía de Fuerza Atómica
Ag	Plata
ADN	Ácido desoxirribonucleico
AMP	Adenosina monofosfato
APTES	(3-aminopropil)trietoxisinalo
ARN	Ácido ribonucleico
Aqa	ácido 8-amino-4-hidroxiquinolina-2-carboxílico
Buffer	Solución tampón
C	Citosina
CD	Dicroísmo Circular
DFT	Teoría de densidad funcional
Cheld	Ácido 4-hidroxipiridín-2,6-dicarboxílico
CheldTp	Ácido 4-(3-(2-(tiofen-2-il)-1H-pirrol-1-il)propoxi)pridín-2,6-dicarboxilico
CMP	Citidina monofosfato
dA	2-deoxyadenosina
Da	Dalton
dC	2-deoxyctidina
DFT	Teorema del funcional de la densidad
di-Py	ácido piridín-2,6-diildimtanamina

dT	2-deoxyatimidina
dX	2-deoxy-7-deazaadenosina
DCM	Diclorometano
DMF	N,N-dimetilfomamida
DMSO	Dimetilsulfóxido
DMSO-D6	Dimetilsulfóxido deuterado
dPy	
eA	9-etil-adenina
EB	Bromuro de etidio
EFM	Microscopía de Fuerza Electrónica
ESI-MS	Ionización por electrospray – Espectrometría de masas
eT	9-etil-timina
Eqv	Equivalentes
EtOH	Etanol
G	Guanina
HF	Metodología de Hartee-Fock
HRP	Peroxidasa del rábano (Horseradish peroxidase)
ICD	Bandas inducidas en dicroísmo circular
ITC	Calorimetría de valoración isotérmica
IR	Espectroscopía de Infrarrojo
mC	1-metil-citosina
MOPS	Ácido (3-(*N*-morpholino)propansulfónico)
MPD	2-metil-2,4-pentanediol
Pd	Paladio
PDB	Protein Data Bank
PEO	Oxido de polietileno
pX	9-propil-7-deaza-guanina

RMN	Resonancia Magnética Nuclear
SAXS	Dispersión de rayos X de ángulo reducido
SNS	2,5-bis(2-tionil)pirrol
T	Timina
Tp	2-(2-tiofenil)pirrol
UV-Vis	Espectroscopía Ultravioleta-visible
W	nucleobases modificadas con 2,5-bis(2-tionil)pirrol
WCF	Puentes de hidrógeno Watson-Crick-Franklin
X	7-deaza-adenina
XRPD	Difracción de Rayos X en polvo
Z	Estados de carga

Capítulo 1

Introducción.

Capítulo 1. Introducción.

1.1. El ADN como biomolécula que condensa la vida.

La historia del ADN es la narrativa de descubrimientos científicos que han transformado nuestra comprensión de la vida. Este relato comienza con los primeros indicios de la existencia de un código genético trasmitido de una generación a otra. A principios del siglo XX, Gregor Mendel sentaría las bases de la genética al describir en sus trabajos las leyes de la herencia genética, aunque por aquel entonces aún se desconocía la naturaleza física de los genes. Pocos años después, en 1871, Johan Friederich Miescher consiguió aislar un precipitado blanquecino durante sus experimentos sobre la composición química del núcleo celular de los leucocitos, presentes en vendas quirúrgicas. Descubrió una sustancia rica en fósforo y nitrógeno a la que denominaría nucleína y, aunque su función seguía siendo desconocida, Miescher sugirió que podría estar implicada en la transmisión de la herencia genética. Aunque desafortunadamente, él mismo desecharía esa misma idea. Los siguientes casi cien años consistieron en una carrera para desentrañar los secretos de la nucleína. Partiendo desde la descripción de las moléculas básicas que componen el ADN (adenina, guanina, citosina y timina), hasta el redescubrimiento de las leyes de Mendel para postular una nueva teoría cromosómica de la herencia. A medida que se fueron sucediendo los distintos descubrimientos, el ADN se posicionó como la molécula que condensa la vida. Debido a su importancia, conocer la estructura del ADN se volvió una de las principales prioridades para la comunidad científica, de donde surgió una de las competiciones científicas más conocidas que, como todas las grandes historias, no ha estado exenta de polémica. Finalmente, el 25 de abril de 1953, la revista *Nature* publica un estudio bajo el título "Molecular structure of Nucleic Acid: A Structure for Deoxyribose Nucleic Acid".[1] En este estudio, James Watson y Francis Crick, junto con las contribuciones de otros científicos entre los que destacan Phoebus Levene, Erwin Chargadd, Rosalind Franklin y Marutice

Wilkins, proponen una estructura helicoidal para del ADN. Este modelo, basado en los datos de difracción de rayos X de Rosalind Franklin, revolucionaría la biología molecular. La estructura helicoidal propuesta sugería además un método claro por el cual la información genética podría replicarle de una célula a otra.

Según describieron Watson y Crick, la formación de la estructura de doble hebra que conforma el ADNes posible gracias a la disposición antiparalela de las dos hebras que la componen, una de ellas dispuesta en sentido 5'-3' y la otra dispuesta en sentido 3'-5' (Figura 1.1). Ambas cadenas, quedan estabilizadas mediante la formación de puentes de hidrogeno, que se generan a partir de las interacciones entre las bases nitrogenadas complementarias púricas y pirimidíncas. La formación de los puentes de hidrogeno sería posible gracias a que los grupos amino se encuentran polarizados sobre el nitrógeno, dejando entonces al átomo de hidrogeno con una cara parcial positiva. Este carácter electrofílico permitirá establecer dichas interacciones entre los grupos amino y carboxilo de la base complementaria. Son estas sutiles interacciones las que dan lugar a la formación de la estructura B dextrógira y le confieren a la doble hebra de ADN una gran estabilidad. Se describió además que, por cada 10 pares de bases se realiza un giro completo de la estructura con un diámetro de 20 Å.

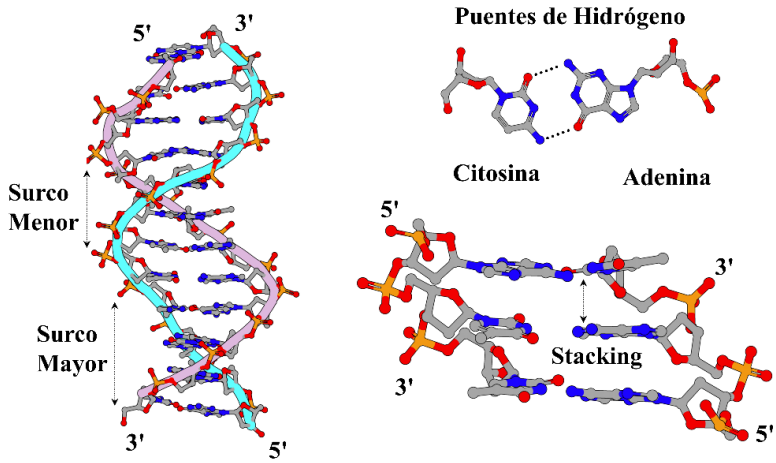

Figura 1.1: Representación esquemática de la doble hebra de ADN, el par de bases complementarias A-C y el apilamiento de las nucleobases.

Con el paso de los años, se fueron descubriendo más secretos sobre la biomolécula de la vida, como su capacidad para auto-replicarse, su capacidad de mutación o su papel crucial en la síntesis de proteínas, responsable de numerosas funciones en las células. Y aunque la estructura helicoidal descrita por Watson-Crick conocida como ADN-B (Figura 1.1), es considerada la estructura más representativa, hoy en día se sabe que es sólo una de las estructuras moleculares descritas.

El plegamiento de diversas conformaciones del ADN y sus interacciones con otras biomoléculas se rigen por la formación de interacciones no covalentes, como los enlaces de hidrógeno, el apilamiento π-π y las interacciones electrostáticas. Todas estas interacciones son determinadas en último término por la posición relativa de las nucleobases que componen la cadena de ADN. Este hecho destaca que la estructura del ADN está íntimamente relacionada con la secuencia de bases que la componen. De hecho, una de las propiedades más importantes de los ácidos nucleicos reside en su habilidad para el reconocimiento de bases. [2–4] Esta propiedad, resulta fundamental a la hora de comprender de qué manera se auto-ensambla esta biomolécula, lo que permite realizar predicciones muy precisas basándonos únicamente en la secuencia de bases. Gracias a esta capacidad, el ADN presenta polimorfismo estructural, lo que ha permitido describir estructuras no canónicas como triplex,[5] estructuras de cruce de tres y cuatro vías [6–8] cuádruples G [9,10] i-motif (Figura 1.2). [11] Aunque en un principio se pensó que estas complejas estructuras pudieran ser artefactos, se ha demostrado que su existencia está relacionada con numerosos procesos de regulación genética.[12–15]

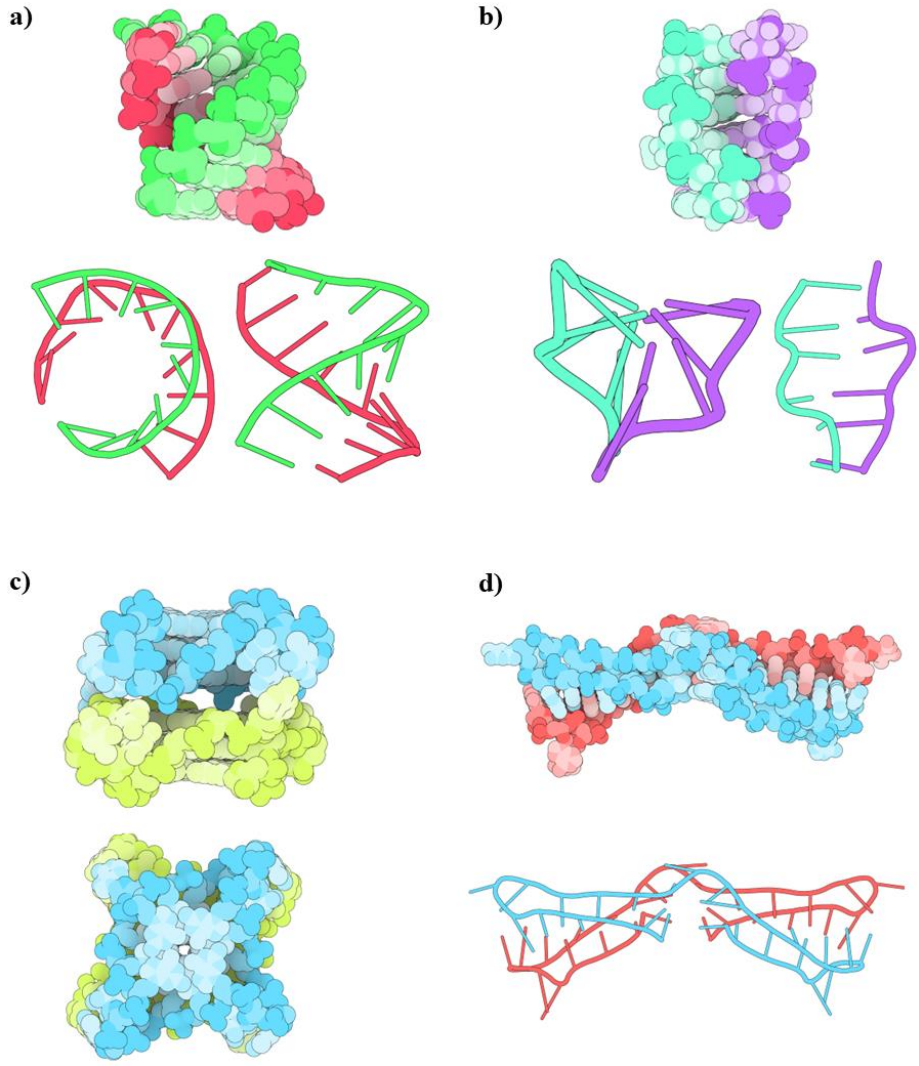

Figura 1.2: Estructuras no canónicas de ADN cristalino; a) A-DNA (PDB: 4IZQ);[16] b) Z-DNA (PDB: 1TNE); [17] c) G-cuadruplex DNA de telómeros humanos (PBD: 6XCL);[18] d) i-motif del área promotora del oncogen HRAS (PBD: 8CXF).[19]

1.2. El ADN como nanomaterial tecnológico.

La introducción del ADN como nanomaterial tecnológico ha experimentado un desarrollo fascinante y revolucionario en las últimas décadas. La flexibilidad y la capacidad de autoensamblaje inherentes lo han convertido en un material prometedor para la construcción de nanoestructuras precisas y funcionales.[20–24] Además, sus capacidades únicas permiten la programación de secuencias específicas para obtener estructuras tridimensionales complejas y a la carta. Una de las técnicas más populares en este sentido es el denominado ADN-origami, [21,25,26] que ha allanado el camino para la creación de nanoestructuras complejas basadas en moléculas de ADN y diseñadas a medida, con aplicaciones potenciales en medicina, electrónica o nanorrobótica.

Pero, el desarrollo de esta tecnología no podría haberse dado sin la Figura clave del profesor **Nadrian Seeman**, lamentablemente fallecido en 2021. En la década de los años 80, **Seeman** planteó por primera vez el concepto de utilizar el ADN como un material de construcción, [24] aunque en un principio sus ideas no tuvieron demasiado apoyo. No fue hasta 1991, cuando él y su estudiante de doctorado, **Junghuei Chen**, lograron sintetizar la primera estructura tridimensional de ADN con la forma de los bordes de un cubo (Figura 1.3), [27] espertando el interés en el campo de la nanotecnología del ADN.

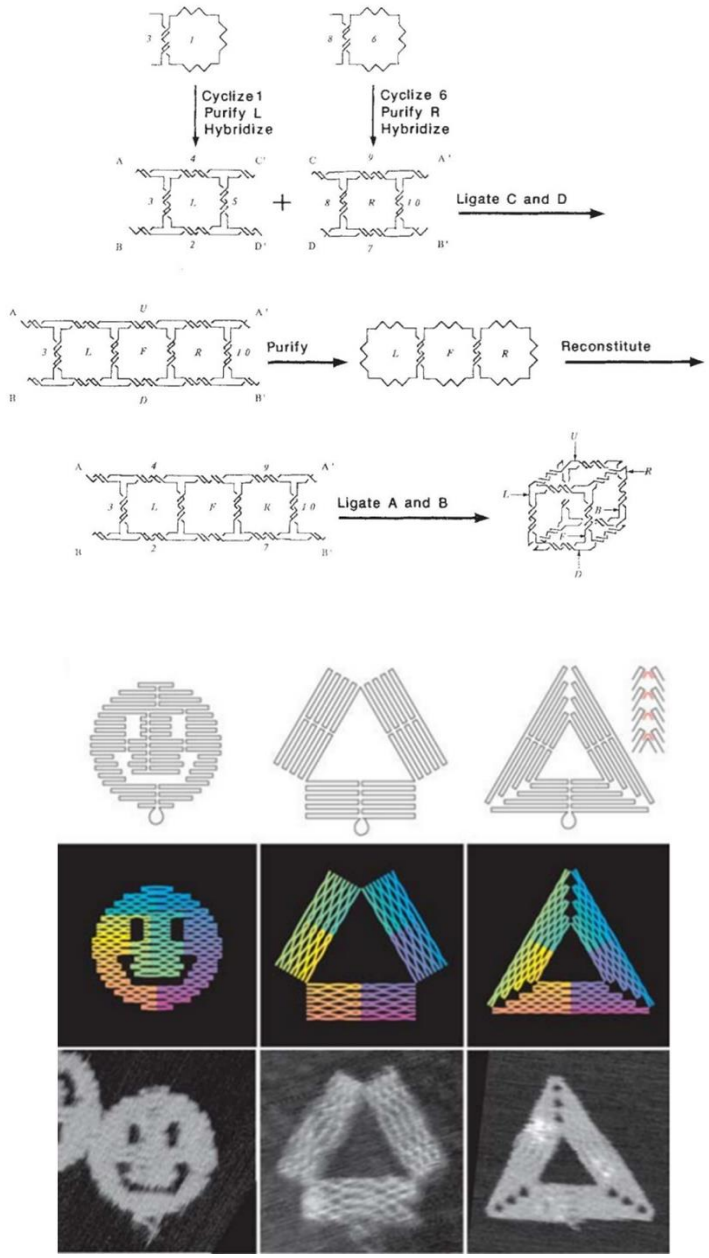

Figura 1.3: Imagen tomada de la publicación de la primera estructura de ADN diseñada por **Seeman** en 1991 (superior) y primeras imágenes de ADN origami publicadas en 2006 (inferior). [28] *Copyright 1991-206 Nature publisin Gruop.*

Desde entonces, el ADN se ha empleado como una increíble herramienta para la fabricación de nanomateriales. **Seeman** y su equipo, demostraron que el ADN puede actuar como plantilla para ensamblar y organizar otros materiales a nivel nanométrico, permitiendo la construcción precisa de dispositivos a pequeña escala. En esta impresionante y prácticamente nueva rama de la ciencia, diversos grupos de investigación centran sus esfuerzos en desarrollar las denominadas "maquinarias de construcción con ADN". [29]

En este ámbito, el trabajo del profesor **Hendrik Dietz** y su equipo sirve para demostrar la importante versatilidad que ofrecen los ácidos nucleicos en el desarrollo nanotecnológico. Este grupo de investigación ha desarrollado estructuras de ADN avanzadas y complejas, controlando y prediseñado una secuencia concreta de nucleobases que posteriormente se autoensamblan mediante un proceso de reconocimiento de pares de bases complementarias. Concretamente, han demostrado que es posible construir con éxito un mecanismo rotatorio nanométrico que emula algunas de las propiedades de la F1-ATP sintasa.[30]

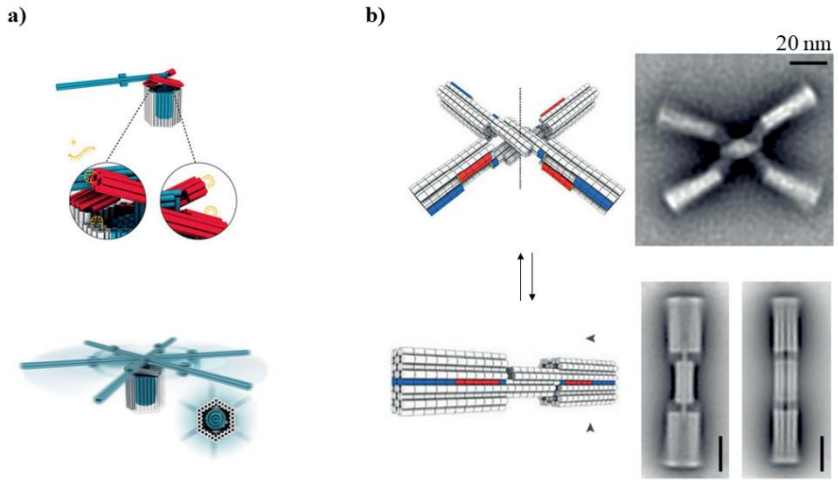

Figura 1.4: a) Diseño y esquema de ensamblaje de un dispositivo rotatorio de ADN. Para el ensamblaje de las partes, las hebras simples de ADN a lo largo de la estructura se unen mediante procesos de autorreconocimiento por complementariedad. **b)** Movimiento de la estructura promovido por la presencia de cloruro de magnesio de 5mM a 25 mM.[30]

Esta máquina molecular, tiene la capacidad de realizar movimientos rotatorios similares a los realizados por la F1-ATP sintasa para obtener la molécula que condensa la energía de las células, el ATP. Aunque aún deben realizar muchos esfuerzos para mejorar el sistema, la versatilidad del diseño y la capacidad de adaptación de este mecanismo nanométrico supone un importante hito para el desarrollo de tecnologías basadas en componentes de ADN móviles, abriendo puertas a diversas aplicaciones nanotecnológicas.

Como se mencionó anteriormente, la comunidad científica ha dedicado numerosos esfuerzos al desarrollo de nanomateriales basados en el ADN. Además, es importante destacar que la gran mayoría se han centrado en el empleo de sistemas de doble hebra, siendo escasos los ejemplos que emplean únicamente hebras simples (ss-ADN) como plantilla de construcción.

Un trabajo importante sobre el uso de moléculas de ss-ADN es el propuesto por **Ulrich** y colaboradores, donde estudiando la interacción entre compuestos bi-funcionalizados y un ADN de cadena simple homotópica de 2-deoxytimidina (**dT_{10}**) soportado sobre una nanopartícula de celulosa (Figura 1.5).[31] Sus investigaciones demostraron cómo compuestos bi-funcionalizados derivados de guanidina (**GuaBi-L**, donde **L** es el ligando modificable) pueden interactuar con el ADN mediante un proceso de auto-ensamblaje molecular promovido por interacciones entre los grupo N-H de **GuaBi** y los grupos fosfodiéster del ADN. Sus resultados indicaron que las interacciones más relevantes para la formación de estructuras supramoleculares estaban promovidas por interacciones de apilamiento (π-π) e interacciones electrostáticas. Las interacciones π- π están promovidas por los ligandos aromáticos (**L**) apilados a lo largo de la estructura fosfodiéster de ADN, mientras que las interacciones electrostáticas estabas promovidas por los grupos guanidinio (**Guabi**) mediante la formacion de puentes salinos con los grupos fosfato. **Ulrich** y colaboradores, demostraron que los derivados que mejor interacciones presentaban para la formación de estructuras supramoleculares eran aquellos derivados de anillos aromáticos.

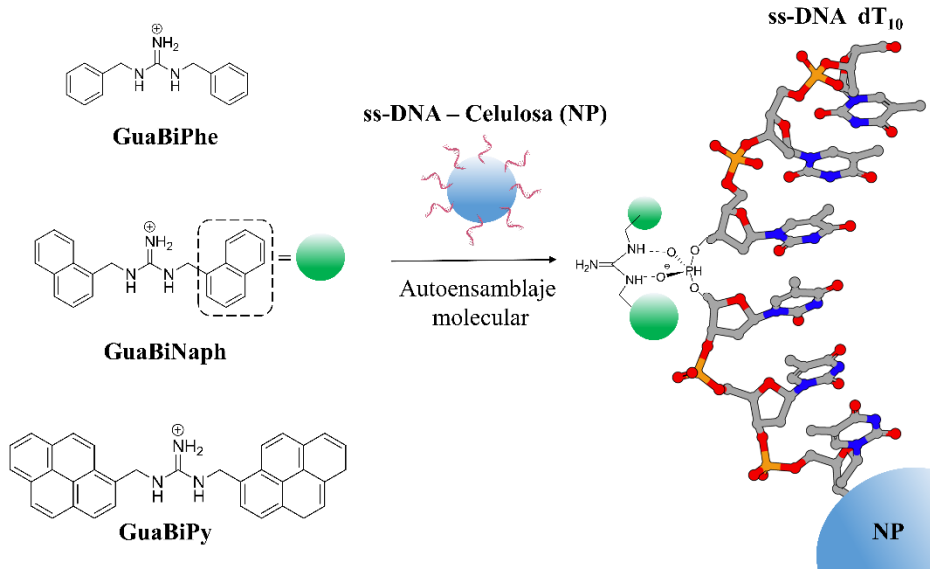

Figura 1.5: Esquema de reacción entre compuestos bi-funcionalizados derivados de guanidina (**GuaBi-L**) y una hebra simple de ADN para la obtención de estructuras supramoleculares de tipo **dT_{10}-GuaBi(L)**. Los estructuras quedan estabilizadas mediante interacciones de apilamiento π-π e interacciones electrostáticas. Las esferas verdes representan a los grupos aromáticos, **L**.[31]

Dentro de este campo, otro de los ejemplos importantes que podemos encontrar y que inspiró directamente esta tesis doctoral, fue el propuesto por **Wagenknecht** y su equipo (Figura 1.6).[32] En sus estudios, han demostrado la viabilidad de emplear derivados de pireno y anilina unidos a nucleósidos de **A** y **U** para crear sistemas miméticos a una doble hebra natural a través de un mecanismo de autoensamblaje molecular, permitiendo, que los nucleósidos modificados reconozcan a sus nucleobases complementarias y se unan mediante puentes de hidrógeno. Esta inteligente estrategia logra ordenar dos grupos cromóforos diferentes a lo largo de la misma hebra ss-ADN con una precisión sin precedentes, únicamente controlando la estequiometría y la secuencia de nucleobases. **Wagenknecht** y su equipo, demostraron que la obtención de estructuras supramoleculares que permiten ordenar grupos cromóforos en el espacio es clave para el desarrollo de materiales funcionales con propiedades fotoquímicas bien definidas. Su principal objetivo fue desarrollar estructuras capaces de redirigir la luz procedente de la energía solar

y controlar los procesos de transferencia de energía y electrones, lo que demuestra el auténtico potencial para el desarrollo nanotecnológico de esta ciencia.

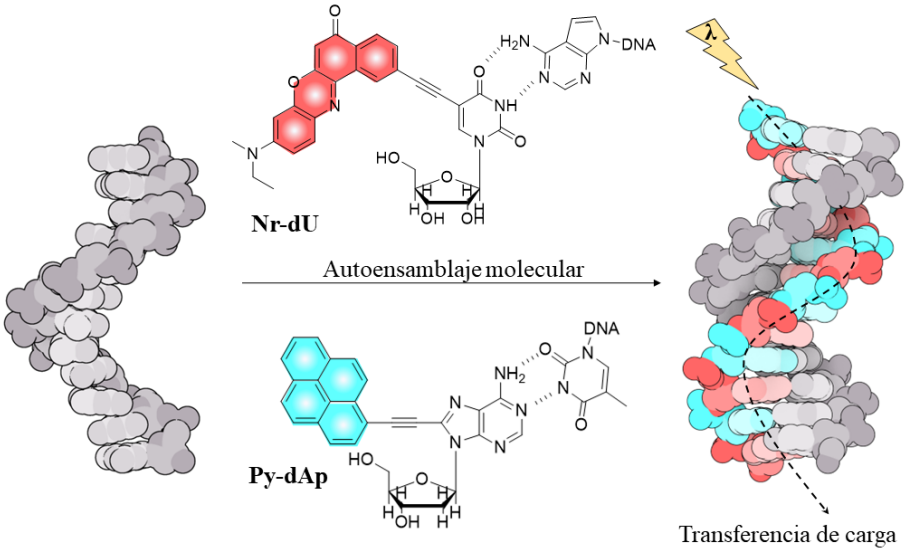

Figura 1.6: Estructura de los derivados Nr-dU y Py-dAp para obtener estructuras cromóforas supramoleculares a través de un mecanismo de autoensamblaje molecular.[32]

Es importante destacar que, si bien hemos abordado algunas de las metodologías mas relevantes en esta sección, existen muchas otras que no ha sido discutidas aquí.[33,34] Estas propuestas innovadoras suponen un vasto campo de investigación, donde diversos grupos de investigación centrar sus esfuerzos. Desde las técnicas de auto-ensamblage hasta los métodos de funcionalización, esta ciencia promete esperanzadores avances para una variedad de campos en desarrollo, desde la medicina hasta la nanotecnología.

1.3. Las interacciones metal-ADN en la naturaleza y en la nanotecnología.

Uno de los problemas asociados al empleo del ADN como nanomaterial tecnológico es que sus propiedades ópticas y electrónicas son limitadas. [35,36] Por tanto, si se pretende extender sus aplicaciones es preciso dotarlo de nuevas propiedades. [37–39] En este sentido, la evidente naturaleza aniónica de los ácidos nucleicos ha promovido, a lo largo de muchas décadas, un intenso estudio de la interacción de cationes metálicos y estructuras de ADN. Hoy día, es sobradamente conocido el papel fundamental que desempeñan los iones metálicos en el correcto funcionamiento de las funciones vitales. Por ejemplo, los iones de Ca^{II} o Mg^{II} desempeñan funciones reguladoras en las células; las metaloproteninas [40] (ricas en iones metálicos) forman parte de todos los organismos vivos actuando como enzimas, proteínas de transporte o almacenamiento; y los iones Zn^{II} o Mg^{II}, evitan la citotoxicidad inducida por Cadmio.[41] Pero el rol de los metales no solo se limita a los encontrados en la naturaleza, el ser humano ha sido capaz de desarrollar de manera racional compuestos basados en metales para el desarrollo de gran cantidad de fármacos. Quizás, el ejemplo más famoso es el del compuesto Cis-platino, $[Pt(NH_3)Cl_2]$,[42] como terapia anticancerígena, y de hecho, los medicamentos que contienen metales han cobrado especial relevancia, debido a su capacidad citotóxica en el tratamiento de enfermedades infecciosas. Hoy en día, la problemática derivada de la resistencia bacteriana y fúngica a los antibióticos se presenta como uno de los mayores retos a los que se enfrenta la humanidad. Es por ello, que el desarrollo de tratamientos antibacterianos o antifúngicos que contienen metales, incluyendo la plata (Ag) y el paladio (Pd), se presentan como una alternativa muy prometedora en la lucha contra este tipo de infecciones.[43]

Si nos centramos en las interacciones de tipo metal-ADN que se dan en la naturaleza, notaremos que existen innumerables ejemplos. Debido a la carga aniónica del ADN, ciertos cationes (cómo el Mg^{II}, Na^{I} o K^{I}) promueven la formación de la estructura secundaria de doble hélice. [44–46] Estos iones, forman parte del medio donde se encuentran los ácidos nucleicos y dan lugar a un ambiente iónico que favorece este tipo de interacciones. [47]

Sin embargo, localizar la posición exacta donde los cationes interaccionan con el ADN ha supuesto un reto mayúsculo y son muchos los grupos de investigación que han centrado su atención en dilucidar este tipo de interacciones. En este sentido se ha demostrado, que cationes divalentes de Mg^{II} son capaces de interaccionar con el surco mayor de la doble hélice, además de promover la formación de puentes de hidrógeno.[48,49] Asimismo, la concentración iónica del medio es también responsable de cambios estructurales más complejos. Por ejemplo, promoviendo una transición de la forma B a la forma Z de la doble hélice, donde los iones de Mg^{II} y iones monovalentes como Na^{I} juegan un papel fundamental. [50,51] En este contexto, las actividades de los metales relacionadas con los ácidos nucleicos resultan fascinantes, abarcando desde el desarrollo de funciones catalizadoras en ribosomas, [52–55] hasta la redistribución de la densidad electrónica para variar el pKa, [56–60] e incluso induciendo transiciones a geometrías o tautómeros más o menos desfavorecidos.[59–61]

Por otra parte, el empleo de metales para el desarrollo tecnológico ha acompañado al ser humano a lo largo de toda su historia. No obstante, en la actualidad, su aplicación ha alcanzado niveles de desarrollo sin precedentes. Las propiedades intrínsecas de los iones metálicos como la luminiscencia, el magnetismo o la transferencia de carga, desempeñan un papel fundamental en el avance de la ciencia basada en las interacciones metal-ADN, conectando de manera inigualable la historia natural de estas interacciones con las innovaciones tecnológicas más recientes.

Son todas estas propiedades las que han permitido que la metalización de los ácidos nucleicos tome especial relevancia en el ámbito de la nanotecnología.[62–65] Las propiedades de los sistemas metal-ADN dependerá de muchos factores, como el metal utilizado, su estado de oxidación o la disposición dentro de la estructura. En general, el ADN ofrece hasta tres posibles puntos de unión con los metales; los átomos de oxígenos de los grupos fosfatos, los átomos de oxígeno del azúcar y los átomos donantes de las nucleobases.[66–71] La coordinación de los iones metálicos está íntimamente relacionada con la electronegatividad o la polarizabilidad de estos grupos.[72] En este sentido, los metales alcalinos y alcalinotérreos, lantánidos y actínidos, tienden a unirse preferentemente a grupos fosfato. Sin embargo, los metales de transición pueden unirse también a las nucleobases, lo que dependerá de su concentración y el tipo de enlace que establezcan con estas.[70,73] Por tanto, la modificación de los ácidos nucleicos con el objetivo de extender sus propiedades tecnológicas se ha abordado desde muchos ángulos distintos.[74–87]

Algunas de las estrategias más relevantes han realizado una metalización completa del ADN, donde la doble hélice actúa como una plantilla para la deposición de iones metálicos (Figura 1.7, izquierda).[88,89] En estos casos, cationes metálicos se unen mediante fuerzas electrostáticas a los grupos fosfato de la doble hebra o enlaces de coordinación a las nucleobases, dependiendo de las características del ión metálico. Posteriormente, estos núcleos metálicos pueden ser reducidos creando puntos metalizados que además actuaran como centros catalíticos para promover la deposición de más átomos metálicos sobre la estructura del ADN. Si bien estos estudios han demostrado que la metalización del ADN afecta significativamente a sus propiedades tecnológicas, aumentando por ejemplo su capacidad para la transferencia de carga a través de su estructura, lamentablemente, no ha logrado controlar de manera precisa el posicionamiento homogéneo de los metales a lo largo de la doble hebra.

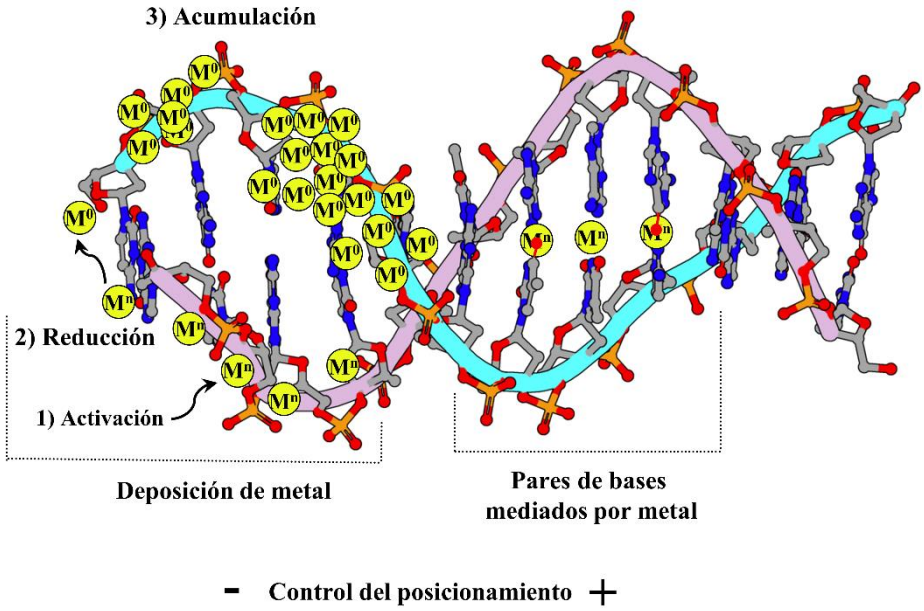

Figura 1.7: Esquema de interacción metal-ADN mediante dos estrategias diferentes. Izquierda; Deposición sin control preciso del metal mediante fuerzas electrostáticas. Derecha; Formación de pares de bases mediados por metales.

Otro novedoso enfoque, se ha centrado en el desarrollo de técnicas que emplean nanopartículas de oro y plata, las cuales se ha demostrado, que tienen una preferencia para unirse a zonas concretas del ADN que contienen dúplex de guanina y citosina.[90] Aunque esta estrategia es capaz de controlar y predecir zonas concretas del ADN para la unión con metales, aún está lejos de controlar de manera precisa la estequiometría y el posicionamiento de los mismos.

Sin duda, la metodología que hasta el momento ha resultado ser la más precisa en cuanto a control de la estequiometria y posicionamiento de los metales en el ADN, es aquella enfocada a la formación de **pares de bases mediados por metales** [91–95] (Figura 1.7, derecha).

Esta metodología consiste en la unión de dos ligandos (bases), iguales o diferentes, que se unen a través de un enlace de coordinación a un ión metálico central, formando un par de base metalizado. Merece la pena mencionar la nomenclatura sugerida por Lippert para referirnos a estos sistemas.[94] Cuando el par de bases se forma sólo en presencia del ión metálico, estamos ante un 'par

de bases *mediado* por ion metálico' (metal-mediated base pair). Sin embargo, en algunos casos, el par de bases existe por sí solo mediante la formación de enlaces de hidrógeno, sin necesidad de que haya iones metálicos. En este caso, cuando un ión metálico sustituye o reemplaza al enlace de hidrógeno original, formando un enlace de coordinación entre las bases, estamos ante un 'par de bases *modificado* por iones metálicos' (metal-modified base pair). Este sería el caso de reemplazar los enlaces de hidrógeno formados entre nucleobases complementarias por iones metálicos.

Anteriormente se mencionó que los metales que mejor interactúan con los diferentes átomos donantes de las nucleobases son el Pt^{II}, Pd^{II} , Rh^{II} , Ag^{I}, Zn^{II} , Hg^{II} y Cu^{II} (metales de transición). Muchos de ellos, como Hg^{II} o Ag^{I} muestran una alta afinidad específica por los nitrógenos endocíclicos orientados en la cara W-C de timina y citosina, respectivamente, formando pares de bases mediados por ion metálico de tipo T-Hg^{II}-T y C-Ag^{I}-C. [96,97]

De hecho, el primer estudio sobre la formación de pares de bases mediados por metales, se dió veinte años antes (1962) de que **Need Seeman** propusiera al ADN como un candidato para desarrollar nanomateriales. En estos estudios, **Sidney Katz** y colaboradores, describieron el mecanismo a través del cual los átomos de mercurio se unían a la doble hélice de ADN indicando que se observaban evidencias de que los complejos del tipo T-Hg^{II}-T eran los más comúnmente formados (Figura 1.8).[98] Estos estudios revelaron que, la introducción de los iones metálicos provocaba una leve perturbación en la estructura del ADN a consecuencia de un desplazamiento axial de la cadena, y además, fue posible evaluar de manera cuantitativa el numero promedio de iones hidrógenos liberados tras la formación de los pares de bases mediados por metales. Aunque en un principio esta metodología no estaba orientada a desarrollar nanomateriales basados en híbridos metal-ADN (ya que no se conocía dicho concepto), sentó las bases para poder controlar de manera precisa el posicionamiento de los metales a lo largo de una hebra de ADN. Este enfoque

ha abierto un nuevo camino para el desarrollo de la tecnología metal-ADN, que se encuentra en continuo estudio y desarrollo.[64,65,99]

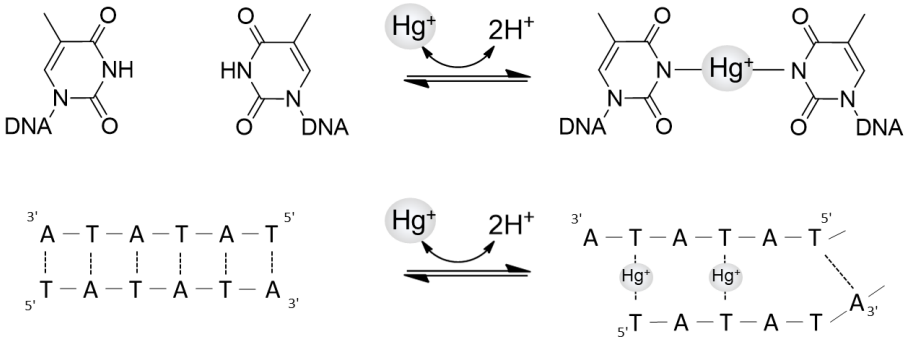

Figura 1.8: Representación esquemáticas de pares de bases mediados por iones de Hg^{II}.[98]

Uno de los principales retos a los que nos enfrentamos al introducir iones metálico en la estructura del ADN es conservar, en la medida de lo posible, su morfología natural y lograr la formación de pares de bases complementarios mediados por metales. Existe una importante problemática significativa con respecto a la interacción entre metales de transición y las nucleobases del ADN, como en el caso de los iones de Hg^{II} o Ag^{I}. Aunque en un principio cabría esperar que estos iones se unieran a través de un enlace de coordinación lineal entre las nucleobases naturales complementarias (A-M^{I}-T o G-M^{I}-C) orientadas en la cara Watson-Crick-Franklin (WCF) de la doble hebra, como vimos en ejemplos anteriores, los resultados obtenidos demuestran lo contrario.[100–102] Esto se debe a que, en condiciones normales de pH neutro y estequiometrias bajas, las posiciones preferentes para la formación de pares de bases mediados por metales son los nitrógenos N7 de la adenina, N7 de la guanina, N3 de la citosina y N3 de la timina. En los casos de **A** y **G**, los nitrógenos endocíclicos N7 y N3 quedan orientados en el exterior de la estructura de la doble hélice (surco mayor y surco menor, respectivamente) (Figura 1.1), mientras que el nitrógeno endocíclico N1, quedará orientado hacia el interior de la estructura, participando en la formación de enlaces de hidrógeno, cerca del eje central.

En 2017, **Jianhua Gan** y colaboradores publicaron el primer ejemplo de pares de bases mediados por metales del tipo G-Ag^I-G vía N7 en una hebra de ADN compuesta por ocho nucleótidos 5'-GCACGCGC-3' a partir de su estructura cristalina (Figura 1.9). En estos estudios demostraron que la formación de pares de bases mediados por iones Ag^I estabilizaban la formación del híbrido metal-ADN. Además, se observó por primera vez como las nucleobases de guanina interaccionan con el ion Ag^I en conformación anti-Hoogteen a través del nitrógeno endocíclico N7. En estos estudios, también fue posible observar la formación de pares de bases metálicos de tipo C-Ag^I-C, que ya habían sido estudiados con anterioridad.

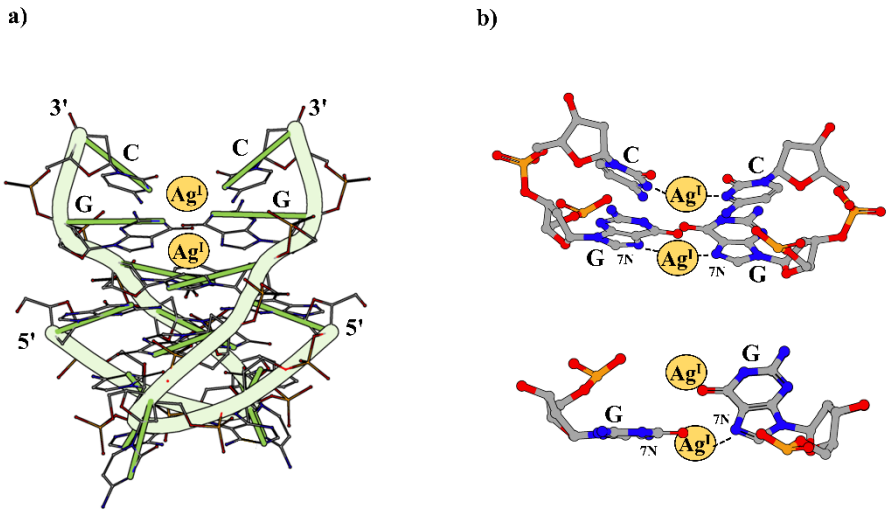

Figura 1.9: Esquema de la formación de pares de bases mediados por metales G-Ag^I-G y C-Ag^I-C. a) Representación general del complejo ADN-Ag^I. Los iones Ag^I se presentan como esferas amarillas y el ADN como líneas verdes. b) Dos puntos de vista del enlace G-Ag^I-G y C-Ag^I-C. Los esquemas muestran la disposición anti-Hoogsten de los pares de bases mediados por metales a través de N7G. Estructura cristalina disponible en PBD:5XJZ.

Jiro Kondo y colaboradores, publicarían también un estudio donde mostraban interacciones de tipo G-Ag^I-G vía N7, aunque en este caso demostraron la posibilidad de saturar todas las posiciones del interior de una doble hebra de ADN. Para esto diseñaron secuencias con hebras compuestas de

tipo 5'-d(CGCGCU^{Br}CU^{Br}CGCG)- 3' (**ODN-I**) (U^{Br} = 5-bromouracilo) donde dos cadenas se unían es sentido antiparalelo según una estructura de doble hélice B. Aunque este dúplex fue originalmente diseñado para formar dos pares de bases de tipo C-AgI-C, buscando replicar los resultados obtenidos para un dúplex de RNA previos,[102] los resultados obtenidos demostraron que los iones Ag^{I} se unían preferentemente a otras posiciones adicionales. Entre ellas, destaca la formación del par G-Ag^{I}-G vía N7, pero además dos nuevos pares de bases fueron encontrados, T-Ag^{I}-T y G-Ag^{I}-C. Este último par mantiene la conformación natural de tipo WCF, de manera que el ión Ag^{I} reemplaza al enlace de hidrógeno central del par G-C, demostrando que los pares de bases WFC pueden ser modificados por un ión metálico central.

En bibliografía existen únicamente dos ejemplos que demuestran que es posible obtener híbridos metal-ADN a través de un enlace de coordinación entre nucleobases complementarias. El primero, fue publicado por **Philipe Dumas** y colaboradores en 2003, donde realizaron un amplio estudio que describía las interacciones de distintos cationes con el ADN. Aquí se describió por primera vez la formación de pares de bases mediados por iones Au^{III} para obtener complejos metal-nucleobase con interacciones WCF de tipo G-Au^{III}-C. [46,100] Por otro lado, como se ha descrito anteriormente, el equipo dirigido por **Jiro Kondo** cristalizó y describió por primera vez la estructura de un sistema Ag-ADN, donde los iones saturaban todas las posiciones disponibles a lo largo de la doble hebra (Figura 1.10). Los datos de difracción revelaron que todos los pares de bases mediados por metales eran del tipo G-Ag^{I}-G, T-Ag^{I}-T o C-Ag^{I}-C a excepción de un par de bases alojado en el extremo de la doble hebra de tipo WCF, G-Ag^{I}-C. Donde la especie G-Ag^{I}-C, representa uno de los primeros ejemplos de pares de bases complementarios mediados por metales. [100,102]

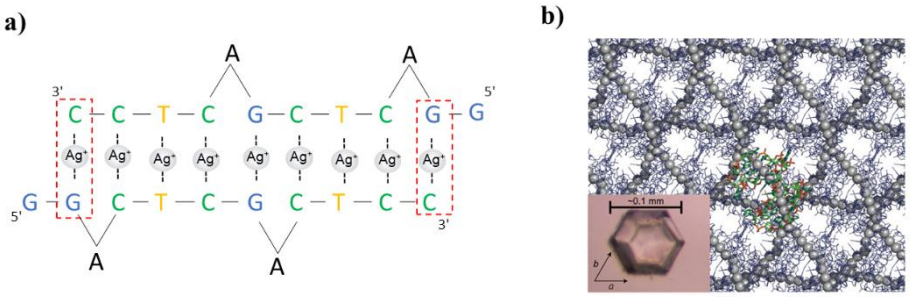

Figura 1.10: **a)** Reacción entre iones de Ag^{i} y un oligonucleótido de doces unidades autoensamblable, para formar un híbrido metal-ADN (recuadro rojo: pares de bases complementarios mediados por metales). **b)** Primer cristal obtenido de un sistema continuo Ag-ADN.[100]

Los resultados anteriores, donde se muestran la formación de pares de bases complementarios mediados por metales (G- Au^{III}-C y G- Ag^{I}-C), aunque sorprendentes, no dejan de ser excepcionales. En este sentido, son numerosos los quipos de investigación que han centrado sus esfuerzos en obtener resultados similares. Por tanto, el hecho de que sólo existan dos ejemplos descritos en bibliografía destaca la dificultad de la metodología. Esto es debido a que la formación de pares de bases mediados por metales en el interior de una doble hebras de ADN puede resultar un proceso impredecible. Por tanto, explorar nuevas metodologías que permitan resolver estos problemas se ha vuelto prioritario.

Nuestro grupo de investigación ha desarrollado una estrategia que consiste en sustituir los nitrógenos endocíclicos N7 de **A** y **G**, por grupos CH para obtener nucleobases modificadas del tipo 7-deaza-adenina (**X**) y 7-deaza-guanina (**Y**) (Figura 1.11). Esta sutil modificación, permite no solo conservar la morfología y la capacidad de auto-reconocimiento del ADN mediante el emparejamiento natural y la formación de enlaces de hidrógeno WCF, sino que también promueve la interacción con los iones metálicos exclusivamente a través de la posición N1-purina y N3-pirimidina de las nucleobases.[103–105] Esta estrategia permite por tanto prediseñar secuencias de ADN que contengan

las nucleobases modificadas **X** e **Y**, y que además, promuevan la unión de iones de Ag^{I} a través de la posición N1.

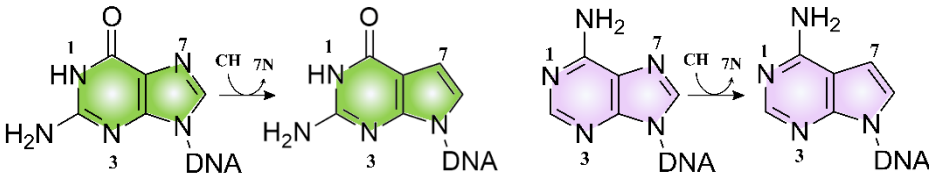

Figura 1.11:Representación esquemática para obtener las nucleobases modificas 7-deaza-guanina (verde) y 7-deaza-adenina (rosa) a partir de las nucleobases naturales.

En este sentido, se estudiaron las interacciones entre iones Ag^{I} y secuencias de ADN donde se introdujo una de las nucleobases modificadas X e Y; como por ejemplo en las hebras 5'-TXT XTX TXT XTX-3' y 5'-YCY CYC YCY CYC YC-3'. Estos estudios revelaron que los iones de Ag^{I} se coordinan a través del nitrógeno endocíclico N1 de la 7-deaza-adenina y el nitrógeno N3 de la timina para formar el par de base **X-Ag^{I}-T**(Figura 1.12). También se demostró que los iones de Ag^{I}, se unen al nitrógeno endocíclico N1 de la 7-deazaguanina y el nitrógeno N3 de la citosina para el par de base **Y-Ag^{I}-C** . Además, estos estudios indicaron que para el caso del par **Y-C**, en comparación con el par **X-T,** se producía una coordinación con dos iones de plata para obtener el complejo **Y-$(Ag^{I})_2$-C**, cuya estructura fue reportada posteriormente por otros autores.[105]

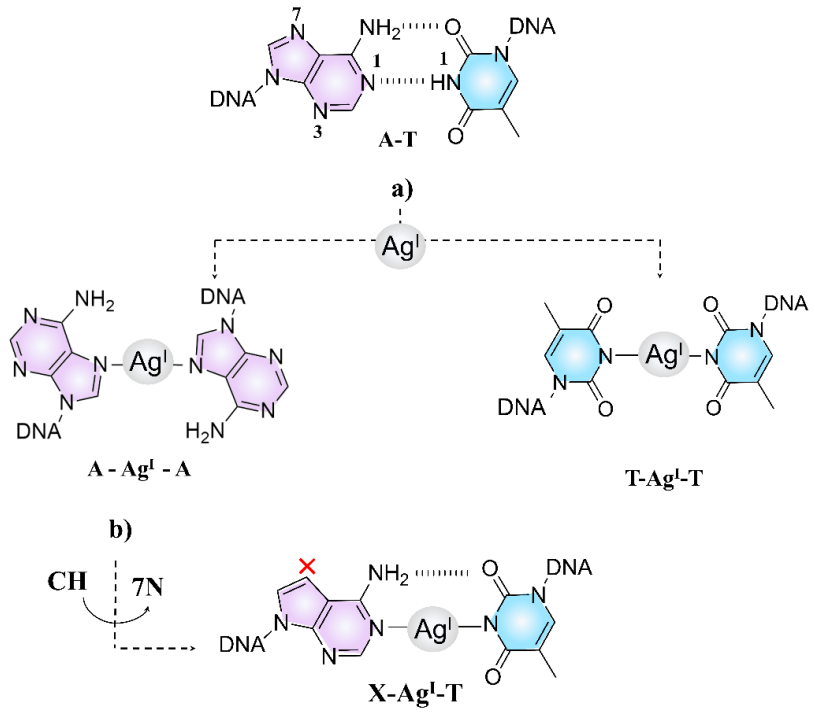

Figura 1.12: Esquema del proceso para la obtención de pares de bases mediados por Ag^{I}. a) Formación de pares de bases no complementarios C-Ag^{I}-C **y** A-Ag^{I}-A promovidas por la interacción del ion de plata vía **N7** b) Modificación en la posición N7 de adenina para obtener el par de bases complementario X-Ag^{I}-T.

Estos resultados permitieron diseñar experimentos más ambicioso donde se empleó una hebra de ADN con una secuencia que incluyeran las dos bases modificadas **X** e **Y**; 5'-CYT XCY TXC YTX XYT XCY-3'. El objetivo era poner a prueba hasta qué punto se puede controlar el posicionamiento y la estequiometría de los iones de plata a lo largo de la estructura del ADN.

En este caso, los resultados indicaron que se obtuvo con éxito un sistema híbrido Ag-ADN donde se obtuvieron pares de bases mediados por metales del tipo X-Ag^{I}-T y Y-Ag^{I}-C a lo largo de toda la estructura. Se pudo concluir que la formación de estos híbridos permitió obtener sistemas altamente estables debido a la sustitución de los puentes de hidrógenos, que se dan entre nucleobases complementarias, por enlaces de coordinación.

Una vez más, se ha demostrado como en la bibliografía podemos encontrar numerosos ejemplos donde se describe la interacción entre iones metálicos y hebras doble de ADN. Sin embargo, son escasos los ejemplos que se centran en utilizar hebras simples como plantilla para la construcción de nanomateriales.

Como se resaltó anteriormente, los estudios realizados por **Wagenknecht** y su equipo (Figura 1.6) han sido fundamentales y han inspirado directamente el desarrollo de esta tesis doctoral. Esto es debido a su propuesta para desarrollar un mecanismo a través del cual, podían organizar moléculas a lo largo de una hebra simple de ADN mediante un mecanismo de autoensamblaje molecular y a través de la formación de puentes de hidrógeno. Tras estos hallazgos, fue lógico pensar que se podrían desarrollar mecanismos análogos para desarrollar sistemas metal-ADN a través de un proceso de autoensamblaje, partiendo de hebras simples de ADN y compuestos de coordinación con características específicas que permitan reconocer las bases de la secuencia empleada.[106–108]

La siguiente cuestión consistió en seleccionar a los candidatos ideales para desarrollar esta idea. Para esto, los complejos metálicos seleccionados deberían estar formados por entidades metálicas capaces de imitar, en la medida de lo posible, las interacciones que se dan entre las nucleobases complementarias del ADN.

Algunas aproximaciones pusieron a prueba la interacción de complejos metálicos con nucleobases aisladas o empleando una hebra simple de ADN. En este contexto **Tuomas Lömnberg** y su equipo realizaron un amplio estudio donde se puso a prueba la afinidad y la selectividad de complejos metálicos por las nucleobases canónicas a nivel individual.[109] En estos estudios se tuvieron en cuenta requisitos tan importantes como la basicidad de los átomos donadores de las nucleobases, los impedimentos estéricos, la estabilización de los posibles pares de bases mediados por metales mediante puentes de hidrógeno o la geometría del complejo de coordinación formado. Además, propusieron, que los iones de Pd^{II} y Pt^{II} eran los mejores candidatos para ser implementados en la formación de pares de bases mediados por metales. Sin embargo, llegaron a

la conclusión de que la especificidad metal-nucleobase aún era un problema por solventar y que era necesario desarrollar metodologías que permitieran estudiar estos fenómenos de manera precisa, sobre todo si se pretendía extender estos descubrimientos al ámbito farmacológico.

Con el objetivo de estudiar la selectividad de los complejos metálicos, como por ejemplo los que contienen iones de Pd^{II}, **Tuomas Lömnberg** y su equipo diseñaron un sistema de hebra simple que se autoensambla y es capaz de interaccionar específicamente (Figura 1.13).[106] Esto permite determinar la selectividad de los complejos metálicos con las nucleobases que quedan en el hueco de la hebra sin aparear, y que además pueden ser seleccionadas simplemente prediseñado la secuencia de bases de la hebra simple. La selectividad se determinó debido a la pérdida de fluorescencia de un grupo cromóforo unido a una nucleobase cercada. Al formarse el par de bases mediados por Pd con el ligando alojado en el hueco de la hebra simple, se produce un quencheo del grupo fluoroforo y por tanto una pérdida de fluorescencia que puede ser medida.

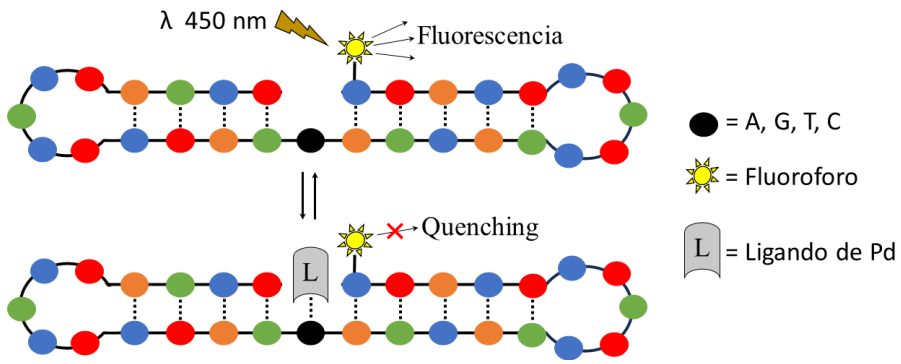

Figura 1.13: Pérdida de fluorescencia de un grupo fluoroforo como consecuencia de la formación de pares de bases mediados por metales entre un complejo de paladio y una nucleobase objetivo. La pérdida de fluorescencia del grupo cromóforo, indica la formación de los enlaces metal-ADN. [106]

Con base en las ideas expuestas, nuestro grupo de investigación se embarcó en el desafío de diseñar sistemas más complejos, donde hebras simples de ADN pudieran alojar complejos metálicos de Pd^{II} a lo largo de toda su estructura. Para esto, no solo se inspiró en el ya mencionado trabajo de **Wagenknecht**, si no que también los descubrimientos de **Shionoya** y colaboradores fueron fundamentales. Estos estudios recogían el primer ejemplo publicado que propuso un mecanismo para organizar iones metálicos mediante la formación de estructuras supramoleculares,[110] resultando ser uno de los ejemplos más inspiradores para la comunidad científica dedicada a la metalización del ADN.

En estos estudios, sintetizaron compuestos quelantes derivados de adenina capaces de interaccionar mediante reconocimiento de pares de bases complementarias con un ADN de cadena simple homotópica de 2-deoxytimidina (**dT_{70}**) a través de la formación de puentes de hidrógeno (Figura 1.14). Además, los derivados quelantes de adenina eran capaces de contener iones de Zn^{II} en su interior. Esto, les permitió obtener estructuras supramoleculares que se asemejaban a una triple hebra formada por una doble hebra natural de tipo **$dT_{70}-A$** y otra hebra formada por iones **Zn^{II}** .

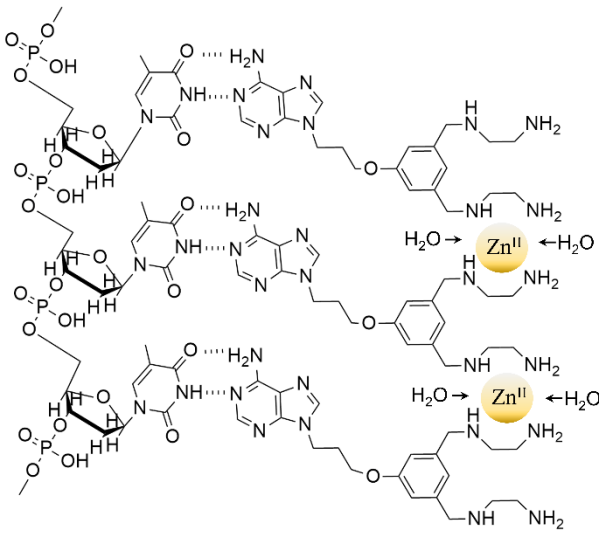

Figura 1.14: Esquema de la reacción entre una hebra simple de **dT_{70}** y compuestos quelantes derivados de adenina que contienen iones Zn^{II}, para obtener una estructura supramolecular de tipo **dT_{70}-A-Zn^{II}** a través de un proceso de auto-ensamblaje molecular mediante reconocimiento de pares de bases. [110]

A lo largo de esta tesis doctoral se explorarán nuevas estrategias que permitan emplear moléculas de ss-ADN como plataforma de construcción de híbridos metal-ADN. Además, se evaluará la capacidad de precisión de estos sistemas para controlar el posicionamiento y la estequiometría de los metales. Este enfoque representa un paso significativo hacia la comprensión de sistemas complejos basados en ADN, ofreciendo resultados valiosos para el diseño y la manipulación de nanoestructuras con potenciales aplicaciones en diversas áreas de la nanotecnología y la ciencia de materiales.

1.4. Bibliografía

1 J. D. Watson and F. H. C. Crick, *Nature*, 1953, **171**, 737–738.

2 K. J. Breslauer, R. Frank, H. Blöcker and L. A. Marky, *Proc. Nat. Acad. Sci.*, 1986, **83**, 3746–3750.

3 R. E. Dickerson and A. Klug, *J Mol Biol*, 1983, **166**, 419–441.

4 F. A. Hays, A. Teegarden, Z. J. R. Jones, M. Harms, D. Raup, J. Watson, E. Cavaliere and P. S. Ho, *Proc. Nat. Acad. Sci.*, 2005, **102**, 7157–7162.

5 C. N. Kunkler, J. P. Hulewicz, S. C. Hickman, M. C. Wang, P. J. McCown and J. A. Brown, *Nucleic Acids Res*, 2019, **47**, 7213–7222.

6 D. R. Duckett, A. I. H. Murchie, S. Diekmann, E. von Kitzing, B. Kemper and D. M. J. Lilley, *Cell*, 1988, **55**, 79–89.

7 D. M. J. Lilley, *Q Rev Biophys*, 2000, **33**, 109–159.

8 C. Altona, J. A. Pikkemaat and F. J. Overmars, *Curr Opin Struct Biol*, 1996, **6**, 305–316.

9 M. Gellert, M. N. Lipsett and D. R. Davies, *Proc. Nat. Acad. Sci.*, 1962, **48**, 2013–2018.

10 D. Sen and W. Gilbert, *Nature*, 1988, **334**, 364–366.

11 K. Gehring, J.-L. Leroy and M. Guéron, *Nature*, 1993, **363**, 561–565.

12 X. Du, D. Wojtowicz, A. A. Bowers, D. Levens, C. J. Benham and T. M. Przytycka, *Nucleic Acids Res*, 2013, **41**, 5965–5977.

13 R. Hänsel-Hertsch, D. Beraldi, S. V Lensing, G. Marsico, K. Zyner, A. Parry, M. Di Antonio, J. Pike, H. Kimura, M. Narita, D. Tannahill and S. Balasubramanian, *Nat Genet*, 2016, **48**, 1267–1272.

14 S. Pandey, A. M. Ogloblina, B. P. Belotserkovskii, N. G. Dolinnaya, M. G. Yakubovskaya, S. M. Mirkin and P. C. Hanawalt, *Nucleic Acids Res*, 2015, **43**, 6994–7004.

15 S. Kendrick, H.-J. Kang, M. P. Alam, M. M. Madathil, P. Agrawal, V. Gokhale, D. Yang, S. M. Hecht and L. H. Hurley, *J Am Chem Soc*, 2014, **136**, 4161–4171.

16 Hall, J. P. ; Ruiz-Morte, S. ; Murray and C. A. ; Cardin, *Full wwPDB X-ray Structure Validation Report i O Title : GGGCATGCCC in the A-DNA Form*, 2020.

17 H. Robinson, A. H. Wang, J. Sugiyama, H. Kawai, K. Matsunaga, A. Fuji-Moto and K. Saito, *Nucleic Acids Res*, 1996, **24**, 1272–1278.

18 C. E. ; Miron, L. M. ; Van Staalduinen, Z. ; Jia and A. Petitjean, *Full wwPDB X-ray Structure Validation Report i ○ Title : Crystal Structure of human telomeric DNA G-quadruplex in complex with a novel platinum(II) complex*, 2023.

19 L. A. ; Yatsunyk and K. S. Li, *Full wwPDB X-ray Structure Validation Report i ○-12:33 PM EDT PDB ID : 8CXF Title : Crystal structure of an i-motif from the HRAS promoter region*, 2023.

20 G. M. Whitesides, J. P. Mathias and C. T. Seto, *Science (1979)*, 1991, **254**, 1312–1319.

21 P. W. K. Rothemund, *Nature*, 2006, **440**, 297–302.

22 Z.-G. Wang and B. Ding, *Acc Chem Res*, 2014, **47**, 1654–1662.

23 N. C. Seeman, *Annu Rev Biochem*, 2010, **79**, 65–87.

24 N. C. Seeman, *J Theor Biol*, 1982, **99**, 237–247.

25 F. Hong, F. Zhang, Y. Liu and H. Yan, *Chem Rev*, 2017, **117**, 12584–12640.

26 N. C. Seeman, *J Biomol Struct Dyn*, 1990, **8**, 573–581.

27 J. Chen and N. C. Seeman, *Nature*, 1991, **350**, 631–633.

28 P. W. K. Rothemund, *Nature*, 2006, **440**, 297–302.

29 H. Ramezani and H. Dietz, *Nat Rev Genet*, 2020, 21, 5–26.

30 P. Ketterer, E. M. Willner and H. Dietz, *Sci. Adv.*, 2016, **2**, 1–8.

31 D. Paolantoni, S. Cantel, P. Dumy and S. Ulrich, *Int J Mol Sci*, 2015, **16**, 3609–3625.

32 R. Hofsäß, S. Sinn, F. Biedermann and H. Wagenknecht, *Chem. Eur. J.*, 2018, **24**, 16257–16261.

33 M. Surin and S. Ulrich, *ChemistryOpen*, 2020, **9**, 480.

34 N. C. Seeman and H. F. Sleiman, *Nat Rev Mater*, 2017, **3**, 17068.

35 F. C. S. Hans-Werner, *letters to nature*, 1999, **398**, 407–410.

36 Y.-W. Kwon, D. Hoon Choi and J.-I. Jin, *Polym J*, 2012, **44**, 1191–1208.

37 N. C. Seeman, *Nat Rev Mater*, 2017, **27**, 1–23.

38 M. Madsen and K. V. Gothelf, *Chem Rev*, 2019, **119**, 6384–6458.

39 E. Stulz, *Molecular Architectonics and Nanoarchitectonics* , Springer Nature, Switzerland, 2022.

40 K. J. Waldron, J. C. Rutherford, D. Ford and N. J. Robinson, *Nature*, 2009, **460**, 823–830.

41 J. Anastassopoulou and T. Theophanides, in *Bioinorganic Chemistry*, Springer Netherlands, Dordrecht, 1995, pp. 209–218.

42 C. J. Williams and J. M. Whitehouse, *BMJ*, 1979, **1**, 1689–1691.

43 A. Bouchoucha, S. Zaater, S. Bouacida, H. Merazig and S. Djabbar, *J Mol Struct*, 2018, **1161**, 345–355.

44 D. E. Draper, D. Grilley and A. M. Soto, *Annu Rev Biophys Biomol Struct*, 2005, 34, 221–243.

45 G. S. Manning, *Acc Chem Res*, 1979, **12**, 443–449.

46 E. Ennifar, P. Walter and P. Dumas, *Nucleic Acids Res*, 2003, **31**, 2671–2682.

47 V. K. Misra, R. Shiman and D. E. Draper, *Biopolymers*, 2003, **69**, 118–136.

48 B. Pullman, *J Biomol Struct Dyn*, 1983, **1**, 773–794.

49 S. A. Strobel and J. A. Doudna, *Trends Biochem Sci*, 1997, **22**, 262–266.

50 N. V Hud, V. Sklenář and J. Feigon, *J Mol Biol*, 1999, **286**, 651–660.

51 L. McFail-Isom, C. C. Sines and L. D. Williams, *Curr Opin Struct Biol*, 1999, **9**, 298–304.

52 J.-H. Chen, B. Gong, P. C. Bevilacqua, P. R. Carey and B. L. Golden, *Biochemistry*, 2009, **48**, 1498–1507.

53 N. Toor, K. S. Keating, S. D. Taylor and A. M. Pyle, *Science (1979)*, 2008, **320**, 77–82.

54 N. J. Reiter, A. Osterman, A. Torres-Larios, K. K. Swinger, T. Pan and A. Mondragón, *Nature*, 2010, **468**, 784–789.

55 M. R. Stahley and S. A. Strobel, *Curr Opin Struct Biol*, 2006, **16**, 319–326.

56 R. K. O. Sigel, E. Freisinger and B. Lippert, *J.B.I.C.*, 2000, **5**, 287–299.

57 R. K. O. Sigel, M. Sabat, E. Freisinger, A. Mower and B. Lippert, *Inorg Chem*, 1999, **38**, 1481–1490.

58 B. Knobloch, R. K. O. Sigel, B. Lippert and H. Sigel, *Angew. Chem. Int. Ed.*, 2004, **43**, 3793–3795.

59 B. Lippert, *Chem Biodivers*, 2008, **5**, 1455–1474.

60 R. Griesser, G. Kampf, L. E. Kapinos, S. Komeda, B. Lippert, J. Reedijk and H. Sigel, *Inorg Chem*, 2003, **42**, 32–41.

61 H. Sigel, *Acid-base properties of purine residues and the effect of metal ions: Quantification of rare nucleobase tautomers**, 2004, vol. 76.

62 K. Tanaka, A. Tengeiji, T. Kato, N. Toyama and M. Shionoya, *Science (1979)*, 2003, **299**, 1212–1213.

63 F. Linares, E. García-Fernández, F. J. López-Garzón, M. Domingo-García, A. Orte, A. Rodríguez-Diéguez and M. A. Galindo, *Chem Sci*, 2019, **10**, 1126–1137.

64 Y. Takezawa, J. Müller and M. Shionoya, *Chem Lett*, 2017, 46, 622–633.

65 B. Jash and J. Müller, *Chem. Eur. J.*, 2017, **23**, 17166–17178.

66 N. V Hud, Ed., *Nucleic Acid–Metal Ion Interactions*, The Royal Society of Chemistry, 2008.

67 N. Hadjiliadis and E. Sletten, Eds., *Metal Complex–DNA Interactions*, Wiley, 2009.

68 H. Sigel, *Chem Soc Rev*, 1993, **22**, 255.

69 Z. Chen, C. Liu, F. Cao, J. Ren and X. Qu, *Chem Soc Rev*, 2018, **47**, 4017–4072.

70 B. Lippert, *Coord Chem Rev*, 2000, **200–202**, 487–516.

71 B. Lippert and P. J. Sanz Miguel, *Acc Chem Res*, 2016, **49**, 1537–1545.

72 J. Schnabl and R. K. Sigel, *Curr Opin Chem Biol*, 2010, **14**, 269–275.

73 S. A. Kazakov and S. M. Hecht, in *Encyclopedia of Inorganic Chemistry*, Wiley, 2005.

74 J. Bath and A. J. Turberfield, *Nat Nanotechnol*, 2007, **2**, 275–284.

75 C. Song, Z. Wang and B. Ding, *Small*, 2013, **9**, 2382–2392.

76 S. M. D. Watson, A. R. Pike, J. Pate, A. Houlton and B. R. Horrocks, *Nanoscale*, 2014, **6**, 4027–4037.

77 I. Grabowska, D. G. Singleton, A. Stachyra, A. Góra-Sochacka, A. Sirko, W. Zagórski-Ostoja, H. Radecka, E. Stulz and J. Radecki, *Chem. Commun.*, 2014, **50**, 4196–4199.

78 E. Paleček and M. Bartošík, *Chem Rev*, 2012, **112**, 3427–3481.

79 A. Abi and E. E. Ferapontova, *J Am Chem Soc*, 2012, **134**, 14499–14507.

80 A. Houlton, A. R. Pike, M. Angel Galindo and B. R. Horrocks, *Chem. Comm.*, 2009, 1797.

81 H. A. Becerril, R. M. Stoltenberg, D. R. Wheeler, R. C. Davis, J. N. Harb and A. T. Woolley, *J Am Chem Soc*, 2005, **127**, 2828–2829.

82 S. A. Farha Al-Said, R. Hassanien, J. Hannant, M. A. Galindo, S. Pruneanu, A. R. Pike, A. Houlton and B. R. Horrocks, *Electrochem commun*, 2009, **11**, 550–553.

83 B. Datta and G. B. Schuster, *J Am Chem Soc*, 2008, **130**, 2965–2973.

84 E. Mayer-Enthart and H. Wagenknecht, *Angew. Chem. Int. Ed.*, 2006, **45**, 3372–3375.

85 J. Huang, L. Lin, D. Sun, H. Chen, D. Yang and Q. Li, *Chem Soc Rev*, 2015, **44**, 6330–6374.

86 K. Li, K. Wang, W. Qin, S. Deng, D. Li, J. Shi, Q. Huang and C. Fan, *J Am Chem Soc*, 2015, **137**, 4292–4295.

87 Y. Wang, G. Ouyang, J. Zhang and Z. Wang, *Chem. Comm.*, 2010, **46**, 7912.

88 S. M. D. Watson, A. R. Pike, J. Pate, A. Houlton and B. R. Horrocks, *Nanoscale*, 2014, **6**, 4027–4037.

89 T. Bayrak, N. Jagtap and A. Erbe, *Int J Mol Sci*, 2018, **19**, 3019.

90 G. Eidelshtein, N. Fardian-Melamed, V. Gutkin, D. Basmanov, D. Klinov, D. Rotem, Y. Levi-Kalisman, D. Porath and A. Kotlyar, *Advanced Materials*, 2016, **28**, 4839–4844.

91 G. H. Clever and M. Shionoya, *Coord Chem Rev*, 2010, **254**, 2391–2402.

92 P. Scharf and J. Müller, *Chempluschem*, 2013, **78**, 20–34.

93 I. Sinha, C. Fonseca Guerra and J. Müller, *Angew. Chem. Int. Ed.*, 2015, **54**, 3603–3606.

94 B. Lippert, *JBIC*, 2022, **27**, 215–219.

95 Y. Takezawa, K. Nishiyama, T. Mashima, M. Katahira and M. Shionoya, *Chem. Eur. J.*, 2015, **21**, 14713–14716.

96 A. Ono, S. Cao, H. Togashi, M. Tashiro, T. Fujimoto, T. Machinami, S. Oda, Y. Miyake, I. Okamoto and Y. Tanaka, *Chem. Comm.*, 2008, 4825.

97 Y. Miyake, H. Togashi, M. Tashiro, H. Yamaguchi, S. Oda, M. Kudo, Y. Tanaka, Y. Kondo, R. Sawa, T. Fujimoto, T. Machinami and A. Ono, *J Am Chem Soc*, 2006, **128**, 2172–2173.

98 S. Katz, *Biochimica et Biophysica Acta (BBA) - Specialized Section on Nucleic Acids and Related Subjects*, 1963, **68**, 240–253.

99 J. Müller, *Coord Chem Rev*, 2019, **393**, 37–47.

100 J. Kondo, Y. Tada, T. Dairaku, Y. Hattori, H. Saneyoshi, A. Ono and Y. Tanaka, *Nat Chem*, 2017, **9**, 956–960.

101 H. Liu, F. Shen, P. Haruehanroengra, Q. Yao, Y. Cheng, Y. Chen, C. Yang, J. Zhang, B. Wu, Q. Luo, R. Cui, J. Li, J. Ma, J. Sheng and J. Gan, *Angew. Chem. Int. Ed.*, 2017, **56**, 9430–9434.

102 T. Atsugi, A. Ono, M. Tasaka, N. Eguchi, S. Fujiwara and J. Kondo, *Angew. Chem. Int. Ed.*, 2022, **61**, 1–7.

103 J. M. Méndez-Arriaga, C. R. Maldonado, J. A. Dobado and M. A. Galindo, *Chem. Eur. J.*, 2018, **24**, 4469–4469.

104 N. Santamaría-Díaz, J. M. Méndez-Arriaga, J. M. Salas and M. A. Galindo, *Angew. Chem. Int. Edi.*, 2016, **55**, 6170–6174.

105 X. Guo, P. Leonard, S. A. Ingale, J. Liu, H. Mei, M. Sieg and F. Seela, *Chem. Eur. J.*, 2018, **24**, 8883–8892.

106 A. Aro-Heinilä and T. Lönnberg, *Chem. Eur. J.*, 2017, **23**, 1028–1031.

107 E. Kimura, H. Kitamura, K. Ohtani and T. Koike, *J Am Chem Soc*, 2000, **122**, 4668–4677.

108 K. E and M. Shionoya, eds. H. Sigel and Astrid. Sigel, 1996, vol. 33, pp. 29–52.

109 S. Taherpour, O. Golubev and T. Lönnberg, *Inorganica Chim Acta*, 2016, **452**, 43–49.

110 A. Hatano, K. Tanaka, M. Shiro and M. Shionoya, *Tetrahedron*, 2002, **58**, 2965–2972.

Capítulo 2

Estudios de Interacción de las Nucleobases con Complejos Metálicos Complementarios. Formación de Híbridos Supramoleculares Pd-ADN Altamente Organizados.

Capítulo 2. Estudios de Interacción de Nucleobases con Complejos Metálicos Complementarios. Formación de Híbridos Supramoleculares ADN-Pd Altamente Organizados.

En este capítulo se describen las estrategias para obtener sistemas híbridos de tipo ADN-metal obtenidos a partir de la interacción de complejos de Pd^{II} con nucleobases complementarias. En cada caso se discutirán los resultados obtenidos para la interacción de los complejos de Pd^{II} con nucleobases modelo de adenina, citosina y timina, y posteriormente empleando la secuencia del oligonucleótido derivada de dicha base. Los estudios con derivados de guanina no se han estudiado en este trabajo de tesis.

Los híbridos ADN-Pd surgen de un proceso de autoensamblaje molecular en fase acuosa que conduce a la formación de la estructura termodinámicamente más estable. Las estructuras resultantes se caracterizan por organizar los complejos metálicos de manera muy precisa, danto lugar a una doble hebra compuesta por pares de bases de tipo nucleobase-Pd^{II}-ligando. Una de las hebras está compuesta por el oligonucleótido empleado y la otra resulta del apilamiento continuo de complejos unidos a las nucleobases. La interacción entre las nucleobases y los complejos se produce por la cara Watson-Crick-Franklin (WCF) de las nucleobases, con la formación de un enlace de coordinación a los nitrógenos endociclícos de las bases y enlaces de hidrógeno complementarios (Figura 2.1).

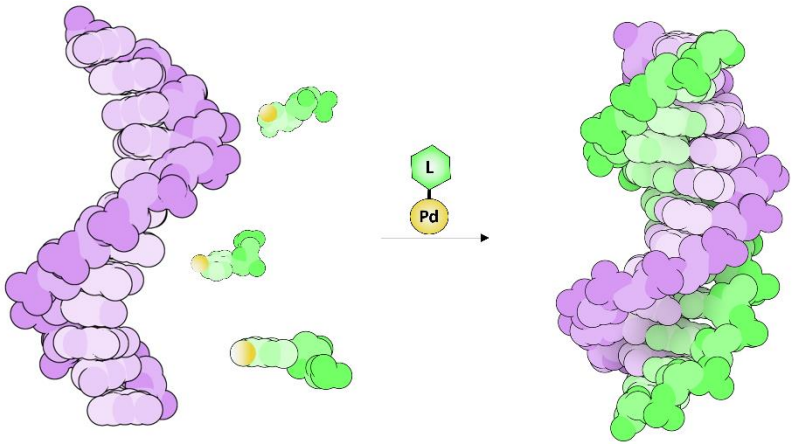

Figura 2.1: Esquema de reacción de autoensamblaje entre una hebra simple de ADN y un complejo metálico de Pd^{II}.

Los complejos metálicos empleados para estos estudios se obtienen a partir de un diseño racional inspirado en las nucleobases. Su estructura se basa en anillos aromáticos que permiten establecer interacciones de apilamiento (stacking) y presentan diferentes grupos funcionales capaces de establecer enlaces por puentes de hidrógenos con nucleobases complementarias. El conjunto de estas interacciones intramoleculares es fundamental para estabilizar la estructura de los híbridos ADN-Pd. Los estudios que se presentan a continuación explotan la capacidad de los complejos de Pd^{II} para coordinarse a través de una geometría plano-cuadrada a los nitrógenos dadores de las nucleobases. Además, su relativa fuerza de enlace les permite participar en reacciones de autoensamblaje con las nucleobases que den lugar a estructuras termodinámicamente más estables.

Para estos estudios se han seleccionado las nucleobases adenina (**A**), citosina (**C**), timina (**T**) y los oligonucleótidos correspondientes compuestos por secuencias homogéneas de quince 2'-deoxyribonucleotidos, $\mathbf{dA_{15}}$, $\mathbf{dC_{15}}$ y $\mathbf{dT_{15}}$. También se ha empleado la base 7-deazaadenina (**X**) y su oligonucleótido $\mathbf{dX_{15}}$, donde el nitrógeno N7 de la adenina se ha sustituido por un grupo CH. Como se adelantó en el Capítulo 1, la necesidad de incluir esta base modificada radica en que los complejos metálicos de Pd^{II} tienen la capacidad de interactuar

con la adenina preferentemente a través de los nitrógenos endocíclicos N1 y N7. Sin embargo, para promover una unión y organización ADN-Pd que se asemeje a una estructura de doble hélice es necesario que esta se produzca a través del átomo N1, localizado la cara WCF de la adenina. La posible unión de los complejos metálicos a través de la posición N7 supondría la formación de híbridos con una geometría distinta a la doble hebra dextrógira deseada. Ante esta situación y dado que en algunos experimentos espectroscópicos (UV-Vis, CD) puede ser complicado conocer con precisión por donde están interaccionando los complejos de Pd^{II} con la adenina, los estudios realizados paralelamente con **X** y $\mathbf{dX_{15}}$ servirán como referencia, ya que excluye la unión de los complejos de Pd^{II} por el átomo N7.

Este capítulo está dividido en tres secciones dependiendo de la naturaleza de las nucleobases, los oligonucleótidos y los fragmentos metálicos empleados.

1) Estudios de interacción del complejo **CH_3CN-Pd-Cheld** con las bases **A** y **X**, y los oligonucleótidos $\mathbf{dX_{15}}$ y $\mathbf{dA_{15}}$.[1]
2) Estudios de interacción del complejo **DMSO-Pd-Aqa** con la base **C** y el oligonucleótido $\mathbf{dC_{15}}$.[2]
3) Estudios de interacción del complejo **DMSO-Pd-dPy** con la base **T** y el oligonucleótido $\mathbf{dT_{15}}$.

2.1. Estudios con derivados de la adenina

Anteriormente se mencionó la posibilidad de que los complejos de Pd^{II} interaccionasen con los nitrógenos endocíclicos de la adenina N1 y N7. Para estudiar estas posibilidades de unión, inicialmente se han realizado estudios con sistemas sencillos complejo-adenina aislados. En esta sección se estudiará en primer lugar la reactividad de las nucleobases modificadas libres, 9-etil-adenina (**eA**) y 9-propil-deazaadenina (**pX**), con el complejo [Pd(Cheld)(CH_3CN)] (**CH_3CN-Pd-Cheld**), derivado del ácido quelidámico (**Cheld**) (Figura 2.2). Las nucleobases de **eA** y **pX** han sido modificadas en la posición N9 con grupos

etilo o propilo, respectivamente, con objeto de impedir interacciones a través de este nitrógeno. Esta estrategia responde a imitar de una manera sencilla el bloqueo que este átomo N9 tiene en el ADN con la unidad de ribosa.

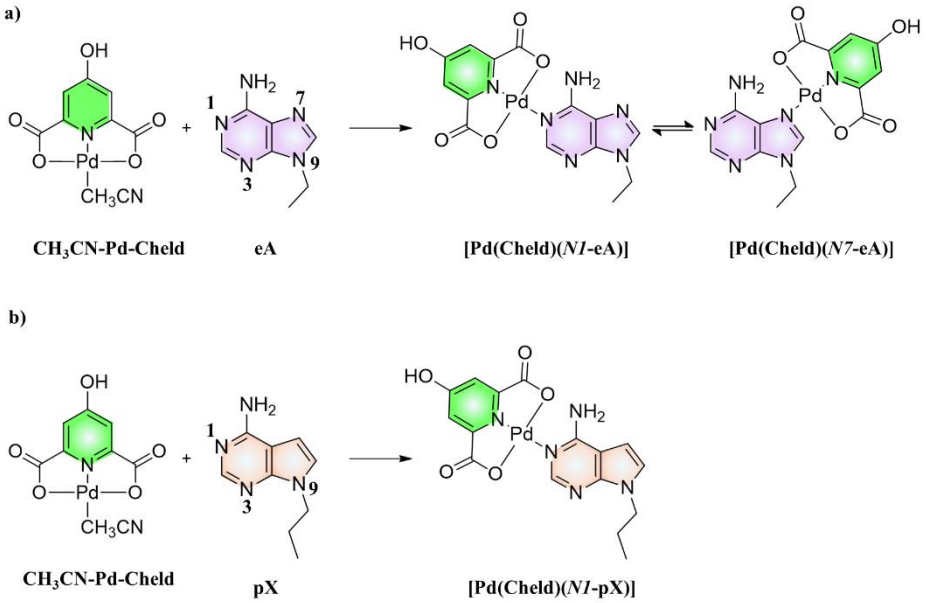

Figura 2.2: Esquema de reacción entre el complejo metálico **Pd-Cheld** y; a) 9-etil-adenina (**eA**), mostrando los dos posibles modos de interacción a través del átomo N1 y N7; b) 9-propil-7-deazaadenina (**pX**), mostrando la interacción por N1. Las etiquetas numéricas sobre las estructuras de **eA** y **pX**, hacen referencia a la nomenclatura de cada nitrógeno.

El estudio de estos sistemas modelo sencillos establecerá las bases para comprender el modo de interacción entre el fragmento metálico [Pd(Cheld)] (**Pd-Cheld**) con sistemas más complejos, como el oligonucleótido **dA$_{15}$**. Para ello, se llevará a cabo la reacción de autoensamblaje entre el fragmento metálico **Pd-Cheld** y los oligonucleótidos **dA$_{15}$** y **dX$_{15}$**, y se hará un estudio comparativo de los resultados obtenidos. El objetivo central es discernir si las diferencias entre la unión a través del átomo N1 y N7 desempeñan un papel crucial en la formación de los sistemas híbridos dA$_x$-Pd.

2.1.a. Síntesis y caracterización del compuesto de coordinación [Pd(Cheld)(CH_3CN)] (**CH_3CN-Pd-Cheld**).

En primer lugar, el complejo metálico **CH_3CN-Pd-Cheld** fue sintetizado y caracterizado. Para esto se mezcló una disolución (CH_3CN) que contenía $Pd(NO_3)_2$ y otra disolución (H_2O) que contenía ácido quelidámico (**Cheld)** (sección 2.5.1). La mezcla se agitó y posteriormente se dejó cristalizar mediante evaporación controlada. Transcurridas 24 horas, aparecieron cristales naranjas en forma de aguja que fueron recolectados, lavados y caracterizados (procedimiento completo descrito en Sección 2.5.1). A continuación, el producto se caracterización en disolución mediante medidas de ^{1}H-RMN (Figura 2.3).

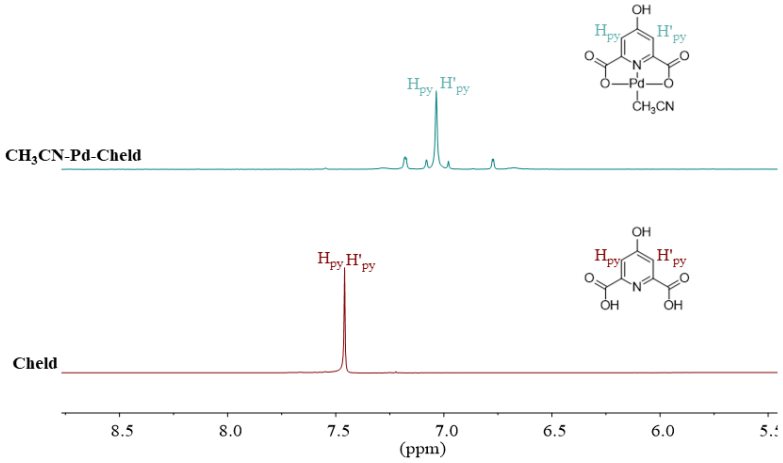

Figura 2.3: ^{1}H-RMN (400Mhz, DMSO-D_6) del ligando comercial ácido quelidámico (**Cheld**) y el complejo metálico **CH_3CN-Pd-Cheld**.

El espectro de ^{1}H-RMN para el ligando **Cheld** libre muestra un singlete a 7.5 ppm correspondiente a los protones aromáticos Hpy y H'py del anillo de piridina. Por otro lado, en el espectro obtenido tras disolver los cristales del complejo **CH_3CN-Pd-Cheld** se observa que el singlete de referencia para **Cheld** libre se ha desplazado a campo alto hasta 7.05 ppm, lo que se puede justificar por la coordinación de los iones de Pd^{II} a su estructura.

Para caracterizar el complejo **CH_3CN-Pd-Cheld** en fase sólida, se realizaron estudios de análisis elemental y espectrometría infrarroja. Los datos de caracterización de ambos procedimientos están descritos y pueden ser consultados en la Sección 2.5.1.

2.1.b. Síntesis y caracterización de compuestos de coordinación con derivados de la adenina; [Pd(Cheld)(eA)] (**eA-Pd-Cheld**) y [Pd(Cheld)(pX)] (**pX-Pd-Cheld**).

Los primeros estudios se realizaron para conocer el modo de interacción entre las nucleobases **eA** y **pX** con el fragmento metálico **Pd-Cheld** en disolución mediante medidas de ^{1}H-RMN. Para ello se prepararon disoluciones de cada una de las bases y se fueron añadiendo cantidades crecientes del complejo **[Pd(Cheld)(CH_3CN)]** hasta alcanzar los tres equivalentes (1 equivalente indica una unidad de **Pd-Cheld** por base) (sección 2.5.1). El estudio de los espectros de ^{1}H-RMN se ha centrado en la región aromática, entre 9.0 y 6.0 ppm, donde se observan las señales para los protones aromáticos más relevantes.

La Figura 2.4 muestra el espectro obtenido tras la valoración de **pX** con **Pd-Cheld**, del que se deduce la formación del compuesto de coordinación **[Pd(Cheld)(pX)]** (**pX-Pd-Cheld**) (espectro completo en Anexo-Figura 1).

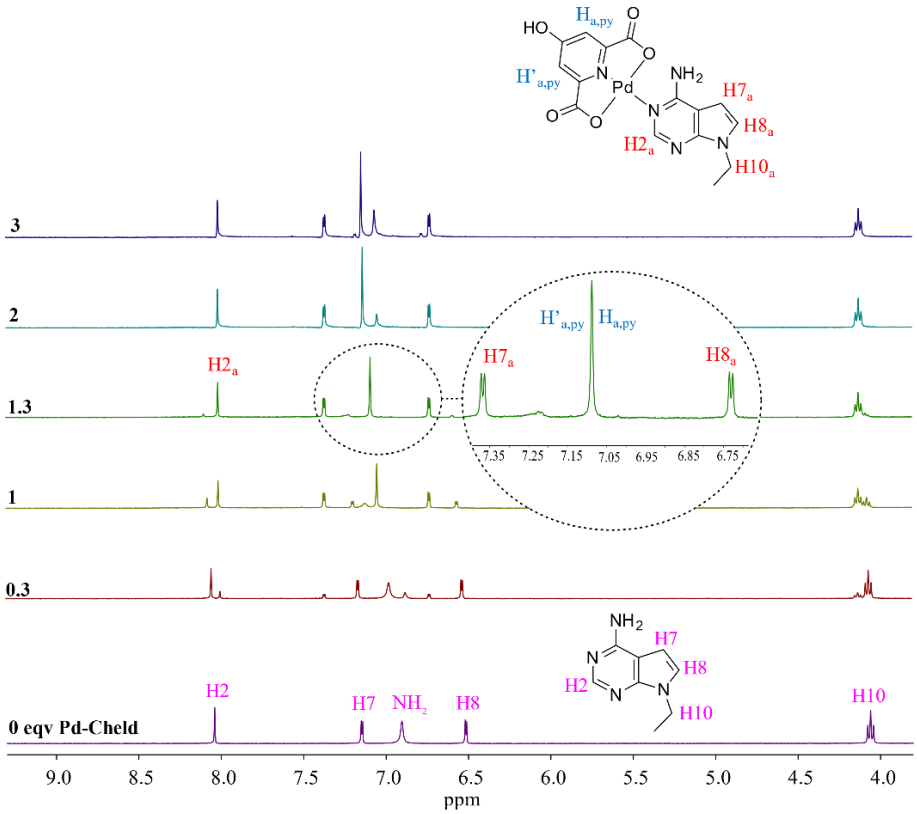

Figura 2.4: ^{1}H-RMN (400Mhz, DMSO-D$_6$). Espectros de la valoración de la nucleobase **pX** mediante la adición controlada del fragmento metálico **Pd-Cheld**, para obtener el complejo **[Pd(Cheld)(pX)]**. Círculo: ampliación de las señales aromáticas.

El espectro de ^{1}H-RMN de la base modificada **pX** libre (espectro inferior) muestra un singlete a 8.1 ppm correspondiente al protón H2, dos dobletes a 7.15 y 6.52 ppm de los protones H7 y H8, respectivamente, un singlete ancho a 6.85 ppm del grupo NH_2 y un triplete a 4.06 ppm correspondiente al grupo CH_2 (H10). A medida que se añaden cantidades crecientes de **Pd-Cheld** se observa como las señales iniciales se desplazan ligeramente. La estabilización de las variaciones se produce cuando se alcanzan los 1.0-1.3 equivalentes de **Pd-Cheld**, indicando la saturación de la interacción, lo que sugiere la formación del complejo **pX-Pd-Cheld**. En el espectro estabilizado la señal singlete H2 se ha desplazado a campo alto, 7.99 ppm (H2a), los dobletes H7 y H8 se han desplazado a campo bajo, 7.34 y 6.71 ppm H7a-H8a respectivamente y la señal correspondiente al grupo NH_2 tiende a desaparecer. Además, se observa la

aparición de una nueva señal singlete a 7.1 ppm correspondiente a los dos protones aromáticos H_{py} y H'_{py} del fragmento **Pd-Cheld**. Estas señales coinciden con la formación de una estructura donde **Pd-Cheld** se une a través de la posición N1 del ligando **pX**, para formar el compuesto de coordinación **[Pd(Cheld)(*N1*-pX)]**. Solo cuando se añade un exceso de **Pd-Cheld** (a partir de 1.7 eqv) aparece un singlete a 7.0 ppm, correspondiente a los protones H_{py} y H'_{py} del fragmento metálico libre.

En cambio, el espectro de valoración de ^{1}H-RMN para obtener el complejo **[Pd(Cheld)(eA)]** (Figura 2.5) muestra diferencias muy significativas con respecto al anterior. (espectro completo en Anexo-Figura 2).

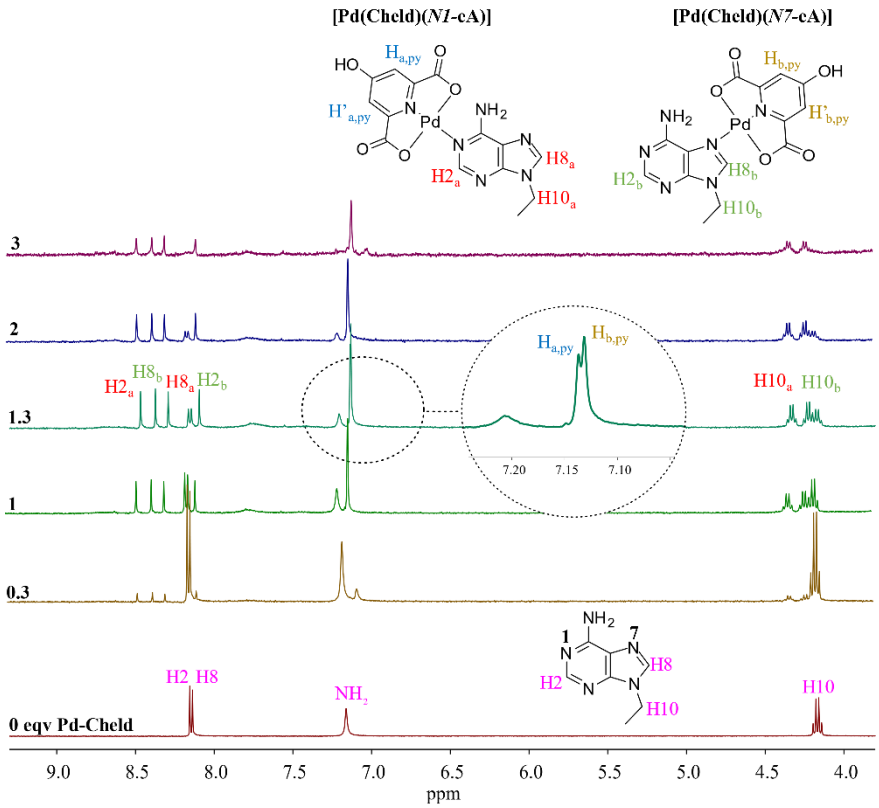

Figura 2.5: ^{1}H-RMN (400Mhz, DMSO-D_6). Espectros de la valoración de la nucleobase **eA** mediante la adicción controlada del fragmento metálico **Pd-Cheld**, para obtener el complejo **[Pd(Cheld)(eA)]**. Círculo: ampliación de las señales aromáticas. Las etiquetas numéricas sobre la estructura de **eA** indican la nomenclatura de cada nitrógeno.

En ausencia de **Pd-Cheld**, la nucleobase **eA** muestra dos señales singletes a 8.16 y 8.14 ppm correspondientes a los protones aromáticos H2 y H8, un singlete ancho a 7.17 ppm del grupo NH_2 y un multiplete a 4.16 ppm correspondiente a los protones H10. Durante la adición de los primeros 0.3 equivalentes de **Pd-Cheld**, se observa la aparición de un nuevo conjunto de señales comprendidas en la región entre 8.5-8.0 ppm. Estos resultados indican una interacción entre **Pd-Cheld** y **eA** más compleja que la mostrada anteriormente usando la base **pX**. Además, la aparición de cuatro señales sugiere la formación de isómeros en equilibrio que resultan de la unión de **Pd-Cheld** por los átomos N1 y N7 de la adenina. La estabilización del espectro ocurre con la adición de 1.0-1.3 equivalentes, a partir de los cuales no se observan cambios significativos. La Figura 2.5 muestra cuatro nuevos singletes, dos a 8.46 y 8.29 ppm que corresponden a los protones $H2_a$ y $H8_a$ del isómero **[Pd(Cheld)(*N1*-eA)]** y dos a 8.37 y 8.09 ppm que corresponden a los protones $H8_b$ y $H2_b$ del isómero **[Pd(Cheld)(*N7*-eA)]**. Esta asignación se ha realizado de acuerdo con los resultados publicados previamente para sistemas comparables.[3] En la zona del espectro en torno a 7.0 ppm se observa un singlete, sin embargo, al ampliar esta zona del espectro (círculo en Figura 2.5) se observan dos señales singlete con un desplazamiento químico casi similar, a 7.14 y 7.13 ppm, correspondiente a los protones aromáticos Ha_{py} y $H'a_{py}$ y Hb_{py} y $H'b_{py}$ del fragmento **Pd-Cheld** para los dos isómeros. De igual manera ocurre para el multiplete correspondiente al grupo CH_2, donde se observan dos conjuntos de señales a 4.33 y 4.22 ppm correspondientes para los protones en posición $H10_a$ y $H10_b$, de cada uno de los isómeros.

Los resultados de ^{1}H-RMN muestran que la presencia del fragmento metálico **Pd-Cheld** en disolución provoca un desplazamiento de las señales aromáticas de las nucleobases **pX** y **eA**, lo que indica la interacción entre ambas moléculas. Cómo se explicó anteriormente, **Pd-Cheld** es capaz de interaccionar con la adenina a través de los átomos endocíclicos N1 y N7, dando lugar a dos isómeros. Existen estudios previos de interacción entre el complejo metálico

$[Pd(dien)]^{2+}$ y derivados de adenina donde se observan comportamientos similares, apoyando los resultados que se presenta en este trabajo de tesis. [3,4]

Para confirmar la existencia de los complejos **[Pd(Cheld)(pX)]** y **[Pd(Cheld)(eA)]** en disolución, se realizaron estudios de espectrometría de masas (ESI-MS, modo positivo). Los espectros de masas obtenidos muestran señales m/z (z = +1) correspondientes a las especies protonadas **[Pd(Cheld)(eA)+H]**$^+$ y **[Pd(Cheld)(pX)+H]**$^+$ a 451.9992 Da y 464.0195 Da, respectivamente, confirmando inequívocamente la formación de ambas especies (teórico 450.9982 Da y 464.0186 Da, respectivamente).

Los siguientes estudios se enfocaron en el análisis de los compuestos en estado sólido. Para ello, se llevaron a cabo experimentos de cristalización de las especies **[Pd(Cheld)(eA)]** y **[Pd(Cheld)(pX)]**. Estos experimentos consistieron en la preparación de las dos disoluciones correspondientes; La primera contenía 0.062 mmol de **eA** disuelta en 1.5 mL de DMF, y la otra de 0.2 mmol de **pX** disuelta en CH_3CN:H_2O (15:15mL). A estas disoluciones se les añadió un equivalente de **Pd-Cheld**, previamente disuelto en DMF. Las disoluciones se dejaron evaporar lentamente, y transcurridos unos días se observó la aparición de pequeños cristales en forma de aguja y color amarillo aptos para estudios a partir de medidas de difracción de rayos X. Las medidas cristalográficas fueron resueltas usando métodos directos del software SHELXS-97.[5]

La especie **[Pd(Cheld)(pX)]** cristaliza en un sistema monoclínico ($p2_1/c$) y la estructura molecular revela la unión del fragmento **Pd-Cheld** al ligando **pX** mediante un enlace de coordinación Pd-N a través del átomo endocíclico N1. El compuesto de coordinación **[Pd(Cheld)(eA)]** también cristalizó en el sistema monocíclico ($p2_1/c$), y de manera similar, la estructura molecular muestra la unión del fragmento **Pd-Cheld** al ligando **eA** mediante un enlace de coordinación Pd-N a través del átomo endocíclico N1 (los datos cristaligráficos completos para ambas especies pueden ser consultados en Anexo-Tabla 1). Sin embargo, no se obtuvieron cristales que demostraran la unión de **Pd-Cheld** a

través del átomo N7 en este ligando. Es decir, sólo se obtuvo la estructura molecular del isómero **[Pd(Cheld)(*N1*-eA)]**. No obstante, con objeto de evaluar si todos los cristales obtenidos corresponden al mismo isómero, se llevó a cabo un estudio más exhaustivo de la muestra cristalizada **[Pd(Cheld)(eA)]** mediante medidas de difracción de rayos X en polvo (XRPD), molturando los cristales recolectados para asegurar una muestra homogénea. Los resultados obtenidos por XRPD mostraron un patrón de difracción igual al correspondiente para la especie **[Pd(Cheld)(*N1*-eA)]** estudiada por difracción en monocristal. La Figura 2.6 muestra el patrón de difracción de la medida experimental por XRPD y la correspondiente al monocristal, donde se aprecia una coincidencia de ambos espectros (línea gris). Estos datos confirmaron por tanto que la especie termodinámicamente más estable en estado sólido corresponde al isómero **[Pd(Cheld)(*N1*-eA)]**.[6] Este resultado puede explicase debido a la mayor basicidad del átomo N1 de la adenina, promoviendo una interacción más favorable de los iones de Pd^{II} a través de esta posición.[7]

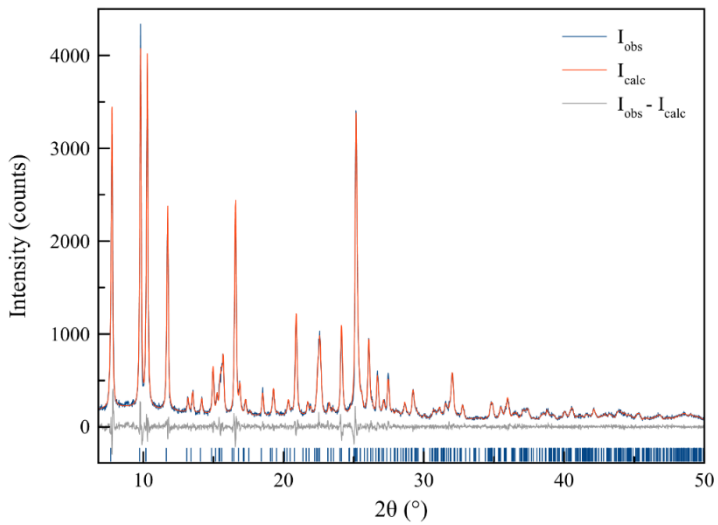

Figura 2.6: Representación gráfica del patrón de las medidas de difracción de rayos X en polvo (realizado con el método de Le Bail) y el calculado para el monocristal de la especie **[Pd(Cheld)(*N1*-eA)]**. Patrones Experimentales (azul), calculados (rojo), patrón de diferencia (gris). La posición de la reflexión de Bragg máxima está indicada con líneas azules. Rp= 0.062, Rwp= 0.082.

Para ambas estructuras **[Pd(Cheld)(*N1*-eA)]** (**eA-Pd-Cheld**) y **[Pd(Cheld)(*N1*-pX)]** (**pX-Pd-Cheld**) (Figura 2.7), el átomo de Pd^{II} adopta una geometría plana cuadrada trans-PdN2O2 y está unido al ligando mediante coordinación μ,κ^3-N10,O2,O4, mientras que las bases se unen a través de la posición N1 en la cara WCF. En ambos casos la distancia Pd1-N11 son comparables, con valores de 2.075 Å para Pd1-N11 en **pX-Pd-Cheld** y 2.04Å en **eA-Pd-Cheld**; mientras que las distancias Pd1-O31 presentan valores de 2.53 y 2.06 Å respectivamente (datos completos en Anexo-Tabla 2). La Figura 2.7 también muestra la formación de enlaces de hidrógeno intramoleculares del tipo WCF entre el grupo amino exocíclico de las bases con el grupo carboxilo del ligando que favorece una ordenación coplanar de las especies, observándose valores de distancia N16-O31 de 2.789 y 2.84 Å para **pX-Pd-Cheld** y **eA-Pd-Cheld.** Para la especie **pX-Pd-Cheld** también se observaron interacciones de tipo stacking entre los fragmentos metálicos **Pd-Cheld** adyacentes con una distancia Pd-Pd de 3.190 Å.

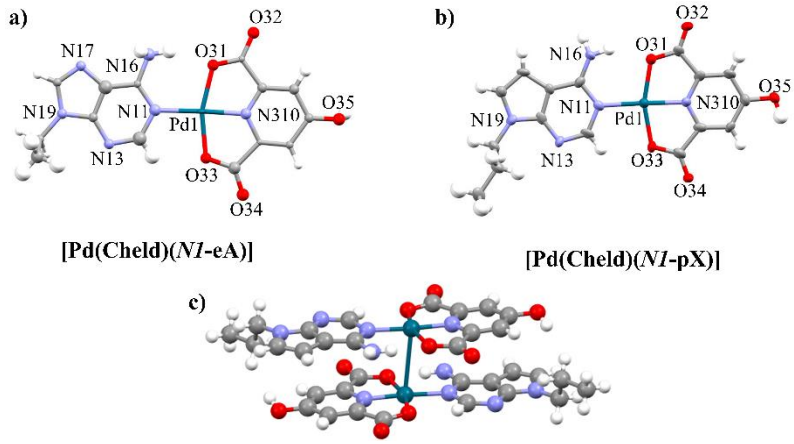

Figura 2.7: Estructura molecular de los complejos; a) **[Pd(Cheld)(*N1*-eA)]**. b) **[Pd(Cheld)(*N1*-pX)]**. c) interacciones de stacking entre los complejos **[Pd(Cheld)(*N1*-pX)]**. Colores de los átomos: Carbonos (Gris), Hidrógenos (blanco), nitrógenos (azul), paladio (turquesa). La numeración de las bases ha seguido la utilizada en los archivos cristalográficos.

Con objeto de estudiar si el isómero **[Pd(Cheld)(*N1*-eA)]** cristalizado existiría en disolución como única especie, se llevaron a cabo estudios en disolución de este cristal. Para ello, se disolvieron aproximadamente 2 mg de

la especie cristalina en DMSO-D_6 y se registraron medidas de ^{1}H-RMN. El espectro resultante reveló la presencia de los dos isómeros derivados de la unión de **Pd-Cheld** a los átomos N1 y N7 de la **eA**, en disolución (Figura 2.5). Este resultado demuestra que la especie termodinámicamente más estable en estado sólido tiene un comportamiento diferente en disolución, lo cual tendrá que ser tenido en cuenta para los siguientes estudios de interacción entre **Pd-Cheld** y hebras de ADN formadas por cadenas de 2'-deoxyadenosina.

2.1.c. Formación y caracterización de los híbridos supramoleculares [{Pd(Cheld)}$_{15}$(dA$_{15}$)] (**dA$_{15}$-Pd-Cheld**) y [{Pd(Cheld)}$_{15}$(dX$_{15}$)] (**dX$_{15}$-Pd-Cheld**).

Los resultados anteriores demostraron que existe una interacción entre el fragmento metálico **Pd-Cheld** y las nucleobases **eA** y **pX** libres. La formación de enlaces de hidrógeno de tipo WCF, la organización coplanar y las interacciones de tipo stacking vistas anteriormente, son también cualidades características en el emparejamiento de las nucleobases naturales del ADN. Por tanto, teniendo todo esto en cuenta, se llevó a cabo un estudio de la formación de los híbridos ADN-metal a partir de la formación de pares de bases mediados por Pd^{II} empleando homopolímeros de 2'-deoxyadenosina y/o 2'-deoxy-7-deaza-adenosina. Es de esperar que mediante el apilamiento de los fragmentos metálicos **Pd-Cheld** a lo largo de la hebra se obtenga un sistema análogo a una doble hebra natural donde los iones de Pd^{II} queden alojados en el eje central de la estructura. Investigaciones anteriores demostraron que el complejo metálico [Cu(mCheld)(H_2O)] no era capaz de interactuar de manera estable con homopolímeros de ADN, a pesar de formar especies discretas con las nucleobases libres.[8] Sin embargo, la presencia de iones de Pd^{II} en el fragmento **Pd-Cheld** da lugar a enlaces Pd-N más fuertes que las correspondientes Cu-N, y por tanto, se puede esperar la formación de híbridos de ADN-Pd más estables.

Con objeto de estudiar la formación de los híbridos ADN-Pd, en primer lugar, se evaluó la interacción entre el fragmento metálico **Pd-Cheld** y monohebras de ADN mediante medidas de Dicroísmo Circular (CD) (Figura 2.8). Para estos estudios se utilizaron ADN de cadena simple homotópica con quince unidades de 2-deoxyadenosina (**dA_{15}**) o 2'-deoxy-7-deazaadenosina (**dX_{15}**).

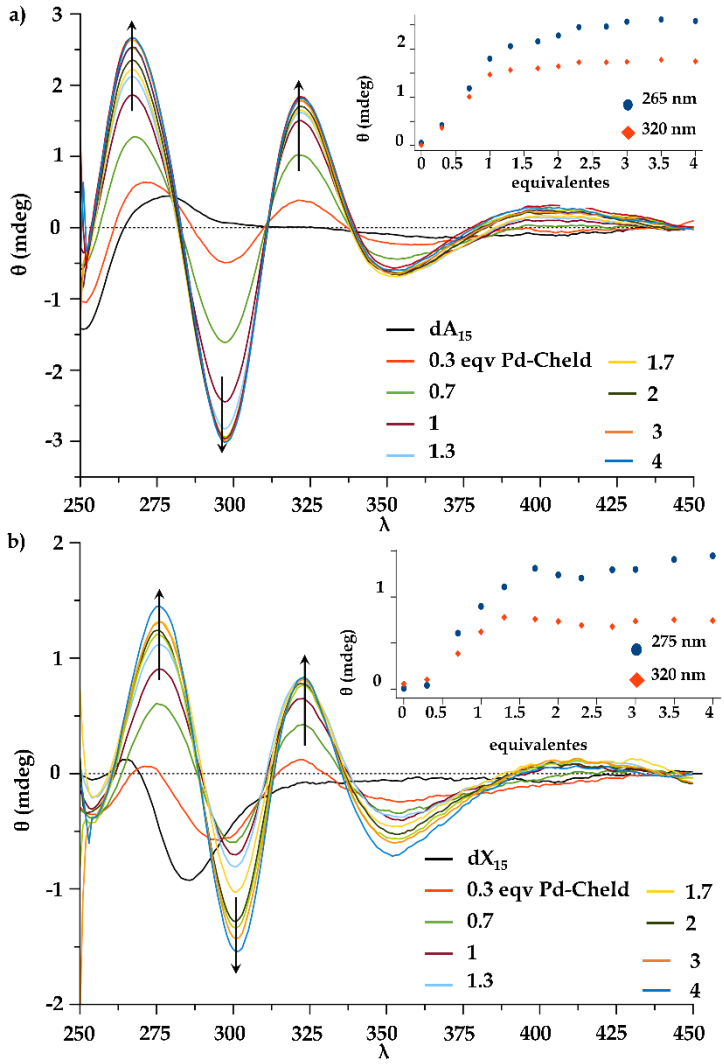

Figura 2.8: Espectros de CD para la valoración de; a) **dA_{15}** y b) **dX_{15}**, en presencia de cantidades crecientes de **Pd-Cheld**. Gráficas interiores: Variación de la elipticidad (θ) a 275 nm y 320 nm respecto a la cantidad de equivalentes de **Pd-Cheld** por base. Condiciones: 2 μM DNA, 0→60 μM **Pd-Cheld**, 100 mM $NaClO_4$, 5 mM MOPS (pH 6.8). Las flechas indican la dirección en los cambios de CD.

Inicialmente se valoró una disolución de **dA_{15}** y **dX_{15}** de 2 μM, 100 mM $NaClO_4$, 5 mM MOPS (pH 6.8), con cantidades crecientes del fragmento **Pd-Cheld** (500 μM en DMF) hasta alcanzar un total de tres equivalentes de **Pd-Cheld** por base. El espectro de CD para **dA_{15}** libre muestra una banda positiva a 279 nm mientras que el espectro para **dX_{15}** libre muestra una banda negativa con un mínimo a 286 nm (Figura 2.8). La diferencia entre ambas señales de CD para los oligonucleótidos libres se justifica por la modificación en la posición N7, que evita la formación de enlaces de hidrógeno por la cara Hoogsteen en el caso de **dX_{15}**, promoviendo diferentes formas de organización supramolecular.

En ambas situaciones, la incorporación gradual de cantidades crecientes de **Pd-Cheld** produjo cambios notables en los perfiles del espectro de CD. Estos cambios se reflejaron en la aparición marcada del efecto Cotton en las curvas, evidenciando así la interacción entre los oligonucleótidos y el fragmento metálico. Merece la pena destacar que las curvas de CD comienzan a ser muy parecidas para ambos sistemas tras la adición de los primeros 0.3 equivalentes de **Pd-Cheld** por base, siendo este efecto más evidente a partir de 1.0 – 1.3 equivalentes, que es el punto exacto donde las señales de CD se estabilizan. La saturación del sistema a aproximadamente 1 equivalente de Pd-Cheld/base demuestra la interacción de quince fragmentos **Pd-Cheld** por oligonucleótido, correspondiente a la cantidad de bases en las hebras de ADN.

Además de los cambios originados en la región del espectro de CD correspondiente a los oligonucleótidos (región entre 250 – 300 nm), se observan cambios en la región a longitudes de onda mayores de 300 nm, correspondientes a la aparición de señales inducidas (ICD). Este tipo de bandas se correlaciona con la región de absorción del fragmento **Pd-Cheld** (UV-Vis Anexo-Figura 3 y 4). Dado que los oligonucleótidos no muestran señal de CD por encima de 300 nm y el fragmento **Pd-Cheld** libre no exhibe señal de CD en todo el espectro, estas señales ICD representan una evidencia inequívoca de la interacción entre el fragmento metálico **Pd-Cheld** y las hebras simples de ADN. Esto se explica porque los oligonucleótidos unidos a **Pd-Cheld** inducen quiralidad en el

fragmento metálico, lo que resulta en la generación de la señal de ICD, la cual se correlaciona con la región de absorción de dicho fragmento.

En ambos casos aparecen dos nuevos máximos a 322 y 404 nm para **dA_{15}-Pd-Cheld**, y a 323 y 412 nm para **dX_{15}-Pd-Cheld** y dos mínimos a 269 - 322 nm y 301 - 353 nm respectivamente. Además, en la representación de los cambios de elipticidad de estas ICD frente a los equivalentes del fragmento metálico se observa como estos se estabilizan a partir de 1.0-1.3 equivalentes, indicando la interacción de un **Pd-Cheld** por cada base.

Estos resultados ponen de manifiesto la formación de sistemas de tipo **dA_{15}-Pd-Cheld** y **dX_{15}-Pd-Cheld** con estructuras de hélice, similar a la del ADN de doble hebra.

Un análisis comparativo de los perfiles de CD para estos experimentos evidencia las similitudes entre ambos. Este hecho revela que los sistemas **dA_{15}-Pd-Cheld** y **dX_{15}-Pd-Cheld** poseen una conformación estructural similar. Los perfiles de las curvas de CD son típicos para conformaciones de dobles hebras dextrógiras de tipo B.[9] Además, el hecho de que el fragmento **Pd-Cheld** solo pueda interaccionar con **dX_{15}** a través de la posición N1 de sus bases, confirma que existe un modo de interacción similar cuando se utiliza **dA_{15}**. Es decir, el fragmento **Pd-Cheld** interacciona preferentemente a través de la posición N1 de las adeninas a pesar de que esta tenga también la posición N7 disponible. Los resultados obtenidos en disolución para **dA_{15}** difieren de los observados en los experimentos de ^{1}H-RMN realizados para la nucleobase libre **eA**, donde se evidenció un equilibrio de unión de **Pd-Cheld** por los átomos N1 y N7. Sin embargo, al emplear hebras de **dA_{15}** la unión por N1 está más favorecida, lo cual puede explicarse por la estabilización de este modo de interacción debido a la presencia de interacciones de apilamiento de los fragmentos **Pd-Cheld** unidos por la cara WCF de las nucleobases, imitando la conformación que ocurre en las dobles hebras de ADN natural.

Para confirmar estos hechos se repitieron las medidas de CD usando **dA_{15}** a pH 4.5. El cambio hacia un pH más ácido provoca que las bases de adenina se protonen en la posición N1, desfavoreciendo la unión del fragmento **Pd-Cheld** a través de este átomo. En estas condiciones, las hebras de poly(2'-deoxyadenosina) forman una doble hélice a través de puentes de hidrógeno generados por los átomos N7-A (que actúa como aceptor de H) de una hebra y los grupos A-NH_2 de otra la hebra (que actúa como donador de H). [10–13]

El perfil de CD observado en estas condiciones difiere notablemente del registrado previamente a pH neutro (Figura 2.9).

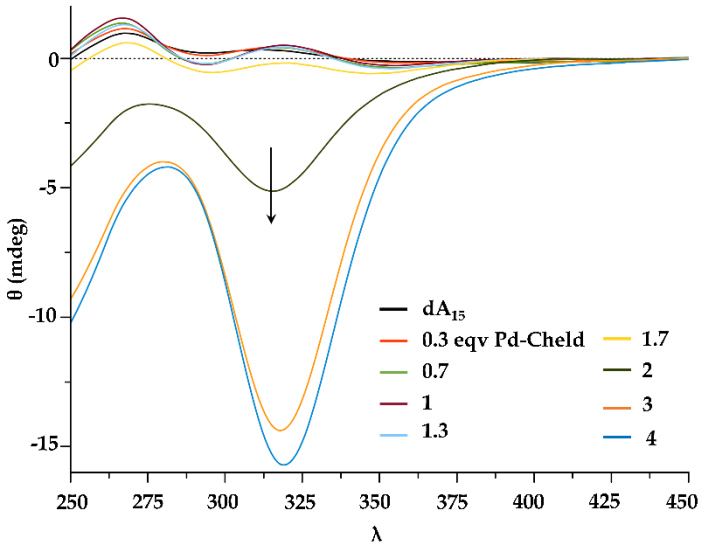

Figura 2.9 Espectros de CD a pH 4.5 para la valoración de **dA_{15}** en presencia de cantidades crecientes de **Pd-Cheld**. Condiciones: 2 µM DNA, 0→60 µM **Pd-Cheld**, 100 mM $NaClO_4$, 5 mM MOPS (pH 4.5). Las flechas indican la dirección en los cambios de CD.

En este caso, la adición controlada de **Pd-Cheld** a la disolución de **dA_{15}** resulta en una marcada reducción de la intensidad del espectro de CD y en una alteración del perfil de la curva. El máximo original a 279 nm disminuye significativamente en intensidad y se acompaña de un ligero desplazamiento hacia los 280 nm. Además, se observa la aparición de una banda ICD a 320 nm con valores negativos muy intensos, lo que sugiere la interacción de **Pd-Cheld** al oligonucleótido. Estos resultados indican que hay interacción entre **Pd-**

Cheld y **dA_{15}**, pero que debe ocurrir a través de una posición distinta al átomo N1 protonado, y por tanto, muy probablemente sucede a través de la posición N7 (descartando N3 por impedimentos estéricos).

Hay que destacar la importancia de estos resultados, ya que evidencia que es posible la formación de híbridos de tipo **[Pd(Cheld)(*N1*-dA_{15})]** a pH 7 de manera espontánea sin la necesidad de emplear nucleobases modificadas como la 7-deaza-adenina (**X)**.

Los hallazgos descritos anteriormente sugieren la formación de una estructura de doble hélice para los sistemas **dA_{15}-Pd-Cheld** y **dX_{15}-Pd-Cheld**. De acuerdo a los resultados obtenidos, estas estructuras estarían compuestas por pares de bases mediados por iones de Pd^{II}, donde la base y el ligando adoptan una conformación coplanar, estabilizada por la formación de puentes de hidrógeno (observados en la estructura molecular de los complejos **[Pd(Cheld)(eA)]** y **[Pd(Cheld)(pX)])**, y permitiendo la formación de interacciones de apilamiento (stacking) a lo largo de la estructura. Finalmente, para demostrar la formación de las interacciones de apilamento, se llevaron a cabo estudios de intercalación con bromuro de etidio (EB), mediante el uso de espectroscopía de fluorescencia. El EB es una molécula plana que presenta poca fluorescencia cuando se encuentra libre en disolución rodeado de moléculas de agua. Sin embargo, tiene la capacidad de intercalarse entre las bases del ADN, provocando que se encuentre en un ambiente más hidrofóbico que da lugar a un aumento de su señal de fluorescencia, muy característica a 620 nm. [14]

Como muestra la Figura 2.10, cuando se excita una disolución de **dA_{15}** y **dX_{15}** que contiene EB con una longitud de onda de 525 nm se observan señales de fluorescencia débiles a 625 nm. Esto es debido a una pobre intercalación de las moléculas de EB entre las bases de una hebra simple. Sin embargo, cuando añadimos un equivalente de **Pd-Cheld** a dichas disoluciones se produce un aumento significativo en la intensidad de la señal.

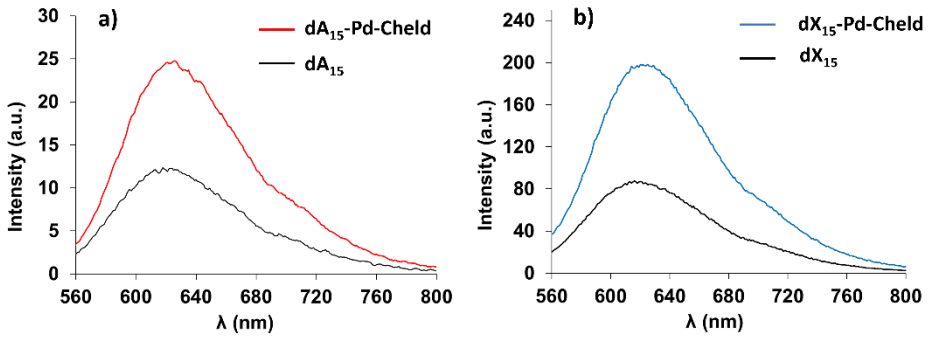

Figura 2.10 Espectros de fluorescencia registrados para a) **EB-[Pd(Cheld)(*N1*-dA$_{15}$)]** y b) **EB-[Pd(Cheld)(*N1*-dX$_{15}$)].** Condiciones: 2 µM dA$_{15}$, 30 µM EB, 30 µM **Pd-Cheld**, 100 mM $NaClO_4$, 5 mM MOPS (pH 6.8).

En ambos casos, esto se puede explicar por la intercalación más efectiva de las moléculas de EB entre los pares de mediados por iones Pd^{II} de las dobles hebras, con mayor capacidad de formar interacciones de stacking que las nucleobases libres de la cadena simple de ADN. Por tanto, los resultados son consistentes con la formación de una estructura de doble hebra donde los pares de bases están estabilizados mediante la formación de interacciones de apilamiento que se establecen entre ellos.

A continuación, se llevaron a cabo medidas de espectrometría de masas (ESI-MS, modo negativo) para confirmar la existencia de los híbridos ADN-Pd en fase acuosa (Figura 2.11). Para esto se prepararon disoluciones de 50 µM de **dA$_{15}$** y 50 µM **dX$_{15}$** a las que se les añadió un equivalente/base de **Pd-Cheld**. Los resultados para **dA$_{15}$** (4636.4 Da) mostraron especies que contenían entre 9 y 15 unidades del fragmento metálico **Pd-Cheld** (287.5 Da) con distinta carga (Z = -4, -5, -6), siendo el pico mayoritario el correspondiente al híbrido **dA$_{15}$-Pd-Cheld** (1488.0 Da, Z = -6) (Tabla 2.1).

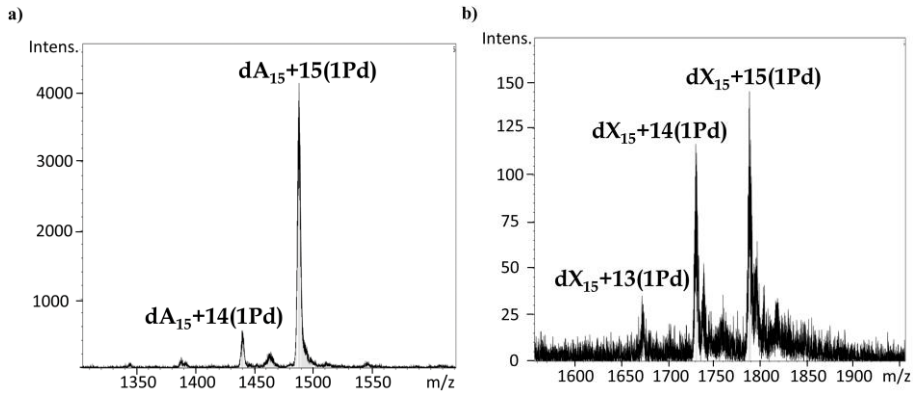

Figura 2.11: Espectro de espectrometría de masas (ESI-MS modo positivo) obtenido para los sistemas; a) **dA$_{15}$-(Pd-Cheld)$_n$** (n = 14, 15) (Z = -6) . b) **dX$_{15}$-(Pd-Cheld)$_n$** (n = 13, 14, 15) (Z = -5). Las etiquetas **1Pd**, hacen referencia el fragmento metálico **Pd-Cheld**.

Tabla 2.1: Masa/carga (m/z) para los diferentes estados de carga (Z) de; a) **dA$_{15}$-(Pd-Cheld)$_n$**. b) **dX$_{15}$-(Pd-Cheld)$_n$**.

a)	**n = 13**	**14**	**15**	**16**
-4	2088.8	2160.7	2232.5	2304.4
-5	1670.8	1728.3	1785.8	1843.3
-6	1392.2	1440.1	1488.0	1535.9

b)	**n = 13**	**14**	**15**	**16**
-4	2092.5	2164.4	2236.2	2308.1
-5	1673.8	1731.1	1788.8	1846.3
-6	1394,7	1442,6	149',5	1538,4

Del mismo modo, los resultados para **dX$_{15}$** (4621 Da) mostraron especies que contenían entre 12-16 unidades de **Pd-Cheld** siendo el pico mayoritario el correspondiente a **dX$_{15}$-(Pd-Cheld)$_{15}$** (1788.68 Da, Z= -6) (Tabla 2.1b). Estos datos confirman la formación de los híbridos supramoleculares descritos y el éxito de la estrategia propuesta en este trabajo de investigación para obtener híbridos ADN-Pd controlando el tamaño de la hebra simple empleada (en Anexo-Tabla 3 pueden consultarse todas las especies obtenidas).

Una vez se ha confirmada la formación de los híbridos **dA_{15}-Pd-Cheld** y **dX_{15}-Pd-Cheld** se llevaron a cabo experiencias que permitieran elucidar detalles estructurales de dichos sistemas. Para ello se realizaron estudios en disolución mediante medidas de dispersión de rayos X a ángulos pequeños (SAXS) y estudios teóricos empleando cálculos computacionales. También se realizaron estudios en estado sólido mediante experimentos de cristalización, aunque como se verá a lo largo del Capítulo 5, los resultados no fueron satisfactorios.

En primer lugar, se realizaron medidas de SAXS, que registran la dispersión de rayos X que inciden en las partículas de una muestra, y permite obtener información sobre las formas, tamaños y organizaciones moleculares, lo que la hace ideal para estudiar proteínas, ácidos nucleicos u otros componentes biológicos en condiciones fisiológicas. No obstante, este experimento solo se realizó para el sistema **dA_{15}-Pd-Cheld** debido a que se necesita una disolución muy concentrada de la muestra (> 1 mM), y obtener una disolución concentrada de la hebra modificada **dX_{15}** resulta muy costoso. Las medidas de SAXS se registraron para disoluciones de **dA_{15}** libre (1 mM) y para el híbrido **dA_{15}-Pd-Cheld** (15 mM), en presencia de un buffer de 5 mM MOPS a pH 6.8. En ambos casos, los resultados muestran una curva con un perfil que se ajusta a una morfología molecular cilíndrica esperada (Figura 2.12).

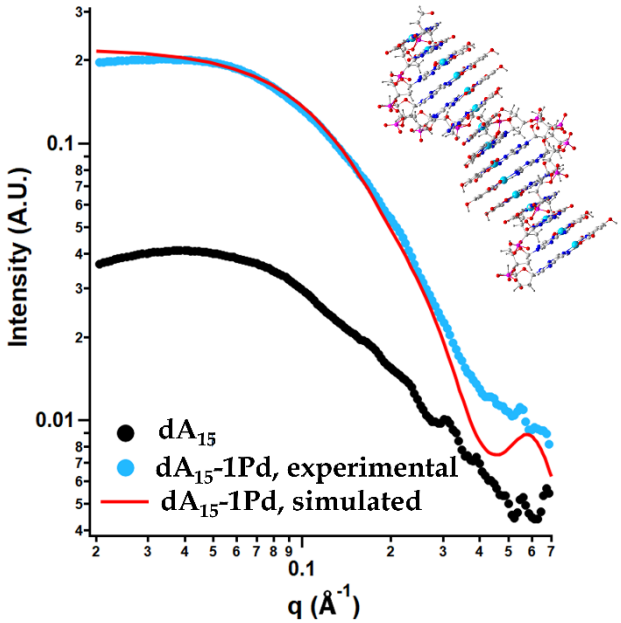

Figura 2.12: Espectro SAXS para: a) **dA15** (negro), **dA15-Pd-Cheld** sintetizado (turquesa) y simulado (rojo) a pH 6.8. Para mayor claridad, la etiqueta 1Pd hace referencia al fragmento metálico **Pd-Cheld**. Condiciones: 1mM **dA15** / **dA15-Pd-Cheld** 5 mM MOPS (pH6.8).

La curva de SAXS del oligonucleótido libre **dA15** (Figura 2.12, curva negra) experimenta cambios evidentes en presencia de un equivalente de **Pd-Cheld** por adenina. En concreto se observa un incremento de la intensidad de la señal y un desplazamiento de la región de Guiner a valores de *q* más bajos, mostrando una pendiente más pronunciada. Esta variación de intensidad es el resultado de la mayor densidad electrónica del sistema cuando se unen los fragmentos de **Pd-Cheld**. Además, a pH 6.8 las curvas para ambos experimentos muestran perfiles que coinciden con la presencia de especies monodispersas, basándonos en el valor de la pendiente a partir de q = 0.06Å^{-1}. El leve descenso de intensidad observado para valores de *q* más bajos es debido a la configuración del instrumento. Esto ocurre cuando las muestras presentan una dispersión débil o una baja concentración, aunque la región de la curva no se tiene en cuenta a la hora de realizar los ajustes.

La curva experimental de SAXS obtenida para **dA15-Pd-Cheld** se comparó con la teórica calculada para un sistema que presentara una estructura de doble hebra dextrógira de conformación B donde los fragmentos de **Pd-Cheld** se

unen a adenina a través de la posición N1. Como muestra la Figura 2.12, la curva experimental (curva azul), se ajusta perfectamente a la curva teórica obtenida para un sistema análogo simulado (cuva roja).

La longitud experimental obtenida a partir de los datos de SAXS, tanto para **dA_{15}** como para el híbrido **dA_{15}-Pd-Cheld,** fue de ≈ 42 Å, muy similar al valor teórico del modelo utilizado de ≈ 36 Å. Sin embargo, el valor experimental del radio cambió notablemente pasando de 5.0 Å a 7.5 Å para **dA_{15}** y **dA_{15}-Pd-Cheld**, respectivamente, lo que es consistente con la coordinación de los ligandos **Pd-Cheld** a la hebra simple de ADN.

Aunque estos resultados indican que el tamaño y forma de los sistemas son los esperados, se llevó a cabo un experimento control a pH 4.3, como ya se realizó en dicroísmo circular. Con esta experiencia se pretendió descartar la posibilidad de que el fragmento **Pd-Cheld** interaccione por el átomo N7 de las adeninas, ya que a pH ácido el átomo N1 se encuentra protonado. Como muestra la Figura 2.13, el espectro de SAXS en estas nuevas condiciones es completamente diferente al mostrado en la experiencia anterior.

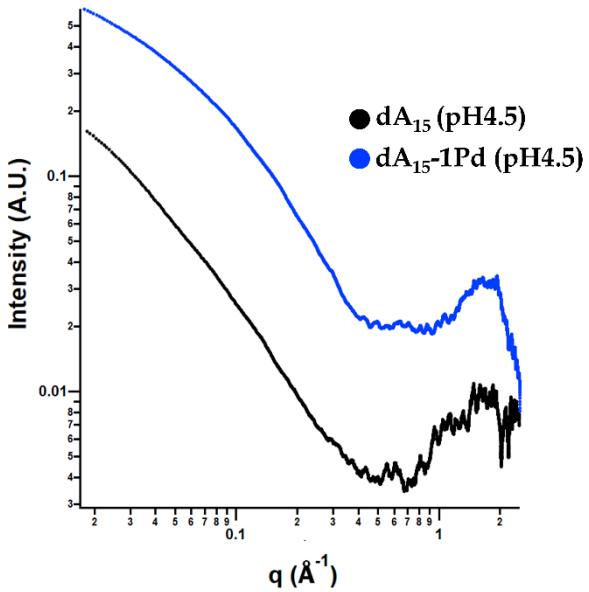

Figura 2.13: Espectro SAXS para: **dA_{15}** y **dA_{15}-Pd-Cheld**. 1mM **dA_{15}** / **dA_{15}-Pd-Cheld** 5 mM MOPS (pH 4.5).

El perfil de la curva correspondiente a **dA_{15}** muestra una pendiente más pronunciada, que es consistente con la formación de estructuras cilíndricas de mayor longitud, donde se obtuvieron un valor de radio de ≈ 12 Å y una longitud de ≈ 3200 Å. Estos resultados coinciden con la formación de estructuras de poliadenina de doble hélice a pH ácido, previamente descritas en bibliografía.[10–12] Cuando se añadió un equivalente de **Pd-Cheld** se observaron valores de diámetro parecido a los experimentos a pH 6.8, sin embargo, la longitud de las moléculas fue de ≈ 107 Å. Presumiblemente, esto puede deberse a la unión entre **Pd-Cheld** y la adenina a través del átomo N7 (la única disponible a pH 4.3 debido a la protonación del átomo N1) dando lugar a nuevas especies en disolución.

En un esfuerzo por entender de manera más precisa como se ordenan las moléculas implicadas en los sistemas híbridos ADN-metal, se llevaron a cabo cálculos computacionales *ab-initio* para fragmentos de doce pares de bases de **dA_{12}-Pd-Cheld** y **dX_{12}-Pd-Cheld.** El uso de hebras más cortas responde a la necesidad de acortar el tiempo para realizar los cálculos computacionales y a su vez proveer de la longitud mínima para completar un giro de la hélice.

La estructura de partida se diseñó de la siguiente forma. En primer lugar, se estableció la geometría para los sistemas de hebra simple **dA_{12}** y **dX_{12}** como se reporta en bibliografía a pH neutro. [13,15] La naturaleza aniónica de los grupos fosfatos del ADN se trató con cationes de Na^{1}. Además, con objeto de simular un medio acuoso se colocaron moléculas de agua cerca de los átomos donares y aceptores de enlaces de hidrógeno de la estructura. A continuación, se añadieron los fragmentos metálicos **Pd-Cheld** a lo largo de la hebra simple de ADN unidos a la posición N1 de las adeninas manteniendo una organización co-planar.

La geometría *ab-initio* optimizada para ambos sistemas, **dA_{12}-Pd-Cheld** y **dX_{12}-Pd-Cheld** reveló resultados en consonancia con los resultados previos. Ambas estructuras están formadas por hélices dextrógiras que contienen pares de bases continuos de tipo **(*N1*-A)-Pd-Cheld** imitando la organización de una

doble hebra de ADN. Estos pares de bases forman puentes de hidrógeno WCF intramoleculares e interacciones de tipo stacking. Los átomos de Pd^{II} se encuentran localizados a lo largo del eje helicoidal en el centro de los pares de bases metal-adenina, con una distancia Pd-N de 3.447-3.765 Å y 3.109-3.819 Å para **dA_{12}-Pd-Cheld** y **dX_{12}-Pd-Cheld**, respectivamente (los datos completos pueden ser consultados en Anexo-Tabla 4). De esta manera, se obtiene una matriz unidimensional e ininterrumpida de átomos de paladio a lo largo de toda la estructura (los átomos de paladio de cada uno de los extremos han sido excluidos debido a los efectos de borde). La Figura 2.14, muestra dos representaciones de la geometría optimizada para **dA_{12}-Pd-Cheld**, a la izquierda se muestra la organización coplanar de los fragmentos metálicos y a la derecha la localización de los iones metálicos ordenados a lo largo de la hebra.

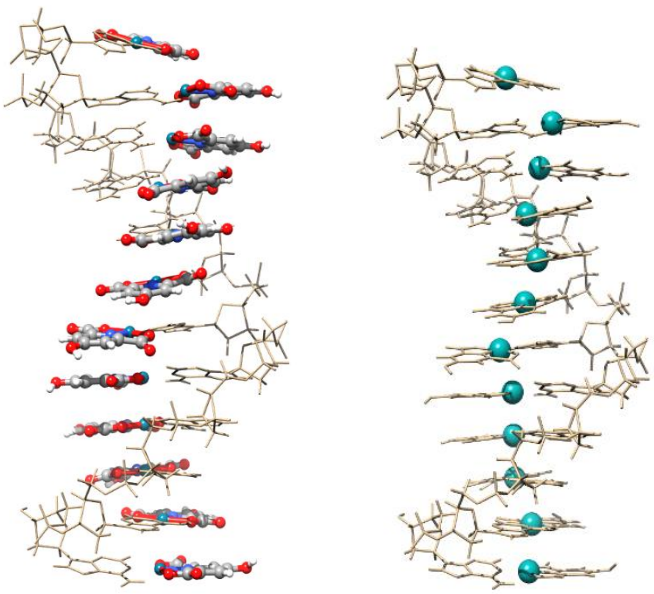

Figura 2.14: Geometría optimizada mediante DFT para el híbrido [**Pd(Cheld)(*N1*-dA_{12})].** A la izquierda se muestra, con esferas de colores, la organización de los fragmentos metálicos **Pd-Cheld** a lo largo de la hebra simple. A la Derecha se muestra, con esferas turquesas, la posición de los iones Pd^{II} a lo largo de la hebra simple.[1]

Todos estos resultados permiten confirmar que se ha desarrollado un método de tipo bottom-up para obtener sistemas híbridos ADN-Pd mediante un proceso de autoensamblaje molecular entre hebras simple de **dA_{15}**, **dX_{15}** y el fragmento metálico **Pd-Cheld** y a través de pares de bases mediados por metales. Como se ha demostrado, estas estructuras quedan además estabilizadas mediante puentes de hidrógeno WCF e interacciones de stacking imitando la organización de una doble hebra natural. Por otro lado, la estructura final es capaz de contener una matriz unidimensional de Pd^{II} localizada en el centro de la hélice cuyo número de unidades queda controlada por la cantidad de bases que contenga la hebra de ADN.

2.2. Estudios con derivados de citosina.

En este apartado describen y discuten los resultados obtenidos en el desarrollo de híbridos ADN-Pd empleando oligonucleótidos con quince unidades de citosina (**dC_{15}**) y el complejo metálico **[Pd(Aqa)(DMSO)]** (**DMSO-Pd-Aqa**) derivado del ácido 8-amino-4-hidroxiquinolina-2-carboxílico (**Aqa**). El fragmento metálico **Pd-Aqa** ha sido diseñado para que incorpore en su estructura grupos funcionales (grupos amino y carboxilo) que le permitan unirse complementariamente con la citosina mediante la formación de puentes de hidrógeno y un enlace de coordinación con el nitrógeno citosina-N3 (Figura 2.15). A continuación, se describirá la síntesis del complejo **DMSO-Pd-Aqa**, los estudios interacción con la nucleobase modelo 1-metil-citosina (**mC**), y finalmente los estudios con el oligonucleótido **dC_{15}** que dan lugar a la formación del híbrido **dC_{15}-Pd-Aqa**.

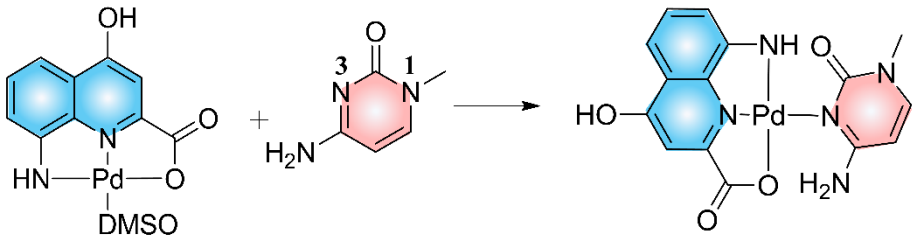

DMSO-Pd-Aqa **mC** **mC-Pd-Aqa**

Figura 2.15: Reacción entre el complejo metálico **DMSO-Pd-Aqa** y la nucleobase modelo **mC,** para obtener el complejo **mC-Pd-Aqa.** Las etiquetas numéricas sobre la estructura de **mC** hacen referencia a la nomenclatura de cada nitrógeno.

2.2.a. Síntesis y caracterización del compuesto de coordinación [Pd(Aqa)(DMSO)] (**DMSO-Pd-Aqa**).

En primer lugar, el ligando **Aqa** fue sintetizado y caracterizado siguiendo una ruta sintética previamente descrita en bibliografía (procedimiento completo en Sección 2.5 y espectro en Anexo-Figura 6).[16] A continuación, se llevó a cabo la síntesis del complejo **DMSO-Pd-Aqa** mediante la adición de un equivalente de $Pd(NO_3)_2$ a una disolución de **Aqa** (sección 2.5.1), cuya reacción se siguió mediante medidas de ^{1}H-RMN (Figura 2.16) (espectro completo en Anexo-Figura 7). El espectro de para el ligando **Aqa** libre muestra un triplete a 7.29 ppm, un doblete a 7.24 ppm, un singlete a 7.25 y un doblete a 6.86 ppm correspondientes a los protones H6, H5, H3 y H7 respectivamente. Tras la adición de un equivalente de $Pd(NO_3)_2$ se observa un desplazamiento de las señales a campo bajo, lo que indica la coordinación del Pd^{II} al ligando **Aqa**. El espectro final muestra la aparición de un singlete ancho a 8.29 ppm correspondiente al grupo NH, dos dobletes a 8.07 y 7.84 ppm, un triplete a 7.77 ppm y un singlete a 7.08 ppm correspondientes a los protones H5, H7, H6 y H3 respectivamente.

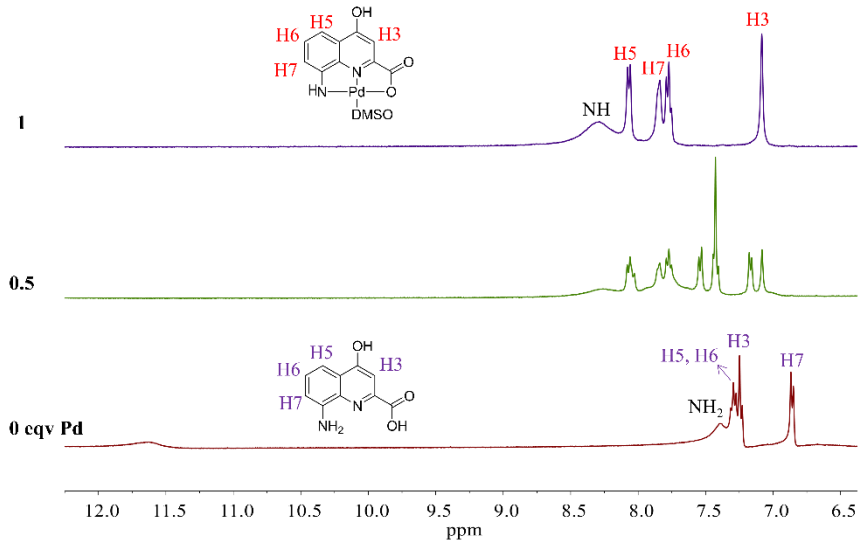

Figura 2.16: ^{1}H-RMN (400Mhz, DMSO-D_6) de la reacción entre **Aqa** y cantidades crecientes de $Pd(NO_3)_2$, hasta alcanzar un equivalente, para obtener el complejo **DMSO-Pd-Aqa**.

Para confirmar la existencia del complejo **[Pd(Aqa)(DMSO)]** en disolución, se realizaron estudios de espectrometría de masas (ESI-MS, modo positivo). Los espectros de masas obtenidos muestran señales m/z (z = +1) correspondientes a la especie protonada **[Pd(Aqa)(DMSO)+H]**$^{+}$ a 386.9682 Da, confirmando la formación del complejo (teórico 385,9553 Da) (espectro completo en Anexo-Figura 9).

Se realizaron numerosos intentos por obtener estructuras cristalinas que nos permitieran caracterizar el complejo **DMSO-Pd-Aqa** en fase sólida, aunque desafortunadamente los resultaos no fueron satisfactorios. Actualmente, se continúan realizando numerosos esfuerzos en este sentido.

2.2.b. Síntesis y caracterización de compuestos de coordinación con derivados de citosina; [Pd(Aqa)(mC)] (**mC-Pd-Aqa**).

Posteriormente se llevó a cabo la preparación y caracterización del complejo **[Pd(Aqa)(mC)]** (**mC-Pd-Aqa**) mediante la reacción entre el complejo metálico **DMSO-Pd-Aqa** y la nucleobase modificada 1-metilcitosina (**mC**) (sección 2.5.1). La reacción se estudió mediante ^{1}H-RMN añadiendo cantidades crecientes de **DMSO-Pd-Aqa** hasta alcanzar un equivalente (Figura 2.17) espectro completo en Anexo-Figura 8)..

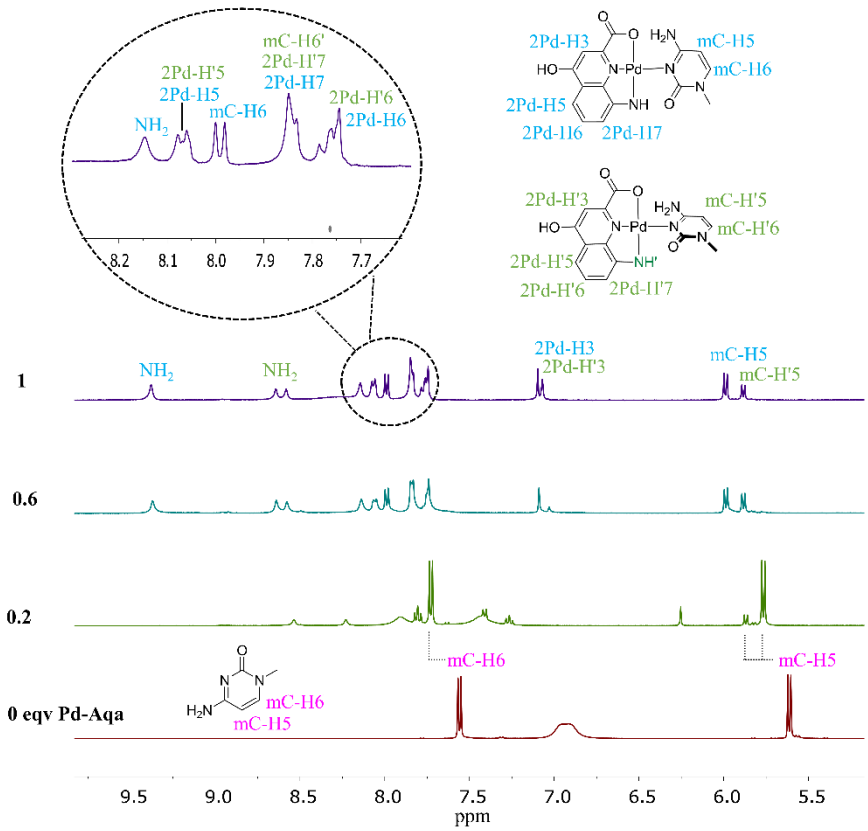

Figura 2.17: ^{1}H-RMN (400Mhz, DMSO-D$_6$) de la reacción entre la nucleobase modificada **mC** y el complejo metálico **DMSO-Pd-Aqa** para obtener el complejo **[Pd(Aqa)(mC)]**.

El espectro para **mC** libre muestra dos dobletes a 7.58 y 5.6 ppm correspondientes a los protones H6 y H5, respectivamente, y un singlete ancho

a 6.95 ppm perteneciente al grupo amino. Al añadir los primeros 0.2 equivalentes de **Pd-Aqa**, se observa un cambio significativo en las señales correspondientes a H6 y H5. El doblete para H6 se desplaza a campo bajo hasta 7.97 ppm, mientras que aparecen dos señales dobletes a campo bajo para H5 a 5.87-5.76 ppm. Esto indica que a pesar de la poca cantidad del fragmento metálico **Pd-Aqa**, existe una tendencia elevada entre las dos moléculas a reaccionar. Sin embargo, los cambios más importantes se observan en presencia de 1 equivalente de **Pd-Aqa** en el medio. Como muestra la Figura 2.17, el doblete a 5.6 ppm H5 de **mC** libre se desdobla en dos dobletes a campo bajo a 6.0 y 5.8 ppm, y el doblete perteneciente a H6 de **mC** libre se desplaza a campo bajo, hasta 8.0 ppm, no observándose a priori el mismo comportamiento que H5. Se observa además la aparición de nuevas señales correspondientes al fragmento **Pd-Aqa**, un doblete a 8.06 ppm de 2Pd-H5, otro doblete a 7.84 ppm de 2Pd-H7, un triplete a 7.75 ppm de 2Pd-H6 y dos singletes a 7.05 ppm correspondientes al protón 2Pd-H3. Además, se muestran cuatro señales a 9.4, 8.6, 8.5 y 8.05 ppm que no pertenecen a ninguna de las especies libres.

La presencia de dos dobletes para H5 de **mC**, y dos singletes para 2Pd-H3 de **Pd-Aqa** sugieren la formación de dos estructuras en equilibrio. Este hecho se puede explicar por la rotación de ambas unidades a través del enlace de coordinación Pd-N3(**mC**), provocando la coexistencia de dos conformaciones diferentes para **mC**-**Pd-Aqa**, y por tanto el desdoblamiento de señales. En una conformación el fragmento **Pd-Aqa** y la **mC** se disponen de manera coplanar, dando lugar a la formación de enlaces de hidrógeno intramoleculares entre los grupos carboxilo y amino, y por tanto aumentando su estabilidad. En la otra conformación ambas unidades se disponen fuera del mismo plano, despareciendo los enlaces de hidrógeno.

Por otra parte, los singletes entre 9.4 - 8.05 ppm deben pertenecer a los grupos NH_2 y NH de ambas moléculas, aunque con la información que aporta el espectro 1D resulta complejo discernir a quien pertenece cada señal.

Para obtener más información sobre la existencia de las diferentes conformaciones, se registró el espectro ^{1}H-RMN a temperatura variable. Este experimento permite estudiar la existencia de dos conformaciones derivadas de la rotación del enlace Pd-N3(**mC**). El espectro de ^{1}H-RMN (Figura 2.18), muestra como algunas señales convergen con el aumento de la temperatura hasta los 100ºC. Concretamente se observa como los cuatro singletes entre 9.4 - 8.05 ppm confluyen en una señal ancha a 8.30 ppm, los dos dobletes de H5 y los dos singletes para H3a convergen en una única señal y el resto de las señales se definen. Esto indica que el aumento de la temperatura provoca una rápida rotación a través del enlace Pd-N3(**mC**), por lo que no se forman dos conformaciones bien diferenciadas como sí ocurre a temperatura ambiente. Por otra parte, el singlete ancho a 8.30 ppm debe pertenecer al grupo NH coordinado a Pd y no al grupo NH_2. Esto es debido a que el grupo amino participa en la formación de puentes de hidrógeno con los grupos carboxilo de **Pd-Aqa** a temperatura ambiente. Dicha interacción desaparece con temperaturas elevadas debido a la rápida rotación del enlace Pd-N3(**mC**). Finalmente, el proceso de calentamiento es reversible, cuando la muestra vuelve a temperatura ambiente se observan las señales originales que corresponden a la existencia de los dos isómeros.

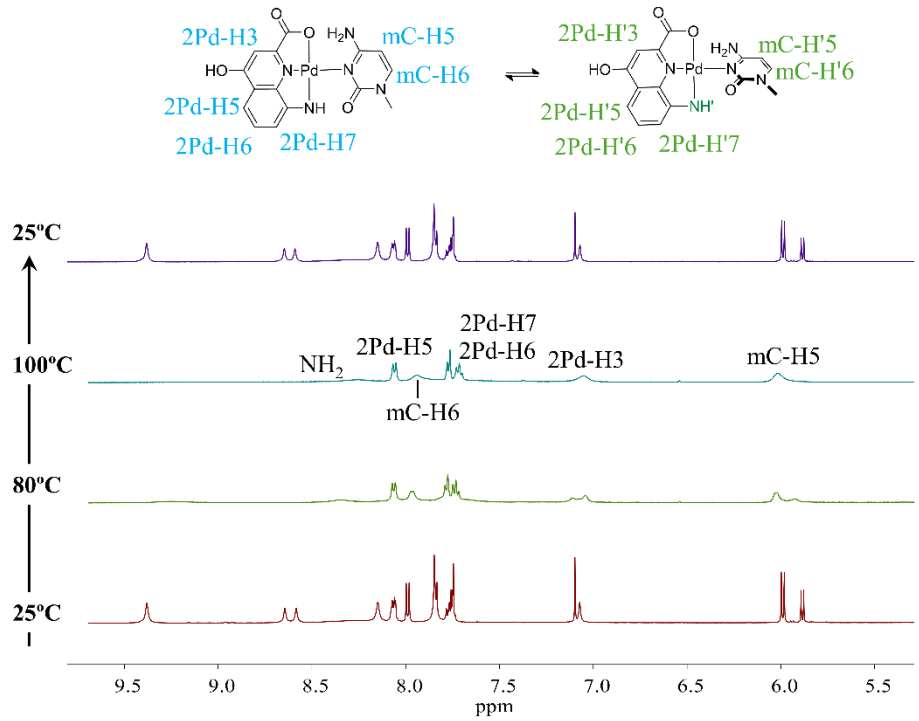

Figura 2.18: ^{1}H-RMN (400Mhz, DMSO-D^{6}) de temperatura varialbe para el complejo **[Pd(Aqa)(mC)]**. Los espectros se presentan desde abajo hasta arriba mostrando los cambios registrados con la variación de temperatura. El último espectro registrado (arriba) corresponde al enfriamiento de la muestra.

Para entender mejor los resultados obtenidos y confirmar las conclusiones extraídas hasta el momento, a la muestra anterior se le realizó una espectroscopía bidimensional de correlación protón/protón (COSY), de orden difusional (DOSY) y de Resonancia Heteronuclear (NH-HSQC). La Figura 2.19 presenta el espectro COSY para el complejo **mC-Pd-Aqa**.

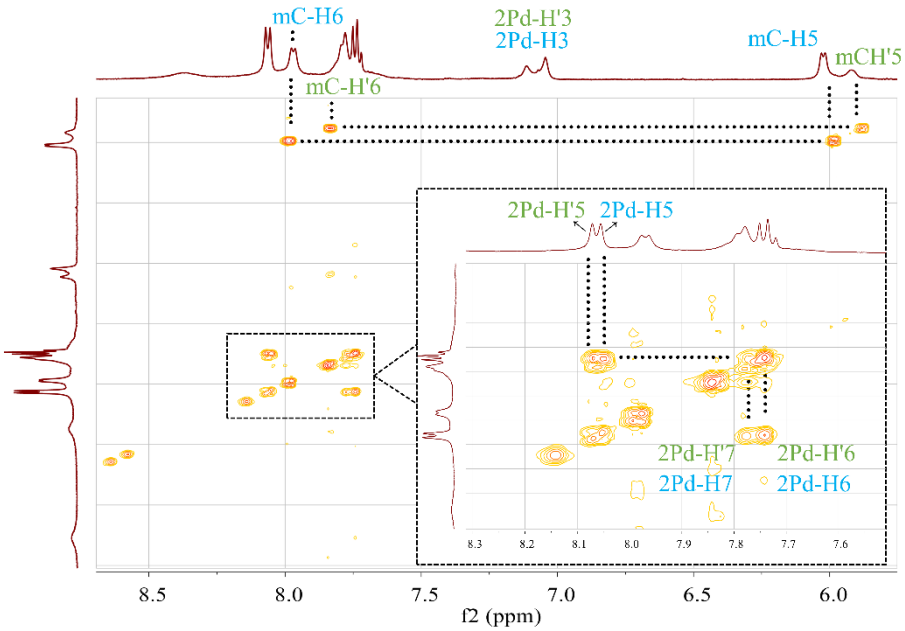

Figura 2.19: ^{1}H-RMN (600Mhz, DMSO-D_6) bidimensional de correlación protón/protón (COSY) para el complejo **[Pd(Aqa)(mC)]**. La ampliación muestra la correlación entre los protones aromáticos del complejo **DMSO-Pd-Aqa**

El espectro muestra una correlación directa entre los protones H6 y H5 de **mC**. Concretamente, se observan dos dobletes a 7.97 y 7.75 ppm, que correlacionan con dos dobletes de H5 a 5.87 y 5.76 descritos en el espectro anterior (Figura 2.18) para las dos estructuras isoméricas. El doblete a 7.97 ppm coincide con la señal descrita anteriormente para H6, del mismo modo, el doblete a 7.75 ppm pertenece al protón H6 de la otra estructura isoméricas, que no pudo ser observada en el espectro 1D debido al solapamiento de las señales en esa región. El espectro COSY también muestra una correlación directa entre las señales para los protones aromáticos 2Pd-H5, 2Pd-H6 y 2Pd-H7 del complejo **DMSO-Pd-Aqa** (Figura 2.19, ampliación), así como el desdoblamiento de señales característico para las dos confirmaciones isoméricas descritas anteriormente. Concretamente, se muestran dos dobletes (solapados) a 8.08 y 8.05 ppm correspondientes a los protones 2Pd-H5 que correlacionan con dos multipletes centrados a 7.77 y 7.74 ppm de los protones 2Pd-H6 y 2Pd-H7.

A la misma muestra se le realizó también un espectro de orden difusional (DOSY). Esta técnica permite separar señales de ^{1}H-RMN de distintas especies en función de su coeficiente de difusión (D). En este proceso, la muestra se irradia con campos pulsados con diferentes intensidades de gradiente. Posteriormente, se analizan los decaimientos de la señal para extraer un conjunto de datos que permitan extraer un valor de D. En la Figura 2.20 se muestra el espectro DOSY tratado para **mC-Pd-Aqa**, donde se pueden ver dos conjuntos de señales bien diferenciadas y marcadas con asteriscos (verde-rojo).

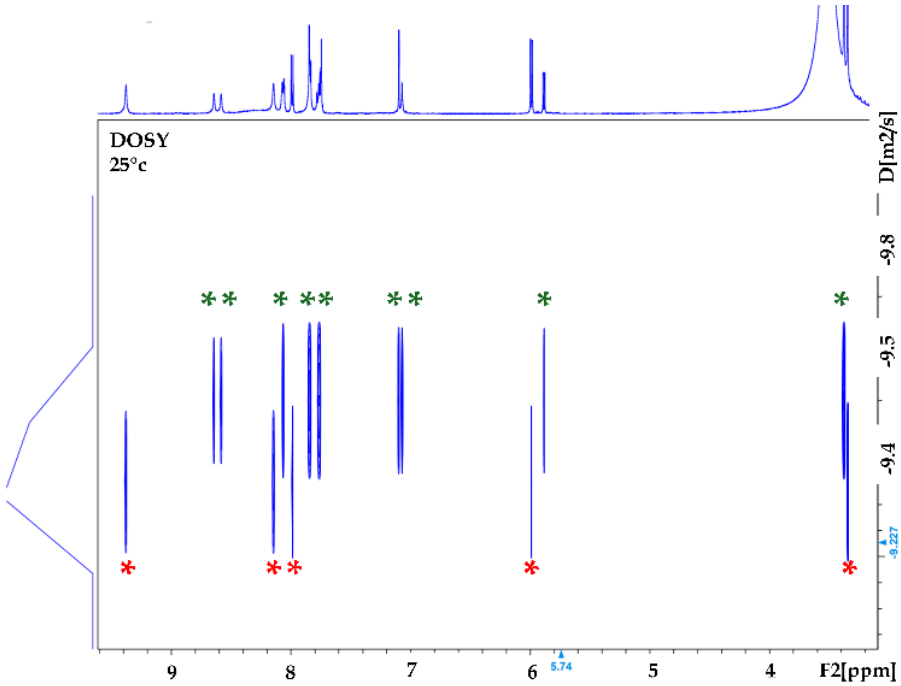

Figura 2.20: ^{1}H-RMN (600Mhz, DMSO-D_6) de orden difusional (DOSY) para el complejo **mC-Pd-Aqa**. Los asteriscos (rojo y verde) representan los conjuntos de señales correspondientes a cada una de las estructuras isoméricas.

A primera vista, podría parecer lógico pensar que dos conjuntos de señales indican la presencia de dos moléculas diferentes; sin embargo, estos datos revelan la existencia de una sola molécula. Esto se debe a la proximidad de los valores de difusión calculados para cada conjunto de señales y el límite de detección del equipo empleado. En este caso, los resultados están de acuerdo con la existencia de dos estructuras isoméricas en equilibrio con coeficientes de

difusión similares. Aunque la diferencia entre ambas es muy pequeña, la sensibilidad del equipo permite detectar ambas estructuras. No obstante, debido a la cercanía de los valores de D, el software no puede aceptar que las señales de dos especies (interpretadas como estructuras distintas) estén tan próximas. Como resultado, genera un valor promedio entre ambas, y en consecuencia, dos conjuntos de señales.

Por último, se realizaron experimentos de NH-HSQC para obtener más información sobre las señales observadas entre 9.40 - 8.05 ppm (consultar Figura 2.17) pertenecientes al grupo amino del complejo **mC-Pd-Aqa**. El espectro de NH-HSQC de la Figura 2.21 muestra dos conjuntos de señales a 9.38 - 8.15 ppm y a 8.65 - 8.59 ppm pertenecientes al grupo amino de **mC**. Este último conjunto de señales (8.65 y 8.59 ppm), puede atribuirse al grupo amino cuando el complejo **mC-Pd-Aqa** se encuentra en una conformación no coplanar, presente en menor proporción. La división de la señal para el grupo NH_2 en dos singletes puede explicarse mediante la rotación restringida del enlace C-NH_2 al unirse al átomo de Pd a través de N3, provocado que ambos protones se encuentren en un ambiente químico distinto. Por otro lado, el conjunto de señales a 9.38 y 8.15 ppm, pertenecen al grupo amino cuando el complejo **mC-Pd-Aqa** se encuentra en conformación coplanar, deducido a partir de la distancia existente entre ambas señales en el espectro. Este hecho puede ser explicado mediante la formación de un enlace de hidrógeno entre el grupo amino y el grupo carboxilo del ligando **Aqa**, lo que provoca un desplazamiento a campo alto de uno de los protones hasta 9.38 ppm.

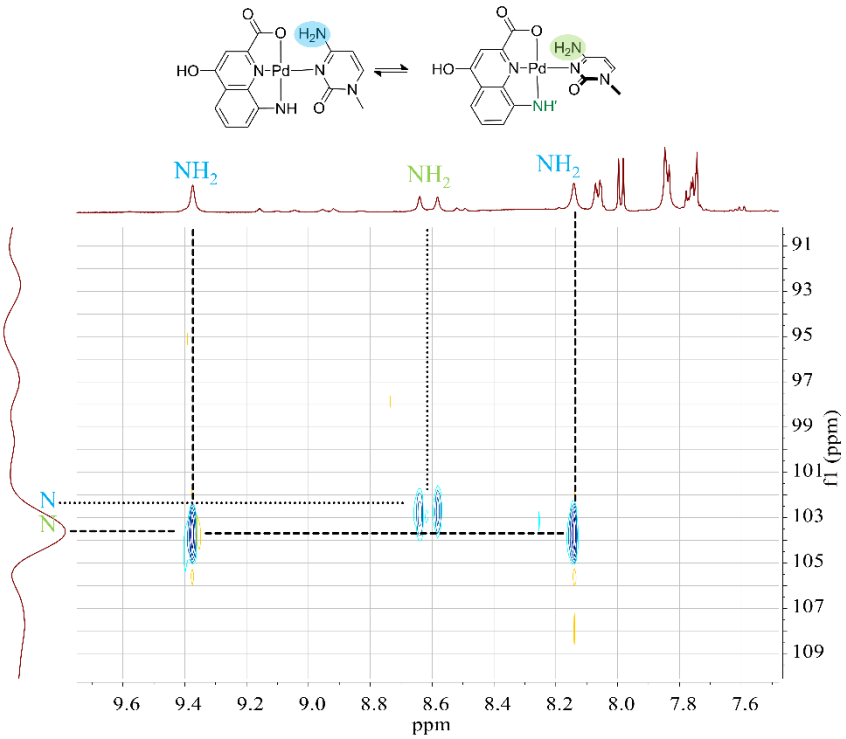

Figura 2.21: ^{1}H-RMN (600Mhz, DMSO-D$_6$). Espectro NH-HSQC para el complejo **mC-Pd-Aqa** donde se muestra las correlaciones N-H en las dos conformaciones isoéricas.

A una alícuota de los experimentos de ^{1}H-RMN anteriores se le realizó un análisis por espectrometría de masas (ESI-MS, modo positivo) que confirmaron de manera inequívoca la formación del complejo **mC-Pd-Aqa** (teórico 434.0081 Da) observándose valores de 433.0074 Da correspondiente al complejo protonado (espectro completo disponibles en Anexo-Figura10)

Una vez realizados los estudios en disolución se intentó realizar la caracterización en estado sólido mediante experiencias de cristalización. Desafortunadamente, todos los esfuerzos para obtener un cristal de la especie **mC-Pd-Aqa** apropiado para medidas de difracción de rayos X han sido infructuosos.

Debido a la imposibilidad de obtener cristales aptos para el estudio de la estructura molecular en detalle, se realizaron cálculos computaciones de densidad funcional teórica (DFT) como una alternativa para conocer detalles estructurales de **mC-Pd-Aqa**. La geometría optimizada mediante DFT reveló que efectivamente las unidades de **Pd-Aqa** y **mC** se organizan de manera coplanar a través del enlace de coordinación y que además dicha estructura queda estabilizada mediante la formación de dos puentes de hidrógeno entre los grupos funcionales complementarios de ambas moléculas (Figura 2.22).

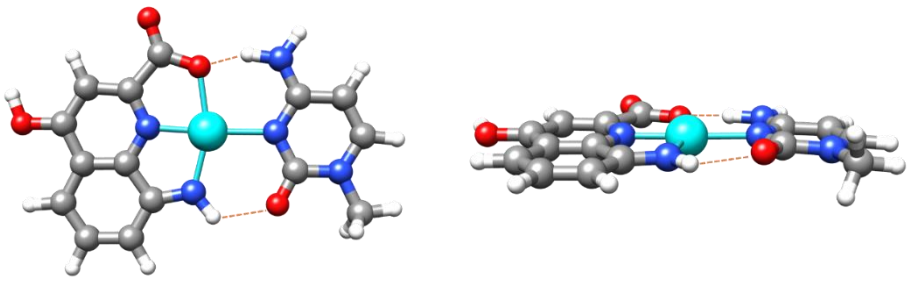

Figura 2.22: Dos perspectivas de la geometría optimizada para **mC-Pd-Aqa** mediante cálculos DFT. Colores de los átomos: gris, carbono; blanco, hidrógeno; azul, nitrógeno; rojo, oxígeno; turquesa; paladio; líneas naranjas punteadas, puentes de hidrógeno entre los grupo amino y carbonilo.[2]

2.2.c. Formación y caracterización del híbrido supramolecular [{Pd(Aqa)}$_{15}$(dC$_{15}$)] (**dC$_{15}$-Pd-Aqa**).

Una vez estudiado y caracterizado el complejo **mC-Pd-Aqa** se realizaron los estudios de interacción entre un ADN de cadena simple homotópica con quince unidades de 2-deoxyacitidina (**dC$_{15}$**) y el fragmento metálico **Pd-Aqa**. Dicha reacción se siguió mediante dicroísmo circular (CD) (Figura 2.23). Para esto, se preparó una disolución de 2 µM de **dC$_{15}$**, 100 mM $NaClO_4$ y 5 mM MOPS (pH6.8) que se valoró con cantidades crecientes de **DMSO-Pd-Aqa** (DMF) a 20ºC hasta alcanzar los cuatro equivalentes por citosina, y manteniendo la concentración inicial de **dC$_{15}$**.

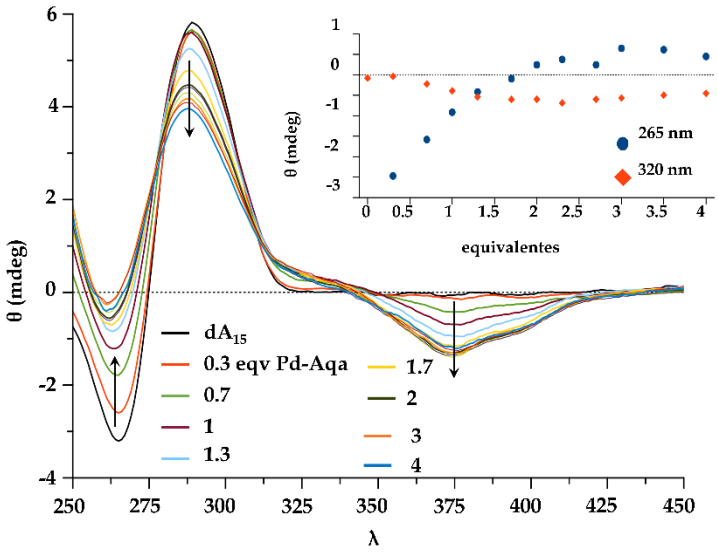

Figura 2.23: Espectro de CD para la valoración de **dC$_{15}$** en presencia de cantidades crecientes de **DMSO-Pd-Aqa**. Gráficas interiores: Variación de la elipticidad (θ) a 265 nm y 320 nm respecto a la cantidad de equivalentes de **Pd-Aqa** por base. Condiciones: 2 µM DNA, 0→60µM **DMSO-Pd-Aqa** (DMF), 100 mM $NaClO_4$, 5 mM MOPS (pH 6.8). Las flechas indican la dirección en los cambios de CD.

El espectro de CD para **dC$_{15}$** libre muestra efecto Cotton con una banda positiva y otra negativa a 283 y 270 nm respectivamente. Cuando añadimos cantidades crecientes de **Pd-Aqa** a la disolución se observa como ambos picos disminuyen su intensidad junto con la aparición de una banda inducida (ICD) a 375 nm, región donde el complejo **DMSO-Pd-Aqa** absorbe (Anexo-Figura 11), demostrando la interacción entre el oligonucleótido y el fragmento metálico, ya que **Pd-Aqa** no presenta señal de CD cuando se encuentra libre en disolución.

En la Figura 2.23 también se observa la estabilización de los cambios experimentados en las curvas de CD. Concretamente, la representación de la variación de elipticidad (θ) frente a los equivalentes **Pd-Aqa**/bases presentes en disolución (grafica interna, para bandas a 265 y 375nm) muestra como los cambios registrados se estabilizan aproximadamente a partir de la presencia de 1.3 equivalente **Pd-Aqa**/base.

El perfil de la curva de CD sugiere la formación de una estructura **dA$_{15}$-Pd-Aqa** helicoidal similar a una doble hebra de ADN. Como en el caso descrito anteriormente para el híbrido **dA$_{15}$-Pd-Cheld**, esta estructura se forma a partir de un proceso de auto-ensamblaje molecular entre los fragmentos metálicos y las bases del oligonucleótido. En este caso, la estructura de **Pd-Aqa** posee dos anillos aromáticos que favorecen la formación de interacciones de tipo stacking entre fragmentos metálicos adyacentes.

El fragmento **Pd-Aqa** se diseñó a partir del ligando **Aqa** con objeto de facilitar la formación de puentes de hidrógeno con el grupo amino y carboxilo de la citosina. Por tanto, se llevó a cabo un experimento control para evaluar si el ligando libre **Aqa** también era capaz de interaccionar con **dC$_{15}$**. Con este objetivo, se realizó una valoración de una disolución de 2 µM de **dC$_{15}$**, 100 mM $NaClO_4$ y 5 mM MOPS (pH6.8) con cantidades crecientes de **Aqa** (Figura 2.24).

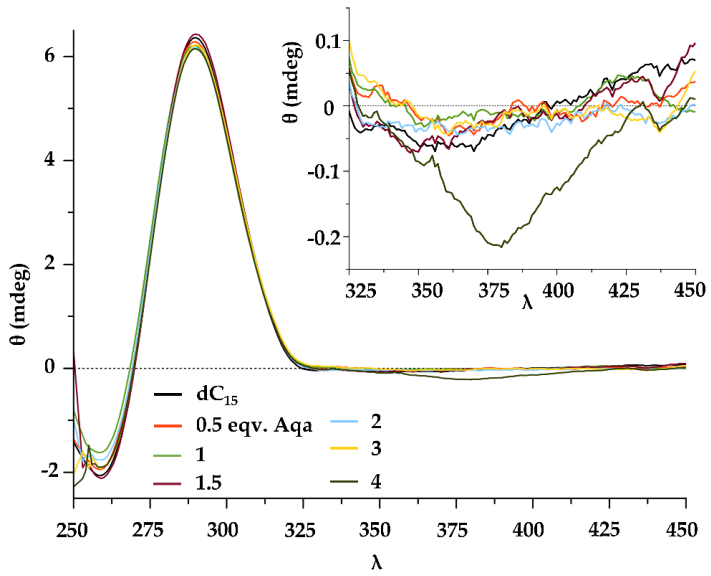

Figura 2.24: Espectro de CD para **dC$_{15}$** en presencia de cantidades crecientes del ligando **Aqa**. Gráfica interior; aumento de la región 325-450 nm donde se observa la aparición de la banda ICD a 375nm. Condiciones: 2 µM dC_{15}, 0→60 µM **Aqa**, 100 mM $NaClO_4$, 5 mM MOPS (pH 6.8).

El espectro de CD no muestra variaciones significativas en presencia de cantidades crecientes del ligando **Aqa**. Sólo se observa una pequeña banda ICD a 380 nm cuando se alcanza los cuatro equivalentes de **Aqa**/base. Estos hechos

sugieren que la interacción entre **Aqa** y **dC$_{15}$** es posible cuando en el medio hay concentraciones altas de ligando. Estos datos refuerzan la importancia de la participación del enlace de coordinación que proporciona **Pd-Aqa** para promover y mejorar la interacción con la hebras simples de ADN, formando así pares de bases mediados por iones Pd^{II}.

Para confirmar la formación del híbrido **dC$_{15}$-Pd-Aqa** se realizaron medidas de espectrometría de masas (ESI-MS, modo negativo) (Figura 2.25). Para ello se analizó una muestra de **dC$_{15}$** (50 μM) con **DMSO-Pd-Aqa** (850 μM) en disolución acuosa con 1.5% de DMSO y 0.2% de Et_3N. Los espectros de masas obtenidos confirman la presencia de diversas especies en disolución, entre las que se encuentran picos correspondientes a **dC$_{15}$** y varios fragmentos **Pd-Aqa**. Concretamente, el espectro muestra especies donde se han unido 14, 15, 16, 17 y 18 fragmentos metálicos (Tabla 2.2) (en Anexo-Tabla 5 pueden consultarse todas las especies obtenidas). La presencia de picos con más de quince unidades de **Pd-Aqa** se puede atribuir a la unión al grupo amino de la citosina, como se ha observado en otros estudios con complejos de Pd^{II} y Pt^{II}.[17,18]

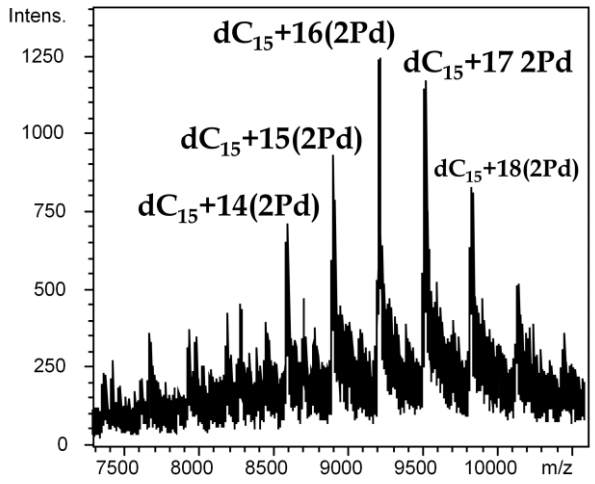

Figura 2.25: Espectro de espectrometría de masas (ESI-MS) obtenido para los sistemas **dC$_{15}$-Pd-Aqa$_{15}$** (z = -5) donde se observan híbridos ADN-metal de 14 a 18 unidades de **Pd-Aqa**. Condiciones: 50 μM **dC$_{15}$** , 850 μM **Pd-Aqa**, 1.5% DMSO y 0.2% Et_3N. La etiqueta 2Pd hace referencia al fragmento metálico **Pd-Aqa**.

Tabla 2.2: Masa/carga (m/z) para los diferentes estados de carga (Z) de; a) **dC$_{15}$-(Pd-Aqa)$_n$**.

a)	**n = 13**	**14**	**15**	**16**	**17**	**18**
-5	8287,5	8596,1	8904,6	9213,2	9521,8	9830,4

Finalmente, para conocer y obtener una geometría optimizada del híbrido ADN-metal se realizaron cálculos DFT para una molécula de doce unidades de citosina (**dC$_{12}$**) que, como se indicó anteriormente, contiene la longitud mínima para completar un giro de la doble hélice. En la estructura de partida, los fragmentos **Pd-Aqa** se unieron a través de un enlace Pd-*N3*(C) manteniendo una estructura coplanar, como se observó en los cálculos realizados para el complejo aislado **mC-Pd-Aqa**. Se añadieron átomos de Na^I para contrarrestar las cargas negativas de los grupos fosfatos y se colocaron moléculas de agua cerca de los átomos dadores/aceptores de enlaces de hidrógeno para simular un medio acuoso. Merece la pena indicar que se ha observado que la omisión de moléculas de agua a la hora de realizar los cálculos provoca una desviación importante de la estructura optimizada deseada, dando lugar a conformaciones estructurales significativamente diferentes. Por tanto, es posible concluir que es de vital relevancia incluir estas moléculas en futuros cálculos donde intervengan estos tipos de sistemas ADN-metal para obtener geometrías más precisas.

La geometría optimizada mostró una configuración de doble hélice para el híbrido **dC$_{12}$-Pd-Aqa**, donde una hebra está compuesta por la cadena monocatenaria del oligonucleótido **dC$_{12}$** y la otra por el apilamiento consecutivo de **Pd-Aqa**, unidos por enlaces de coordinación a las citosinas, e interaccionando entre ellos mediante fuerzas de tipo stacking. Por tanto, esta estructura está formada por pares de bases mediados por iones de Pd^{II}, donde los iones quedan ubicados en el eje central de la estructura formando una cadena 1D (Figura 2.26). Los pares de bases se apilan unos sobre otros con una distancia Pd···Pd de 3.083-3.232 Å, mientras que los ángulos de torsión oscilan entre los 7.42-21.3º (excluyendo a las bases terminales), permitiendo la

interacción mediante puentes de hidrógeno entre el fragmento metálico **Pd-Aqa** y las unidades de citosina de la hebra simple de ADN.

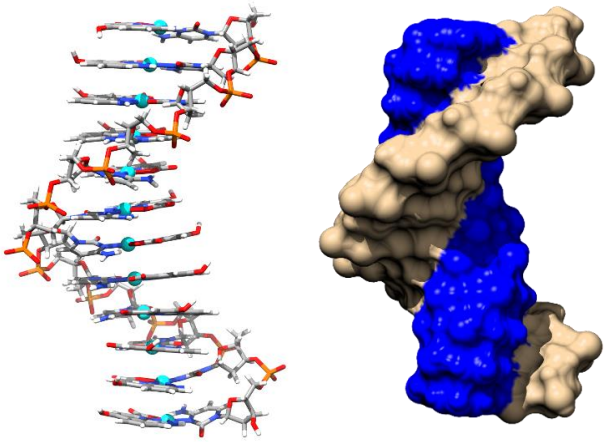

Figura 2.26: Geometría optimizada mediante DFT para **dC_{12} -Pd-Aqa**. Colores de los átomos: gris, carbono; blanco, hidrógeno; azul, nitrógeno; rojo, oxígeno; turquesa; paladio; naranja; fosforo.

Los resultados para la caracterización del complejo **[Pd(Aqa)(mC)]** y los estudios de interacción del complejo **DMSO-Pd-Aqa** con **dC_{15}**, han permitido confirmar la formación del híbrido **dC_{15} -Pd-Aqa** cuya estructura es similar a una doble cadena dextrógira de ADN. Estos datos confirman que este hibrido contiene una matriz unidimensional de iones de Pd^{II} a lo largo de su eje central obtenido a partir de una reacción de autoensamblaje de complejos de paladio y una hebra simple de ADN. Además, estos resultados son comparables con los obtenidos en la sección anterior para el híbrido **dA_{15} -Pd-Cheld**, lo que demuestra la consistencia y reproducibilidad del método propuesto en este trabajo de tesis.

2.3. Estudios con derivados de timina.

Dentro de la complejidad para obtener sistemas híbridos ADN-metal utilizando la estrategia planteada en este trabajo de tesis, la adenina y la citosina pueden considerarse las nucleobases más sencillas. Esto se debe a que poseen un átomo de nitrógeno donador en la cara WCF, accesible para participar en enlaces de coordinación con iones de Pd^{II}. En cambio, si se observa detenidamente las estructuras de la timina (**T**) y la guanina (**G**) se observa que el nitrógeno orientado en la cara WCF (posición N3 para timina y N1 para guanina) se encuentra protonado. Este protón tiene un rol fundamental en la estabilización de la doble hebra natural, a través del cual se forma un puente de hidrógeno en las interacciones T-A y G-C

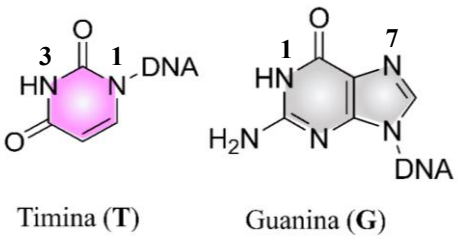

Figura 2.27: Estructura química de las nucleobases naturales timina (**T**) y guanina (**G**). Las etiquetas numéricas sobre la estructura de **eT**, hacen referencia a la nomenclatura de cada nitrógeno.

En estos casos y para promover una reacción del tipo Pd-*N1*G o Pd-*N3*T, es necesario desprotonar las nucleobases en esta posición, lo que supone un reto por la complejidad a la hora de preparar las muestras adecuadamente, ya que un aumento del pH puede dar lugar a la formación de nuevas especies en presencia de iones metálicos. Además, tratar de obtener estos sistemas mediante guanina es un desafío aún mayor, pues como en el caso de la adenina, también tiene disponible la posición N7 y en esta ocasión la interacción metal-nucleobase podría verse especialmente favorecida en esta posición.

En esta sección se presentan los resultados obtenidos para estudios de interacción del complejo [Pd(dPy)(DMSO)] (dPy = 2,6-piridina-

dicarboxamida) (**Pd-dPy-DMSO**) con la nucleobase modelo 1-etil-timina (e**T**) y el oligonucleótido $\mathbf{dT_{15}}$. Los estudios con la nucleobase de guanina y sus derivados no han sido objeto de estudio en este trabajo de tesis.

2.3.a. Síntesis y caracterización del compuesto de coordinación [Pd(dPy)(DMSO)] (**DMSO-Pd-dPy**).

Al igual que en las secciones anteriores, se han preseleccionado ligandos orgánicos con la capacidad de unirse a iones de Pd^{II} y cuya estructura, en términos teóricos, es complementaria a timina. En esta ocasión, se estudió la posibilidad de emplear hasta dos estructuras químicas derivadas de piridina, 2,6-piridina-dimetanamina (**dPy**) (espectro completo en Anexo-Figura 12). y 2,6-piridina-dicarboxamida (**Dyc**) (Figura 2.28a). Finalmente, el candidato mejor posicionado para realizar los estudios de interacción metal nucleobase fue aquel derivado de la 2,6-piridina-dimetanamina (**dPy)**, para formar el complejo [Pd(dPy)(DMSO)] (**DMSO-dPy-Pd**) (Figura 2.28b) espectro completo en Anexo-Figura 13). Esta propuesta se inspira en estudios anteriores donde se empleó el ligando **Dyc** para obtener complejos metálicos del tipo **[Pd(Dyc)(Cl)]**$^{-}$,[19] y que demostraron tener poca eficiencia a la hora de coordinarse con nucleósidos de timina y citosina en comparación con ligandos derivados de 2,6-Bis(3,5-dimetil-1H-pirazol-1-il)-9-(b-D-ribofuranosil)-9H-purina. Otros estudios emplearon el ligando **Dyc** para demostrar la formación de pares de bases mediados por Pd^{II} en los extremos de un dúplex corto, y aunque demostraron que pueden ser grupos estabilizadores, no se acomodaban fácilmente mediante apilamiento a lo largo de la estructura.[20]

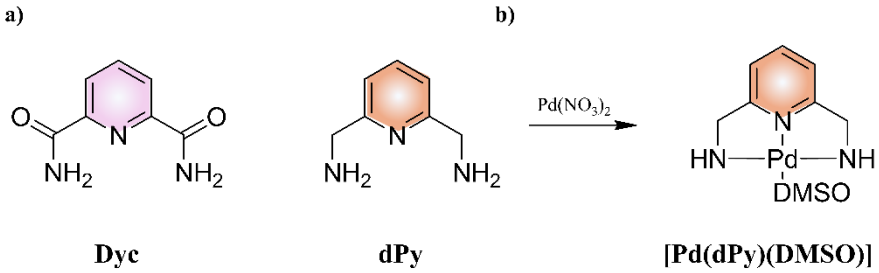

Figura 2.28: a) Estructuras químicas de los ligandos 2,6-dimetanamina (**dPy**) y 2,6-piridina-dicarboxamida (**Dyc**). b) Reacción entre **dPy** y un equivalente de Pd^{II} para obtener el complejo **[Pd(dPy)(DMSO)].**

2.3.b. Síntesis y caracterización del compuesto de coordinación con derivados de la timina; [Pd(dPy)(eT)] (**eT-Pd-dPy**).

En primer lugar, se estudiaron las condiciones necesarias para promover la interacción entre el fragmento metálico **Pd-dPy** y **eT**. Para ello se llevó a cabo una optimización de las condiciones experimentales adecuadas que favorecieran la formación del complejo **eT-Pd-dPy**. Cómo se ha comentado anteriormente, para promover la formación de estos sistemas es necesario que primero tenga lugar la deprotonación de la posición H-*N3*eT (Figura 2.29).

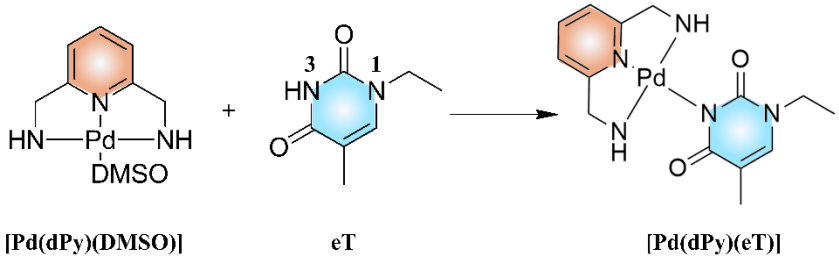

Figura 2.29: Reacción entre el complejo metálico **DMSO-Pd-dPy** y **eT** para obtener el complejo **eT-Pd-dPy**. Las etiquetas numéricas sobre la estructura de **eT**, hacen referencia a la nomenclatura de cada nitrógeno.

La primera experiencia de reacción entre las unidades **DMSO-Pd-dPy** y **eT** se realizó en DMSO-D_6 y fue seguida mediante medidas de ^{1}H-RMN. Los resultados obtenidos en estas condiciones no fueron concluyentes, y aunque se observaron nuevas señales que pueden sugerir la formación de la especie **eT-Pd-dPy**, también se observaron picos mayoritarios para las especies libres en disolución (Figura 2.30). Esto puede explicarse observando el singlete a 11.2 ppm correspondiente al protón H-*N3*eT. El espectro muestra como a medida que se añaden cantidades crecientes de nucleobase, la señal para NH aumenta en intensidad, lo que imposibilita que se promueva la reacción entre ambas entidades.

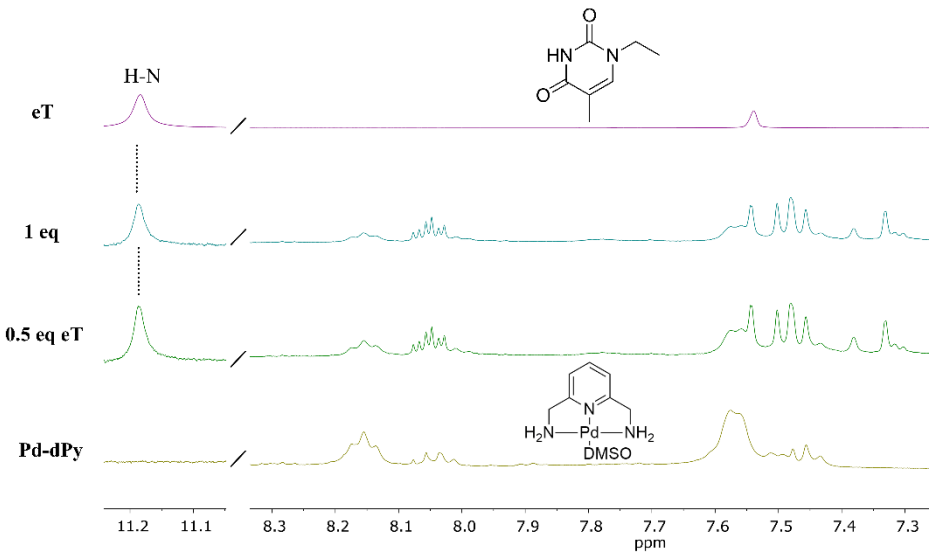

Figura 2.30. Región aromática de los espectros de ^{1}H-RMN (400Mhz, DMSO-D_6) para la reacción entre complejo metálico **DMSO-Pd-dPy** con cantidades crecientes de **eT**.

La segunda experiencia se realizó empleando una mezcla de disolventes D_2O:DMSO-D_6 (1:1) con objeto de facilitar la deprotonación en la posición H-*N3*(**eT**) en presencia de agua. La Figura 2.31 muestra el espectro de ^{1}H-RMN resultante en estas condiciones para una valoración de **DMSO-Pd-dPy** con cantidades crecientes de **eT (**espectro completo en Anexo-Figura 14). El espectro del complejo libre muestra dos señales anchas y poco intensas a 7.93 y 7.32 ppm que corresponden a los protones dPy-H4, dPy-H3 del anillo de piridina. A medida que se añade **eT**, hasta alcanzar los 1.25 equivalentes/base,

estas señales se definen mejor, observándose un triplete a 7.91 ppm para dPy-H4 y un doblete a 7.33 ppm para dPy-H3. Junto a ellos, a 7.26 ppm se observa un singlete perteneciente al protón eT-H6 (ampliación, Figura 2.31). En el espectro no se observan señales correspondientes al grupo H-*N3*eT (espectro de referencia para **eT** libre, rosa). Esto es indicativo de la deprotonación del grupo H-*N3*eT y en consecuencia, de la formación de pares de bases mediados por metales a través de un enlace de coordinación con iones de Pd^{II}.

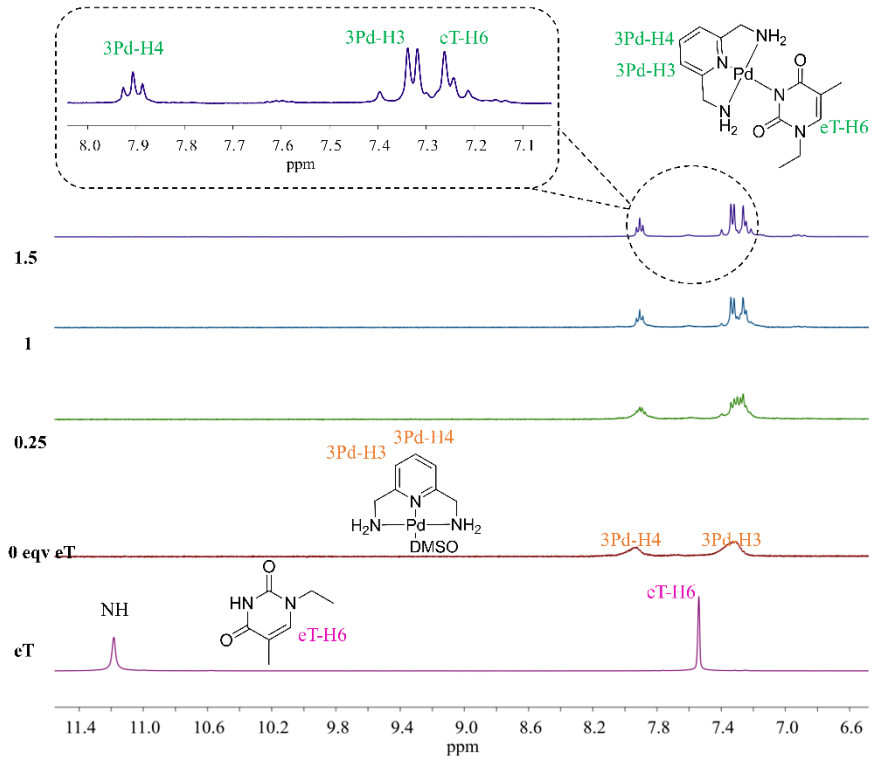

Figura 2.31. Región aromática de los espectros de ^{1}H-RMN (400Mhz, DMSO-D_6) para la valoración de **DMSO-Pd-dPy** con cantidades crecientes de **eT**. El espectro inferior (rosa) muestra el espectro para **eT** libre. La etiqueta **3Pd** hace referencia al fragmento metálico Pd-dPy.

Con objeto de estudiar la formación de **eT-Pd-dPy** se realizó un estudio de ^{1}H-RMN a temperatura variable, sin sobrepasar 80°C debido a la presencia de agua en el medio. La zona aromática del espectro en la Figura 2.32, muestra como a 80°C solo se produce un ligero desplazamiento a campo bajo para los

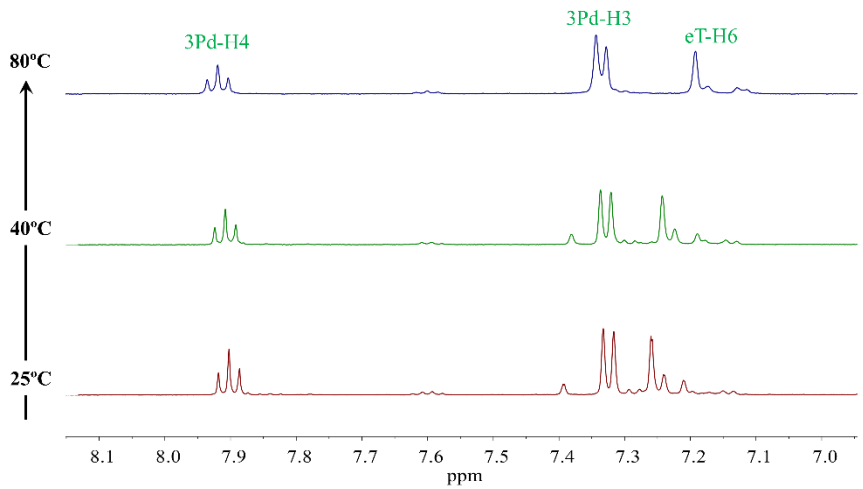

protones 3Pd-H4 y 3Pd-H3de **Pd-dPy**. Por otro lado, el singlete para eT-H6 de **eT**, sufre un desplazamiento a campo alto hasta los 7.18 ppm y además el conjunto de señales sin identificar a 7.25, 7.23 y 7.20 ppm parecen disminuir en intensidad.

Figura 2.32. ^{1}H-RMN (400Mhz, DMSO-D^{6}) de temperatura varialbe para el complejo **[Pd(dPy)(eT)]**. Los espectros se presentan desde abajo hasta arriba mostrando los cambios registrados con la variación de temperatura. La etiqueta 3Pd hace referencia al fragmento metálico **Pd-dPy**.

Estos datos sugieren que la interacción de tipo **eT-Pd-dPy** es posible y que, además, la deprotonación de **eT** se ve favorecida por la presencia de un medio acuoso. No obstante, es necesario seguir optimizando las condiciones para obtener espectros de resonancia magnética nuclear mejor definidos. Actualmente se está trabajando en una serie de valoraciones a pH ligeramente básico controlado. Para esto se ha planteado preparar distintas disoluciones madre de **eT** a pH 8, 8.5 y 9, que nos permitan estudiar las condiciones óptimas

de pH para promover la deprotonación de **eT** y la posterior interacción con el fragmento **Pd-dPy**.

A la disolución empleada para los estudios anteriores se le realizó un análisis mediante medidas de espectrometría ESI (modo positivo). Los resultados confirmaron la presencia del complejo **eT-Pd-dPy** ($C_{14}H_{18}N_5O_2Pd$, masa teórica = 394.0652 Da), observándose valores experimentales para la estructura protonada, **[Pd(dPy)(eT)+H]**$^+$, de 395.6 Da (espectro completo en Anexo-Figura 1.15).

2.3.c. Formación y caracterización del híbrido supramolecular [{Pd(dPy)}$_{15}$(dA$_{15}$)] (**dA$_{15}$-Pd-dPy**).

Una vez estudiado y caracterizado el complejo **eT-Pd-dPy** se realizaron los estudios de interacción entre un ADN de cadena simple homotópica con quince unidades de 2-deoxytimidina (**dT$_{15}$**) y el fragmento metálico **Pd-dPy**. Para ello, inicialmente se realizaron estudios de CD donde se valoró una disolución de 2 μM de **dT$_{15}$**, 100 mM $NaClO_4$ y 5 mM Tris (pH 8.5) con cantidades crecientes de **DMSO-Pd-dPy** (Figura 2.33). En estos ensayos, se ha modificado el pH hasta 8.5 empleando una disolución de Tris, a diferencia de los estudios anteriores para las estructuras supramoleculares **Pd-Cheld** y **dC$_{15}$-Pd-Aqa**, donde se empleó una disolución de MOPS a pH6.8. La modificación hasta pH 8.5 responde a la necesidad de facilitar la deprotonación del grupo H-*N3*eT, favoreciendo la interacción entre el fragmento metálico **Pd-dPy** y la hebra simple de ADN.

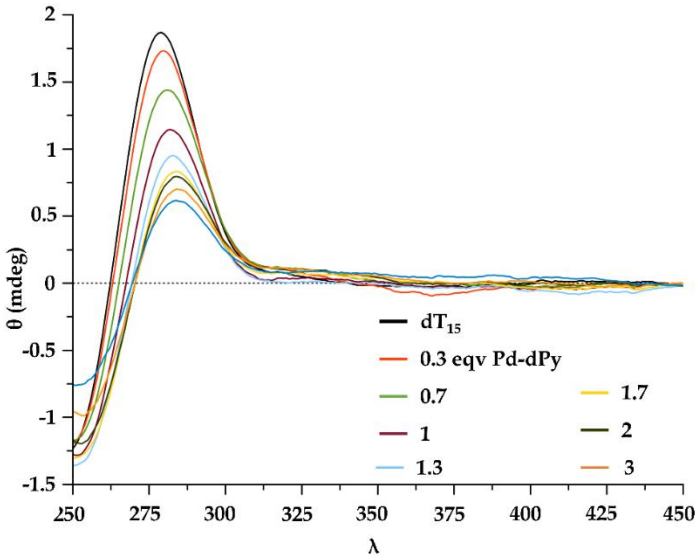

Figura 2.33: Espectro de valoración para CD **dT_{15}** con cantidades crecientes de **Pd-dPy**. Condiciones: 2 µM DNA, 0→60 µM **Pd-dPy**, 100 mM $NaClO_4$, 5 mM Tris (pH 8.5).

El espectro para **dT_{15}** libre muestra efecto Cotton con un máximo a 275 nm y un mínimo a 250 nm. Tras la adición de cantidades crecientes de **DMSO-Pd-dPy**, el máximo experimenta un desplazamiento hasta longitudes de ondas más altas a 286 nm acompañado de una disminución drástica de la intensidad, que se estabiliza en torno a los 1.3 equivalentes. Por otro lado, el mínimo a 250 nm experimenta únicamente una disminución en la intensidad. En el espectro de CD no se observa la aparición de ninguna banda de tipo ICD por encima de 300nm, en la región en la que el complejo **DMSO-Pd-dPy** absorbe (espectro completo en Anexo-Figura 16).La ausencia de estos cambios sugiere que la interacción entre ambas entidades no está siendo efectiva y que por tanto no se está formado la estructura supramolecular **dT_{15}-Pd-dPy**. Si el fragmento metálico se hubiera unido a la hebra ADN se esperaría ver una quiralidad inducida en los fragmentos **Pd-dPy**, y por tanto señal de CD. Una de las posibles causas puede ser la no deprotonación del grupo H-*N3*eT de la hebra simple, lo que imposibilitaría la formación de pares de bases mediados por metales. Por tanto, los cambios que ocurren en la región de la hebra de ADN pueden ser derivados de procesos de intercalación del complejo metálico entre

las bases, y no por coordinación del mismo. No obstante, esta suposición es meramente especulativa y se requiere un trabajo más detallado para entender lo que está ocurriendo.

Lamentablemente, al tiempo de escritura de esta memoria de tesis no se han terminado los estudios necesarios para confirmar correctamente la formación de las estructuras supramoleculares **dT$_{15}$-Pd-dPy**. A pesar de ello, los resultados preliminares descritos indican que es posible la formación de las especies **eT-Pd-dPy** y, por tanto, sugieren que podría obtenerse el hibrido **dT$_{15}$-Pd-dPy.** En este caso, es necesario optimizar aún más las condiciones experimentales para favorecer la deprotonación de las nucleobases de timina en la hebra simple para promover una adecuada coordinación vía Pd-*N3*(T). La complejidad de los procesos involucrados ha generado ciertas limitaciones experimentales que han afectado a la obtención de resultados concluyentes. Por otra parte, la falta de tiempo ha impedido explorar a fondo las variables y ajustar los parámetros de manera exhaustiva. Aunque estos hallazgos no permiten confirmar la formación de estas especies, proporcionan una base inicial para futuras investigaciones.

2.4. Conclusiones.

En esta sección se ha presentado una estrategia exitosa para obtener híbridos ADN-Pd empleando complejos metálicos de Pd^{II} y hebras simples de ADN. Se ha demostrado que es posible obtener sistemas supramoleculares híbridos a través de un mecanismo de auto-ensamblaje mediante la formación de pares de bases mediados por iones de Pd^{II}, a través de un enlace de coordinación entre los fragmentos metálicos y los nitrógenos endocíclicos de las nucleobases. Además, se han sintetizado y caracterizado ligandos orgánicos cuya estructura ha sido diseñada racionalmente para promover un reconocimiento mediante complementariedad con las nucleobases de adenina, citosina y timina y promover mecanismos de interacción racionales.

Mediante el empleo de distintas técnicas de caracterización se ha demostrado la posibilidad de ordenar los iones de Pd^{II} mediante la formación de un sistema que imita la organización de una doble hebra de ADN donde los iones metálicos quedan alojados en el eje central. Por tanto, esta estrategia sintética nos permite formar matrices unidimensionales de iones de Pd^{II} con una longitud deseada controlando únicamente la longitud de la hebra simple de ADN empleada. Se han conseguido caracterizar con éxito sistemas híbridos para monohebras de adenina y citosina, **dA_{15}-Pd-Cheld** y **dC_{15}-Pd-Aqa,** y se ha comenzado a establecer las bases para desarrollar sistemas análogos del tipo **dT_{15}-Pd-dPy**, aunque en este último caso aún es necesario poner a punto las condiciones experimentales. Investigaciones posteriores a esta tesis doctoral deberán centrarse en desarrollar un método para el estudio y caracterización de monohebras de guanina, para de este modo obtener híbridos ADN-metal para cada una de las nucleobases.

2.5. Materiales y métodos.

2.5.1. Síntesis de materiales

2.5.1.a. Síntesis del ligando ácido 8-amino-4-hidroxiquinolina-2-carboxílico

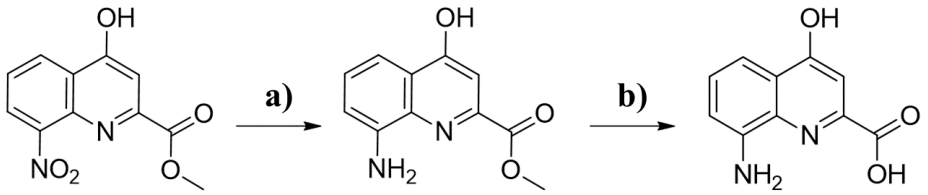

1 **2** **Aqa**

Esquema 1: Ruta sintética para obtener el ligando ácido 8-amino-4-hidroxiquinolina-2-carboxílico (**Aqa**).[16]

El ligando 8-nitro-4-hidroxi-1,4-dihidroquinolina-2carboxilato de metilo, (**1**); se obtuvo siguiendo una ruta sintética descrita previamente en bibliografía.

a) A una disolución de **1** (1.3 g, 4.96 mmol) en MeOH (120 mL) se le añade una cantidad catalítica de Pd/C (130 mg). La mezcla se mantiene en atmósfera de H_2 (1 atm) a temperatura ambiente durante 24 horas. Se filtra con *cellite*® y el disolvente se evapora para obtener **2** en forma de precipitado amarillo. Rendimiento: 100 %. ^{1}H-RMN (400 MHz; DMSO-D6): δ 7.49 (s, 1H, C*H*), 7.37 (t, *J*=7.9 Hz, 1H, C*H*), 7.28 (d, *J*=8.2 Hz, 1H, C*H*), 6.96 (dd, *J*=2.2 y 7.6, 1H, CH), 4.08 (s, 3H, CH_3) 3.94 (s, 3H, CH_3). HRMS (ESI): m/z calculado para $C_{12}H_{12}N_2O_3[M+H]^+$: 233.0926 Da; encontrado: 233.0845 Da.

b) A una disolución de **2** (300 mg, 1.5 mmol) en EtOH (100mL) se le añade NaOH (1M, 2 mL) y se mantiene en agitación 24 horas. La mezcla de reacción se evapora, se redisuelve en H_2O y se acidifica con HNO_3 (1M) hasta alcanzar pH3 y la aparición de un precipitado. El precipitado se filtra, lava y seca para obtener **Aqa** en forma de polvo marrón. Rendimiento: 95%. ^{1}H-RMN (400

MHz; DMSO-D6): δ 7.29 (t, 1H, J= 8.5 Hz, CH_{ar}), 7.24 (d, 1H, J= 7.5 Hz, CH_{ar}) 7.25 (s, 1H, CH_{ar}), 6.86 (d, 1H, J= 8.0 Hz, CH_{ar}), 7.08. HRMS (ESI): m/z calculado para $C_{11}H_{10}N_2O_3[M+H]^+$: 204.0378 Da; encontrado: 205.0605 Da.

2.6.1.b. Síntesis del ligando ácido piridín-2,6-diildimtanamina (**dPy**).

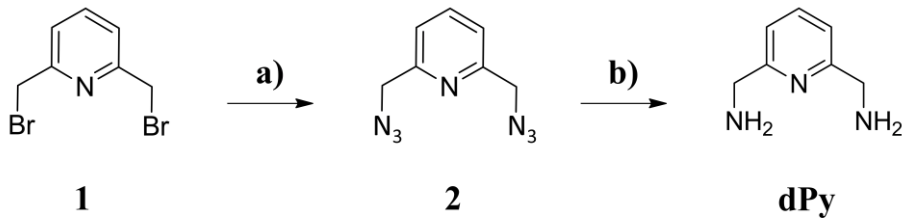

Esquema 2: Ruta sintética para obtener el ligando ácido piridín-2,6-diildimtanamina (**di-Py**).

a) A una disolución de 2,6-bis(bromometil)piridina (**1**) (0.25 g, 1 mmol) en EtOH:H_2O (10:1) se le añade azida de sodio (0.62 g, 10 mmol) y la mezcla se mantiene a reflujo durante 48 horas. El disolvente se elimina en el rotavapor y se añade DCM (100mL). Se realiza un lavado con hidrogeno carbonato de sodio al 10% (100mL) y con cloruro de sodio (100mL). La fase orgánica se recoge, se seca con sulfato de magnesio, se filtra y se concentra hasta obtener **2** en forma de sirupo amarillo. Rendimiento: Cuantitativo. ^{1}H-RMN (400 MHz; DMSO-D6): δ 7.89 (td, *J*=1.2 y 7.8 Hz, 1H, C*H*); 7.38 (d, *J*=7.7 Hz, 2H, C*H*); 4.51 (s, 4H, CH_2). ^{13}C-RMN (400 MHz; DMSO-D6): δ 54.66 (CH_2), 122.07 (C*H*), 138.75 (C*H*), 156.21 (C). IR (ν/cm^{-1}): 2929 (d), 2109 (mf), 1718 (d), 1594 (m), 1576 (m), 1458 (m), 1435 (d), 1332 (m), 1280 (f), 1159 (d), 1095 (md), 996 (d), 902 (md), 979 (d), 762 (m), 655 (d), 566 (d).

b) A una disolución de 2,6-bis(azidometil)piridina (**2**) (40 mg, 0.3 mmol) en MeOH (3mL) previamente purificado con carbón activo, se le añade una cantidad catalítica de Pd/C (6 mg). La mezcla se deja agitando en atmósfera de H_2 (3 atm) durante 16 horas, se filtra con *cellite*® y el disolvente se evapora

para obtener **dPy** en forma de sirupo amarillo. Rendimiento: Cuantitativo. ^{1}H-RMN (400 MHz; DMSO-D6): δ 7.88 (t, *J*=7.7 Mz, 1H, C*H*), 7.40 (d, *J*=7.7, 2H, C*H*), 4.52 (s, 4H, CH_2). ^{13}C-RMN (400 MHz; DMSO-D6): δ 54.67 (CH_2), 122.07 (C*H*), 138.74 (C*H*), 156.19 (C*H*). HRMS (ESI): m/z calculado para $C_7H_{11}N_3[M+H]^+$: 138.1031 Da; encontrado: 138.1029 Da.

2.6.1.c. Síntesis del complejo [Pd(Cheld)(CH_3CN)] (**Pd-Cheld**).

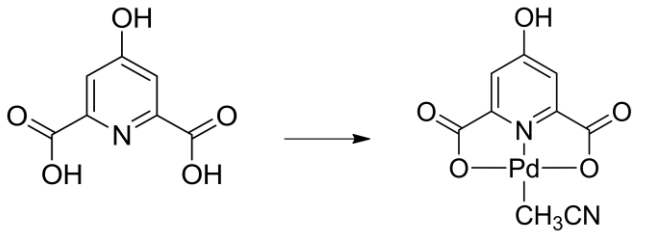

Cheld **[Pd(Cheld)(CH_3CN)]**

Esquema 3: Ruta sintética para obtener el complejo **[Pd(Cheld)(CH_3CN)].**

Una suspensión de $Pd(NO_3)_2$ (350 mg, 2mmol) en CH_3CN (60 mL) se mantiene a reflujo durante 30 minutos hasta su completa disolución. Se filtra a temperatura ambiente para eliminar impurezas y a continuación se le añade una disolución de ácido quelidámico (Cheld) (366 mg, 2 mmol) en H_2O (50 mL). La mezcla se mantiene a reflujo durante 12 horas. Posteriormente se deja enfriara temperatura ambiente, apareciendo **CH_3CN-Pd-Cheld** como cristales naranjas en forma de aguja. Los cristales se filtran, se lavan y se secan. Rendimineto: 70%. ^{1}H-RMN (400 MHz; DMSO-D6): δ 7.05 (s, 2H, CH_{py}), 2.03 (s, 3H, CH_3CN). IR (ν/cm^{-1}): 3458 (m), 3022 (m), 2928 (m), 2716 (d), 2334 (m), 2309 (md), 1684 (mf), 1628 (mf), 1582 (md), 1458 (f), 1359 (mf), 1269 (m), 1228 (m), 1176 (md), 1085 (mf), 924 (m), 911 (m), 799 (m), 757 (m), 701 (md), 638 (m), 571 (m), 638 (m), 571 (m), 460 (m).

2.6.1.d. Síntesis del complejo [Pd(Aqa)(DMSO)] (**Pd-Aqa**).

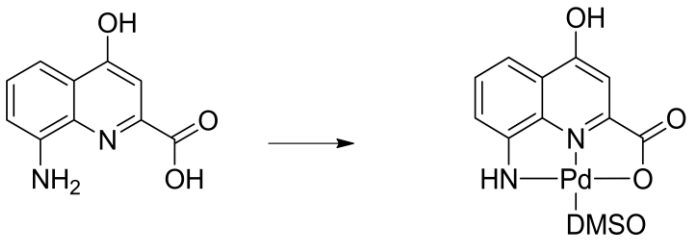

Aqa **[Pd(Aqa)(DMSO)]**

Esquema 4: Ruta sintética para obtener el complejo **[Pd(Aqa)(DMSO)]**.

A una disolución de **Aqa** (204 mg, 1mmol) en DMSO (500 µL) se le añade una disolución de $Pd(NO_3)_2$ (267 mg, 1 mmol) gota a gota. La mezcla se deja en agitando durante 30 minutos. ^{1}H-RMN (400 MHz; DMSO-D6): δ 8.07 (d, 1H, J= 8.5 Hz, C*H*$_{ar}$), 7.84 (d, 1H, J= 7.5 Hz, C*H*$_{ar}$) 7.77 (t, 1H, J= 8.0 Hz, *CH*$_{ar}$), 7.08 (s, 1H, C*H*$_{ar}$). HRMS (ESI): m/z calculado para $C_{10}H_6N_2O_3$ (DMSO)$[M+H]^+$: 385,9553 Da; encontrado: 386.9682 Da.

2.6.1.e. Síntesis del complejo [Pd(dPy)(DMSO)] (**Pd-dPy**).

dPy **[Pd(dPy)(DMSO)]**

Esquema 5: Ruta sintética para obtener el complejo **[Pd(dPy)(DMSO)]**.

A una disolución de **dPy** (133 mg, 1mmol) en DMSO (500 µL) se le añade una disolución de $Pd(NO_3)_2$ (267 mg, 1 mmol) gota a gota agitando la mezcla durante 30 minutos. ^{1}H-RMN (400 MHz; DMSO-D6): δ 7.94 (s, 1 H, C*H*$_{ar}$), 7.94 (s, 2H, C*Har*), 4.53 (s, 4H, CH_2). . ^{13}C-RMN (400 MHz, DMSO-D6): δ 54.81 (C), 120.20 (CH_2), 140.20 (C*H*), 162.89 (C*H*).

2.6.1.f. Síntesis del complejo [Pd(Cheld)(pX)] (**pX-Pd-Cheld**).

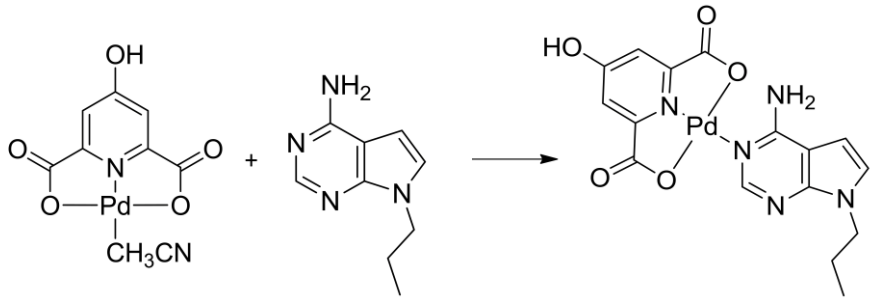

CH_3CN-Pd-Cheld **pX** **[Pd(Cheld)(pX)]**

Esquema 6: Ruta sintética para obtener el complejo **[Pd(Cheld)(pX)]**.

El complejo **CH_3CN-Pd-Cheld** (70 mg, 0.2 mmol) se suspende en una disolución de CH_3CN:H_2O (15:15 mL) y se deja a reflujo hasta completa disolución. Posteriormente, la disolución se filtra y se mezcla con una disolución de **pX** (375 mg, 0.2 mmol) en H_2O (20 mL). La mezcla se agita y se calienta a 60ºC durante 90 minutos en oscuridad. Finalmente, el complejo **pX-Pd-Cheld** aparece como un precipitado amarillo que se filtra, lava y seca. Rendimiento: 72.21%. Parte del producto se disuelve en DMF, dejando la mezcla evaporarse poco a poco para obtener cristales amarillos en forma de aguja del complejo **pX-Pd-Cheld** para ser caracterizados en fase sólida. ^{1}H-RMN (400 MHz; DMSO-D6): δ 7.99 (s, 1H, C*H*), 7.34 (d, 1H, C*H*, J=3.4 Hz), 7.10 (s, 2H, CH_{py}), 6.71 (d, 1H, C*H*, J=3.4 Hz), 4.11 (t, 2H, CH_2, J=7.0 Hz), 1.76 (dq, 2H, CH_2, J=7.2 Hz), 0.81 (t, 3H, CH_3, J=7.4 Hz). IR (ν/cm-1): 3389, 3225, 1664, 1603, 1502, 1461, 1370, 1254, 1084, 797, 733. HRMS (ESI): m/z calculado para $C_{16}H_{15}N_5O_5Pd[M+H]^+$: 464.0186 Da; encontrado: 464.0195 Da.

2.6.1.g. Síntesis del complejo [Pd(Cheld)(eA)] **(eA-Pd-Cheld**).

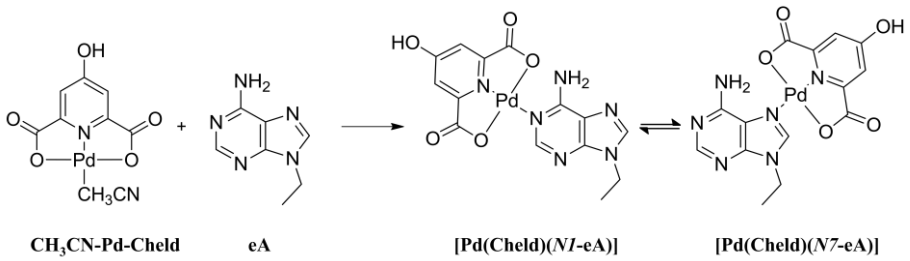

Esquema 7: Ruta sintética para obtener el complejo **[Pd(Cheld)(eA)]**.

A una disolución de eA (10.9 mg, 0.062 mmol) en DMF (1.5 mL) se le añade gota a gota una disolución de **CH_3CN-Pd-Cheld** (18.8 mg, 0.062 mmol) en DMF (3.5 mL). La mezcla se deja cristalizar hasta la aparición del complejo **eA-Pd-Cheld** en forma de cristales amarillos. El precipitado se filtra se lava y se seca para ser caracterizado. ^{1}H-RMN (400 MHz; DMSO-D6): δ 8.46 (s, 1H, CH_{2a}), 8.37 (s, 1H, CH_{8b}), 8.29 (s, 1H, CH_{8a}), 8.09 (s, 1H, CH_{2b}), 7.22 (d, 2H, NH_2), 7.14-7.13 (d, 2H, CH_{py}), 4.32-4.23 (q, 2H, CH_2, J=7.2 Hz), 1.39 (t, 3H, CH_3, J=7.2 Hz). IR (ν/cm-1): 3320, 3225, 3069, 1665, 1613, 1343, 1080, 791, 641, 560, 453. HRMS (ESI): m/z calculado para $C_{14}H_{13}N_6O_5Pd[M+H]^+$: 450.9982 Da; encontrado: 450.9992 Da.

2.6.1.g. Síntesis del complejo [Pd(Aqa)(mC)] **(mC-Pd-Aqa**).

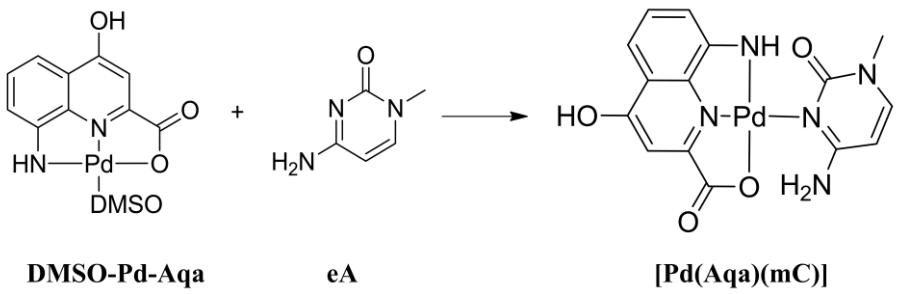

DMSO-Pd-Aqa **eA** **[Pd(Aqa)(mC)]**

Esquema 8: Ruta sintética para obtener el complejo **mC-Pd-Aqa**.

A una disolución de **mC** (1mmol) en DMSO (500 µL) se le añade otra disolución de Pd-Aqa (1 mmol) en DMSO (500 µL) gota a gota. No se pudo aislar el complejo **mC-Pd-Aqa** en fase sólida, por tanto, la disolución obtenida fue apropiadamente caracterizada. ^{1}H-RMN (400 MHz; DMSO-D6): δ 9.38 (s, 1H, NH_2-mC), 8.66 (s, NH_2-mC), 8.59 (s, NH_2-mC), 8.15 (s, NH_2-mC), 8.06 (d, 1H, 2P-H), 8.06 (d, 1H, 2Pd-H5), 8.00 (d,0.7H, mC-H6), 7.84 (m, 1.3 H, 2Pd-H7 y mC-H'6), 7.76 (m, 1H, 2Pd-H6), 7.05 (s, 0.5 H, 2Pd-H3), 6.00 (d, 0.6H, mC-H5), 5.88 (d, 0.4H, mC-H'5), 3.38 (s, 1.5H, CH_3), 3.38-3.35 (s, CH_3). HRMS (ESI): m/z calculado para $C_{15}H_{13}N_5O_4Pd[M+H]^+$: 434.0075 Da; encontrado: 434.0081 Da.

2.6.1.h. Síntesis del complejo [Pd(dPy)(eT)] (**eT-Pd-dPy**).

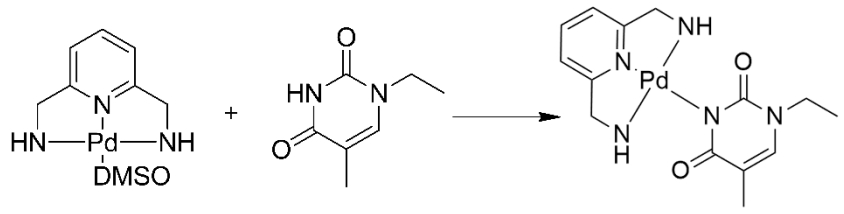

[Pd(dPy)(DMSO)] **eT** **[Pd(dPy)(eT)]**

Esquema 9: Ruta sintética para obtener el complejo **eT-Pd-dPy**.

A una disolución de **eT** (1 mmol) en una mezcla DMSO:H_2O (1:1) se le añade gota a gota otra disolución de **Pd-dPy** (1 mmol) en DMSO. No se pudo aislar el complejo **eT-Pd-dPy** en fase sólida, por tanto, la disolución obtenida fue apropiadamente caracterizada. ^{1}H-RMN (400 MHz; DMSO-D6): δ 7.91 (t, 1H, 3Pd-H4), 7.33 (d, 2H, 3Pd-H3), 7.26 (s, 1H, eT-H6), 4.48 (s, 4H, CH_2), 3.64 (q, 2H, CH_2), 1.79 (s, 3H, CH_3), 1.15 (t, 3H, CH_3). HRMS (ESI): m/z calculado para $C_{14}H_{20}N_5O_2Pd[M+H]^+$: = 394.0652Da; encontrado: 395.6024 Da.

2.5.2. Técnicas de caracterización.

2.5.2.a. Resonancia Magnética Nuclear (^{1}H-RMN).

Los espectros de ^{1}H-RMN se han registrado a temperatura ambiente en un espectrómetro de 400 MHz (2 canales) de alta definición Bruker Nanobay Avance III HD. Este equipo cuenta con una sonda BBDO de 5mm, observación directa de núcleos 31P-109Ag y observación 1H, 19F y desacoplamiento de 1H con gradiente Z. Además, cuenta con un sistema ATM de sintonización automática. Los espectros de ^{1}H-RMN con gradiente de temperatura se han registrado en un espectrómetro de 500 MHz (2 canales) de alta definición Bruker Avance NEO. Este equipo cuenta con sonda Smart Probe BBFO de 5mm, observación directa de núcleos 31P-109Ag y observación 1H, 19F y desacoplamiento de 1H con gradiente Z. Además, cuenta con un sistema ATM de sintonización automática mediante robot 24h. Estos equipos están disponibles en el Centro de Investigación Científica (CIC) de la Universidad de Granada.

Preparación de muestras: Todas las muestras se han disuelto en disolventes deuterados adquiridos en la casa comercial *Eurisotop.*

2.5.2.b. Espectrometría de Masas (ESI-MS).

La espectrometría de masas de ionización por electrospray (ESI-MS) de alta resolución se llevó a cabo en un espectrómetro Waters LCT Premier para los complejos metálicos, mientras que la caracterización de los oligonucleótidos se llevó a cabo mediante espectrometría de masas MALDI-TOF en un espectrómetro Bruker Autoflex. La Determinación de la masa molecular de los híbridos ADN-metal se llevó a cabo mediante ESI-MS utilizando un instrumento Micro Tof-Q (Bruker Daltonics GmbH, Bremen, Alemania) equipado con un analizador de tiempo de vuelo (ESO-TOF-MS), calibrado con Na^I (200 ppm de Na^I en una mezcla 1:! De H2O:isopropanol), conectado a una bomba HPLC Agilent technologies Series 1100 HPLC y equipado con un auto muestreador, ambos controlados por el software Compass. La interacción de los complejos metálicos con las hebras de ADN (50 μM) se realizó en modo negativo, inyectando 10 μL de la muestra a 40 $\mu Lmin^{-1}$, con un voltaje e electrodo de contador capilar a 3,9-4,2 kV; la temperatura de desolvatación se fijó en 100ºC, y se hizo fluir gas seco a 6 $Lmin^{-1}$, utilizando una mezcla 90:10 de acetato de amino 15mM y acetonitrilo (pH7) como portador de líquido. Los espectros se recogieron en un intervalo m/z de 800 a 3000.

2.5.2.c. Espectroscopía UV-Vis (UV-Vis) y de Fluorescencia.

Los espectros de absorción UV-Vis y de fluorescencia se registraron en un espectrofotómetro Varían Cary-Eclipse equipado con una lámpara Xe (potencia pico de 75 kW), un monocromador CZERNY-Turner y un tubo fotomultiplicador R-298 sensible al rojo.

2.5.2.d. Difracción de Rayos X en polvo (XRPD).

Se depositó una muestra en polvo (50 mg) de **eA-Pd-Cheld** en la cavidad de un portamuestras de fondo libre de silicio de 0,2 mm de profundidad (Assing S.r.l., Monterotondo, Italia). La adquisición de datos de difracción de rayos X en polvo se realizó con un difractómetro de barrido vertical θ:θ Bruker AXS D8 Advance, equipado con un tubo de rayos X (Cu Kα, λ = 1. 5418 Å), un detector lineal sensible a la posición Bruker Lynxeye, un filtro de níquel en el haz difractado y los siguientes componentes ópticos: rendijas Soller del haz primario (apertura 2,5°), rendija de divergencia fija (apertura 0,5°), rendija antidispersión (apertura 8 mm). El generador se ajustó a 40 kV y 40 mA. Los datos se adquirieron en el intervalo 2θ 5,0-50,0°, con pasos de 0,02° y un tiempo por paso de 0,2 s. Un refinamiento del patrón de polvo completo con el método de Le Bail, empleando los parámetros de la celda unitaria de **[Pd(Cheld)(N1-eA)]**, nos permitió evaluar que el polvo a granel sólo contiene la fase **[Pd(Cheld)(N1-eA)]**.

2.5.2.e. Difracción de Rayos X de monocristal (XR).

Los datos de difracción de rayos X para **[Pd(Cheld)(N1-pX)]** se recogieron a T = 100 K utilizando un difractómetro automatizado Bruker X8 Proteum equipado con un ánodo giratorio de enfoque fino (Cu Kα, λ = 1.5418 Å), un detector de área Smart 6000 CCD y un aparato de refrigeración Oxford Cryostream 700. La reducción de datos se realizó con el software SAINT V6.36A,[21] mientras que la corrección de datos para absorción se llevó a cabo utilizando el software SADABS.[22] Los datos de difracción de rayos X para **[Pd(Cheld)(N1-eA)]** se recogieron a T = 150 K utilizando un difractómetro automatizado Bruker AXS Apex II equipado con un tubo de rayos X sellado (Mo Kα, λ = 0,71,03 Å), un detector de área CCD y un aparato de refrigeración Bruker Kryoflex. La reducción de datos se realizó con el software SAINT. No se llevó a cabo ninguna corrección de datos por absorción. En ambos casos, la

estructura cristalina se resolvió mediante métodos directos implementados en SHELXS-97,[5] que permitieron la localización de la mayoría de los átomos de la unidad asimétrica. Todos los átomos (que no eran hidrógeno) restantes se localizaron a partir de mapas de diferencia de Fourier calculados a partir de sucesivos ciclos de refinamiento por mínimos cuadrados de matriz completa en F2 utilizando SHELXL-2018/3.[23] En el caso de **[Pd(Cheld)(N1-pX)]** se asignaron parámetros de desplazamiento térmico anisótropos a todos los átomos distintos del hidrógeno. En cuanto a **[Pd(Cheld)(N1-eA)]**, la muy baja calidad de la difracción de los monocristales impidió la adopción de parámetros térmicos anisótropos. Para intentar solucionar este problema, se ensayaron sin éxito varios monocristales del mismo lote, así como monocristales de lotes diferentes, obtenidos al modular las condiciones de cristalización. Dada la relevancia de la información estructural desvelada por estas determinaciones de estructura para complementar y corroborar los demás resultados científicos presentados en este trabajo, es necesario presentar los detalles estructurales de [1Pd(N1-A)] a pesar de la limitada calidad de los datos de los que se obtuvieron. Los átomos de hidrógeno se localizaron en posiciones idealizadas utilizando instrucciones HFIX, y se describieron con parámetros de desplazamiento térmico isótropo fijados en 1,2 o 1,5 veces los del átomo al que estaban unidos. La información cristalográfica principal, así como los detalles experimentales y de tratamiento de datos se proporcionan en Anexo-Tabla 1.

2.5.2.f. Dicroísmo Circular (CD).

Los espectros de CD se registraron en un espectropolarímero de dicroísmo circular JASCO modelo-J815 dotado con sistema de termostatización por Pertier. Los datos fueron tratados con el Software Spectra Mánager Administrative Tool V 1.03.02, todo disponible en el Centro de Investigación Científica (CIC) de la Universidad de Granada.

Para estudiar la formación de los híbridos [Pd(Cheld)(dX_{15})], [Pd(Cheld)(dA_{15})], [Pd(Aqa)(dC_{15})] y [Pd(dPy)(dT_{15})], se prepararon y evaluaron disoluciones de:

- 2 μM de **dA_{15}**, 100 mM $NaClO_4$ y 5 mM MOPS (Ph6.8), 0→60 μM **Pd-Cheld** (500μM, DMSO).
- 2 μM de **dX_{15}**, 100 mM $NaClO_4$ y 5 mM MOPS (Ph6.8), 0→60 μM **Pd-Cheld** (500μM, DMSO).
- 2 μM de **dC_{15}**, 100 mM $NaClO_4$ y 5 mM MOPS (Ph6.8), 0→60 μM **Pd-Aqa** (500μM, DMSO).
- 2 μM de **dC_{15}**, 100 mM $NaClO_4$ y 5 mM MOPS (Ph6.8), 0→60 μM **Aqa** (500μM, DMSO).
- 2 μM de **dT_{15}**, 100 mM $NaClO_4$ y 5 mM MOPS (Ph6.8), 0→60 μM **Pd-dPy** (500μM, DMSO).

Parámetros experimentales; 250-450 nm, 5 scans, T=25°C.

2.5.2.g. Difracción de Rayos X de Ángulo pequeño (SAXS).

Los espectros de SAXS para **dA_{15}** y **dA_{15}-Pd-Cheld** se midieron en un instrumento Anton-Park SAXSess con radiación Cu-Kα (1.54 Å). El equipo está equipado con un plato de imagen 2D para la colección de datos con un rango de q=0.018-2.5 Å. El valor mínimo de q está limitado por el atenuador de campo. Se emplearon disoluciones de aproximadamente 1mM de **dA_{15}** y **dA_{15}-Pd-Cheld** que fueron medidas en un capilar de 1.5 mm (Hampton Research). Se recogieron datos de dispersión del disolvente puro para la sustracción del fondo. La dispersión se midió durante 30 minutos en cada experimento. Se utilizó el software SAXSQUANT para la recogida y el tratamiento de los datos (normalización, eliminación del haz primario, sustracción del fondo, y suavizado para eliminar el ruido adicional creado por la rutina).

2.6 Bibliografía.

1 A. Pérez-Romero, A. Domínguez-Martín, S. Galli, N. Santamaría-Díaz, O. Palacios, J. A. Dobado, M. Nyman and M. A. Galindo, *Angew. Chem. Int. Ed*, 2021, **133**, 10177–10182.

2 A. Pérez-Romero, M. Cano-Muñoz, C. López-Chamorro, F. Conejero-Lara, O. Palacios, J. A. Dobado and M. A. Galindo, *Angew. Chem. Int. Ed. 2024. e20240026*.

3 T. Mihály, M. Garijo Añorbe, F. M. Albertí, P. J. Sanz Miguel and B. Lippert, *Inorg Chem*, 2012, **51**, 10437–10446.

4 K. H. Scheller, V. Scheller-Krattiger and R. B. Martin, *J Am Chem Soc*, 1981, **103**, 6833–6839.

5 G. M. Sheldrick, *SHELXS-97 and SHELXL-97, Program for Crystal Structure Solution and Refinement. Univ. Gottingen, Gottingen. 1997*.

6 E. Meggers, P. L. Holland, W. B. Tolman, F. E. Romesberg and P. G. Schultz, *J Am Chem Soc*, 2000, **122**, 10714–10715.

7 L. E. Kapinos, B. P. Operschall, E. Larsen and H. Sigel, *Chem. Eur. J.*, 2011, **17**, 8156–8164.

8 A. Dominguez-Martin, S. Galli, J. A. Dobado, N. Santamaría-Díaz, A. Pérez-Romero and M. A. Galindo, *Inorg Chem*, 2020, **59**, 9325–9338.

9 J. Kypr, I. Kejnovska, D. Renciuk and M. Vorlickova, *Nucleic Acids Res*, 2009, **37**, 1713–1725.

10 M. L. Gleghorn, J. Zhao, D. H. Turner and L. E. Maquat, *Nucleic Acids Res*, 2016, **44**, 8417–8424.

11 A. Rich, D. R. Davies, F. H. C. Crick and J. D. Watson, *J Mol Biol*, 1961, **3**, 71-IN19.

12 A. Schreiber, M. S. Lüth, A. Erxleben, E. C. Fusch and B. Lippert, *J Am Chem Soc*, 1996, **118**, 4124–4132.

13 S. Chakraborty, S. Sharma, P. K. Maiti and Y. Krishnan, *Nucleic Acids Res*, 2009, **37**, 2810–2817.

14 J. L. Alderfer and S. L. Smith, *J Am Chem Soc*, 1971, **93**, 7305–7314.

15 J. Isaksson, S. Acharya, J. Barman, P. Cheruku and J. Chattopadhyaya, *Biochemistry*, 2004, **43**, 15996–16010.

16 N. P. Peet, L. E. Baugh, S. Sunder and J. E. Lewis, *J Med Chem*, 1985, **28**, 298–302.

17 M. Krumm, I. Mutikainen and B. Lippert, *Inorg Chem*, 1991, **30**, 884–890.

18 W.-Z. Shen and B. Lippert, *J Inorg Biochem*, 2008, **102**, 1134–1140.

19 O. Golubev, T. Lönnberg and H. Lönnberg, *Helv Chim Acta*, 2013, **96**, 1658–1669.

20 O. Golubev, G. Turc and T. Lönnberg, *J Inorg Biochem*, 2016, **155**, 36–43.

21 *SAINT v6.36A. Bruker AXS inc.; Madison, WI, USA: 2002*.

22 G. M. Sheldrick, *G. M. Sheldrick, SADABS 2016/2. Program for Empirical Absorption Correction of Area Detector Data, University Of Göttingen, Germany,* 2016.

23 G. M. Sheldrick, *Acta Crystallogr. Sect. C Struct. Chem.* , 2015, **71**, 3–8.

2.7. Anexo.

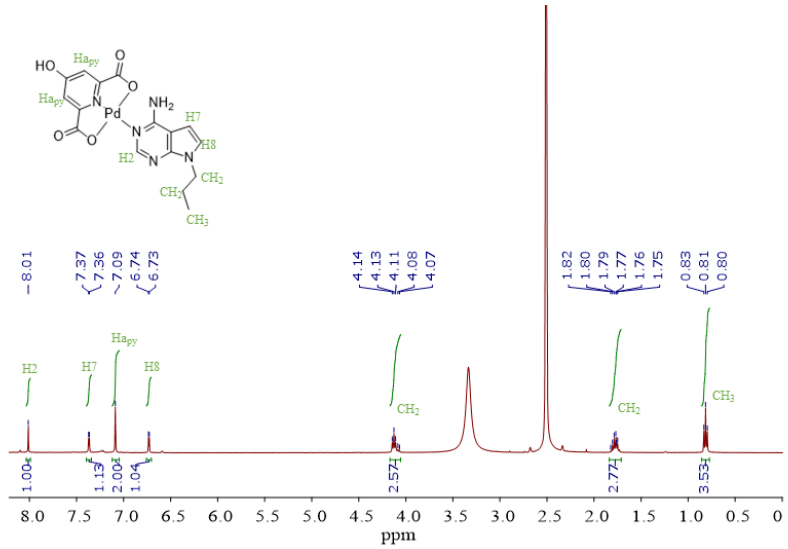

Anexo-Figura 1: ^{1}H-RMN (400Mhz, DMSO-D^{6}) del complejo **Pd(Cheld)(pX)]**.

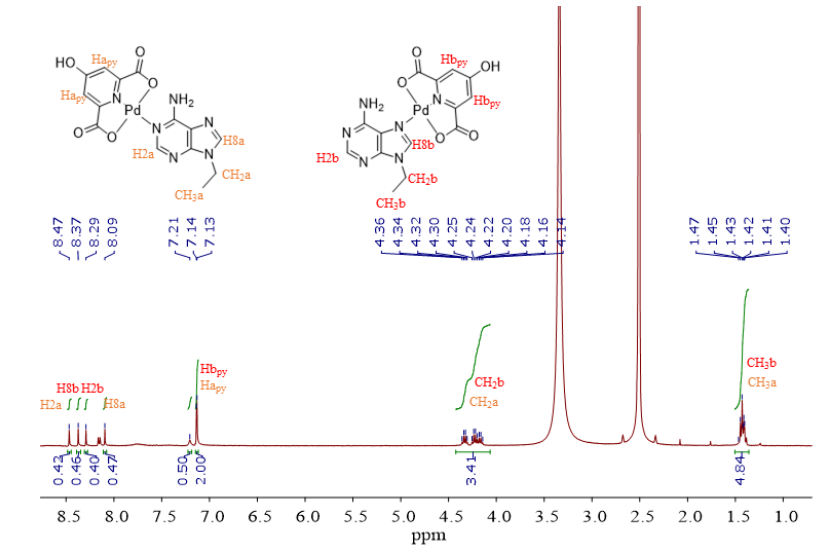

Anexo-Figura 2: ^{1}H-RMN (400Mhz, DMSO-D^{6}) de los complejos **[Pd(Cheld)(N1-eA)]** y **[Pd(Cheld)(N7-eA)]** (**eA-Pd-Cheld**).

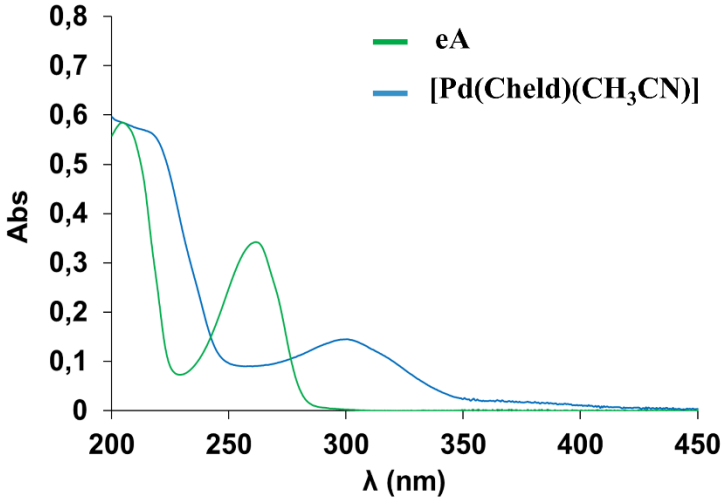

Anexo-Figura 3: Espectro UV-Vis para **eA** y el complejo **[Pd(Cheld)(CH$_3$CN)]**. 0.1 mM H_2O con 25% de DMF.

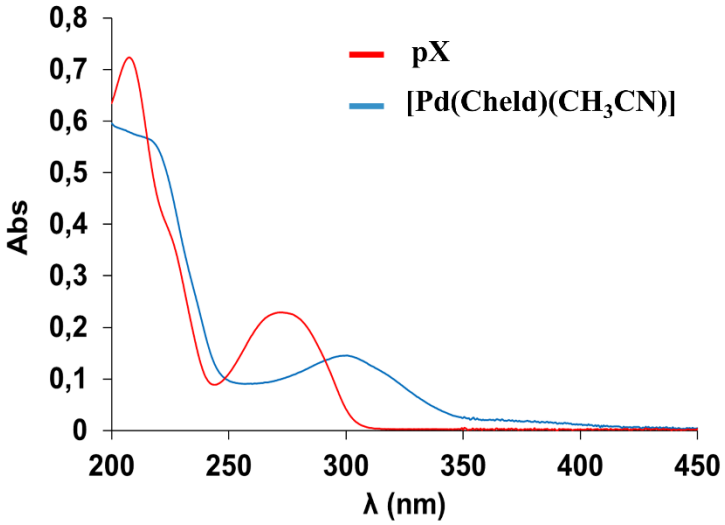

Anexo-Figura 4: Espectro UV-Vis para **pX** el complejo **[Pd(Cheld)(pX)]**. 0.1 mM H_2O con 25% de DMF.

Anexo-Tabla 1: Resumen de los datos cristalográficos experimentales para **eA-Pd-Cheld** y **pX-Pd-Cheld**.

	[Pd(Cheld)(*N1*-eA)]	**[Pd(Cheld)(*N1*-pX)]**
Asymmetric unit formula	$C_{17}H_{15}N_7O_6Pd$	$C_{35}H_{39}N_{11}O_6Pd$
MW [g/mol]	519.75	1018.57
T [K]	150	100
Color, habit	Yellow, needle	Yellow, needle
Dimensions [mm^3]	0.34x0.15x0.08	0.18x0.03x0.02
Crystal system	Monoclinic	Monoclinic
Space group	$P2_1/c$	$P2_1/c$
Z, Z'	4, 4	4, 4
a [Å]	11.515(8)	18.1949(14)
b [Å]	13.148(9)	28.525(2)
c [Å]	12.803(9)	7.4952(6)
α [°]	90	90
β [°]	99.732(17)	101.268(2)
γ [°]	90	90
V [Å^3]	1910(2)	3815.1(5)
F(000)	1052	2056
μ [cm^{-1}]	1.026	8.296
ρ [g cm^{-3}]	1.818	1.773
θ range [°]	2.2-19.0	2.5-66.4
	-10<h<10	-21<h<21
h, k, l ranges	-11<k<11	-33<k<28
	-11<l<11	-8<l<8
Tot., indep., obs. [I_o>2σ(I_o)] refl.	10054, 1528, 1185	49544, 6593, 4081
R_{int}, R_σ	0.167, 0.094	0.226, 0.138
Param., restr.	139, 5	560, 9
Indep. refl. R1	0.161[a]	0.126
Obs. refl. R1	0.134[a]	0.075
wR2	0.306[a]	0.215
GoF	1.324	1.010
Highest peak [e Å^{-3}]	1.67	1.32
Deepest hole [e Å^{-3}]	-1.01	-1.28
CCDC number	2044056	2044057

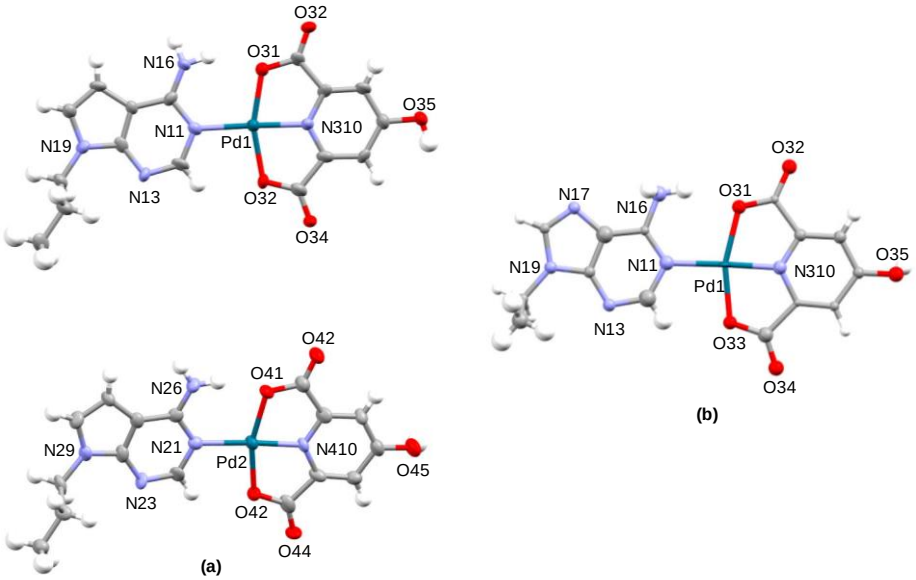

Anexo-Figura 5: Representación esquemática (50% de probabilidad) de la estructura molecular del complejo; a) **[Pd(Cheld)(eA)]** . b) **[Pd(Cheld)(pX)] .** Las etiquetas corresponden a la numeración empleada en la sección 2.1. Colores de los átomos: carbón (gris), hidrógeno (blanco), nitrógeno (azul), oxígeno (rojo), paladio (turquesa). Las moléculas de disolvente se han omitido para mayor claridad.

Anexo-Tabla 2: Comparación de las distancias de enlaces más relevantes y los ángulos interplanares en relació a Pd-Cheld/base de **[Pd(Cheld)(eA)]** y **[Pd(Cheld)(pX)]** .Consultar etiquetas de átomos en Anexo-Figura 5.

	[Pd(Cheld)(*N1*-X)]	**[Pd(Cheld)(*N1*-A)]**
Pd1-N11, Pd2-N21	2.075(9), 2.073(9)	2.04(2)
Pd1-N310, Pd2-N410	1.937(9), 1.912(9)	1.91(2)
Pd-O31, Pd-O41	2.053(6), 2.050(7)	2.06(2)
Pd-O33, Pd-O43	2.051(7), 2.028(7)	2.035(19)
N16-O31, N26-O41	2.789(12), 2.768(10)	2.84(3)
Interplanar angle	3.0(4), 2.2(4)	1.3(11)

Anexo-Tabla 3: Masa/carga (m/z) para los diferentes estados de carga (Z) de; a) **dA$_{15}$-(Pd-Cheld)$_n$**. b) **dX$_{15}$-(Pd-Cheld)$_n$**.

a)	**0**	**9**	**10**	**11**	**12**	**13**	**14**	**15**	**16**
-4	1154.3	1801.3	1873.1	1945.0	2015.9	2088.8	2160.7	2232.5	2304.4
-5	923.3	1440.8	1498.3	1555.8	1613.3	1670.8	1728.3	1785.8	1843.3
-6	769.2	1200.5	1248.4	1296.3	1344.3	1392.2	1440.1	1488.0	1535.9

b)	**0 eqv.**	**12**	**13**	**14**	**15**	**16**
-4	1158	2020.6	2092.5	2164.4	2236.2	2308.1
-5	926.6	1616.3	1673.8	1731.1	1788.8	1846.3
-6	771.6967	1346,7	1394,7	1442,6	149',5	1538,4

Anexo-Tabla 4: Comparación de las distancias de enlaces más relevantes de **A-Pd-Cheld** y **X-Pd-Cheld** encontrados y calculados para las estructuras **dX$_{12}$-Pd-Cheld** y **dA$_{12}$-Pd-Cheld**

Distance (Å)	**dX$_{12}$-Pd-Cheld**	**dA$_{12}$-Pd-Cheld**
Pd-N1	2.024-2.057	2.031 - 2.074
Pd-N10	1.932-1.941	1.929 – 1.942
Pd-O1	1.993-2.045	1.982 – 2.038
Pd-O3	1.977-2.011	1.986 – 2.012
N6-O1	2.678-2.774	2.665 – 2.889
Pd-Pd[1]	3.819-3.109	3.447 – 3.765

Anexo-Tabla 5: Masa/carga (m/z) para los diferentes estados de carga (Z) de; a) **dC$_{15}$-(Pd-Aqa)$_n$**

Z

-5	n = 0	1	2	3	4	5	6
	4275,8	4584,4	4893,0	5201,6	5510,2	5818,7	6127,3
	7	8	9	10	11	12	13
	6435,9	6744,5	7053,1	7361,7	7670,3	7978,9	8287,5
	14	15	16	17	18	19	
	8596,1	8904,6	9213,2	9521,8	9830,4	10139,0	10447,6

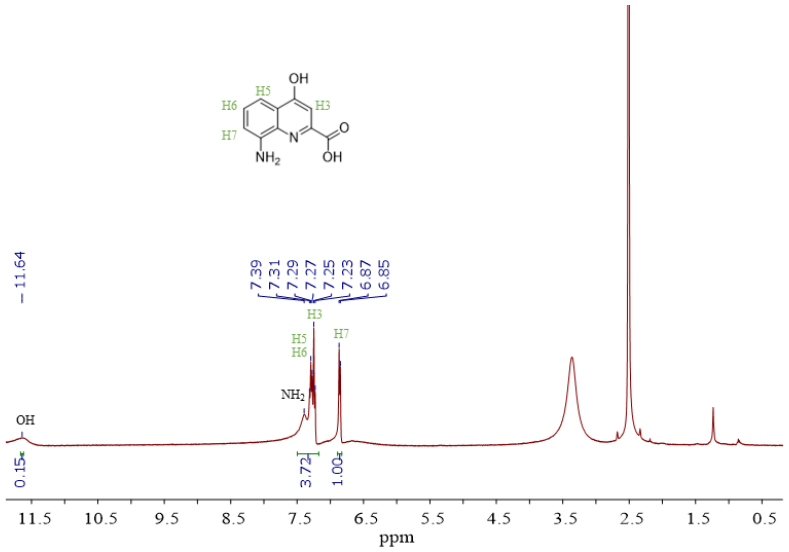

Anexo-Figura 6: [1]H-RMN (400Mhz, DMSO-D[6]) del ligando 8-amino-4-hidroxiquinolina-2-carboxílico, **Aqa.**

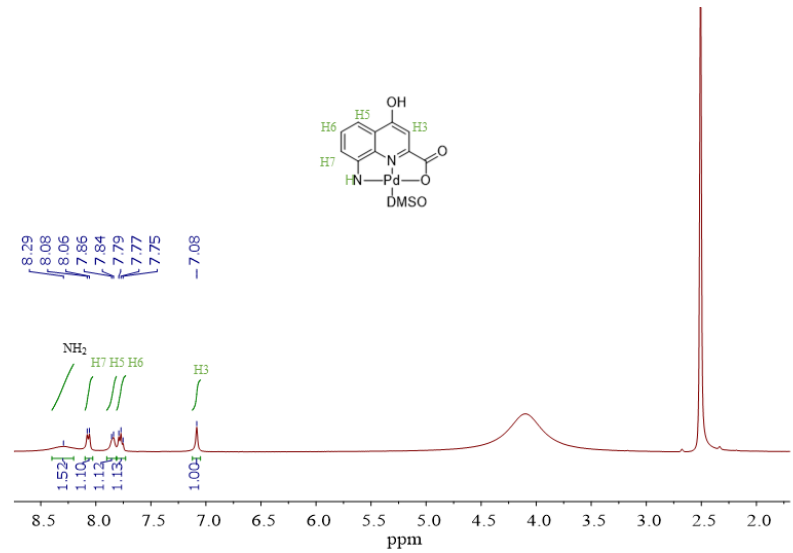

Anexo-Figura 7: [1]H-RMN (400Mhz, DMSO-D[6]) del complejo [**Pd(Aqa)(DMSO)**].

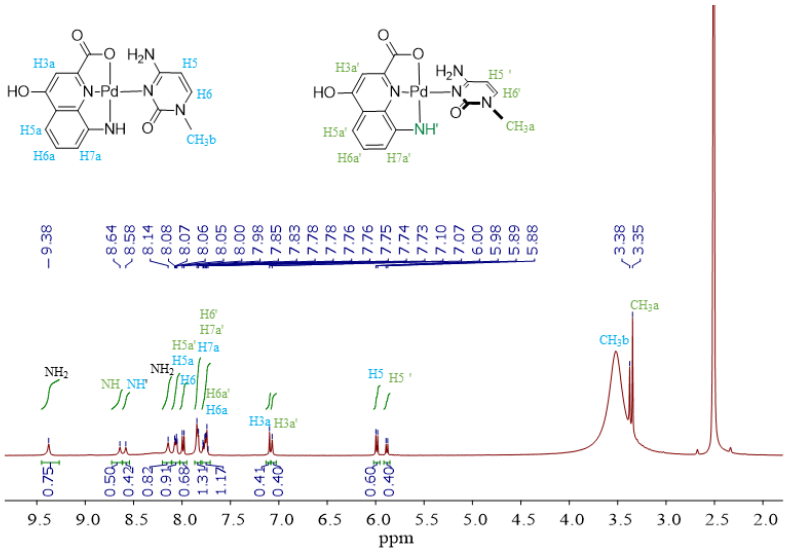

Anexo-Figura 8: ^{1}H-RMN (400Mhz, DMSO-D^{6}) del complejo [**Pd(Aqa)(mC)**].

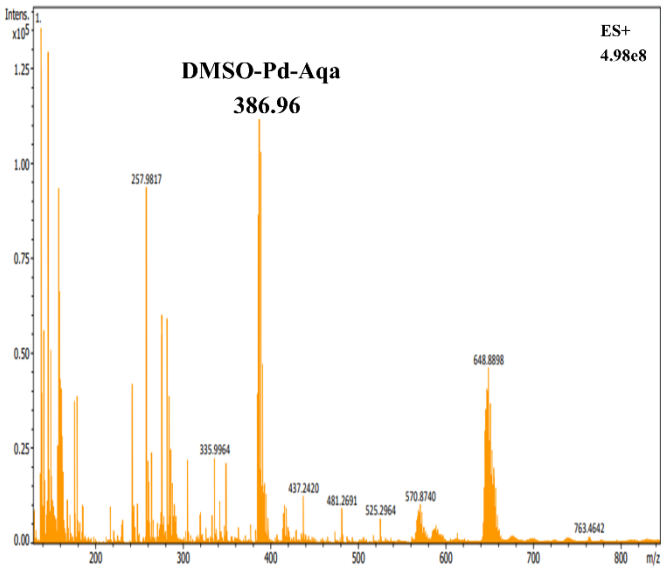

Anexo-Figura 9: Espectro ESI-MS (+) para el complejo [**Pd(Aqa)(DMSO)**].

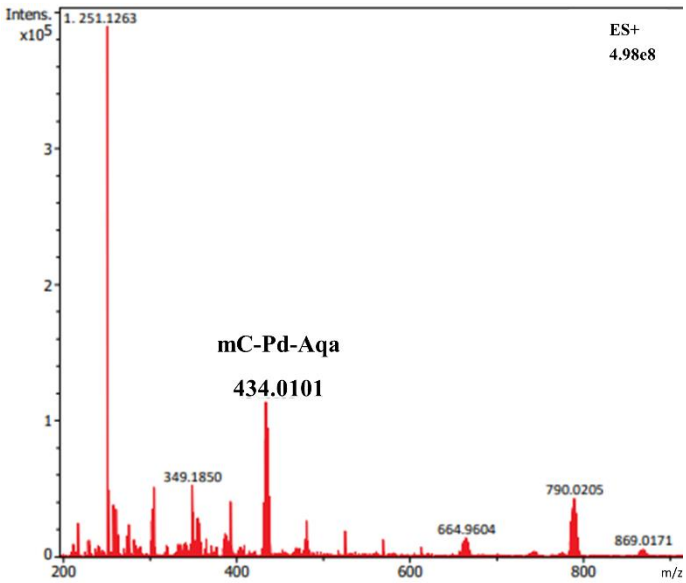

Anexo-Figura 10: Espectro ESI-MS (+) para el complejo [**Pd(Aqa)(mC)**].

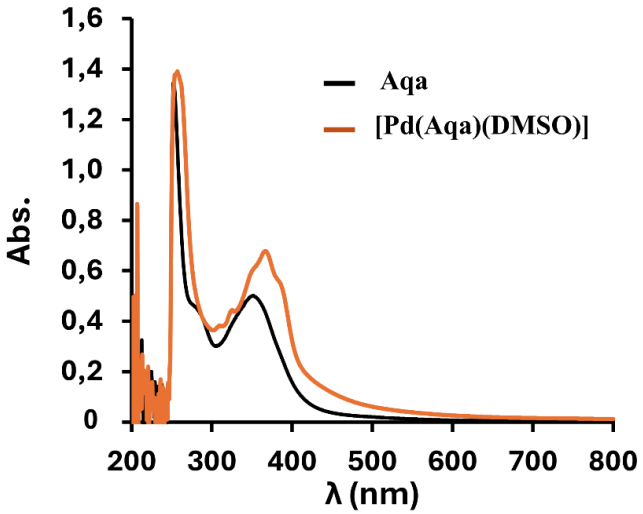

Anexo-Figura 11: Espectro UV-Vis para el ligando **Aqa** y el complejo [**Pd(Aqa)(DMSO)**]. Condiciones: 0.1 mM H_2O con 25% de DMF.

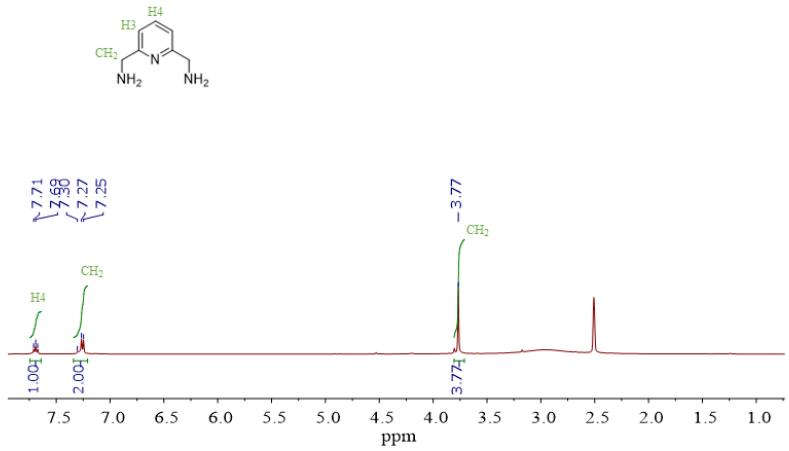

Anexo-Figura 12: ^{1}H-RMN (400Mhz, DMSO-D^{6}) del ligando piridín-2,6-diildimtanamina, **dPy.**

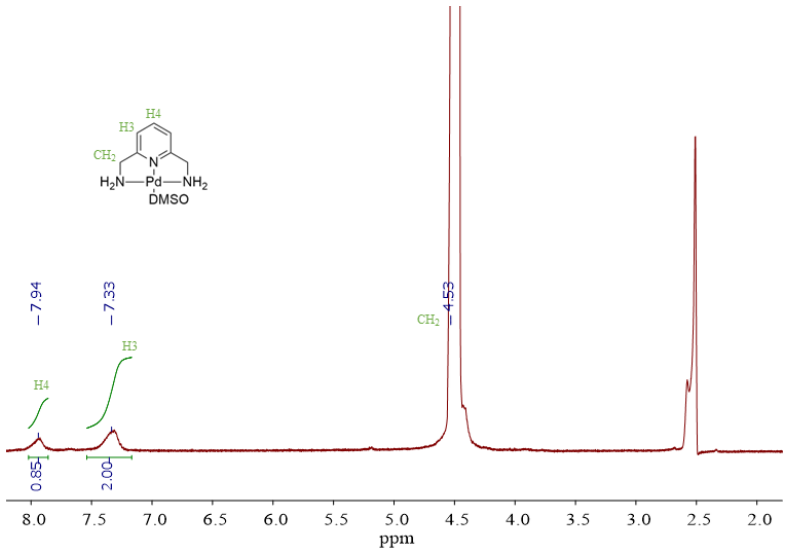

Anexo-Figura 13: ^{1}H-RMN (400Mhz, DMSO-D^{6}) del complejo [**Pd(dPy)(DMSO)**].

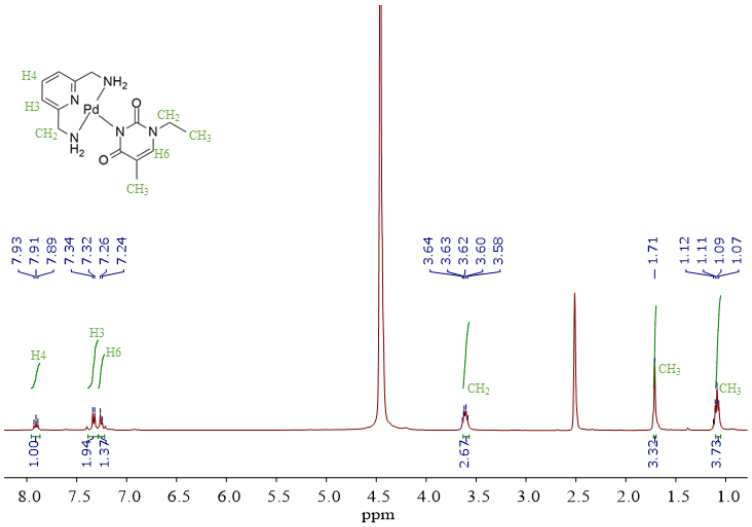

Anexo-Figura 14: ^{1}H-RMN (400Mhz, DMSO-D^{6}) del complejo [**Pd(dPy)(eT)**].

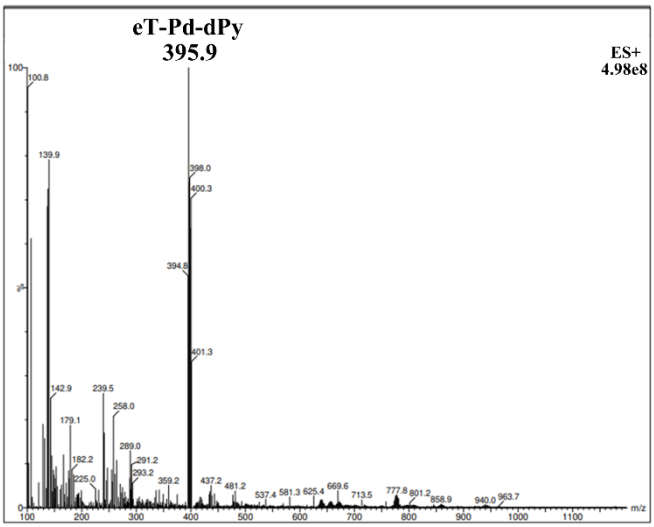

Anexo-Figura 15: Espectro ESI-MS (+) para el complejo [**Pd(dPy)(eT)**].

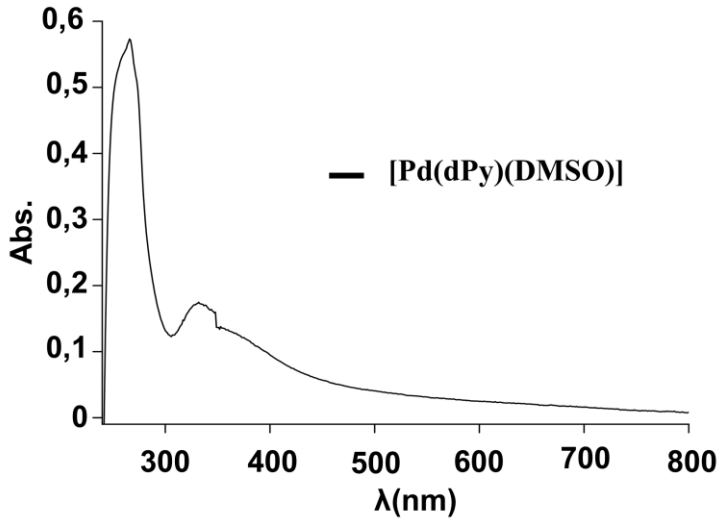

Anexo-Figura 16: Espectro UV-Vis para el complejo [**Pd(dPy)(DMSO)**]. Condiciones: 0.1 mM H_2O con 25% de DMF.

Capítulo 3

Estudios de Competitividad Entre Fragmentos Metálicos de Pd^{II} y Moléculas de ADN.

Capítulo 3. Estudios de Competitividad entre Fragmentos Metálicos de Pd^{II} y Moléculas de ADN.

En esta sección se presentan los resultados obtenidos para los estudios de competitividad entre los fragmentos metálicos [Pd(Cheld)] (**Pd-Cheld**) y [Pd(Aqa)] (**Pd-Aqa**) con las nucleobases de adenina y citosina a nivel individual, así como cuando forman parte de oligonucleótidos de cadena simple homotópica con unidades de 2'-dexoycitidina (**dC_{15}**), 2'-dexoyadenosina (**dA_{15}**), y de cadena heterotópica con una mezcla de unidades de 2'-dexoyadenosina y 2'-dexoycitidina 5'-d-(CCCACACACC)-3' (**dC_7A_3**). En el capítulo anterior, se demostró que era posible obtener sistemas supramoleculares híbridos del tipo **dA_{15}-Pd-Cheld** y **dC_{15}-Pd-Aqa**, donde fragmentos metálicos y ADN se unen formando pares de bases mediados por iones de Pd^{II}, cuya estructura supramolecular queda estabilizada por la formación de puentes de hidrógeno intramoleculares e interacciones de tipo stacking. En este sentido, las diferencias estructurales entre los ligandos orgánicos **Cheld** y **Aqa** brindan una oportunidad única para explorar la especificidad de cada uno de ellos con respecto a su nucleobases complementarias. A través de estos estudios, se aborda la posibilidad de diseñar sistemas heterolépticos ADN-metal compuestos por dos ligandos de distinta naturaleza dentro de la misma hebra simple de ADN (Figura 3.1).

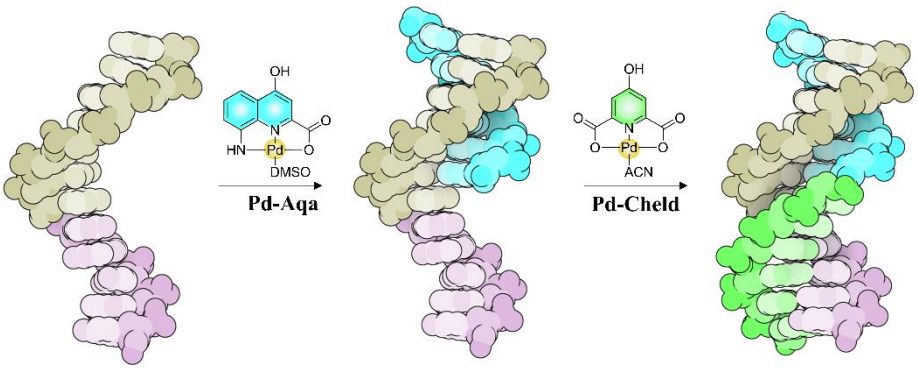

Figura 3.1: Representación esquemática de una posible estructura supramolecular híbrida basada en sistemas heterolepticos ADN-metal.

3.1. Estudios de competitividad metal-nucleobase.

En el capítulo anterior se estudió y caracterizó la formación de los complejos [Pd(Cheld)(eA)] (**eA-Pd-Cheld**) y [Pd(Aqa)(mC)] (**mC-Pd-Aqa**) (Figura 3.2), diseñados para que los ligandos empleados formen enlaces complementarios con la nucleobase correspondiente. En esta sección se estudiará la afinidad de dichos fragmentos por sus nucleobases complementarias, y se evaluará además la posible formación de interacciones de tipo no complementario. Estos estudios tienen como objetivo establecer las bases para el diseño y la preparación racional de sistemas heterolépticos de tipo ADN-metal, donde los fragmentos metálicos interactúen de manera específica con las nucleobases mediante un enfoque racional.

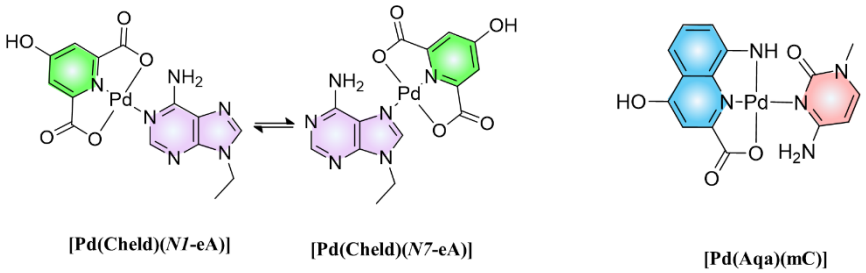

Figura 3.2: Esquema de los complejos complementarios **eA-Pd-Cheld** (izquierda) y **mC-Pd-Aqa** (derecha).

3.1.a. Estudios de competitividad entre los fragmentos metálicos [Pd(Cheld)] (**Pd-Cheld**) y [Pd(Aqa)] (**Pd-Aqa**) con las nucleobases adenina y citosina.

En primer lugar, se estudiaron las interacciones entre los fragmentos metálicos **Pd-Cheld** y **Pd-Aqa** con las nucleobases 1-metil-citosina (**mC**) y 9-etil-adenina (**eA**), respectivamente, con el fin de investigar la formación de complejos considerados como no complementarios **[Pd(Cheld)(mC)]** y **[Pd(Aqa)(eA)]**, los cuales no habían sido estudiados hasta el momento (Figura 3.3).

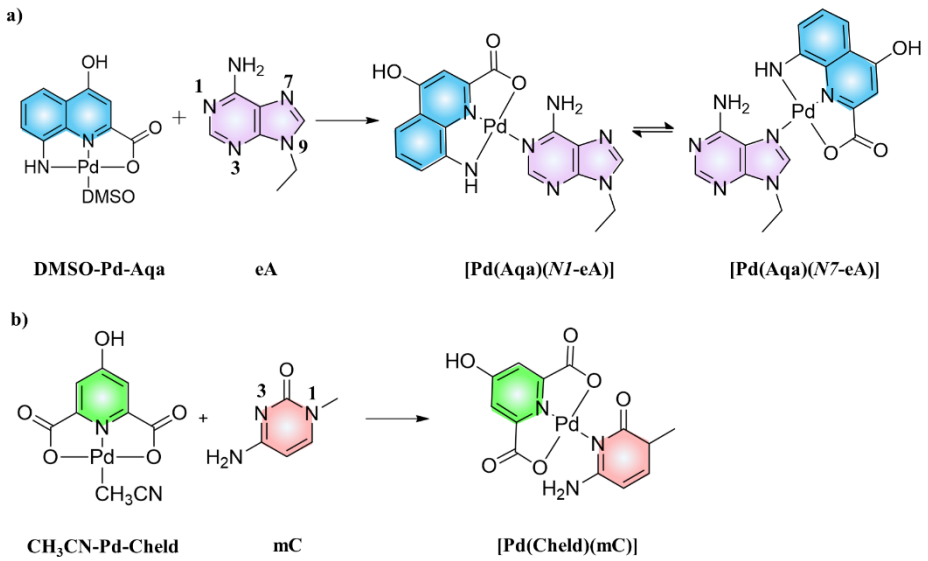

Figura 3.3: Esquema de reacción para la obtención de complejos formados por unidades no complementarias. a) Reacción entre el complejo metálico **DMSO-Pd-Aqa** y **eA** para obtener **eA-Pd-Aqa**. En el esquema se muestran los dos posible isómeros vía N1 y N7. b) Reacción entre el complejo metálico **CH_3CN-Pd-Cheld** y **mC** para obtener **mC-Pd-Cheld**. Las etiquetas numéricas sobre las estructuras de **eA** y **mC**, hacen referencia a la nomenclatura de cada nitrógeno.

Los datos obtenidos serán importantes para establecer una correlación posterior entre las especies, complementarias y no complementarias, que se forman en disolución en los experimentos de competitividad. Merece la pena indicar que el fragmento **Pd-Aqa** y la nucleobase **eA** podrían ser considerados como complementarios ya que pueden formar un enlace de hidrógeno intramolecular, aunque el grupo amino de **Pd-Aqa** no participe en este tipo de interacciones.

Los estudios competitivos entre nucleobases y fragmentos metálicos se estudiaron en disolución mediante medidas de ^{1}H-RMN. La Figura 3.4, muestra los espectros para la formación de los complejos **mC-Pd-Cheld** y **eA-Pd-Aqa**, así como los espectros de referencia de para las nucleobases **eA** y **mC** libres.

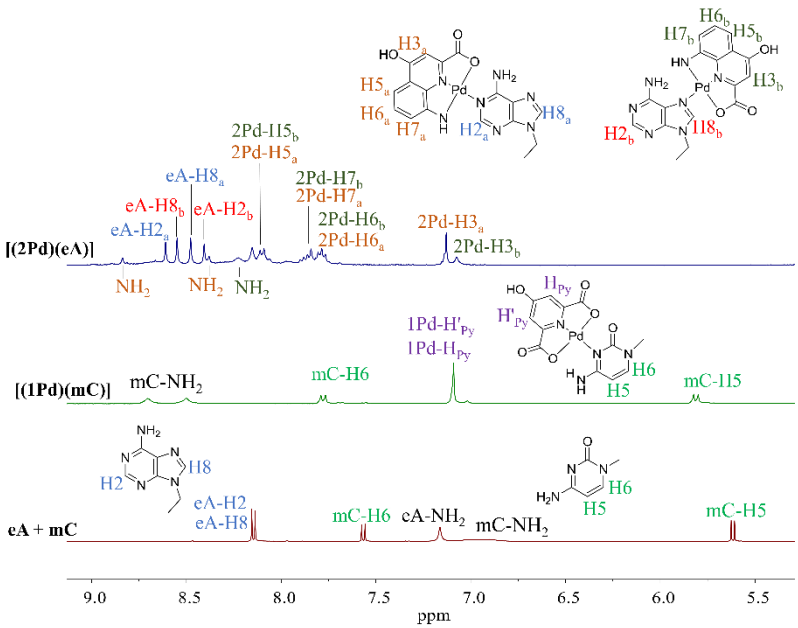

Figura 3.4: Espectro de ^{1}H-RMN (400 MHz; DMSO-D_6) para la mezcla de nucleobases **eA+mC** (abajo), complejo **mC-Pd-Cheld** (en medio) y complejo **eA-Pd-Aqa** (superior). En el espectro superior. Los códigos **1Pd** y **2Pd** hacen referencia a los fragmentos metálicos **Pd-Cheld** y **Pd-Aqa**, respectivamente.

El espectro obtenido para **mC-Pd-Cheld** (en medio) muestra dos dobletes a 7.76 y 5.78 ppm correspondientes a los protones H6 y H5 de **mC**, respectivamente. Además, se muestra un singlete a 7.07 ppm perteneciente a los protones aromáticos H_{py} y H'_{py} del fragmento **Pd-Cheld** y dos singletes anchos a 8.69 y 8.48 ppm correspondientes a los protones del grupo NH_2. Estos dos singletes anchos indican que tras formarse la especie **mC-Pd-Cheld**, el grupo amino pierde la rotación debido a que el enlace C-NH_2 adquiere carácter de doble enlace, lo que fija las posiciones de los H.

Por otro lado, en el espectro correspondiente al complejo **eA-Pd-Aqa** (azul), se muestran singletes a 8.60, 8.54, 8.47 y 8.40 ppm para los protones $H2_a$, $H8_b$, $H8_a$ y $H2_b$ consistentes con la formación de dos isómeros conformacionales que resultan de la unión del fragmento **Pd-Aqa** a través de la

posición N1 y N7 de la adenina para formar los complejos **[Pd(Aqa)(*N1*-eA)]** y **[Pd(Aqa)(*N7*-eA)]** que coexisten en equilibrio. Así mismo, se observan dos singletes a 7.12 y 7.07 ppm correspondientes al protón Aqa-H3a/b del fragmento **Pd-Aqa**, consistente con la formación de los dos isómeros. Las señales pertenecientes a los protones Aqa-$H5_{a/b}$ (multiplete), Aqa-$H7_{a/b}$ (multiplete) y Aqa-$H6_{a/b}$ (multiplete) aparecen en la región comprendida entre 8.20 – 7.70 ppm. Estos datos indican que los fragmentos **Pd-Cheld** y **Pd-Aqa** también son capaces de formar pares de bases no complementarios en disolución. Los espectros de ^{1}H-RMN completos para los complejos no complementarios, **eA-Pd-Aqa** y **mC-Pd-Cheld** aislados, pueden ser consultados en Anexo-Figura 1 y 2.

Se llevaron a cabo numerosos intentos para cristalizar estas especies con objeto de realizar medidas de difracción de rayos X y obtener datos de su estructura molecular en estado sólido. Desafortunadamente, solo se obtuvieron cristales aptos para su medida de la especie **mC-Pd-Cheld** (Figura 3.5 y Tabla 3.1) (Los datos cristalográficos completos se presentan en Anexo-Tabla 1).

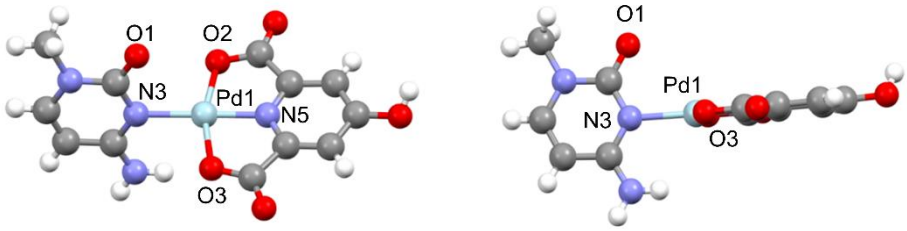

Figura 3.5: Dos perspectivas de la estructura molecular del complejo **[Pd(Cheld)(mC)]** resuelto mediante difracción de rayos X. Colores de los átomos: Carbono (Gris), Hidrógeno (blanco), Nitrógeno (azul), Oxígeno (rojo), Paladio (turquesa) (Anexo-Tabla 1).

Tabla 3.1. Datos cristalográficos más relevantes para el compuesto de coordinación **[Pd(Cheld)(mC)]**.

Código	**[Pd(Cheld)(mC)]**
Fórmula Empírica	$C_{12}H_{16}N_4O_9Pd$
Peso Molecular	466.69
Temperatura/K	100(2)
Sistema Cristalino	triclínico
Grupo Espacial	P-1
a/Å	6.7020(3)
b/Å	9.8320(5)
c/Å	13.1889(7)
α/°	95.501(2)
β/°	93.318(2)
γ/°	107.373(2)
Volumen/Å^3	822.17(7)
Z	2
R indexado final [I>=2σ (I)]	R_1 = 0.0395, wR_2 = 0.0984
R indexado final [completo]	R_1 = 0.0425, wR_2 = 0.1025
Distancias de enlace	
Pd1-N3	2.061 Å
Pd1-N5	1.910 Å
Pd1-O2	2.038 Å
Pd1-O3	2.044 Å

En este caso, la estructura molecular indica que el ion de Pd^{II} está coordinado según una geometría plana cuadrada al ligando **Cheld** en un sistema de coordinación μ,κ3-N3,O2,O4. La estructura obtenida reveló que la citosina se une a través de la posición N3 localizada en su cara WCF. Además, existe una desviación en la coplanariedad de la estructura debido a las fuerzas de repulsión entre los dos grupos cetona, que resulta en un ángulo entre planos de 75.63°. Esta sutil desviación podría ser la responsable de impedir la formación de un enlace de hidrógeno entre ambas moléculas. La distancia de enlace calculadas para Pd1-N3, fue de 2.061 Å, muy similar a las distancias observadas para las estructuras **eA-Pd-Cheld** y **pX-Pd-Cheld**, de 2.04 y 2.05 Å (capítulo 2, sección 2.1.b).

Con objeto de estudiar la formación de enlaces de hidrógeno intramoleculares entre entidades, se realizaron cálculos computacionales a nivel DFT (Figura 3.6). Para ello se calculó la energía de diferentes estructuras (single point) derivadas de rotar el enlace Pd-N en los complejos **mC-Pd-Cheld** y **mC-Pd-Aqa**. Los resultados mostraron que la estructura más estable para el complejo **mC-Pd-Cheld** es aquella en que las unidades **mC** y **Pd-Cheld** se desvían de la coplanariedad, concretamente para ángulos diedros <O-Pd-N-C de 45º y 150º, coincidiendo con los puntos valle de mínima energía relativa.

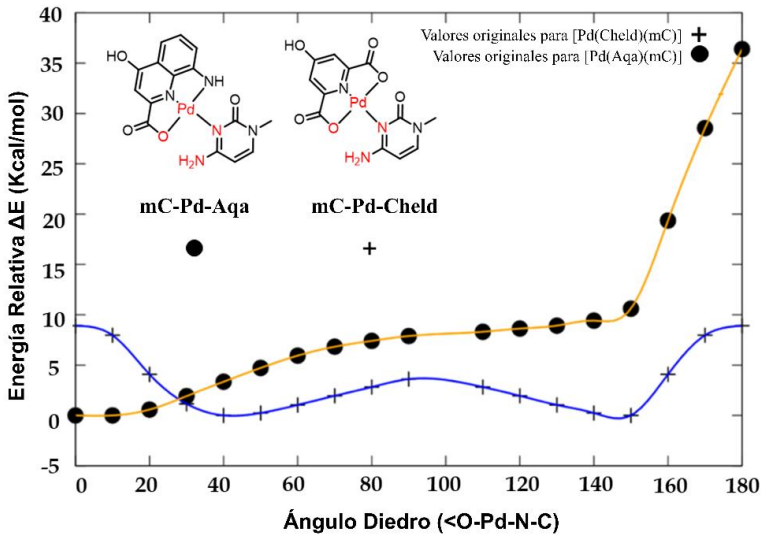

Figura 3.6: Variación en las energías de barrera torsional (Kcal/mol), determinadas mediante cálculos DFT a nivel PBEh-3c para estructuras de un solo punto generadas mediante rotaciones incrementales del ligando citosina en intervalos de 10º para los complejos **[Pd(Cheld)(mC)]** (+) y **[Pd(Aqa)(mC)]** (•). Las geometrías iniciales se ilustran en la figura, señalando en rojo los átomos que participan en el ángulo diedro (<0-Pd-N-C) de 0º.

Los datos obtenidos para el complejo **mC-Pd-Aqa**, cuya estructura es capaz de formar enlaces de hidrógeno complementarios, se muestran en la Figura 3.6. En esta ocasión, la estructura más estable es aquella donde ambas moléculas están orientadas en el mismo plano, para un ángulo diedro <O-Pd-N-C de 0º, lo que permite establecer interacciones mediante puentes de hidrógeno entre los grupo amino y cetona de ambas especies tal y como se comprobó en el capítulo 2. Por el contrario, la estructuras más desfavorecida es aquella donde los dos

grupos aminos y cetona, quedan enfrentados, respectivamente, es decir, para un ángulo diedro <O-Pd-N-C de 180º. Es precisamente esta cualidad la que se pretende explotar en esta investigación, pues cabría esperar que en un sistema más complejo que contenga hebras de ADN, la formación de los pares de bases complementarios (**mC-Pd-Aqa**) se vea favorecida en detrimento de los pares de bases no complementarios (**mC-Pd-Cheld**).

A continuación se comenzaron los estudios de especificidad de los fragmentos metálicos frente a ambas nucleobases. Para ello se realizaron medidas de ^{1}H-RMN para una mezcla de los fragmentos metálicos **Pd-Cheld** y **Pd-Aqa** con las nucleobases modelo **eA** y **mC**. El experimento consistió en disolver una mezcla de las nucleobases libres sobre las cuales se añadió cantidades crecientes de cada uno de los complejos hasta alcanzar un equivalente. La Figura 3.7 muestra la evolución del espectro de valoración para esta experiencia en el rango entre 9.5–5.5 ppm, que es la zona donde se observan los protones aromáticos más característicos para determinar las especies presentes en disolución (el espectro completo puede ser consultado en Anexo-Figura 3).

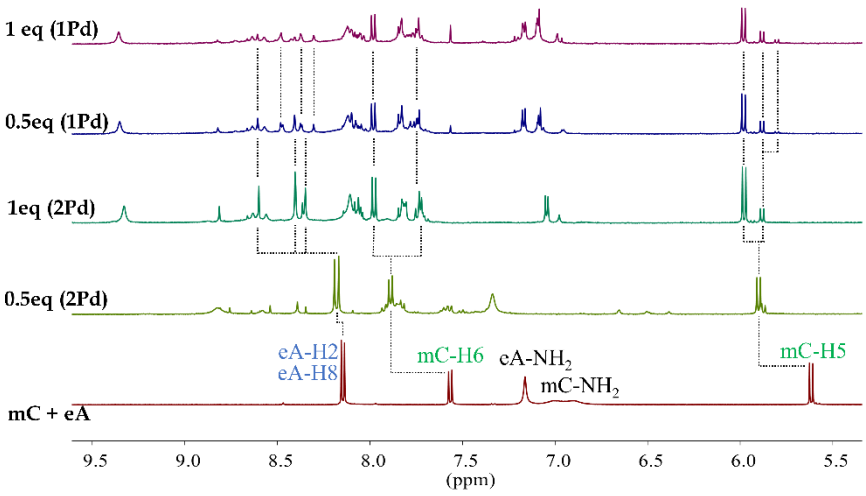

Figura 3.7: Espectro de ^{1}H-RMN (400 MHz; DMSO-D_6) para la valoración de una mezcla de las nucleobases **eA** y **mC** con los fragmentos metálicos **Pd-Cheld** y **Pd-Aqa**. Las líneas punteadas muestran los cambios generales más significativos de los desplazamientos de **eA** y **mC**.

En primer lugar, a la mezcla de nucleobases libres **mC** y **eA** se le añadió una cantidad creciente de **Pd-Aqa**. Tras añadir los primeros 0.5 equivalentes de **Pd-Aqa**, el espectro de ^{1}H-RMN muestra cambios con respecto a las señales de **mC** iniciales. Los dobletes correspondientes a los protones H6 y H5 de **mC** experimentaron un desplazamiento a campo bajo, pasando de 7.57 y 5.62 ppm hasta 7.89 y 5.9 ppm, respectivamente. Sin embargo, los protones H2 y H8 de **eA** no experimentaron cambios significativos. Esto indica que tras añadir una pequeña cantidad de **Pd-Aqa** y ante la posibilidad de reaccionar con ambas bases libres, preferentemente y al inicio, lo hace con su nucleobase complementaria **mC**. Finalmente, tras añadir un equivalente de ambos ligandos, se observa un espectro completamente diferente al inicial (Figura 3.7, rosa).

La Figura 3.8, muestra el espectro final obtenido tras el proceso de valoración y los espectros de referencia para las especies esperadas **eA-Pd-Cheld** y **mC-Pd-Aqa.**

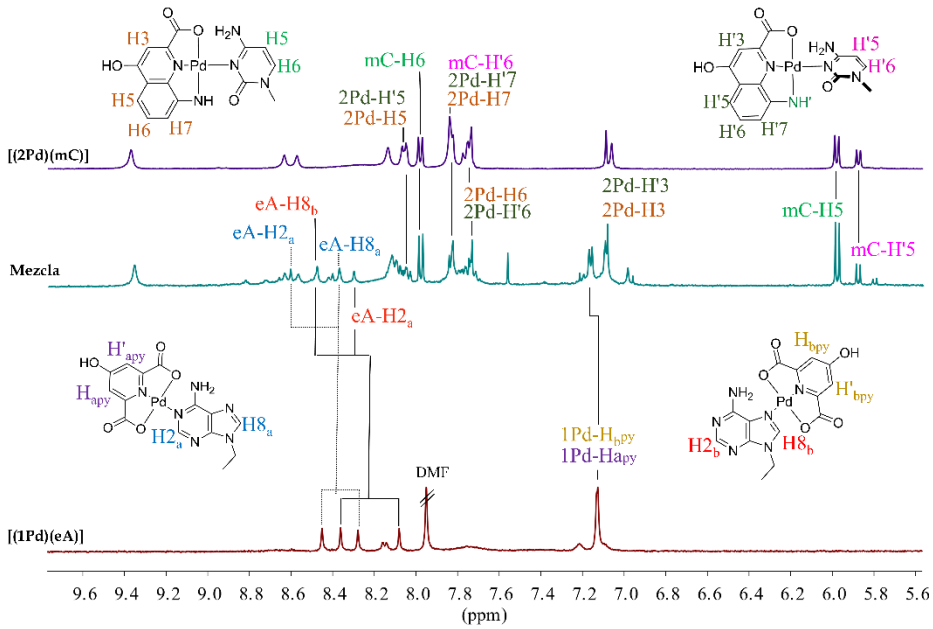

Figura 3.8: Espectros de ^{1}H-RMN (400 MHz; DMSO-D_6) para; una mezcla de los complejos **eA-Pd-Cheld** y **mC-Pd-Aqa** en disolución (medio) y los espectros de referencia para; la adición de 1 equivalente de **Pd-Cheld** con respecto a **eA** (abajo) y para la adición de 1 equivalente de **Pd-Aqa** con respecto a **mC** (superior). Los códigos **1Pd** y **2Pd** hacen referencia a los fragmentos metálicos **Pd-Cheld** y **Pd-Aqa**, respectivamente.

En primer lugar, cabe destacar la presencia de dos dobletes a 5.98 y 5.88 ppm correspondientes al protón H5 de **mC** que coinciden con la formación del complejo **mC-Pd-Aqa**. Como se demuestra en el capítulo 2, este desdoblamiento está causado por la rotación del enlace Pd-*N3*-mC en la estructura del complejo, lo que provoca la formación de dos isómeros conformacionales (coplanar y no coplanar). Esto mismo se observa con la formación de dos singletes a 7.09 y 7.08 ppm correspondientes al protón Aqa-H3 del fragmento metálico **Pd-Aqa**. Además, aparecen dos dobletes y un triplete a 8.06, 7.83 y 7.75 ppm, respectivamente, correspondientes a los protones Aqa-H5, Aqa-H7 y Aqa-H6. El espectro muestra también cuatro singletes a 9.37, 8.64, 8.57 y 8.14 ppm correspondientes a los protones del grupo Aqa-NH_2 para la conformación coplanar y no coplanar, observadas para el complejo **mC-Pd-Aqa** (Capítulo 2, Figura 2.17). Por otro lado, el espectro muestra dos singletes a 7.17 y 7.16 ppm correspondientes a los protones Cheld-H_{py} del fragmento **Pd-Cheld**, así como cuatro singletes a 8.61, 8.48, 8.37 y 8.30 ppm correspondientes a los protones eA-H2 y eA-H8 de los isómeros conformacionales **[Pd(Cheld)(*N1*-eA)]** y **[Pd(Cheld)(*N7*-eA)]**. En el espectro también aparecieron señales minoritarias para la formación de los pares de bases no complementarios **[Pd(Cheld)(mC)]** y **[Pd(Aqa)(eA)]** (anexo-Figura 4). Esto puede explicarse por la existencia de un equilibrio termodinámico que está más desplazado hacia la formación de las especies más estables **mC-Pd-Aqa** y **eA-Pd-Cheld**, y cuyas señales son mayoritarias. Por tanto, es poco probable obtener un espectro limpio donde únicamente se observe la formación de las especies objetivo. Este hecho sugiere que, a pesar de que todas las especies pueden formarse en disolución (tal y como se ha visto al inicio de este capítulo), los fragmentos metálicos **Pd-Cheld** y **Pd-Aqa** son capaces de discriminar entre las nucleobases de adenina y citosina, dando lugar a pares de bases con su estructura complementaria, mediadas por un enlace de coordinación a un ión central Pd^{II}.

Posteriormente se realizaron medidas de espectrometría de masas ESI (en modo positivo) a partir de una alícuota de la disolución estudiada mediante ^{1}H-RMN. Los resultados indicaron la formación de un pico mayoritario para la especie **[(mC-Pd-Aqa)+H]**$^{+}$ (teórico: 435.017 Da; encontrado: 434.009 Da), y dos picos minoritarios para las especies **[(eA-Pd-Aqa)+H]**$^{+}$ (teórico: 472.036 Da; encontrado: 473.034 Da) y **[(mC-Pd-Cheld)+H]**$^{+}$ (teórico: 412.650 Da; encontrado: 413.770 Da) (los espectros están disponibles en Anexo-Figura 5 y 6). Aunque no se encontraron picos correspondientes a la especie **eA-Pd-Cheld**, en la muestra podía apreciarse gran cantidad de [(**eA)+H]**$^{+}$ libre (teórico: 163.085 Da; encontrado: 164.093 Da). Este hallazgo sugiere una estabilidad dispar de los compuestos de coordinación durante el proceso de ionización, lo que podría conllevar a la ruptura del enlace de coordinación de las muestras con **eA**. Cabe destacar que la formación de esta especie quedó confirmada en el Capítulo 2, sección 2.1.b, donde se encontraron picos que confirmaban la formación de la especie **[**(**eA-Pd-Cheld)+H]**$^{+}$ (teórico: 450.9982 Da; encontrado: 451.9992 Da).

3.2. Formación de sistemas ADN-Pd heterolépticos.

Los resultados de competitividad obtenidos al emplear nucleobases libres proporcionaron el fundamento para diseñar experimentos más complejos utilizando ADN de cadena simple homotópica con unidades de 2'-deoxicitidina (**dC$_{15}$**). Para estos experimentos se registraron los cambios en el espectro de CD del oligonucleótido **dC$_{15}$** en presencia de cantidades crecientes de los fragmentos metálicos **Pd-Aqa** y **Pd-Cheld**. De acuerdo con los resultados obtenidos en los experimentos de ^{1}H-RMN, el fragmento **Pd-Aqa** tiene mayor preferencia por la unión a la citosina, por lo que la formación del híbrido **dC$_{15}$-Pd-Aqa** debe ser preferencial en contraposición a la formación del híbrido **dC$_{15}$-Pd-Cheld.**

3.2.a. Estudios de competitividad entre los fragmentos metálicos [Pd(Cheld)] (**Pd-Cheld**) y [Pd(Aqa)] (**Pd-Aqa**) con monohebras de **dC$_{15}$**.

Para registrar el espectro de CD se preparó una disolución de 2 µM de **dC$_{15}$,** 100 mM $NaClO_4$ y 5 mM MOPS (pH6.8) y se realizaron tres experimentos complementarios. La primera experiencia, consistió en añadir 1.3 equivalentes de **Pd-Cheld** para formar el híbrido **dC$_{15}$-Pd-Cheld**, y posteriormente añadir cantidades crecientes de **Pd-Aqa** con objeto de observar si se produce un desplazamiento del fragmento **Pd-Cheld (**Figura 3.9). En la segunda experiencia, se añadió 1.3 equivalente de **Pd-Aqa** para formar el híbrido **dC$_{15}$-Pd-Aqa**, y a continuación se valoró con cantidades crecientes de **Pd-Cheld**, para evaluar si se produce un desplazamiento del fragmento **Pd-Aqa** (Figura 3.10). Finalmente, en la experiencia tercera, se valoró una disolución de **dC$_{15}$** con una disolución que contenía una mezcla a 1.3 equivalentes de **Pd-Cheld** y **Pd-Aqa** para evaluar el híbrido supramolecular que se forma preferentemente, **dC$_{15}$-Pd-Aqa** , **dC$_{15}$-Pd-Cheld** , o una mezcla de ambos. (Figura 3.11).

La Figura 3.9 muestra el espectro de CD para la valoración inicial de una mezcla **dC$_{15}$** y 1.3 equivalentes de **Pd-Cheld**, a la que se añadieron cantidades crecientes de **Pd-Aqa**.

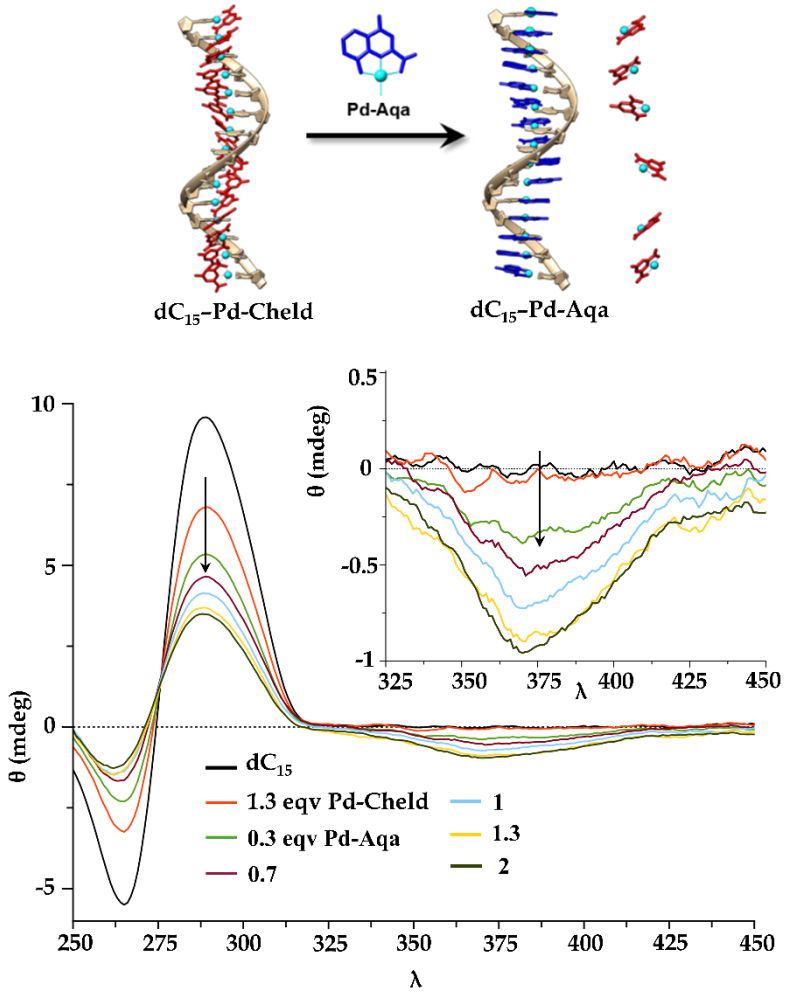

Figura 3.9: Esquema de la reacción de competitividad investigada y espectros de CD para la valoración de **dC$_{15}$** con 1.3 eqv. **Pd-Cheld** y cantidades crecientes de **Pd-Aqa**. **Pd-Aqa**. Condiciones: 2 µM DNA, 36 µM **Pd-Cheld** 0→60 µM **Pd-Aqa**, 100 mM $NaClO_4$, 5 mM MOPS (pH 6.8). Las flechan indican la dirección de los cambios del CD.

Inicialmente, el espectro muestra efecto Cotton con una banda positiva y otra negativa a 283 y 270 nm, respectivamente, correspondiente a **dC$_{15}$** libre. Tras añadir 1.3 equivalentes de **Pd-Cheld** no se observa la aparición de bandas ICD, aunque no son de esperar, ya que el complejo **mC-Pd-Cheld** no absorbe en esta región (espectro UV-Vis disponible en Anexo-Figura 7). En este caso, el espectro solo muestra una disminución en la intensidad del máximo y mínimo mencionados anteriormente, indicando cierto grado de interacción entre **dC$_{15}$** y **Pd-Cheld** (Para estudiar esta interacción con más detalle, se realizó una valoración adicional en la que se investigó la interacción de **dC$_{15}$** con cantidades crecientes de **Pd-Cheld**. Los estudios de CD revelaron cambios en la región del correspondiente a **dC$_{15}$** (< 300nm) pero en ningún caso se mostraron bandas ICD en la zona de 370 nm, como se observa en la figura Anexo-Figura 8).

A continuación, se añadieron cantidades crecientes de **Pd-Aqa** dando lugar a la aparición de una banda ICD centrada a 375 nm, y cuyos cambios se estabilizan a partir de 1.3 equivalentes (Figura 3.9). Este hecho indica que el fragmento **Pd-Aqa** es capaz de unirse a **dC$_{15}$** en presencia de **Pd-Cheld**, y que por tanto posee una mayor afinidad por esta secuencia de ADN.

En el segundo experimento se valoró una disolución de **dC$_{15}$** y 1.3 equivalente de **Pd-Aqa**, a la que se le añadieron cantidades crecientes de **Pd-Cheld**. La Figura 3.10 muestra el espectro registrado para este experimento donde inicialmente se observa un efecto Cotton con una banda positiva y otra negativa a 283 y 270 nm, respectivamente, correspondiente a **dC$_{15}$** libre. Tras añadir 1.3 equivalentes de **Pd-Aqa**, el espectro sufre cambios drásticos, derivados de la formación del híbrido **dC$_{15}$ -Pd-Aqa**, como se describió en el Capítulo 2, sección 2.2.c. Tanto el mínimo como el máximo experimentan un desplazamiento hipsocrómico hasta los 260 y 280 nm, así como una bajada drástica de intensidad. Además, aparece una banda ICD a 375 nm correspondiente a la interacción entre la hebra simple y el fragmento metálico **Pd-Aqa**. A continuación, y tras añadir cantidades crecientes de **Pd-Cheld**, el espectro de CD solo mostró una ligera disminución en la intensidad de todas

las señales registradas. Estos datos indican que el fragmento **Pd-Cheld** no es capaz de desplazar al fragmento **Pd-Aqa** cuando éste forma parte del sistema **dC$_{15}$-Pd-Aqa**, reforzando la idea de una interacción preferente entre el fragmento metálico complementario a citosina, **Pd-Aqa**, en contraposición del fragmento metálico no complementario, **Pd-Cheld**.

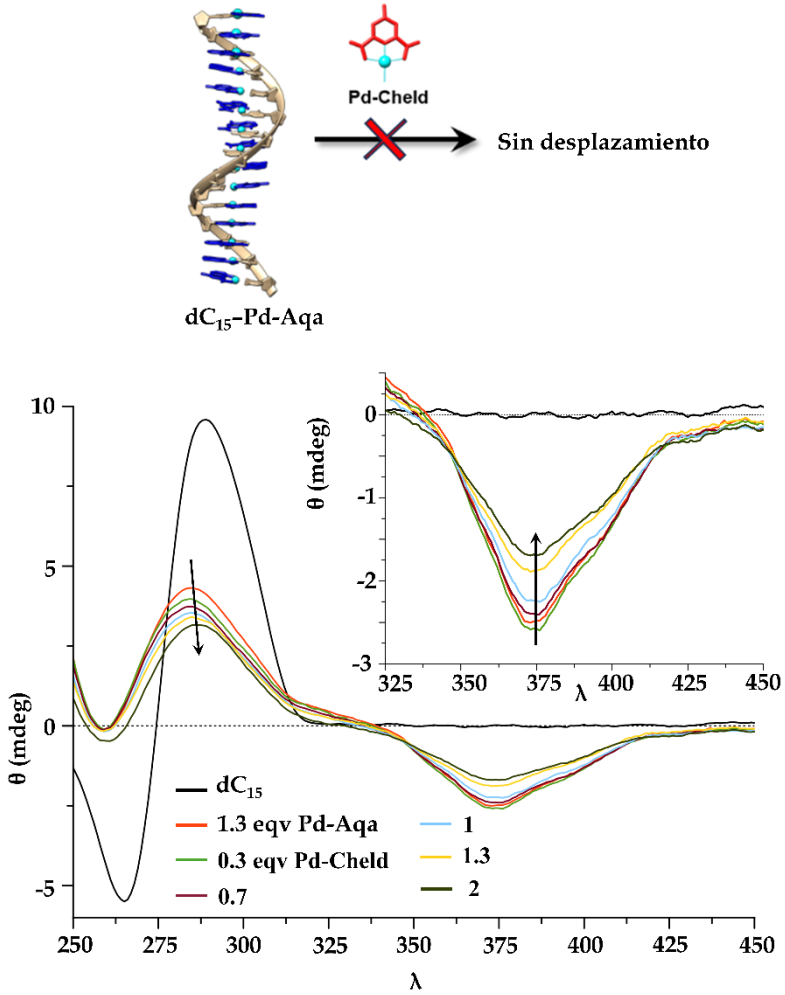

Figura 3.10: Esquema de la reacción de competitividad investigada y espectros de CD para la valoración de **dC$_{15}$** con 1.3 eqv. **Pd-Aqa** y cantidades crecientes de **Pd-Cheld**. En la imagen superior se muestra la representación esquemática del proceso. Condiciones: 2 µM DNA, 36 µM **Pd-Aqa,** 0→60 µM **Pd-Chel,** 100 mM $NaClO_4$, 5 mM MOPS (pH 6.8). Las flechan indican la dirección de los cambios del CD.

El último experimento consistió en valorar una disolución de **dC$_{15}$** con otra disolución que contenía una mezcla de 1.3 equivalentes de **Pd-Cheld** y **Pd-**

Aqa. La Figura 3.11 muestra el espectro inicial típico para la hebra simple **dC$_{15}$** con una banda positiva y otra negativa a 283 y 270 nm, respectivamente. Tras añadir 1.3 equivalentes de la mezcla de los fragmentos metálicos, el perfil de CD muestra un efecto Cotton muy pronunciado con la aparición de un mínimo a 250 nm correspondiente a una banda ICD. Estos resultados son similares a los observados en las experiencias anteriores (Figura 3.9 y 3.10). Esta experiencia muestra inequívocamente como, ante la posibilidad de interaccionar con cualquiera de los ligandos, la hebra de **dC$_{15}$** lo hace preferentemente con el fragmento complementario **Pd(Aqa)**.

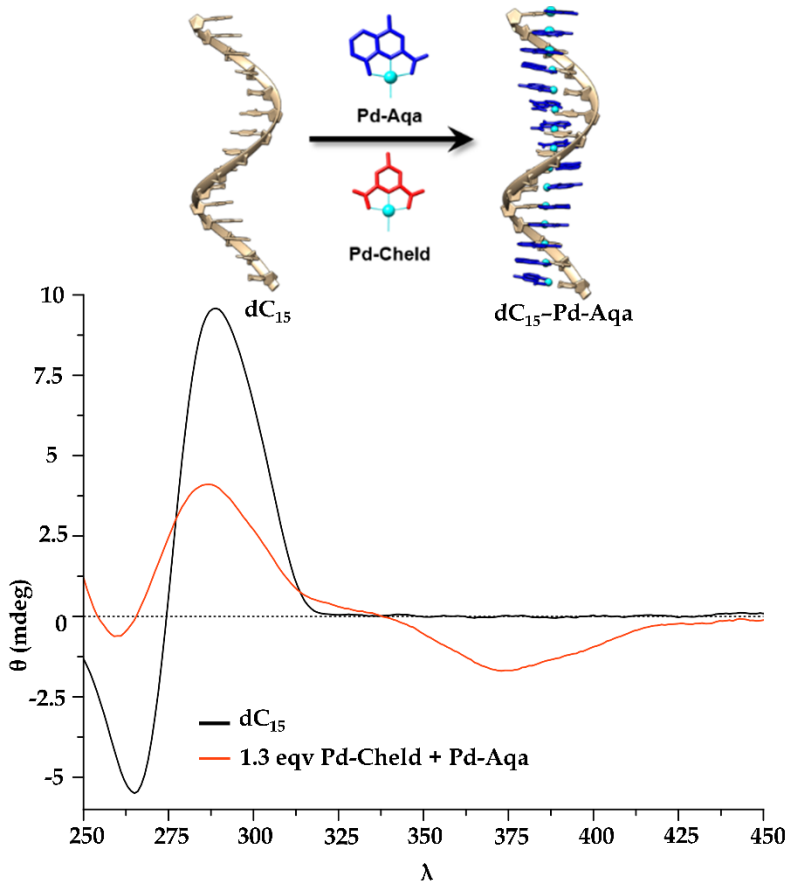

Figura 3.11: Esquema de la reacción de competitividad investigada y espectro de CD para la valoración de **dC$_{15}$** con 1.3 eqv. de **Pd-Aqa** y **Pd-Cheld**. En la imagen superior se muestra la representación esquemática del proceso Condiciones: 2 µM DNA, 36 µM **Pd-Cheld,** 36 µM **Pd-Aqa**, 100 mM $NaClO_4$, 5 mM MOPS (pH 6.8).

Los datos de CD obtenidos, son consistentes con los resultados de ^{1}H-RMN presentados en la sección 3.1.a., donde se ha demostrado que el fragmento metálico **Pd-Aqa** es capaz de desplazar a **Pd-Cheld** para unirse preferentemente a su nucleobase complementaria mediante pares de bases mediados por metales.

Finalmente, y con objeto de conocer los aspectos termodinámicos de las interacciones de los fragmentos **Pd-Cheld** y **Pd-Aqa** con respecto a la citosina libre y el oligonucleótido **dC$_{15}$**, se realizaron experimentos de calorimetría de titulación isotérmica (**ITC**). Estos experimentos comenzaron estudiando las interacciones más sencillas entre los fragmentos metálicos **Pd-Cheld** y **Pd-Aqa** con citidina-monofosfato (**CMP**) y posteriormente, las interacciones de sistemas más complejos con la hebra simple **dC$_{15}$**. En este caso, el empleo de **CMP** y no de la nucleobase modificada **mC** responde a la mayor solubilidad de la citidina. También se realizaron experimentos con **dA$_{15}$**, aunque desafortunadamente estos resultados no fueron concluyentes. Cabe destacar que la sensibilidad del equipo de **ITC** obliga a que todas las disoluciones contengan exactamente las mismas concentraciones de sales o disolventes orgánicos. Esto se debe a que cualquier variación del sistema (como un porcentaje distinto de disolvente orgánico entre muestras) producirá calores de dilución que serán detectados por el equipo cuando ambas disoluciones se mezclen, y por tanto, afectará a una correcta medida de los parámetros termodinámicos.

Para estudiar la interacción de los fragmentos metálicos con **CMP** y **dC$_{15}$** se prepararon disoluciones de 100 µM **Pd-Cheld** o **Pd-Aqa**, 10 mM MOPS (pH6.8), 10 mM $NaClO_4$ en un 5% DMF. Estas disoluciones se valoraron con otra disolución que contenía 2 mM **CMP** o **dC$_{15}$**, 10 mM MOPS (pH6.8), 10 mM $NaClO_4$ con un 5% DMF. Para realizar la titulación, se colocó el complejo metálico bajo estudio en la celda calorimétrica y se valoró inyectando volúmenes constantes de 10 µL de **CMP** o **dC$_{15}$**, según corresponda. Estas adiciones fueron modificando la ratio Pd/base a lo largo de la experiencia desde

0 hasta alcanzar al menos 3 equivalentes. La Figura 3.12 muestra dos tipos de diagramas de ITC obtenidos para estas experiencias.

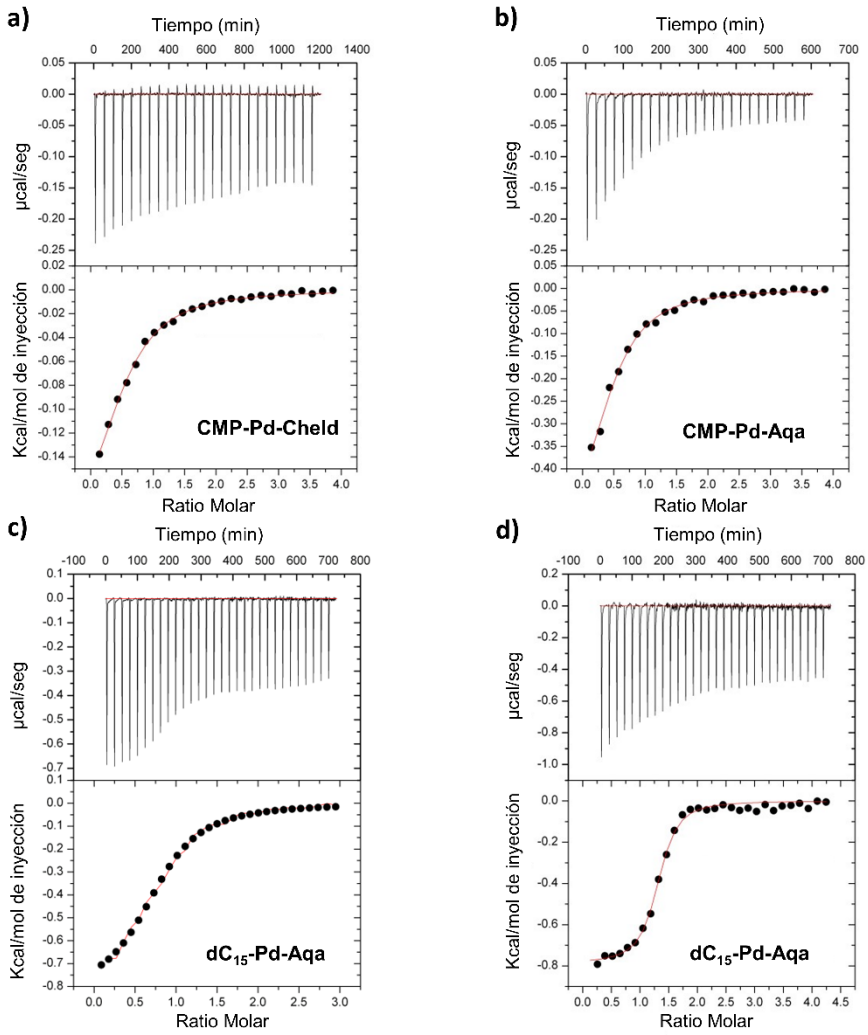

Figura 3.12: Gráficas de ITC para las interacciones entre: a) **Pd-Cheld** y **CMP**. b) **Pd-Aqa** y **CMP**. c) **Pd-Cheld** y **dC$_{15}$**. d) **Pd-Aqa** y **dC$_{15}$**. Las gráficas superiores muestran los termogramas experimentales donde se observan las inyecciones realizadas frente al tiempo de recuperación. Las gráficas inferiores muestran los valores de calor normalizados por mol de ligando inyectado frente a la relación molar. Condiciones: 2 mM **dC$_{15}$**, 100 µM **Pd-Cheld,** 100 µM **Pd-Aqa**, 100 mM $NaClO_4$, 5 mM MOPS (pH 6.8) y 5% DMF.

Por un lado, se representan los termogramas experimentales que muestran los efectos calóricos (µcal/seg) de las inyecciones realizadas de **CMP** ó **dC_{15}** sobre la disolución del fragmento metálico correspondiente (parte superior de las gráficas). Los termogramas muestran picos cuya intensidad disminuye a medida que transcurre el tiempo. Cada pico indica el momento de la inyección, y el área de cada pico es la medida del calor correspondiente. La separación entre ellos representa el tiempo de estabilización del sistema hasta realizar la siguiente inyección.

Por otro lado, se representan los valores de calor normalizados (Kcal/mol) de **CMP** o **dC_{15}** inyectado frente a la relación molar ADN:Pd (parte inferior de las gráficas), donde se obtienen perfiles de curvas sigmoidales. A partir de estos gráficos, se pueden extraer los parámetros termodinámicos correspondientes a las interacciones ADN-metal. Es importante mencionar que, solo en casos óptimos, se observarán perfiles de curvas sigmoidales tal y como muestra la Figura 3.12 para la valoración con **dC_{15}**. Sin embargo, a veces los perfiles de las curvas pueden resultar más complejos, como los observados para la valoración con **CMP**, donde se observan perfiles parabólicos.

La Tabla 3.1 muestra los parámetros termodinámicos calculados para la unión entre **Pd-Cheld** y **Pd-Aqa** con **CMP** y **dC_{15}** derivados del ajuste de las cruvas de unión de ITC utilizando un modelo de unión de sítios equivalentes e independientes. En esta tabla se muestran además los valores de la constante de unión (K_b), que nos indican la afinidad de cada uno de los ligandos por **CMP** y **dC_{15}**. Todos estos datos, serán comentados a continuación.

Tabla 1: Parámetros termodinámicos de unión entre, **Pd-Cheld** y **Pd-Aqa** con **CMP** y **dC_{15}** derivados del fitting de los termogramas de ITC.

	CMP		**dC_{15}**	
	Pd-Aqa	**Pd-Cheld**	**Pd-Aqa**	**Pd-Cheld**
K_b ($\cdot 10^3$ M^{-1})	35 ± 12	27 ± 6	540 ± 140	54 ± 12
K_d (μM)	29 ± 10	37 ± 9	1.8 ± 0.5	18 ± 4
ΔG_b (kJ·mol^{-1})	−6.19 ± 0.21	−6.04 ± 0.14	−7.82 ± 0.15	−6.46 ± 0.13
ΔH_b (kJ·mol^{-1})	−0.65 ± 0.16	−0.26 ± 0.05	−0.76 ± 0.02	−1.06 ± 0.02
$-T\cdot\Delta S_b$ (kJ·mol^{-1})	−5.6 ± 0.4	−5.78 ± 0.18	−7.06 ± 0.18	−5.40 ± 0.15
N	0.46 ± 0.07	0.50 ± 0.05	1.26 ± 0.02	0.79 ± 0.03

La Figura 3.13, muestra una representación de los valores termodinámicos calculados mediante un diagrama de barras para las interacciones de los fragmentos metálicos con **CMP** y **dC_{15}**.

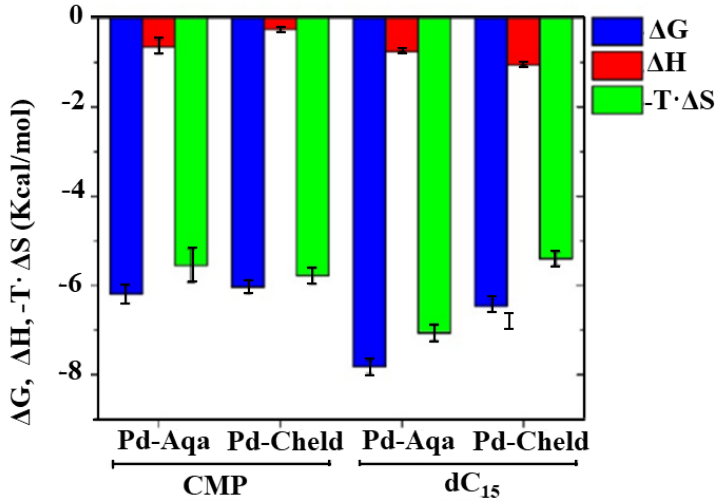

Figura 3.13: Parámetros termodinámicos (energía libre, entalpía y entropía) representados mediante diagramas de barras para los enlaces de **Pd-Cheld** y **Pd-Aqa** con **CMP** y **dC_{15}**.

En este tipo de uniones, los factores entálpicos y entrópicos contribuyen positivamente a la afinidad de unión global (**ΔG**). Los gráficos de la Figura 3.13 (izquierda) muestran como la interacción de ambos ligandos con **CMP** tienden predominantemente hacia una naturaleza entrópica (-T·ΔS). Los datos termodinámicos calculados para la entropía y la entalpía de **CMP-Pd-Cheld** y **CMP-Pd-Aqa** fueron de, -5.78 y -5.6 kJ·mol^{-1}, -0.26 y -0.65 kJ·mol^{-1}, respectivamente. Finalmente, estas pequeñas diferencias se contrarrestan y las afinidades de unión entre ambos sistemas fueron muy similares, 27.10^3 M^{-1} y 35. 10^3 M^{-1}.

La principal contribución energética para los sistemas **CMP-Pd** proviene de la entropía, impulsada principalmente por la liberación de agua que acompaña a la formación de los pares de bases mediados por Pd^{II}. Las curvas de ITC para estos ensayos se ajustaron según un modelo que considera sitios de unión independientes y equivalentes, lo que dio como resultado una estequiometría de unión aproximadamente 0.5:1 (Figura 3.12). Estos resultados indican que dos fragmentos metálicos podrían unirse a **CMP**. De hecho, este evento no se puede descartar, ya que se ha documentado la unión de dos complejos de Pd^{II} a derivados de citidina, con la participación del átomo N3 del grupo amino.[1,2]

La formación de los enlaces entre **CMP** y los fragmentos metálicos implica la ruptura de enlaces de hidrógeno que se establecen entre el nucleósido y las moléculas de agua circundantes. En ambos procesos hay implicada una energía similar, que se contrarrestan y derivan en los bajos valores de entalpía calculados.

Por otro lado, si se observa la representación de los valores termodinámicos calculados para las interacciones de los fragmentos metálicos con **dC_{15}** , los datos de ITC muestran una mayor afinidad para la formación del híbrido complementario **dC_{15}-Pd-Aqa** (K_b = 540. 10^3 M^{-1}) en comparación con la estructura no complementaria, **dC_{15}-Pd-Cheld** (K_b = 54. 10^3 M^{-1}) (Tabla 1).

Al igual que en los estudios con **CMP**, ambos complejos exhiben una contribución energética entálpica y entrópica favorable al interactuar con la hebra simple. Sin embargo, aunque la entalpía de unión es similar, -0.76 kJ·mol^{-1} **(dC$_{15}$-Pd-Aqa)** y -1.06 kJ·mol^{-1} (**dC$_{15}$-Pd-Cheld)**, el factor entrópico ahora es significativamente mayor para el fragmento **Pd-Aqa**. Concretamente, se obtuvieron valores de entropía para el híbrido **dC$_{15}$-Pd-Aqa** de -7.06 kJ·mol^{-1}, y de -5.40 kJ·mol^{-1} para **dC$_{15}$-Pd-Cheld**. Para entender estos resultados, cabe indicar que estudios previos han demostrado que las secuencias ricas en citosina pueden adoptar estructuras altamente organizadas a pH 7, [3–5] como se observa en el perfil de CD para **dC$_{15}$** libre (Capítulo 2, Figura 2.23), cuya máximo a 280 nm es especialmente intenso si se compara con la misma señal para **dA$_{15}$** libre (Capítulo 2, Figura 2.8). Este comportamiento puede justificar las bajas entalpías de unión en comparación con contribuciones altas de entropía.

En este escenario, la pérdida de entropía conformacional y traslacional-rotacional producida por la unión de **Pd-Aqa** se compensa con la ganancia de entropía asociada a los procesos de desolvatación que ocurren junto con los eventos de apilamiento. Cabe destacar que, a diferencia de los estudios con **CMP**, la unión de la hebra **dC$_{15}$** con los fragmentos metálicos implica la formación de interacciones de apilamiento entre pares de bases adyacentes. Por tanto, la formación del híbrido **dC$_{15}$-Pd-Aqa** exhibirá interacciones de apilamiento más favorables que **dC$_{15}$-Pd-Cheld**. Esto es causado por la propia estructura del ligando, pues **Pd-Aqa** presenta dos anillos aromáticos y por tanto la coplanariedad está favorecida para la formación del complejo **dC$_{15}$-Pd-Aqa,** en contraposición a **dC$_{15}$-Pd-Cheld**. Estas observaciones concuerdan con estudios que destacan la importancia de las interacciones de apilamiento de bases en la estabilidad de las hélices de ADN.[6]

La estequiometría de unión para **dC$_{15}$** ahora se acerca más a n = 1, lo que sugiere que la unión de más de un complejo de Pd^{II} a las bases de citosina está más impedida cuando se emplea la hebra simple, al contrario que en el caso de

CMP. La Figura 3.12 muestra los termogramas de ITC para la titulación con **dC_{15}** sobre los complejos metálicos, y las curvas de unión para ambas experiencias. El perfil de la curva de unión para el sistema **dC_{15}-Pd-Aqa** muestra una mayor forma que el correspondiente perfil del sistema **dC_{15}-Pd-Cheld**, lo que concuerda con la idea expuesta anteriormente sobre una formación preferente de los pares de bases complementarios mediados por Pd^{II}.

La información obtenida a partir de los estudios de ITC ofrece ideas esenciales para entender por qué **Pd-Aqa** muestra una mayor afinidad por la citosina que el fragmento metálico **Pd-Cheld**. Además, servirán como base para establecer un método que permita comprender las interacciones entre nuevos complejos metálicos complementarios a las nucleobases.

3.2.b. Estudios de competitividad entre los fragmentos metálicos [Pd(Cheld)] (**Pd-Cheld**) y [Pd(Aqa)] (**Pd-Aqa**) con monohebras de **dA_{15}**.

Como se comentó anteriormente, se realizaron experimentos análogos de ITC empleando ADN de cadena simple homotópica con unidades de 2'-deoxiadenosina (**dA_{15}**) y los fragmentos metálicos **Pd-Cheld** y **Pd-Aqa** (Figura 3.14). Para esto se prepararon disoluciones que contenían 100 µM **Pd-Cheld** o **Pd-Aqa**, 10 mM MOPS (pH6.8), 10 mM $NaClO_4$ en un 5% DMF. Estas disoluciones se valoraron con otra disolución que contenía 2 mM **dA_{15}**, 10 mM MOPS (pH6.8), 10 mM $NaClO_4$ con un 5% DMF.

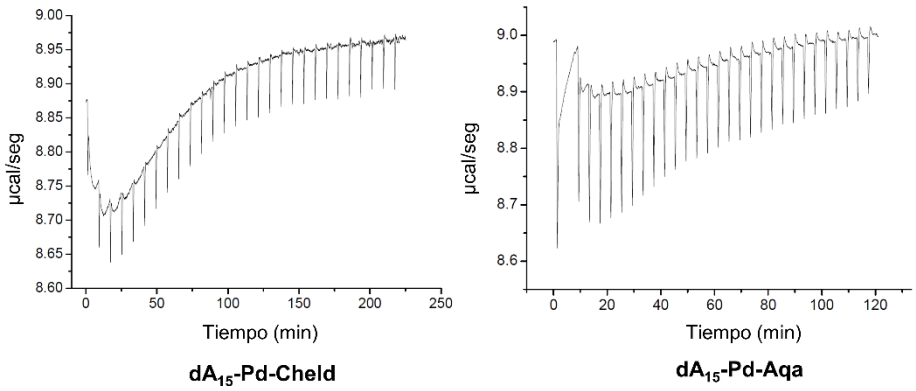

Figura 3.14: Gráficas de ITC de los termogramas experimentales para las interacciones entre: a) **Pd-Cheld** y **dC$_{15}$**. b) **Pd-Aqa** y **dC$_{15}$**.

En los termogramas obtenidos para estas experiencias, se aprecia como el área de las inyecciones para cada pico, solapa con el área del siguiente pico, comportamiento que no fue observado para los experimentos análogos con **dC$_{15}$** (Figura 3.12 c y d). Este es debido a que el proceso de unión entre **dA$_{15}$** y los fragmentos metálicos para formar los híbridos supramoleculares **dC$_{15}$-Pd-Aqa** y **dC$_{15}$-Pd-Cheld** es muy lento, provocando que el sistema no tenga tiempo suficiente para reajustarse y estabilizarse antes de la siguiente inyección. Un problema importante derivado de esta causa es la propia limitación del equipo de ITC, que no puede realizar medidas tan prolongadas en el tiempo como las requeridas para esta experiencia. Por tanto, los hechos aquí presentados, impiden extraer correctamente los datos termodinámicos derivados de los termogramas.

Es importante señalar, que las causas que motivan la lenta interacción entre **dA$_{15}$** y los fragmentos metálicos no pueden ser extraídas con claridad y son meramente especulativas. La ruptura de los enlaces de hidrógeno entre hebras de ADN y el agua circundante para formar enlaces de tipo ADN-metal podría ser uno de los motivos. Otra posible causa podría ser que la presencia de los nitrógenos N1 y N7 en la adenia, que ralentiza la organización de los fragmentos metálicos de Pd^{II} debido a una interacción en ambas posiciones

hasta el completo reajuste y la formación de la estructura vía N1 orientada en la cara WCF de la hebra simple.

Desafortunadamente, los datos recolectados para estos sistemas fueron limitados y son necesarios realizar ajustes que ayuden a mejorar los valores termodinámicos obtenidos. Además, será necesario comparar los valores de ITC de los homopolímeros de **dA_{15}** con cadenas simples homotópicas con unidades de 2'-deoxi-deaza-adenosina (**dX_{15}**) donde el nitrógeno en la posición N7 se ha cambiado por un grupo CH, tal y como se hizo a lo largo del capítulo 2 para los estudios de interacción ADN-metal.

3.2.b. Formación de sistemas heterolépticos de tipo ADN-Pd**.**

Finalmente, como prueba de concepto para demostrar la formación de sistemas heterolepticos de tipo ADN-Pd, se realizaron estudios ESI-MS de la reacción entre los fragmentos metálicos **Pd-Cheld**, **Pd-Aqa** y oligonucleótidos con secuencia 5'-d(CCCACACACC)-3' (**dC_7A_3**). Para realizar estos estudios se empleó una disolución que contenía 50 µM **dC_7A_3**, sobre la que se añadieron disoluciones de **Pd-Cheld** y **Pd-Aqa** 750 µM en agua y un 15% DMSO. Las muestras se incubaron a 40ºC durante 30 minutos. Para estas experiencias, se evitó añadir buffer o sales a la disolución, pues pruebas preliminares demostraron que dificultaban las medidas ESI-MS.

La Figura 3.15 muestra el espectro ESI-MS obtenido para estos estudios, donde se observan picos mayoritarios para la especie objetivo **dC$_7$A$_3$-7(Pd-Aqa)-3(Pd-Cheld)** (6008 Da).

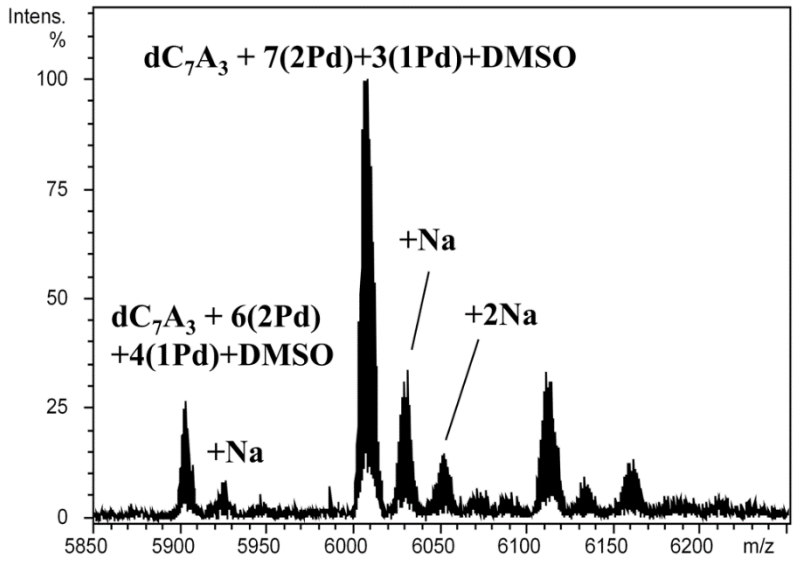

Figura 3.15: Espectro ESI-MS tras la incubación de **dC$_7$A$_3$** con una mezcla de **Pd-Aqa** y **Pd-Cheld**. Condiciones: 50 µM **dC$_7$A$_3$** , 750 µM **Pd-Cheld** (15%DMSO), 750 µM **Pd-Aqa** (15% DMSO). Las etiquetas **1Pd** y **2Pd**, hacen referencia a los fragmentos metálicos **Pd-Cheld** y **Pd-Aqa**, respectivamente.

Estos resultados preliminares indican que la adición de la misma concentración de fragmentos metálicos a una disolución de **dC$_7$A$_3$,** resulta en la unión de siete unidades de **Pd-Aqa** y tres unidades de **Pd-Cheld** para formar el híbrido **dC$_7$A$_3$-7(Pd-Aqa)-3(Pd-Cheld)**. Además, estos datos muestran un comportamiento similar a los obtenidos mediante ^{1}H-RMN, CD e ITC, quedando en evidencia que los fragmentos metálicos son capaces de discriminar entre las bases del ADN para unirse a su nucleobase complementaria mediante pares de bases mediados por metales.

Actualmente, nuestro grupo de investigación está trabajando en sistemas análogos que emplean hebras simples con secuencia 5'-d(AAACACACAA)-

3’ (**dC_3A_7**), d(AAAAACCCCC)-3’ (**dC_5A_5**), **dC_{15}** , **dA_{15}** a las cuales se les añaden cantidades equivalentes de ambos fragmentos metálicos para observar la formación de las especies supramoleculares híbridas con la estequiometría esperada.

3.3. Conclusiones.

En este capítulo, se han presentado los resultados obtenidos para los estudios de competitividad y selectividad de los fragmentos metálicos **Pd-Cheld** y **Pd-Aqa** frente a nucleobases de adenina y citosina, y frente a oligonucleótidos de cadena simple que contengan dichas nucleobases. Estos estudios han revelado cómo el diseño racional de los ligandos orgánicos facilita el auto-rreconocimiento con sus nucleobases complementarias, lo que a su vez permite la formación de pares de bases mediados por iones Pd^{II} estables. Para estos estudios, se han empleado técnicas de caracterización como la resonancia magnética nuclear, dicroísmo circular, espectrometría de masas y calorimetría de titulación isotérmica (ITC), que ha proporcionado información valiosa para comprender la naturaleza de estos sistemas.

Los estudios presentados en este capítulo han contribuido a posicionar al complejo metálico [**Pd(Aqa)(DMSO)]** como un compuesto capaz de participar en un proceso de autoensamblaje con oligonucleótidos para dar lugar a la formación de pares de bases mediados por paladio del tipo **[Pd(Aqa)(mC)]**, generando estructuras supramoleculares de ADN-Pd que imitan la estructura de doble hélice del ADN natural. Uno de los aspectos más destacados de estos hallazgos es la preferencia natural del fragmento **Pd-Aqa** para unirse a citosina en lugar de adenina. En consecuencia, **Pd-Aqa** ha demostrado tener una mayor afinidad por interactuar con secuencias $\mathbf{dC_{15}}$ en comparación con $\mathbf{dA_{15}}$.

Basándonos en las propiedades selectivas mostradas de los complejos metálicos, una nueva vía de investigación prometedora podría consistir en cargar cada uno de los ligandos con átomos de distinta naturaleza, como el cobre o el platino. Para así, aplicando los mecanismos expuestos en este capítulo, evaluar si somos capaces de formar sistemas heteropelticos multimetálicos basados en ADN.

3.4. Materiales y Métodos.

3.3.1. Síntesis de materiales.

Las síntesis de los materiales necesarios para el desarrollo de este capítulo han sido incluidas en el capítulo 2, sección 2.5.1.

3.3.2. Técnicas de caracterización.

3.3.2.a. Resonancia Magnética Nuclear, (^{1}H-RMN).

Los espectros de ^{1}H-RMN se han registrado a temperatura ambiente en un espectrómetro de 400 MHz (2 canales) de alta definición Bruker Nanobay Avance III HD. Este equipo cuenta con una sonda BBDO de 5mm, observación directa de núcleos 31P-109Ag y observación 1H, 19F y desacoplamiento de 1H con gradiente Z. Además, cuenta con un sistema ATM de sintonización automática. Los espectros de ^{1}H-RMN con gradiente de temperatura se han registrado en un espectrómetro de 500 MHz (2 canales) de alta definición Bruker Avance NEO. Este equipo cuenta con sonda Smart Probe BBFO de 5 mm, observación directa de núcleos 31P-109Ag y observación 1H, 19F y desacoplamiento de 1H con gradiente Z. Además, cuenta con un sistema ATM de sintonización automática mediante robot 24h. Estos equipos están disponibles en el Centro de Investigación Científica (CIC) de la Universidad de Granada.

Preparación de muestras: Todas las muestras se han disuelto en disolventes deuterados adquiridos en la casa comercial *Eurisotop.*

2.5.2.b. Espectrometría de Masas (ESI-MS).

La espectrometría de masas de ionización por electrospray (ESI-MS) de alta resolución se llevó a cabo en un espectrómetro Waters LCT Premier para los

complejos metálicos, mientras que la caracterización de los oligonucleótidos se llevó a cabo mediante espectrometría de masas MALDI-TOF en un espectrómetro Bruker Autoflex. La Determinación de la masa molecular de los híbridos ADN-metal se llevó a cabo mediante ESI-MS utilizando un instrumento Micro Tof-Q (Bruker Daltonics GmbH, Bremen, Alemania) equipado con un analizador de tiempo de vuelo (ESO-TOF-MS), calibrado con Na^I (200 ppm de Na^I en una mezcla 1:! De H2O:isopropanol), conectado a una bomba HPLC Agilent technologies Series 1100 HPLC y equipado con un auto muestreador, ambos controlados por el software Compass. La interacción de los complejos metálicos con las hebras de ADN (50 µM) se realizó en modo negativo, inyectando 10 µL de la muestra a 40 $\mu L min^{-1}$, con un voltaje e electrodo de contador capilar a 3,9-4,2 kV; la temperatura de desolvatación se fijó en 100ºC, y se hizo fluir gas seco a 6 $L min^{-1}$, utilizando una mezcla 90:10 de acetato de amino 15mM y acetonitrilo (pH7) como portador de líquido. Los espectros se recogieron en un intervalo m/z de 800 a 3000.

2.5.2.c. Espectroscopía UV-Vis (UV-Vis) y de Fluorescencia.

Los espectros de absorción UV-Vis y de fluorescencia se registraron en un espectrofotómetro Varían Cary-Eclipse equipado con una lámpara Xe (potencia pico de 75 kW), un monocromador CZERNY-Turner y un tubo fotomultiplicador R-298 sensible al rojo.

3.3.2.d. Dicroísmo Circular, (CD).

Los espectros de CD se registraron en un espectropolarímero de dicroísmo circular JASCO modelo-J815 dotado con sistema de termostatización por Pertier. Los datos fueron tratados con el Software Spectra Mánager

Administrative Tool V 1.03.02, todo disponible en el Centro de Investigación Científica (CIC) de la Universidad de Granada.

Para estudiar la formación de los híbridos **[Pd(Aqa)(dC$_{15}$)]** y **[Pd(Cheld)(dC$_{15}$)]** a pH6.8 se prepararon y evaluaron disoluciones de:

- 2 µM de **dC$_{15}$**, 100 mM $NaClO_4$ y 5 mM MOPS (Ph6.8), 0→60 µM **Pd-Cheld** (500µM, DMSO).
- 2 µM de **dC$_{15}$**, 100 mM $NaClO_4$ y 5 mM MOPS (Ph6.8), 36 µM **Pd-Cheld** , 0→60 µM **Pd-Aqa** (500µM, DMSO).
- 2 µM de **dC$_{15}$**, 100 mM $NaClO_4$ y 5 mM MOPS (Ph6.8), 36 µM **Pd-Aqa**, 0→60 µM **Pd-Cheld** (500µM, DMSO).
- 2 µM de **dC$_{15}$**, 100 mM $NaClO_4$ y 5 mM MOPS (Ph6.8), 36 µM **Pd-Aqa**, 36 µM **Pd-Cheld** (500µM, DMSO).

Parámetros experimentales; 250-450 nm, 5 scans, T=25°C.

3.3.2.e. Difracción de Rayos X de monocristal (XR).

Los datos de difracción de rayos X para el complejo **[Pd(Cheld)(mC)]** fueron colectados en un equipo Bruker AXS Photon 100 detector con kryoflex II cooling. Los datos fueron tratados con el software APEX3,[7] mientras que la corrección de la absorción fue tratado con SADABS.[8] La estructura cristalina fue resuelta mediante el método de Patterson y refinada empleando la minimización cuadrada con SHELX[9] e integrada en OLEX2.[10] Se ha descubierto que una de las moléculas de agua presenta desorden en tres posiciones con ocupaciones 0.43, 0.35 y 0.22. Los átomos de hidrógeno para esta molécula no se han incluido en el modelo.

3.3.2.f. Calorimetría de titulación isotérmica (ITC)

Los experimentos de ITC se llevaron a cabo en un microcalorímetro Microcal VP-ITC (Malvern Panalytical, Malvern, Reino Unido) a 25ºC.

Disponible en el departamento de Química-Física de la Universidad de Granada.

Para estudiar la formación de los híbridos **[Pd(Aqa)(dC$_{15}$)]** y **[Pd(Cheld)(dC$_{15}$)]** a pH6.8 se prepararon y evaluaron disoluciones de:

- 100 µM de **Pd-Aqa**, 100 mM $NaClO_4$ y 5 mM MOPS (Ph6.8) (5% DMF).
- 100 µM de **Pd-Cheld**, 100 mM $NaClO_4$ y 5 mM MOPS (Ph6.8)(5% DMF).
- 2 mM de **dC$_{15}$**, 100 mM $NaClO_4$ y 5 mM MOPS (Ph6.8) (5% DMF).
- 2 mM de **dA$_{15}$**, 100 mM $NaClO_4$ y 5 mM MOPS (Ph6.8) (5% DMF).

La celda del calorímetro que contenía la disolución de complejo metálico se tituló desde la jeringa con la disolución de ADN. Las titulaciones se realizaron con inyecciones de 10 µL a intervalos de 28 o 48 minutos. Los termogramas experimentales se corrigieron sustrayendo la línea base ajustada manualmente y los picos se integraron para determinar el calor producido por cada inyección de ADN. Los calores residuales debidos a la unión no específica o la dilución del ligando se estimaron a partir de los picos finales de las titulaciones. Cada calor se normalizó por mol de monómero de nucleótido inyectado. Las isotermas de unión resultantes se ajustaron utilizando un modelo de unión con n sitios independientes y equivalentes, lo que permitió la determinación de la constante de unión aparente, Kb, la entalpía de unión, ΔHb, y la estequiometría de unión, n. La energía libre de Gibbs estándar aparente y la entropía se calcularon de acuerdo con la ecuación:

$$\Delta G_b = -RT \cdot lnK_b = \Delta H_b - T \cdot \Delta S_b \qquad \text{(eq 1)}$$

Donde R es la constante de los gases y T la temperatura absoluta.

3.3.2.g. Modelado molecular

Para la completa optimización del complejo **[Pd(Aqa)(mC)]**, se empleó el programa computacional ORCA 5.0.2.[11,12] Los cálculos cuánticos de DFT se llevaron a cabo empleando el método de Grimme PBEh-3c,[13] que incorpora un conjunto de bases de tipo gaussiano doble zeta de alta calidad. Para corregir el error de superposición de conjuntos de bases (BSSE), se aplicó el algoritmo de corrección geométrica de contrapeso gCP.[14] Además, se implementó la corrección de dispersión pacon al esquema de amortiguación Becke-Johnson (D3BJ).[15,16] Para caracterizar la naturaleza de los puntos estacionarios, se realizó un cálculo de frecuencia vibracional, dando como resultado todas las frecuencias positivas, indicativas de un mínimo.

Para la completa optimización del híbrido **[Pd(Aqa)(dC$_{15}$)]** se empleó el software Avogadro.[17,18] Se inició el ensamblaje de sistemas neutros introduciendo 12 contraiones de sodio a los grupos fosfato. Para considerar efectos de solvente, se incorporaron 70 moléculas de agua a los sistemas modelo. La optimización de la geometría se llevó a cabo mediante cálculos ab initio de mecánica cuántica utilizando el método DFT, que incluye el esquema de corrección de dispersión D3. Los cálculos DFT se realizaron con el software NWChem[19] (versión 7.0.2) para investigar la optimización de la geometría de un sistema multifacético que consta de 844 átomos. Este sistema incluye 12 iones de palado (Pd^{II}), 12 iones de sodio (Na^{I}) que actúan como contraiones y 70 moléculas de agua.

Para los cálculos de la estructura electrónica, se aplicó el conjunto de bases SBKJC-VDZ (Valence Double Zeta with Effective Core Potentials) a los iones Pd^{II}, acompañado por el conjunto de bases ECP (Effective Core Potential) para considerar con precisión los electrones centrales. Se seleccionó la funcional híbrida PBE0 (Perdew-Burke-Ernzerhof) como funcional de intercambio-correlación debido a su mayor precisión para describir propiedades estructurales y electrónicas.[20,21] Además, se incorporó la corrección D3 para

abordar las fuerzas de dispersión, especialmente relevantes en sistemas con interacciones no covalentes como agregados moleculares.[15,16] Se realizó una optimización exhaustiva de la geometría para minimizar la energía total del sistema con respecto a las coordenadas nucleares

3.5. Bibliografía

1 W.-Z. Shen and B. Lippert, *J Inorg Biochem*, 2008, **102**, 1134–1140.

2 S. Coşar, M. B. L. Janik, M. Flock, E. Freisinger, E. Farkas and B. Lippert, *J. Chem. Soc., Dalton Trans.*, 1999, 2329–2336.

3 J. Kypr, I. Kejnovska, D. Renciuk and M. Vorlickova, *Nucleic Acids Res*, 2009, **37**, 1713–1725.

4 Y. Dong, Z. Yang and D. Liu, *Acc Chem Res*, 2014, **47**, 1853–1860.

5 T. Miyahara, H. Nakatsuji and H. Sugiyama, *J Phys Chem A*, 2013, **117**, 42–55.

6 A. Vologodskii and M. D. Frank-Kamenetskii, *Phys Life Rev*, 2018, **25**, 1–21.

7 *APEX3 Software, V2016.1; Bruker AXS: Madison, WI, USA,* 2016.

8 G. M. Sheldrick, *G. M. Sheldrick, SADABS 2016/2. Program for Empirical Absorption Correction of Area Detector Data, University Of Göttingen, Germany,* 2016.

9 G. M. Sheldrick, *Acta Crystallogr A*, 2008, **64**, 112–122.

10 O. V. Dolomanov, L. J. Bourhis, R. J. Gildea, J. A. K. Howard and H. Puschmann, *J Appl Crystallogr*, 2009, **42**, 339–341.

11 F. Neese, *Wiley Interdiscip. Rev. Computa. Mol. Sci.*, 2018, **8**.

12 F. Neese, *Wiley Interdiscip. Rev. Computa. Mol. Sci.*, 2012, **2**, 73–78.

13 S. Grimme, J. G. Brandenburg, C. Bannwarth and A. Hansen, *J Chem Phys*, 2015, **143**.

14 H. Kruse and S. Grimme, *J. Chem. Phys.* , 2012, **136**, 1–16.

15 S. Grimme, S. Ehrlich and L. Goerigk, *J Comput Chem*, 2011, **32**, 1456–1465.

16 S. Grimme, J. Antony, S. Ehrlich and H. Krieg, *J. Chem. Phys.*, 2010, **132**, 154104.

17 M. D. Hanwell, D. E. Curtis, D. C. Lonie, T. Vandermeersch, E. Zurek and G. R. Hutchison, *J Cheminform*, 2012, **4**, 17.

18 Avogadro: An Open-Source Molecular Builder and Visualization Tool. Version 1.2.0. https://avogadro.cc/, .

19 E. Aprà, E. J. Bylaska, W. A. de Jong, N. Govind, K. Kowalski, T. P. Straatsma, M. Valiev, H. J. J. van Dam, Y. Alexeev, J. Anchell, V. Anisimov, F. W. Aquino, R. Atta-Fynn, J. Autschbach, N. P. Bauman, J. C. Becca, D. E. Bernholdt, K. Bhaskaran-Nair, S. Bogatko, P. Borowski, J. Boschen, J. Brabec, A. Bruner, E. Cauët, Y. Chen, G. N. Chuev, C. J. Cramer, J. Daily, M. J. O. Deegan, T. H. Dunning, M. Dupuis, K. G. Dyall, G. I. Fann, S. A. Fischer, A. Fonari, H. Früchtl, L. Gagliardi, J. Garza, N. Gawande, S. Ghosh, K. Glaesemann, A. W. Götz, J. Hammond, V. Helms, E. D. Hermes, K. Hirao, S. Hirata, M. Jacquelin, L. Jensen, B. G. Johnson, H. Jónsson, R. A. Kendall, M. Klemm, R. Kobayashi, V. Konkov, S. Krishnamoorthy, M. Krishnan, Z. Lin, R. D. Lins, R. J. Littlefield, A. J. Logsdail, K. Lopata, W. Ma, A. V. Marenich, J. Martin del Campo, D. Mejia-Rodriguez, J. E. Moore, J. M. Mullin, T. Nakajima, D. R. Nascimento, J. A. Nichols, P. J. Nichols, J. Nieplocha, A. Otero-de-la-Roza, B. Palmer, A. Panyala, T. Pirojsirikul, B. Peng, R. Peverati, J. Pittner, L. Pollack, R. M. Richard, P. Sadayappan, G. C. Schatz, W. A. Shelton, D. W. Silverstein, D. M. A. Smith, T. A. Soares, D. Song, M. Swart, H. L. Taylor, G. S. Thomas, V. Tipparaju, D. G. Truhlar, K. Tsemekhman, T. Van Voorhis, Á. Vázquez-Mayagoitia, P. Verma, O. Villa, A. Vishnu, K. D. Vogiatzis, D. Wang, J. H. Weare, M. J. Williamson, T. L. Windus, K. Woliński, A. T. Wong, Q. Wu, C. Yang, Q. Yu, M. Zacharias, Z. Zhang, Y. Zhao and R. J. Harrison, *J. Chem.l Phys.*, 2020, **152**, 184102.

20 J. P. Perdew, K. Burke and M. Ernzerhof, *Phys Rev Lett*, 1996, **77**, 3865–3868.

21 C. Adamo and V. Barone, *J Chem Phys*, 1999, **110**, 6158–6170.

3.6. Anexo.

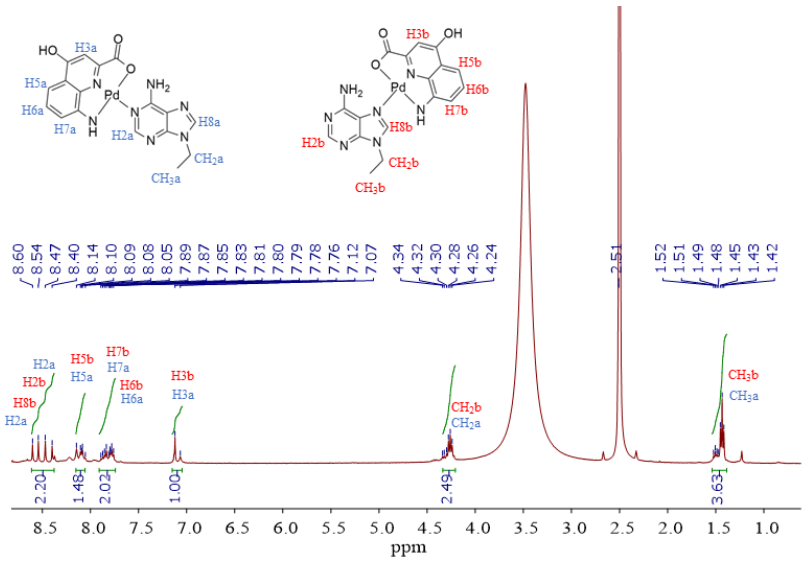

Anexo-Figura 1: Espectro ^{1}H-RMN (400Mhz DMSO-D_6) del complejo **[Pd(Aqa)(eA)]**.

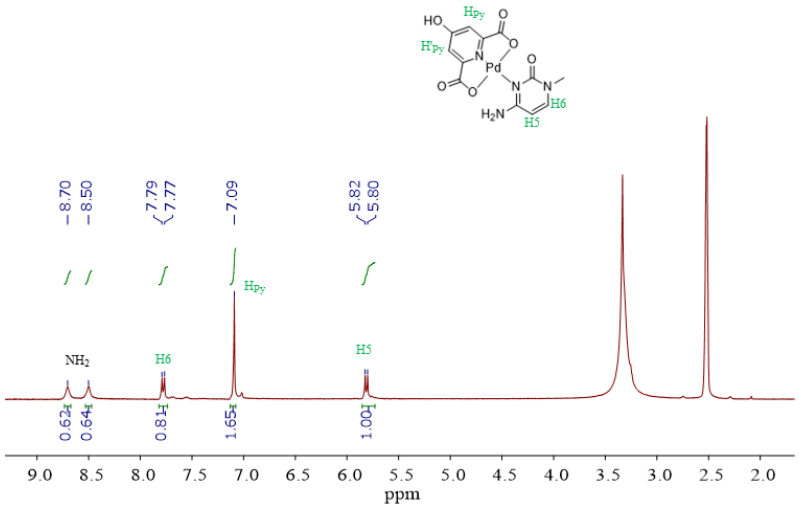

Anexo-Figura 2: Espectro ^{1}H-RMN (400Mhz DMSO-D_6) del complejo **[Pd(Cheld)(mC)]**.

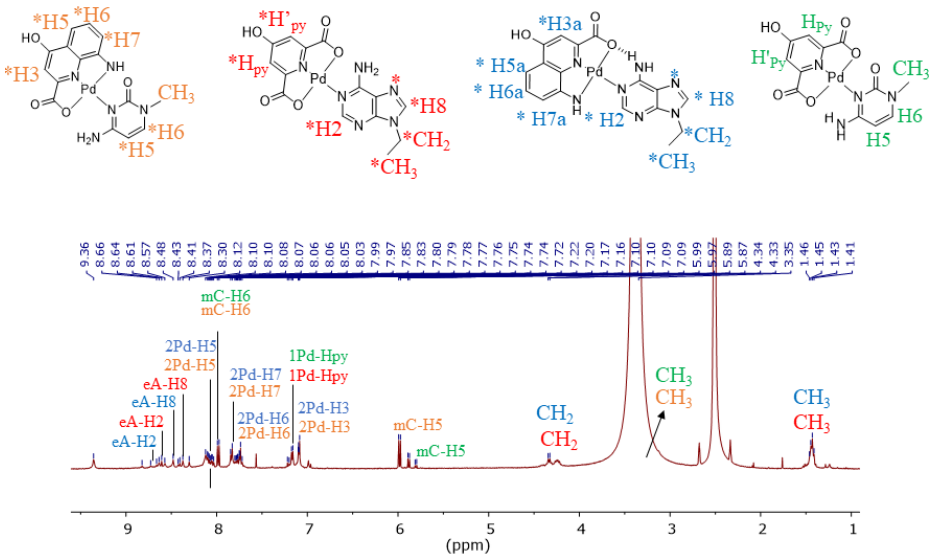

Anexo-Figura 3: ^{1}H-RMN (400Mhz DMSO-D$_6$) del espectro final para la valoración de **eA** y **mC** con los fragmentos metálicos **Pd-Cheld** y **Pd-Aqa**. Por claridad, las estructuras isoméricas no han sido incluidas en el espectro. Los asteriscos junto a las etiquetas numéricas hacen referencia a la presencia de estructuras isoméricas.

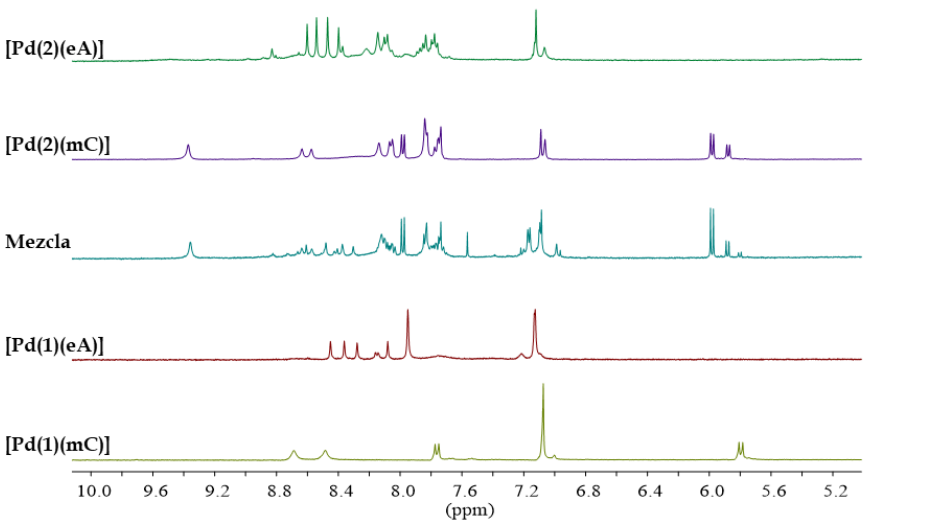

Anexo-Figura 4: Ampliación de ^{1}H-RMN (400Mhz DMSO-D$_6$) para el espectro de la mezcla final tras la valoración de **eA** y **mC** con **Pd-Cheld** y **Pd-Aqa** (en medio). Se incluyen las referencias de los espectros para los pares de bases complementarios, **eA-Pd-Cheld** y **mC-Pd-Aqa** y los pares de bases no complementarios **eA-Pd-Aqa** y **mC-Pd-Cheld.** Las etiquetas **1Pd** y **2Pd** hacen referencia a los fragmentos metálicos **Pd-Cheld** y **Pd-Aqa**, respectivamente**.**

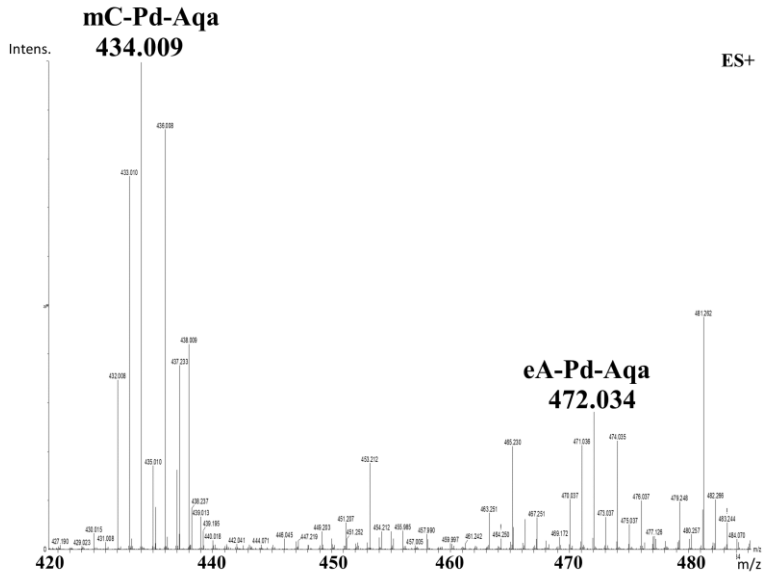

Anexo-Figura 5: Espectro ESI-MS(+) para los complejos **[Pd(Aqa)(mC)]** y **[Pd(Aqa)(eA)]**.

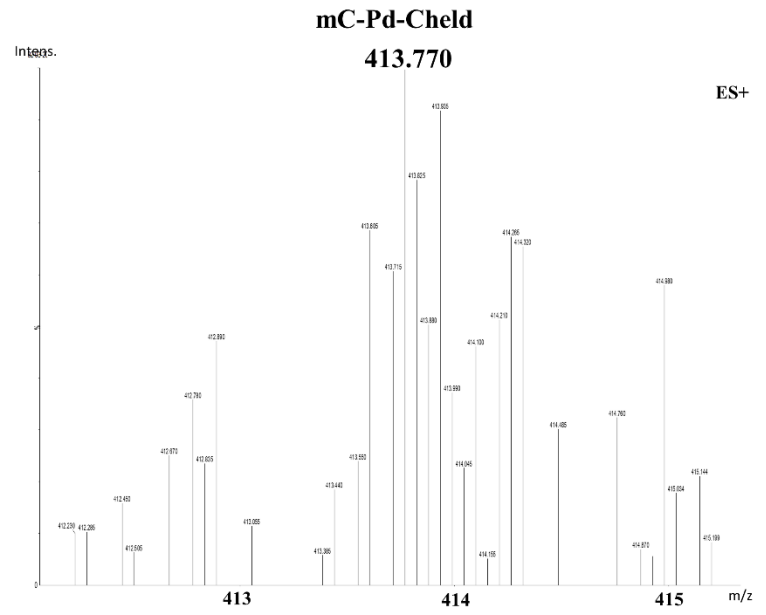

Anexo-Figura 6: Espectro ESI-MS(+) para el complejo **[Pd(Cheld)(mC)]**.

Anexo-Tabla 1: Información cristalográfica de difracción de rayos X para el compejo **mC-Pd-Cheld**

Código	**[Pd(Cheld)(mC)]**
Fórmula empírica	$C_{12}H_{16}N_4O_9Pd$
Peso molecular	466.69
Temperatura/K	100(2)
Sistema cristalino	triclinico
Grupo estpacial	P-1
a/Å	6.7020(3)
b/Å	9.8320(5)
c/Å	13.1889(7)
α/°	95.501(2)
β/°	93.318(2)
γ/°	107.373(2)
Volumen/$Å^3$	822.17(7)
Z	2
$\rho_{calc}g/cm^3$	1.885
μ/mm^{-1}	9.662
F(000)	468.0
Tamaño de cristal/mm^3	0.120 × 0.120 × 0.080
Radiación	CuKα (λ = 1.54178)
2Θ Rango para la recogida de datos/°	6.76 to 133.114
Rangos indexados	-7 ≤ h ≤ 7, -11 ≤ k ≤ 11, -15 ≤ l ≤ 15
Reflexiones colectadas	11629
Reflexiones independientes	2848 [R_{int} = 0.0403, R_{sigma} = 0.0307]

Datos/restricción/parametros	2848/4/267
Goodness-of-fit on F^2	1.148
R final indexado [I>=2σ (I)]	R_1 = 0.0395, wR_2 = 0.0984
R final indexados [all data]	R_1 = 0.0425, wR_2 = 0.1025
Pico de mayor diferencia/hole / e $Å^{-3}$	0.78/-1.83

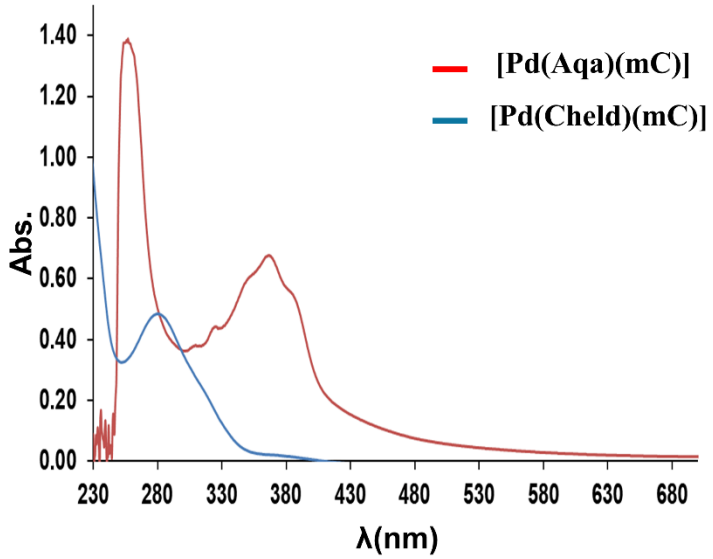

Anexo-Figura 7: Espectro UV-Vis para los complejos **[Pd(Aqa)(mC)]** y **[Pd(Cheld)(mC)]** (0.1 mM, H2O:DMSO; 75:25)

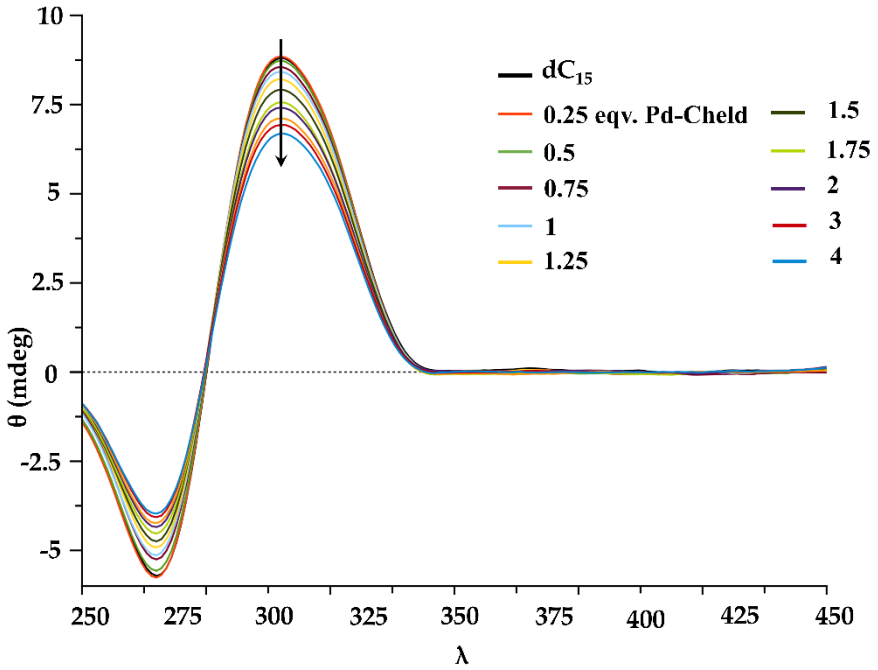

Anexo-Figura 8: Espectro de CD para la valoración de **dC$_{15}$** con el fragmento metálico **Pd-Cheld**, para obtener el híbrido **[Pd(Cheld)(dC$_{15}$)]**. Condiciones: Condiciones: 2 µM **dC$_{15}$**, 0→60 µM **Pd-Chel,** 100 mM $NaClO_4$, 5 mM MOPS (pH 6.8). Las flechan indican la dirección de los cambios de CD.

.

Chapter 4

Supramolecular DNA-Pd Hybrids Integrated with Conducting Polymers

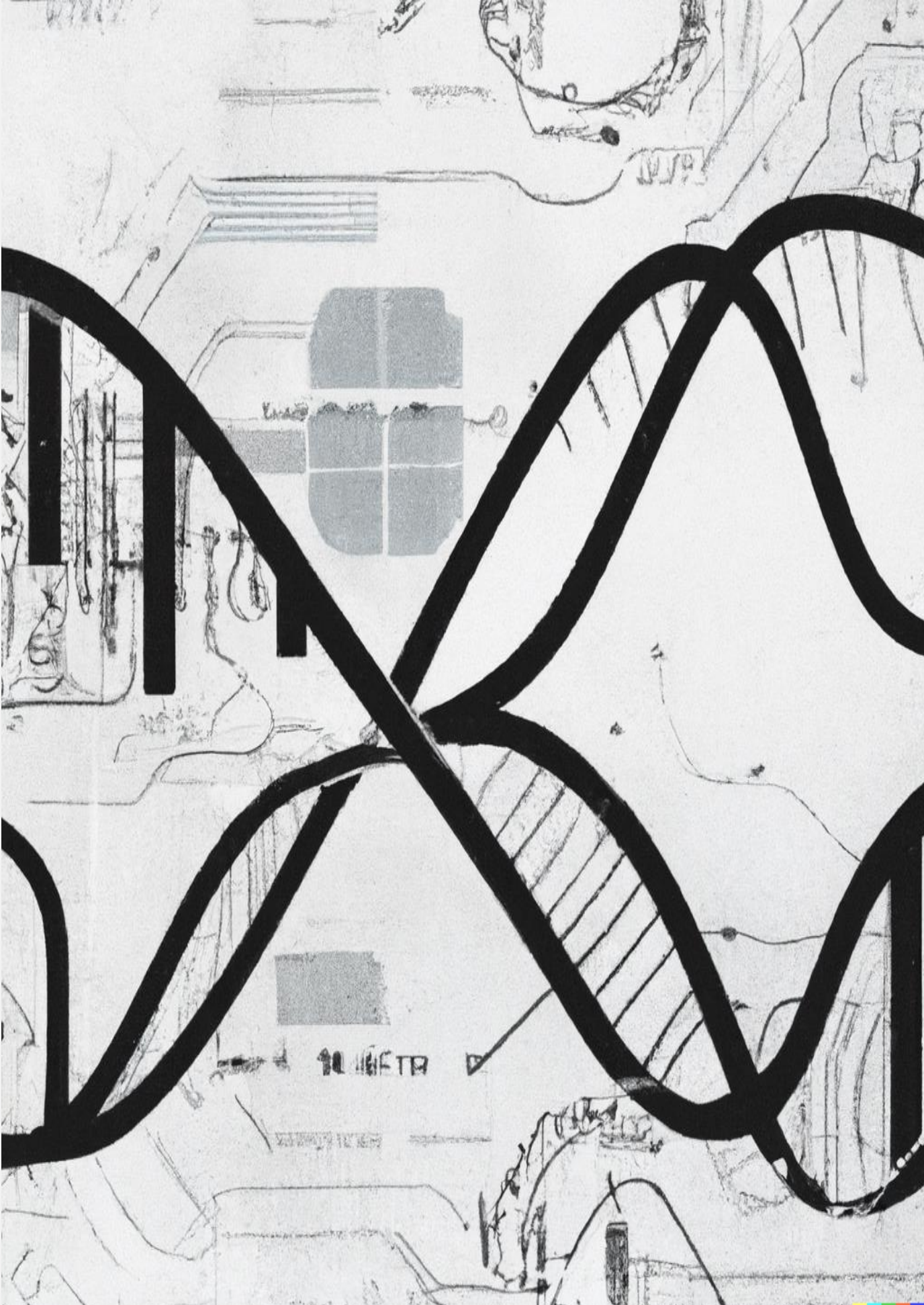

Chapter 4. Supramolecular DNA-Pd Hybrids Integrated With Conducting Polymers

In Chapter 1, the significance of DNA molecules in advancing new nanomaterials, as well as the existing challenge concerning their limited additional properties relevant to nanotechnology applications, was discussed. This is mainly due to the non-conducting nature of nucleic acids (despite some controversy on this topic)[1–7] and the lack of magnetic or fluorescent properties, all of which are highly demanded in nanotechnology.

To expand DNA applications in nanotechnology, it is essential to explore new approaches that allow improving its properties. In previous chapters, it was demonstrated how DNA metallization strategies provide significant alternatives in this regard.[8] In this context, metals can provide electrical conductivity, magnetism and photoactivities properties.[9] However, the control over the position and stoichiometry to obtain well-defined metal-DNA systems still represents a big challenge. Despite these difficulties, promising results have been presented in previous chapters for obtaining supramolecular DNA-Pd hybrids with precise control over the positioning of the metal throughout ss-DNA sequences. Consequently, Pd^{II} complexes are promising for building metal-DNA hybrids via palladium-mediated base pairs. Yet, they would need to be reduced to Pd^{0} to increase conductivity. While reducing Pd^{II} in DNA-Pd hybrids might lead to DNA-Pd conducting wires, this potential remains unexplored in our group due to concerns about linear wire formation versus uncontrolled aggregation events. Therefore, this chapter will explore the integration of conducting polymers, like pyrrole-thiophene derivatives, in Pd^{II}-DNA.[10]

To improve DNA properties, this study presents a methodology to modify the organic structure of 4-hydroxipyridine-2,6-dicarboxylic acid (Cheld) studied in previous chapters. To do this, monomer units capable of creating

conductive polymers have been incorporated into the Cheld ligand and, subsequently, into the DNA-Pd structure.

In this context, the monomeric fragment 2-(2-thienyl)pyrrole (**TP**) (Figure 4.1) and its derivatives have found extensive application as a precursor for synthesizing conductive polymers, which can further lead to the development of DNA-based conducting polymers. [11–16] **TP** has emerged as an exceptional candidate with unique properties in the field of nanomaterials and organic electronics. These copolymers, which combine units of thiophene and pyrrole in their structure, offer several significant advantages over polymers such as polyamides. [17–22]

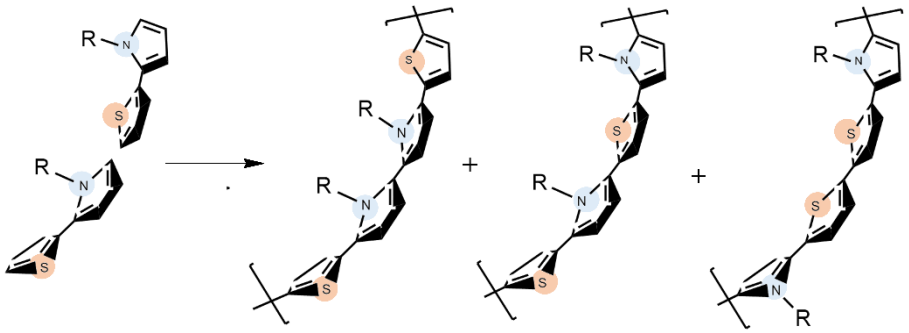

Figure 4.1: Schematic representation of the **TP** monomers polymerization. Three polymer organizations via TP-PT, TP-TP and PT-TP are presented. Colour code: Blue (nitrogen); orange (sulphur).

The main advantage lies in their high electrical conductivity when the polymer is formed. The polymerization of these heterocyclic units allows for the formation of highly conjugated structures that facilitates the transport of charge through the material. This makes them excellent candidates for developing electronic nanodevices like organic transistors or solar cells.[17,23]

Furthermore, these copolymers also exhibit good thermal-chemical stability and are resistant to degradation caused by environmental factors. In the **TP** structure, it is also possible to introduce different chemical groups, providing them additional properties such as affinity for specific substrates or external

stimuli.[24] In recent years, the use of these kind polymers has become a very popular approach to endow DNA electrical conductivity.[16,19] However, most examples involve complex modifications of the nucleobases structures in DNA to include **TP**, and related monomer units. [16,20,21] These modifications allow **TP** monomers to be introduced at specific positions along DNA duplex and subsequently proceed with their polymerization.

Previous chapters have detailed a novel approach for organizing metal complexes along ss-DNA strands by using Pd-mediated base pairs. Building upon this foundation, this chapter will focus on exploiting this knowledge to arrange **TP** monomers along a single-stranded DNA. By forming DNA-Pd-TP hybrids, it would be possible to facilitate the polymerization process of adjacent **TP** monomers, meticulously organized along the ss-DNA. This process is envisioned to culminate in developing a conjugated polymer extending along the DNA structure. (Figure 4.2).

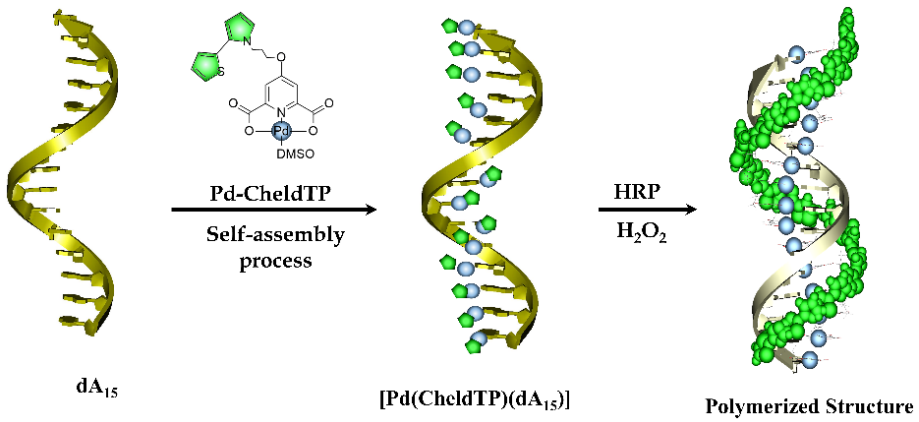

Figure 4.2: Schematic representation of self-assembly process between a ss-DNA **dA_{15}** and **Pd-ChledTP** complex to obtain **[Pd(CheldTP)(dA_{15})]** hybrid and the subsequence polymerization process of **TP** monomers along a DNA template.

4.1. Synthesis and characterization of 4-hydroxypyridine-2,6-dicarboxylic acid (Cheld) functionalized with 2-(2-thienyl)pyrrole (TP).

First, 2-(2-thienyl)pyrrole (**TP**) was modified with 3-bromopropane to obtain 1-(3-bromopropyl)-2-(2-thienyl)pyrrole (**Br-TP**) (Figure 4.3a). Then, NaH was added to a **DMF** solution containing diethyl 4-hydroxypyridine-2,6-dicarboxilate (**$(OEt)_2$Cheld**), and the mixture was stirred for 30 minutes. Afterwards, a solution of **Br-TP** was added to give diethyl 4-(3-(2-(2-thienyl)pyrrole)propoxy)pyridine-2,6-dicarboxylate (**$(OEt)_2$CheldTP)** (Figure 4.3b). Finally, a solution of sodium methoxide (1M) was added dropwise into a solution of **$(OEt)_2$CheldTP** in MeOH to yield 4-(3-(2-(2-thienyl)pyrrole)propoxy)pyridine-2,6-dicarboxylic acid (**CheldTP**) as a white powder (Figure 4.3c).

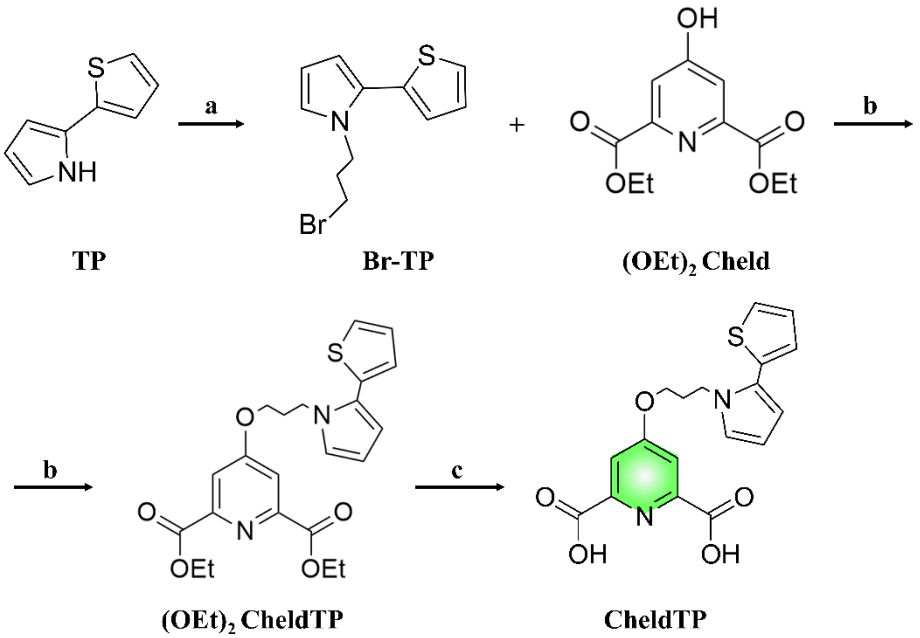

Figure 4.3: Scheme route for the synthesis of **CheldTP**. a) Anhydrous DMF (300 mL), 1,3-Bromopropane, NaH (2 g). Yield: 95%. b) Anhydrous DMF (15 mL), NaH (0.1 g). Yield: 95%. c) Anhydrous MeOH (30 mL), MeONa (3 mL, 1M), 60ºC. Yield: Quantitative. All reaction conditions are available in section 4.7.

The reaction to obtain **CheldTP** was followed by ^{1}H-NMR (Figure 4.4). The spectra show a singlet at 7.61 ppm corresponding to Hpy and H'py protons of the **Cheld** structure. Additionally, signals at 7.43 (H17), 7.09 (H15), 7.04 (H16), 6.94 (H12), 6.20 (H14) and 6.07 (H13) ppm were observed for the **TP** fragment. At high field, signals at 4.23, 4.09 and 2.08 ppm for the three CH_2 groups were observed. (available in Appendix-Figure 1).

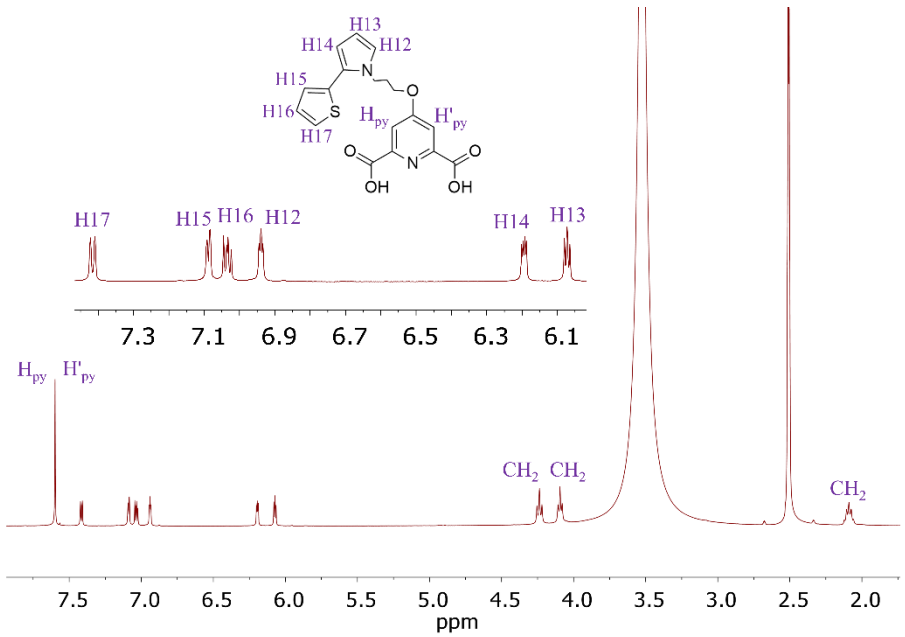

Figure 4.4: ^{1}H-NMR (400Mhz DMSO- D_6) spectra for **CheldTP**.

Finally, to confirm the formation of **CheldTP** in solution, an aliquot of the ^{1}H-NMR samples was studied using mass spectrometry (ESI-MS, positive mode). The mass spectrum showed the presence of $[(CheldTP)+H]^{+}$ compound at 373.0844 Da (theoretical mass 372.0858 Da) (available in Appendix-Figure 2). UV-Vis measurements were also conducted, showing a maximum absorption band centred at 270 nm (available in Appendix-Figure 4).

A small amount of **CheldTP** was measured by IR to characterize its solid state (Appendix-Figure 3). The spectra exhibited two characteristic bands at

3500 and 1700 cm^{-1} corresponding to the alcoholic and keto groups, along with the signals atributed to the **TP** unit.

4.2. Synthesis and characterization of metal complex [Pd(CheldTP)(DMSO)] (DMSO-Pd-CheldTP).

The metal complex was synthesized by a reaction between **CheldTP** and one equivalent of $Pd(NO_3)_2$ (Figure 4.5). This reaction was followed by ^{1}H-NMR. For this task, solutions of **CheldTP** (DMSO-D_6) and $Pd(NO_3)_2$ (DMSO-D_6) were prepared and mixed, and the corresponding NMR was registered.

Moreover, several efforts were made to obtain and characterize the resultant Pd^{II} complex in a solid state, such as powder or crystals. Unfortunately, only a meagre quantity of powder, inadequate for complete characterization, was obtained.

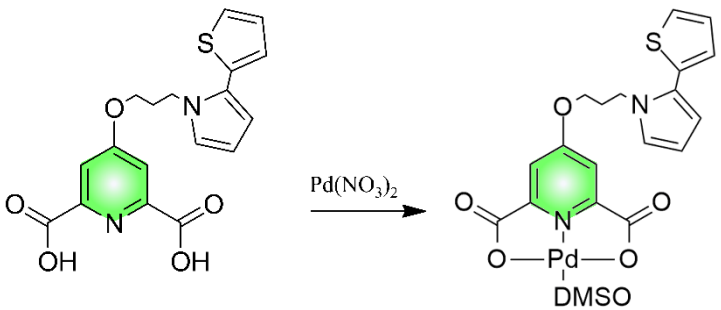

CheldTp **Pd-CheldTp**

Figure 4.5: Reaction scheme between **CheldTP** and one equivalent of $Pd(NO_3)_2$ to obtain **[Pd(CheldTP)(DMSO)]** complex. The reaction monitored by H^1-NMR (400 Mhz DMSO-D_6) and the synthesis procedure is described in section 4.5.

Figure 4.6 shows the spectrum after the reaction between **CheldTP** and increasing amounts of $Pd(NO_3)_2$. As the amount of Pd^{II} increased, the singlet at 7.61 ppm tended to disappear, while a new set of signals emerged at high field at 7.28, 7.22 and 6.8 ppm. These signals are related to aromatics H_{py} and H'_{py} protons of **CheldTP**. The interpretation of this splitting is due to the formation of a dimeric structure in solution via Pd^{II}-coordination to the carboxylic acid of different **Pd-CheldTP** complexes, as previously reported.[25] Signals for the **TP**

monomer were also observed in the same region as reported for the **CheldTP** ligand ^{1}H-NMR (Figure 4.4) (available in Appendix-Figure 5).

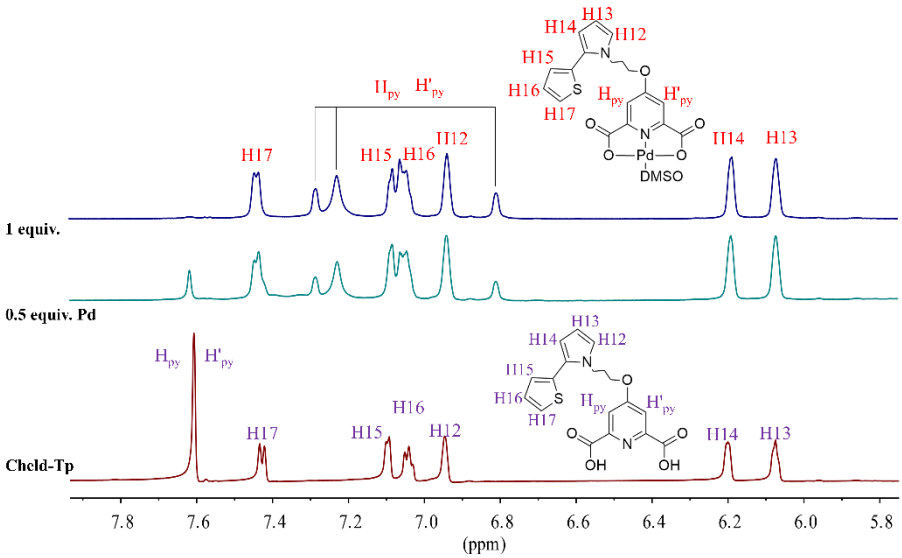

Figure 4.6: ^{1}H-NMR (400Mhz DMSO- D_6) titration spectra for the reaction between **CheldTP** and one equivalent of $Pd(NO_3)_2$ to obtain **[Pd(CheldTP)(DMSO)]** complex.

To gain further insights into these findings, a ^{1}H-NMR spectra at variable temperatures were conducted (Figure 4.7). It is important to note that the temperature was limited to 75ºC to prevent the possibility of inducing polymerization in the **TP** monomers. As the temperature increased, the spectrum gradually simplified, and the three singlets at 7.28, 7.22 and 6.8 ppm converged in one singlet at 7.20 ppm. Notably, the original ^{1}H-NMR spectra reappeared after cooling the sample back to room temperature. These results confirm the formation of dimeric structure between two Pd^{II} complexes at room temperature, as described in bibliography.[25]

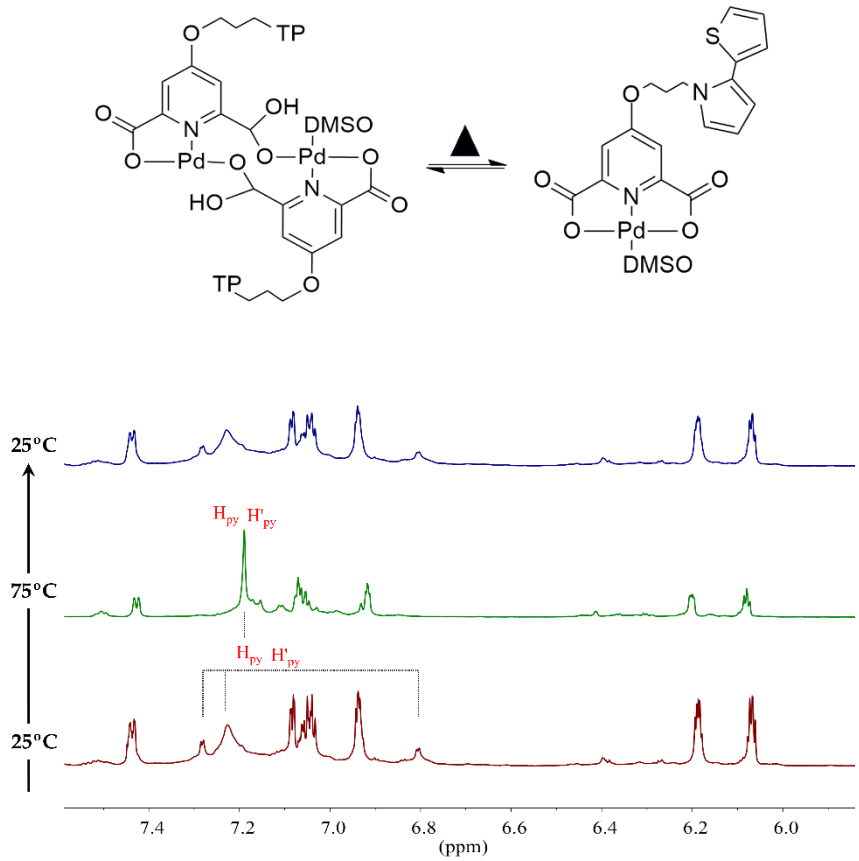

Figure 4.7: ^{1}H-NMR (400Mhz DMSO-D_6) spectra at variable temperature for **[Pd(CheldTP)(DMSO)]** complex. The spectra are presented bottom-to-top, illustrating the progression of the temperature changes. The spectrum at the top represents the initial starting temperature after heating the sample. The top scheme shows the dimeric structure formation between two **Pd-CheldTP** complexes at room temperature and the subsequence dissociation at higher temperatures.

To confirm the formation of **DMSO-Pd-CheldTP** complex, an aliquoted from ^{1}H-NMR experiments was studied by ESI-MS(positive mode). The mass spectrum showed the presence of $[Pd(CheldTP)(DMSO)+H]^{+}$ complex at 555.9798 Da (theoretical mass 554.9880 Da), confirming the complex formation. The spectrum also showed the presence of the dimeric structure described in ^{1}H-NMR experiments at 954.9378 Da (theoretical mass 953.9321 Da) (spectra available in Appendix-Figure 6).

To characterize **DMSO-Pd-CheldTP** in its solid phase, a small amount of sample was analyzed by IR (Appendix-Figure 3). Upon comparing the spectra of **DMSO-CheldTP** and **DMSO-Pd-CheldTP**, notable differences were observed. In the latter, the band corresponding to the carboxylic -OH group at 3500 cm^{-1} was absent, while a band at 1600 cm^{-1} attributed to Keto groups remained. These observations are agree with the coordination of Pd^{II} ions to the carboxylic groups.

4.3. Synthesis and characterization of metal complex with adenine derivative: [Pd(CheldTP)(eA)] (eA-Pd-CheldTP).

After synthesizing and characterizing the **Pd-CheldTP** complex, its interaction with the model nucleobase 9-ethyl-adenine (**eA**) was investigated. This study served as a preliminary step toward the formation of supramolecular DNA-Pd hybrids that incorporate the **TP** unit.

With this aim, the interaction between **Pd-CheldTP** and **eA** to form [Pd(CheldTP)(eA)] (**eA-Pd-CheldTP**) complex was followed by ^{1}H-NMR. Figure 4.8a illustrates the spectral data resulting from titrating a solution of **Pd-CheldTP** with increasing amounts of **eA**, up to one equivalent. Upon addition of **eA**, a new set of signals appeared at 8.53 (s), 8.46 (s), 8.38 (s), 8.43 (s) and 8.13 (s) ppm which can be assigned to the H2 and H8 protons for two different **eA-Pd-CheldTP** isomers, **[Pd(CheldTP)(*N1*-eA)]** and **[Pd(CheldTP)(*N7*-eA)]**. These isomers exist due the possible interaction of the metal **Pd-CheldTP** fragment binding to **eA** via N1 or N7 atom, as previously observed for the formation of [Pd(Chled)(eA)] (**eA-Pd-Cheld**) (Chapter 2, Section 2.1.b).[26] Moreover, the signals at 8.53 and 8.52 (two singlets), 7.33 and 7.31 ppm (two singlets) correspond to NH_2 and H_{py} for the **Pd-CheldTP** fragment, respectively (available in Appendix-Figure 7).

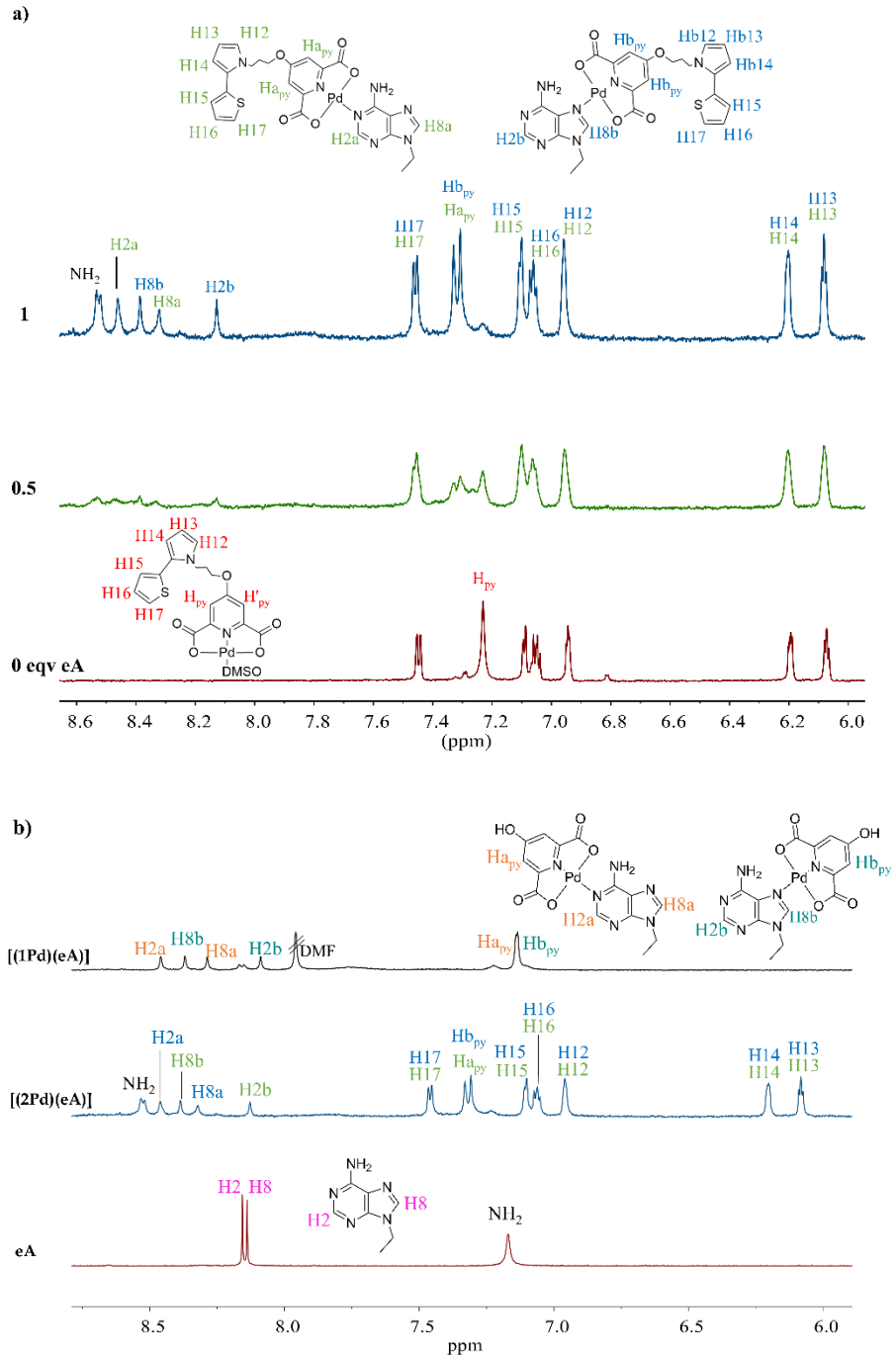

Figure 4.8: ^{1}H-NMR (400Mhz DMSO-D$_6$). a) Titration spectra for the reaction between **Pd-CheldTP** and one equivalent of **eA**. b) Comparison of the spectra for, botton-to-top, free **eA**, **eA-Pd-CheldTP** and **eA-Pd-Cheld** complexes**.** For clarity, a code for the Pd^{II} complexes is used, (**1Pd**) = **Pd-Cheld** and (**2Pd**)= **Pd-CheldTP.**

The figure 4.8b shows the spectrum for **eA-Pd-CheldTP** complex in comparison to the free **eA** and **eA-Pd-Cheld** complex. Singlet signals between 8.53 and 8.13 ppm for H2 and H8 of **eA** are consistent with the formation of two different structures that coexist in equilibrium as a consequence of the N1 and N7 coordinated isomers. Additionally, singlets at 7.33 and 7.31 ppm, which correspond to aromatics Ha_{py} and Hb_{py} protons isomers, are also observed. Finally, singlets at 8.53 and 8.52 ppm can be attributed to the NH_2 group of **eA**.

So far, it has not been possible to obtain a mass spectrum to confirm the presence of the complex in solution. Therefore, at the time of this thesis, more experiments will needed in this regard.

4.4. Synthesis and characterization of supramolecular hybrid [{Pd(CheldTP)}$_{15}$(dA$_{15}$)] (dA$_{15}$-Pd-CheldTP).

Section 4.3 demonstrated the formation and solution behaviour of the **eA-Pd-CheldTP** complex, akin to that of **eA-Pd-Cheld** without the **TP** unit (Chapter 2, section 2.2.b).[26] Therefore, these results suggest that this complex could also interact with oligonucleotide sequences containing adenosine to form a supramolecular system [{Pd(CheldTP)}$_{15}$(dA$_{15}$)] (**dA$_{15}$-Pd-CheldTP)**, where the **TP** units can be arranged according to the single-stranded oligonucleotide structure. To study this, the interaction between **dA$_{15}$** and **Pd-CheldTP** was followed by circular dichroism experiments. A solution of 2 μM DNA, 100 mM $NaClO_4$, 5mM MOPS (pH6.8) was prepared and titrated with increasing amounts of **Pd-CheldTP** dissolved in DMSO (Figure 4.9).

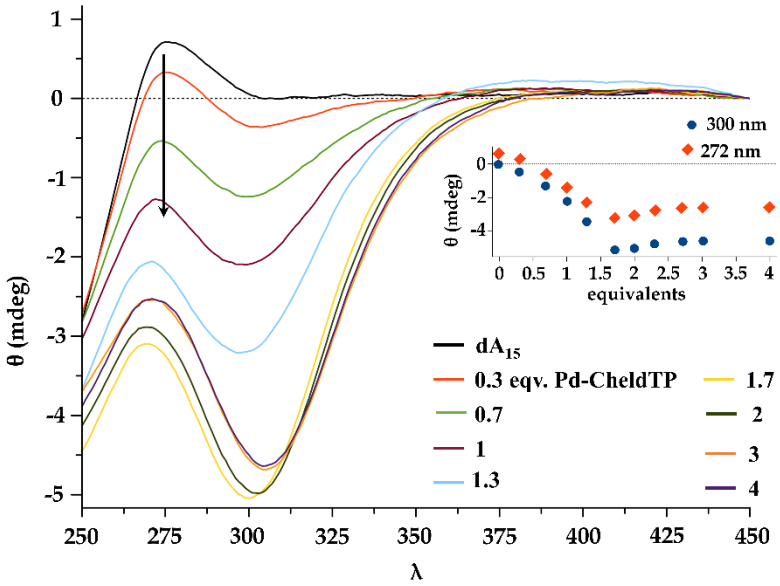

Figure 4.9: CD titration spectra for **dA15** upon the addition of controlled amounts of **Pd-CheldTP**. Insets: Ellipticity changes at 272 and 300 nm as a function of equivalents of **Pd-CheldTP** added. Conditions: 2 μM DNA, 0→60 μM **Pd-CheldTP** (DMSO), 100 mM $NaClO_4$, 5 mM MOPS (pH 6.8). The arrow indicates the direction in which UV-Vis changes..

The spectra of free **dA15** exhibited both negative and positive bands within the range of 245-300 nm, where DNA typically absorbs. Upon the controlled addition of **Pd-CheldTP**, distinct Cotton effects were observed along with induced circular dichroism (ICD) bands appearing in the region above 300 nm, where **Pd-CheldTP** absorb (UV-Vis, available in Appendix-Figure 4). Specifically, an intense negative band at 307 nm and a small broad positive band between 350 and 400 nm emerged, accompanied by a decrease in the **dA15** band as Pd^{II} complex was added. These ICD bands illustrate the interaction between the **Pd-CheldTP** fragment and **dA15**. Importantly, upon introducing the Pd^{II} complex, the presence of the ascending band at 275 nm remains, albeit with a shift towards negative ellipticity values. Furthermore, the plot of ellipticity (θ) values at 272 and 300 nm against equivalents of Pd^{II}/base indicates that the CD spectra changes stabilize at approximately 1.3 equivalents, consistent with the saturation of binding at the adenosine position.

These findings, together with studies using isolated adenine derivatives described above, suggest that **Pd-CheldTP** units are organized along the single strand of DNA by binding to adenine bases, and the system retains a helical structure, suggesting the formation of a supramolecular hybrid of the **dA_{15}-Pd-CheldTP** type.

The necessity for the DNA-Pd interaction to be established through the N1 nitrogen of adenine to maintain a natural DNA-like double helix structure was discussed in Chapter 2. To confirm these facts, a similar CD titration experiment was conducted using a reference oligonucleotide comprising 7-deazaadenosine (**dX_{15}**), therefore restricting the binding of the Pd^{II} fragment towards the N1-atom at WCF face of adenine. With this aim, a solution of 2 µM **dX_{15}**, 100 mM $NaClO_4$, 5mM MOPS (pH6.8) was titrated with 1.3 equivalents (Pd^{II} /base) of **Pd-CheldTP** in DMSO (Figure 4.10).

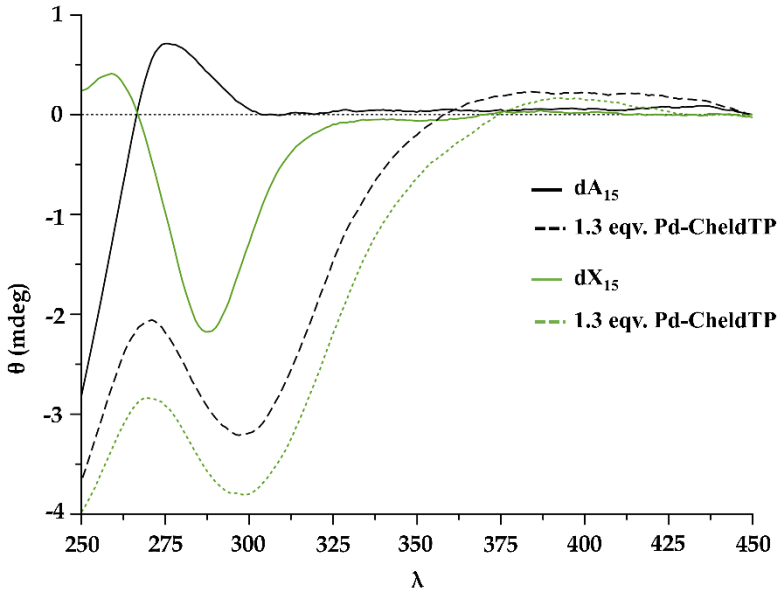

Figure 4.10: CD spectrums for the interaction between **dA_{15}** and **dX_{15}** with 1.3 equivalent of **Pd-CheldTP**. Conditions: 2 µM DNA, 39 µM **Pd-CheldTP** (DMSO), 100 mM $NaClO_4$, 5 mM MOPS (pH 6.8). Colour code: **dA_{15}** (black line), **dX_{15}** (dotted black line), **[Pd(CheldTP)(dA_{15})]** (green line) and **[Pd(CheldTP)(dX_{15})]** (dotted green line)

Figure 4.10 shows the CD spectra for both ss-DNA (**dA_{15}** and **dX_{15}**) experiment when a 1.3 equivalent of **Pd-CheldTP** were added. Spectra for free **dX_{15}**, shows a positive and a negative band in the range of 250-300 nm, respectively. However, in the presence of **Pd-CheldTP**, comparable spectra are observed for both **dA_{15}-Pd-CheldTP** and **dX_{15}-Pd-CheldTP** supramolecular systems. The CD spectra exhibited a similar interaction pattern, resembling the formation of a helix structure and confirming the binding of the **Pd-CheldTP** fragment via *N1*-adenine position. This behaviour can be attributed to the fact that **dX_{15}** strand only offers the *N1*-7-deaza-adenine position for binding.

In addition, analogous control CD experiments were conducted to rule out the interactions of **dA_{15}** with free **CheldTP** ligand or $Pd(NO_3)_2$, respectively. To achieve this, a solution of 2 µM **dA_{15}**, 100 mM $NaClO_4$, 5 mM MOPS (pH 6.8) was titrated with **CheldTP** (in DMSO**)** or $Pd(NO_3)_2$ (in DMSO) (available in Appendix-Figures 8 and 9). In both cases, the CD titration spectra exhibited different outcomes compared to those previously discussed, indicating that these interactions did not occur in our initial study involving **dA_{15}** and **Pd-CheldTP**.

The CD data obtained for **dA_{15}-Pd-CheldTP** hybrids at pH 6.8 provided the possibility to design an analogous experiment to investigate the polymerization process of **TP** fragments. In this regard, Horseradish peroxidase (**HRP**) enzyme is commonly used to carry out these polymerization processes. **HRP** has an essential role in facilitating reactions involving the formation of conductive polymers, even if it is not directly involved in the polymerization of the monomers.[27]

HRP role is based on its ability to catalyze the oxidation of organic compounds, including **TP** monomers. For this purpose, hydrogen peroxide is employed as a substrate to promote an electron cascade that facilitates the polymerization process. This process needs a catalytic amount of 2,2'-azino-bis(3-ethylbenthiothiazoline-6-sulfonate) (**ABTS**). It has been demonstrated

that ABTS acts as a redox mediator in this process by facilitating electron transfer between the **TP** monomers and **HRP**.[28] **ABTS** initiates the process by donating electrons to **HRP** in the presence of H_2O_2, which activates the enzyme and regenerates its oxidized form. Once **HRP** is oxidated, it can generate free radicals from the **TP** monomers, which, as previously mentioned, are highly reactive and will bind to each other to from covalent bonds, creating polymeric chains.

In this context, **HRP** can intervene in several key aspects. Firstly, it plays a primary role in the initial stage of polymerization by catalyzing the oxidation of **TP** monomers, forming highly reactive free radicals. These free radicals initiate the cascade polymerization reaction, allowing the monomers to bond and form polymeric chains. Moreover, **HRP** can promote additional binding of additional monomers to create longer and complex structures and act as a regulator of the reaction, controlling the kinetics of the process.

This process must develop the correct specific conditions. This requirement includes the presence of suitable substrates, optimal enzyme and reactant concentrations, and precise control over pH and temperature conditions. In this section, a method to ensure the effective operation of **HRP** for the polymerization of the **TP** moieties in the **dA_{15}-Pd-CheldTP** structures is presented. The maximum activity of **HRP** has been described at pH 4.5 and 40ºC, using water as a solvent or, alternatively, a mixture of water and dimethyl sulfoxide (DMSO).[29–31]

The polymerization reaction for **dA_{15}-Pd-CheldTP** was initially monitored using UV-vis spectroscopy. According to the literature, the polymerization of **TP** derivatives can exhibit a characteristic band around 350-400 nm for short polymer chains and beyond 800 nm for longer chains. [17,21,22] The UV-vis experiment was performed following the procedure outlined in the previous CD experiment to prepare the **dA_{15}-Pd-CheldTP** system: 2 µM **dA_{15}**, 1.3 equivalent of **Pd-CheldTP** (in DMSO), 100 mM $NaClO_4$ and 5 mM Citrate

(pH 6.8). The use of citrate buffer responds to the need to vary the pH from 6.8 to 4.5, and no difference between MOPS or Citrate buffer was observed for the formation of the supramolecular **dA_{15}-Pd-CheldTP** structure. To initiate the polymerization process, a pH 4.5 and oxidizing environment were required. To achieve this, nitric acid (20 µL, 0.5M) was added to adjust pH from 6.8 to 4.5. Subsequently, ABTS (10 µL, 10 µM), HRP (2 µL, 1mg/mL) and H_2O_2 (5 µL, 15%v/v) were added into the solution.

Additionally, a control experiment was also performed using a solution containing 2 µM **dA_{15}** in the presence of 1.3 equivalent **CheldTP** (in DMSO), excluding the Pd^{II} ions (Figure 4.11). This comparison aimed to elucidate the differences in the polymerization process of **CheldTP** units when they are organized along the **dA_{15}** strand versus when they are free in solution.

Figure 4.11 shows the UV-Vis spectra of **dA_{15}-Pd-CheldTP** before and after polymerization, as well as the UV-Vis spectra for the control experiment using **dA_{15}** and **CheldTP.**

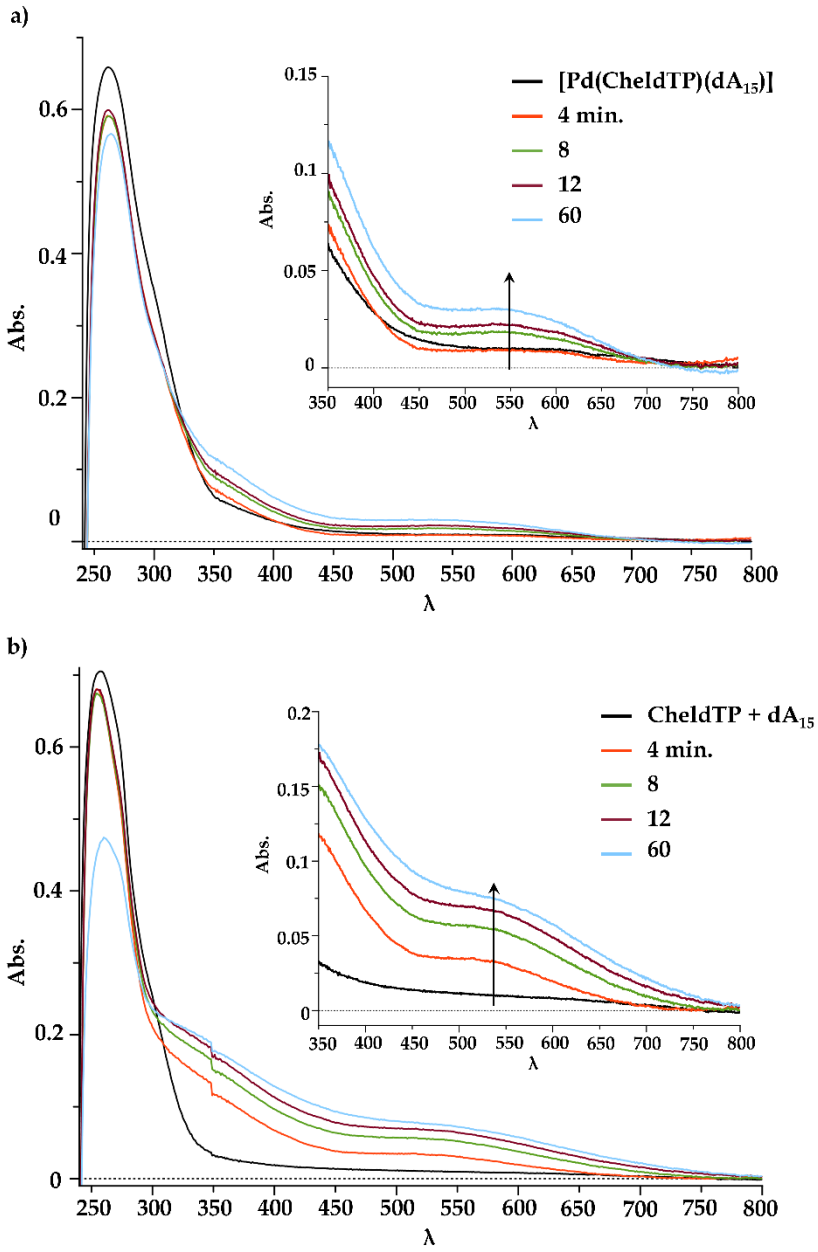

Figure 4.11: UV-Vis spectra for the interaction of: a) **dA$_{15}$** and 1.3 equivalent of **Pd-CheldTP**. b) **dA$_{15}$** and 1.3 equivalent of **CheldTP**. Both spectra show signals for the polymerization process during 60 minutes. Conditions: 2 μM DNA, 39 μM **Pd-CheldTP** or **CheldTP** (DMSO), 100 mM $NaClO_4$, 5 mM Citrate (pH 6.8→4.5). The increasing signals from 4 to 60 minutes centred at 525 nm illustrate the polymerization process. The arrow indicates the direction in which UV-Vis changes.

For **dA_{15}-Pd-CheldTP**, UV-Vis exhibit an intense peak at 266 nm, characteristic of **dA_{15}**, alongside a shoulder band centred at approximately 350 nm, corresponding to the absorption of the **Pd-CheldTP** fragment, which participates in the formation of the Pd-mediated base pairs. Upon the addition of polymerization reactants (HRP/APTS/H_2O_2), a new broad absorption band emerged within the range of 450 – 700 nm, and its intensity increased over time. As mentioned before, this absorption agrees with the formation of **$(TP)_n$** polymers, thus indicating the occurrence of polymerization events. Notably, no absorption bands were registered in the region above 700 nm. In addition, the absorption band for **dA_{15}** shows minimal changes, thus suggesting non-significant alteration of the oligonucleotide strand. These results suggest the formation of polymer strands, likely influenced by the organized arrangement of **TP** moieties along the ss-DNA via metal-mediated base pairs, leading to the polymerized system **dA_{15}-Pd-CheldTP^{polym}**. It is worth mentioning that this process might result in some end-to-end polymerization events, potentially leading to the formation of longer polymerized structures beyond the anticipated 15-mer. However, The studies conducted here did not yield conclusive evidence regarding this possibility.

To investigate the impact of Pd^{II} ions on the organization of the **CheldTP** unit in the supramolecular system, a similar UV-Vis experiment was conducted using **dA_{15}** and **CheldTP** (Figure 4.11b). In this experiment, the absence of Pd^{II} ions resulted in significant changes observed in the spectra. Initially, the UV-Vis spectrum displayed the characteristic peak for **dA_{15}**, with a less pronounced shoulder, which can be related to the absence of Pd-mediated base pair formation. Notably, upon polymerization, a broader absorption band within the range of 450-800 nm exhibited a rapid increase in intensity, suggesting the accelerated formation of various lengths of **$(TP)_n$** polymer chains, including longer ones, as the absorption band reaches wavelengths beyond 750nm. Furthermore, the absorption band of **dA_{15}** underwent significant changes upon polymerization, indicative of the formation of **$(TP)_n$** polymers and their

interaction with the oligonucleotide, thereby altering its absorption band. This interaction can be attributed to spontaneous electrostatic interactions between the cationic polymer and the anionic ss-DNA strand.[32] Additionally, control experiments were conducted, including UV-Vis spectra for free **Pd-CheldTP** and **CheldTP**, without the presence of **dA_{15}**, which also displayed significantly different polymerization outcomes, underscoring the distinct polymerization pattern for the **dA_{15}-Pd-CheldTP^{polym}** supramolecular system (Appendix-Figure 10 and 11).

It is worth mentioning that, except for **dA_{15}-Pd-CheldTP^{polym}**, all polymerization experiments resulted in precipitate formation within 60 minutes. To further investigate this phenomenon, once the UV-Vis experiments were concluded, the solutions were centrifuged at 10.000 rpm for 15 minutes. The samples containing **dA_{15}/CheldTP**, **Pd-CheldTP** or **CheldTP** exhibited a dark precipitate, which was more evident for the samples without the oligonucleotide. However, in the experiments involving **dA_{15}-Pd-CheldTP^{polym}**, a clear solution was observed. Figure 4.12 shows an image for experimental Eppendorfs containing the samples studied by UV-Vis polymerization experiments.

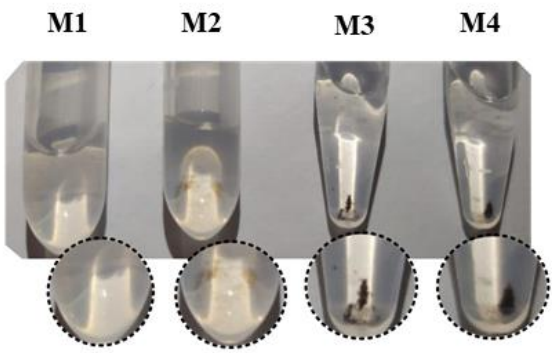

Figure 4.12: Image taken of the Eppendorf tubes after UV-Vis polymerization experiments. M1; (**dA_{15}-Pd-CheldTP**). M2; (**dA_{15}-CheldTP**). M3; (**Pd-CheldTP**). M4; (**CheldTP**).

Furthermore, the formation of the shorter TP-TP polymer was investigated, as previously reported for the related 2,5-bis(2-thienyl)-pyrrole (SNS) monomer. To explore this, a single strand 5'-TTTTTAATTTTT-3' (**dT_5AAT_5**), containing two adenine bases flanked by five thymine bases was employed. Thymines were selected because their interaction with **Pd-CheldTP** fragment is less favoured due to the protonated H-N3T position. The addition of one equivalent of the metal fragment per base would then lead to its binding to the adenine base, placed in the middle of the oligonucleotide sequence.

The experiment was performed by the addition of **Pd-ChelTP** to the oligonucleotide **dT_5AAT_5**, followed by polymerization, as described previously. As mentioned earlier, short polymers exhibit a maximum around 350- 450 nm. [17,21,22] Figure 4.13 shows the UV-Vis spectra for 2 µM **dT_5AAT_5**, 100 mM $NaClO_4$, 5 mM Citrate (pH 6.8) with 1.3 equivalent/adenine **Pd-CheldTP** (in DMSO).

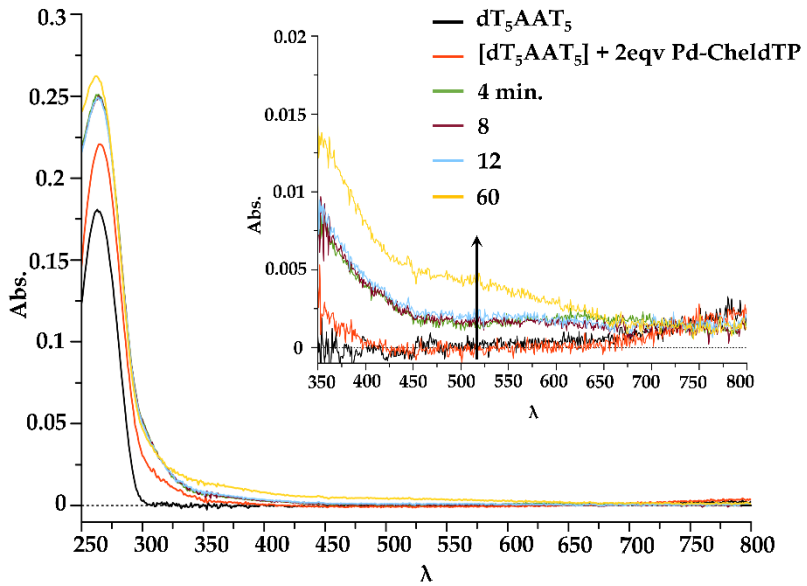

Figure 4.13: a) UV-Vis spectra for the interaction of **dT_5AAT_5** and 2 equivalent of **Pd-CheldTP** (Pd(II)/A). Conditions: 2 µM DNA, 4 µM **Pd-CheldTP** (DMSO), 100 mM $NaClO_4$, 5 mM Citrate (pH 6.8→4.5). The increasing signals from 4 to 60 minutes centred at 525 nm illustrate the polymerization process. The arrow indicates the direction in which UV-Vis changes.

The UV-Vis spectrum reveals the emergence of a small peak centred at 525 nm during the polymerization process, presenting a result comparable to previous related systems published by Schuster and collaborators.[22] This prior study employed modified ds-DNA incorporating 2,5-bis(2-thionyl)pyrrole (**SNS**) covalently attached to cytosine bases. Despite significant differences with the systems reported herein, involving a single strand with the **TP** units coordinated to adenine base, the emergence of a peak at 525 nm suggests the formation of shorter polymers, likely due to TP-TP dimers, stabilized by the oligonucleotide strand. Indeed, a comparison of the UV-Vis spectra of the experiments performed with the oligonucleotides **dA$_{15}$** and **dT$_5$AAT$_5$** clearly reveals a different polymerization event (Figure 4.13). In the case of **dA$_{15}$**, the UV-Vis spectrum exhibited a broad absorption band between 450-700 nm, consistent with the formation of polymers comprising few units. However, in case of **dT$_5$AAT$_5$** only a small band at 410 nm is observed, indicative of the formation of smaller polymers and pointing to the presence of the TP-TP dimers.

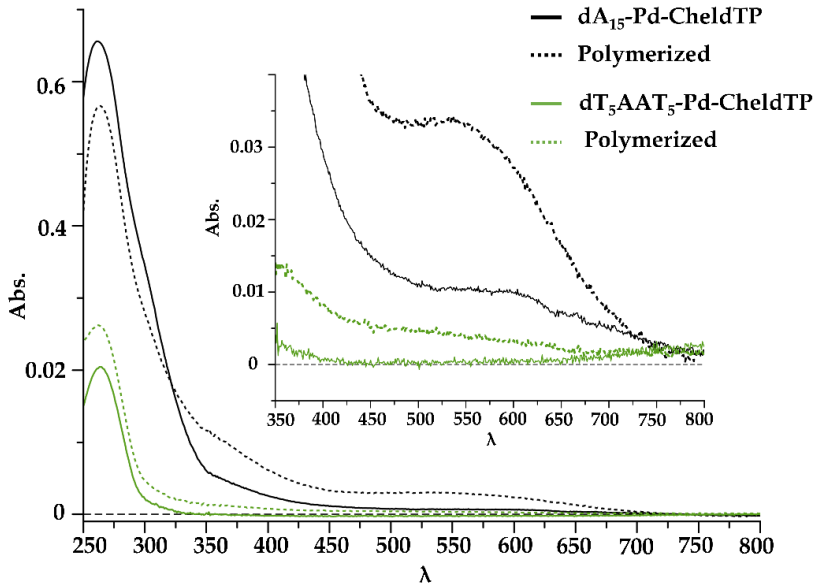

Figure 4.14: A comparison of the UV-Vis spectra of the experiments performed with the oligonucleotides **dA$_{15}$** and **dT$_5$AAT$_5$** with **Pd-CheldTP** (Pd^{II}/A). Conditions: 2 µM DNA, 2 µM **Pd-CheldTP** (DMSO), 100 mM $NaClO_4$, 5 mM Citrate (pH 6.8→4.5).

A CD was carried out to gain more insight into how this process could affect the geometrical disposition of **dA_{15}-Pd-CheldTP** hybrids (Figure 4.15). This study was conducted using a solution containing 2 µM dA_{15}, 100 mM $NaClO_4$, Citrate (pH 6.8), and 1.3 **Pd-CheldTP (**in DMSO). To initiate the polymerization process, a pH 4.5 and oxidizing environment were required. To achieve this, nitric acid (20 µL, 0.5M) was added to adjust pH from 6.8 to 4.5. Subsequently, ABTS (10 µL, 10 µM), HRP (2 µL, 1mg/ml) and H_2O_2 (5 µL, 15%v/v) were added into the solution.

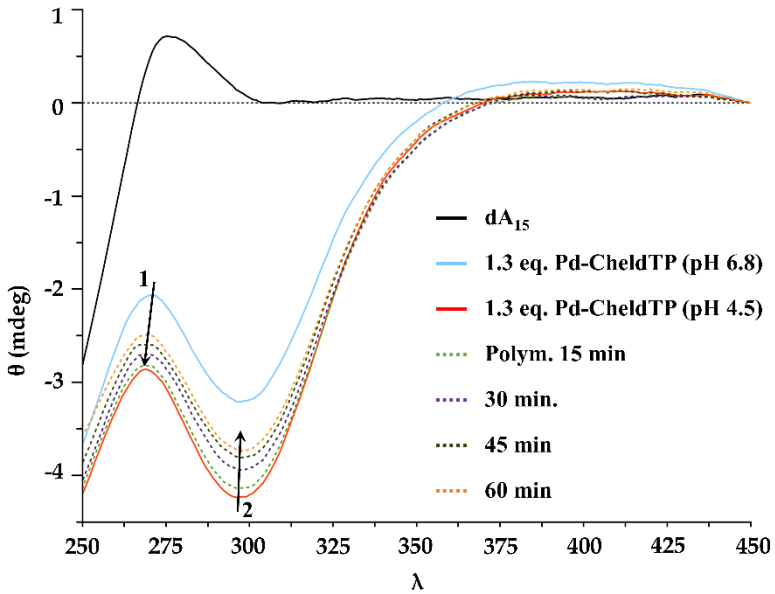

Figure 4.15: CD titration spectra for **dA_{15}** upon adding 1.3 equivalent of **Pd-CheldTP**. The spectra show CD signal for the polymerization process every 15 min. Conditions: 2 µM DNA, 39 µM **Pd-CheldTP** (DMSO), 100 mM $NaClO_4$, 5 mM Citrate (pH 6.8→4.5). The arrows and the numeric labels indicate the direction in which UV-Vis changes.

CD spectra exhibit the formation of **dA_{15}-Pd-CheldTP** at pH 6.8, as described previously in Figure 4.9. Following pH adjustment to 4.5, the CD curve maintained its profile with two ascending bands at 264 and 400 nm, and a descending band at 307 nm. Subsequently, the sample underwent polymerization upon adding the reactants (HRP/H_2O_2/ABTS) and the corresponding CD was measured at different stages of the polymerization

process. The CD spectra before and after polymerization display comparable profiles, with a slight increase in ellipticity observed post-polymerization. Additionally, the broadband within 350-450nm seems to disappear and leads to the suppression of the initial ICD band before polymerization, which is related to the absorbance changes of the polymer in this region (as observed in the UV-Vis spectrometry experiment).

The results obtained from UV-Vis and CD spectroscopy indicate that the helix's conformation does not significant alter upon polymerization of the **TP** units, suggesting a match between the polymer structure and the helicity of the single strand. To further evaluate this structural aspect, computational studies for the polymerized **dA$_{15}$-Pd-CheldTP^{polym}** system were conducted. In this regard, its optimized geometry was calculated employing Hartee-Fock (HF) methodologies.

The geometries of the molecules calculated (DNA-polymer) in this doctoral thesis were initially generated using the Avogadro 1.2.0 molecular software editor.[33,34] Avogadro is a Computational Chemistry program that allows the construction and optimization of molecule geometries based on molecular mechanics (MM) methods.[35]

In the second phase, the geometries obtained with Avogadro were used as a starting point to get the most accurate geometries possible with quantum mechanical methods. Neutral theoretical models were constructed with hydrogens and sodium atoms as counterions for the DNA-polymer system. Neutral systems were assembled by introducing 11 sodium counterions to the phosphate groups.

HF quantum mechanical calculations were performed using the ORCA 5.0.3 program,[36,37] employing the HF-3c method corrected by Grimme.[38] It corrects some systematic deficiencies of a HF calculation with a small basis set and is employed as a high-speed quantum mechanical method. Base overlap errors are corrected through the geometrical counterpoise (gCP) scheme,

dispersion is addressed through Grimme's well-established D3 approach, and short-range basis incompleteness is also corrected.

All calculations were carried out on the Albaicín cluster of the supercomputing service belonging to the Center for Information and Communication Networks and Services (CSIRC) of the University of Granada (htTPs://hpc.ugr.es).

Figure 4.16 displays the optimized geometry obtained for the polymerized **dA$_{15}$-Pd-CheldTP^{polym}**. The optimized geometry structure unveils a double-helix configuration that accommodates the polymer. One strand is formed by a **dA$_{15}$** and the other strand comprises **Pd-CheldTP^{polym}** units. As demonstrated for **dA$_{15}$-Pd-Cheld** supramolecular structures (Chapter 2, Section 2.1.c), **Pd-CheldTP** complexes are also stacked along the ss-DNA. The supramolecular structure is formed by continuous Pd-mediated base pairs with the Pd^{II} ions binding at the N1-adenine position. The optimized structure also shows that the Pd-mediated base pairs form intramolecular hydrogen bonds between the keto and amino groups orientated in the WCF face of the helix. The structure is further stabilized by stacking interactions between contiguous Pd^{II} complexes, and the metal ions run along the helical axis at the centre of the metal-adenine base pairs.

The arrangement of the Pd^{II} complexes along the ss-DNA facilitates the correct positioning of the **TP** monomers for subsequent polymerization. It should be noted that **TP** is a non-symmetrical unit linked to the **Cheld** ligand via an alkyl chain that is attached to the pyrrole unit. Therefore, three possible scenarios are possible to connect adjacent monomers upon polymerization: **TP-TP**, **TP-PT** and **PT-TP** (Figure 4.1). Our preliminary calculations (not shown) indicated that the most favourable arrangement for the units to be accommodated and close to each other for polymerization is the **TP-TP** arrangement. Thus, this organization was chosen for our geometry optimization calculation. However, the other scenarios could be also possible and may

deserve further exploration. However, these theoretical studies were out of the scope of this thesis work. [16]

Figure 4.16 shows that the polymer nicely follows the helicity of the DNA strand and fits within the structure dimension without alteration of the Pd-base pairs. Although this structure only consists of 12 bases to complete a helix turn, the results suggest that longer strands could also accommodate the formation of the $(TP)_n$ polymers.

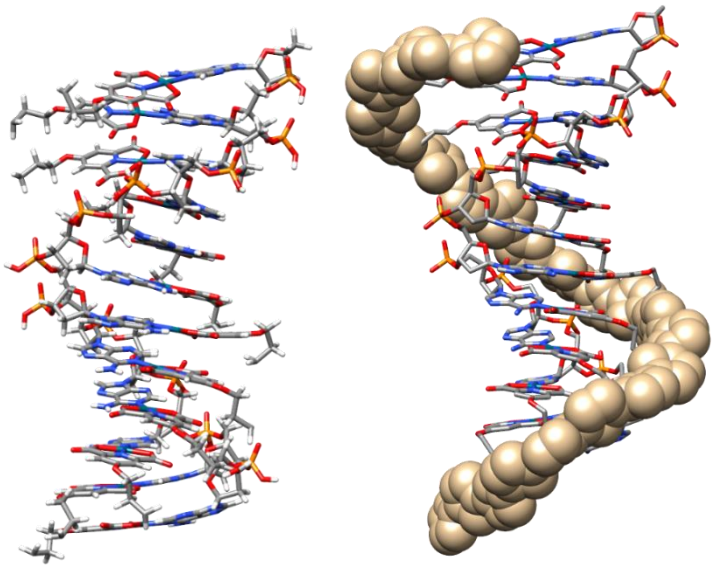

Figure 4.16. Left: Geometry-optimized structure of **dA$_{15}$-Pd-CheldTP** showing the organization of the **Pd-CheldTP** complexes along the structure. Right: The surface displays the polymer along the DNA strands (brown spheres: polymerized **TP**). Sodium counterions and hydrated water molecules have been omitted for clarity. Colour code: Carbon (grey), Hydrogen (white), Nitrogen (blue), Phosphorus (red), Sulphur (orange), Palladium (turquoise). The polymer is represented as brow balls.

4.5. Studies of the conducting properties of the polymerized supramolecular dA_{15}-Pd-CheldTP^{polym} system

Thus far, this chapter has explored the utilization of custom-designed Pd^{II} complexes to create Pd-mediated base pairs integrating polymerizable TP moieties. Given the proven effectiveness of TP-derived polymers in generating electrically conductive structures,[18,39] this section will delve into the properties of **dA_{15}-Pd-CheldTP^{polym}** hybrid systems.

To accomplish this, scanning probe microscopy, particularly Atomic Force Microscopy (AFM) and Electronic Force Microscopy (EFM) were conducted.[40,41] These techniques are acknowledged as powerful tools in nanotechnology studies because they can characterize samples across nanometric to micrometric dimensions.

The previously studied **dA_{15}** strand and the subsequent **dA_{15}-Pd-CheldTP^{polym}** hybrid may prove too short for microscopy studies. It is worth mentioning that our efforts to observe this short hybrid system on surfaces were unsuccessful. However, these unsuccessful attempts could provide evidence suggesting that more extended structures resulting from end-to-end polymerization did not occur under the conditions employed.

To address the challenge of working with strands that were too short for surface characterization, poly(adenylic) acid, **poly(A)**, with a variable length between 2.100 and 10.000 nucleotides, was employed to create longer **[Pd(CheldTP)(poly(A))]** structures (**poly(A)-Pd-CheldTP^{polym}**). RNA is more delicate than its DNA counterpart, but at the time of this study, **poly(A)** was more readily accessible to our laboratory.

Two surfaces were employed to study different characteristics of the poly(A)-Pd systems. On one hand, the mica surface was chosen to obtain stretched structure images. On the other hand, a silicon oxide (SiO_2) surface

was chosen to conduct electrical measurements, despite hindered reproducibility in obtaining stretched structures,

Before conducting AFM studies, it is crucial to appropriately functionalize the surfaces to enhance the electrostatic attraction between the surfaces and nucleic acids, ensuring correct deposition and, ideally, stretched strands. The functionalized surface must interact correctly with the sample to provide adequate resolution. In this regard, (3-aminopropyl)triehoxysilane (APTES) has been commonly employed to functionalize mica surfaces for DNA deposition.[42] APTES facilitates the creation of positive charges on the mica surface, enabling interaction with negatively charged biomolecules such as nucleic acids.[43] It is important to note that there is no singular method for functionalizing AFM surfaces, and each deposition protocol should be thoroughly studied for each sample.

Mica surface was initially employed to deposit samples of free **poly(A)**, supramolecular **poly(A)-Pd-Cheld** system, non-polymerized **poly(A)-Pd-CheldTP** and polymerized **poly(A)-Pd-CheldTP^{polym}**. To achieve this, solutions containing 3 µM **poly(A)**, 1.3 equivalent **Pd-CheldTP** (DMSO), 50 mM $NaNO_3$, 3 mM Tris (pH7), and 0.3 mM EDTA were employed. Before sample deposition, the mica surface underwent functionalization following established procedures (Section 4.5). The surface was exfoliated and treated with APTES (0.1%), after which 20 µL of sample was deposited for 3-5 minutes. [43–45] Figure 4.17 shows the protocol for sample deposition on mica.

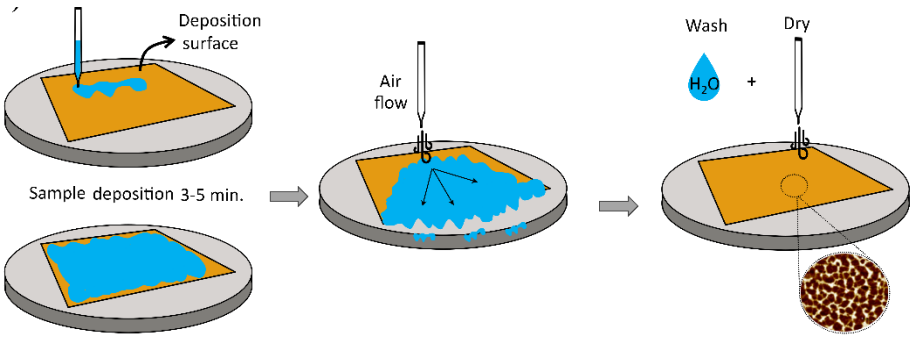

Figure 4.17: Scheme for free **poly(A)**, supramolecular **poly(A)-Pd-Cheld** system, non-polymerized **poly(A)-Pd-CheldTP** and polymerized **poly(A)-Pd-CheldTP^{polym}** sample deposition on mica Surface. Complete the procedure described in section 4.5.

The structural images for each sample are shown in Figure 4.18. The results indicate that, in general, the absence of the **Pd-Cheld** complex resulted in aggregation, with rounded structures observed for **poly(A)**. This observation corresponds to the inherent tendency of single-stranded RNA molecules to adopt complex structures, often leading to globular aggregation.

In contrast, when **Pd-Cheld** is present in the sample, the images show elongated and stretched strands, with widths ranging between 10-20 nm and heights of around 1nm, forming a densely interconnected network, in agreement with the formation of **poly(A)-PdCheld** structures. This transformation can be attributed to the disruption of hydrogen bond formation within **poly(A)** strands due to the formation of Pd-mediated base pairs, thus preventing aggregation.

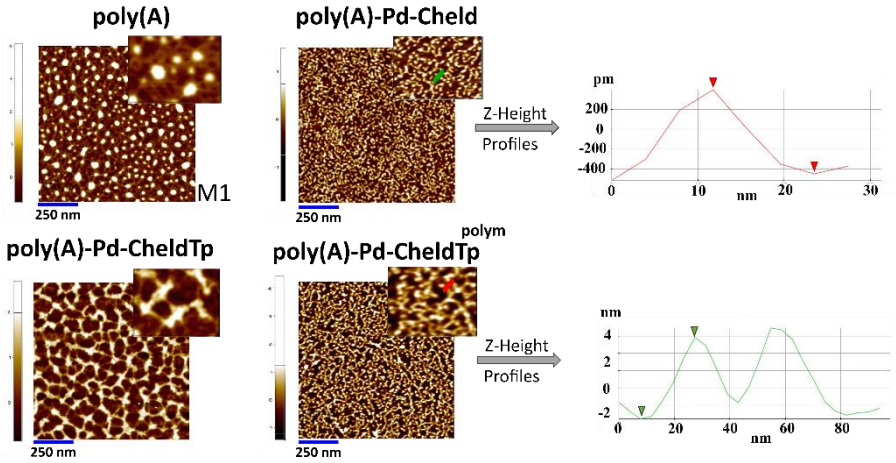

Figure 4.18: Left) AFM image on mica Surface for; **poly(A)**, **poly(A)-Pd-CheId**, **poly(A)-Pd-CheldTP**, **poly(A)-Pd-CheldTP^{polym}**. Right) Height/width profiles for **poly(A)-Pd-CheId** (red plot) and **poly(A)-Pd-CheldTP^{polym}** (green plot). Conditions: 3 µM **poly(A)**, 1.3 equivalent of **Pd-CheldTP** (DMSO), 50 mM $NaNO_3$, 3 mM Tris (pH7), 0.3 mM EDTA.

The images registered for **poly(A)-Pd-CheldTP** system also revealed elongated structures, but in this case, resulting in a more distinct interconnected network with strands showing a width between 10-20 nm and height around 2 nm. Finally, the polymerized **poly(A)-Pd-CheldTP^{polym}** sample exhibited an intricate, densely interconnection network between strands of broad nodes, that can be related to the polymerization process. In this sample, the width and height of the strands exceeded that of any other case, with widths ranging from 30-40 nm and heights around 3nm.

Consequently, it can be concluded that forming Pd-mediated base pairs promotes the development of more extended and interconnected structures. Still, more detailed studies are needed to fully understand cross-polymerization events between **poly(A)** molecules. This could explain the presence of more connected and broader nodes in **poly(A)-Pd-CheldTP^{polym}** structures.

After investigating the formation of supramolecular **poly(A)-Pd-CheldTP^{polym}** hybrids by AFM, their electrical properties were studied. As mentioned above, polymers derived from **TP** have been demonstrated to be

effective in creating electrically conductive structures.[18,39] For this purpose, electrostatic force microscopy (EFM) characterization was conducted. EFM is a technique utilized to analyze the electrical characteristics of a sample surface. It operates by detecting the electrostatic force between the surface and a biased AFM tip. By applying a voltage between the sample and the tip while the cantilever oscillates above the surface without contact, EFM generates images showing changes in oscillation amplitude and phase. Consequently, EFM images offer insights into the surface electrical properties, such as charge distribution. In this thesis, the measurements carried out in EFM mode simultaneously acquire the topography information of the sample in NCM (Non-contact Mode).

To study the electrical properties of **poly(A)-Pd-CheldTP** supramolecular hybrids, SiO_2 surfaces were chosen. SiO_2 wafers are commonly employed for this task and have been evaluated as proper candidates for electrical studies.[46] Again, samples of free **poly(A)**, supramolecular **poly(A)-Pd-Cheld**, non-polymerized **poly(A)-Pd-CheldTP** and polymerized **poly(A)-Pd-CheldTP^{polym}** were deposited and characterized (Figure 4.16). For these studies, SiO_2 surface was treated with piranha solution (H_2SO_4:H_2O_2 4:1), chlorotrimethyl-silane and 20-40 μL of samples were deposited for 1 minute.[19,47,48] Figure 4.19 shows a schematic representation of the protocol to deposit the sample on SiO_2. Subsequently, the samples were studied using AFM and EFM.

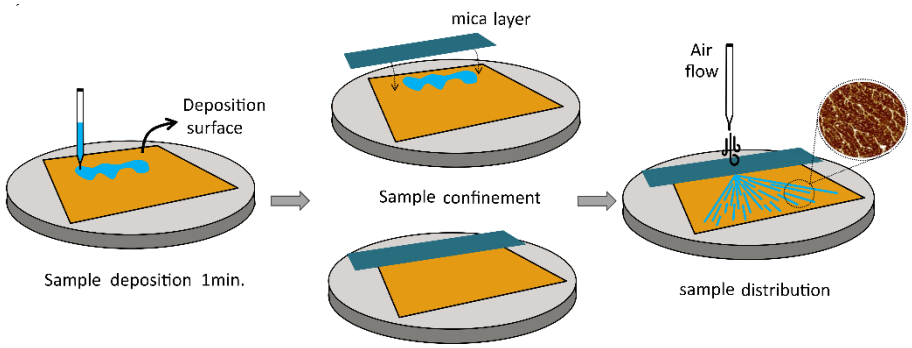

Figure 4.19: Scheme for free **poly(A)**, supramolecular **poly(A)-Pd-Cheld** system, non-polymerized **poly(A)-Pd-CheldTP** and polymerized **poly(A)-Pd-CheldTP^{polym}** sample deposition on SiO_2 Surface. Complete procedure described in section 4.5.

As observed in the AFM experiments using SiO_2, free **poly(A)** strands tend to form granular structures (Figure 4.20a). As expected by the non-conducting nature of these structures, the corresponding electrical signal amplitude and phase acquired by EFM (from -5V to 5V) did not display any charge distribution over the sample. The images recorded for **poly(A)-Pd-Cheld** structures exhibited an irregular strand organization, with multiple overlapping layers and poor strand stretching with structures ranging from 20 to 40 nm (Figure 4.20a). These results are different from those conducted on mica for **poly(A)-Pd-Cheld** hybrid. Unfortunately, all attempts to obtain images showing stretched **poly(A)-Pd-Cheld** strands on SiO_2 were unsuccessful. Nonetheless, EFM measurements were conducted for these **poly(A)-Pd-Cheld** irregular structures and no electrical signal amplitude or phase was observed. These results also indicate that the presence of **Pd-Cheld** does not lead to noticeable changes in the conductive characteristic of this material.

AFM experiments were them conducted for **poly(A)-Pd-CheldTP** on SiO_2 (Figure 4.20a), revealing granular and slightly elongated structures with widths ranging from 50 to 100 nm. Unfortunately, no stretched structures were observed. Nevertheless, EFM was conducted on the deposited material, and as expected, no electrical signal amplitude or phase was detected. This behaviour is consistent with the above findings, as neither the presence of **Pd-Cheld** nor

Pd-CheldTP monomers change the conductive characteristic of **poly(A)-Pd-CheldTP** hybrids.

Finally, the AFM studies performed on polymerized **poly(A)-Pd-CheldTP^{polym}** samples yielded promising results. Figure 4.20a displays the initial AFM topography on SiO_2 studies, showing stretched and continuous structures with intercalated small nodes along the structures. Graphics for Z-height profiles present a cross-section of the structures (Figure 4.20a, right), revealing that the heights range between 1nm for thinner structures and 4 nm for wider structures. These results suggest that the formation of isolated polymer stranded (Z_Height ≈ 1 nm) is accompanied by the deposition of several ones (Z_Height ≈ 4 nm), although possible cross-polymerization processes leading to wider and more complex structures cannot be ruled out. On the other hand, the width for **poly(A)-Pd-CheldTP^{polym}** structures ranges from 100 to 200 nm, in contrast with the 50 to 100 nm found for **poly(A)-Pd-CheldTP**. The significant difference in thickness between both samples suggests a better elongation when the polymer is formed, and probably, two or more strands should adhere together over the silicon oxide surface.

Moreover, a comparison of AFM topography between mica and SiO_2 surfaces for **poly(A)-Pd-CheldTP^{polym}**, shows that the silicon surface facilitates the stretching of the strands and the formation of single layers. It is worth mentioning that the depositions of these samples proved to be challenging and required tedious and meticulous procedures to yield reproducible data.

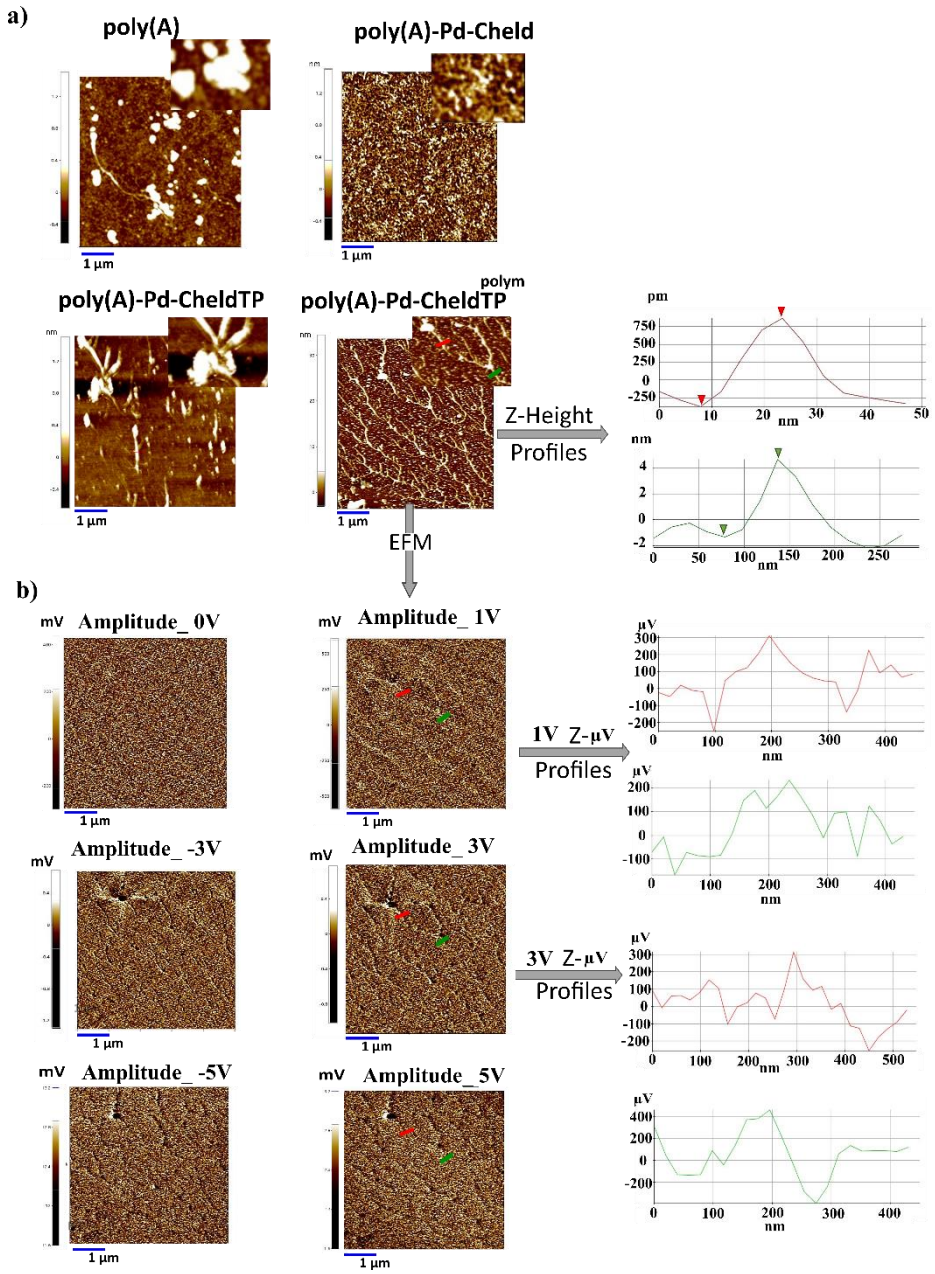

Figure 4.20: a) AFM image and Z-Height/width profiles on SiO_2 Surface for; **poly(A)**; poly**(A)-Pd-Cheld**; **poly(A)-Pd-CheldTP** ;**poly(A)-Pd-CheldTP^{polym}**. b) EFM image and Z-µV profiles for sample **poly(A)-Pd-CheldTP^{polym}** (-5 to 5V). Conditions: 3 µM **poly(A)**, 1.3 equivalent of **Pd-Cheld/Pd-CheldTP** (DMSO), 50 mM $NaNO_3$, 3 mM Tris (pH7), 0.3 mM EDTA.

Subsequently, the conducting characteristics of **poly(A)-Pd-CheldTP^{polym}** structures were investigated by EFM measurements. The corresponding electrical signal amplitude and phase acquired at different voltages (-5V to 5V) are presented in Figure 4.20b. The amplitude signals indicate that the charge distribution in the sample follows the topography observed by AFM, where a multitude of structures were visualized between -3 and 3 V, following the topographic signal. Graphics for Z-μV profiles present a cross-section for the amplitude signal (Figure 4.20b, right), and a comparison of Z-μV profiles for the same cross-section (red line or green line) at 1V and 3V are presented. In all the experiences, Z-μV profiles exhibit values ranging from 400 to 600 μV and a width of 200 nm, indicating the existence of charge conduction in this case.

Comparing these results with EFM experiments for **poly(A)**, **poly(A)-Pd-Cheld** and **poly(A)-Pd-CheldTP^{polym}**, only for samples containing polymerized **TP** structures along the ss-DNA template, electrostatics properties were observed. Overall, the results obtained in this research provide initial evidence suggesting that **polyA-Pd-CheldTP^{poly}** structures can be conductive. However, it is important to clarify that while these supramolecular structures have exhibited EFM signals, this does not necessarily imply intrinsic conductivity. Complementary studies, such as conductive AFM (c-AFM) experiments, would be necessary to study the electrical conductivity of these systems more deeply. In this regard, Houlton and co-workers have made significant advances in studying DNA-based material using c-AFM measurements, demonstrating that polymers derived from thiophene/pyrrole systems deposited on DNA molecules can act as conducting material. [13,49–51]

4.6. Conclusions.

In Chapter 4, a strategy to obtain metal-DNA hybrids with potential nanotechnological properties has been presented. Initially, the functionalization of the **CheId** ligand with 2-(2-thienyl)pyrrole (**TP**) monomers was described. Afterwards, the formation and characterization of the **[Pd(CheldTP)(DMSO)]** complex was described. Subsequently, interaction studies between **Pd-CheldTP** and the model nucleobase 9-ethyl-adenine (**eA**) confirmed the formation of the **[Pd(CheldTP)(eA)]** complex, serving as a preliminary step toward the formation of supramolecular DNA-Pd hybrids that incorporate the **TP** unit.

Following the methodologies described in this thesis, the formation of the supramolecular **[{Pd(CheldTP)$_{15}$}(dA$_{15}$)]** hybrid was confirmed. This structure resembles a helix due to the binding of the **Pd-CheldTP** fragment via ***N1***-adenine position, with one strand formed by **dA$_{15}$** and the other one by **Pd-CheldTP** complexes. Furthermore, the organization of **TP** monomers along the ss-DNA template makes them suitable for further reactions. The subsequent polymerization of these monomers was studied by UV-Vis, CD, and computational studies, confirming that the conformation of the nucleic acid helix does not significantly alter upon polymerization of the **TP** units.

Finally, preliminary investigations were conducted to determine the potential conductive properties of the polymeric structures, **[{Pd(CheldTP)$_{15}$}(dA$_{15}$)]^{polym}** , using EFM. While these results suggest that the supramolecular structures exhibit charge distribution, they do definitively confirm conductivity. More profund studies in this regard need to be conducted dut to the difficulty in obtaining reproducible samples with stretched polymeric structures suitable for c-AFM.

4.7. Materials and Methods.

4.7.1. Synthesis and characterization of compounds.

4.5.1.a. Synthesis of 4-(3-(2-(2-thienyl)pyrrole)propoxy)pyridine-2,6-dicarboxylic acid, **CheldTP.**

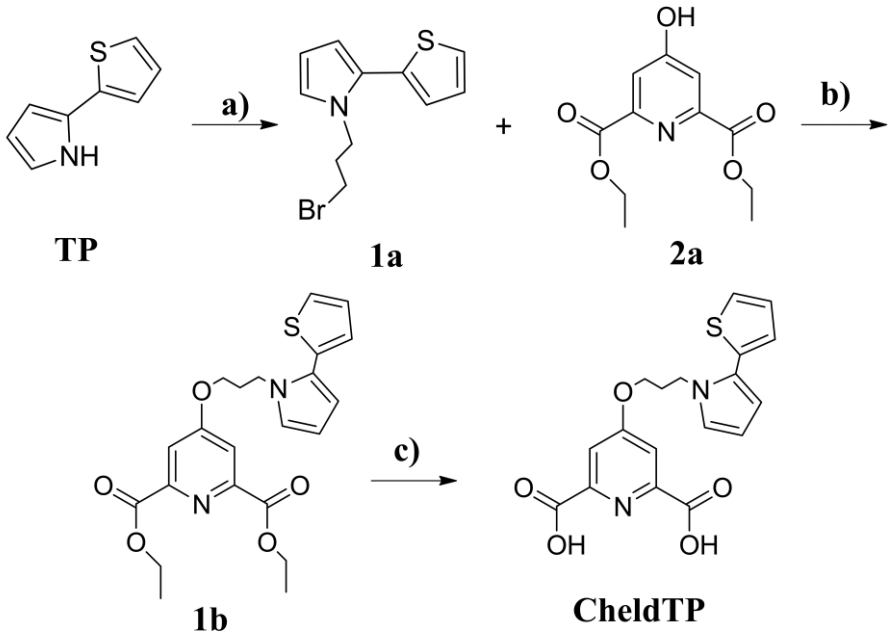

Scheme 4.1: Synthesis route to obtain 4-(3-(2-(thiophen-2-yl)-1H-pyrrol-1-yl)propoxy)pyridine-2,6-dicarboxylic acid, **CheldTP.**

Compound 2-(2-thienyl)pyrrole, **TP**; was obtained following a synthetic route previously described in the literature.[52]

Compound diethyl 4-hydroxypyridine-2,6-dicarboxilate, **2a**; was obtained following a synthetic route previously described in the literature.[53]

a) 1-(3-bromopropyl)-2-(2-thienyl)pyrrole, **1a**. To a solution of **TP** (3g, 20 mmol) in anhydrous N,N-dimethylformamide (DMF) (300 mL) was added 100 mL (1 mmol) of 1,3-dibromopropane under N_2 atmosphere. The mixture was

stirred for five minutes, and sodium hydride (NaH) (2 g, 0.005 mmol) was added. The reaction flask was stirring for five days and protected from light. The solvent was removed by rotavapor to obtain a yellow oil. The product was dissolved in ethyl acetate (200 mL), wash with three portions of water (100 mL), and the organic phase was collected, dry with magnesium sulphate ($MgSO_2$) and concentrated to obtain a garnet oil. The product was purified by silica column in hexane as mobile phase. Product fractions were combined and concentrated. Yield: 95 %. ^{1}H-NMR (400 MHz; DMSO-D_6): δ 7.51 (dd, J=7.0-4.5 Hz, 1H, *CH*), 7.11 (m, 2H, *CH*), 6.92 (s, 1H, *CH*), 6.21 (m, 1H, *CH*), 6.09 (n, 1H, *CH*), 4.15 (t, J=7.0 Hz, 2H, CH_2), 3.40 (t, J=6.4 Hz, 2H, CH_2), 2.12 (m, 2H, CH_2). HRMS (ESI): m/z: calculated for $C_{11}H_{12}NSBr[M+H]^+$: 269.9952 Da; found: 269.9949 Da.

b) Diethyl 4-(3-(2-(2-thienyl)pyrrole)propoxy)pyridine-2,6dicarboxylate, **1b**. Into a solution of **1a** (0.5 g, 2 mmol) in anhydrous DMF (15 mL), NaH (0.1 g, 2.5 mmol) was added under N_2 atmosphere. The mixture was stirred for 30 minutes. A solution of **2a** (0.4 g, 1.5 mmol) in anhydrous DMF (20 mL) was added and the mixture was stirred for five days. The solvent was removed to obtain a yellow oil. The product was dissolved in dichloromethane (DCM) (100 mL) and washed with three portions of water (100 mL). Organic phase was dry with $MgSO_2$ and concentrated to obtain **1b** as a yellow oil. Yield: 75 %. ^{1}H-NMR (400 MHz; DMSO-D_6): 7.61 (s, 2H, *CH*), 7.42 (dd, J=0.9-5.0 Hz, 1H, *CH*), 7.08 (dd, J=0.9-3.3 Hz, 1H, *CH*), 7.03 (dd, J=3.6-5.0 Hz, 1H, *CH*), 6.94 (dd, J=1.9-2.5 Hz, 1H, *CH*), 6.19 (dd, J=1.7-3.4 Hz, 1H, *CH*), 6.07 (dd, J=2.9-3-4 Hz, 1H, *CH*), 4.38 (q, J=7.1 Hz, 4H, CH_2) 4.24 (t, J=6.8 Hz, 2H, CH_2), 4.07 (t, J=5.5 Hz, 2H, CH_2), 2.10 (dd, J=7.9-3.7 Hz, 2H, CH_2), 1.34 (t, J=7.1 Hz, 6H, CH3). HRMS (ESI): m/z: Calculated for $C_{22}H_{25}N_2O_5S[M+H]^+$: 429.1418 Da; found: 429.1492 Da.

c) 4-(3-(2-(2-thienyl)pyrrole)propoxy)pyridine-2,6-dicarboxylic acid, **CheldTP.** Into a solution of **1b** (0.7 g, 1.5 mmol) in anhydrous MeOH (30 mL) sodium methoxide (3 ml, 1M) was added dropwise. The mixture was stirred at 60°C until the appearance of a precipitate. The pH was adjusted with Amberlite® to neutral pH. The mixture was filtered, and the solvent removed by vacuum to obtain **1c** as a white powder. Yield: Quantitative. ^{1}H-NMR (400 MHz; DMSO-D_6): δ 7.6 (s, 2H, *CH*), 7.42 (dd, J=1.1-5.1, 1H, *CH*), 7.09 (dd, J=1.1-5.1, 1H, *CH*), 7.03 (dd, J=3.6-5.1, 1H, CH), 6.94 (dd, J=1.7-2.5, 1H, CH), 6.19 (dd, J=1.8-3.5, 1H, CH), 6.07 (t, 1H, *CH*), 4.23 (t, J=6.9, 2H, CH_2) 4.09 (t, J=5.8 Hz, 2H, CH_2), 2.08 (dt, J=6.1-12.6 Hz), 2H CH_2). HRMS (ESI): m/z: Calculated for $C_{18}H_{17}N_2O_5S[M+H]^+$: 373.0858; Found: 373.0844. IR (ν/cm^{-1}):: 3224 (m), 2921 (mf), 2857 (m), 1729 (mf), 1603 (m), 1447 (m), 1400 (mf), 1361 (mf), 1194 (f), 1105 (m), 1038 (m), 773 (m), 684 (m).

4.5.1.b. Synthesis of [Pd(CheldTP)(DMSO)], **Pd-CheldTP**.

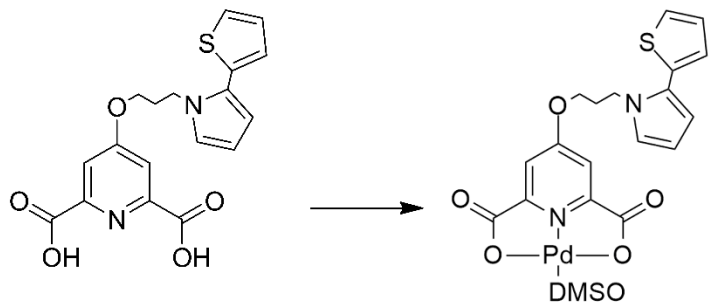

CheldTP **Pd-CheldTP**

Scheme 4.2: Synthesis route to obtain [Pd(CheldTP)(DMSO)] complex, **Pd-CheldTP**.

Into a solution of **CheldTP** (2 mg, 5 mmol) in DMSO-D_6 a solution of $Pd(NO_3)_2$ (1.5 mg, 5 mmol) was added. The mixture was stirred 15 minutes and heat at 45°C. The complex was directly characterized in solution. ^{1}H-NMR (400 MHz; DMSO-D_6): δ 7.45 (dd, J=1.1-5.1, 1H, *CH*), 7.23 (s, 2H, *CH*), 7.09 (dd, J=1.1-5.1, 1H, *CH*), 7.05 (dd, J=3.6-5.1, 1H, CH), 6.94 (dd, J=1.7-2.5, 1H, CH),

6.19 (dd, J=1.8-3.5, 1H, CH), 6.07 (t, 1H, *CH*), 4.23 (t, J=6.9, 2H, CH_2) 4.15 (t, J=5.8 Hz, 2H, CH_2), 2.07 (dt, J=6.1-12.6 Hz), 2H CH_2). HRMS (ESI): m/z: Calculated for $C_{18}H_{15}N_2O_5SPd(DMSO)[M+H]^+$: 554.9798 Da; found: 554.9880 Da.

4.5.1.c. Synthesis of [Pd(CheldTP)(eA)], **eA-Pd-CheldTP**.

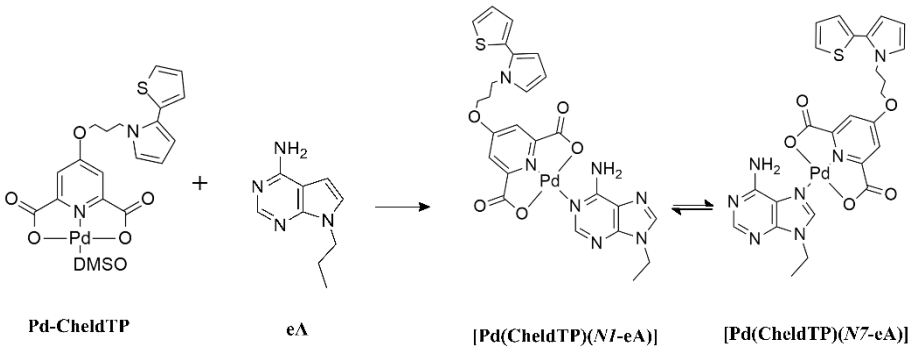

Scheme 4.3: Synthetic reoute to obtain [Pd(CheldTP)(*N1*-eA)] and [Pd(CheldTP)(*N7*-eA)] complexes.

Into a solution of **eA** (2 mg, 15 mmol) in DMSO-D_6 a solution of **Pd-CheldTP** (1 equivalent) was added. The mixture was stirred 15 minutes and heat at 45°C. The complex was directly characterized in solution. ^{1}H-NMR (400 MHz; DMSO-D_6): δ 8.53 (s, 1H, A-NH_2), 5.52 (s, 1H, A-NH_2), 8.46 (s, 1H, *CHa*), 8.38 (s, 1H, *CHb*), 8.32 (s, 1H, *CHb*), 8.13 (s, 1H, *CHa*), 7.46 (dd, J=1.1-5.1, 1H, *CH*), 7.33 (s, 2H, CHa_{py}), 7.31 (s, 2H, CHb_{py}), 7.11 (dd, J=1.1-5.1, 1H, *CH*), 7.06 (dd, J=3.6-5.1, 1H, CH), 6.96 (dd, J=1.7-2.5, 1H, CH), 6.20 (dd, J=1.8-3.5, 1H, CH), 6.08 (t, 1H, *CH*), 4.36 (q, J=7.2, 2H, CH_2), 4.23 (t, J=6.9, 2H, CH_2) 4.15 (t, J=5.8 Hz, 2H, CH_2), 2.07 (dt, J=6.1-12.6 Hz), 2H CH_2), 1.44 (t, J=7.2 Hz, 3H, CH_3).

4.7.2. Characterization techniques.

4.7.2.a. Nuclear Magnetic Resonance (^{1}H-NMR).

The ^{1}H-NMR spectra have been recorded at room temperature on a 400 MHz (2 channels) high-definition Bruker Nanobay Avance III HD. This equipment features a 5mm BBDO probe, direct observation of 31P-109Ag nuclei, and observation of 1H, 19F, and 1H decoupling with Z gradient. Additionally, it includes ATM automatic tuning system. The ^{1}H-NMR spectra with temperature gradient have been recorded on a 500 MHz (2 channels) high-definition Bruker Avance NEO spectrometer. This equipment is equipped with a 5mm Smatr probe BBFO, direct observation of 31P-109Ag nuclei, and observation of 1H, 19F, and 1H decoupling with Z gradient. It also includes ATM automatic tuning system with a 24-hour robot. These instruments are available at Scientific Research Center (CIC) of the University of Granada.

Samples preparation: All simples have been disolved in deuterated solvents acquired from Eurisotop.

4.7.2.b. Mass Espectrometry (ESI-MS)

High-resolution electrospray ionization mass spectrometry (ESI-MS) was carried out on a Waters LCT Premier spectrometer for the metal complexes, while the characterization of the **dX15** oligonucleotide was carried out by MALDI-TOF mass spectrometry on a Bruker Autoflex spectrometer. Molecular mass determination for **1Pd-DNA** was performed by ESI-MS using a Micro Tof-Q Instrument (Bruker Daltonics GmbH, Bremen, Germany) equipped with a time-of-flight analyzer (ESI-TOF MS), calibrated with NaI (200 ppm NaI in a 1:1 H2O:isopropanol mixture), interfaced with an AgilentTechnologies Series 1100 HPLC pump and equipped with an autosampler, both controlled by the Compass Software. The interaction of the

metallic complexes with the DNA hybrids (50 μM) was analyzed in negative mode, injecting 10 μL of the sample at 40 μL min-1, with capillary-counter electrode voltage at 3.9-4.2

kV; the desolvation temperature was set at 100 °C, and dry gas was flowed at 6 L min-1, using a 90:10 mixture of 15 mM ammonium acetate and acetonitrile (pH 7.0) as a liquid carrier. The spectra were collected throughout an m/z range from 800 to 3000.

4.7.2.c. Circular Dichroism (CD).

CD spectra were recorded on a JASCO model J815 spectropolarimiter equipped with a Peltier temperature control system. The data were processed using Spectra Mánager Administrative Tool V 1.03.02 sowftware, available at the Scientific Research Center (CIC) of the University of Granada.

To study **[Pd(CheldTP)(dA_{15})]** and **[Pd(CheldTP)(dX_{15})]** hybrid at pH6.8, the following samples were prepared:

- 2 uM de **dA_{15}**, 100 mM $NaClO_4$, 5 mM MOPS (pH6.8) and **Pd-CheldTP** (500μM, DMSO).
- 2 uM de **dX_{15}**, 100 mM $NaClO_4$, 5 mM MOPS (pH6.8) and **Pd-CheldTP** (500μM, DMSO).

Experimental parameters; 250-450 nm, 5 scans, T=25°C.

To study **[Pd(CheldTP)(dA_{15})]** hybrid at pH4.5, the following samples were prepared:

- 2 uM de **dA_{15}**, 100 mM $NaClO_4$, 5 mM Citrate (pH6.8→4.5) and **Pd-CheldTP** (500μM, DMSO).

4.7.2.d. UV-Vis spectrometry.

UV-Vis spectra were recorded on an Agilent Technologies Cary 100 spectrophotometer, equipped with a Cary Temperature Controller, available in the Department of Inorganic Chemistry at University of Granada.

To study the polymerization process of **CheldTP** ligand after **[Pd(CheldTP)(dA$_{15}$)]** hybrid formation, the following samples were prepared:

- 2 uM de **dA$_{15}$**, 100 mM $NaClO_4$, 5 mM Citrato (pH 6.8→4.5) and **Pd-CheldTP** (500µM, DMSO).
- 2 uM de **dA$_{15}$**, 100 mM $NaClO_4$, 5 mM Citrato (pH 6.8→4.5) amd **CheldTP** (500µM, DMSO).
- 100 mM $NaClO_4$, 5 mM Citrato (pH 6.8→4.5) and **CheldTP** (500µM, DMSO).
- 100 mM $NaClO_4$, 5 mM Citrato (pH 6.8→4.5) and $Pd(NO_3)_2$ (500µM, DMSO).

Polymerization was carried out by the addition of 10 µL **ABTS** (10µ M), 2µL **HRP** (1g/mL) and 5 µL **H_2O_2** (15%).

Experimental parameters; 250-800 nm, 1 scans / 4 minutes (total time; 60 minutes), T=10°C.

4.7.2.e. Atomic Force Microscopy and Electronic Force Microscopy (AFM-EFM).

AFM-EFM images were recorded by a motorized atomic force microscope with a platinum stage (XY route: 150 nm; Z route: 25 mm); wafer fixation by vacuum and multi-sample stage (up to 16). It features a single-reflection XY scanning module with closed-loop control, scanning range of 100 µm x 100 µm, 20-bit position control, and 24-bit position sensor. Additionally, it is

equipped with 10x lenses (0.21 NA) for ultra-long working distance, objective in the sample surface viewing axis, cantilever, and a coupled objective lens 10x field of view (840 x 630 µm). These instruments are available at Scientific Research Center (CIC) of the University of Granada.

To study the polymerization process in **[Pd(CheldTP)(dA$_{15}$)]** hybrid samples deposited on mica surfaces, the following samples were prepared:

- 2.5 µM **poly(A)**, 50 µM NaNO3, 3 µM Tris (pH 7), 0.3 µM EDTA.
- 3 µM **poly(A)**, 50 µM NaNO3, 3 µM Tris (pH 7), 0.3 µM EDTA and 4.5 µM **Pd-Cheld**.
- 3 µM **poly(A)**, 50 µM NaNO3, 3 µM Tris (pH 7), 0.3 µM EDTA and 4.5 µM **Pd-CheldTP**.

Protocol for sample deposition on mica surface:

Over the metallic support, a double-sided adhesive was placed. Them a mica layer were added and exfoliated twice. 40 µL APTES (0.1% in H_2O) solution was added over the mica surface for one minute. Mica Surface was them washed with 1 mL of H_2O and dry with N_2 flow. 20 µL of samples (**poly(A)**, **poly(A)-Pd-Cheld**, **poly(A)-Pd-CheldTP**) were deposit for 3 minutes. The samples were blown with nitrogen flow and the mica surface was washed with 2 mL of H_2O and dry with a N_2 flow. [43–45]

To study the polymerization process in **[Pd(CheldTP)(dA$_{15}$)]** hybrid samples deposited on SiO_2 surfaces, the following samples were prepared:

- 2.5 µM **poly(A)**, 50 µM NaNO3, 3 µM Tris (pH 7), 0.3 µM EDTA.
- 3 µM **poly(A)**, 50 µM NaNO3, 3 µM Tris (pH 7), 0.3 µM EDTA and 4.5 µM **Pd-Cheld**.
- 3 µM **poly(A)**, 50 µM NaNO3, 3 µM Tris (pH 7), 0.3 µM EDTA and 4.5 µM **Pd-CheldTP**.

Protocol for sample deposition on SiO_2 surface:

The SiO_2 surface was firstly washed with acetone, ethanol, and water and dry with air flow. The SiO_2 surface was submerged in a "piranha" solution (4:1 H_2SO_4:H_2O_2) for 60 minutes and them washed with water and dry by an air flow. The SiO_2 surface was heated in oven at 100°C for 30 minutes. Them, SiO_2 surface was place into a desiccator containing Chlorotimethylsinale vapor for 10 minutes. A 20-40 µL of samples were deposited and a mica layer was placed on top 1 minute. With an intense air flow, the sample was distributed over the surface as a spry. Them, SiO_2 surface was washed with 1mL of water and dry with an air flown.

5.7. Bibliography

1 M. R. Arkin, E. D. A. Stemp, R. E. Holmlin, J. K. Barton, A. Hörmann, E. J. C. Olson and P. F. Barbara, *Science (1979)*, 1996, **273**, 475–480.

2 F. D. Lewis, T. Wu, Y. Zhang, R. L. Letsinger, S. R. Greenfield and M. R. Wasielewski, *Science (1979)*, 1997, **277**, 673–676.

3 H.-W. Fink and C. Schönenberger, *Nature*, 1999, **398**, 407–410.

4 E. Braun, Y. Eichen, U. Sivan and G. Ben-Yoseph, *Nature*, 1998, **391**, 775–778.

5 Z. Kutnjak, C. Filipič, R. Podgornik, L. Nordenskiöld and N. Korolev, *Phys Rev Lett*, 2003, **90**, 098101.

6 V. D. Lakhno, *Physics of Particles and Nuclei Letters*, 2008, **5**, 231–235.

7 J. D. Slinker, N. B. Muren, S. E. Renfrew and J. K. Barton, *Nat Chem*, 2011, **3**, 228–233.

8 Z. Chen, C. Liu, F. Cao, J. Ren and X. Qu, *Chem Soc Rev*, 2018, **47**, 4017–4072.

9 Z. Chen, C. Liu, F. Cao, J. Ren and X. Qu, *Chem Soc Rev*, 2018, **47**, 4017–4072.

10 J. J. Gossett and S. C. Harvey, *Nano Lett*, 2011, **11**, 604–608.

11 P. Nickels, W. U. Dittmer, S. Beyer, J. P. Kotthaus and F. C. Simmel, *Nanotechnology*, 2004, **15**, 1524–1529.

12 R. Nagarajan, W. Liu, J. Kumar, S. K. Tripathy, F. F. Bruno and L. A. Samuelson, *Macromolecules*, 2001, **34**, 3921–3927.

13 L. Dong, T. Hollis, S. Fishwick, B. A. Connolly, N. G. Wright, B. R. Horrocks and A. Houlton, *Chem. Eur. J.*, 2007, **13**, 822–828.

14 S. Pruneanu, S. A. F. Al-Said, L. Dong, T. A. Hollis, M. A. Galindo, N. G. Wright, A. Houlton and B. R. Horrocks, *Adv Funct Mater*, 2008, **18**, 2444–2454.

15 R. Hassanien, M. Al-Hinai, S. A. Farha Al-Said, R. Little, L. Šiller, N. G. Wright, A. Houlton and B. R. Horrocks, *ACS Nano*, 2010, **4**, 2149–2159.

16 M. A. Galindo, J. Hannant, R. W. Harrington, W. Clegg, B. R. Horrocks, A. R. Pike and A. Houlton, *Org Biomol Chem*, 2011, **9**, 1555.

17 W. Chen, G. Güler, E. Kuruvilla, G. B. Schuster, H.-C. Chiu and E. Riedo, *Macromolecules*, 2010, **43**, 4032–4040.

18 S. M. D. Watson, A. R. Pike, J. Pate, A. Houlton and B. R. Horrocks, *Nanoscale*, 2014, **6**, 4027–4037.

19 S. M. D. Watson, J. H. Hedley, M. A. Galindo, S. A. F. Al-Said, N. G. Wright, B. A. Connolly, B. R. Horrocks and A. Houlton, *Chem. Eur. J.*, 2012, **18**, 12008–12019.

20 W. Chen and G. B. Schuster, *J Am Chem Soc*, 2012, **134**, 840–843.

21 W. Chen and G. B. Schuster, *J Am Chem Soc*, 2013, **135**, 4438–4449.

22 W. Chen and G. B. Schuster, *Org. Biomol. Chem.*, 2013, **11**, 35–40.

23 W. Su, M. Schuster, C. R. Bagshaw, U. Rant and G. A. Burley, *Angew. Chem.*, 2011, **123**, 2764–2767.

24 G. G. Abashev, A. Y. Bushueva and E. V. Shklyaeva, *Chem Heterocycl Compd (N Y)*, 2011, **47**, 130–154.

25 P. Espinet, J. A. Miguel, S. García-Granda and D. Miguel, *Inorg Chem*, 1996, **35**, 2287–2291.

26 A. Pérez-Romero, A. Domínguez-Martín, S. Galli, N. Santamaría-Díaz, O. Palacios, J. A. Dobado, M. Nyman and M. A. Galindo, *Angew. Chem. Int. Ed*, 2021, **133**, 10177–10182.

27 H.-K. Song and G. T. R. Palmore, *J Phys Chem B*, 2005, **109**, 19278–19287.

28 H.-K. Song and G. T. R. Palmore, *Adv. Mater.*, 2006, **18**, 1764–1768.

29 R. Santucci, E. Laurenti, F. Sinibaldi and R. P. Ferrari, *Biochimica et Biophysica Acta (BBA) - Protein Structure and Molecular Enzymology*, 2002, **1596**, 225–233.

30 A. M. Azevedo, D. M. F. Prazeres, J. M. S. Cabral and L. P. Fonseca, *J Mol Catal B Enzym*, 2001, **15**, 147–153.

31 B. Datta and G. B. Schuster, *J Am Chem Soc*, 2008, **130**, 2965–2973.

32 S. M. D. Watson, M. A. Galindo, B. R. Horrocks and A. Houlton, *J Am Chem Soc*, 2014, **136**, 6649–6655.

33 M. D. Hanwell, D. E. Curtis, D. C. Lonie, T. Vandermeersch, E. Zurek and G. R. Hutchison, *J Cheminform*, 2012, **4**, 17.

34 Avogadro: An Open-Source Molecular Builder and Visualization Tool. Version 1.2.0. https://avogadro.cc/, .

35 U. Burkert and N. Allinger, *Molecular Mechanics*, Washington D.C, 1982, vol. 177.

36 F. Neese, *Wiley Interdiscip. Rev. Computa. Mol. Sci.*, 2012, **2**, 73–78.

37 F. Neese, F. Wennmohs, U. Becker and C. Riplinger, *The Journal of Chemical Physics* , 2020, **152**.

38 R. Sure and S. Grimme, *J Comput Chem*, 2013, **34**, 1672–1685.

39 G. G. Abashev, A. Y. Bushueva and E. V. Shklyaeva, *Chem Heterocycl Compd (N Y)*, 2011, **47**, 130–154.

40 A. Y. Lushnikov, A. Bogdanov and Y. L. Lyubchenko, *J.B.C.*, 2003, **278**, 43130–43134.

41 H. G. Hansma, I. Revenko, K. Kim and D. E. Laney, *Nucleic Acids Res*, 1996, **24**, 713–720.

42 Y. L. Lyubchenko and L. S. Shlyakhtenko, *Proc. Natl. Acad. Sci.* , 1997, **94**, 496–501.

43 L. S. Shlyakhtenko, A. A. Gall, A. Filonov, Z. Cerovac, A. Lushnikov and Y. L. Lyubchenko, *Ultramicroscopy*, 2003, **97**, 279–287.

44 C. Ke, A. Loksztejn, Y. Jiang, M. Kim, M. Humeniuk, M. Rabbi and P. E. Marszalek, *Biophys J*, 2009, **96**, 2918–2925.

45 N. Crampton, W. A. Bonass, J. Kirkham and N. H. Thomson, *Langmuir*, 2005, **21**, 7884–7891.

46 J. Castellon, D. El Khoury and R. Arinero, *Int J Nanosci*, 2019, **18**, 1940038.

47 G. Soliveri, V. Pifferi, R. Annunziata, L. Rimoldi, V. Aina, G. Cerrato, L. Falciola, G. Cappelletti and D. Meroni, *J.Phys. Chem.*, 2015, **119**, 15390–15400.

48 E. L. Sciuto, C. Bongiorno, A. Scandurra, S. Petralia, T. Cosentino, S. Conoci, F. Sinatra and S. Libertino, *Chemosensors*, 2018, **6**, 59.

49 S. M. D. Watson, A. R. Pike, J. Pate, A. Houlton and B. R. Horrocks, *Nanoscale*, 2014, **6**, 4027–4037.

50 A. Houlton, A. R. Pike, M. Angel Galindo and B. R. Horrocks, *Chem. Comm.*, 2009, 1797.

51 S. M. D. Watson, A. R. Pike, J. Pate, A. Houlton and B. R. Horrocks, *Nanoscale*, 2014, **6**, 4027–4037.

52 R. E. Niziurski-Mann and M. P. Cava, *Adv. Mater.*, 1993, **5**, 547–551.

53 I. Kim, B. H. Han, C.-S. Ha, J.-K. Kim and H. Suh, *Macromolecules*, 2003, **36**, 6689–6691.

5.8. Appendix

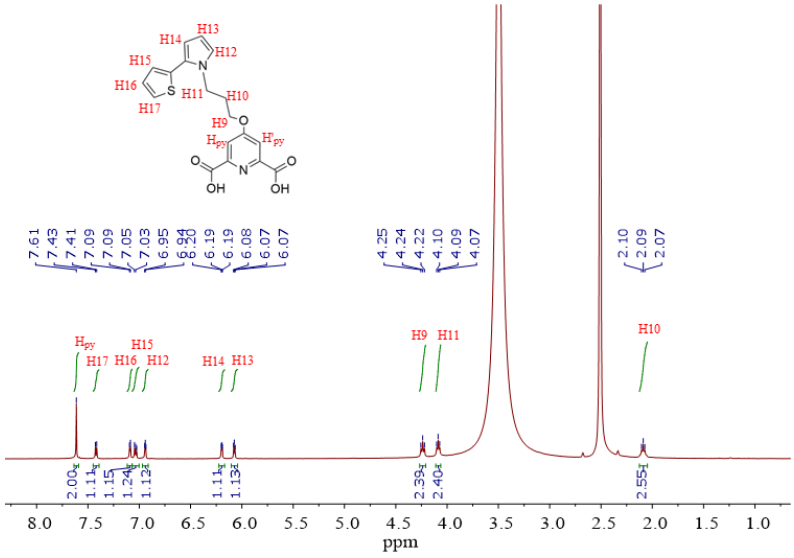

Appendix-Figure 1: [1]H-NMR (400Mhz DMSO-D_6) spectra for 4-(3-(2-(thiophen-2-il)-1H-pyrrole-1-yl)propoxi)pyriden-2,6-dicarboxylic acid, **CheldTP**.

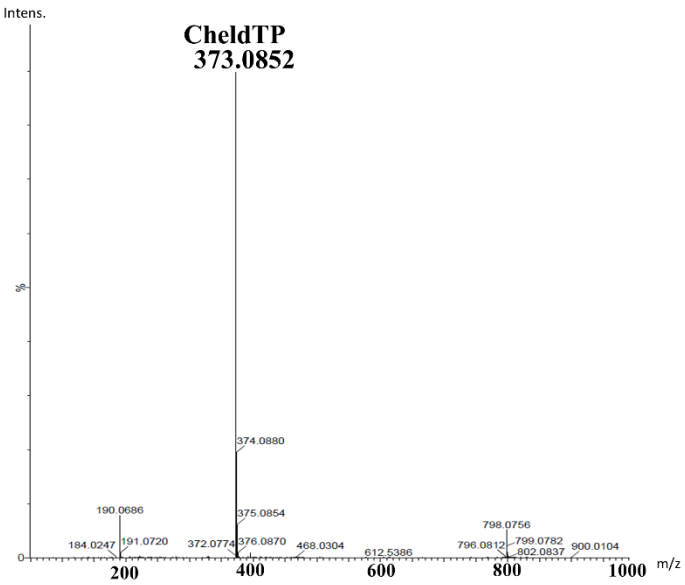

Appendix-Figure 2: ESI-MS(+) spectra for **CheldTP** ligand.

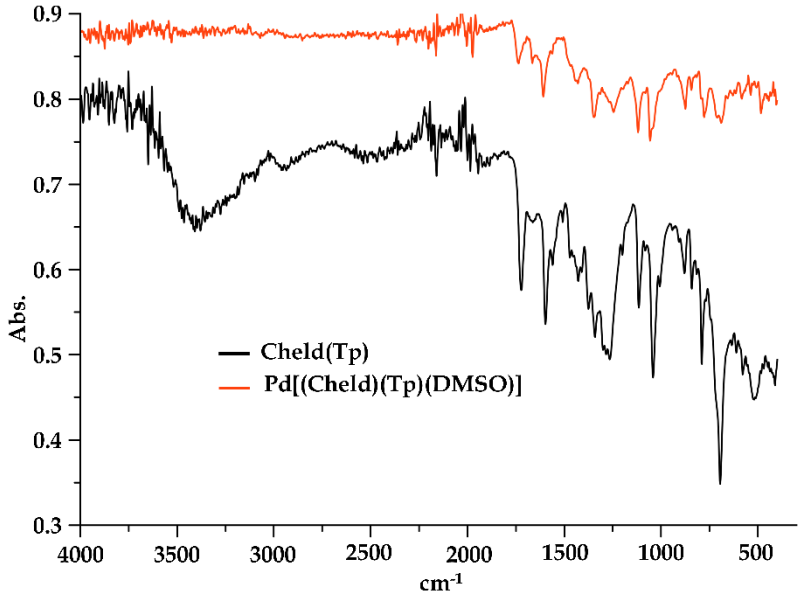

Appendix-Figure 3: IR spectra for **CheldTP** and **[Pd(CheldTP)(DMSO)]**.

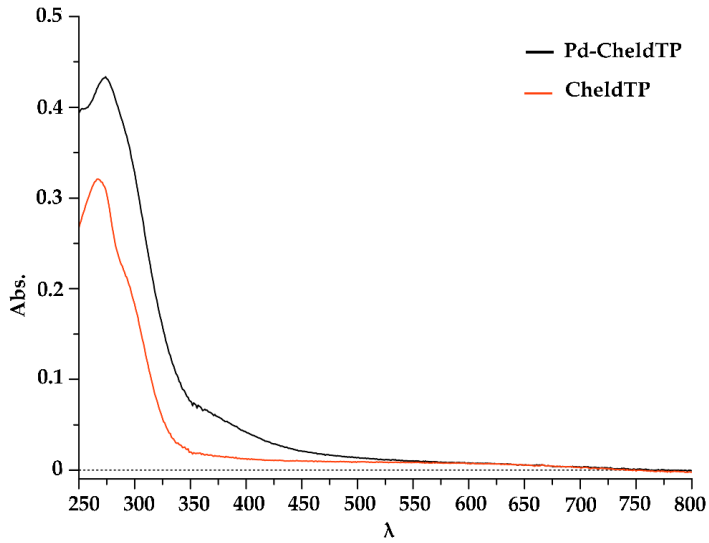

Appendix-Figure 4: UV-Vis for **[Pd(CheldTP)(DMSO)]** and **CheldTP**. Conditions: 39 µM **Pd-CheldTP** or **CheldTP (**DMSO), 100 mM $NaClO_4$, 5 mM MOPS (pH 6.8).

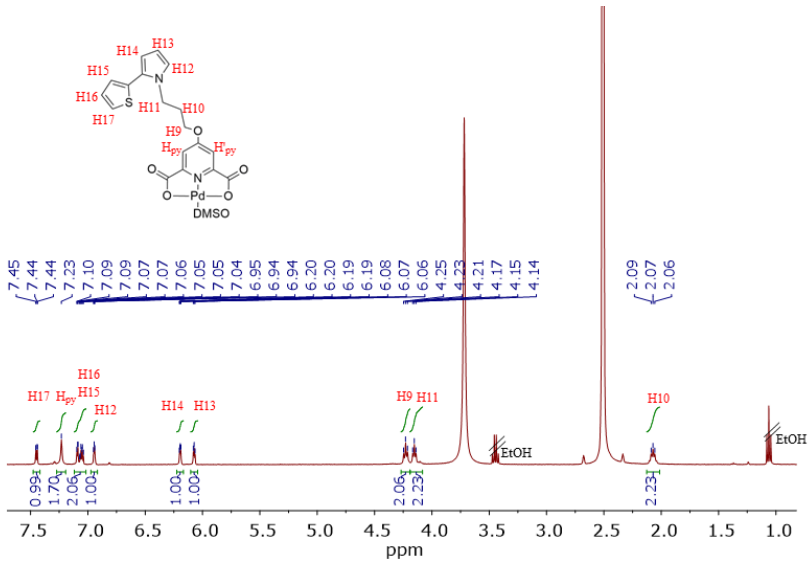

Appendix-Figure 5: ^{1}H-NMR (400Mhz DMSO-D_6) spectra for **[Pd(CheldTP)(DMSO)]** complex.

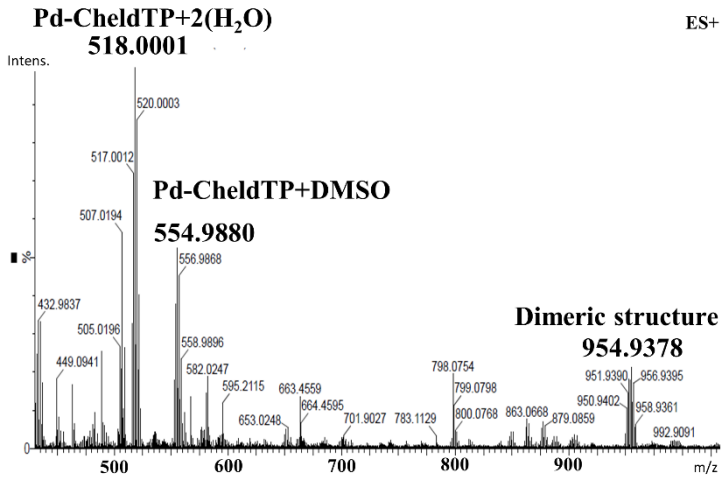

Appendix-Figure 6: ESI-MS(+) spectra for **[Pd(CheldTP)(DMSO)]** complex.

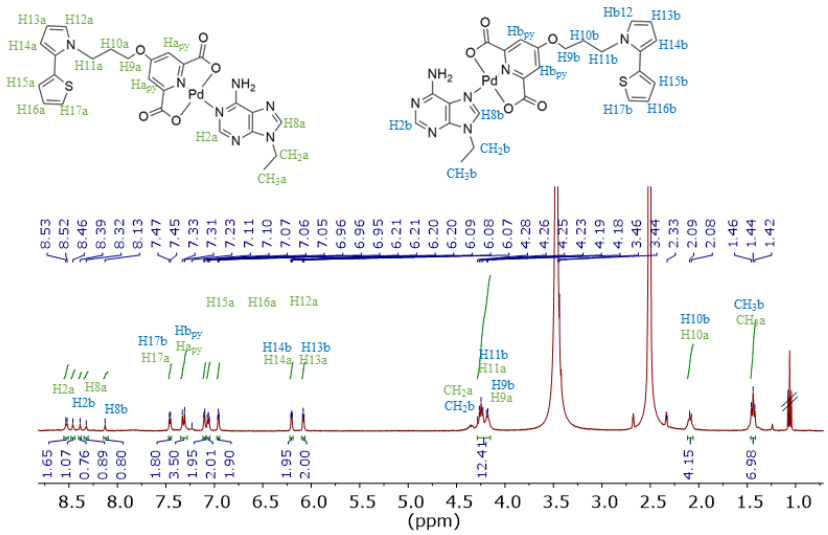

Appendix-Figure 7: ^{1}H-NMR (400Mhz DMSO-D_6) spectra for **[Pd(CheldTP)(eA)]**.

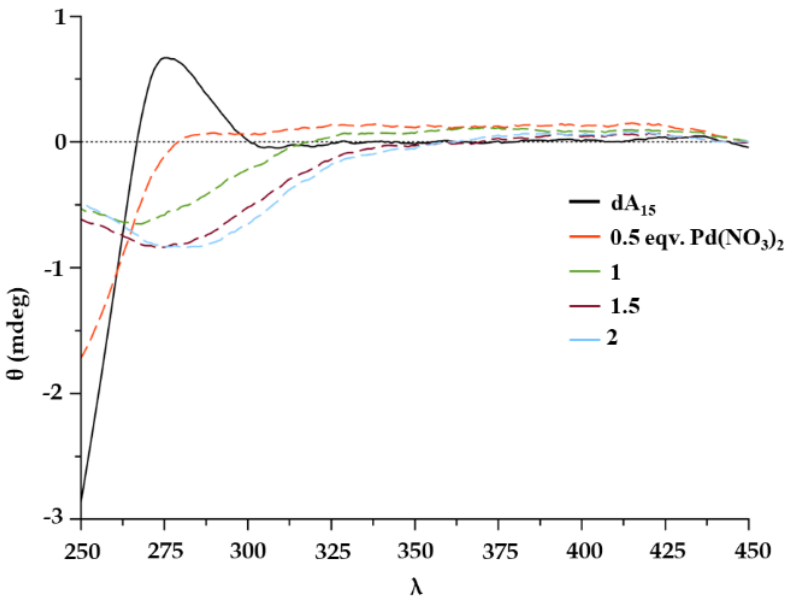

Appendix-Figure 8: CD titration spectra for **dA_{15}** upon controlled addition of $Pd(NO_3)_2$. Conditions: 2 µM DNA, 0→30 µM $Pd(NO_3)_2$. (DMSO), 100 mM $NaClO_4$, 5 mM MOPS (pH 6.8)

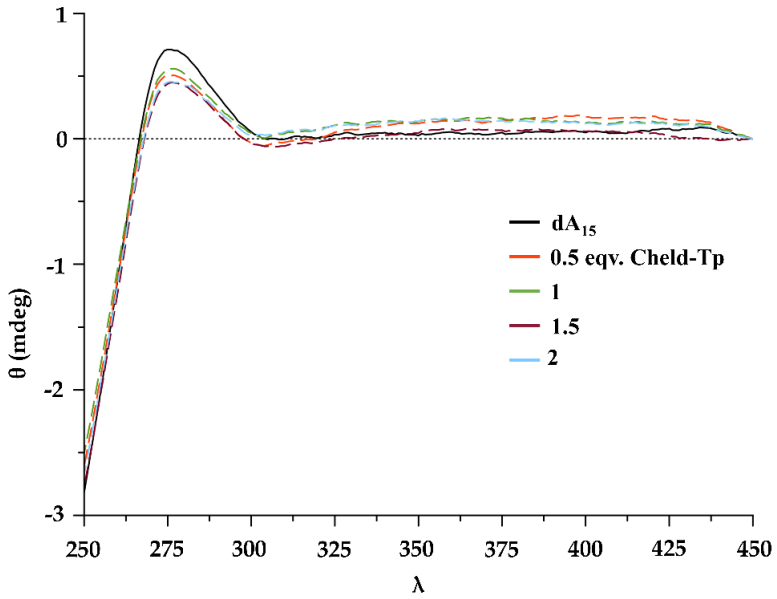

Appendix-Figure 9: CD titration spectra for **dA_{15}** upon controlled addition of **CheldTP**. Conditions: 2 μM DNA, 0→30 μM $Pd(NO_3)_2$. (DMSO), 100 mM $NaClO_4$, 5 mM MOPS (pH 6.8).

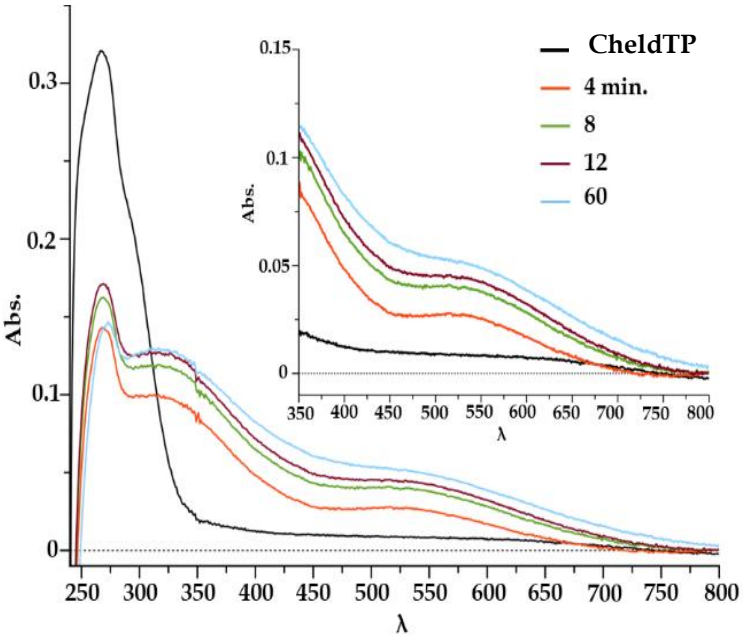

Appendix-Figure 10: UV-Vis spectra for **CheldTP** complex. Spectra shows signal for polymerization process for 60 minutes. Conditions: 39 μM **CheldTP** (DMSO), 100 mM $NaClO_4$, 5 mM Citrate (pH 6.8→4.5).

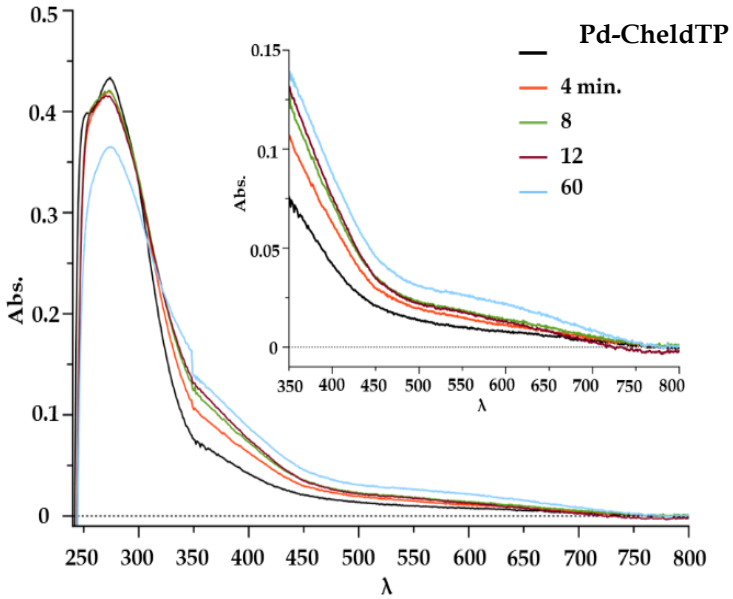

Appendix-Figure 11: UV-Vis spectra for **[Pd(CheldTP)(DMSO)]** complex. Spectra shows signal for polymerization process for 60 minutes. Conditions: 39 µM **Pd-CheldTP** (DMSO), 100 mM $NaClO_4$, 5 mM MOPS (pH 6.8→4.5).

Chapter 5

Crystallization of Biomolecules

Chapter 5. Crystallization of Metal-DNA Hybrids.

5.1. Crystallization of Biomolecules.

Crystallization is a key process for understanding the structural arrangement of biomolecules in solid-state. This process allows the obtaining of 3D data by X-ray diffraction measurements to determine the arrangements of atoms in the crystals, revealing fundamental details about molecular structures.

Crystals provide a unique opportunity to study the complex interactions between biomolecules such as protein-ligand, protein-protein or enzyme-metal, among many others.[1–3] However, developing the technique for obtaining the first crystals from a biomolecule and determining their structure through X-ray diffraction was a big challenge that brought together the brightest minds of the 20th century. To understand the significance of these advancements, between 1901 and 2013, forty-two Nobel Prizes in chemistry (30) and Physics (12) were awarded in this regard. One of the most influential researchers was **Max Perutz**,[4], who was among the first scientists to discover how to determine the structure of proteins by X-rays and apply this technique to reveal the structure of hemoglobin.[5] He was awarded the Nobel Prize in 1962 for this groundbreaking work, shared with his colleague **John Kendrew**. Moreover, he was the mentor of the well-known **James. D. Watson** y **Francis Crick**, two of those responsible for solving the crystal structure of DNA.

In Chapter 1, the importance of unravelling the crystal structure of DNA was mentioned, along with all the advances resulting from these discoveries. Furthermore, the importance of DNA metallization in developing new nanomaterials was discussed. However, it was emphasized that only two approaches could obtain crystals for metal-DNA systems by metal-mediated base pairs that respect the natural complementarity of the base pairs rules. [6,7]

This chapter will describe the protocols for attempting to obtain crystals for DNA-Pd hybrids and Ag-modified Watson-Crick base pairs, along with efforts to

conduct corresponding X-ray diffraction analysis. It is worth mentioning that the studies involving the use of Ag^{I} ions inside ds-DNA molecules are also part of the group research projects, focusing on obtaining ds-DNA-Ag systems where a coordination bond has replaced all base pairs.[8,9] Regrettably, it must be acknowledged that the X-ray structures of the desired systems could not be fully resolved in this thesis. Nevertheless, documenting the intensive effort and resources invested in this endeavour deserves inclusion in this thesis, as it may provide valuable insights for future research in this direction.

This work is part of the international mobility program carried out in the Department of Chemistry of Biomacromolecules at the "Universidad Nacional Autónoma de México" under the supervision of Prof. Dr. **Abel Moreno Cárcamo**. The international mobility program has been funded by the Ibero-American University Postgraduated Association (AUIP) and the "Universidad Nacional Autónoma de México"

5.2. Crystallization of silver-modified Watson-Crick-Franklind base pairs complexes.

As mentioned in Chapter 1, when two free nucleobases bind through a coordination bond with metal ions, they usually tend to form non-canonical metal-mediated base pairs such as A-M^{n+}-A, T-M^{n+}-T, C-M^{n+}-C or G-M^{n+}-G.[10] The only reported examples of canonical metal-modified base pairs have been published within a ds-DNA.[6,7,11] So far, no crystalline structures for isolated metal-modified Watson-Crick-Franklin base pairs have been described. At this point, the reader may have noticed the subtle differences between the expressions "metal-mediated base pairs" and "metal-modified base pairs". Occasionally, both definitions are used synonymously, and as proposed by Prof. **Bernhard Lippert**, a more precise differentiation is desirable.[12] In this respect, metallo-base pairs between complementary nucleobases should be termed "metal-modified base pairs" and

metal cross-links between non-complementary nucleobases should name "metal-mediated base pairs". As far as this thesis is concerned, "metal-modified base pairs" refer to DNA-Ag-DNA structures, while "metal-mediated base pairs" referring to DNA-Pd structures.

The first objective in this section consisted of obtaining the canonical metal-modified base pairs [Ag(eA)(eT)] complex (**eA-Ag^{I}-eT**). It is important to clarify that to promote the formation of a linear coordination bond between both, **eA** and **eT** nucleobases via ***N1*eA-A^{I}-*N1*eT**, it is necessary the loss of the proton HN3-thymine (pKa 2´-deoxytimidine = 10.03 ± 0.3)[13]. In the first experiment, the formation of a hydrogen bonded **eA-eT** pair is promoted, followed by diffusion of Ag^{I} ions (with no pH modification) to study if silver ions are able to replace hydrogen bonds. Alternatively, an analogous experiment was carried out employing a solution of **eT** with one equivalent of KOH to obtain the deprotonated nucleobase $(eT)^{-}$ $(K)^{+}$. The potassium thymine salt was then mixed with **eA**, followed by diffusion of Ag^{I} ions.

The experiments were conducted as follows. Initially, a 2 M mixture solution of **eA-eT** (DMSO) and 2 M solution of $AgNO_3$ (H_2O) were prepared. Subsequently, a crystallization gel was prepared by mixing polyethylene oxide (**PEO**) and 1,2-dichloroethane. [14,15] Then, a solution (250 µL) of DMSO containing a mixture of **eA** and **eT** was added into the **PEO** (**PEO** gel preparation is described in Section 4.6.2.a).

Two different strategies were employed to promote the crystallization process (Figure 5.1):

a) Crystallization in Pasteur pipettes.

b) Crystallization in a TG40 device. TG40 is a portable temperature-controlled microplate system designed to optimize crystallization temperature for biomolecule experiments.

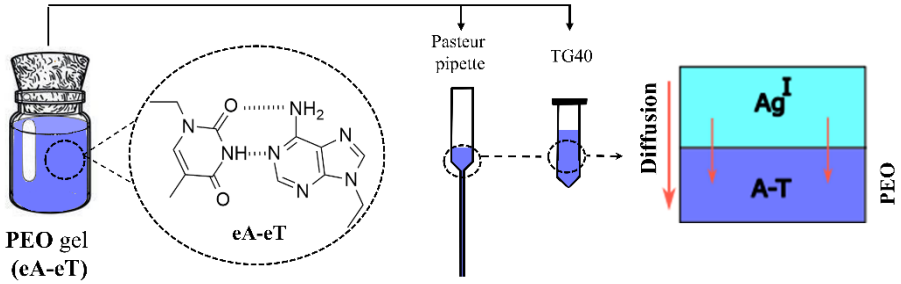

Figure 5.1: Scheme of the crystallization process to obtain **eA-Ag^{I}-eT**. a) A Pasteur pipette is used as a gel carrier. b) Using a glass tube for TG40 device as a gel carrier. In both cases, the solution of Ag^{I} was added to the gel to promote the diffusion of metal ions.

For both strategies, the **PEO**-nucleobase (1,2-dichloroethane:DMSO 1:1) solution was introduced in the appropriate containers and the mixture was allowed to gel for 30 minutes. Subsequently, a solution of $AgNO_3$ was added to the gels at 0.25, 0.5, 0.75 and 1 equivalent, with respect to **eA** and **eT**. As mentioned above, this methodology aims twofold: first, to achieve the **eA-eT** base pair structure within the **PEO** gel, and to facilitate the diffusion of Ag^{I} ions throughout the gel to promote the formation of the **eA-Ag^{I}-eT** complexes.

The Pasteur pipettes containing the samples were placed in a temperature controller cabinet at 25°C and 10°C in darkness for 5 days. The TG40 device was positioned as follows (Figure 5.2):

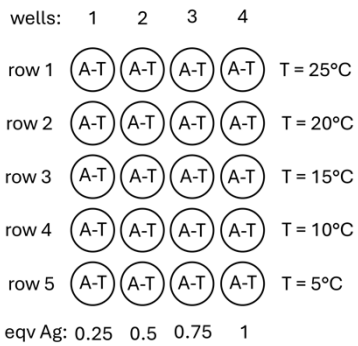

Figure 5.2: TG40 device scheme. The concentration in all wells is 1.5 M **eA-eT**. Increasing amounts of Ag^{I}, 0.25 to 1 equivalent, were added and the temperature range between 5 to 25ºC was fixed.

Both methodologies were designed to study different crystallization parameters to optimize the process. **PEO** gel crystallization by Pasteur pipettes provided favourable conditions for promoting diffusion-driven processes. The length of the Pasteur pipettes (230 nm) and their width (1 mm) facilitate a slow diffusion process of Ag^{I} ions. **PEO** gel crystallization by TG40 offers a good screening process to determine the optimal temperature conditions.

After 5-15 days, the appearance of crystalline structures was observed. Figure 5.3a shows crystals obtained inside the Pasteur pipettes for samples that contain 1.5 M **eA-eT** and 1 equivalent of Ag^{I} at 10ºC. On the other hand, Figure 5.3b shows crystals obtained in TG40 devices for samples that contain 1.5 M e**A-eT** and 1 equivalents of Ag^{I} at 10ºC. As shown, there are differences in the morphology of the crystals for both crystallization methods, probably due to the difference in the Ag^{I} diffusion.

a)

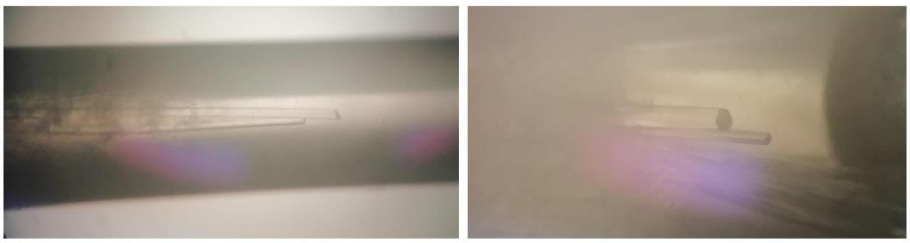

b)

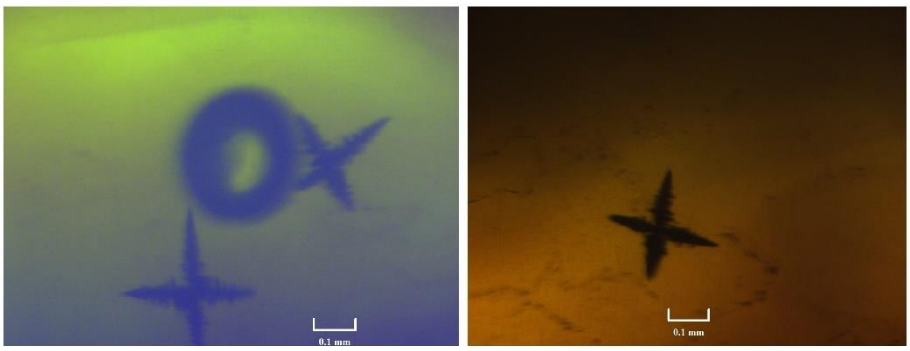

Figure 5.3: Images after crystallization process in **PEO** gel of samples containing 1.5 M **eA-eT** and 1 equivalents Ag^{I}; a) In a Pasteur pipette. b) In a TG40 devices.

Unfortunately, after collecting and analyzing the crystals by X-ray diffraction, the data revealed that the crystalline structures belonged to analogous **T-Ag^{I}-T** base pairs previously described in the literature. [16]

Alternatively, experiments were carried out employing a solution of **eT** with KOH to obtain the deprotonated nucleobase $(eT)^{-}$ $(K)^{+}$, aiming to promote the formation of the heterotopic **eA-Ag^{I}-eT** complex. These crystallization experiments were conducted under the same conditions described above. However, no crystalline structures or amorphous precipitates were observed in either the Pasteur pipette or TG40 crystallizers. Usually, the absence of precipitates in crystallization experiments can be considered a good indicator. It suggests that the concentration of the target compounds is optimal, indicating that they have not reached saturation in the crystallization solution. Consequently, these conditions serve as an excellent initial step for subsequent tests. Adjustments to pH, temperature, or the addition of different precipitating agents can be made to facilitate crystallization.

A potential approach to obtaining **eA-Ag^{I}-eT** structures could involve conducting more in-depth temperature studies using Pasteur pipette crystallizers. Alternatively, specific crystallization kits for nucleobases, such as the *Nucleic Acis MiniScreem*® designed by *Hampton-Research*® could be utilized. However, these experiments would most likely require the use of different crystallization protocols.

5.3. Crystallization of DNA-Ag and DNA-Pd supramolecular structures.

In this section, the experimental procedures for obtaining crystals of metal-DNA hybrids will be outlined. Firstly, crystallization processes to obtain crystals of modified DNA-Ag structures will be studied. As detailed in Section 4.1, our research group has proposed a methodology for obtaining metal-modified base pairs with WCF-like features, wherein hydrogen bonds are replaced by coordination bonds (Chapter 1, Section 1.3, Figure 1.11 and 1.12). [8,9] In this approach, the endocyclic *N7* position in adenine and guanine nucleobases has been replaced by a *CH* group. These modifications promote the coordination of Ag^I ions to the *N1*-position of the purine nucleobases and the *N3*-position of pyrimidine nucleobases, thereby facilitating the formation of WCF-like base pairs **^{7c}A(*N1*)-Ag^I-(*N3*)T** and **^{7c}G(*N1*)-Ag^I-(*N3*)C** (7c = 7-deaza-nucleobase). These metallized base pairs retain the canonical arrangement, and therefore, the metal-DNA duplex retains the double-helical structure similar to the unmetallated one.

Secondly, crystallization processes for supramolecular DNA-Pd structures described in this thesis will be discussed.

5.3.a. Crystallization and characterization of the supramolecular hybrid $[\{Ag\}_{12}(dY_4C_4T_2X_2)]$ (**ODN1-Ag**).

In previous chapters, the issue arising from the coordination sites of Ag^I ions to multiple sites on DNA nucleobases was introduced, along with our research group's method to address it using 7-deazapurine bases.

In this regard, our effort to crystallize deaza-DNA molecules containing Ag^I within the duplex involved utilizing the non-canonical sequence 5'-d(YYX CTC YXY TCC)-3' (**ODN1**) (X= 7-deaza-adenine; Y= 7-deaza-guanine). The formation and solution structure of this DNA-Ag system has been investigated

using ^{1}H-NMR, SAXS, CD and ESI-MS. As of the writing of this thesis, these results are currently under revision in Nature Communication.[17]

To obtain crystals of the DNA-Ag duplex suitable for X-ray diffraction, two different protocols have been followed:

- Capillary Crystallization methods
- Sitting drop Crystallization methods.

5.3.a.1. Capillary crystallization methods.

For these experiences, HR6-160 capillaries from Hampton-Research® were used (length: 80 mm, internal diameter: 0.5 nm, glass thickness: 0.01 mm). This crystallizer offers the advantage that once the crystals are obtained, they can be directly measured by X-ray diffraction without needing to be removed from the capillary. Table 5.1 provides information on the initial solutions of DNA, Ag^{I}, buffers and salts used for crystallization, as well as the final concentration for each assay.

Table 5.1: Concentration values for the crystallization of **ODN1-Ag** hybrid. Initial and final concentrations, once introduced in capillary, are presented.

	Stock solutions	Sample ODN1-Ag	Sample ODN1
DNA solutions			
ODN1	8 mM	2 mM	-
ODN1	8 mM	-	2 mM
Ag^{I} solutions			

$AgNO_3$	24 mM	24 mM	-
Buffer and salts solutions			
MOPS pH7	200 mM	50 mM	50 mM
Spermine	40 mM	10 mM	10 mM
KNO_3	1200 mM	300 Mm	300 Mm
MPD	40 %	10 %	10 %

First, a 0.2% agarose gel was prepared, and adequate amounts of DNA (**ODN1**), MOPS (pH 7), spermine, KNO_3, MPD and $AgNO_3$ (where applicable) were added and carefully mixed. The sample was introduced into the capillary using capillary action, which involves placing an open-ended capillary into the solution and allowing the solution to ascend. Then, the capillary tip was sealed, and the mixture was allowed to gel for 10 minutes (Figure 5.4a). Subsequently, a solution of $AgNO_3$ was added to the top of the capillary (only for **ODN1-Ag** assays) (Figure 5.4b). The system was then stored at 5ºC in darkness until crystals appeared.

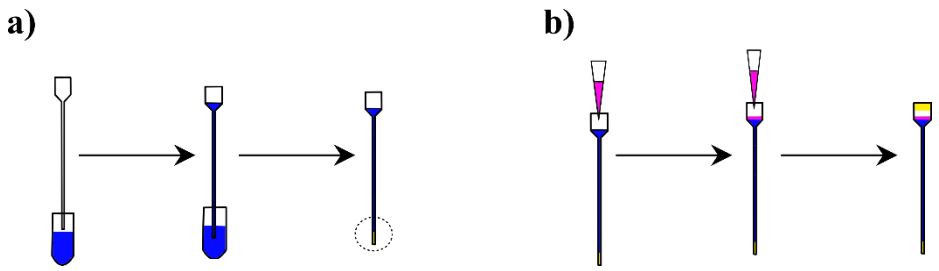

Figure 5.4: Scheme for capillary crystallization system: a) Assembly of agarose-DNA mixture in the capillary by suction from an Eppendorf. b) The Ag^I solution is added for diffusion along the gel. Colour code; Blue: agarose-DNA solution. Pink: Ag^I solution. Yellow: sealant.

Figure 5.5 illustrates the crystals obtained for **ODN1-Ag** experiments. In the center of the figure, a previouly published crystal obtained for a DNA-Ag molecule with an uninterrupted array of Ag^{I} ions running through the center of the helix is also shown for comparison reference.[6] The crystals obtained for **ODN1-Ag** exhibit a similar appearance of hexagonal crystalline structure (Figure 5.5.a, b and c). Additionally, other crystals with star-shaped structures were observed (Figure 5.5d), commonly identified as salts and, therefore, discarded from further resolution experiments.

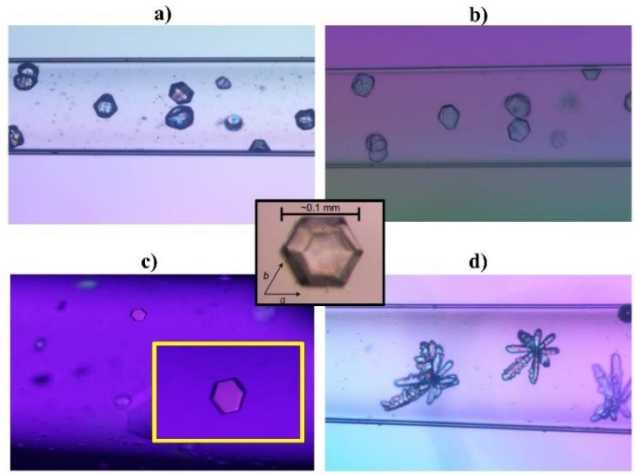

Figure 5.5: Images of the crystals obtained after capillary crystallizations through Ag^{I} ions diffusion. Conditions: 2 mM **ODN1**, 24 mM Ag^{I}, 50 mM MOPS (pH 7), 10 mM Spermine, 300 mM KNO_3 and 10%v/v MPD. Central image: DNA-Ag reference crystal reported by **Jiro Kondo**.[6]

The crystals were sent to the *European Synchrotron Radiation Facility* (**ESRF**) for X-ray diffraction measurements. Figure 5.6 shows the diffraction pattern for crystals obtained in a capillary (Figure 5.5c). Unfortunately, the chosen crystals did not diffract properly. However, the diffraction pattern suggested the presence of biological molecules, ruling out the possibility of it being a salt pattern. This result is very encouraging, as DNA molecules have been successfully crystallized despite confronting poor diffraction from the obtained crystals. Currently, modifications have been made to the conditions to obtain crystals that exhibit better diffraction properties.

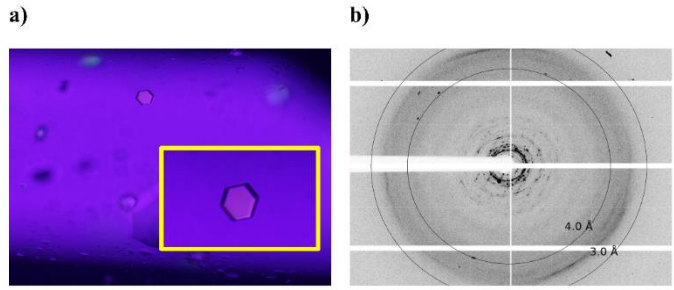

Figure 5.6: a) Crystals for **ODN1-Ag**. b) Diffraction pattern for **ODN1-Ag**. Conditions: 2 mM **ODN1,** 24 mM Ag^{I}, 50 mM MOPS (pH7), 10 mM Spermine, 300 mM KNO_3 and 10%v/v MPD.

5.3.a.2. Sitting drop crystallization.

For these processes, 6x4 well-sitting drop plates from *Hampton-Research*® were used. The crystallization samples were prepared using a *Natrix-HR-116*®, *Natrix-HR-117*® and *Nucleic Acid MiniScreen*® (NAM) from *Hampton-Research*®. Natrix solutions are a complete reagent kit designed to provide a rapid screening method for the crystallization of nucleic acids. This screen is simple and practical for finding initial crystallizations conditions, as well as determining the solubility of nucleic acids in a wide range of precipitants and pH. The methodology for sample deposition in a sitting drop crystallizer is shown in Figure 5.7.

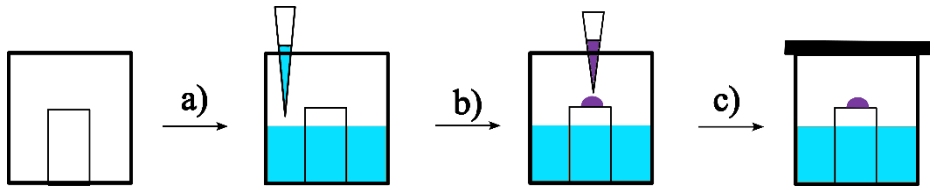

Figure 5.7: Scheme for sitting drop crystallization system. a) Addition of precipitant agent (blue). b) Addition of the sample. c) Hermetic sealing.

For this purpose, a stock solution containing 4 mM **ODN1** and a 48 mM $AgNO_3$ in H_2O was prepared. Then, a precipitation agent solution (400 µL) from *Natrix-HR-116*, *Natrix-HR-117* or *Nucleic Acid MiniScreen* was added to the

reservoir. Subsequently, 10 µL of reservoir solution, 5 µL **ODN1** and 5 µL $AgNO_3$ were placed and mixed on top of the central well support to obtain **ODN1-Ag** crystals. The protocol was repeated for blank samples containing **ODN1** and no silver salts. Finally, the system was sealed with specifically provided adhesive tape, and the crystallization plates were stored at 5ºC. The final concentrations for sample drops of **ODN1-Ag** and **ODN1** are presented in Table 5.2

Table 5.2: Table of concentration values for the crystallization of **ODN1-Ag** and **ODN1**. Initial and final concentrations, once supported in crystallization plates, are presented.

	Stock solutions	Final **ODN1-Ag** Samples concentration	Final **ODN1** Samples concentration
ODN1	1.8 mM	1 mM	1 mM
$AgNO_3$	24 mM	12 mM (1 equivalent)	-

Figure 5.8 shows the crystals obtained for these experiments. Images a and b depict examples of crystal morphology obtained after the **ODN1-Ag** crystallization process. As illustrated, amorphous precipitates were formed, and only hard crystals associated with salts were obtained. However, in the absence of Ag^I ions, crystals with hexagonal shapes were found (Figure 5.8.c and d). As discussed earlier, these hexagonal structures are commonly observed in DNA crystals. These crystals were obtained under the following conditions:

- 2 mM **ODN1**, 0.02 M $MgCl_2 \cdot (H_2O)_6$, 0.05 MES pH6.0, 15%v/v 2-propanol.
- 2 mM **ODN1**, 0.04 $MgAc_2$ $(H_2O)_4$, 0.05M sodium cacolidate pH 6.0, 30%v/v(+/-) MPD.

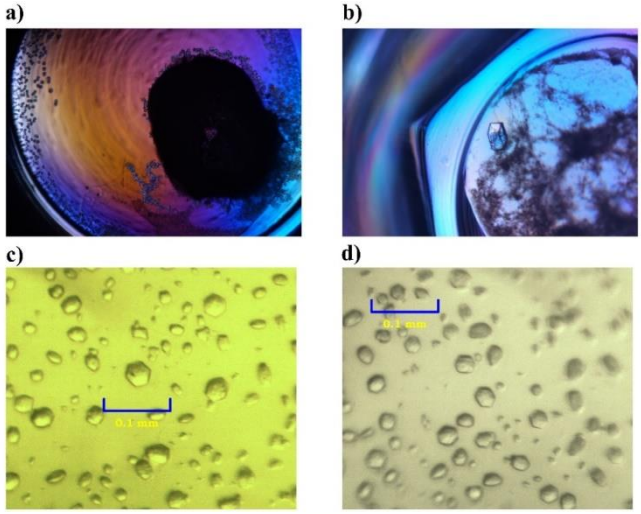

Figure 5.8: Image after crystallization process by sitting drop kit of: a,b) 1 mM **ODN1**, 12 mM Ag^{I}. c) 1mM **ODN1**, 0.02 M $MgCl_2 \cdot (H_2O)_6$, 0.05 MES pH6.0, 15%v/v 2-propanol. d) 1mM **ODN1**, 0.04 $MgAc_2 \cdot (H_2O)_4$, 0.05M sodium cacolidate pH 6.0, 30%v/v(+/-) MPD. Temperature conditions, 5ºC.

These findings suggest that the presence of Ag^{I} ions significantly affects the crystallization process, promoting the precipitation of the systems under the given conditions. Consequently, a new set of experiments were conducted to attempt the crystallization of **ODN1-Ag**. In this revised approach, solutions containing 0.2, 0.4, 0.6 and 0.8 equivalents of Ag^{I} were added to a 1 mM solution of **ODN1**. Importantly, no precipitate was observed following the preparation of sitting drops and the subsequent addition of the Ag^{I} solution to the final drop sample.

In these new experiments, the characteristic DNA crystal structures were not observed. However, there were no appearances of amorphous precipitates either, indicating a positive or encouraging result. These findings suggest that samples and ions/salts concentration were appropriate, allowing them to remain in solution. A possible solution to obtain crystals of **ODN1** under these conditions could involve conducting a study to determine the optimal crystallization temperature. These studies are planned for future work.

Crystallization plates containing samples c and d were taken to the *National Synchrotron Light Source II, beanline 17-ID-2*, at *Brookhaven National Laboratory*, which belongs to the United States Department of Energy, in New York. The samples were included in the research project led by Prof. Dr. **Abel Moreno Cárcamo**. Once again, after conducting single-crystal scattering measurements, it was concluded that while samples did not appear to be salts, none of them exhibited enough diffraction to provide adequate data for the structural resolution.

5.3.b. Crystallization and characterization of the supramolecular hybrid [{Pd(Cheld)}$_{15}$(dA$_{15}$)] (**dA$_{15}$-Pd-Cheld**).

This thesis has presented a methodology to obtain supramolecular **dA$_{15}$-Pd-Cheld** hybrids, which has been described and discussed (Chapter 2).[18] There is currently no existing literature on crystallization methodology for these types of compounds. Consequently, the crystallization of these systems was also investigated.

To obtain suitable structures of **dA$_{15}$-Pd-Cheld** for structural resolution, a sitting drop crystallization methodology was followed. Figure 5.9 shows the crystallization plates employed in these processes, acquired from *Hampton-Research*®. These crystallization plates have 96 compartments, each divided into four wells: three for sample deposition and one for reservoir. In all experiments, samples containing **dA$_{15}$**, **Pd-Cheld** and Natrix solutions (from *Hampton-Research*®) were deposited in reservoir 1. In addition, blank solutions containing **dA$_{15}$** and Natrix solutions were placed in reservoirs 2 and 3.

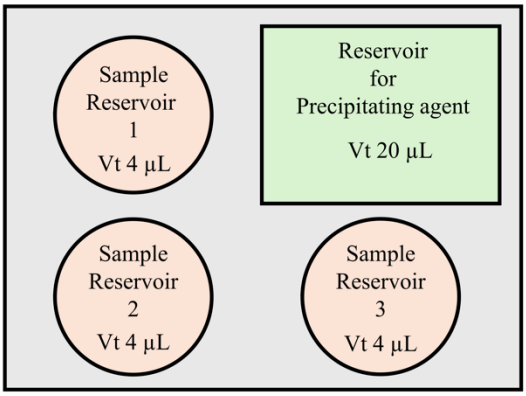

Figure 5.9: Scheme for the individual crystallization plate from *Hampton-Research*®. Samples of **dA$_{15}$**, **Pd-Cheld** and Natrix solutions were placed in reservoir 1. Samples with **dA$_{15}$** and Natrix solutions were added to reservoirs 2 and 3.

Table 5.2: Table of concentration values for the crystallization of **dA$_{15}$-Pd-Cheld** hybrid. Initial and final concentrations in crystallization plates are presented.

	Stock solutions	**dA$_{15}$ -Pd-Cheld** Samples	**dA$_{15}$** Samples
dA$_{15}$	1.8 mM	0.72 mM	0.9 mM
Pd-Cheld	24 mM	5.2 mM	-

Table 5.2 contains information on the initial concentration of **dA$_{15}$** and **Pd-Cheld** solutions, as well as the final concentration for each experiment. Figure 5.1 displays images of the crystals obtained for **dA$_{15}$-Pd-Cheld** crystallization processes. These structures seem to appear as hexagon crystals, although not as clear as those observed for **ODN1-Ag** systems. These samples were obtained under the following conditions:

- 0.72 mM **dA$_{15}$** , 4.8 mM **Pd-Cheld**, 0.1 M $(NH_4)_2SO_4$, 0.01M $MgCl_2{\cdot}(H_2O)_6$, 0.5 MES pH5.6, 20%v/v PEG 8000.
- 0.72 mM **dA$_{15}$** , 4.8 mM **Pd-Cheld**, 0.1 M KCl, 0.005M $MgSO_4{\cdot}H_2O$, 0.05 M HEPES pH7, 5%v/v(+/-) MPD.

- 0.72 mM **dA$_{15}$** , 4.8 mM **Pd-Cheld**, 0.2 M KCl, 0.01 M $MgCl_2 \cdot (H_2O)_6$, 0.05 M HEPES pH 7, 1.7 M 1,6-hexanediol.

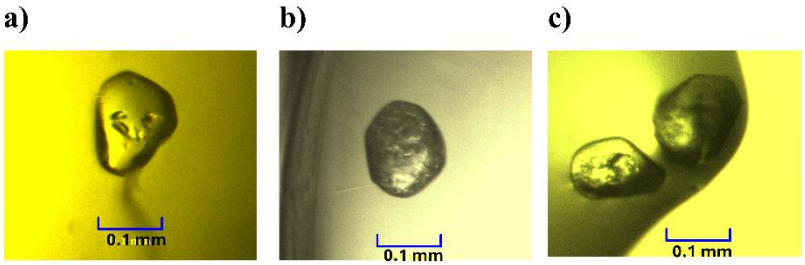

Figure 5.10: Images obtained for **dA$_{15}$ -Pd-Cheld** crystallization processes. Conditions: 0.72 mM **dA$_{15}$** , 4.8 mM **Pd-Cheld** and the corresponding Natrix solution

The above samples a, b and c were measured in the *National Synchrotron Light Source II, beamline 17-ID-2*, in New York. Figure 5.11 show the diffraction pattern obtained for the sample b.

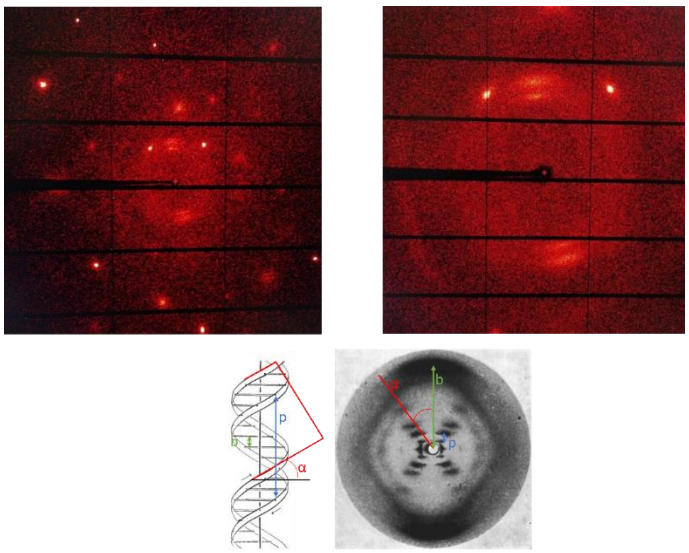

Figure 5.11: The diffraction pattern obtained for **dA$_{15}$ -Pd-Cheld** crystals measurement by X-ray. On the left, the complete pattern for **dA$_{15}$ -Pd-Cheld (**0.72 mM **dA$_{15}$** , 4.8 mM **Pd-Cheld)** is presented. On the right, zoom of the central area. At the bottom, the diffraction pattern of a ds-DNA obtained by Rosalind Franklin.[19]

Unfortunately, the resolution of the crystals was inadequate to acquire data for resolving the corresponding molecular structure. Based on the limited data obtained, the diffraction pattern indicates the presence of biological molecules and also suggests the presence of a coordination compound (related to the presence of **Pd-Cheld** complex). The diffraction pattern bears some similarities with the diffraction pattern of a DNA molecule, such as that published by J**. Watson** and **F. Crick**. , but with apparent differences, as in our case, it is a single strand. This statement is pure speculation derived from personal reflection.

A possible solution to obtain suitable DNA crystals is to employ strands containing the so-called "sticky ends". These ss-DNA molecules have end bases that can hybridized with other complementary strands, forming sturdy 2D or 3D structures that help with crystallization. Indeed, the formation of structures comprising sticky ends, even unintentionally, has been responsible for obtaining the crystal structures for already published DNA-Ag structures where all base pairs are metallized (Figure 1.10).[6,11]

5.4. Conclusions.

Chapter 5 presents the results obtained for the crystallization of metal-DNA structures. Specifically, the experimental procedures to get the metal-modified Watson-Crick-Franklin base pairs **eA-Ag^{I}-eT**, the duplex **ODN1-Ag** and the supramolecular **dA$_{15}$-Pd-Cheld** hybrids. For this purpose, several strategies for nucleic acid crystallization have been followed, and specific crystallization kits have been used.

Although suitable crystals for target structures were not isolated, some data indicate that the experimental procedures are adequate. DNA crystals are relatively easily obtained but usually do not provide sufficient diffraction for X-ray studies. As presented in Chapter 1, there are very few examples where similar structures have been isolated and resolved.[6] Therefore, the difficulty in obtaining suitable crystals allows us to consider the possibility of using different strategies to achieve this goal. One possible strategy is to use ss-DNA sequences with "sticky ends", a method proven to facilitate the formation of DNA-Ag crystal structures. [6,20,21]

Currently, our research group is dedicating significant efforts to learning and developing methodologies aimed at achieving this goal. The acquisition of specialized materials and participation in training sessions, including the international mobility program held in the Department of Chemistry of Biomacromolecules at the "Universidad Nacional Autónoma de México", aim to enhance understanding and expertise in this field.

5.5. Material and Methodology.

5.6.1. Crystallization plates and Kits.

All the crystallization materials, HR6-160 capillaries, 6x4 well-sitting drop plates and 96x3 well-sitting drop plates were acquired in *Hampton-Research*®. Natrix reagent kits, Natrix-HR-116, Natrix-HR-117 and Nucleic Acid MiniScreen (NAM) were acquired in *Hampton-Research*®.

4.6.2. Crystallization protocols.

4.6.2.a Preparation of PEO gel for crystallization in Pasteur pipette and TG40.

A solution of 250 µL 1,2-dichloroethane and 125 mg of polyethylene oxide (**PEO**) was prepared. Then, a 250 µL DMSO containing **eA** and **eT** was added and mixed, and the mixture was allowed to gel for 30 minutes. Subsequently, a solution of $AgNO_3$ (2 M) was added on top of the gel at 0.25, 0.5, 0.75 and 1 equivalent with respect to **eA** and **eT.** Samples were stored at 25 and 5 ºC.

4.6.2.b. Preparation of agarose gel for capillaries crystallization of **ODN1** and **ODN1-Ag**.

A solution of 200 mg agarose in 1000 µL of H2O was prepared to obtain 0.2% agarose gel. Then, 64 µL agarose (0.2%), 25 µL **ODN1** (4 mM), 1 µL MPOS (pH7) (200 mM), 5 µL Spermine (40 mM), 0.2 µL KNO_3 (1200 mM) and 5 µL MPD (40%v/v) were carefully added and mixed. The mixture was introduced into capillaries and allowed to gel for 30 minutes at 5ºC. Over the gel, 10 µL of $AgNO_3$ (24 mM) was added. The capillaries were stored at 5ºC, the time required until crystal formation.

For samples without Ag^I, 64 µL agarose (0.2%), 25 µL **ODN1** (4 mM), 1 µL MPOS (pH7) (200 mM), 5 µL Spermine (40 mM), 0.2 µL KNO_3 (1200 mM) and 5 µL MPD (40%v/v) were carefully added and mixed. The mixture was

introduced into capillaries and allowed to gel for 30 minutes at 5ºC. The capillaries were then stored at 5ºC the time required until crystal formation.

4.6.2.c. Sitting drop crystallization of **ODN1** and **ODN1-Ag**.

A initial stock solutions of 4 mM **ODN1** and 24 mM $AgNO_3$ were prepared. Next, 400 µL of precipitation agent solutions from Natrix-HR-116, Natrix-HR-117 and Nucleic Acid MiniScreen were added to the reservoir. Subsequently, 10 µL of reservoir solution, 5 µL **ODN1** and 5 µL Ag^I were mixed and placed on the central well support to obtain **ODN1-Ag** crystals. The samples were stored at 5ºC, the time required until crystal formation.

For samples without Ag^I, 10 µL of reservoir solution, 5 µL **ODN1** and 5 µL H_2O were mixed and placed on the central well support to obtain **ODN1** crystals. The crystallization plates were stored at 5ºC, the time required until crystal formation.

4.6.2.d. Sitting drop crystallization of **dA_{15}** and **dA_{15}-Pd-Cheld**.

A initial solution of 1.8 mM **dA_{15}** and 82 mM **Pd-Cheld** (DMSO) were prepared. Then, 20 µL of precipitation agent solutions from Natrix-HR-116, Natrix-HR-117 and Nucleic Acid MiniScreen were added in to the reservoir. Subsequently, 1 µL of reservoir, 1 µL **dA_{15}** and 0.5 µL of **Pd-Cheld** were mixed and placed in reservoir sample 1. For samples with no Pd^{II}, 1 µL of reservoir and 1 µL **dA_{15}** were mixed and placed in reservoir samples 2 and 3. The crystallization plates were stored at 5ºC, the time required until crystal formation.

5.6. Bibliography.

1 R. Giegé, *FEBS Journal*, 2013, **280**, 6456–6497.

2 M. Jaskolski, Z. Dauter and A. Wlodawer, *FEBS J*, 2014, **281**, 3985–4009.

3 A. McPherson, in *Methods in Molecular Biology*, 2017, vol. 1607, pp. 17–50.

4 H. E. Huxley, *Nature*, 2002, **415**, 851–852.

5 M. F. Perutz, M. G. Rossmann, A. F. Cullis, H. Muirhead, G. Will and A. C. T. North, *Nature*, 1960, **185**, 416–422.

6 J. Kondo, Y. Tada, T. Dairaku, Y. Hattori, H. Saneyoshi, A. Ono and Y. Tanaka, *Nat Chem*, 2017, **9**, 956–960.

7 E. Ennifar, P. Walter and P. Dumas, *Nucleic Acids Res*, 2003, **31**, 2671–2682.

8 J. M. Méndez-Arriaga, C. R. Maldonado, J. A. Dobado and M. A. Galindo, *Chem. Eur. J.*, 2018, **24**, 4469–4469.

9 N. Santamaría-Díaz, J. M. Méndez-Arriaga, J. M. Salas and M. A. Galindo, *Angew. Chem. Int. Edi.*, 2016, **55**, 6170–6174.

10 J. Müller, *Coord Chem Rev*, 2019, **393**, 37–47.

11 T. Atsugi, A. Ono, M. Tasaka, N. Eguchi, S. Fujiwara and J. Kondo, *Angew. Chem. Int. Ed.*, 2022, **61**, 1–7.

12 B. Lippert, *JBIC*, 2022, **27**, 215–219.

13 J. C. González-Olvera, J. Martínez-Reyes, E. González-Jasso and R. C. Pless, *Biophys Chem*, 2015, **206**, 58–65.

14 Z. Pietras, H.-T. Lin, S. Surade, B. Luisi, O. Slattery, K. M. Pos and A. Moreno, *J Appl Crystallogr*, 2010, **43**, 58–63.

15 D. Choquesillo-Lazarte and J. M. García-Ruiz, *J Appl Crystallogr*, 2011, **44**, 172–176.

16 F. Guay and A. L. Beauchamp, *J Am Chem Soc*, 1979, **101**, 6260–6263.

17 U. Javornik, A. Pérez-Romero, R. Smith, C. López-Chamorro, J. Dobado, O. Palacios, M. Bera, M. Nyam, J. Plavec and M. A. Galindo, *Nat. Comm. NCOMMS-23-62967-T*.

18 A. Pérez-Romero, A. Domínguez-Martín, S. Galli, N. Santamaría-Díaz, O. Palacios, J. A. Dobado, M. Nyman and M. A. Galindo, *Angew. Chem. Int. Ed*, 2021, **133**, 10177–10182.

19 J. D. Watson and F. H. C. Crick, *Nature*, 1953, **171**, 737–738.

20 S. Vecchioni, B. Lu, W. Livernois, Y. P. Ohayon, J. B. Yoder, C. Yang, K. Woloszyn, W. Bernfeld, M. P. Anantram, J. W. Canary, W. A. Hendrickson, L. J. Rothschild, C. Mao, S. J. Wind, N. C. Seeman and R. Sha, *Adv. Mater.*, 2023, **35**, 1–11.

21 Y. P. Ohayon, C. Hernandez, A. R. Chandrasekaran, X. Wang, H. O. Abdallah, M. A. Jong, M. G. Mohsen, R. Sha, J. J. Birktoft, P. S. Lukeman, P. M. Chaikin, S. L. Ginell, C. Mao and N. C. Seeman, *ACS Nano*, 2019, **13**, 7957–7965.

Publicaciones

Publications

Publicaciones / Publications.

1. Comparative Structural Study of Metal-Mediated Base Pairs Formed Outside and Inside DNA Molecules.

Inorganic Chemistry. **2020**, 59, 9325-9338.
Alicia Domínguez-Martín, Simona Galli, José A. Dobado, Noelia Santamaría-Díaz, **Antonio Pérez-Romero**, M. A. Galindo.

2. Single-Stranded DNA as Supramolecular Template for One-Dimensional Palladium (II) Arrays.

Angewanted Chemical International Edition. **2021**, 60, 10089-10094.
Antonio Pérez-Romero, Alicia Domínguez-Martín, Simona Galli, Noelia Santamaría-Díaz, Oscar Palacios, José A. Dobado, May Nyman, M. A. Galindo.

3. Selective Formation of Pd-DNA Hybrids Using Tailored Palladium-Mediated Base Pairs: Towards Heteroleptic Pd-DNA Systems.

Angewanted Chemical International Edition. **2024**, 63, e202400261.
Antonio Pérez-Romero, Mario Cano-Muñoz, Carmen López-Chamorro, Francisco Conejero-Lara, Oscar Palacios, José A. Dobado, , M. A. Galindo

4. Supramolecular DNA-Pd Hybrids Integrated With Conducting Polymers.

This results will submitted for publication.
Antonio Pérez-Romero, Carmen López-Chamorro, Fátima Linares, José A. Dobado, M. A. Galindo

The following publication has not been included in this thesis:

5. Unveiling The B-Form Structure of a DNA With Contunuous Silver-Modified Watson-Crick Base Paris.

Under revision in Nature Communication.
Uros Javornik, **Antonio Pérez-Romero**, Rachelle M. Smith, Carmen López-Chamorro, José A. Dobado, Oscar Palacios, Mrinal K. Bera, May Nyman, Janez Plavec, M. A. Galindo.

Bioinorganic Chemistry Hot Paper

How to cite: *Angew. Chem. Int. Ed.* **2021**, *60*, 10089–10094
International Edition: doi.org/10.1002/anie.202015554
German Edition: doi.org/10.1002/ange.202015554

Single-Stranded DNA as Supramolecular Template for One-Dimensional Palladium(II) Arrays

*Antonio Pérez-Romero, Alicia Domínguez-Martín, Simona Galli, Noelia Santamaría-Díaz, Oscar Palacios, José A. Dobado, May Nyman, and Miguel A. Galindo**

Abstract: *Atomic-level control over the position and growth of a single and continuous metal chain is an ambitious goal that often requires complex and costly processes. Herein, we demonstrate that* ***1Pd-DNA*** *molecules, comprising a continuous single chain of Pd^{II} ions, can be prepared by a simple self-assembly reaction between the complex [Pd(Cheld)(CH_3CN)] (**1Pd_CH_3CN**) (Cheld = chelidamic acid) and single-stranded DNA homopolymers (ss-DNA) containing adenine (**A**) or 7-deazaadenine (**X**) bases. The single Pd^{II}-base pairs* ***[1Pd(N1-A)]*** *and* ***[1Pd(N1-X)]*** *were synthesized and characterized in solution and solid-state (X-ray diffraction) revealing an arrangement similar to that of natural Watson–Crick base pairs. Subsequently,* ***1Pd-DNA*** *hybrids were prepared, characterized, and their structures studied by small-angle X-ray scattering (SAXS) and ab-initio calculations. The results indicate that the* ***1Pd-DNA*** *structures resemble that of double-stranded DNA, with one strand being replaced by a supramolecular stack of continuous Pd^{II} complexes.*

Introduction

DNA is an important tool for applications in nanoscience and nanotechnology.[1–3] This is due to their easy processing (both chemically and enzymatically), water solubility, and importantly, the ability to predict and control DNA structures via base sequence programming. These characteristics have led to strategic synthesis of many DNA-based assemblies with nanoscale to microscale dimensions. Typically, two or more complementary DNA strands are programmed to obtain double-stranded DNA (ds-DNA) molecules with the desired shape.[4–6] Nonetheless, single-stranded DNA (ss-DNA) can also participate in the preparation of new nanoscale systems, especially when they are employed to template the assembly of different functional materials in a "bottom-up" approach.[7–14] Moreover, DNA can also be modified to carry specific functionalities.[15] In this context, special attention has been paid to DNA metallization.[16] Metals provide differentiating properties that are not intrinsic to DNA including conductivity, catalytic activity, magnetism, and photoactivity. The rational and programmed organization of metal ions in DNA molecules is not straightforward, due to the many possible positions to bind metals in the DNA structure (i.e. phosphate groups and nucleobases). A smart approach to guide the metal interaction towards specific locations is achieved using the so-called "metal-mediated base pairs", typically employed in ds-DNA molecules.[17–19] However, preparing DNA molecules that contain unlimited metal-mediated base pairs has turned out to be an enormous challenge, and only a few results have been reported towards this goal.[20–25] In this regard, ss-DNA molecules have rarely been used to assemble metalized 1D DNA systems,[26] due to the difficulty of controlling the interaction of metals at specific positions on the single strand. A simple approach to directly control the formation of a single contiguous metal ion matrix within DNA molecules would yield DNA-based systems applicable in nanotechnology.

Herein, we propose a bottom-up approach, based on a self-assembly reaction between ss-DNA molecules and a specific Pd^{II} complex, to prepare novel metal-DNA helical systems comprising contiguous Pd^{II}-mediated base pairs (Scheme 1). To the best of our knowledge, this is the first report in which Pd^{II} ions are guided to bind at all DNA Watson–Crick (W-C) positions with precise control, leading to a Pd-DNA rod-like polymer (Scheme 1).

For these studies, the complex [Pd(*Cheld*)(CH_3CN)] (**1Pd_CH_3CN**) was synthesized by the reaction of $Pd(NO_3)_2$ and chelidamic acid (*Cheld*). Subsequently, **1Pd_CH_3CN** was reacted with the nucleoside derivatives 9-propyl-7-deazaadenine (**X**) and 9-ethyladenine (**A**) for the preparation of the metal complexes **[1Pd(*N1*-X)]** and **[1Pd(*N1*-A)]**, respectively, to study the structural arrangement of these palladium-mediated base pairs. The base **X** is different from **A** in that

[*] A. Pérez-Romero, Dr. A. Domínguez-Martín, Dr. N. Santamaría-Díaz, Dr. M. A. Galindo
Departamento de Química Inorgánica.
Unidad de Excelencia de Química Aplicada a Biomedicina y Medioambiente, Universidad de Granada
Avda Fuentenueva s/n, 18071 Granada (Spain)
E-mail: magalindo@ugr.es

Dr. S. Galli
2 Dipartimento di Scienza e Alta Tecnologia, Università dell'Insubria
Via Valleggio 11, 22100 Como (Italy)

Dr. O. Palacios
Departament de Química, Facultat de Ciències,
Universitat Autònoma de Barcelona
Campus Bellaterra s/n, 08193 Cerdanyola del Vallès, Barcelona (Spain)

Prof. J. A. Dobado
Grupo de Modelización y Diseño Molecular,
Departamento de Química Orgánica, Universidad de Granada
Avda Fuentenueva s/n, 18071 Granada (Spain)

Prof. M. Nyman
Department of Chemistry, Oregon State University
Corvallis, OR 97331-4003 (USA)

Supporting information and the ORCID identification number(s) for the author(s) of this article can be found under: https://doi.org/10.1002/anie.202015554.

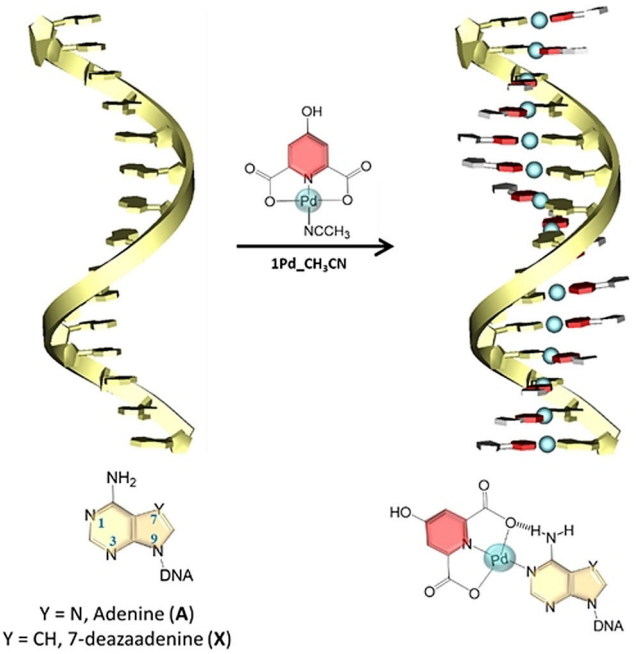

Scheme 1. Schematic representation of the formation of Pd-DNA hybrids from a self-assembly reaction between ss-DNA, comprising adenine (**A**) or 7-deazaadenine (**X**), and **1Pd_CH$_3$CN**.

a CH group replaces the N7 atom. This subtle modification promotes the exclusive interaction of the Pd^{II} complex towards the N1 atom, placed at the W-C face, and therefore **X** becomes a reference to evaluate the interaction of the metal fragment [Pd(*Cheld*)] (**1Pd**) towards **A**, where both the N1 and N7 position are available. Finally, the preparation of Pd-DNA was achieved by reaction between **1Pd_CH$_3$CN** and the ss-DNA homopolymers **dXn** or **dAn** (n = number of bases).

Results and Discussion

The reaction between **1Pd_CH$_3$CN** and the individual bases, **X** and **A**, was first studied in solution using ^{1}H-NMR ([D$_6$]DMSO) spectroscopy. The NMR spectra obtained during the addition of a controlled amount of **1Pd_CH$_3$CN** complex to a solution of **X** showed the disappearance of the signals of the free base and the appearance of a new set of resonances, corresponding to the formation of the new complex **[1Pd(*N1*-X)]** (Figure S1). On the other hand, when the same experiment was repeated using the base **A**, in addition to the disappearance of the signals of the free base, two new sets of signals appeared with increasing addition of **1Pd_CH$_3$CN** (Figure S2). These signals are consistent with the formation of two different Pd^{II} complexes that co-exist in equilibrium in solution in comparable amount. These are the *N1*- and *N7*-coordinated isomers **[1Pd(*N1*-A)]** and **[1Pd(*N7*-A)]**, respectively, as previously demonstrated for the interaction between [Pd(dien)]$^{2+}$ and adenine derivatives.[27,28] Importantly, an excess of **1Pd_CH$_3$CN** did not lead to new additional signals, indicating that the formation of bispalladium complexes via *N1*,*N7*-coordination can be ruled out. Spectrometric characterization using ESI-MS confirmed the formation of the purported complexes **[1Pd(A)]** (*m*/*z* found 450.9992, corresponding to M+H$^+$) and **[1Pd(N1-X)]** (*m*/*z* found 464.0195, corresponding to M+H$^+$) (see Supporting Information).

Following solution studies, we crystallized the observed complexes for solid-state characterization. Whilst the **[1Pd(*N1*-X)]** and **[1Pd(*N1*-A)]** compounds were successfully characterized by single-crystal X-ray diffraction (see Supporting Information, Table S1), all attempts to isolate suitable single crystals of the **[1Pd(*N7*-A)]** isomer were fruitless. In both **[1Pd(*N1*-X)]** and **[1Pd(*N1*-A)]**, the Pd^{II} ion adopts a trans-PdN$_2$O$_2$ square planar geometry (Figure 1). The *Cheld* ligand binds the metal ion in a μ,κ^3-N10,O2,O4-coordination mode, and the bases **X** and **A** through their N1-atom placed at the W-C face.

The Pd–N and Pd–O bond distances involving the metal center in **[1Pd(*N1*-X)]** and **[1Pd(*N1*-A)]** are comparable (Table S2). Remarkably, both complexes show an intramolecular W-C hydrogen bond between the exocyclic amine group of the bases and the carboxylic group of the *Cheld* ligand (Figure 1), which facilitates a coplanar arrangement of the units (Table S2). The structure of **[1Pd(*N1*-X)]** also shows the formation of stacking interactions between the *Cheld* ligand and the **X** base of nearby complexes, leaving a Pd···Pd distance of 3.190(1) Å (Figure S6). These three features—that is, intramolecular W-C hydrogen bonds, coplanar organization of the units, and formation of stacking interactions—are characteristics of natural base pairing, thereby suggesting that these Pd^{II}-mediated base pairs could be adequately prepared in a DNA structure, although some prior studies refuted this claim.[29]

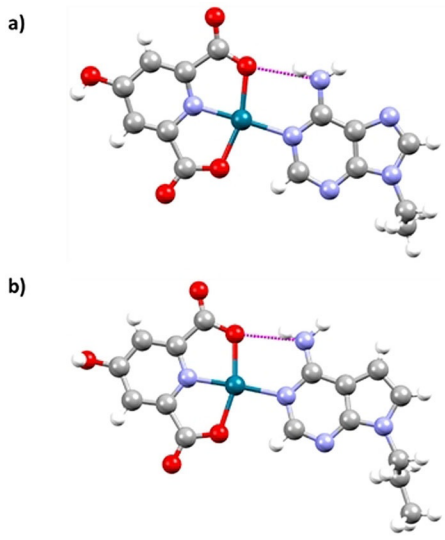

Figure 1. Molecular structure of the complexes a) **[1Pd(*N1*-A)]** and b) **[1Pd(*N1*-X)]** as determined by single-crystal X-ray diffraction.[41] In the former case, one of the two independent complexes has been arbitrarily chosen for the sake of simplicity. For an Ortep image, the reader is referred to the Supplementary Information (Figures S5). Atom colour code: grey, carbon; white, hydrogen; blue, nitrogen; red, oxygen; cyan, palladium; hydrogen bonds, dashed fuchsia line.

Powder X-ray diffraction (PXRD) of a polycrystalline bulk **[1Pd(A)]** verified the purity of the *N1*-isomer, by comparison to the calculated diffraction pattern from the single-crystal X-ray diffraction structure (Figure S7). Interestingly, upon dissolution of crystallized **[1Pd(*N1*-A)]**, ^{1}H-NMR shows again the presence of both *N1*- and *N7*-isomers (Figure S4), as observed in the NMR titration experiments (vide supra). The presence of only one isomer in the solid-state might be related to the highest basicity of the *N1*-atom in adenine,[30] which may favor the exclusive formation of the *N1*-isomer during the crystallization process.

The characteristics of the herein reported single base pairs inspired us to prepare larger Pd-DNA complexes by a self-assembly reaction between **1Pd_CH$_3$CN** and single-stranded DNA homopolymers comprising **X** or **A**. According to the above reported results, the resultant Pd-DNA hybrid molecule would have a contiguous array of stacked Pd^{II}-mediated base pairs that mimic the natural base pairing arrangement and, consequently, the DNA helical structure (Scheme 1). It is worth mentioning that our first attempt to apply this strategy was carried out using the [Cu(mCheld)(H$_2$O)$_2$] complex (mCheld = 4-methoxypyridine-2,6-dicarboxylic acid) and DNA homopolymers, in an effort to prepare Cu-DNA hybrids. However, the Cu-mediated base pairs were not suitable for this task which may be attributed to its coordination plasticity.[31]

To demonstrate our hypothesis, a titration experiment was initially performed by the addition of a controlled amount of **1Pd_CH$_3$CN** to ss-DNA homopolymers, namely: **dX$_{15}$** or **dA$_{15}$**, and followed by circular dichroism (CD). The CD spectrum for free **dX$_{15}$** shows a negative band in the range 270–300 nm, whilst **dA$_{15}$** displays a positive band in the same region (Figure 2). However, in presence of **1Pd**, comparable spectra are measured. This indicates the formation of well-defined helical structures with very similar profiles, in both cases stabilized by 1.0–1.3 equivalents of **1Pd** per base (Figure 2). Cotton effects are displayed in spectra with the appearance of new induced circular dichroism (ICD) bands in the region over 300 nm, where the palladium-mediated base pairs absorb (Figures S8). Specifically, two positive bands with a maximum centered at 325 nm and 400 nm, and a negative band with a minimum at 360 nm are observed. Complex **1Pd_CH$_3$CN** has no CD signal; therefore, the presence of these ICD bands confirms the interaction between **1Pd** and the oligonucleotides **dX$_{15}$** and **dA$_{15}$**. Moreover, four comparable isodichroic points are observed in both spectra, suggesting the transition between the two-state populations. These results are remarkable since they indicate that a similar binding mode occurs between **1Pd** and **dX$_{15}$** or **dA$_{15}$**, thus resulting in comparable **1Pd_ dX$_{15}$** and **1Pd_dA$_{15}$** helical structures, that can be related to a B-form polymorphism comprising palladium-mediated base pairs.[32] Based on these results, and considering the fact that **1Pd** would only bind **dX$_{15}$** through the N1-position W-C face of the helix, we propose the same for the interaction between **1Pd** with **dA$_{15}$** in solution. In addition, the formation of a double helix with a metallized adenine-N1 atom and pairs of hydrogen bonds between opposite adenine-N7 and adenine-N6H$_2$ groups can

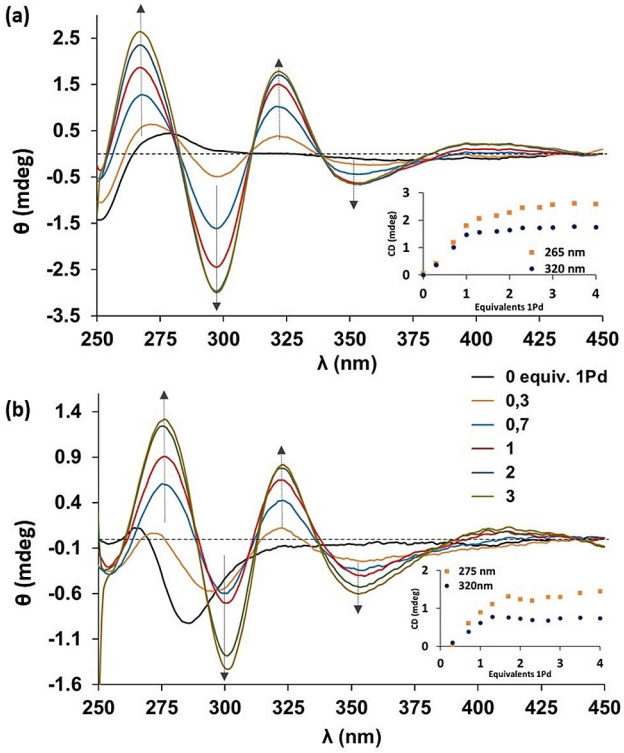

Figure 2. CD titration spectra for the reaction between **1Pd_CH$_3$CN** and a) **dA$_{15}$** and b) **dX$_{15}$**. Insets: CD signal as a function of equivalents of Pd^{II} ions added in (a) and (b). Conditions: 2 μM ss-DNA, 0 → 60 μM **1Pd** (in DMF), 100 mM NaClO$_4$, 5 mM MOPS buffer pH 6.8. Note: 1 equivalent means **1Pd** per base.

be excluded, since **1Pd-dX$_{15}$** cannot participate in this type of interactions.

However, the fact that **1Pd** could also interact with **dA$_{15}$** through adenine-N7 position in solution (vide supra) required more solution phase study of **1Pd-dA$_{15}$**. For this purpose, we performed an analogous CD titration experiment at pH 4.3. It is well-known that single-stranded poly(A) molecules are protonated at the adenine-N1 atom at pH 4.3, leading to a double helical structure with base pairs formed by two reciprocal hydrogen bonds involving the N7 atom as H-acceptor and the exocyclic N6-amino group of the opposite base as H-donor.[33,34] Thus, in acidic environment, the protonation of the adenine-N1 atom would hinder the binding of **1Pd** at this position, and favor metal interaction via the N7-atom instead.[35] The CD titration spectra at pH 4.3 (Figure S9) are completely different from those observed at pH 6.8 (Figure 2a), thereby pointing towards a different interaction mode between **1Pd** and **dA$_{15}$**. The absence of significant change in the CD spectrum upon adding the first equivalent of **1Pd** agrees with the participation of the N7 atom in the formation of hydrogen bonding in the interior of protonated **dA$_{15}$** double helix, hindering binding of **1Pd** at this position.

The preferred interaction of **1Pd** towards adenine-N1 in **1Pd-dA$_{15}$** at pH 6.8 would lead to the formation of planar W-C Pd^{II}-mediated base pairs that are further stabilized by stacking interactions, leading to a DNA-like helical structure. To verify the presence of stacking interactions, we carried out

intercalation studies using ethidium bromide (**EB**) and fluorescence spectroscopy. **EB** is a planar molecule that has a characteristic fluorescent peak at 620 nm when it intercalates between DNA stacked bases. The reaction between **EB** and free $\mathbf{dA_{15}}$ or $\mathbf{dX_{15}}$ provokes the insurgence of a small fluorescent band at 620 nm, upon excitation at 525 nm (Figure 3), consistent with the formation of stacking interactions in free poly(dA) or poly(dX).[36] However, the addition of one equivalent of **1Pd** to such solutions leads to a significant enhancement of the fluorescence intensity, as a consequence of a more hydrophobic environment for the **EB** molecules when stacked between the larger base pairs. These results are in agreement with the intercalation of **EB** between the Pd^{II}-mediated base pairs formed in $\mathbf{1Pd\text{-}dA_{15}}$ and $\mathbf{1Pd\text{-}dX_{15}}$ and further support the formation of consecutive planar and stacked Pd^{II}-mediated base pairs in helical structures.

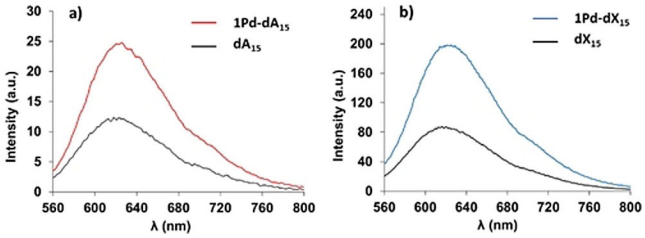

Figure 3. Fluorescence emission spectra for **EB** in the presence of a) $\mathbf{dA_{15}}$ and $\mathbf{1Pd\text{-}dA_{15}}$, and b) $\mathbf{dX_{15}}$ and $\mathbf{1Pd\text{-}dX_{15}}$. Conditions: 2 μM ss-DNA, 30 μM **EB**, 30 μM **1Pd** (in DMF), 100 mM $NaClO_4$, 5 mM MOPS buffer pH 6.8. Excitation: 525 nm.

Electrospray ionization mass spectrometry (ESI-MS) was employed to further demonstrate the existence of the Pd-DNA hybrids in solution (Figures S10 and S11). The deconvoluted mass spectrum for the $\mathbf{1Pd\text{-}dA_{15}}$ complex shows $\mathbf{dA_{15}}$ (4636.2 $g\,mol^{-1}$) with 14–15 **1Pd** metal fragments (287.5 $g\,mol^{-1}$) bound (Figure 4). It is worth mentioning that the addition of excess (3×) of $\mathbf{1Pd\_CH_3CN}$ did not give rise to a spectrum with a higher amount of bound **1Pd**. Equally, the mass spectrum for the $\mathbf{1Pd\text{-}dX_{15}}$ complex shows $\mathbf{dX_{15}}$ (4621.4 $g\,mol^{-1}$) with 15 **1Pd** moieties bound (Tables S3 and S4).

The solution phase speciation of $\mathbf{dA_{15}}$ and $\mathbf{1Pd\text{-}dA_{15}}$ was studied using bench-top small-angle X-ray scattering (SAXS, Figure 5). At pH 6.8, both scattering curves indicate monodisperse species, based on the flattering of the curve below

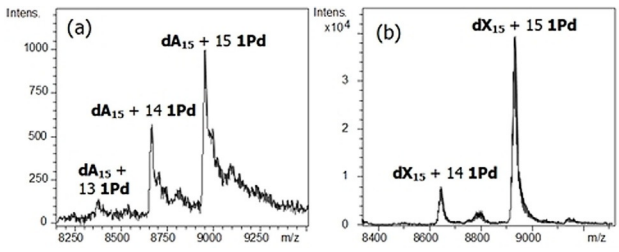

Figure 4. Deconvoluted ESI-MS spectra of a) $\mathbf{dA_{15}}$ and b) $\mathbf{dX_{15}}$, both incubated with 15 equivalents of **1Pd**.

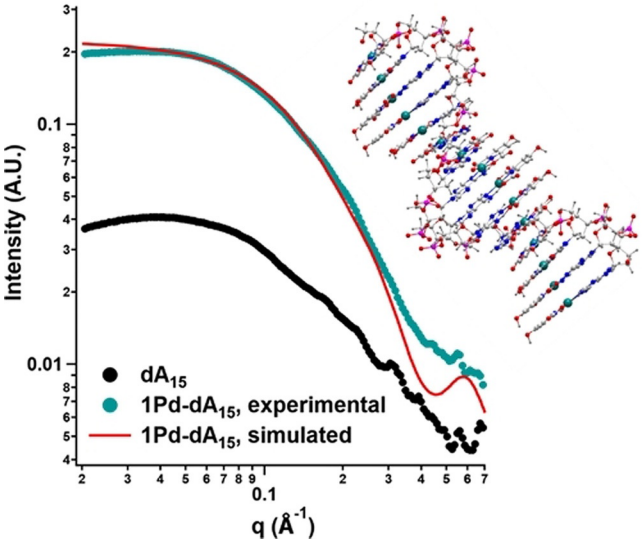

Figure 5. Left: Small-angle X-ray scattering spectra of $\mathbf{dA_{15}}$ (black), experimental $\mathbf{1Pd\text{-}dA_{15}}$ (turquoise), and simulated $\mathbf{1Pd\text{-}dA_{15}}$ (red). Conditions: 1 mM $\mathbf{dA_{15}}$, 15 mM **1Pd**, 5 mM MOPS buffer pH 7. Right: Model of $\mathbf{1Pd\text{-}dA_{15}}$ from which the scattering data were simulated. (Note: the descent in intensity in both experimental curves between $q \approx 0.02$–0.03 $Å^{-1}$ is an instrumental artifact due to the position of the beam attenuator).

$q = 0.06$ $Å^{-1}$.[37] Free $\mathbf{dA_{15}}$ undergoes significant changes in presence of one equivalent of **1Pd**, that is, the intensity of the curve increases and the Guinier region ($q \approx 0.06$–0.2 $Å^{-1}$) moves to a lower q-range, showing a steeper slope. The intensity increase is related to both electron density of the scattering species ($I(q) \propto$ (atomic number)^2) and size ($I(q) \propto$ (radius)^6). We simulated the scattering data for different $\mathbf{1Pd\text{-}dA_{15}}$ conformations. The simulated scattering data that best matched the experimental results are those obtained from a right-handed B-like conformation of the $\mathbf{1Pd\text{-}dA_{15}}$ molecule in which the **1Pd** fragments bind at the N1-position of each base in the $\mathbf{dA_{15}}$ oligonucleotide (Figure 5).

Based on the expected shape of $\mathbf{dA_{15}}$ and $\mathbf{1Pd\text{-}dA_{15}}$, we fit both these scattering curves with a cylindrical model. The length of both species described by the cylindrical model fit is ≈42 Å, roughly similar to the end-to-end (Pd-Pd) measured distance of simulated $\mathbf{1Pd\text{-}dA_{15}}$ (36 Å). The radius from the cylindrical model fit increases from 5.0 to 7.5 Å, which is consistent with the addition of the **1Pd**. The physical diameter is more difficult to measure in the $\mathbf{1Pd\text{-}dA_{15}}$ model since the helix shape has a complex topology. However, the good agreement between experimental and simulated SAXS data supports the solution species proposed by CD and ESI-MS for $\mathbf{1Pd\text{-}dA_{15}}$ at pH 6.8.

On the other hand, the scattering data for $\mathbf{dA_{15}}$ and $\mathbf{1Pd\text{-}dA_{15}}$ at pH 4.3 reveal completely different species (Figure S12). The steep slopes of both curves suggest elongated species; again, the curves were suitably fit with cylindrical models. According to this data analysis, $\mathbf{dA_{15}}$ at pH 4.3 has a cylinder radius of ≈12 Å and a length of 3200 Å. This result agrees with the formation of a double helix, as described for poly(A) at low pH. The significant elongation can be

explained because all the bases are the same and, therefore, the double-helix formation can occur by staggered and offset-linking of the **dA$_{15}$** chains.[34] Upon addition of **1Pd** to the **dA$_{15}$** solution at pH 4.3, the **1Pd** fragment binds, presumably, through the adenine-N7 atom, leading to a different species in solution. We observe a similar diameter as that of **1Pd-dA$_{15}$** at near neutral pH, but the length is ≈107 Å, suggesting, on average, possible dimer-to-trimer formation.

Based on all the obtained data, we performed ab-initio calculations for the **1Pd-dA$_{12}$** and **1Pd-dX$_{12}$** molecules, in an effort to get a more precise understanding of the molecule arrangement (see Supporting Information). For this task, we chose smaller oligonucleotides, namely dodecamers, since they provide the minimum length needed to complete a helix turn. The starting geometries were obtained from **dA$_{12}$** and **dX$_{12}$** single helix structures, respectively, with the bases in an anti-conformation, as previously reported at neutral pH.[36,38,39] The **1Pd** metal fragments were bound to the N1 atom of the bases in a co-planar organization, as observed in the crystal structures (vide supra). The anionic nature of the phosphate groups was treated with Na cations, and water molecules were placed close to the donor and acceptor atoms. To the best of our knowledge, this is the first example of a DNA molecule with Pd^{II} ions, sodium cations, and water molecules studied at this computational level. Our previous reported example at this level included only one Cu^{II}-mediated base pair and no water molecules.[31] The geometry-optimized structures show that **1Pd-dA$_{12}$** and **1Pd-dX$_{12}$** consist of right-handed helical molecules comprising consecutively stacked Pd^{II}-mediated base pairs that mimic natural base pair organization in double-stranded DNA, that is, with the presence of Watson–Crick hydrogen bonds and stacking interactions (Figures 6, S14, and S15). The Pd^{II} ions are located along the helical axis that runs through the center of the metallo-base pairs, in close contact with each other at 3.447–3.765 and 3.109–3.819 Å,[40] for **1Pd-dA$_{12}$** and **1Pd-dX$_{12}$**, respectively, and leading to an uninterrupted 1D array.

Simulated small-angle X-ray scattering data from the optimized structure agrees with the experimental scattering of **1Pd-dA$_{12}$**, dissolved at pH 6.8 in MOPS buffer, similarly to the above-described study of **1Pd-dA$_{15}$** (Figure S13). We also measured the small-angle X-ray scattering of **dA$_{12}$**. Similar to the SAXS study of **dA$_{15}$**, the addition of **1Pd** increased the scattering intensity (due to an increase in electron density) without significantly changing the curve shape, and both curves could be fitted with a cylindrical model. This suggests that the complex formation between **1Pd** and **dA$_{15}$**, or **dA$_{12}$** is essentially identical.

Conclusion

We developed a bottom-up approach to prepare customized Pd-DNA hybrid systems by a self-assembly reaction between single-stranded **dA$_{15}$** or **dX$_{15}$** homopolymers and the **1Pd** complex, capable of forming metal-mediated base pairs. The **1Pd** fragments bind to the bases through a coordination bond and a W-C hydrogen bond, and are further stabilized by stacking interactions, mimicking the organization of natural base pairs in a ds-DNA molecule. Importantly, the final Pd-DNA structure contains an uninterrupted 1D array of Pd^{II} ions running through the center of the helix and the number of **1Pd** moieties is controlled by the template. We believe that this strategy can be applied to strategically assemble ss-DNA-based functional materials at the nanoscale. In principle, the **1Pd** fragment can be designed with different functionalities (i.e. chromophores or monomers precursor of conducting polymers) that could be precisely organized at the nanoscale by the ss-DNA templates. This is the focus of our current efforts.

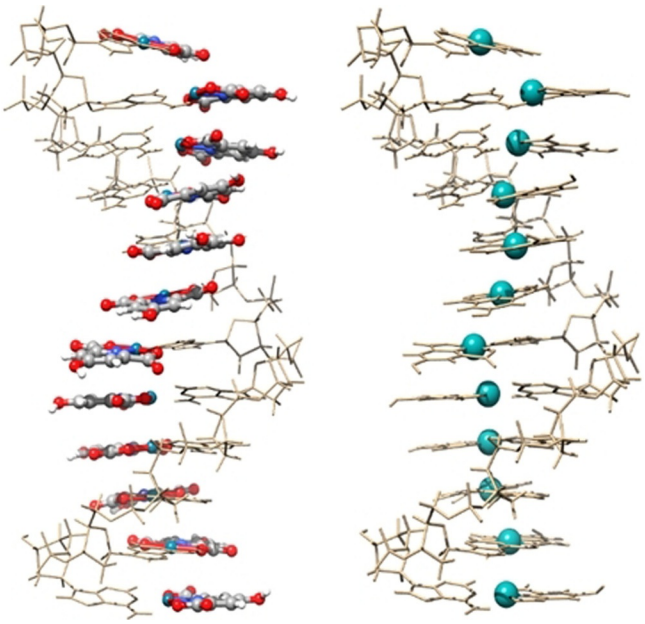

Figure 6. Two different representations of the geometry-optimized structure of **1Pd-dA$_{12}$** showing the organization of the **1Pd** complex along the structure (left) and the formation of a continuous 1D array of Pd^{II} ions (right). Sodium cations and water molecules have been omitted for clarity. Atom color code: carbon, grey; hydrogen, white; nitrogen, light blue; oxygen, red; palladium, cyan; **dA$_{12}$**, tan (in left and right image); *Cheld*, tan (in right image).

Acknowledgements

Financial support from Spanish MINECO (CTQ2017-89311-P), Spanish MICIU (Salvador Madariaga Program, Ref. PRX19/00290), University of Granada (A-FQM-465-UGR18), and Junta de Andalucía (FQM-293 and FQM-283). We also thank the "Centro de Servicios de Informática y Redes de Comunicaciones" (CSIRC) (UGRGrid), Universidad de Granada, for providing computing time. ADM acknowledges support by COST Action CA-18202 (European Cooperation in Science and Technology). OP is a member of the "Grup de Recerca de la Generalitat de Catalunya" (Ref. 2017SGR-864) and he wants to acknowledge the Spanish MICINN and FEDER (BIO2015-67358-C2-2-P). We thank Dr. Jean-Luc Brousseau of Anton-Paar USA (Ashland, VA) for performing the SAXS measurements of dA_{12} and 1Pd-dA_{12}. MN acknowledges support from the U.S. Department of

Energy, Office of Basic Energy Sciences, Division of Material Sciences and Engineering, under award DE SC0010802 for data collection and analysis of the SAXS data.

Conflict of interest

The authors declare no conflict of interest.

Keywords: bioinorganic chemistry · DNA · metal-mediated base pair · palladium · self-assembly

[1] N. C. Seeman, H. F. Sleiman, *Nat. Rev. Mater.* **2018**, *3*, 17068.
[2] X. Dai, Q. Li, A. Aldalbahi, L. Wang, C. Fan, X. Liu, *Nano Lett.* **2020**, *20*, 5604 – 5615.
[3] S. K. Vittala, D. Han, *ACS Appl. Bio Mater.* **2020**, *3*, 2702 – 2722.
[4] M. R. Jones, N. C. Seeman, C. A. Mirkin, *Science* **2015**, *347*, 1260901.
[5] P. W. K. Rothemund, *Nature* **2006**, *440*, 297 – 302.
[6] N. R. Kallenbach, R. I. Ma, N. C. Seeman, *Nature* **1983**, *305*, 829 – 831.
[7] R. Iwaura, K. Yoshida, M. Masuda, M. Ohnishi-Kameyama, M. Yoshida, T. Shimizu, *Angew. Chem. Int. Ed.* **2003**, *42*, 1009 – 1012; *Angew. Chem.* **2003**, *115*, 1039 – 1042.
[8] R. Iwaura, F. J. M. Hoeben, M. Masuda, A. P. H. J. Schenning, E. W. Meijer, T. Shimizu, *J. Am. Chem. Soc.* **2006**, *128*, 13298 – 13304.
[9] P. G. A. Janssen, J. Vandenbergh, J. L. J. Van Dongen, E. W. Meijer, A. P. H. J. Schenning, *J. Am. Chem. Soc.* **2007**, *129*, 6078 – 6079.
[10] L. A. Fendt, I. Bouamaied, S. Thöni, N. Amiot, E. Stulz, *J. Am. Chem. Soc.* **2007**, *129*, 15319 – 15329.
[11] P. G. A. Janssen, S. Jabbari-Farouji, M. Surin, X. Vila, J. C. Gielen, T. F. A. De Greef, M. R. J. Vos, P. H. H. Bomans, N. A. J. M. Sommerdijk, P. C. M. Christianen, et al., *J. Am. Chem. Soc.* **2009**, *131*, 1222 – 1231.
[12] M. V. Ishutkina, A. R. Berry, R. Hussain, O. G. Khelevina, G. Siligardi, E. Stulz, *Eur. J. Org. Chem.* **2018**, 5054 – 5059.
[13] P. Ensslen, H. A. Wagenknecht, *Acc. Chem. Res.* **2015**, *48*, 2724 – 2733.
[14] M. Surin, S. Ulrich, *ChemistryOpen* **2020**, *9*, 480 – 498.
[15] T. J. Bandy, A. Brewer, J. R. Burns, G. Marth, T. N. Nguyen, E. Stulz, *Chem. Soc. Rev.* **2011**, *40*, 138 – 148.
[16] Z. Chen, C. Liu, F. Cao, J. Ren, X. Qu, *Chem. Soc. Rev.* **2018**, *47*, 4017 – 4072.
[17] J. Müller, *Coord. Chem. Rev.* **2019**, *393*, 37 – 47.
[18] S. Naskar, R. Guha, J. Müller, *Angew. Chem. Int. Ed.* **2020**, *59*, 1397 – 1406; *Angew. Chem.* **2020**, *132*, 1413 – 1423.
[19] Y. Takezawa, M. Shionoya, J. Müller, *Comprehensive Supramolecular Chemistry II*, Elsevier, Amsterdam, **2017**, pp. 259 – 293.
[20] F.-A. Polonius, J. Müller, *Angew. Chem. Int. Ed.* **2007**, *46*, 5602 – 5604; *Angew. Chem.* **2007**, *119*, 5698 – 5701.
[21] D. A. Megger, C. Fonseca Guerra, J. Hoffmann, B. Brutschy, F. M. Bickelhaupt, J. Müller, *Chem. Eur. J.* **2011**, *17*, 6533 – 6544.
[22] N. Santamaría-Díaz, J. M. Méndez-Arriaga, J. M. Salas, M. A. Galindo, *Angew. Chem. Int. Ed.* **2016**, *55*, 6170 – 6174; *Angew. Chem.* **2016**, *128*, 6278 – 6282.
[23] J. Kondo, Y. Tada, T. Dairaku, Y. Hattori, H. Saneyoshi, A. Ono, Y. Tanaka, *Nat. Chem.* **2017**, *9*, 956 – 960.
[24] J. M. Méndez-Arriaga, C. R. Maldonado, J. A. Dobado, M. A. Galindo, *Chem. Eur. J.* **2018**, *24*, 4583 – 4589.
[25] S. M. Swasey, F. Rosu, S. M. Copp, V. Gabelica, E. G. Gwinn, *J. Phys. Chem. Lett.* **2018**, *9*, 6605 – 6610.
[26] A. Hatano, K. Tanaka, M. Shiro, M. Shionoya, *Tetrahedron* **2002**, *58*, 2965 – 2972.
[27] T. Mihály, M. Garijo Añorbe, F. M. Albertí, P. J. Sanz Miguel, B. Lippert, *Inorg. Chem.* **2012**, *51*, 10437 – 10446.
[28] K. H. Scheller, V. Scheller-Krattiger, R. B. Martin, *J. Am. Chem. Soc.* **1981**, *103*, 6833 – 6839.
[29] E. Meggers, P. L. Holland, W. B. Tolman, F. E. Romesberg, P. G. Schultz, *J. Am. Chem. Soc.* **2000**, *122*, 10714 – 10715.
[30] L. E. Kapinos, B. P. Operschall, E. Larsen, H. Sigel, *Chem. Eur. J.* **2011**, *17*, 8156 – 8164.
[31] A. Dominguez-Martin, S. Galli, J. A. Dobado, N. Santamaría-Díaz, A. Pérez-Romero, M. A. Galindo, *Inorg. Chem.* **2020**, *59*, 9325 – 9338.
[32] J. Kypr, I. Kejnovská, D. Renčiuk, M. Vorlíčková, *Nucleic Acids Res.* **2009**, *37*, 1713 – 1725.
[33] A. Rich, D. R. Davies, F. H. C. Crick, J. D. Watson, *J. Mol. Biol.* **1961**, *3*, 71 – 86.
[34] M. L. Gleghorn, J. Zhao, D. H. Turner, L. E. Maquat, *Nucleic Acids Res.* **2016**, *44*, 8417 – 8424.
[35] A. Schreiber, M. S. Lüth, A. Erxleben, E. C. Fusch, B. Lippert, *J. Am. Chem. Soc.* **1996**, *118*, 4124 – 4132.
[36] J. L. Alderfer, S. L. Smith, *J. Am. Chem. Soc.* **1971**, *93*, 7305 – 7314.
[37] At the lowest q-values, the curve exhibits a downward dip in intensity; this is an instrument artifact observed for weakly scattering species and/or low concentration solutions, and is not evaluated in the curve fitting described subsequently.
[38] S. Chakraborty, S. Sharma, P. K. Maiti, Y. Krishnan, *Nucleic Acids Res.* **2009**, *37*, 2810 – 2817.
[39] J. Isaksson, S. Acharya, J. Barman, P. Cheruku, J. Chattopadhyaya, *Biochemistry* **2004**, *43*, 15996 – 16010.
[40] The Pd ions at each end of the structure have not been considered due to the border effect.
[41] Deposition Numbers 2044056 (for **[1Pd(*N1*-A)]**) and 2044057 (for **[1Pd(*N1*-X)]**) contain the supplementary crystallographic data for this paper. These data are provided free of charge by the joint Cambridge Crystallographic Data Centre and Fachinformationszentrum Karlsruhe Access Structures service www.ccdc.cam.ac.uk/structures.

Manuscript received: November 21, 2020
Revised manuscript received: January 15, 2021
Accepted manuscript online: February 9, 2021
Version of record online: March 24, 2021

Angewandte Chemie
Eine Zeitschrift der Gesellschaft Deutscher Chemiker

Supporting Information

Single-Stranded DNA as Supramolecular Template for One-Dimensional Palladium(II) Arrays

*Antonio Pérez-Romero, Alicia Domínguez-Martín, Simona Galli, Noelia Santamaría-Díaz, Oscar Palacios, José A. Dobado, May Nyman, and Miguel A. Galindo**

anie_202015554_sm_miscellaneous_information.pdf

CONTENTS

GENERAL METHODS 1
METAL COMPLEXES PREPARATION 2
NMR SPECTROSCOPY 4
SINGLE-CRYSTAL X-RAY DIFFRACTION STRUCTURE DETERMINATION 8
POWDER X-RAY DIFFRACTION 11
UV-VIS SPECTROSCOPY 12
CIRCULAR DICHROISM 13
MASS SPECTROMETRY FOR 1Pd-DNA 14
SAXS MEASUREMENTS 16
MOLECULAR MODELLING 17
OLIGONUCLEOTIDE SYNTHESIS 56
REFERENCES 57

GENERAL METHODS

^{1}H-NMR spectra were recorded at room temperature on a Varian Direct Drive 400 instrument. Chemical shifts are given in ppm (δ) relative to tetramethylsilane. Abbreviations used are s = singlet, d = doublet, t = triplet, q = quartet, m = multiplet, dq = double quartet. Infrared (IR) spectra were acquired on a Thermo Nicolet IR200 spectrometer or a Bruker Tnesor 27 Fourier transform infrared spectrometer. Elemental analyses were carried out on a Thermo Scientific Flash 2000 instrument with a precision microbalance or a Flash EA1112 CHNS-O Thermo Finnigan instrument with a Mettler Toledo MX5 electronic microbalance. CD spectra were recorded on a Jasco J-815 Mettler Toledo MX5 instrument equipped with a Peltier temperature controller. UV-Vis absorption and fluorescence spectra were recorded on a Varian Cary-Eclipse spectrophotometer equipped with a Xe lamp (peak power 75 kW), a CZERNY-Turner monochromator, and an R-298 red-sensitive photomultiplier tube.

High-resolution electrospray ionization mass spectrometry (ESI-MS) was carried out on a Waters LCT Premier spectrometer for the metal complexes, while the characterization of the **dX_{15}** oligonucleotide was carried out by MALDI-TOF mass spectrometry on a Bruker Autoflex spectrometer. Molecular mass determination for **1Pd-DNA** was performed by ESI-MS using a Micro Tof-Q Instrument (Bruker Daltonics GmbH, Bremen, Germany) equipped with a time-of-flight analyzer (ESI-TOF MS), calibrated with NaI (200 ppm NaI in a 1:1 H_2O:isopropanol mixture), interfaced with an Agilent Technologies Series 1100 HPLC pump and equipped with an autosampler, both controlled by the Compass Software. The interaction of the metallic complexes with the DNA hybrids (50 µM) was analyzed in negative mode, injecting 10 µL of the sample at 40 µL min^{-1}, with capillary-counter electrode voltage at 3.9-4.2 kV; the desolvation temperature was set at 100 °C, and dry gas was flowed at 6 L min^{-1}, using a 90:10 mixture of 15 mM ammonium acetate and acetonitrile (pH 7.0) as a liquid carrier. The spectra were collected throughout an m/z range from 800 to 3000.

METAL COMPLEXES PREPARATION

Materials

9-ethyl-adenine and 9-propyl-7-deaza-adenine were synthesized according to literature procedures.[1,2] Chelidamic acid (Cheld), $Pd(NO_3)_2$, and K_2PtCl_4 were purchased from Sigma-Aldrich. All the chemicals and solvents were used without further purifications.

Synthesis procedures

Synthesis of complex [Pd(Cheld)(CH_3CN)], 1Pd_CH_3CN

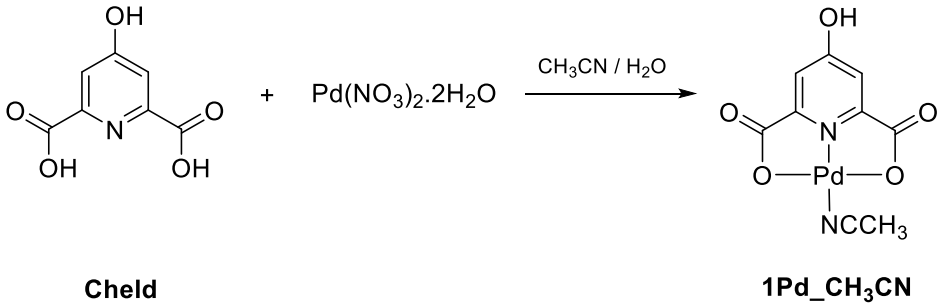

Cheld **1Pd_CH_3CN**

Scheme S1. Synthetic route to **1Pd_CH_3CN**

A suspension of palladium(II) nitrate hydrate (800 mg, 3 mmol) in CH_3CN/H_2O (30:30 mL) was stirred at reflux until completely dissolved. A solution of chelidamic acid (Cheld) (603 mg, 3 mmol) in H_2O/CH_3CN (90:60 mL) was then added dropwise, stirred and refluxed for 5 h. Subsequently, the mixture was cooled, filtered off and the solution was left to concentrate by slow evaporation at room temperature. After 12 h, an orange powder appeared, was collected by filtration, washed with water (1 mL) and dried with ethanol (1mL) and ether (1 mL), affording **1Pd_CH_3CN** (760 mg, yield 77%). ^{1}H-NMR (400 MHz, DMSO-d_6), δ (ppm) = 7.05 (s, 2H, *CH*), 2.03 (s, 3H, *CH_3*). IR (v/cm^{-1}) = 3458, 3022, 2716, 2597, 2334, 2309, 1684, 1628, 1582, 1458, 1269, 1228, 1176, 1085, 924, 911, 799, 757, 701, 638, 571, 460. Elem. Anal. for [Pd($C_7H_3NO_5$)(CH_3CN)], (M_W = 328.6), Calcd. % (Found %): C, 32.92 (32.65); H, 1.83 (1.96); N, 8.53 (8.51).

Synthesis of complex [Pd(*N1*-(7-deazaadenine))], [1Pd(*N1*-X)]

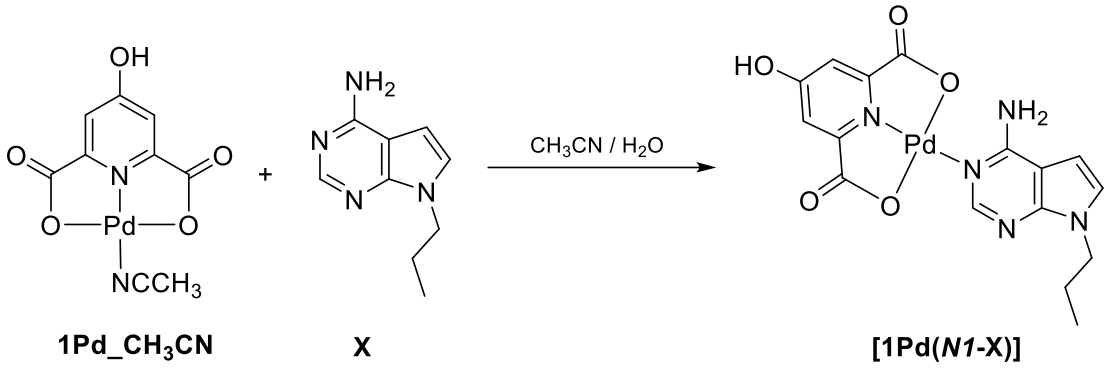

Scheme S3. Synthetic route to **[1Pd(*N1*-X)]**

Compound **1Pd_CH_3CN** (70 mg, 0.2 mmol) was suspended in CH_3CN/H_2O (15:15 mL) and the suspension was refluxed until complete dissolution of the complex. The solution was then filtered off using a syringe filter and an aqueous solution (20 mL) of 9-propyl-7-deaza-adenine (**X**) (375 mg, 0.2 mmol) was added. The mixture was stirred at 60 ℃ for 90 min in darkness. The title **[Pd(*N1*-X)]** compound appeared as a yellow powder that was filtered, washed with water (1 mL) and dried with ethanol (1 mL) and ether (1 mL) (71.5 mg, yield 72.1%). Part of the product was recrystallized from *N,N*-dimethylformamide by slow evaporation at room temperature, obtaining yellow crystals suitable for X-ray diffraction. ^{1}H-NMR (400 MHz, DMSO-d_6, Figure S3) δ (ppm) = 7.99 (s, 1H, *CH*), 7.34 (d, 1H, *CH*, J = 3.4 Hz), 7.10 (s, 2H, CH_{py}), 6.71 (d, 1H, *CH*, J = 3.4 Hz), 4.11 (t, 2H, CH_2, J = 7.0 Hz), 1.76 (dq, 2H, CH_2, J = 7.2, 14.4 Hz), 0.81 (t, 3H, CH_3, J = 7.4 Hz). IR: (v/cm^{-1}) = 3389, 3225, 1664, 1603, 1502, 1461, 1370, 1254, 1084, 797, 733. Elem. Anal. for [Pd($C_{16}H_{15}N_5O_5$)(H_2O)$_{1.8}$], (Mw = 496.1), Calcd. % (Found %): C, 38.73 (38.55); H, 3.78 (4.28); N, 14.11 (14.51). HRMS (ESI): m/z calcd. for $C_{16}H_{16}N_5O_5Pd$ [M + H]$^+$, 464.0186; found, 464.0195.

Synthesis of complex [1Pd(*N1*-(9-ethyladenine))], [1Pd(*N1*-A)]

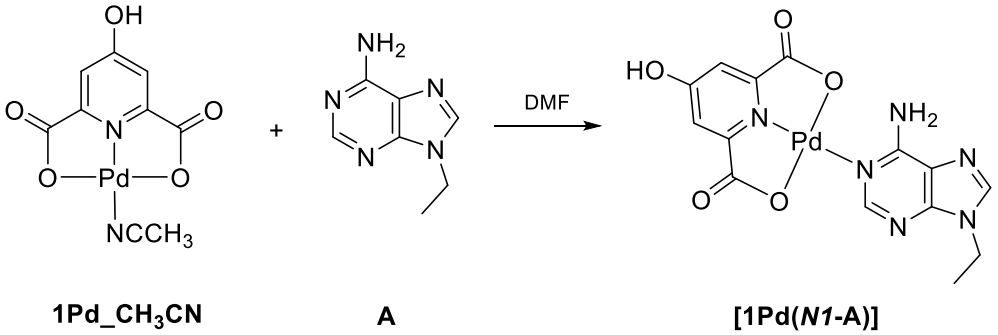

Scheme S2. Synthetic route to **[1Pd(*N1*-A)]**

To a slowly stirred solution of 9-ethyladenin (**A**) (10.9 mg, 0.062 mmol) in DMF (1.5 mL) was added drop wise a solution of **1Pd_CH$_3$CN** (18.8 mg, 0.062 mmol) in DMF (3.5 mL). The mixture was left crystallize and [Pd(*N1*-9-ethyladenine)], **[1Pd(*N1*-A)]**, appeared as small yellow crystals suitable for X-ray diffraction (no yield calculated). The precipitate was filtered, dried and characterized. ^{1}H-NMR (400 MHz, DMSO-d_6, Figure S4), δ (ppm) = 8.46 (s, 1H, CH_{8b}), 8.37 (s, 1H, CH_{8a}), 8.29 (s, 1H, CH_{3b}), 8.09 (s, 1H, CH_{3a}), 7.22 (s, 2H, NH_2), 7.14-7.13 (d, 2H, CH_{PY}), 4.32-4.23 (q, 2H, CH_2, J = 7.2 Hz), 1.39 (t, 3H, CH_3, J = 7.2 Hz). IR (ν/cm^{-1}) = 3320, 3225, 3069, 1665, 1613, 1343, 1080, 791, 641, 560, 453. Elem. Anal. for [$C_{14}H_{12}N_6O_5Pd\cdot(H_2O)_{0.85}$], ($M_W$ = 467.02), Calcd. % (Found %): C, 36.01 (36.58); N, 18.00 (17.54); H, 3.17 (3.87). HRMS (ESI): m/z calcd. for $C_{14}H_{13}N_6O_5Pd$ [M + H]$^+$, 450.9982; found, 450.9992.

NMR SPECTROSCOPY

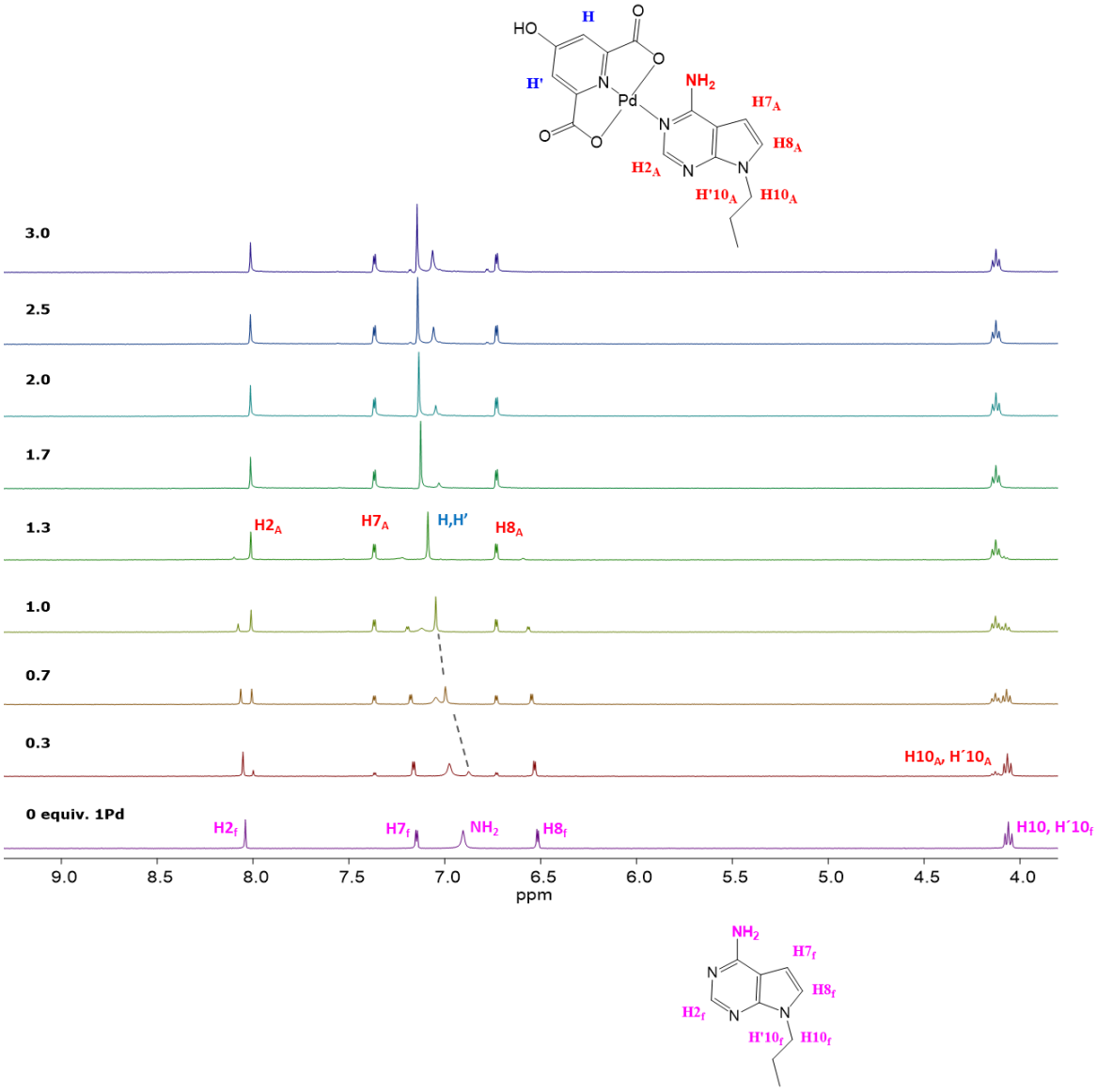

Figure S1. ^{1}H-NMR (400 MHz, DMSO-d_6) titration spectra revealing the formation of the complex **[1Pd(X)]**, upon addition of a controlled amount of **1Pd** over a solution containing the nucleobase **X**.

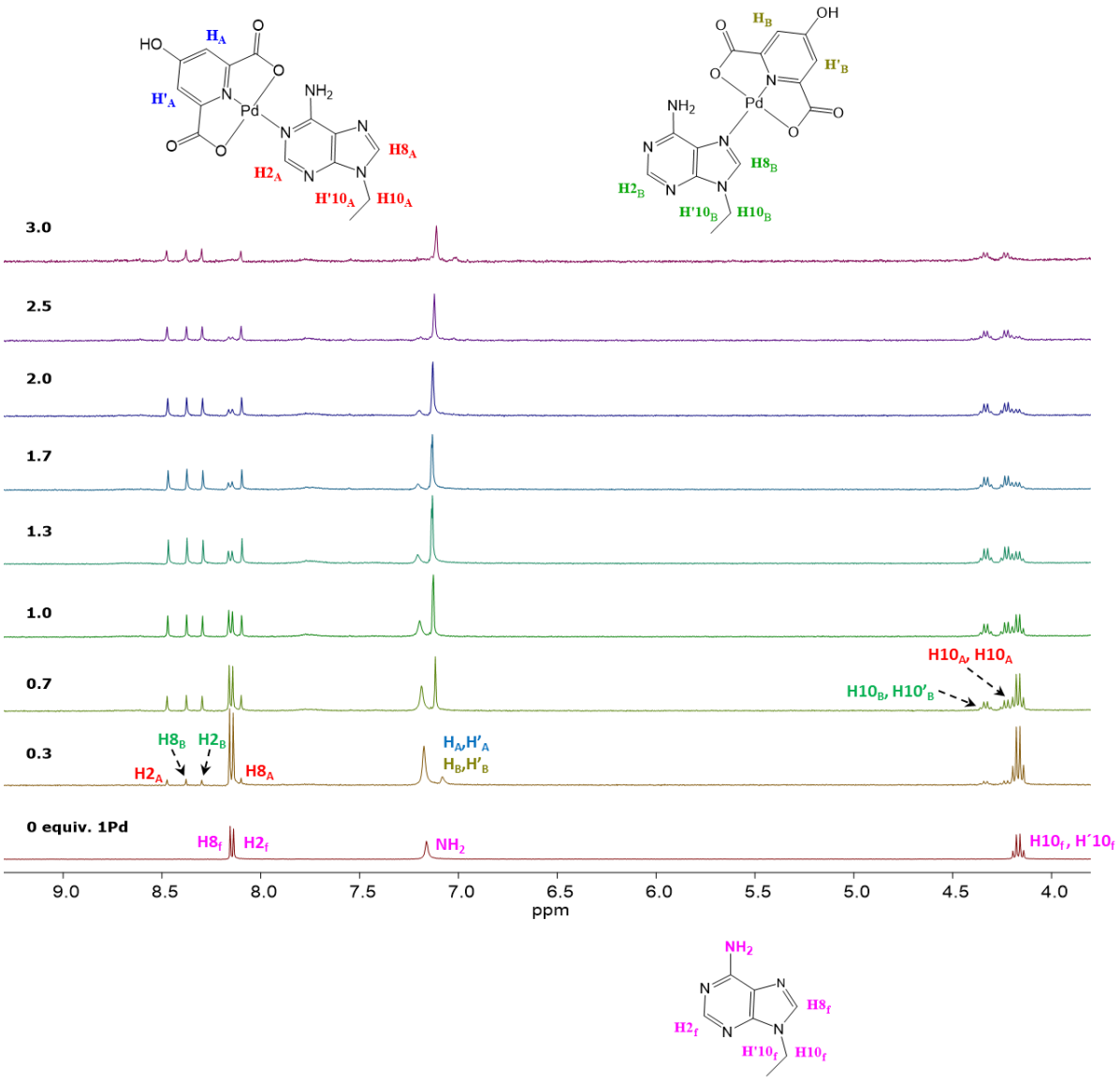

Figure S2. ^{1}H-NMR (400 MHz, DMSO-d_6) titration spectra revealing the formation of the complexes **[1Pd(*N1*-A)]** and **[1Pd(*N7*-A)]** upon addition of a controlled amount of **1Pd** over a solution containing the nucleobase **A**. Note: the H2 and H8 resonances of the adenine ligand have been assigned according to the literature. [3]

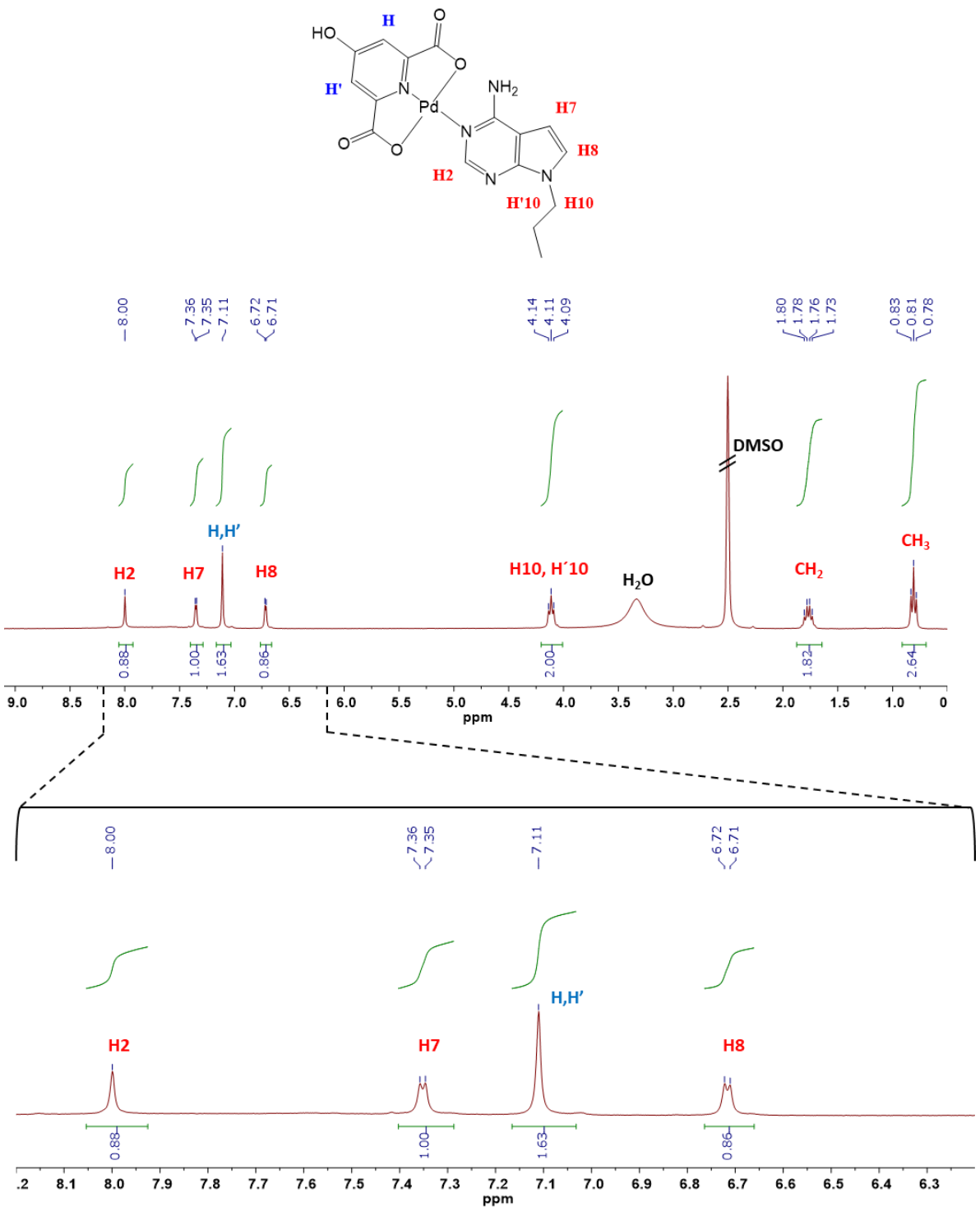

Figure S3. ^{1}H-NMR (400 MHz, DMSO-d_6) spectrum of the single crystals obtained for complex **[1Pd(*N1*-X)]** and employed for X-ray diffraction studies.

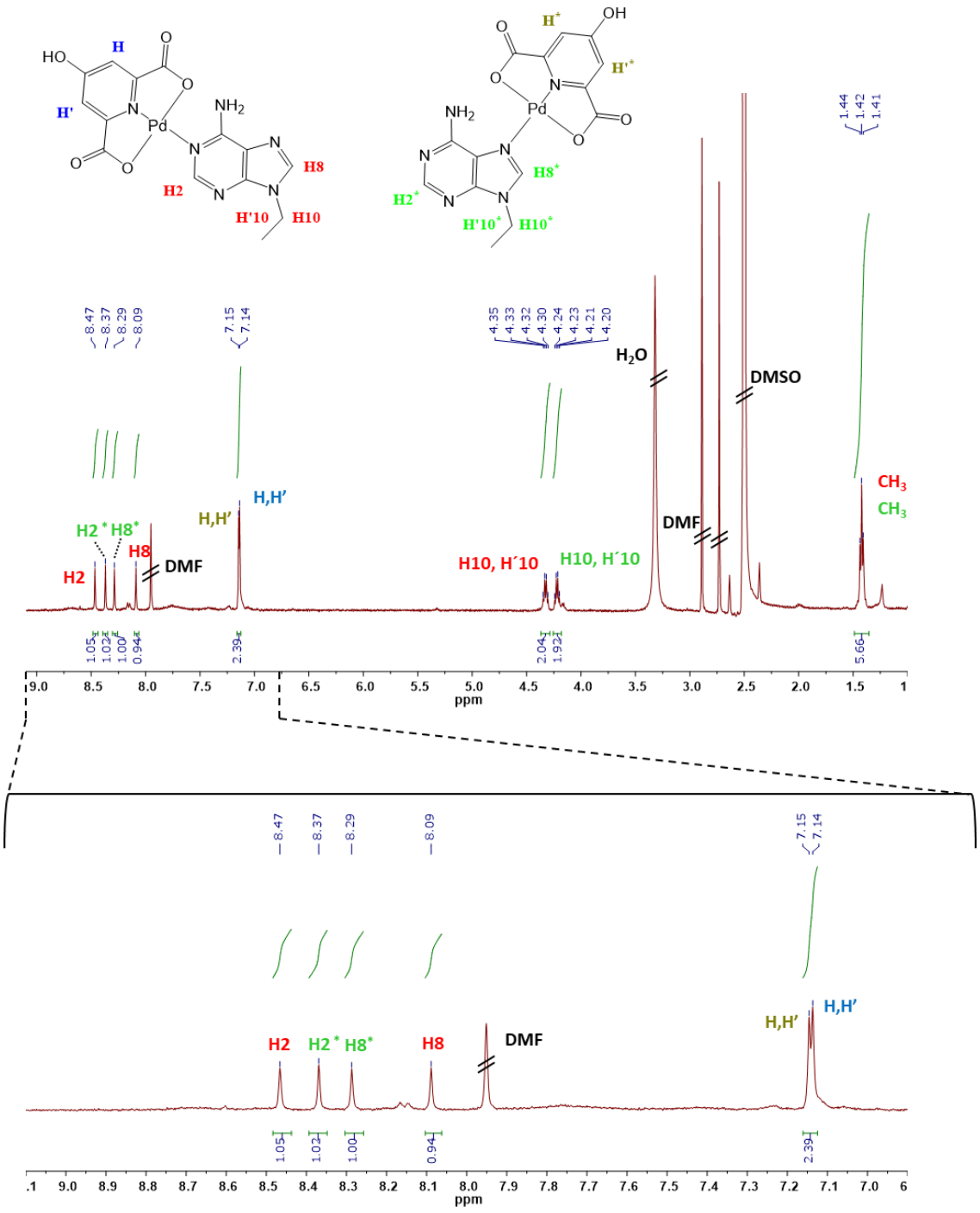

Figure S4. ^{1}H-NMR (400 MHz, DMSO-d_6) spectrum of the single crystals obtained for complex **[1Pd(*N1*-A)]** and employed for X-ray diffraction studies.

SINGLE-CRYSTAL X-RAY DIFFRACTION STRUCTURE DETERMINATION

X-ray diffraction data for **[1Pd(*N1*-X)]** were collected at T = 100 K using a Bruker X8 Proteum automated diffractometer equipped with a fine-focus rotating anode (Cu Kα, λ = 1.5418 Å), a Smart 6000 CCD area detector, and an Oxford Cryostream 700 cooling apparatus. Data reduction was performed with the software SAINT V6.36A,[4] while data correction for absorption was carried out using the software SADABS.[5] X-ray diffraction data for **[1Pd(*N1*-A)]** were collected at T = 150 K using a Bruker AXS Apex II automated diffractometer equipped with a sealed X-ray tube (Mo Kα, λ = 0.7103 Å), a CCD area detector and a Bruker Kryoflex cooling apparatus. Data reduction was performed with the software SAINT V6.36A. No data correction for absorption was carried out. In both cases, the crystal structure was solved by direct methods as implemented in SHELXS-97,[6] which allowed the location of most of the atoms of the asymmetric unit. All the remaining non-hydrogen atoms were located from difference Fourier maps calculated from successive full-matrix least-squares refinement cycles on F^2 using SHELXL-2018/3.[7] Anisotropic thermal displacement parameters were assigned to all the non-hydrogen atoms in the case of **[1Pd(*N1*-X)]**. As for **[1Pd(*N1*-A)]**, the very low quality of the single-crystals diffraction prevented the adoption of anisotropic thermal parameters. To try and fix this issue, several single crystals of the same batch, as well as single crystals from different batches, obtained upon modulating the crystallization conditions, were tested without success. Given the relevance of the structural information unveiled by these structure determinations to complement and corroborate the other scientific results presented in this work (see *e.g.* the coordination mode, *N1* vs. *N7*, of the A base), we believe it necessary to present the structural details of **[1Pd(*N1*-A)]** despite the limited quality of the data from which they were retrieved. Rephrasing, the crystallographic studies are not shared with the scientific community *per se*, yet as a valuable part of a comprehensive work. The hydrogen atoms were located at idealized positions using HFIX instructions, and described with isotropic thermal displacement parameters fixed at 1.2 or 1.5 times those of the atom to which they were bound. The main crystallographic information, as well as experimental and data treatment details are provided in Table S1.

Table S1. Summary of crystallographic information and relevant X-ray diffraction experimental details for **[1Pd(*N1*-A)]** and **[1Pd(*N1*-X)]**. [a]The reader is addressed to the previous section.

	[1Pd(*N1*-A)]	**[1Pd(*N1*-X)]**
Asymmetric unit formula	$C_{17}H_{15}N_7O_6Pd$	$C_{35}H_{39}N_{11}O_{12}Pd_2$
MW [g/mol]	519.75	1018.57
T [K]	150	100
Color, habit	Yellow, needle	Yellow, needle
Dimensions [mm^3]	0.34x0.15x0.08	0.18x0.03x0.02
Crystal system	Monoclinic	Monoclinic
Space group	$P2_1/c$	$P2_1/c$
Z, Z'	4, 4	4, 4
a [Å]	11.515(8)	18.1949(14)
b [Å]	13.148(9)	28.525(2)
c [Å]	12.803(9)	7.4952(6)
α [°]	90	90
β [°]	99.732(17)	101.268(2)
γ [°]	90	90
V [Å^3]	1910(2)	3815.1(5)
F(000)	1052	2056
μ [cm^{-1}]	1.026	8.296
ρ [g cm^{-3}]	1.818	1.773
θ range [°]	2.2-19.0	2.5-66.4
	-10<h<10	-21<h<21
h, k, l ranges	-11<k<11	-33<k<28
	-11<l<11	-8<l<8
Tot., indep., obs. [I_o>2σ(I_o)] refl.	10054, 1528, 1185	49544, 6593, 4081
R_{int}, R_σ	0.167, 0.094	0.226, 0.138
Param., restr.	139, 5	560, 9
Indep. refl. R1	0.161[a]	0.126
Obs. refl. R1	0.134[a]	0.075
wR2	0.306[a]	0.215
GoF	1.324	1.010
Highest peak [e Å^{-3}]	1.67	1.32
Deepest hole [e Å^{-3}]	-1.01	-1.28
CCDC number	2044056	2044057

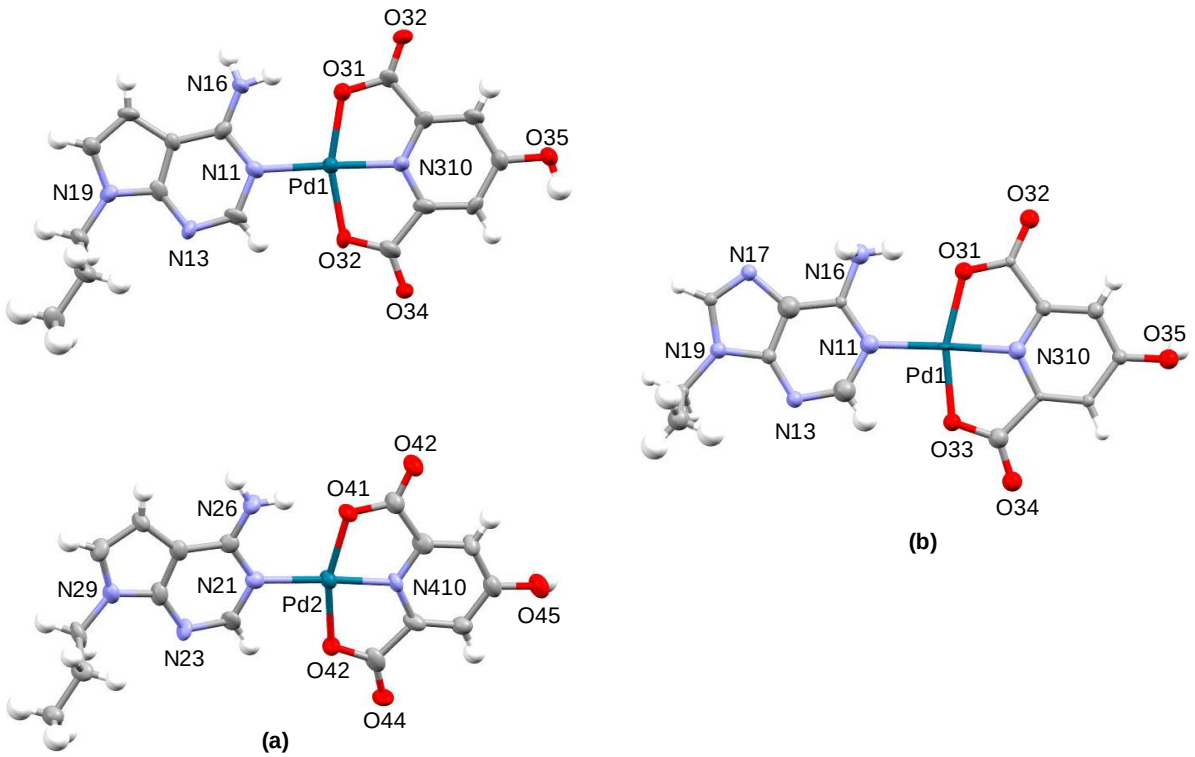

Figure S5. Ortep drawing (50% probability level) of the molecular structure of complex (a) **[1Pd(*N1*-X)]** and (b) **[1Pd(*N1*-A)]**, with the labels used throughout the paper. Atom colour code: carbon, grey; hydrogen, white; nitrogen, light blue; oxygen, red; palladium, cyan. The solvent molecules have been omitted for the sake of clarity.

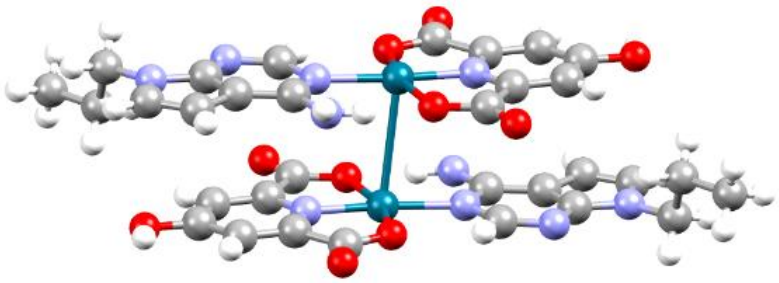

Figure S6. Molecular structure of the complex **[1Pd(N1-X)]** displaying the stacking interactions between the Cheld ligand and the **X** base. The metallophilic Pd···Pd interactions (3.190(1)Å) is represented by a solid cyan line.

Table S2. Comparison of relevant bond distances (Å) and Cheld/base interplanar angles (deg) in the **[1Pd(*N1*-X)]** and **[1Pd(*N1*-A)]** complexes. For the atom labels, see Figure S5.

	[1Pd(*N1*-X)]	**[1Pd(*N1*-A)]**
Pd1-N11, Pd2-N21	2.075(9), 2.073(9)	2.04(2)
Pd1-N310, Pd2-N410	1.937(9), 1.912(9)	1.91(2)
Pd-O31, Pd-O41	2.053(6), 2.050(7)	2.06(2)
Pd-O33, Pd-O43	2.051(7), 2.028(7)	2.035(19)
N16-O31, N26-O41	2.789(12), 2.768(10)	2.84(3)
Interplanar angle	3.0(4), 2.2(4)	1.3(11)

POWDER X-RAY DIFFRACTION

A powdered sample (~50 mg) of **[1Pd(A)]** was deposited in the cavity of a silicon free-background sample-holder 0.2 mm deep (Assing S.r.l., Monterotondo, Italy). The powder X-ray diffraction (PXRD) data acquisition was carried out with a Bruker AXS D8 Advance vertical-scan θ:θ diffractometer, equipped with a sealed X-ray tube (Cu Kα, λ = 1.5418 Å), a Bruker Lynxeye linear position-sensitive detector, a filter of nickel in the diffracted beam and the following optical components: primary beam Soller slits (aperture 2.5°), fixed divergence slit (aperture 0.5°), anti-scatter slit (aperture 8 mm). The generator was set at 40 kV and 40 mA. The data were acquired in the 2θ range 5.0-50.0°, with steps of 0.02° and time *per* step of 0.2 s. A whole powder pattern refinement with the Le Bail method, employing the unit cell parameters of **[1Pd(*N*1-A)]**, enabled us to assess that the bulk powder only contains the phase **[1Pd(*N*1-A)]** (i.e. **[1Pd(*N*1-A)]** is representative of the bulk) (Figure S7).

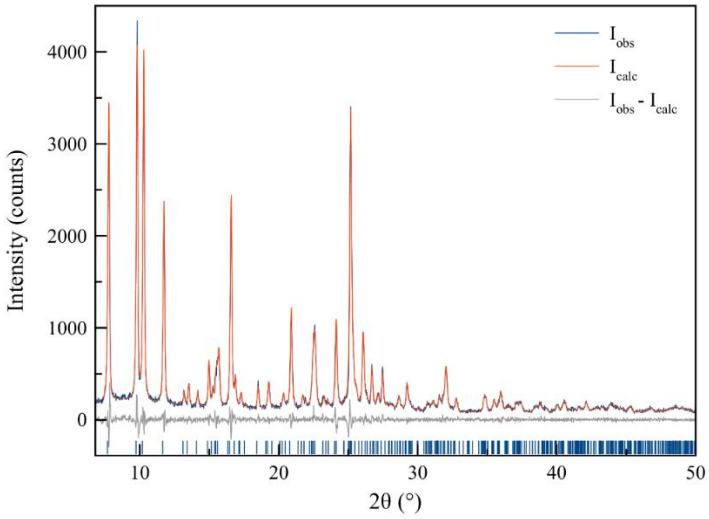

Figure S7. Graphical representation of the final stage of the whole powder pattern refinement carried out with the Le Bail method on bulk **[1Pd(A)]**. Experimental, calculated, difference patterns: blue, red, gray traces, respectively. The positions of the Bragg reflections maxima are indicated with blue thicks at the bottom. R_p = 0.062, R_{wp} = 0.082.

UV-VIS SPECTROSCOPY

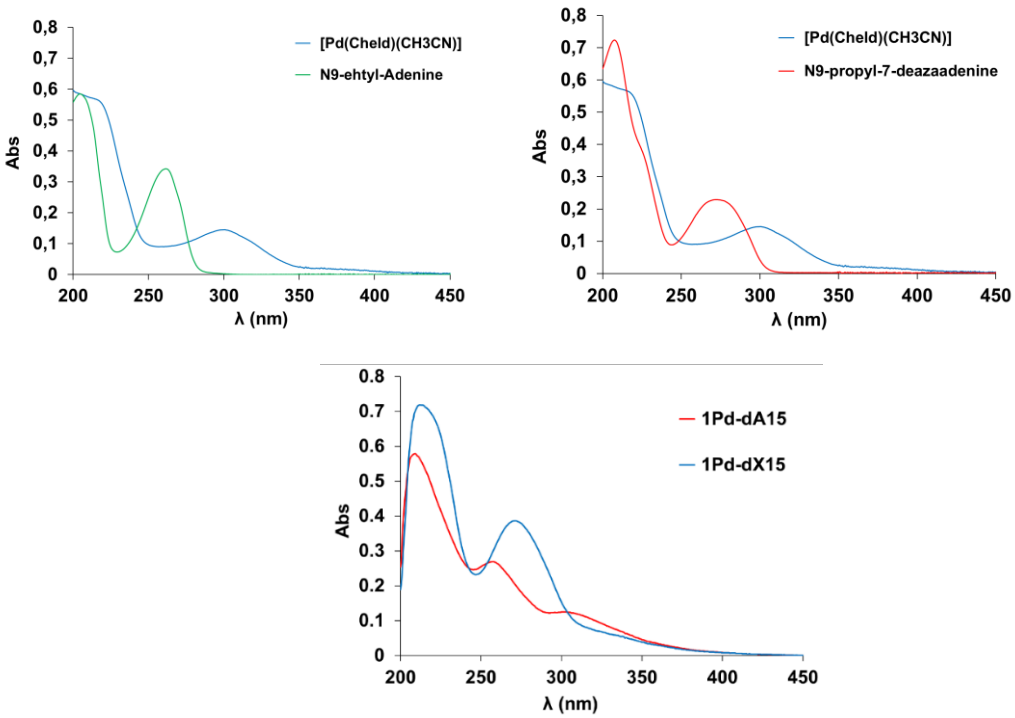

Figure S8. UV-Vis spectra for the complex **1Pd_CH$_3$CN**, 9-ethyl-adenine (**A**), 9-propyl-7-deazaadenine (**X**) (0.025M), **1Pd-dA$_{15}$** and **1Pd-dX$_{15}$** (ssDNA 2µM, **1Pd** 60 µM, 100 mM $NaClO_4$, 5mM MOPS pH 6.8) employed in this work.

CIRCULAR DICHROISM

The **1Pd-dA$_{15}$** and **1Pd-dX$_{15}$** samples for the CD spectroscopy titration series keeping the oligonucleotide concentration constant were undertaken by dissolving 2 µM of oligonucleotide in 700 µL of water containing 5 mM buffer and 100 mM $NaClO_4$. To this solution, the aliquotes from a stock solution of **1Pd** (500 µM, DMF) were added, along with comparable aliquotes from an oligonucleotide stock solution (4 µM DNA, 10 mM buffer, 200 mM $NaClO_4$) to keep the concentration constant. At the end of the titration experiments, when 4 equivalents of **1Pd** were present in the solution, the final solution had 24% of DMF.

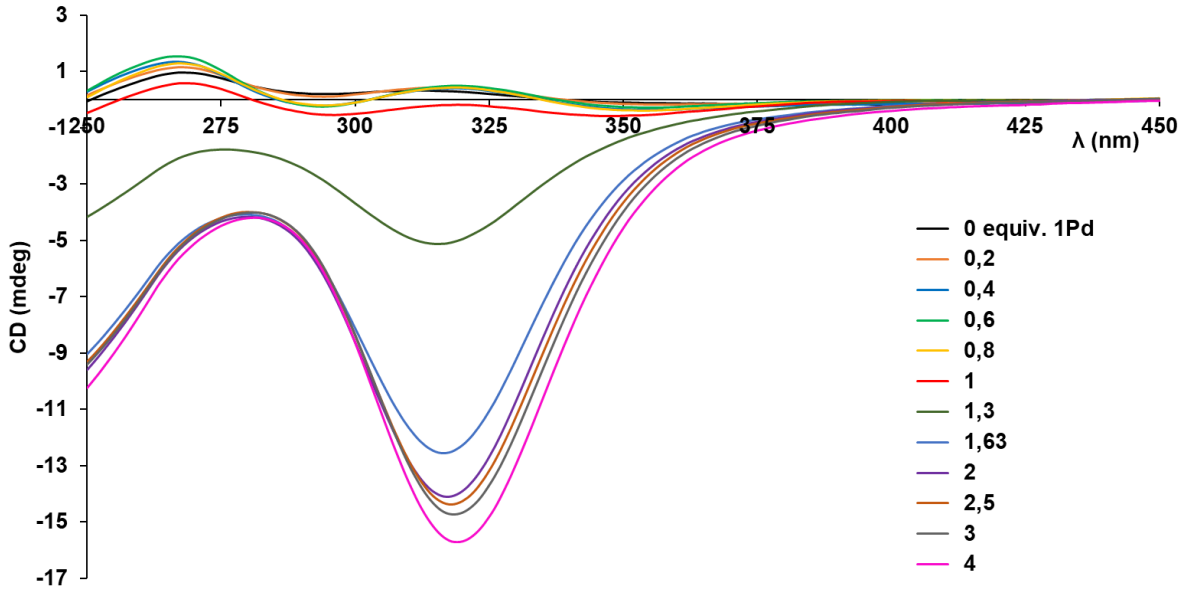

Figure S9. CD spectra at pH 4.3 for the titration experiment performed on **dA$_{15}$** upon the addition of a controlled amount of **1Pd_CH$_3$CN**. Conditions: 2µM **dA$_{15}$**, 0 → 60 µM **1Pd_CH$_3$CN** (in DMF), 100 mM $NaClO_4$, 5 mM acetate buffer pH 4.3. Note: 1 equivalent means **1Pd_CH$_3$CN** per adenine base (**A**).

MASS SPECTROMETRY FOR 1Pd-DNA

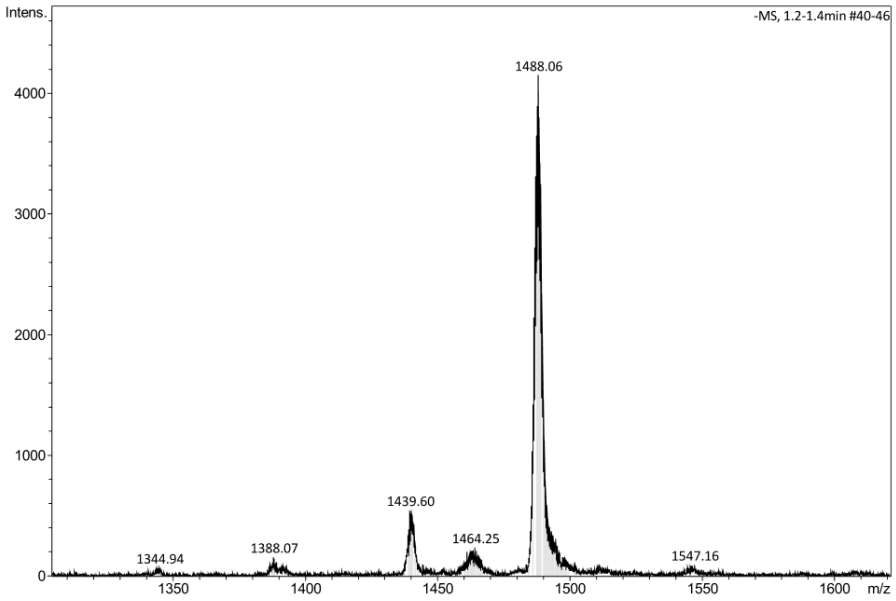

Figure S10. ESI-MS spectrum (Z = -6) of **dX_{15}** incubated with 15 equivalents of **1Pd_CH_3CN**.

Table S3. Theoretical mass ratio corresponding to the different states of charge (Z) of the **dX_{15}+1Pd** system**.**

Number of **1Pd** moieties coordinated to **dX_{15}**

Charge (Z)	0	9	10	11	12	13	14	15	16
-4	1154,3	1801,3	1873,1	1945,0	2016,9	2088,8	2160,7	2232,5	2304,4
-5	923,3	1440,8	1498,3	1555,8	1613,3	1670,8	1728,3	1785,8	1843,3
-6	769,2	1200,5	1248,4	1296,3	1344,3	1392,2	1440,1	1488,0	1535,9

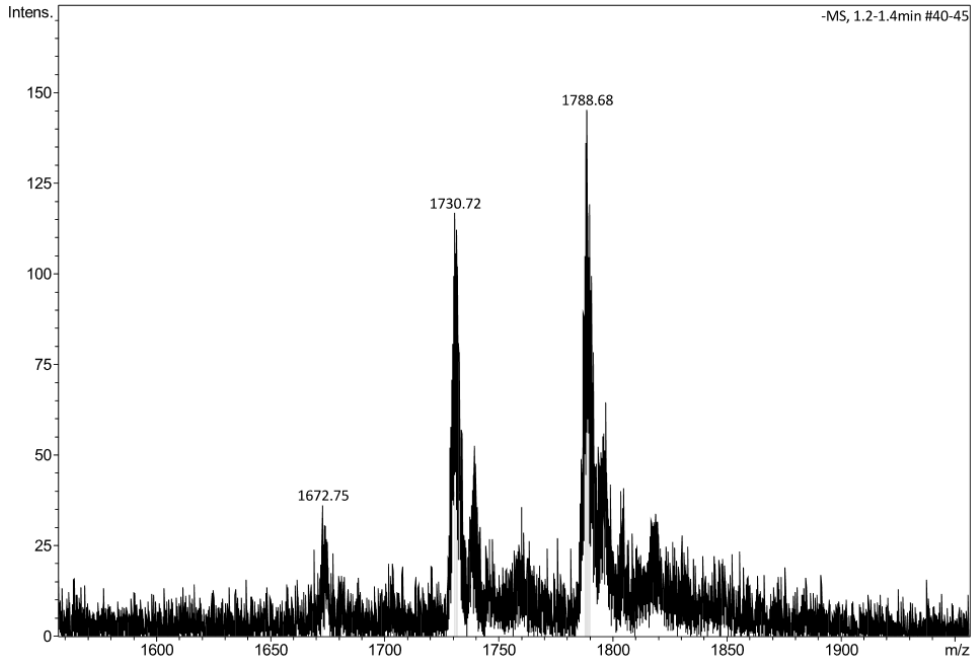

Figure S11. ESI-MS spectrum (Z = -5) of **dA_{15}** incubated with 15 equivalents of **1Pd_CH_3CN**.

Table S4. Theoretical mass ratio corresponding to the different states of charge (Z) of the **dA_{15}+1Pd** system.

Number of **1Pd** moieties coordinated to **dA_{15}**

Charge (Z)	0	12	13	14	15	16
-4	1158	2020,6	2092,5	2164,4	2236,2	2308,1
-5	926,2	1616,3	1673,8	1731,3	1788,8	1846,3
-6	771,6967	1346,7	1394,7	1442,6	1490,5	1538,4

SAXS MEASUREMENTS

The measurements on the **dA$_{15}$** and **1Pd-dA$_{15}$** complexes were performed on an Anton-Paar SAXSess instrument using Cu-Kα radiation (1.54 Å) and line collimation. The instrument was equipped with a 2-D image plate for data collection in the q = 0.018-2.5 Å^{-1} range. The lower q resolution is limited by the beam attenuator. Approximately 1 mmolar (**dA$_{15}$**, **1Pd** = 15 mmolar in DMF) solutions were measured in 1.5 mm glass capillaries (Hampton Research). Scattering data of neat solvent was collected for background subtraction. Scattering was measured for 30 min for every experiment. We used SAXSQUANT software for data collection and treatment (normalization, primary beam removal, background subtraction, desmearing, and smoothing to remove the extra noise created by the desmearing routine). The measurements on the **dA$_{12}$** and **1Pd-dA$_{12}$** complexes were performed on an Anton-Paar SAXSpoint 2.0 equipped with a 50W Cu-Kα micro-source and 2 sets of scatter-less slits for a tunable beam size, in this case giving a q range of 0.006-0.6 Å^{-} with a sample to detector distance of 575 mm. The data collection was performed on a noise-free Eiger R 1M (Dectris Ltd., Baden-Daettwil, Switzerland) detector. Solutions were measured for 30 minutes in a 1mm quartz capillary. Data reduction was carried out using the SAXSanalysis software (Anton-Paar, Graz, Austria). The curve fitting (cylindrical models) was carried out utilizing IRENA macros within the IgorPro 8 (Wavemetrics) software.[8] To simulate the scattering data from the **1Pd-dA$_{15}$** and **1Pd-dA$_{12}$** models, we used the SolX software.[9]

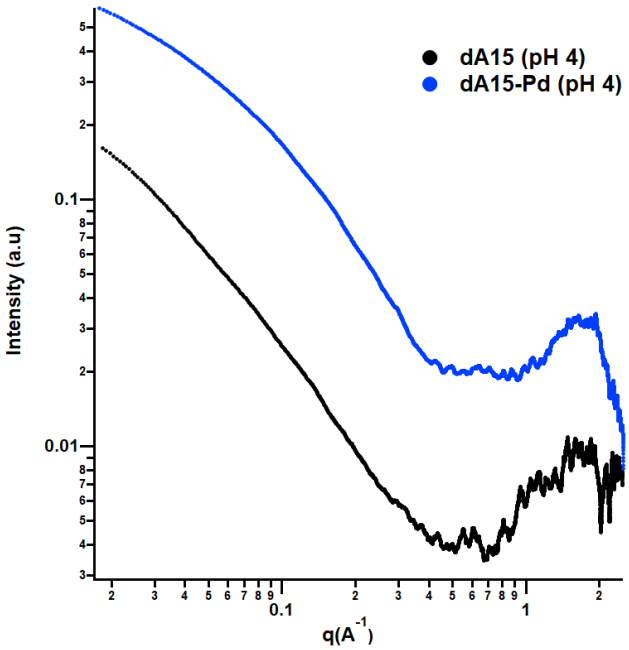

Figure S12. SAXS data for **dA$_{15}$** (black) and **1Pd-dA$_{15}$** (blue). Conditions: 1 mM **dA$_{15}$**, 15 mM **1Pd**, 5 mM Acetate buffer pH 4.3.

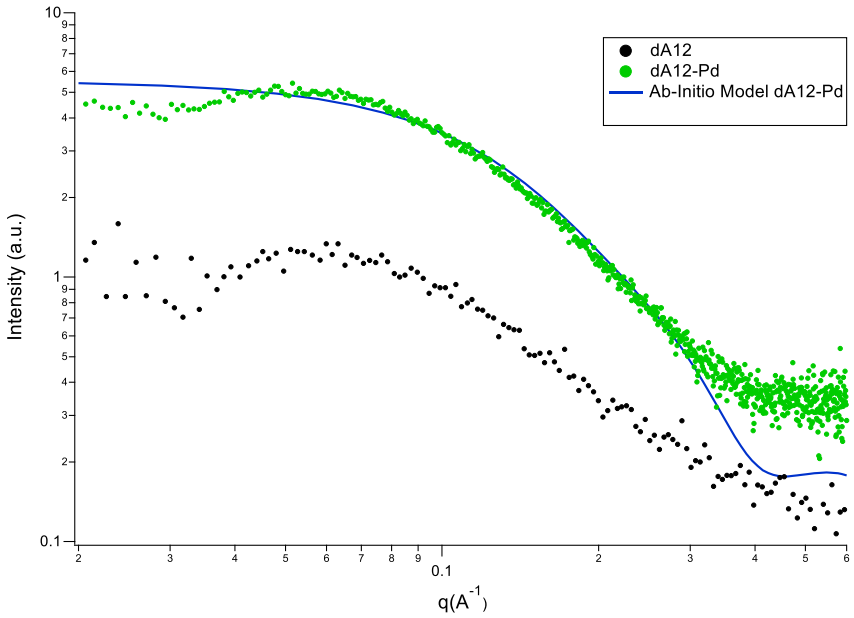

Figure S13. SAXS data for **dA$_{12}$** (black) and **1Pd-dA$_{12}$** (green). Conditions: 1mM **dA$_{12}$**, 15 mM **1Pd**, 5mM MOPS buffer pH 6.8. The fit (blue line) has been calculated from the geometry optimized model obtained from an ab-initio calculation (see below). (Note: the descent in intensity in both experimental curves between q~0.02 - 0.04 Å^{-1} is an instrumental artifact due to the position of the beam attenuator).

MOLECULAR MODELLING

Theoretical models were built from scratch using the Avogadro software.[10] Sodium counterions were added to the phosphate groups, thus resulting in neutral model systems. Besides, 95 water molecules were included in the model system to account for the solvent effect. After a partial geometry optimization of these molecules, using semiempirical methods (PM3) within the ORCA 4.2.1 computational program,[11,12] a suitable geometry was obtained for further full optimization by quantum mechanics ab initio calculations using the HF-3c method.[13] The latter method included the so-called MINIX basis set and a correction of the basis set superposition error (BSSE) using the geometrical counterpoise gCP correction algorithm,[14] as well as the atom-pairwise London dispersion energy from the D3 dispersion correction scheme with the Becke-Johnson damping scheme (D3BJ).[15–17]

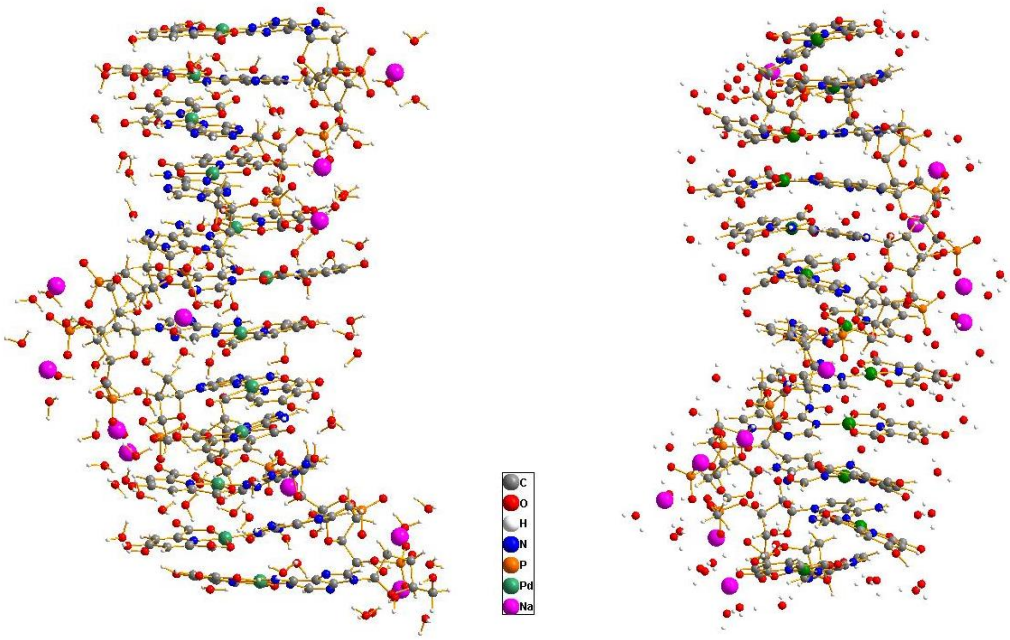

Figure S14. Ab-initio (HF-3C) geometry-optimized structures for **1Pd-dA$_{12}$** (left) and **1Pd-dX$_{12}$** (right).

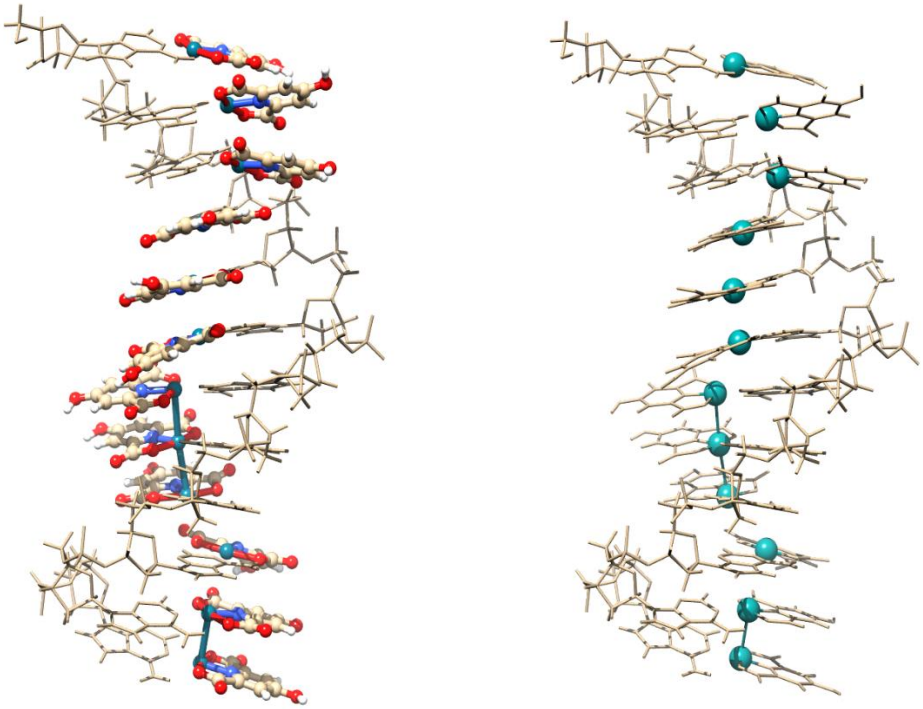

Figure S15. Two different representations of the geometry optimized structure of **1Pd-dX$_{12}$** showing the organization of the **1Pd** complex lengthways the structure (left) and the formation of a continuous 1D array of Pd^{II} ions (right). Sodium cations and water molecules have been omitted for clarity. Atom colour code: carbon, grey; hydrogen, white; nitrogen, light blue; oxygen, red; palladium, cyan. **dX$_{12}$**, tan (in left and right figure); *Cheld*, tan (in right figure). The metallophilic Pd···Pd interactions (3.091-3.109Å) is represented by a solid cyan line.

Table S5. Comparison of the relevant bond distance ranges (Å) in **[1Pd(*N1*-X)]** and **[1Pd(*N1*-A)]** base pairs found in the calculated structures of **1Pd-dX$_{12}$** and **1Pd-dA$_{12}$**, respectively.

Distance (Å)	1Pd-dX$_{12}$	1Pd-dA$_{12}$
Pd-N1	2.024-2.057	2.031 - 2.074
Pd-N10	1.932-1.941	1.929 – 1.942
Pd-O1	1.993-2.045	1.982 – 2.038
Pd-O3	1.977-2.011	1.986 – 2.012
N6-O1	2.678-2.774	2.665 – 2.889
Pd-Pd[1]	3.819-3.109	3.447 – 3.765

[1] The Pd ions at each end of the structure have not been considered due to the border effect.

Table S6. Cartesian coordinates (Å) for geometry-optimized (HF-3c, MINIX basis set) **1Pd-dA$_{12}$** structure (883atoms).

C	-10.87164485112949	4.04079424859873	-0.22450311010417
C	-9.87947578648696	5.08224248126979	-0.80605252012244
C	-10.36828919134629	6.37500921979557	-0.08863105231094
C	-11.90417263012315	6.06574355761274	0.17056226731597
C	-12.82267177461353	7.03647142149909	-0.64923577513078
O	-12.12988996680209	4.70840663350190	-0.23698263054096
H	-10.55884054560695	3.82064427921792	0.80382025450203
H	-9.99983408829843	5.17242439507365	-1.88044086102303
H	-8.85203586210632	4.84747328975537	-0.55815461640883
H	-10.28480844917380	7.24224805145614	-0.75121230028966
H	-12.11145494205845	6.17399006787844	1.24181399161142
H	-12.74351581585318	8.02445025049705	-0.18513250075607
H	-13.86274855754226	6.70505047985484	-0.54280136848184
O	-9.63610794687063	6.65193488267879	1.07063896085736
N	-9.61919200770279	-0.73482447862464	0.59727767910850
C	-9.87071319562337	0.30348852202676	1.44210269429666
N	-10.37214908471919	1.47016545746310	1.12008627134123
C	-10.56245260191051	1.61398511578127	-0.21535704147581
C	-10.40190663074058	0.62458539188221	-1.16631516505888
C	-9.94956703234063	-0.65825827503533	-0.71380465311949
N	-9.84960958967628	-1.70721827618757	-1.51695443451322
N	-10.66091814652625	1.15958231021490	-2.43737543446450
C	-10.93857370619712	2.41117948497698	-2.25241108098506
N	-10.90190725420898	2.75726731638000	-0.88779743551902
H	-9.61417703408605	0.10781107946525	2.48000050610591
H	-9.48536282696393	-2.58202989869553	-1.15745804912076
H	-10.13488783232638	-1.62927149342879	-2.51044768570721
H	-11.19401023476832	3.14357449635364	-3.01473627232469
O	-9.04705364991625	4.52422085981252	2.04512813299541
C	-6.27722536102213	2.35621933996976	0.47150025493947
C	-5.94189582758727	3.87086893810073	0.51371726524865
C	-6.20938521777790	4.21678850215304	2.00688897456452
C	-7.16786306721951	3.04934013518329	2.47903605679134

OLIGONUCLEOTIDE SYNTHESIS

Oligonucleotides **dA_{15}** and **dA_{12}** were purchased from Sigma-Aldrich with HPLC purification. The synthesis of oligonucleotide **dX_{15}** was performed in an Applied Biosystems 3400 DNA synthesizer following standard protocols and using the appropriated phosphoramidites purchased from Glen Research, VA, USA. The cleavage and deprotection of the oligonucleotide involved treatment with aqueous ammonium hydroxide 30% for 16 h at 55 °C. The purification was performed by RP-HPLC using a Thermo Scientific P4000 instrument in association with a Spectra System UV8000 detector and a Phenomenex Clarity 3µ column (Figure Sa). After purification, the oligonucleotide was desalted by gel filtration using a Shepadex G-25 column. The desalted oligonucleotide was characterized by MALDI-TOF mass spectrometry on a Bruker Autoflex spectrometer using a 3-hydropicolinic acid/ammonium citrate matrix (Calcd. for **dX_{15}** $[C_{165}H_{196}N_{60}O_{73}P_{14}+H]^+$): 4618.97 Da, found: 4620.06 Da) (Figure S2).

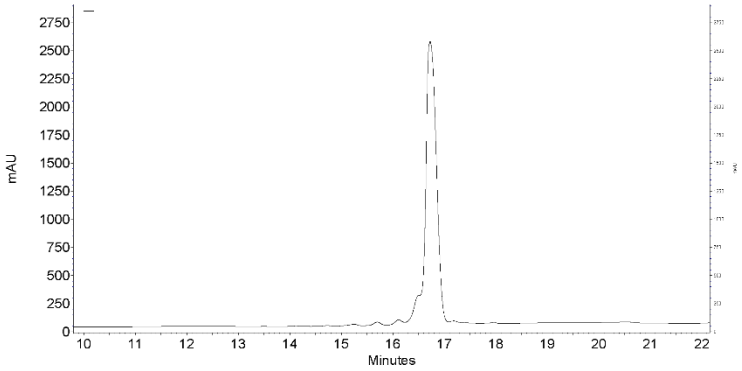

Figure S14. HPLC trace for oligonucleotide **dX_{15}**. The solvent gradient was made up of solvent A (10% acetonitrile in water containing TEAA buffer pH 6.5) and solvent B (65 % acetonitrile in water containing TEAA buffer pH 6.5), increasing from 0% B to 35% B over 25 min and returning to 100% A at 30 min.

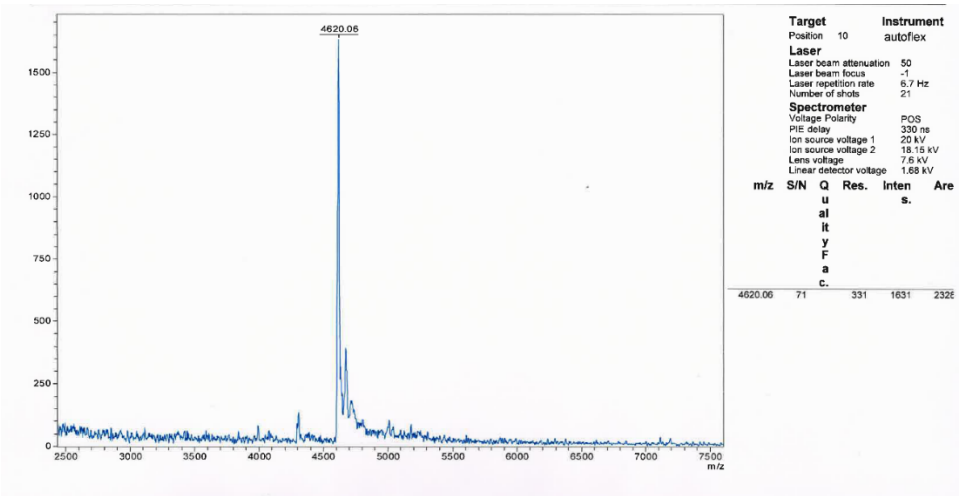

Figure S15. MALDI-TOF spectrum for oligonucleotide **dX_{15}**. Calcd. for **dX_{15}** $[C_{165}H_{196}N_{60}O_{73}P_{14}+H]^+$): 4618.97 Da, found: 4620.06 Da.

REFERENCES

(1) Nowick, J. S.; Chen, J. S.; Noronha, G. Molecular Recognition in Micelles: The Roles of Hydrogen Bonding and Hydrophobicity in Adenine-Thymine Base-Pairing in SDS Micelles. *J. Am. Chem. Soc.* **1993**, *115* (17), 7636–7644.

(2) Dominguez-Martin, A.; Galli, S.; Dobado, J. A.; Santamaría-Díaz, N.; Pérez-Romero, A.; Galindo, M. A. Comparative Structural Study of Metal-Mediated Base Pairs Formed Outside and inside DNA Molecules. *Inorg. Chem.* **2020**, *59* (13), 9325–9338.

(3) Mihály, T.; Añorbe, M. G.; Albertí, F. M.; Sanz Miguel, P. J.; Lippert, B. Multiple Metal Binding to the 9-Methyladenine Model Nucleobase Involving N1, N6, and N7: Discrete Di- and Trinuclear Species with Different Combinations of Monofunctional PdII and PtII Entities. *Inorg. Chem.* **2012**, *51* (19), 10437–10446.

(4) SAINT v6.36A. Bruker AXS Inc.; Madison, WI, USA: 2002.

(5) Sheldrick, G. M. SADABS 2016/2. Program for Empirical Absorption Correction of Area Detector Data. University of Göttingen, Germany. 2016.

(6) Sheldrick, G. M. SHELXS-97 and SHELXL-97, Program for Crystal Structure Solution and Refinement. *Univ. Gottingen, Gottingen, 1997*.

(7) Sheldrick, G. M. Crystal Structure Refinement with SHELXL. *Acta Crystallogr. Sect. C Struct. Chem.* **2015**, *71* (1), 3–8.

(8) Ilavsky, J.; Jemian, P. R. Irena: Tool Suite for Modeling and Analysis of Small-Angle Scattering. *J. Appl. Crystallogr.* **2009**, *42* (2), 347–353.

(9) Zuo, X.; Cui, G.; Merz, K. M.; Zhang, L.; Lewis, F. D.; Tiede, D. M. X-Ray Diffraction "Fingerprinting" of DNA Structure in Solution for Quantitative Evaluation of Molecular Dynamics Simulation. *Proc. Natl. Acad. Sci. U. S. A.* **2006**, *103* (10), 3534–3539.

(10) Hanwell, M. D.; Curtis, D. E.; Lonie, D. C.; Vandermeerschd, T.; Zurek, E.; Hutchison, G. R. Avogadro: An Advanced Semantic Chemical Editor, Visualization, and Analysis Platform. *J. Cheminform.* **2012**, *4* (8), 17.

(11) Neese, F. The ORCA Program System. *Wiley Interdiscip. Rev. Comput. Mol. Sci.* **2012**, *2* (1), 73–78.

(12) Neese, F. Software Update: The ORCA Program System, Version 4.0. *Wiley Interdiscip. Rev. Comput. Mol. Sci.* **2018**, *8* (1), e1327.

(13) Sure, R.; Grimme, S. Corrected Small Basis Set Hartree-Fock Method for Large Systems. *J. Comput. Chem.* **2013**, *34* (19), 1672–1685.

(14) Kruse, H.; Grimme, S. A Geometrical Correction for the Inter- and Intra-Molecular Basis Set Superposition Error in Hartree-Fock and Density Functional Theory Calculations for Large Systems. *J. Chem. Phys.* **2012**, *136* (15), 154101.

(15) Becke, A. D.; Johnson, E. R. A Density-Functional Model of the Dispersion Interaction. *J. Chem. Phys.* **2005**, *123* (15), 154101..

(16) Johnson, E. R.; Becke, A. D. A Post-Hartree–Fock Model of Intermolecular Interactions. *J. Chem. Phys.* **2005**, *123* (2), 024101.

(17) Johnson, E. R.; Becke, A. D. A Post-Hartree-Fock Model of Intermolecular Interactions: Inclusion of Higher-Order Corrections. *J. Chem. Phys.* **2006**, *124* (17), 174104.

Zitierweise: *Angew. Chem. Int. Ed.* **2024**, *63*, e202400261
doi.org/10.1002/anie.202400261

Supramolecular Chemistry

Selective Formation of Pd-DNA Hybrids Using Tailored Palladium-Mediated Base Pairs: Towards Heteroleptic Pd-DNA Systems

*Antonio Pérez-Romero, Mario Cano-Muñoz, Carmen López-Chamorro, Francisco Conejero-Lara, Oscar Palacios, José A. Dobado, and Miguel A. Galindo**

Dedicated to Professor Andrew Houlton

Abstract: The formation of highly organized metal-DNA structures has significant implications in bioinorganic chemistry, molecular biology and material science due to their unique properties and potential applications. In this study, we report on the conversion of single-stranded polydeoxycytidine (dC_{15}) into a Pd-DNA supramolecular structure using the [Pd(Aqa)] complex (Aqa = 8-amino-4-hydroxyquinoline-2-carboxylic acid) through a self-assembly process. The resulting Pd-DNA assembly closely resembles a natural double helix, with continuous [Pd(Aqa)(C)] (C = cytosine) units serving as palladium-mediated base pairs, forming interbase hydrogen bonds and intrastrand stacking interactions. Notably, the design of the [Pd(Aqa)] complex favours the interaction with cytosine, distinguishing it from our previously reported [Pd(Cheld)] complex (Cheld = chelidamic acid). This finding opens possibilities for creating heteroleptic Pd-DNA hybrids where different complexes specifically bind to nucleobases. We confirmed the Pd-DNA supramolecular structural assembly and selective binding of the complexes using NMR spectroscopy, circular dichroism, mass spectrometry, isothermal titration calorimetry, and DFT calculations.

Introduction

The integration of DNA into the fabrication of supramolecular assemblies has led to a groundbreaking era in the advancement of nanomaterials.[1–4] Notably, significant attention is focused on advancing metal-DNA systems, wherein the metal entities are precisely arranged along specific sequences. This precision aims to construct dynamic metal-DNA hybrids, gathering significant thought for their potential to stimulate diverse applications.[5–9] In this context, the possibility of scheduling specific sequences for rational self-assembly through base pairs recognition has made DNA an ideal candidate for building highly organized functional systems at the nanoscale. Complementary DNA strands (ds-DNA) are frequently employed for this task, but single-stranded DNA (ss-DNA) can also serve as a template to yield customized supramolecular systems.[10,11] In this scenario, the binding of molecules to ss-DNA has traditionally relied on intermolecular forces acting on the nucleobases or phosphate groups, thus facilitating the assembly of structures. In recent years, this field of research has witnessed remarkable advancements, resulting in noteworthy outcomes.[12] However, the arrangement of metal entities along ss-DNA has received comparatively less attention. Building upon prior knowledge, our research has explored a novel strategy for designing metal-DNA templated systems. We employed specifically designed Pd^{II}-coordination compounds endowed with a unique capability to bind nucleobases along ss-DNA through both coordinating bonds and Watson–Crick complementary hydrogen bonds.[13] While some previous studies focused on the interaction of Pd^{II}-coordination compounds with nucleobases at monomeric level[14–16] or at single-nucleotide gap in double helixes,[17] our strategy aims to precisely organize a continuous one-dimen-

[*] A. Pérez-Romero, C. López-Chamorro, Dr. M. A. Galindo
Departamento de Química Inorgánica. Unidad de Excelencia Química Aplicada a Biomedicina y Medioambiente. Facultad de Ciencias. Universidad de Granada
Avda Fuentenueva s/n, 18071 Granada (Spain)
E-mail: magalindo@ugr.es

Dr. M. Cano-Muñoz, Prof. Dr. F. Conejero-Lara
Departamento de Química Física, Instituto de Biotecnología y Unidad de Excelencia Química Aplicada a Biomedicina y Medioambiente. Facultad de Ciencias. Universidad de Granada
Avda Fuentenueva s/n, 18071 Granada (Spain)

Dr. O. Palacios
Departament de Química, Facultat de Ciències. Universitat Autònoma de Barcelona.
Campus Ballaterra s/n, 08193 Cerdanyola del Vallès, Barcelona (Spain)

Prof. Dr. J. A. Dobado
Grupo de Modelización y Diseño Molecular, Departamento de Química Orgánica. Facultad de Ciencias. Universidad de Granada.
Avda Fuentenueva s/n, 18071 Granada (Spain)

sional array of Pd^{II} ions and ligands along specific ss-DNA sequences. It is noteworthy that these ligands can be customized to create Pd^{II} complexes with tailored substituents, thereby enhancing their affinity for nucleobases and/or introducing enhanced functionalities. The inherent moderate strength of Pd^{II} coordination bonds ensures system stability while allowing for self-correction interactions, guiding the system towards a thermodynamically stable configuration.

We have previously shown that metal complex [Pd(Cheld)(CH_3CN)] (**Pd-Cheld**) (Cheld = chelidamic acid) self-assembles with a single-stranded polydeoxyadenosine (dA_{15}), resulting in the formation of a supramolecular Pd-DNA hybrid structure.[13] Our current research focuses on expanding this strategy to design and synthesize new metal complexes capable of recognizing other nucleobases in DNA sequences. Specifically, we are exploring competitive designs of metal complexes to selectively bind to specific bases, thereby paving the way for developing heteroleptic metal-DNA hybrids.

In this work, we report the synthesis and characterization of complex [Pd(Aqa)(DMSO)] (**Pd-Aqa**) (Aqa = 8-amino-4-hydroxyquinoline-2-carboxylic acid) and demonstrate its capability to bind to cytosine resulting in the formation of Pd-mediated base pair [Pd(Aqa)(Cyt)] (**Cyt-Pd-Aqa**) (Cyt = 1-methylcytosine). Furthermore, we demonstrate that these palladium-mediated base pairs can be prepared on a single-stranded 15mer deoxycytidine (**dC_{15}**) to yield a Pd-DNA helical supramolecular structure. This system comprises continuous **Cyt-Pd-Aqa** base pairs organized similarly to canonical base pairs in DNA double helix. Notably, the Pd^{II} ions are successfully accommodated throughout the double-stranded structure, forming a continuous one-dimensional (1D) metal array (Scheme 1). In addition, we performed competitive binding assays using circular dichroism (CD) titration experiments and isothermal titration calorimetry (ITC) measurements to demonstrate the preferential binding of **Pd-Aqa** to cytosine compared to **Pd-Cheld**. This strategy, using metal complexes complementary to bases, offers exciting possibilities for developing advanced metal-DNA supramolecular hybrids that can be personalized by selecting specific DNA sequences and complementary metal complexes, allowing for rational customization of their structure and properties.

Results and Discussion

The complex **Pd-Aqa** was synthesized in solution by reacting equimolar amounts of $Pd(NO_3)_2$ and the **Aqa** ligand. The formation of the complex was confirmed by ^1H NMR spectroscopy and ESI-MS spectrometry. The changes in the NMR (DMSO-D_6) spectrum provided a means to follow the formation of the complex (Supp. Info., Figure S1–S2). In the presence of increased amounts of Pd^{II} ions, the **Aqa** spectrum shifted downfield, indicating the interaction of the metal ions with the ligand. Upon adding one equivalent of Pd^{II} only signals for a distinct species were observed, with no signals for the free **Aqa** ligand, in agreement with the complete formation of **Pd-Aqa** complex. The solution was subjected to analysis using ESI-MS spectrometry (positive mode), showing a mass-to-charge ratio (m/z) peak of 386.9630 Da and providing clear evidence for the formation of the complex [Pd(Aqa)(DMSO)] + H^+ with a theoretical mass of 386.9635 Da (Supp. Info., Figure S3). This result also revealed the deprotonation of the amino group upon coordination of the Pd^{II} ions, resulting in the formation of a neutral **Pd-Aqa** complex.

The **Pd-Aqa** design was conceived to promote the formation of cytosine-complementary hydrogen bonds along with a central Pd-coordination bond with the cytosine-N3 atom. This strategic design aims to facilitate the formation of a stable Pd-mediated **Cyt-Pd-Aqa** base pair, mimicking the natural Watson–Crick arrangement (Scheme 2a). Consequently, we investigated the formation of **Cyt-Pd-Aqa** complex by following the reaction between **Pd-Aqa** and Cyt. The reaction was monitored using ^1H NMR spectroscopy by

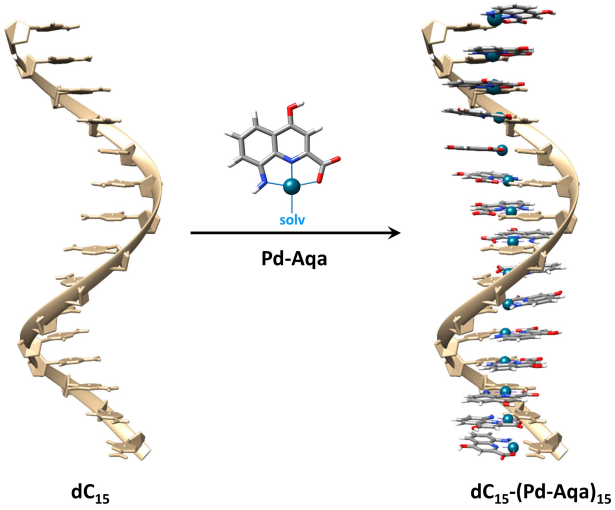

Scheme 1. Schematic representation of the self-assembly reaction between oligonucleotide **dC_{15}** and complex **Pd-Aqa**, outlining the proposed structure for the Pd-DNA hybrids.

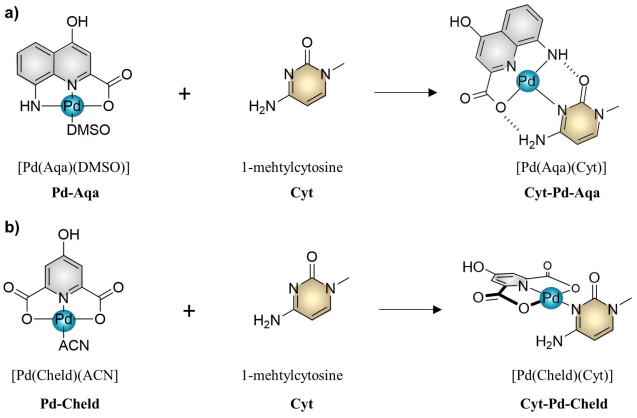

Scheme 2. Schematic representation of the formation of palladium-mediated base pairs a) [Pd(Aqa)(Cyt)] (**Cyt-Pd-Aqa**) and b) [Pd(Cheld)-(Cyt)] (**Cyt-Pd-Cheld**). (DMSO, dimethylsulfoxide; ACN, acetonitrile.)

adding controlled amounts of **Pd-Aqa** to Cyt (Supp. Info., Figure S4–S5).

The NMR (DMSO-D_6) spectra demonstrated that the Cyt signals gradually vanished while a new set emerged when **Pd-Aqa** was present. Interestingly, at equimolar quantities, the spectrum revealed the splitting of the signals, indicating the formation of two different molecular species. This was significantly evident from the observation of two different doublets for the Cyt-H5 proton at 5.97 and 5.87 ppm, and two singlets for the Aqa-H3 proton at 7.10 and 7.07 ppm. Additionally, new peaks emerged at 9.38, 8.65, 8.59, and 8.15 ppm, differing from the spectra of the free molecules. To gain further insights into these findings, we conducted NH-HSQC NMR experiment and H NMR at variable temperatures. The HSQC NMR experiment ([D_6]DMSO) facilitated the assignment of amino group hydrogen peaks, revealing that the peaks at 9.38 and 8.15 ppm can be associated with one amino group, while those at 8.65 and 8.59 ppm correspond to a different one (Supp. Info., Figure S6). The latter can be attributed to the amino group of a non-coplanar **Cyt-Pd-Aqa** arrangement formed in a smaller proportion. Similar findings were observed for the amino protons in the non-coplanar complex [Pd(Cheld)(Cyt)] (**Cyt-Pd-Cheld**), as described below. The splitting and downshift of this amino group are explained by the restricted rotation of the C-NH_2 bond upon Pd-binding at the Cyt-N3 atom. In contrast, the signals from the other amino group may be attributed to a more prevalent co-planar **Cyt-Pd-Aqa** arrangement, given their distinct separation at 9.38 and 8.15 ppm, respectively. This observation suggests the formation of a hydrogen bond with the carboxylic group of the Aqa ligand, leading to the subsequent downshift of one of the protons (at 9.38 ppm). The ^{1}H NMR spectra at variable temperatures provided additional evidence of the variable structural arrangement of the complex (Supp. Info., Figure S7). As the temperature increased, the spectrum gradually simplified, and the signals related to the amino proton groups shifted and converged into broader signals, disappearing from the downfield region at high temperatures. Remarkably, the original NMR spectra reappeared after cooling the sample back to room temperature. This solution behaviour can be explained by the varied configurations **Cyt-Pd-Aqa** can adopt. The organizational diversity arises from the rotational dynamics of the (Cyt)N3-Pd bond, a process influenced by the presence of intramolecular hydrogen bonds between the keto and amino groups of cytosine and Aqa unit. This situation prompts the **Cyt-Pd-Aqa** to adopt two conformations, including a more stable co-planar configuration stabilized by the formation of hydrogen bonds. However, the system also allows deviating from this coplanarity, leading to an equilibrium between conformations, as revealed by the NMR experiments. To date, our attempts to obtain crystals of **Cyt-Pd-Aqa** suitable for X-ray diffraction analysis have been unsuccessful. Alternatively, we employed density functional theory (DFT) calculations as an alternative approach to studying the **Cyt-Pd-Aqa** molecular arrangement. The DFT studies revealed the formation of a co-planar arrangement between the units, which was stabilized by forming intramolecular hydrogen bonds (Aqa-O···H_2N-Cyt, d_{O-H} 1.606 Å, $<_{O-H-N}$ 158° ; Aqa-NH···O-Cyt, d_{H-O} 2.108 Å, $<_{N-H-O}$ 118.3°) (Figure 1a). This co-planar configuration remained unchanged regardless of the initial dihedral angle between the units. Additionally, single-point structures resulting from incremental rotations of the cytosine ligand in 10° steps were calculated. The outcomes consistently demonstrated that the **Cyt-Pd-Aqa** complex achieves maximum stability at a dihedral angle of 0 degrees, emphasizing a clear preference for a co-planar conformation (Supp. Info. Figure S17).

Further investigations using ESI-MS spectrometry unequivocally confirm the formation of the **Cyt-Pd-Aqa** base pair, as indicated by the m/z peak found at 433.0081 Da corresponding to the $[Pd(Aqa)(Cyt)]^+$ complex (Supp. Info. Figure S8).

After preparing and studying the formation of **Cyt-Pd-Aqa** base pairs, we investigated the formation of a supramolecular Pd-DNA system. Toward this purpose, we performed a self-assembly reaction between the pentadecamer homopolymer **dC_{15}** and complex **Pd-Aqa**. The reaction was initially followed by circular dichroism titration measurements.

The CD spectrum of free **dC_{15}** exhibited a pattern with an intense positive and negative Cotton effect centred at 288 nm and 265 nm, respectively (Figure 2). Upon the controlled addition of **Pd-Aqa**, the CD profile underwent significant changes. The intensity of the original bands decreased and shifted, while a new induced band (ICD) emerged at 375 nm corresponding to the absorption of the **Cyt-Pd-Aqa** complex (Supp. Info., Figure S10), thus indicating the binding of **Pd-Aqa** to the oligonucleotide. The alteration in the CD profile stabilizes with a slight excess of more than one equivalent of **Pd-Aqa** per cytosine base, with a substantial transformation occurring for the 290 nm band when reaching an equivalence of one complex per cytosine base (Figure 2, insets). Notably, the bands maintained a similar sinusoidal shape throughout the experiment despite intensity variations. These results provide strong evidence

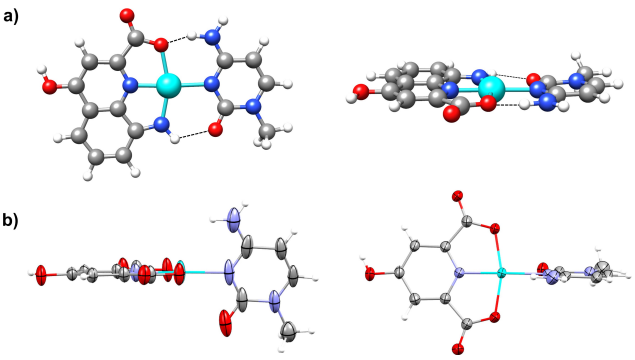

Figure 1. a) Two views for the DFT geometry-optimized structure of [Pd(Aqa)(Cyt)] (**Cyt-Pd-Aqa**). b) Two views for the X-ray structure of [Pd(Cheld)(Cyt)] (**Cyt-Pd-Cheld**), with atoms represented by ellipsoids.[18] Atom colour code: grey, carbon; white, hydrogen; blue, nitrogen; red, oxygen; cyan, palladium. Hydrogen bonds are represented by black dashed lines.

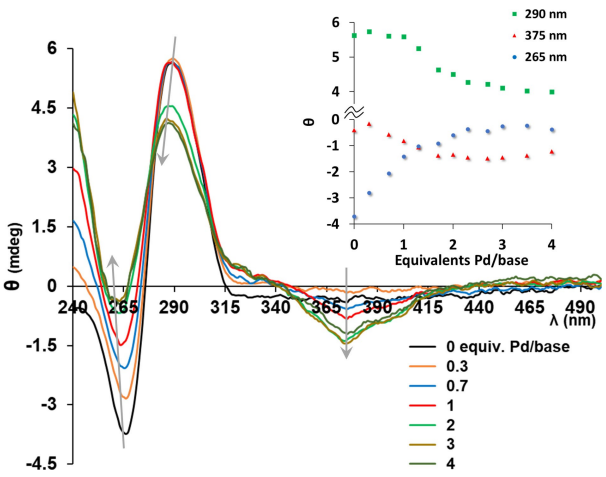

Figure 2. CD titration spectra of **dC_{15}** upon adding controlled amounts of **Pd-Aqa**. Insets: Ellipticity changes at 265, 290, and 375 nm as a function of equivalents of Pd-Aqa added. Conditions: 2 μM **dC_{15}**, 0 to 120 μM complex (in DMSO), 100 mM $NaClO_4$, 5 mM MOPS buffer pH 6.8. Note: 1 equivalent means one Pd^{II} complex per base.

for the formation of a helical **dC_{15}-(Pd-Aqa)$_{15}$** hybrid structure that closely resembles a DNA double helix. The structure is characterized by a continuous stack of **Cyt-Pd-Aqa** base pairs, reminiscent of the previously observed with **dA_{15}-(Pd-Cheld)$_{15}$** base pairs.[13] The similarity in the structural features observed in both cases suggests a consistent and reproducible self-assembly process involving cytosine-complementary **Pd-Aqa** complexes and **dC_{15}** fragment, yielding a well-defined **dC_{15}-(Pd-Aqa)$_{15}$** supramolecular structure.

ESI-MS analysis further supports the formation of the proposed structure, as evidenced by the mass spectra obtained using **dC_{15}** and a two-fold excess of the complex per base. The spectra reveal the presence of the **dC_{15}-(Pd-Aqa)$_{15}$** hybrid, alongside the occurrence of other hybrids containing a slight deficit or excess of bound complexes (Figure 3 and Supp. Info. Table S2). The presence of additional bound complexes can be attributed to the reasonable binding of palladium complexes to the cytosine amino group, as elucidated in previous studies.[19,20]

Considering all previous experimental data, we conducted density functional theory (DFT) calculations on a

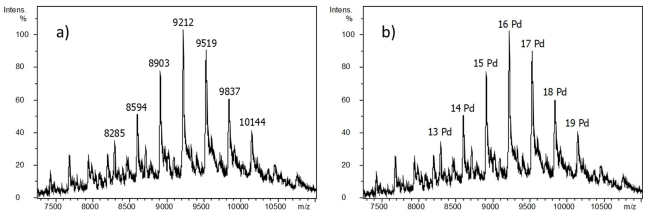

Figure 3. Deconvoluted ESI-MS spectrum recorded after incubation of **dC_{15}** (50 μM) with the **Pd-Aqa** complex (1500 μM). a) Spectrum with the experimental masses measured; b) spectrum indicating the species found, where *Pd* means one equivalent of **Pd-Aqa** per cytosine base.

dC_{12}-(Pd-Aqa)$_{12}$ supramolecular hybrid to evaluate its optimal geometry. The initial starting geometry consisted of a dodecamer oligonucleotide dC_{12} (instead of dC_{15}), representing the minimum length required to complete a helix turn while simultaneously optimizing the computational demands for the calculation. Subsequently, **Pd-Aqa** complex was bound to each base pair via Cyt-N3 atom, maintaining a co-planar arrangement between the units as described previously. Sodium cations were introduced into the system to address the ionic phosphate groups. Additionally, water molecules were strategically positioned near the donor and acceptor atoms to simulate an aqueous environment. The DFT-optimized geometry structure unveils a double-helix configuration, composed of one strand consisting of dC_{12} and the other strand comprising stacked Pd^{II} complexes, each bound explicitly to the Watson–Crick faces of the cytosine bases (Figure 4). As a result, the system forms a continuous array of Pd-mediated base pairs, with the Pd^{II} ions stacking throughout the central axis of the double helix

The resemblance of this arrangement to a natural DNA double helix is noticeable. The Pd-mediated base pairs are stacked on top of each other with a Pd···Pd distance falling within the range of 3.083–3.232 Å. The base propeller twist angles of the base pairs range from 7.42–21.3° (excluding terminal base pairs), allowing hydrogen bonds formation between the **Cyt** and **Aqa** units. The structural similarities observed in **dC_{12}-(Pd-Aqa)$_{12}$** system are comparable with our previously studied **dA_{12}-(Pd-Cheld)$_{12}$** system and underscore the consistency and reproducibility of our methodology to form supramolecular Pd-DNA-based assemblies.

Notably, the different molecular designs of our herein-reported **Pd-Aqa** complex and our previous **Pd-Cheld** complex offer an exciting opportunity for nucleobases to discriminate between the complexes, which could open the door to creating tailor-made heteroleptic metal-DNA systems. To demonstrate this concept, we investigated the relative preference of **Pd-Aqa** and **Pd-Cheld** to bind to **Cyt** and **dC_{15}**.

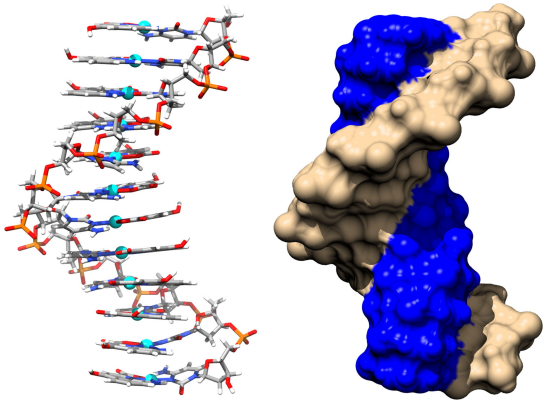

Figure 4. Left: DFT Geometry-optimized structure of **dC_{12}-(Pd-Aqa)$_{12}$** showing the organization of the **Pd-Aqa** complexes along the structure. Right: Hydrophobicity surface displaying the two different strands that form the supramolecular structure (tan; **dC_{12}**, blue; **Pd-Aqa** complexes). Sodium counterions and hydration water molecules have been omitted for clarity.

Initially, we prepared the [Pd(Cheld)(Cyt)] (**Cyt-Pd-Cheld**) complex to get insight into the structural characteristics of this base pair (Scheme 1b), using ^{1}H NMR and X-ray diffraction. The NMR spectrum analysis for the reaction between **Pd-Cheld** and Cyt showed the downshift of the cytosine's protons and the splitting of the amino signal (Supp. Info., Figure S9). These changes are consistent with the binding of **Pd-Cheld** via the Cyt-N3 atom. The non-appearance of signals at the lower field indicates the absence of intramolecular hydrogen bonds, which contrasts with the observations in complex **Cyt-Pd-Aqa** (vide supra). However, in this case, it was possible to isolate **Cyt-Pd-Cheld** in a crystalline form suitable for X-ray diffraction measurements (Supp. Info. Table S1).[18] The molecular structure reveals that the Pd^{II} ion adopts a trans-PdN2O2 square planar geometry (Scheme 1b). The **Cheld** ligand binds to Pd^{II} in a μ,κ3-N10,O2,O4-coordination mode, while the Cyt binds through its N3-atom located at the Watson–Crick face. Notably, there is a significant deviation from the coplanarity of the two ligands due to the repulsion between the keto groups, resulting in an angle of 75.63° between the r.m.s. planes of the Cyt and [Pd(Cheld)] units. This specific arrangement is responsible for the absence of intramolecular hydrogen bond formation between Cyt-amino and Cheld-keto groups. Furthermore, DFT calculations utilizing single-point structures derived from incremental rotations of the cytosine ligand consistently highlight that the most stable **Cyt-Pd-Cheld** structure deviates from coplanarity (Supp. Info. Figure S17).

Subsequently, CD titration experiments were conducted to follow the reaction between **dC$_{15}$** and **Pd-Cheld** and assess the formation of supramolecular **dC$_{15}$-(Pd-Cheld)$_{15}$** molecules. The CD spectra showed that the addition of **Pd-Cheld** to **dC$_{15}$** only causes variations in the intensity of both positive and negative bands upon adding more than one equivalent of Pd-complex per base (Supp. Info., Figure S11). Moreover, these variations did not reach a stabilization point, indicating a relatively weak interaction with the oligonucleotide. It is worth noting that the complex **Cyt-Pd-Cheld** does not absorb beyond 330 nm, so the appearance of an ICD band is not expected upon the interaction (Supp. Info., Figure S10). These results suggest a weaker interaction of **Pd-Cheld** to **dC$_{15}$** than that observed for **Pd-Aqa** complex described previously.

Then, CD competitive binding studies were conducted to evaluate whether cytosine can discriminate between our **Pd-Aqa** and **Pd-Cheld** complexes. In the first study, controlled amounts of **Pd-Aqa** were added to a solution already containing **dC$_{15}$** and **Pd-Cheld** in a 1:1.3 ratio (Figure 5a and Supp. Info., Figure S12). Before adding **Pd-Aqa**, the initial CD spectrum exhibited the expected positive and negative bands described before, thus indicating some degree of interaction between **Pd-Cheld** and **dC$_{15}$**. Upon adding **Pd-Aqa**, these bands underwent intensity alterations, and a new ICD band appeared at 370 nm. These changes stabilized when one equivalent of the complex was present. The resulting CD profile resembled the one previously observed for **dC$_{15}$-(Pd-Aqa)$_{15}$** (Figure 2). Based on these results, it is evident that the **Pd-Aqa** complex can bind to **dC$_{15}$** independently of the presence of the **Pd-Cheld** fragment. In contrast, no significant changes were observed when the CD titration was reversed, i.e., when pre-formed **dC$_{15}$-(Pd-Aqa)$_{15}$** was titrated with **Pd-Cheld** (Figure 5b and Supp. Info., Figure 13). This finding indicates that **Pd-Aqa** can displace **Pd-Cheld** bound to **dC$_{15}$** but not the other way around, suggesting a more specific and stronger binding interaction between **Pd-Aqa** and **dC$_{15}$**. In a final experiment, an equimolar mixture of **Pd-Cheld** and **Pd-Aqa** was added to a solution containing **dC$_{15}$** (Figure 5c and Supp. Info., Figure S13). Once again, the resulting CD spectra profile supported the preferential formation of **dC$_{15}$-(Pd-Aqa)$_{15}$**. This selectivity highlights the two complexes's distinct and

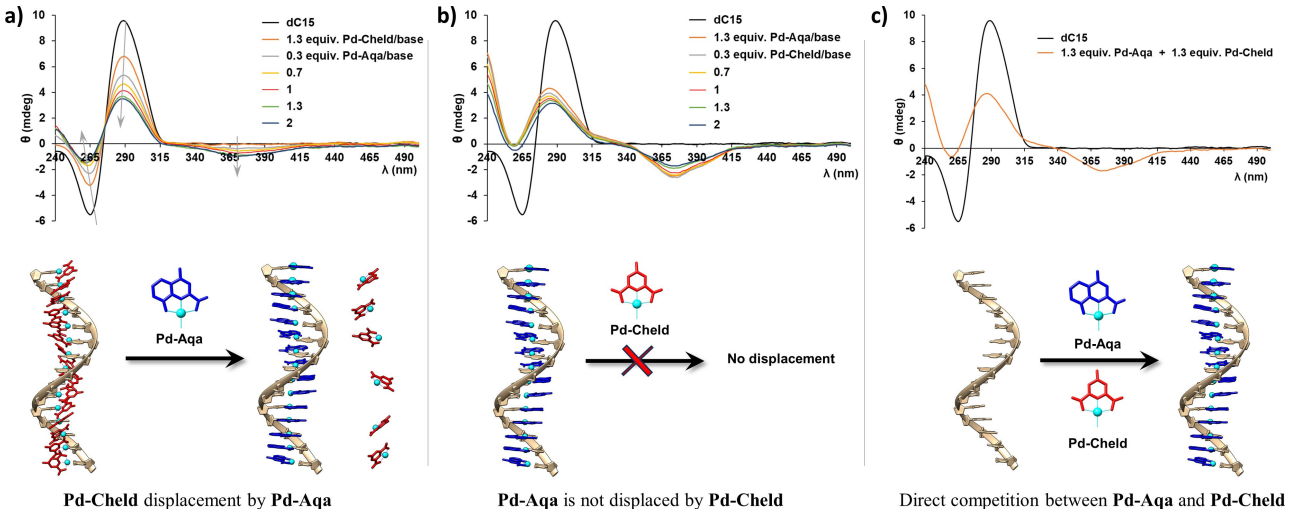

Pd-Cheld displacement by **Pd-Aqa** | **Pd-Aqa** is not displaced by **Pd-Cheld** | Direct competition between **Pd-Aqa** and **Pd-Cheld**

Figure 5. CD titration spectra and reaction Scheme for: a) formation of **dC$_{15}$:Pd-Cheld** and subsequent addition of controlled amounts of **Pd-Aqa**, b) formation of **dC$_{15}$:Pd-Aqa** and subsequent addition of controlled amounts of **Pd-Cheld**, c) **dC$_{15}$** upon addition of an equimolar mixture of **Pd-Cheld** and **Pd-Aqa**. Conditions: 2 μM **dC$_{15}$**, 0–60 μM Pd-complex (in DMSO), 100 mM $NaClO_4$, 5 mM MOPS buffer pH 6.8. Note: 1 equivalent means one Pd-complex per base

non-interchangeable binding behaviours to the **dC_{15}** molecule.

To get more insight into the binding affinities of **Pd-Cheld** and **Pd-Aqa** towards **dC_{15}**, we conducted ITC experiments to measure their binding affinities and investigate the thermodynamics of these interactions (Figure 6 and Supp. Info. Figure S15). For these experiments, we used cytidine monophosphate (**CMP**) and **dC_{15}** and determined the thermodynamic characteristic of the palladium-mediated base pairs when they are formed isolated or along the oligonucleotide strand.

The ITC data indicated that the binding affinity between **Pd-Aqa** and **CMP**, as well as between **Pd-Cheld** and **CMP**, are very similar. The thermodynamic characteristics portrayed as binding signature plots in Figure 6b provide an understanding of these interactions (see also Supp. Info. Table S3). Enthalpic and entropic factors positively contribute to the overall binding affinity (ΔG) but, notably, the plots distinctly illustrate that the interaction with **CMP** leans predominantly towards an entropic nature. The enthalpy change (ΔH) upon binding to **Pd-Aqa** demonstrates a somewhat more favourable outcome with respect to **Pd-Cheld**.

However, since the overall binding affinities of the two compounds for CMP are very similar, the slight enthalpy distinction appears to be counteracted by an increased binding entropy (△S) associated with **Pd-Cheld**, although this difference is not significant within the error of the measurements.

The slightly higher enthalpy observed for the binding of **Pd-Aqa** to **CMP** could be attributed to the formation of intrabase hydrogen bonds (see above). Nevertheless, these hydrogen bonds make a relatively minor contribution to the overall bond enthalpy due to the necessity of breaking initial hydrogen bonds formed between the amino and keto groups and water molecules. As a result, the primary energy contribution of the binding arises from the entropy, primarily driven by the release of water accompanying the formation of the Pd-mediated base pairs.

The ITC binding curves for **CMP** were fitted with a model considering independent and equivalent binding sites (Supp. Info. Figure S15), yielding a binding stoichiometry of approximately 0.5:1 ratio (CMP:complex). These results suggest that two metal complexes can bind to **CMP**, which cannot be dismissed, given that the binding of two Pd^{II} complexes to cytidine derivatives, via the N3 atom and the amino group, has been documented.[20,21] On the other hand, the ITC analysis using oligonucleotide **dC_{15}** revealed an even higher binding affinity of **Pd-Aqa** compared to **Pd-Cheld** (Figure 6). Like the interaction with **CMP**, both complexes exhibit a slightly favourable binding enthalpy and a large positive entropic energy contribution upon interaction with **dC_{15}**. However, although the binding enthalpy is more alike, the entropic factor is now considerably higher for **Pd-Aqa**. It is well-known that cytosine-rich sequences adopt highly organized structures, even at pH 7, as observed in the CD profile for **dC_{15}** in the absence of complex (Figure 2).[22–24] This fact can justify the low binding enthalpies compared to higher entropy contributions. In this scenario, the relatively small loss of conformational entropy produced by **Pd-Aqa** binding could be compensated by the entropy associated with desolvation processes occurring alongside stacking events. It should be noted that, unlike the **CMP** studies, the binding to the **dC_{15}** strand involves the formation of stacking interactions between adjacent base pairs. The formation of **dC_{15}-(Pd-Aqa)$_{15}$** will exhibit more favourable stacking interactions than **dC_{15}-(Pd-Cheld)$_{15}$**, owing to the larger aromatic ring of the Aqa ligand, favouring the coplanarity of the rings in the **Cyt-Pd-Aqa** base pairs compared to non-coplanar **Cyt-Pd-Cheld**. These observations align with studies highlighting the importance of base-stacking interactions in DNA duplex stability.[25]

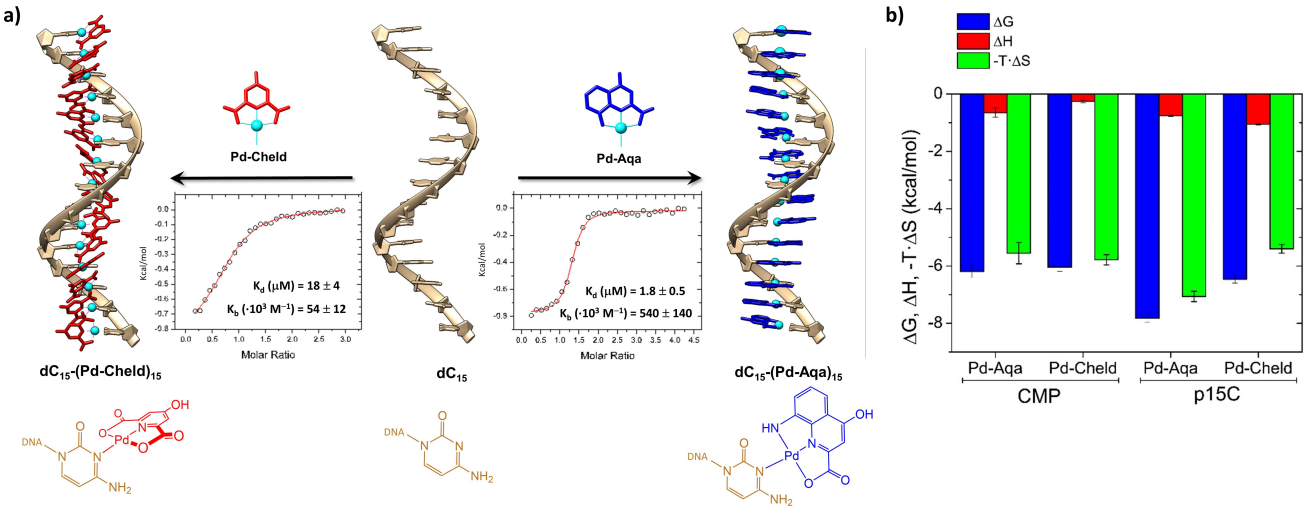

Figure 6. a) Schematic representation illustrating the binding of **dC_{15}** with **Pd-Cheld**, and **Pd-Cheld**, resulting in the formation of the supramolecular Pd-DNA hybrids. The Figure incorporates the titration plot versus the molar ratio of [Pd-complex]/[dC_{15}], obtained from the ITC profiles (Supp. Inf. Figure S14). b) The thermodynamic parameters (free energy, binding enthalpy and entropy factor) plotted for the binding of **Pd-Cheld** and **Pd-Aqa** to **CMP** and **dC_{15}**.

The binding stoichiometry for **dC_{15}** is now closer to $n=1$, suggesting that binding the binding of more than one Pd^{II} complex to cytidine bases is more hindered in **dC_{15}** than in free **CMP** (Supp. Info. Table S3).

The analysis of ITC data provided crucial insights into elucidating the stronger affinity of **Pd-Aqa** for **dC_{15}** compared to **Pd-Cheld**, as also observed in the CD competitive binding studies. This heightened affinity can be ascribed not only to the ability of **Pd-Aqa** to form intrabase hydrogen bonds with cytosine but also to its capacity to induce the formation of more extensive stacking interactions. These findings highlight the intricate interplay between the promotion of intramolecular hydrogen bonds and the significance of stacking interactions in the design of complementary nucleobase complexes. The latter is indispensable for stabilizing these complexes along DNA strands.

Finally, as a proof of concept for the formation of heteroleptic Pd-DNA systems, we obtained an ESI-MS spectrum illustrating the interaction between **Pd-Aqa** and **Pd-Cheld** with the oligonucleotide sequence 5′-d-(CCCACACACC)-3′ **$d(C_7A_3)$**, comprising a mixture of cytosine and adenine, specifically, seven cytosine and three adenine bases (Supp. Info. Figure S16). These preliminary results indicate that adding equal amounts of the complexes to **$d(C_7A_3)$** results in the binding of seven **Pd-Aqa** and three **Pd-Cheld** complexes, aligning with the preferential binding of the complexes to the nucleobases described herein. Nevertheless, our group is conducting ongoing research and additional experiments to deepen our understanding of this process. We are optimistic that the findings presented here will contribute to the advancement of Pd-DNA heteroleptic systems.

Conclusion

This study establishes **Pd-Aqa** as a complementary nucleobase complex capable of engaging in self-assembly reactions with polycytidine ss-DNA strands. These assemblies involve the formation of consecutive planar palladium-mediated base pairs, specifically **Cyt-Pd-Aqa** pairs, creating supramolecular Pd-DNA assemblies that closely mimic the double helix structure of natural DNA. This study's significance is underscored by the extraordinary advantage demonstrated by the purposefully designed **Pd-Aqa** complex in binding with **dC_{15}**. This complex exhibited a superior affinity for engaging with **dC_{15}**, surpassing the interaction observed with the earlier complex, **Pd-Cheld**, designed for complementary binding to adenine. These results underscore the impact of precise design in augmenting the discrimination capacity nucleobases for the binding of specific complementary complexes. Such heightened selectivity not only highlights the potential for creating heteroleptic Pd-DNA assemblies but also emphasizes the importance of strategic complex design and consideration of DNA sequence. This marks a promising avenue for future exploration in this field. From this result, our ongoing efforts are centred on the investigation of the selective binding properties of complementary nucleobase complexes to DNA sequences encompassing different nucleobases.

Supporting Information

Acknowledgements

The authors have cited additional references within the Supporting Information.[13,26–38]

Acknowledgements

Financial support from Spanish Ministerio de Ciencia e Innovación (projects PID2020-120186RB-I00 and PID2022-138479NB-I00), Junta de Andalucia (project P20_00702). We thank the "Centro de Servicios de Informática y Redes de Comunicaciones" (CSIRC) (UGRGrid), Universidad de Granada, for providing computing time on the Alhambra and Dr Ali Haidour Benamin, from Centro de Instrumentación Cientifica (UGR), for his support, assistance, and expertise in conducting NMR experiments.

Conflict of Interest

The authors declare no conflict of interest.

Data Availability Statement

The data that support the findings of this study are available from the corresponding author upon reasonable request.

Keywords: cytosine · metal-mediated base pairs · DNA · palladium · supramolecular chemistry

[1] X. Dai, Q. Li, A. Aldalbahi, L. Wang, C. Fan, X. Liu, *Nano Lett.* **2020**, *20*, 5604–5615.
[2] S. K. Vittala, D. Han, *ACS Appl Bio Mater* **2020**, *3*, 2702–2722.
[3] M. R. Jones, N. C. Seeman, C. A. Mirkin, *Science* **2015**, *347*, 1260901.
[4] D. A. Rusling, A. R. Chandrasekaran, Y. P. Ohayon, T. Brown, K. R. Fox, R. Sha, C. Mao, N. C. Seeman, *Angew. Chem. Int. Ed.* **2014**, *53*, 3979–3982.
[5] B. Jash, J. Müller, *Chem. Eur. J.* **2017**, *23*, 17166–17178.
[6] Z. Chen, C. Liu, F. Cao, J. Ren, X. Qu, *Chem. Soc. Rev.* **2018**, *47*, 4017–4072.
[7] S. Naskar, R. Guha, J. Müller, *Angew. Chem. Int. Ed.* **2020**, *59*, 1397–1406.
[8] Y. Takezawa, K. Mori, W.-E. Huang, K. Nishiyama, T. Xing, T. Nakama, M. Shionoya, *Nat. Commun.* **2023**, *14*, DOI 10.1038/s41467-023-40353-3.
[9] K. Mori, Y. Takezawa, M. Shionoya, *Chem. Sci.* **2023**, 1DYMMY.
[10] M. Balaz, S. Tannir, K. Varga, *Coord. Chem. Rev.* **2017**, *349*, 66–83.
[11] M. Surin, S. Ulrich, *ChemistryOpen* **2020**, *9*, 480–498.

[12] J. García Coll, S. Ulrich, *ChemBioChem* **2023**, e202300333.
[13] A. Pérez-Romero, A. Domínguez-Martín, S. Galli, N. Santamaría-Díaz, O. Palacios, J. A. Dobado, M. Nyman, M. A. Galindo, *Angew. Chem. Int. Ed.* **2021**, *60*, 10089–10094.
[14] O. Golubev, T. Lönnberg, H. Lönnberg, *J. Inorg. Biochem.* **2014**, *139*, 21–29.
[15] O. Golubev, T. Lönnberg, H. Lönnberg, *Helv. Chim. Acta* **2013**, *96*, 1658–1669.
[16] O. Golubev, T. Lönnberg, H. Lönnberg, *Molecules* **2014**, *19*, 16976–16986.
[17] A. Aro-Heinilä, T. Lönnberg, *Chem. Eur. J.* **2017**, *23*, 1028–1031.
[18] Deposition number 2313312 (for **Cyt-Pd-Cheld**) contains the supplementary crystallographic data for this paper. These data are provided free of charge by the joint Cambridge Crystallographic Data Centre and Fachinformationszentrum Karlsruhe Access Structures service. Data have also been deposited at the Crystallography Open Database (COD ID 3000467) and can be freely downloaded from www.crystallography.net.
[19] M. Krumm, I. Mutikainen, B. Lippert, *Inorg. Chem.* **1991**, *30*, 884–890.
[20] W.-Z. Shen, B. Lippert, *J. Inorg. Biochem.* **2008**, *102*, 1134–1140.
[21] S. Coşar, M. B. L. Janik, M. Flock, E. Freisinger, E. Farkas, B. Lippert, *Dalton Trans.* **1999**, 2329–2336.
[22] J. Kypr, I. Kejnovská, D. Renčiuk, M. Vorlíčková, *Nucleic Acids Res.* **2009**, *37*, 1713–1725.
[23] Y. Dong, Z. Yang, D. Liu, *Acc. Chem. Res.* **2014**, *47*, 1853–1860.
[24] T. Miyahara, H. Nakatsuji, H. Sugiyama, *J. Phys. Chem. A* **2013**, *117*, 42–55.
[25] A. Vologodskii, M. D. Frank-Kamenetskii, *Phys. Life Rev.* **2018**, *25*, 1–21.
[26] E. Greco, A. E. Aliev, V. G. H. Lafitte, K. Bala, D. Duncan, L. Pilon, P. Golding, H. C. Hailes, *New J. Chem.* **2010**, *34*, 2634–2642.
[27] N. P. Peet, L. E. Baugh, S. Sunder, J. E. Lewis, *J. Med. Chem.* **1985**, *28*, 298–302.
[28] APEX3 Software,V2016.1; Bruker AXS: Madison, WI, USA, **2016**.
[29] G. M. Sheldrick, *SADABS 2016/2. Program for Empirical Absorption Correction of Area Detector Data*, University Of Göttingen, Germany., **2016**.
[30] G. M. Sheldrick, *Acta Crys.* **2008**, *64*, 112–122.
[31] O. V. Dolomanov, L. J. Bourhis, R. J. Gildea, J. A. K. Howard, H. Puschmann, *J. Appl. Crys.* **2009**, *42*, 339–341.
[32] M. D. Hanwell, D. E. Curtis, D. C. Lonie, T. Vandermeersch, E. Zurek, G. R. Hutchison, *J. Cheminf.* **2012**, *4*, 17.
[33] *Avogadro: An Open-Source Molecular Builder and Visualization Tool. Version 1.2.0.* https://avogadro.cc/.
[34] E. Aprà, E. J. Bylaska, W. A. de Jong, N. Govind, K. Kowalski, T. P. Straatsma, M. Valiev, H. J. J. van Dam, Y. Alexeev, J. Anchell, V. Anisimov, F. W. Aquino, R. Atta-Fynn, J. Autschbach, N. P. Bauman, J. C. Becca, D. E. Bernholdt, K. Bhaskaran-Nair, S. Bogatko, P. Borowski, J. Boschen, J. Brabec, A. Bruner, E. Cauët, Y. Chen, G. N. Chuev, C. J. Cramer, J. Daily, M. J. O. Deegan, T. H. Dunning Jr, M. Dupuis, K. G. Dyall, G. I. Fann, S. A. Fischer, A. Fonari, H. Früchtl, L. Gagliardi, J. Garza, N. Gawande, S. Ghosh, K. Glaesemann, A. W. Götz, J. Hammond, V. Helms, E. D. Hermes, K. Hirao, S. Hirata, M. Jacquelin, L. Jensen, B. G. Johnson, H. Jónsson, R. A. Kendall, M. Klemm, R. Kobayashi, V. Konkov, S. Krishnamoorthy, M. Krishnan, Z. Lin, R. D. Lins, R. J. Littlefield, A. J. Logsdail, K. Lopata, W. Ma, A. V. Marenich, J. Martin Del Campo, D. Mejia-Rodriguez, J. E. Moore, J. M. Mullin, T. Nakajima, D. R. Nascimento, J. A. Nichols, P. J. Nichols, J. Nieplocha, A. Otero-de-la-Roza, B. Palmer, A. Panyala, T. Pirojsirikul, B. Peng, R. Peverati, J. Pittner, L. Pollack, R. M. Richard, P. Sadayappan, G. C. Schatz, W. A. Shelton, D. W. Silverstein, D. M. A. Smith, T. A. Soares, D. Song, M. Swart, H. L. Taylor, G. S. Thomas, V. Tipparaju, D. G. Truhlar, K. Tsemekhman, T. Van Voorhis, Á. Vázquez-Mayagoitia, P. Verma, O. Villa, A. Vishnu, K. D. Vogiatzis, D. Wang, J. H. Weare, M. J. Williamson, T. L. Windus, K. Woliński, A. T. Wong, Q. Wu, C. Yang, Q. Yu, M. Zacharias, Z. Zhang, Y. Zhao, R. J. Harrison, *J. Chem. Phys.* **2020**, *152*, 184102.
[35] J. P. Perdew, M. Ernzerhof, K. Burke, *J. Chem. Phys.* **1996**, *105*, 9982–9985.
[36] C. Adamo, V. Barone, *J. Chem. Phys.* **1999**, *110*, 6158–6170.
[37] S. Grimme, J. Antony, S. Ehrlich, H. Krieg, *J. Chem. Phys.* **2010**, *132*, 154104.
[38] S. Grimme, S. Ehrlich, L. Goerigk, *J. Comput. Chem.* **2011**, *32*, 1456–1465.

Manuscript received: January 4, 2024
Accepted manuscript online: January 21, 2024
Version of record online: February 5, 2024

Supporting Information

Selective Formation of Pd-DNA Hybrid Using Tailored Palladium-Mediated Base Pairs: Towards Heteroleptic Pd-DNA Systems

Antonio Pérez-Romero,[a] Mario Cano-Muñoz,[b] Carmen López-Chamorro,[a] Francisco Conejero-Lara,[b] Oscar Palacios,[c] José A. Dobado,[d] and Miguel A. Galindo*[a]

[a] Mr A. Pérez-Romero, Dr M. A. Galindo
Departamento de Química Inorgánica. Unidad de Excelencia Química Aplicada a Biomedicina y Medioambiente. Facultad de Ciencias.
Universidad de Granada
Avda Fuentenueva s/n, 18071 Granada (Spain)
E-mail: magalindo@ugr.es

[b] Dr M. Cano-Muñoz, Prof Dr F. Conejero-Lara
Departamento de Química Física, Instituto de Biotecnología y Unidad de Excelencia Química Aplicada a Biomedicina y Medioambiente. Facultad de Ciencias
Universidad de Granada
Avda Fuentenueva s/n, 18071 Granada (Spain)

[c] Dr O. Palacios
Departament de Química, Facultat de Ciències
Universitat Autònoma de Barcelona
Campues Ballaterra s/n, 08193 Cerdanyola del Vallès, Barcelona (Spain).

[d] Prof Dr J. A. Dobado
Grupo de Modelización y Diseño Molecular, Departamento de Química Orgánica
Universidad de Granada
Avda Fuentenueva s/n, 18071 Granada (Spain)

Content

GENERAL METHODS 4

SYNTHESIS AND CHARACTERIZATION OF COMPOUNDS 4

Materials 4

Synthesis of complex [Pd(Aqa)(DMSO)], **Pd-Aqa**. 5

Figure S1. ^{1}H-NMR ([D$_6$]DMSO) spectra for the formation of [Pd(Aqa)(DMSO)] (**Pd-Aqa**) 5

Figure S2. ^{1}H-NMR ([D$_6$]DMSO) spectrum for [Pd(Aqa)(DMSO)] (**Pd-Aqa**). 6

Figure S3. Mass spectrum for [Pd(Aqa)(DMSO)] (**Pd-Aqa**) 6

Synthesis of complex [Pd(Aqa)(Cyt)], **Cyt-Pd-Aqa** 7

Figure S4. ^{1}H-NMR ([D$_6$]DMSO) spectra for the formation of [Pd(Aqa)(Cyt)] (**Cyt-Pd-Aqa**) 7

Figure S5. ^{1}H-NMR ([D$_6$]DMSO) spectrum for [Pd(Aqa)(Cyt)] (**Cyt-Pd-Aqa**)..... 8

Figure S6. ^{1}H-NMR ([D$_6$]DMSO) spectra at variable temperature for [Pd(Aqa)(Cyt)] (**Cyt-Pd-Aqa**)..... 8

Figure S7. Mass spectrum for [Pd(Aqa)(Cyt)] (**Cyt-Pd-Aqa**)..... 9

Synthesis of complex [Pd(Cheld)(Cyt)], **Cyt-Pd-Cheld** 9

Figure S8. ^{1}H-NMR ([D6]DMSO) spectra for [Pd(Cheld)(Cyt)] (**Cyt-Pd-Cheld**)..... 10

SINGLE-CRYSTAL X-RAY DIFRACTION STRUCTURE DETERMINATION..... 10

Table S1. Summary of crystallographic information and relevant X-ray diffraction experimental details for [Pd(Cheld)(Cyt)] (**Cyt-Pd-Cheld**) 10

UV-VIS SPECTROSCOPY..... 11

Figure S9. UV-Vis spectra for [Pd(Aqa)(Cyt)] (**Cyt-Pd-Aqa**) and [Pd(Cheld)(Cyt)] (**Cyt-Pd-Cheld**)..... 11

MASS SPECTROMETRY..... 12

Table S2. Theoretical masses corresponding to dC$_{15}$ and the adducts with "n" equivalents of the **Pd-Aqa** complex. 12

CIRCULAR DICHROISM..... 12

Figure S10. CD titration spectra for dC$_{15}$ upon adding controlled amounts of **Pd-Cheld**. 12

Figure S11. CD titration spectra for **dC$_{15}$:Pd-Cheld** upon adding controlled amounts of **Pd-Aqa**..... 13

Figure S12. CD titration spectra for **dC_{15}:Pd-Aqa** upon adding controlled amounts of **Pd-Cheld** 13

Figure S13. CD for dC_{15} upon addition of an equimolar mixture of **Pd-Cheld** and **Pd-Aqa**. 14

ISOTHERMAL TITRATION CALORIMETRY 14

Figure S14. ITC plots of heat values against molar ratio 15

Table S3. Thermodynamic parameters of binding of **Pd-Cheld** and **Pd-Aqa** to CMP and dC_{15} 16

MOLECULAR MODELLING 16

Theoretical methodology for [Pd(Aqa)(Cyt)] (**Cyt-Pd-Aqa**) structure 16

Theoretical methodology for **dC_{15}-(Pd-Aqa)$_{15}$** structure 16

Coordinates of the DFT calculated [Pd(Aqa)(Cyt)] (**Cyt-Pd-Aqa**) structure. 17

Coordinates of the DFT calculated **dC_{12}-(Pd-Aqa)$_{12}$** structure. 18

REFERENCES 26

GENERAL METHODS

NMR spectra were recorded at room temperature on a Varian Direct Drive 400 instrument. Chemical shifts are given in ppm (δ) relative to tetramethylsilane. Abbreviations used are s = singlet, d = doublet, t = triplet, q = quartet, m = multiplet, dq = double quartet. Infrared (IR) spectra were acquired on a Thermo Nicolet IR200 spectrometer or a Bruker Tensor 27 Fourier transform infrared spectrometer. Elemental analyses were carried out on a Thermo Scientific Flash 2000 instrument with a precision microbalance or a Flash EA1112 CHNS-O Thermo Finnigan instrument with a Mettler Toledo MX5 electronic microbalance. CD spectra were recorded on a Jasco J-815 Mettler Toledo MX5 instrument equipped with a Peltier temperature controller. UV-Vis absorption and fluorescence spectra were recorded on a Varian Cary-Eclipse spectrophotometer equipped with a Xe lamp (peak power 75 kW), a CZERNY-Turner monochromator, and an R-298 red-sensitive photomultiplier tube.

Molecular mass determination for Pd^{II}-metal complexes was by ESI-MS using a Compact Q-TOF Bruker Instrument, in positive mode, with set capillarity at 4.5 kV, set end plate offset at -500V, set charging voltage at 2000V, set dry gas 9 L·min^{-1} and dry heater at 220°C.

Molecular mass determination for the **dC_{15}(Pd-Aqa)$_n$** system was performed by ESI-MS using a Micro Tof-Q Instrument (Bruker Daltonics GmbH, Bremen, Germany) equipped with a time-of-flight analyzer (ESI-TOF MS), with ESI-L Low Concentration Tuning Mix (Agilent Technologies, USA), interfaced with an Agilent Technologies Series 1100 HPLC pump and equipped with an autosampler, both controlled by the Compass Software. The interaction of the **Pd-Aqa** with the **dC_{15}** (50 µM) was analyzed in negative mode, injecting 10 µL of the sample at 40 µL min^{-1} , with capillary-counter electrode voltage at 3.9-4.2 kV; the desolvation temperature was set at 100 °C, and dry gas was flowed at 6 L min^{-1} , using a 90:10 mixture of 15 mM ammonium acetate and acetonitrile (pH 7.0) as a liquid carrier. The spectra were collected throughout an m/z range from 800 to 3000.

SYNTHESIS AND CHARACTERIZATION OF COMPOUNDS

Materials

1-methyl-citosine,[1] 8–amino–4–hydroxy–1,4–dihydroquinoline-2 carboxylate (Aqa)[2] and [Pd(*Cheld*)(CH_3CN)] (**Pd-Cheld**)[3] were synthesized according to literature procedures. Oligonucleotide dC_{15} was purchased from Sigma-Aldrich at HPLC grade and used without further purification.

Synthesis of complex [Pd(Aqa)(DMSO)], **Pd-Aqa**.

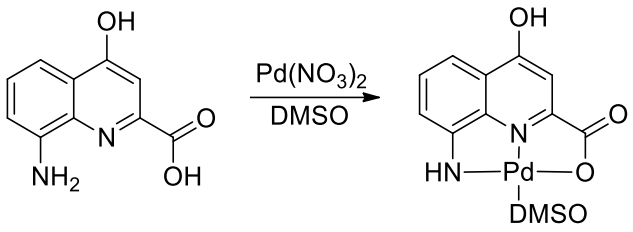

Scheme S1: Synthetic route to **Pd-Aqa**

The Aqa ligand (1mmol) was dissolved in DMSO (500µL) and a DMSO solution (100µL) of $Pd(NO_3)_2$ (1mmol) was added dropwise. Despite our efforts, attempts to isolate the product as a pure solid were unsuccessful. The formation of **Pd-Aqa** was confirmed in solution by nuclear magnetic resonance and mass spectrometry. ^{1}H-RMN (400 MHz, [D_6]DMSO, ppm): δ = 8.34 (b, 1H; *NH*), 8.07 (d, 1H; *C-H5*), 7.84(b, 1H; *C-H7*), 7.77(t, 1H; *C-H6*), 7.08 (s, 1H; *C-H3*). HRMS (ESI): *m/z* calcd for $C_{12}H_{12}N_2O_4PdS+H^+$: 386.9635 [*M*+H]$^+$; found: 386.9630.

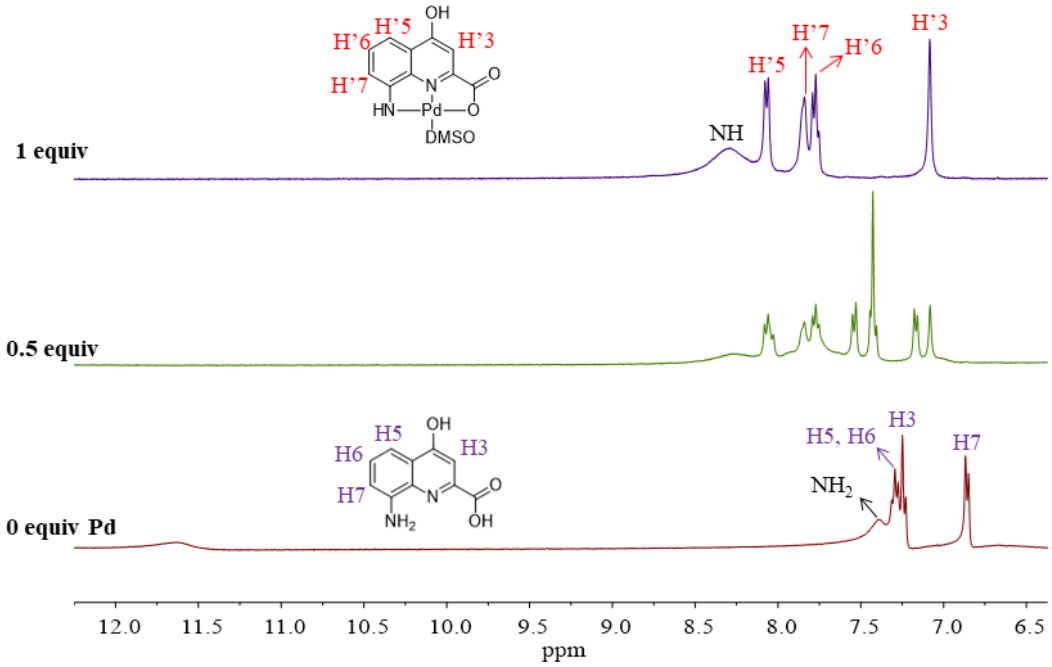

Figure S1. ^{1}H-NMR ([D_6]DMSO) spectra for the formation of [Pd(Aqa)(DMSO)] (**Pd-Aqa**) (top) upon addition of $Pd(NO_3)_2$ to ligand 8-amino-4-hydroxyquinoline-2-carboxylic acid (Aqa) (bottom).

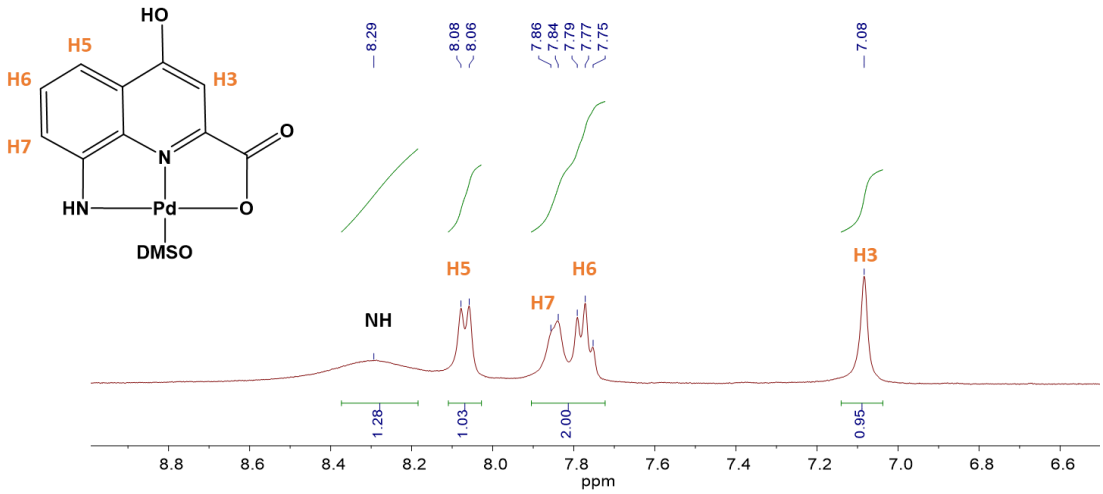

Figure S2. ^{1}H-NMR ([D_6]DMSO) spectrum for [Pd(Aqa)(DMSO)] (**Pd-Aqa**).

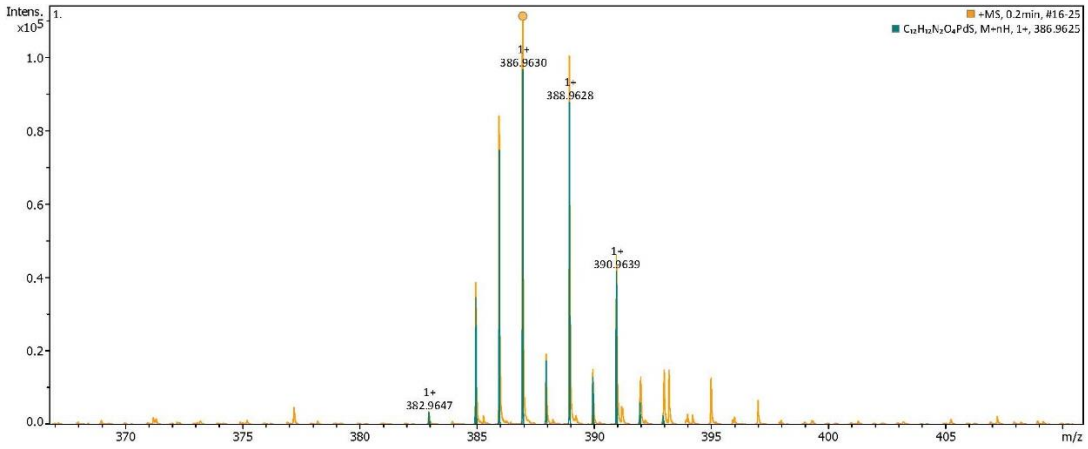

Figure S3. Mass spectrum (ESI-MS, positive mode) for [Pd(Aqa)(DMSO)] (**Pd-Aqa**) displaying the simulated (blue) and experimental (orange) isotopic patterns.

Synthesis of complex [Pd(Aqa)(Cyt)], **Cyt-Pd-Aqa**

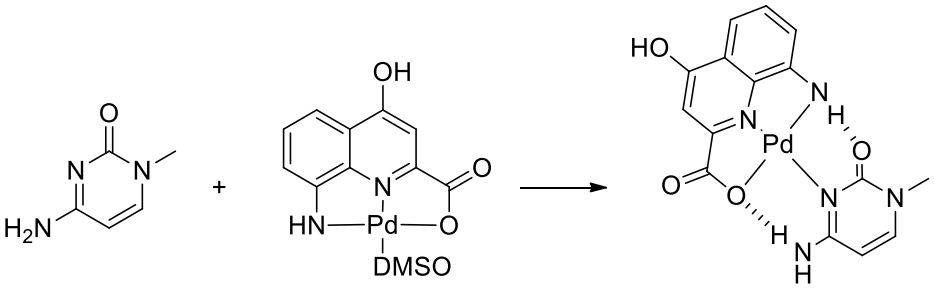

Scheme S2: Synthetic route to **Cyt-Pd-Aqa**.

1-methylcytosine (Cyt) (1mmol) was dissolved in DMSO (500µL) and a DMSO solution (500µL) of Pd-Aqa (1mmol) was added dropwise. Despite our efforts, attempts to isolate the product as a pure solid were unsuccessful. The formation of **Cyt-Pd-Aqa** complex was confirmed in solution by nuclear magnetic resonance and mass spectrometry. ^{1}H-RMN (400 MHz, [D_6]DMSO, ppm): δ = 9.38 (s, 1H; *cyt-NH$_2$*), 8.66-8.59 (d, 1H; *aqa-NH*), 8.15 (s, 1H; *cyt-NH$_2$*) 8.06 (d, 1H; *aqa-H14*), 7.99 (d, 0.7H; *cyt-H6*), 7.84 (m, 1.3H; *cyt-H6'* & *aqa-H16*), 7.76 (m, 1H; *aqa-H15*), 7.10 (s, 0.5H; *aqa-H10*), 7.07 (s, 0.5H; *aqa-H10'*), 5.99 (d, 0.6H; ; *cyt-H5*) 5.88 (d, 0.4H; *cyt-H5'*), 3.38 (s, 1.5H; *CH$_3$*), 3.38 & 3.35 (s; *CH$_3$*). HRMS (ESI): *m/z* calcd for $C_{15}H_{13}N_5O_4Pd+H^+$: 434.0075 [*M*+H^+], found: 434.0081.

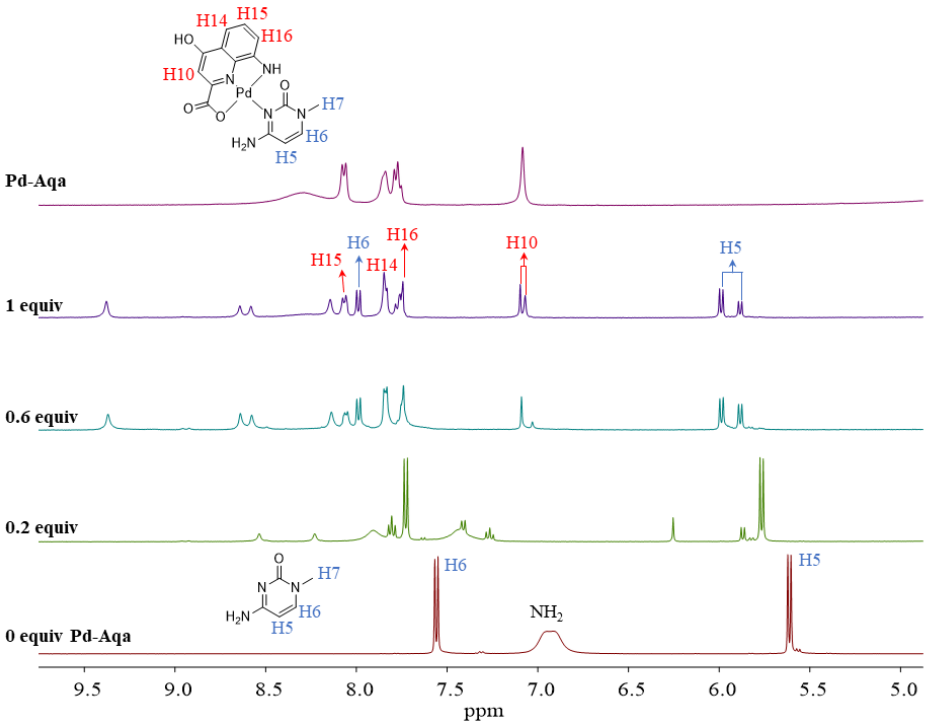

Figure S4. ^{1}H-NMR ([D_6]DMSO) spectra for the formation of [Pd(Aqa)(Cyt)] (**Cyt-Pd-Aqa**) upon addition of [Pd(Aqa)(DMSO)] (**Pd-Aqa**) to ligand 1-methylcytosinie (Cyt).

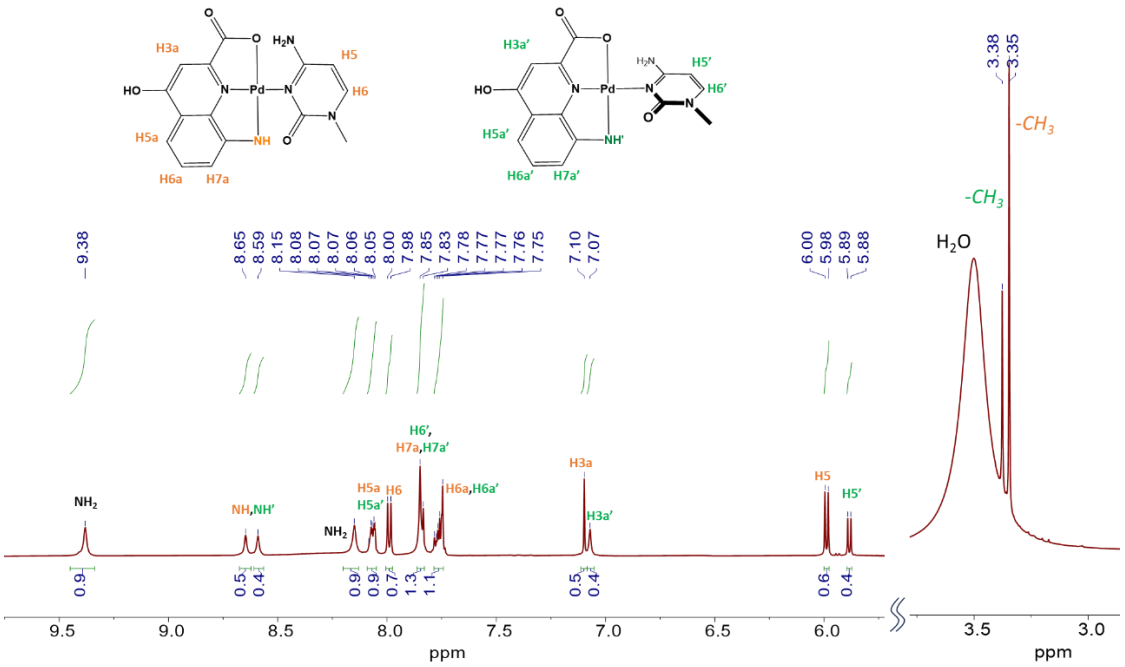

Figure S5. ^{1}H-NMR ([D$_6$]DMSO) spectrum for [Pd(Aqa)(Cyt)] (**Cyt-Pd-Aqa**).

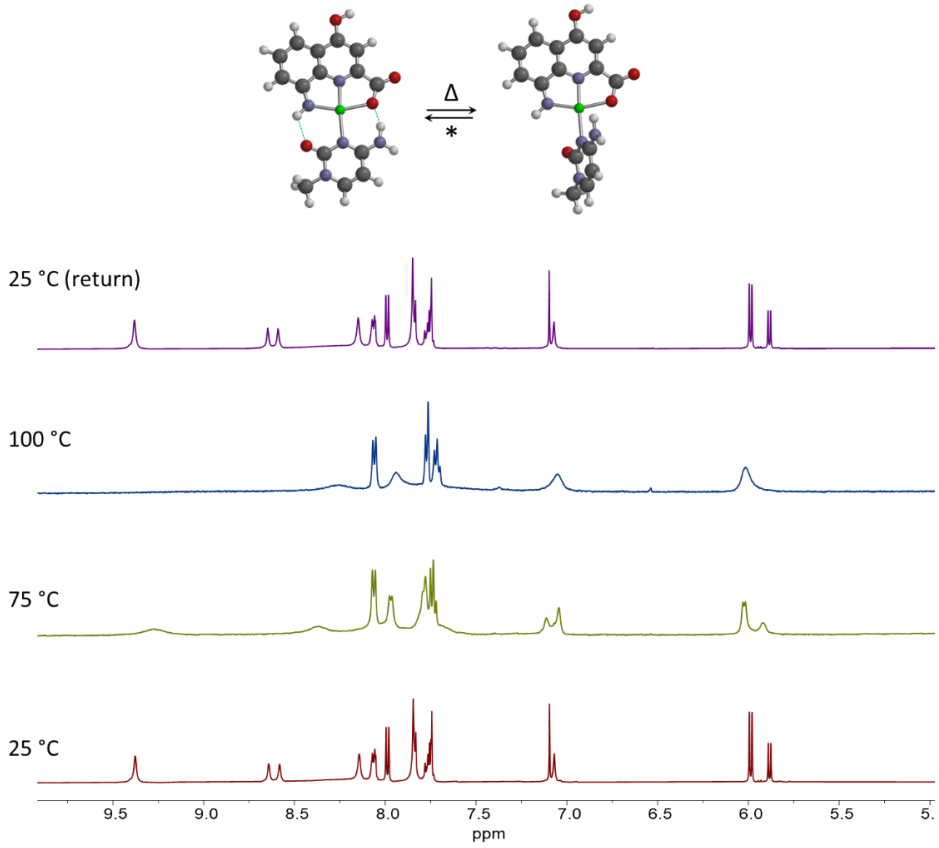

Figure S6. ^{1}H-NMR ([D$_6$]DMSO) spectra at variable temperature for [Pd(Aqa)(Cyt)] (**Cyt-Pd-Aqa**). The spectra are presented bottom-to-top, illustrating the progression of temperature changes. The spectrum at the top corresponds to the initial starting temperature after heating the sample.

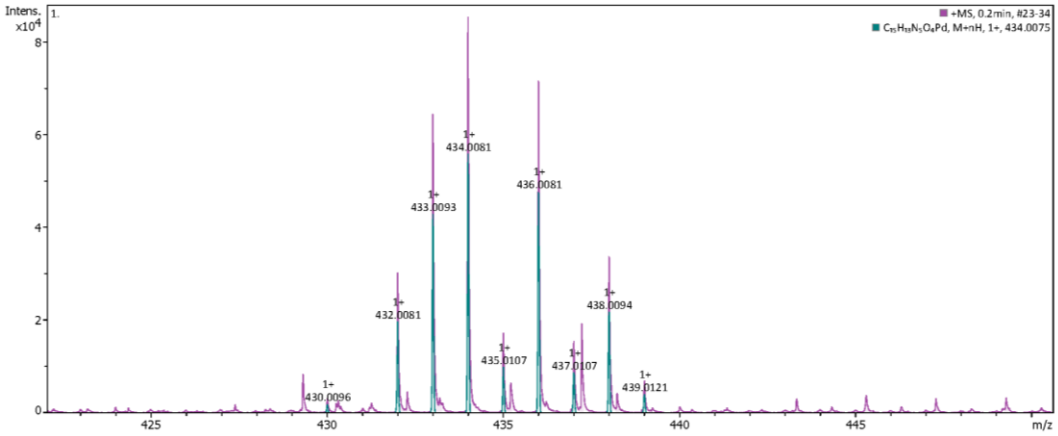

Figure S7. Mass spectrum (ESI-MS, positive mode) for [Pd(Aqa)(Cyt)] (**Cyt-Pd-Aqa**) displaying the simulated (blue) and experimental (purple) isotopic patterns.

Synthesis of complex [Pd(Cheld)(Cyt)], **Cyt-Pd-Cheld**

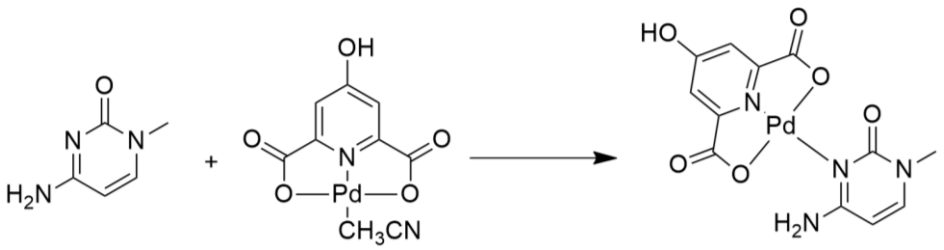

Scheme S3: Synthetic route to **Cyt-Pd-Cheld**.

Pd-Cheld (50.0 mg, 0.15 mmol) was suspended in water (20 mL) and then added a solution of 1-methylcytosine (Cyt) (18.75 mg, 0.15 mmol) in water (10 mL). The mixture was stirred at 50°C in the dark for 12 hours (pH=5.3). Following this period, the titled compound appeared as a yellow precipitate, which was filtered, washed, and dried. The compound was recrystallized in *N,N*-dimethylformamide, yielding orange crystals suitable for X-ray diffraction analysis. Yield: 45 mg (71.2%). Elemental analysis calcd (%) for $PdC_{12}H_{10}N_4O_6{\cdot}(H_2O)_{3.3}$: C, 30.54; H, 3.52; N, 11.87; found: C, 30.98; H, 3.59; N, 11.76. ^{1}H-RMN (400 MHz, [D_6]DMSO, ppm): δ = 2.08 (s, 3H; *cyt-CH$_3$*), 5.78 (d, *J*=7.3 Hz, 1H; *cyt-H5*), 7.07 (s, 2H; *CH$_{py.}$*), 7.76 (d, *J*=7.3 Hz, 1H; *cyt-H6*), 8.50 (s, 1H; *cyt-NH*), 8.71 (s, 1H; *cyt-NH*). IR (cm-1): $\tilde{\nu}$= 3437 (s), 1637 (ms), 1515 (w), 1461 (w), 1366 (m), 1261 (m), 1175 (w), 1090 (m), 931 (w), 880 (w), 793 (w), 771 (mw), 755 (mw).

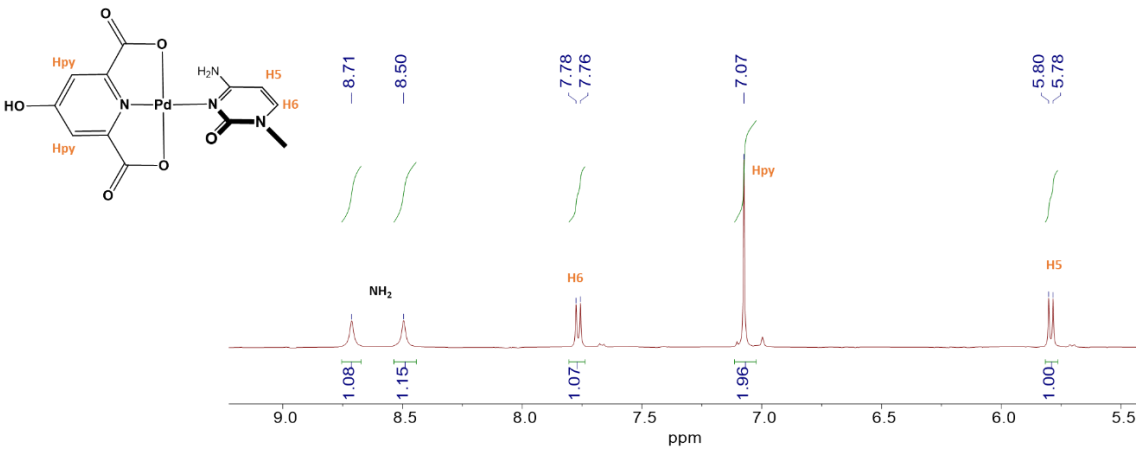

Figure S8. ^{1}H-NMR ([D6]DMSO) spectra for [Pd(Cheld)(Cyt)] (**Cyt-Pd-Cheld**)

SINGLE-CRYSTAL X-RAY DIFRACTION STRUCTURE DETERMINATION

X-ray diffraction data for complex [Pd(Cheld)(Cyt)] (**Cyt-Pd-Cheld**) were collected on a Bruker D8 Venture diffractometer equipped with either a Cu (λ= 1.54178 Å) X-ray tube, a Bruker AXS Photon 100 detector, and a Kryoflex II cooling apparatus. Data reduction was performed with the software APEX3,[4] while data correction for absorption was carried out using the software SADABS.[5] the structures were solved by Patterson method and refined using least squares minimization with the SHELX suite of programs[6] integrated in OLEX2.[7] One of the water molecules has been found to be disordered between three positions with occupancies 0.43, 0.35 and 0.22, H-atoms for this molecule have not been included in the model.

Table S1. Summary of crystallographic information and relevant X-ray diffraction experimental details for [Pd(Cheld)(Cyt)] (**Cyt-Pd-Cheld**)**.**

Identification code	**[Pd(Cheld)(Cyt)]**
Empirical formula	$C_{12}H_{16}N_4O_9Pd$
Formula weight	466.69
Temperature/K	100(2)
Crystal system	triclinic
Space group	P-1
a/Å	6.7020(3)
b/Å	9.8320(5)

c/Å	13.1889(7)
α/°	95.501(2)
β/°	93.318(2)
γ/°	107.373(2)
Volume/Å^3	822.17(7)
Z	2
ρ_{calc}g/cm^3	1.885
μ/mm^{-1}	9.662
F(000)	468.0
Crystal size/mm^3	0.120 × 0.120 × 0.080
Radiation	CuKα (λ = 1.54178)
2Θ range for data collection/°	6.76 to 133.114
Index ranges	-7 ≤ h ≤ 7, -11 ≤ k ≤ 11, -15 ≤ l ≤ 15
Reflections collected	11629
Independent reflections	2848 [R_{int} = 0.0403, R_{sigma} = 0.0307]
Data/restraints/parameters	2848/4/267
Goodness-of-fit on F^2	1.148
Final R indexes [I>=2σ (I)]	R_1 = 0.0395, wR_2 = 0.0984
Final R indexes [all data]	R_1 = 0.0425, wR_2 = 0.1025
Largest diff. peak/hole / e Å^{-3}	0.78/-1.83

UV-VIS SPECTROSCOPY

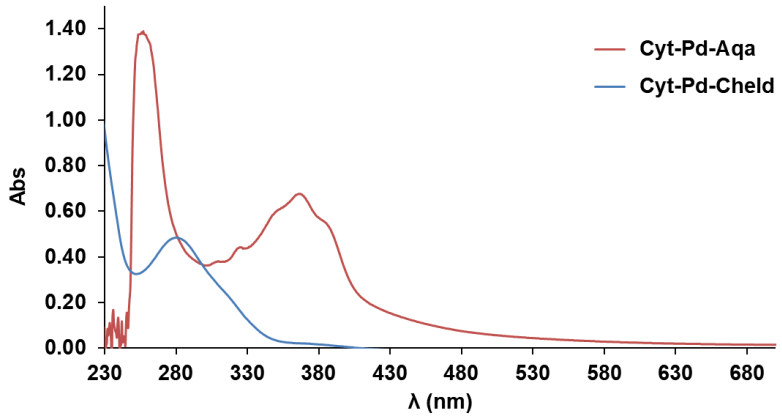

Figure S9. UV-Vis spectra for [Pd(Aqa)(Cyt)] (**Cyt-Pd-Aqa**) (0.1 mM, water with 25% DMF) and [Pd(Cheld)(Cyt)] (**Cyt-Pd-Cheld**) (0.025 mM, water with 25% ACN).

MASS SPECTROMETRY

Table S2. Theoretical masses corresponding to dC_{15} and the adducts with "n" equivalents of the **Pd-Aqa** complex.

n	0	1	2	3	4	5	6
Mass	4275,8	4584,4	4893,0	5201,6	5510,2	5818,7	6127,3

n	7	8	9	10	11	12	13	14
Mass	6435,9	6744,5	7053,1	7361,7	7670,3	7978,9	8287,5	8596,1

n	15	16	17	18	19	20	21	22
Mass	8904,6	9213,2	9521,8	9830,4	10139,0	10447,6	10756,2	11064,8

CIRCULAR DICHROISM

The **Pd-Aqa-dC$_{15}$** samples for the CD spectroscopy titration series keeping the oligonucleotide concentration constant were undertaken by dissolving 2 µM of oligonucleotide in 700 µL of water containing 5 mM buffer and 100 mM NaClO4. To this solution, the aliquotes from a stock solution of **Pd-Aqa** (500 µM, DMF) were added, along with comparable aliquotes from an oligonucleotide stock solution (4 µM DNA, 10 mM buffer, 200 mM NaClO4) to keep the concentration constant. At the end of the titration experiments, when 4 equivalents of **Pd-Aqa** were present in the solution, the final solution had 24% of DMF.

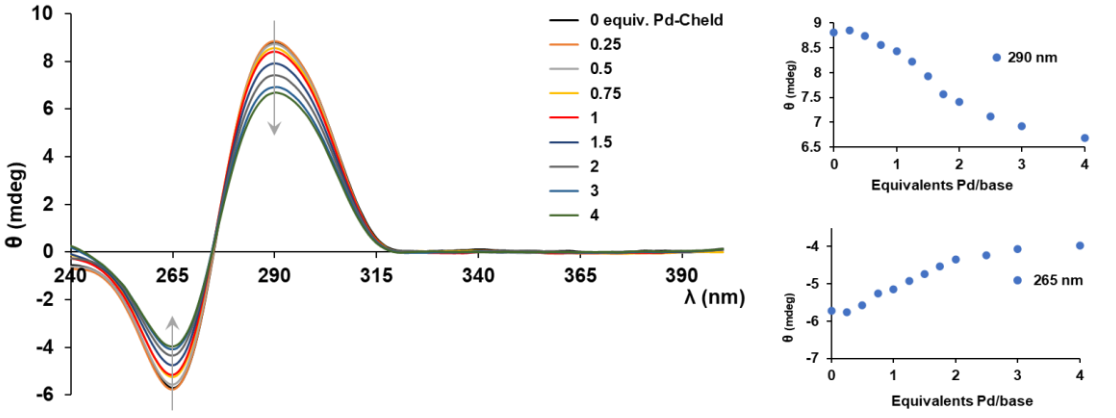

Figure S10. CD titration spectra for dC_{15} upon adding controlled amounts of **Pd-Cheld**. Insets: Ellipticity changes at 265 and 290 nm as a function of equivalents of **Pd-Cheld.** added.Conditions: 2 µM dC_{15}, 0 to 120 µM complex (in DMSO), 100mM $NaClO_4$, 5mM MOPS buffer pH 6.8. Note: 1 equivalent means one Pd^{II} complex per base.

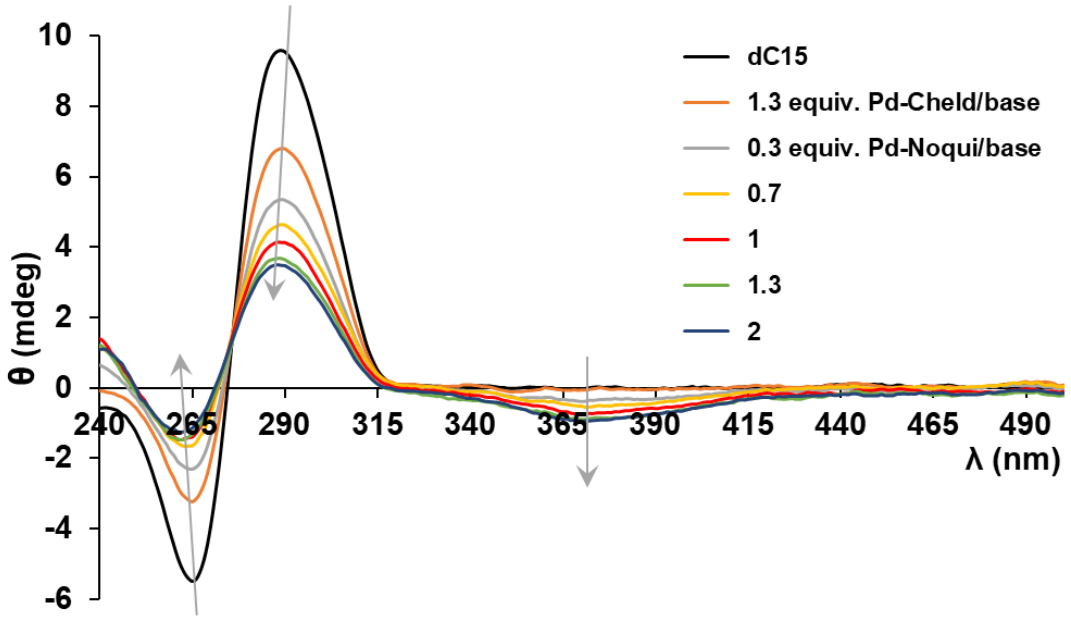

Figure S11. CD titration spectra for **dC_{15}:Pd-Cheld** (in 1:1.3 ratio) upon adding controlled amounts of **Pd-Aqa**. Conditions: 2 µM dC_{15}, 0 to 60 µM complex (in DMSO), 100mM $NaClO_4$, 5mM MOPS buffer pH 6.8. Note: 1 equivalent means one Pd^{II} complex per base.

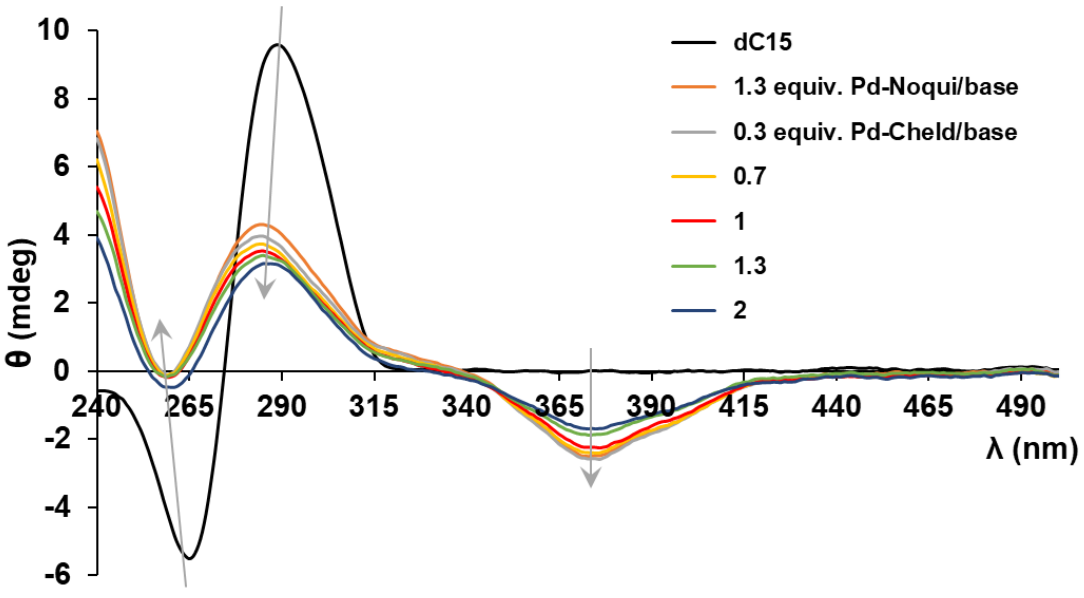

Figure S12. CD titration spectra for **dC_{15}:Pd-Aqa** (in 1:1.3 ratio) upon adding controlled amounts of **Pd-Cheld**. Conditions: 2 µM dC_{15}, 0 to 60 µM complex (in DMSO), 100mM $NaClO_4$, 5mM MOPS buffer pH 6.8. Note: 1 equivalent means one Pd^{II} complex per base.

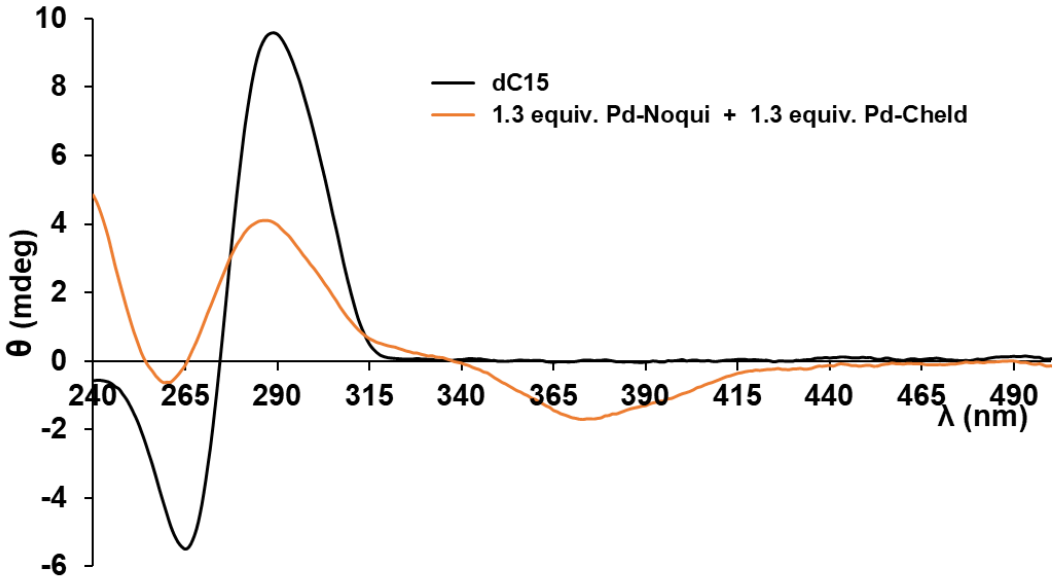

Figure S13. CD for dC_{15} upon addition of an equimolar mixture of **Pd-Cheld** and **Pd-Aqa**. Conditions: 2µM dC_{15}, 39 µM complex (in DMSO), 100mM $NaClO_4$, 5mM MOPS buffer pH 6.8. Note: 1 equivalent means one Pd^{II} complex per base.

ISOTHERMAL TITRATION CALORIMETRY

ITC experiments were carried out in a Microcal VP-ITC microcalorimeter (Malvern Panalytical, Malvern, UK) at 25°C. A solution of 100 µM [Pd(Aqa)(DMSO)] (**Pd-Aqa**) or [Pd(Cheld)(CH_3CN)] (**Pd-Cheld**) in the calorimeter's cell was titrated from the syringe with cytidine monophosphate (**CMP**) or single-stranded 15mer deoxycytidine (**dC_{15}**) at 2 mM total nucleotide concentration. Titrations were carried out with 10 µL injections at intervals of 24 or 48 min. Buffer conditions were the same as in the CD experiments. The experimental thermograms were baseline corrected and the peaks were integrated to determine the heats produced by each ligand injection. Residual heats due to unspecific binding or ligand dilution were estimated from the final peaks of the titrations. Each heat was normalized per mole of injected nucleotide monomer. The resulting binding isotherms were fitted using a binding model of n-independent and equivalent sites, allowing the determination of the apparent binding constant, K_b, the binding enthalpy, ΔH_b, and the binding stoichiometry, n. The apparent standard Gibbs energy and entropy of binding were calculated according to equation (1),

$$\Delta G_b = -RT \cdot lnK_b = \Delta H_b - T \cdot \Delta S_b \text{ (eq 1)},$$

Where R is the gas constant and T the absolute temperature.

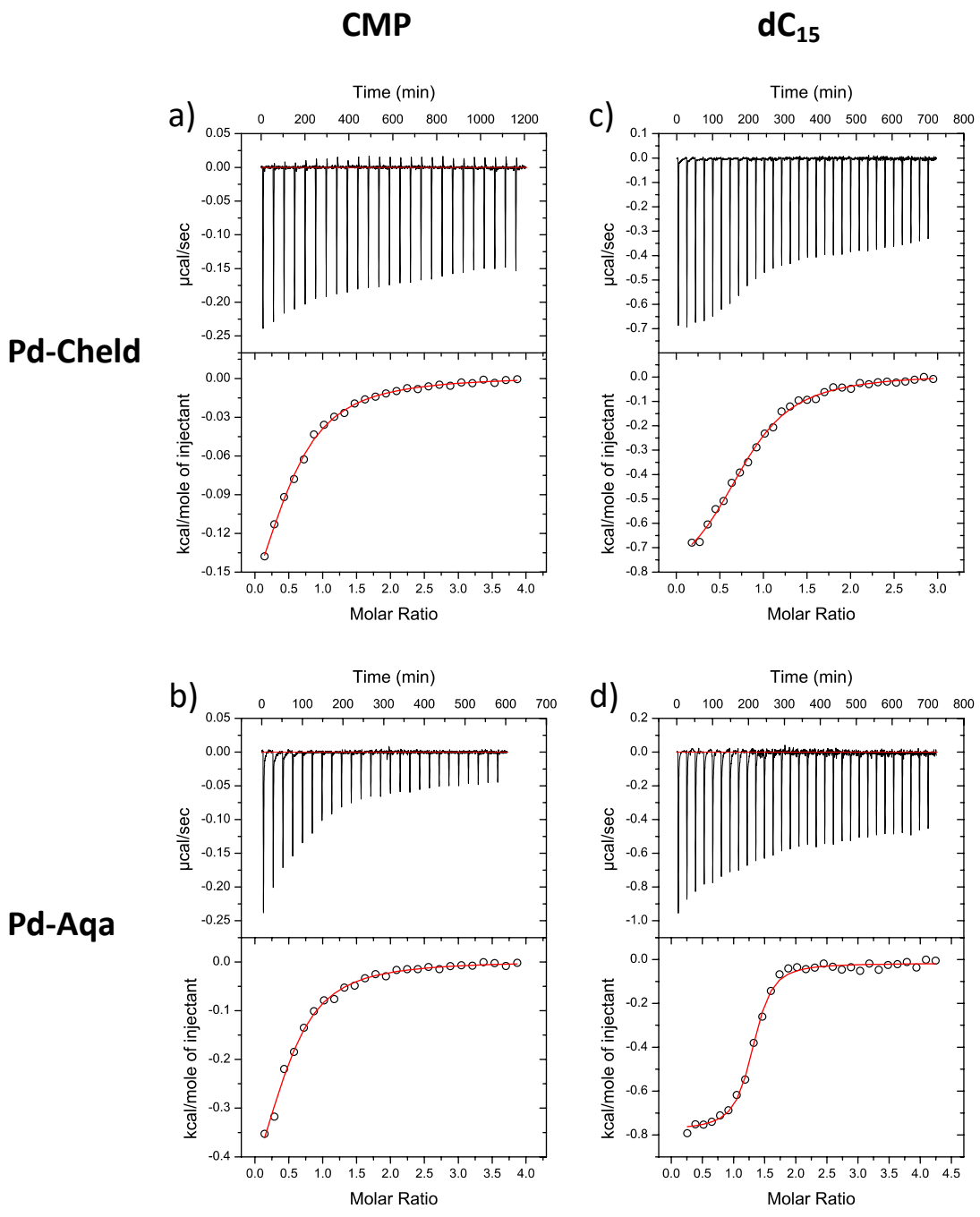

Figure S14. ITC plots of heat values against the molar ratio of: a) **Pd-Cheld** and CMP, b) **Pd-Aqa** and CMP, c) **Pd-Cheld** and dC_{15} and d) **Pd-Aqa** and dC_{15}

Table S3. Thermodynamic parameters of binding of **Pd-Cheld** and **Pd-Aqa** to CMP and dC_{15} derived from the fittings of the ITC thermograms shown in Figure S14 using a binding model of "n" independent and identical sites.

	CMP		**dC_{15}**	
	Pd-Aqa	**Pd-Cheld**	**Pd-Aqa**	**Pd-Cheld**
K_b ($\cdot 10^3$ M^{-1})	35 ± 12	27 ± 6	540 ± 140	54 ± 12
K_d (μM)	29 ± 10	37 ± 9	1.8 ± 0.5	18 ± 4
ΔG_b (kJ·mol^{-1})	-6.19 ± 0.21	-6.04 ± 0.14	-7.82 ± 0.15	-6.46 ± 0.13
ΔH_b (kJ·mol^{-1})	-0.65 ± 0.16	-0.26 ± 0.05	-0.76 ± 0.02	-1.06 ± 0.02
$-T\cdot\Delta S_b$ (kJ·mol^{-1})	-5.6 ± 0.4	-5.78 ± 0.18	-7.06 ± 0.18	-5.40 ± 0.15
N	0.46 ± 0.07	0.50 ± 0.05	1.26 ± 0.02	0.79 ± 0.03

Errors in the parameters were estimated as 95% confidence intervals of the fits. Kb; binding constant; Kd, dissociation constant; ΔG_b, free energy; ΔH_b, enthalpy; ΔS_b, enthalpy; T, temperature; n, stoichiometry (per base).

MOLECULAR MODELLING

Theoretical methodology for [Pd(Aqa)(Cyt)] (**Cyt-Pd-Aqa**) structure

The ORCA 5.0.2 computational program[8,9] was employed for the complete geometry optimization of small systems, specifically **Cyt-Pd-Aqa** complex. Quantum mechanics DFT calculations were conducted using Grimme's PBEh-3c method,[10] which is a hybrid functional incorporating a double zeta Gaussian-type basis set quality. To correct for basis set superposition error (BSSE), the geometrical counterpoise gCP correction algorithm was applied.[11] Additionally, the atom-pairwise dispersion correction with the Becke-Johnson damping scheme (D3BJ) was implemented.[12,13] For characterizing the nature of stationary points, a vibrational frequency calculation was performed, yielding all positive frequencies, indicative of a minimum.

Theoretical methodology for **dC_{15}-$(Pd\text{-}Aqa)_{15}$** structure

Theoretical model were constructed using Avogadro software,[14,15] beginning with the assembly of neutral systems by introducing 12 sodium counterions to phosphate groups. To consider solvent effects, 70 water molecules were incorporated into the model systems. The geometry optimization was conducted through quantum mechanics ab

initio calculations employing the DFT method, inclusive of the D3 dispersion correction scheme. The DFT calculations were executed using the NWChem software package[16] (version 7.0.2) to investigate the geometry optimization of a multifaceted system consisting of 844 atoms. This system encompasses 12 palladium ions (Pd^{II}), 12 sodium ions (Na^{I}) serving as counterions, and 70 water molecules.

For electronic structure calculations, the SBKJC-VDZ (Valence Double Zeta with Effective Core Potentials) basis set was applied to Pd^{II} ions, accompanied by the ECP (Effective Core Potential) basis set to accurately consider core electrons. The PBE0 (Perdew-Burke-Ernzerhof hybrid functional) was selected as the exchange-correlation functional due to its enhanced accuracy in describing both structural and electronic properties.[17,18] Additionally, the D3 correction was incorporated to address dispersion forces, especially relevant in systems featuring non-covalent interactions such as molecular aggregates.[12,13] A comprehensive geometry optimization was performed to minimize the overall system energy with respect to nuclear coordinates.

Coordinates of the DFT calculated [Pd(Aqa)(Cyt)] (**Cyt-Pd-Aqa**) structure.

C	-0.11006967560296	-5.14946487767188	2.09063272710077
N	0.11629559149095	-4.36524055076325	0.88996780669518
C	0.05022789387015	-2.96952072302463	1.01961021622606
O	-0.15271332378572	-2.52701449258144	2.12458150103840
N	0.21486280061085	-2.20109899739565	-0.11243514895625
C	0.50984682209342	-2.78816101593749	-1.28312150113968
N	0.70401880002404	-2.08111335902586	-2.38056885831979
C	0.62376188786619	-4.21151115573830	-1.38922336274584
C	0.40748858866341	-4.94654372945097	-0.28661068803173
H	0.64891690451563	-1.05133261085606	-2.41507845047828
H	0.91119641529428	-2.56687685988884	-3.23346075800134
H	0.86256167537221	-4.68017908498128	-2.33103888164603
H	0.46076712391271	-6.02659322635216	-0.29703500073628
H	-0.07937971147553	-6.20416798349116	1.82856637062203
H	-1.08269470273113	-4.92186649128121	2.52045696541409
H	0.65345970453500	-4.94631869377709	2.83876650845325
H	-0.01101560079408	4.49436446422677	-1.83367069455552
C	-0.21086391983011	3.93094195169642	-0.93010833158500
C	-0.60096847098004	4.53776742376933	0.24929308253553
N	-0.29525162885459	1.83905005807116	0.11289364147576
C	-0.85522932294469	3.76506007244458	1.41944629399777
C	-0.06321886720519	2.54425556920195	-0.96540588273490
C	-0.68069396467403	2.38245278306742	1.27750020160257
C	-1.24609104510509	4.25135637635877	2.67913770307837
C	-1.43535204869359	3.33386412456890	3.69532638807131
H	-1.39150935486613	5.30692901426084	2.85081994504341
H	-1.73494196088770	3.69966190356275	4.66979513081980
C	-1.26180192258632	1.95375484713277	3.54762434931340
H	-1.43132749548156	1.29836490803637	4.39214587195743

H	-10.949385450	-2.271983730	3.953410020	H	-15.166025020	1.647821150	2.859347660
H	-12.159249030	-2.100424400	2.905152050	O	-17.681094770	4.859714940	1.085054670
O	-14.743520110	1.111766020	3.562644270	H	-16.867406920	5.355420840	1.355051260
H	-13.985647300	1.622157740	3.943001510	H	-17.975327150	5.169599420	0.202220440

REFERENCES

[1] E. Greco, A. E. Aliev, V. G. H. Lafitte, K. Bala, D. Duncan, L. Pilon, P. Golding, H. C. Hailes, *New J. Chem.* **2010**, *34*, 2634–2642.

[2] N. P. Peet, L. E. Baugh, S. Sunder, J. E. Lewis, *J. Med. Chem.* **1985**, *28*, 298–302.

[3] A. Pérez-Romero, A. Domínguez-Martín, S. Galli, N. Santamaría-Díaz, O. Palacios, J. A. Dobado, M. Nyman, M. A. Galindo, *Angew. Chem. Int. Ed.* **2021**, *60*, 10089–10094.

[4] APEX3 Software,V2016.1; Bruker AXS: Madison, WI, USA, **2016**.

[5] G. M. Sheldrick, *SADABS 2016/2. Program for Empirical Absorption Correction of Area Detector Data*, University Of Göttingen, Germany., **2016**.

[6] G. M. Sheldrick, *Acta Crys.* **2008**, *64*, 112–122.

[7] O. V. Dolomanov, L. J. Bourhis, R. J. Gildea, J. A. K. Howard, H. Puschmann, *J. Appl. Crys.* **2009**, *42*, 339–341.

[8] F. Neese, *Wiley Interdiscip. Rev. Comput. Mol. Sci.* **2018**, *8*, e1327.

[9] F. Neese, *Wiley Interdiscip. Rev. Comput. Mol. Sci.* **2012**, *2*, 73–78.

[10] S. Grimme, J. G. Brandenburg, C. Bannwarth, A. Hansen, *J. Chem. Phys.* **2015**, *143*, 054107.

[11] H. Kruse, S. Grimme, *J. Chem. Phys.* **2012**, *136*, 154101.

[12] S. Grimme, S. Ehrlich, L. Goerigk, *J. Comput. Chem.* **2011**, *32*, 1456–1465.

[13] S. Grimme, J. Antony, S. Ehrlich, H. Krieg, *J. Chem. Phys.* **2010**, *132*, 154104.

[14] M. D. Hanwell, D. E. Curtis, D. C. Lonie, T. Vandermeersch, E. Zurek, G. R. Hutchison, *J. Cheminform.* **2012**, *4*, 17.

[15] *Avogadro: An Open-Source Molecular Builder and Visualization Tool. Version 1.2.0*. https://avogadro.cc/

[16] E. Aprà, E. J. Bylaska, W. A. de Jong, N. Govind, K. Kowalski, T. P. Straatsma, M. Valiev, H. J. J. van Dam, Y. Alexeev, J. Anchell, V. Anisimov, F. W. Aquino, R. Atta-Fynn, J. Autschbach, N. P. Bauman, J. C. Becca, D. E. Bernholdt, K. Bhaskaran-Nair, S. Bogatko, P. Borowski, J. Boschen, J. Brabec, A. Bruner, E. Cauët, Y. Chen, G. N. Chuev, C. J. Cramer, J. Daily, M. J. O. Deegan, T. H. Dunning Jr, M. Dupuis, K. G. Dyall, G. I. Fann, S. A. Fischer, A. Fonari, H. Früchtl, L. Gagliardi, J. Garza, N. Gawande, S. Ghosh, K. Glaesemann, A. W. Götz, J. Hammond, V. Helms, E. D. Hermes, K. Hirao, S. Hirata, M. Jacquelin, L. Jensen, B. G. Johnson, H. Jónsson, R. A. Kendall, M. Klemm, R. Kobayashi, V. Konkov, S. Krishnamoorthy, M. Krishnan, Z. Lin, R. D. Lins, R. J. Littlefield, A. J. Logsdail, K. Lopata, W. Ma, A. V. Marenich, J. Martin Del Campo, D. Mejia-Rodriguez, J. E. Moore, J. M. Mullin, T. Nakajima, D. R. Nascimento, J. A. Nichols, P. J. Nichols, J. Nieplocha, A. Otero-de-la-Roza, B. Palmer, A. Panyala, T. Pirojsirikul, B. Peng, R. Peverati, J. Pittner, L. Pollack, R. M. Richard, P. Sadayappan, G. C. Schatz, W. A. Shelton, D. W. Silverstein, D. M. A. Smith, T. A. Soares, D. Song, M. Swart, H. L. Taylor, G. S. Thomas, V. Tipparaju, D. G. Truhlar, K. Tsemekhman, T. Van Voorhis, Á. Vázquez-Mayagoitia, P. Verma, O. Villa, A. Vishnu, K. D. Vogiatzis, D. Wang, J. H. Weare, M. J. Williamson, T. L. Windus, K. Woliński, A. T. Wong, Q. Wu, C. Yang, Q. Yu, M. Zacharias, Z. Zhang, Y. Zhao, R. J. Harrison, *J. Chem. Phys.* **2020**, *152*, 184102.

[17] J. P. Perdew, M. Ernzerhof, K. Burke, *J. Chem. Phys.* **1996**, *105*, 9982–9985.
[18] C. Adamo, V. Barone, *J. Chem. Phys.* **1999**, *110*, 6158–6170.

Inorganic Chemistry

pubs.acs.org/IC Article

Comparative Structural Study of Metal-Mediated Base Pairs Formed outside and inside DNA Molecules

Alicia Dominguez-Martin, Simona Galli, José A. Dobado, Noelia Santamaría-Díaz, Antonio Pérez-Romero, and Miguel A. Galindo*

Cite This: *Inorg. Chem.* 2020, 59, 9325−9338 Read Online

ACCESS | Metrics & More | Article Recommendations | Supporting Information

ABSTRACT: The formation of copper(II)-mediated base pairs involving pyridine-2,6-dicarboxylate derivatives and canonical nucleosides has proven to be a smart approach to introduce copper(II) ions at specific locations of DNA duplexes. However, the structural characteristics of these metalized base pairs have not yet been revealed, and their effect on DNA structures is difficult to assess. Herein, for the first time, we report on the different structural details of copper-mediated base pairs formed by themselves and in DNA duplexes. The individual base pairs [Cu(mcheld)(*N3*-Cyt)(H_2O)]·3H_2O (**1Cu_Cyt**), [Cu(mcheld)(*N7*-Ade)(H_2O)$_2$]·2H_2O (**1Cu_Ade**), [Cu(mcheld)(*N7*-Gua)(H_2O)] (**1Cu_Gua**), and [Cu(mcheld)(*N1*-^{7C}Ade)(H_2O)]·H_2O (**1Cu_^{7C}Ade**) were obtained from the reaction of the metal complex [Cu(mcheld)(H_2O)$_2$] (**1Cu**) (mcheld = 4-methoxypyridine-2,6-dicarboxylic acid) with model nucleosides (Cyt = *N1*-methylcytosine, Ade = *N9*-ethyladenine, Gua = *N9*-propylguanine, ^{7C}Ade = *N9*-propyl-7-deazaadenine). The crystal structure of the five complexes was determined by means of single-crystal X-ray diffraction. Furthermore, the formation of the **1Cu_Cyt** and **1Cu_Gua** base pairs in the middle of DNA duplexes, duplex **DNA$_{15}$** (917 atoms) and **DNA$_{10}$** (649 atoms), respectively, was studied using highly demanding *ab initio* computational calculations. These theoretical studies aimed to validate, from a structural point of view, whether base pairs of the kind **1Cu_nucleosides** can be included in a DNA double helix and how this situation affects the double-helical structure. The results indicate that the **1Cu_Cyt** and **1Cu_Gua** base pairs can be formed in a DNA molecule without significant structural constraints. In addition, the double-helix DNA structure remains virtually unchanged when it contains these Cu(II)-mediated base pairs.

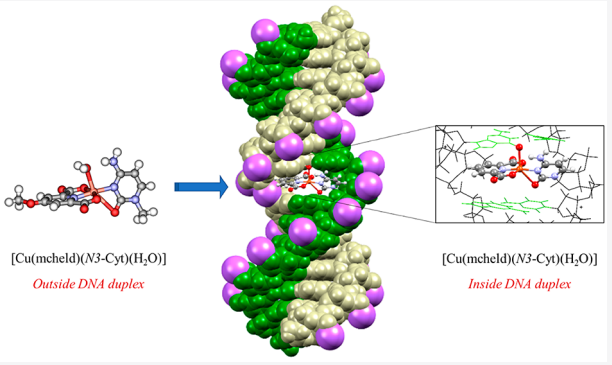

INTRODUCTION

The development of DNA-based nanotechnology has received deep attention due to the remarkable properties of nucleic acids.[1] DNA is very soluble in water, and its synthesis is well established, making it an ideal biopolymer for research purposes. The code programmability of DNA derives from the natural self-assembly capabilities of adenine−thymine (A-T) and guanine−cytosine (G-C) base pairs. The DNA structure and conformation can be rationally preprogrammed on the basis of the self-recognition abilities of DNA sequences,[2] leading to tailored structures that range from the nanometer to the micrometer scale.[3] In addition, the DNA genetic code can be further expanded if novel ligand-type nucleobases (LTNs), i.e. specific ligands replacing canonical nucleobases, are employed.[4] In this regard, different LTNs have been demonstrated to self-assemble inside DNA in the presence of metal ions, forming the so-called metal-mediated base pairs.[5] This strategy, first proposed by Shionoya's research group[6] and first achieved by Schultz,[4] has led to the formation of smart metal-mediated base pairs with different combinations, which include LTN-M-LTN and LTN-M-nucleobase pairs (M = metal ion).[7,8] Among the LTNs, some nucleobase analogues are capable of mimicking either Watson−Crick or Hoogsteen pairing in both the absence and presence of metal ions.[9−12] Remarkably, the use of LTNs has led to short oligonucleotides featuring specific transition-metal ions situated at precise locations inside a DNA double helix, with applications ranging from sensing to electron transport processes.[13−17] The formation of metal-mediated base pairs inside DNA is normally determined in solution using spectroscopic and spectrometric methodologies. However, unraveling the structural organization of these systems can be a complicated task due to the difficulty in either obtaining

Received: April 23, 2020
Published: June 18, 2020

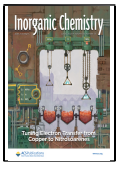

https://dx.doi.org/10.1021/acs.inorgchem.0c01210
Inorg. Chem. 2020, 59, 9325−9338

crystals suitable for single-crystal X-ray diffraction, or performing structural high-resolution NMR studies. Notably, in some cases, solid-state crystallographic investigations and solution NMR studies have been carried out for DNA molecules containing metal-mediated base pairs.[18] Alternatively, theoretical computational procedures can help in revealing the structural aspects of metal-mediated base pairs. Such calculations are commonly performed for individual base pairs,[19,20] with few cases involving the DNA framework.[21,22]

The ligand pyridine-2,6-dicarboxylic acid (Cheld, a planar tridentate ligand) and its carboxyamide derivative[23] were among the pioneering ligands to be employed in the formation of metal-mediated base pairs. Cheld has been widely used in the preparation of metalated double-stranded DNA (ds-DNA) molecules via the formation of metal-mediated base pairs. Initially, Cheld and pyridine were employed to introduce Cu(II) ions into DNA duplexes by forming unsymmetrical [3 + 1] metal−base pairs. This approach led to the formation, in solution, of DNA duplexes containing Cheld-Cu-nucleobase mismatches, which showed higher thermal stability in comparison to the unmetalated counterparts.[4] The stabilization of these mismatches followed the trend adenine > cytosine > guanine, with no data for thymidine mismatches. These results demonstrated that the ligand Cheld can be employed to form metal-mediated base pairs with canonical bases within ds-DNA molecules.

The crystal structure of a DNA duplex containing one Cheld-Cu-pyridine metallo-base pair was determined,[24] as well as the crystal structure of the complex itself,[25,26] demonstrating the predictable coplanar arrangement between Cheld and pyridine in both cases. However, no further studies have been performed to fully reveal the structure and conformation of Cheld-Cu-nucleoside systems, where noncoplanar arrangements between the units can be anticipated. In this regard, it is important to compare the structure of metal-mediated base pairs when they are prepared inside and outside a double helix, in order to determine the effect of the DNA scaffold on the final arrangement. In this respect, Cheld-Cu-nucleoside systems are important representative examples.

To the best of our knowledge, only the crystal structure of the Cheld-Cu-adenine ternary complex[27] and the interaction of other iminodiacetic acid based copper(II) complexes toward adenine derivatives[28] have been reported. Though the molecular structure of Cheld-Cu-nucleoside systems could be foretold in principle on the basis of these previously described systems, detailed, experimentally derived structural information at the molecular and crystal-packing level is still needed to accurately understand the structural implications that the Cheld-Cu-nucleoside systems can have in DNA molecules.

Ultimately, determining the crystal and molecular structure of metal-mediated base pairs will provide fundamental information that can be used in the design of novel metal−DNA systems, potentially finding applications in different areas, from catalysis to charge transport.

In this context, we report herein the preparation and solid-state characterization of complexes of the type Cheld-Cu-nucleoside as well as, utilizing *ab initio* theoretical calculations, their organization inside DNA duplexes, in an effort to get some insight into the molecular arrangement of these systems when they are prepared by themselves and in the context of a DNA molecule.

EXPERIMENTAL SECTION

Materials and Methods. 1-Methylcytosine (Cyt),[29] *N*9-ethyladenine (Ade),[30] and diethyl-4-hydroxypyrimidine-2,6-carboxylic acid (decheld)[31] were synthesized according to literature procedures. 6-Amino-7-deazapurine, 6-chloro-2-amino-7-deazapurine, adenine, sodium hydride (60% oil dispersion), anhydrous *N*,*N*-dimethylformamide, 1-iodopropane, and the oligonucleotides $d(Ade)_{15}$, $d(^{7C}Ade)_{15}$, $d(Cyt)_{15}$ and $d(Gua)_{10}$ were purchased from Sigma-Aldrich. ^{1}H NMR spectra were recorded with a Bruker AMX instrument working at 300 MHz. ^{13}C NMR spectra were recorded with a Bruker Neo 500 MHz spectrometer. Elemental analyses were carried out with a Fisons-Carlo Erba Model EA 1108 analyzer. CD spectra were recorded on a JASCO J-815 spectrometer. High-resolution electrospray mass spectrometry was performed with a Waters LCT Premier XE mass spectrometer. Infrared (IR) spectra were registered with a Bruker Tensor-27 FT-IR spectrometer.

Synthesis of the Ligands. *Diethyl-4-methoxypyrimidine-2,6-dicarboxylic Acid (demcheld).* To a solution of decheld (3.00 g, 12.50 mmol) in anhydrous *N*,*N*-dimethylformamide (150 mL) was added sodium hydride (0.50 g, 12.50 mmol) under N_2. The reaction mixture was stirred for 30 min at room temperature. After this time, iodomethane (0.79 mL, 12.50 mmol) was added and the mixture was stirred under N_2 for 48 h. The solvent was then removed under reduced pressure, and the product was diluted in dichloromethane (150 mL) and washed with aqueous sodium hydrogen carbonate (10% m/m, 150 mL) and brine (150 mL). The organic layers were collected, dried over magnesium sulfate, filtered off, and concentrated in vacuo, giving the title compound as a white powder (3.00 g, 94% yield). ^{1}H NMR (300 MHz, DMSO-d_6): δ (ppm) 7.72 (s, 2H; *CH*), 4.38 (q, J = 7.1 Hz, 4H; CH_2), 3.98 (s, 3H; CH_3), 1.34 (t, J = 7.1 Hz, 6H; CH_3). HRMS (ESI): m/z calcd for $C_{12}H_{16}NO_5$ $[M + H]^+$, 254.1028; found, 254.1037.

4-Methoxypyridine-2,6-dicarboxylic Acid (mcheld). demcheld (2.00 g, 8.37 mmol) was dissolved in 0.5 M aqueous sodium hydroxide (25 mL), and the solution thus obtained was refluxed overnight. Then, the solution was acidified with concentrated hydrochloric acid until the pH reached 3.6 and was concentrated under reduced pressure to give the title compound as a white precipitate, which was filtered off and dried under vacuum (1.21 g, 58% yield). ^{1}H NMR (300 MHz, DMSO-d_6): δ (ppm) 7.36 (s, 2H; *CH*), 3.80 (s, 3H; CH_3). IR (ν/cm^{-1}): 3564.7, 3429.8, 3084.3, 2923, 1722, 1631.5, 1601, 1574.7, 1465.8, 1439.5, 1410.2, 1372.5, 1312.1, 1234, 1165.4, 1112.3, 1047.7, 892.7, 865.1, 814.9, 783, 696.7, 579.6. HRMS (ESI): m/z calcd for $C_8H_8NO_5$ $[M + H]^+$, 198.0402; found, 198.0406.

N9-Propyl-7-deazaadenine (^{7C}Ade). To a solution of 6-amino-7-deazapurine (1.00 g, 7.23 mmol) in anhydrous *N*,*N*-dimethylformamide (200 mL) was added NaH (0.10 g, 2.48 mmol) under argon. The reaction mixture was stirred for 30 min until H_2 evolution ceased. 1-Iodopropane (0.22 mL, 2.26 mmol) was then added, and the reaction mixture was stirred at room temperature for 24 h under argon. The solvent was removed under reduced pressure. The crude residue was dissolved in dichloromethane (200 mL) and washed with an aqueous solution of sodium hydrogen carbonate (10% m/m, 150 mL) and brine (150 mL). The organic layer was collected, dried over magnesium sulfate, filtered off, and concentrated in vacuo. The precipitate was recrystallized from dichloromethane to give the title compound in the form of a powder (0.70 g, 55% yield). ^{1}H NMR (300 MHz, DMSO-d_6): δ (ppm) 8.04 (s, 1H; *CH*), 7.13 (d, J = 3.4 Hz, 1H; *CH*), 6.87 (s, 2H; NH_2), 6.51 (d, J = 3.4 Hz, 1H; *CH*), 4.05 (t, J = 7.1 Hz, 2H; CH_2), 1.90−1.61 (m, 2H; CH_2), 0.81 (t, J = 7.4 Hz, 3H; CH_3). ^{13}C NMR (500 MHz, DMSO): δ (ppm) 157.84 (C6), 151.89 (C2), 150.01 (C4), 124.52 (C8), 102.77 (C5), 98.68 (C7), 45.76 (C10), 23.70 (C11), 11.54 (C12). IR (ν/cm^{-1}): 1680, 1639.6, 1612.6, 1568.2, 1502.7, 1467.9, 1415.8, 1363.8, 1334.8, 1305.9, 1215.2, 1084.1, 1047.4, 1022.3, 960.62, 925.9, 879.6, 792.8, 752.3, 733, 700, 673.2. HRMS (ESI): m/z calcd for $C_9H_{13}N_4$ $[M + H]^+$, 177.1140; found, 177.1113.

https://dx.doi.org/10.1021/acs.inorgchem.0c01210
Inorg. Chem. 2020, 59, 9325−9338

*N9-Propyl-6-chloro-2-amino-7-deazapurine (**Cl-^{7C}Gua**).* 6-Chloro-2-amino-7-deazapurine (1.00 g, 5.90 mmol) was dissolved in anhydrous *N*,*N*-dimethylformamide (100 mL), and NaH (0.24 g, 6.00 mmol) was added under argon. The reaction mixture was stirred until H_2 evolution ceased. 1-Iodopropane (0.58 mL, 6.00 mmol) was then added, and the solution was stirred for 24 h at room temperature under argon. The solvent was removed under reduced pressure. The crude precipitate was dissolved in dichloromethane (200 mL) and washed with aqueous sodium hydrogen carbonate (10% m/m, 150 mL) and brine (150 mL). The organic layer was collected, dried over magnesium sulfate, filtered, and concentrated in vacuo. The sample was then recrystallized from dichloromethane to give the title compound in the form of a powder (0.85 g, 68% yield). ^{1}H NMR (300 MHz, DMSO-d_6): δ (ppm) 7.17 (d, J = 3.5 Hz, 1H; *CH*), 6.61 (s, 2H; NH_2), 6.28 (d, J = 3.4 Hz, 1H; *CH*), 3.97 (t, J = 7.1 Hz, 2H; CH_2), 1.73 (m, 2H; CH_2), 0.82 (t, J = 7.3 Hz; 3H; CH_3). HRMS (ESI): m/z calcd for $C_9H_{12}ClN_4$ $[M + H]^+$, 211.0750; found, 211.0732.

*N9-Propyl-7-deazaguanine (**^{7C}Gua**).* **Cl-^{7C}Gua** (0.40 g, 1.90 mmol) was refluxed in a hydrochloric acid (25 mL, 1 M) and ethanol (5 mL) mixture for 2 h. After the mixture was cooled to room temperature, the pH was adjusted to ca. 7 using sodium hydroxide and the suspension was cooled in an ice bath for 1 h. The precipitate was collected by filtration and dried in vacuo to afford the title compound in the form of crystals (0.05 g, 15% yield). ^{1}H NMR (300 MHz, DMSO-d_6): δ (ppm) 10.22 (s, 1H; *NH*), 6.71 (d, J = 3.2 Hz, 1H; *CH*), 6.19 (d, J = 3.3 Hz, 2H; NH_2), 6.17 (s, 1H; *CH*), 3.85 (t, J = 7.0 Hz, 2H; CH_2), 1.68 (m, 2H; CH_2), 0.82 (t, J = 7.3 Hz, 3H; CH_3). ^{13}C NMR (500 MHz, DMSO-d_6): δ (ppm) 159.1 (C6), 152.9 (C2), 150.5 (C4), 120.4 (C8), 101.4 (C7), 100.3 (C5), 45.81 (C10), 23.7 (C11), 11.5 (C12). IR (ν/cm^{-1}): 3402.7, 3173.1, 2874.1, 1660.8, 1608.7, 1539.3, 1508.4, 1433.2, 1410.1, 1369.6, 1334.8, 1304, 1213.3, 1180.5, 1072.5, 889.2, 850.7, 785.1, 717.8, 677.1, 601.8, 555.5. HRMS (ESI): m/z calcd for $C_9H_{13}N_4ONa$ $[M + H]^+$, 193.1089; found, 193.1086.

Synthesis of the Complexes. *[Cu(mcheld)(H_2O)$_2$] (**1Cu**).* To an aqueous solution of $Cu(CH_3COO)_2$ (0.09 g, 0.50 mmol) was added an aqueous solution of mcheld (0.10 g, 0.50 mmol) dropwise with stirring. The resulting solution was heated to 90 °C and left at this temperature with stirring for 30 min. A light blue precipitate appeared, which was filtered off and washed with water, ethanol, and ether. The filtrate was left to crystallize by slow evaporation from the aqueous solution. After a few days, blue single crystals suitable for X-ray diffraction were collected (0.07 g, 50% yield). Anal. Calcd for $C_8H_9CuNO_7$: C, 32.60; H, 3.08; N, 4.75. Found: C, 32.55; H, 3.75; N, 4.81.

*[Cu(mcheld)(N3-Cyt)(H_2O)]·3H_2O (**1Cu_Cyt**).* To a warm aqueous solution (15 mL) of 1-methylcytosine (0.09 g, 0.07 mmol) was added an aqueous solution (10 mL) of **1Cu** (0.02 g, 0.07 mmol) dropwise. The solution was heated to 65 °C and left at this temperature with stirring for 30 min. When the solution appeared clear, it was left to crystallize by slow solvent evaporation at room temperature. After a few days, blue single crystals suitable for X-ray diffraction were formed (0.01 g, 40% yield). Anal. Calcd for $C_{13}H_{14}CuN_4O_7{\cdot}3H_2O$: C, 34.25; H, 4.42; N, 12.29. Found: C, 34.55; H, 4.50; N, 12.54.

*[Cu(mcheld)(N7-Ade)(H_2O)]·2H_2O (**1Cu_Ade**).* To a warm aqueous solution (15 mL) of *N9*-ethyladenine (0.02 g, 0.10 mmol) was added an aqueous solution (15 mL) of **1Cu** (0.03 g, 0.10 mmol) dropwise. The solution was heated to 65 °C and left at this temperature with stirring for 30 min. The precipitate was collected by filtration and dried in vacuo to afford the title compound in the form of a powder (0.04 g, 87% yield). Anal. Calcd for $C_{15}H_{16}CuN_6O_6{\cdot}6.6H_2O$: C, 32.03; H, 5.30; N, 14.94. Found: C, 31.84; H, 4.93; N, 15.45. The precipitate was recrystallized by room-temperature slow evaporation in DMF, giving blue single crystals suitable for X-ray diffraction after a few days. The detection of higher water content by elemental analysis than by X-ray diffraction (*vide infra*) could be due to the presence of surface-absorbed moisture.

*[Cu(mcheld)(N7-Gua)(H_2O)] (**1Cu_Gua**).* To an aqueous solution (15 mL) of *N9*-propylguanine (0.02 g, 0.10 mmol) was added an aqueous solution (10 mL) of **1Cu** (0.03 g, 0.10 mmol) dropwise. The solution was heated to 65 °C and left at this temperature with stirring for 30 min. A very thin precipitate was formed and eliminated by filtration. The clear solution was then left to crystallize at room temperature by slow solvent evaporation. After a few days, blue single crystals suitable for X-ray diffraction were collected (0.02 g, 47% yield). Anal. Calcd for $C_{16}H_{18}CuN_6O_7(H_2O)$: C, 39.39; H, 4.13; N, 17.23. Found: C, 39.71; H, 4.22; N, 17.12. The detection of higher water content by elemental analysis than by X-ray diffraction (*vide infra*) could be due to the presence of surface-absorbed moisture.

*[Cu(mcheld)(N1-^{7C}Ade)(H_2O)$_2$]·H_2O (**1Cu_^{7C}Ade**).* To an aqueous solution (15 mL) of **1Cu** (0.02 g, 0.07 mmol) was added an aqueous solution (10 mL) of the ligand (0.01 g, 0.07 mmol) dropwise. The solution was heated to 60 °C and left at this temperature with stirring for 30 min. A thin precipitate was formed and eliminated by filtration. The clear solution was then left to crystallize at room temperature by slow solvent evaporation. After a few days, blue single crystals suitable for X-ray diffraction were recovered (0.01 g, 32% yield). Anal. Calcd for $C_{17}H_{19}CuN_5O_6(H_2O)$: C, 43.35; H, 4.49; N, 14.87. Found: C, 43.18; H, 4.92; N, 14.70.

Single-Crystal X-ray Diffraction Structure Determination. X-ray diffraction data for **1Cu_^{7C}Ade** were collected using a Bruker X8 Proteum diffractometer equipped with a Cu (λ = 1.54178 Å) sealed rotating anode X-ray tube, a Bruker AXS Smart 6000 CCD detector, and an Oxford Cryostream 700 plus cooling apparatus. X-ray diffraction data for **1Cu**, **1Cu_Ade**, and **1Cu_Gua** were collected on a Bruker D8 Venture diffractometer equipped with either a Cu (λ = 1.54178 Å) or a Mo (λ = 0.71073 Å) X-ray tube, a Bruker AXS Photon 100 detector, and a Kryoflex II cooling apparatus. For all four of the complexes, data reduction was performed with the software APEX3,[32] while data correction for absorption was carried out using the software SADABS.[33] X-ray diffraction data for **1Cu_Cyt** were collected using a Bruker SMART APEX I diffractometer equipped with a Mo (λ = 0.71073 Å) X-ray tube and a Kryoflex cooling apparatus. In this case, data reduction was performed with the software SAINT V6.36A, while data correction for absorption was carried out using SADABS.[33] The structures were solved by direct methods as implemented in SHELXS-97,[34] which allowed the location of most of the atoms of the asymmetric unit. All the remaining non-hydrogen atoms were located from difference Fourier maps calculated from successive full-matrix least-squares refinement cycles on F^2 using SHELXL-2018/3.[34] The electron densities around the propyl group in **1Cu_Gua** and **1Cu_^{7C}Ade** were ill-defined: the central carbon atom of the propyl group was found to be disordered into two positions. Isotropic thermal displacement parameters were refined for the three carbon atoms of the propyl group, and no hydrogen atoms were located on them. Anisotropic thermal displacement parameters were assigned to all the other non-hydrogen atoms. The hydrogen atoms were located at idealized positions using HFIX instructions and described with isotropic thermal displacement parameters fixed at 1.2 or 1.5 times those of the atom to which they were bound. The main crystallographic information and experimental and data treatment details are provided in Table S1 in the Supporting Information.

Computational Details. Theoretical models were built from scratch using the Avogadro software.[35] Sodium counterions or protons were added to the phosphate groups, thus resulting in neutral model systems. After a partial geometry optimization of these molecules, using semiempirical methods (PM3) within the ORCA 4.2.1 computational program,[36,37] a suitable geometry was obtained for further full optimization by quantum mechanics *ab initio* calculations using the HF-3c method.[38] The latter method includes the so-called MINIX basis set and a correction of the basis set superposition error (BSSE) by means of the geometrical counterpoise gCP correction algorithm,[39] as well as the atom-pairwise London dispersion energy from the D3 dispersion correction scheme with the Becke−Johnson damping scheme (D3BJ).[40−42] The solvent effect was included by the so-called "implicit solvent model". Thus, the solute was placed in a cavity of roughly molecular shape, and the solvent was described by a continuum that interacts with the charges on the cavity

https://dx.doi.org/10.1021/acs.inorgchem.0c01210
Inorg. Chem. 2020, 59, 9325−9338

Scheme 1. Synthesis of the Model Nucleosides *N9*-Propyl-7-deazaadenine (^{7C}Ade) and *N9*-Propyl-7-deazaguanine (^{7C}Gua)[a]

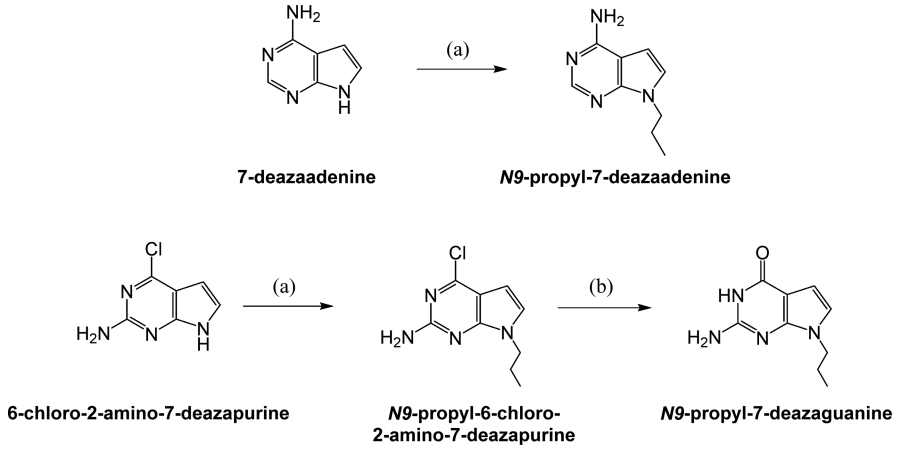

[a]Legend: (a) sodium hydride, 1-iodopropane, anhydrous *N*,*N*-dimethylformamide, rt, 24 h; (b) hydrochloric acid (1 M), reflux, 2 h.

surface. Specifically, the conductor-like polarizable continuum model (CPCM) was used for the computations of the DNA structure comprising only three base pairs (**DNA$_3$**), using water as a solvent, which is an efficient way of accounting for solvent effects in quantum chemical calculations.[43] The solvent effect was not included for the calculations of larger **DNA$_{15}$** and **DNA$_{10}$** models, composed of 971 and 649 atoms, respectively, due to the extremely costly computational demand.

RESULTS AND DISCUSSION

Synthesis of 4-Methoxypyridine-2,6-dicarboxylic Acid (mcheld) and Model Nucleosides. The synthetic route to prepare 4-methoxypyridine-2,6-dicarboxylic acid (mcheld) consists of three steps (Scheme S1). The synthesis is initiated from the commercially available 4-hydroxypyridine-2,6-dicarboxylic acid, which is converted to diethyl-4-hydroxypyridine-2,6-carboxylate (decheld) in good yields, as described previously.[31] The successive reaction steps consist of the methylation of the hydroxyl functional group of decheld, using sodium hydride and iodomethane, to obtain diethyl 4-methoxypyridine-2,6-dicarboxylate (demcheld) in 94% yield. Finally, the demcheld ester is converted into the carboxylic acid mcheld using sodium hydroxide in water, affording it in 58% yield.

The model nucleosides *N9*-propyl-7-deazaadenine (^{7C}**Ade**) and *N9*-propyl-7-deazaguanine (^{7C}**Gua**) were prepared by following an adaptation of previous synthesis protocols (Scheme 1).[30,44] The synthesis of ^{7C}**Ade** was achieved in good yield via N-alkylation of the commercially available 7-deazaadenine using sodium hydride and 1-bromopropane, in anhydrous *N*,*N*-dimethylformamide. In the case of *N9*-propyl-7-deazaguanine (^{7C}**Gua**), the synthesis starts from 6-chloro-2-amino-7-deazapurine and the N9 position is blocked by introducing a propyl chain via N-alkylation, to form *N9*-propyl-6-chloro-2-amino-7-deazapurine. Then, a hydroxyl group displaces the chlorine atom by nucleophilic aromatic substitution in acidic conditions (1 M hydrochloric acid) to obtain ^{7C}**Gua**.

Synthesis and Crystal Structure of [Cu(mcheld)(H$_2$O)$_2$] (1Cu). The reaction of copper(II) acetate and mcheld was carried out in water at 90 °C, leading to a light blue precipitate. The latter was recovered by filtration and recrystallized in water, isolating blue single crystals which were characterized by elemental analysis and single-crystal X-ray diffraction according to the formula [Cu(mcheld)(H$_2$O)$_2$] (**1Cu**).

1Cu crystallizes in the monoclinic space group $P2_1/n$ (Table S1). The asymmetric unit contains one copper(II) ion, one mcheld molecule, and two water molecules, all in general positions. The copper(II) ion is five-coordinated and adopts a distorted-square-pyramidal geometry (τ = 0.08)[45] (Figure S1), as already observed in [Cu(Cheld)(H$_2$O)$_2$].[46] In **1Cu**, the mcheld ligand[56] shows the μ,κ^3-N$_{10}$,O$_2$,O$_4$ coordination mode (Cu−N10 1.900(2) Å, Cu−O2 2.056(1) Å, Cu−O4 2.043(2) Å) and occupies three basal positions. Two water molecules complete the coordination sphere, occupying the basal position opposite to the pyrimidine nitrogen atom (Cu−O2w 1.939(2) Å) and the apical position (Cu−O1w 2.174(2) Å). The latter water molecule forms a slightly elongated Cu−O bond, in agreement with the Jahn−Teller distortion that typically occurs in five- or six-coordinated Cu(II) complexes.[47] Intermolecular hydrogen bonds[56] are present among neighboring [Cu(mcheld)(H$_2$O)$_2$] complexes, involving the carboxylic oxygen atoms of mcheld and the water molecules (O1w···O2w 2.925(2) Å, O1w···O3 2.706(2) Å, O1w···O5 2.698(2) Å, O2w···O2 2.693(2) Å, O2w···O4 2.973(2) Å, O2w···O5 2.712(2) Å) (Figure S2). Overall, these interactions bring about the formation of a 3D supramolecular network. The methylation of the hydroxyl group of mcheld avoids the formation of intermolecular hydrogen bonds via this position.[48,49] As shown below, this feature is important regarding the coordination of the [Cu(mcheld)] fragment to nucleobases and nucleosides, since it favors the formation of hydrogen bonds exclusively between the carboxylic groups of mcheld and the donor or acceptor groups of the nucleobase moiety.[55]

Synthesis and Crystal Structure of mcheld-Cu-Nucleoside Complexes. The interaction of **1Cu** with a number of model nucleobases (Scheme 2) was studied in the solid state and solution by means of single-crystal X-ray diffraction and CD spectroscopy, respectively.

The general procedure to obtain complexes of the type [Cu(mcheld)(model nucleoside)] consisted of adding a warm aqueous solution of **1Cu** to a warm solution of the appropriate model nucleobase and leaving the mixture to react at 65 °C for 30 min with stirring. The precipitate was then filtered off and left to crystallize by slow evaporation (in DMF or water; see

https://dx.doi.org/10.1021/acs.inorgchem.0c01210
Inorg. Chem. 2020, 59, 9325−9338

Scheme 2. Model Nucleosides Employed in the Present Work[a]

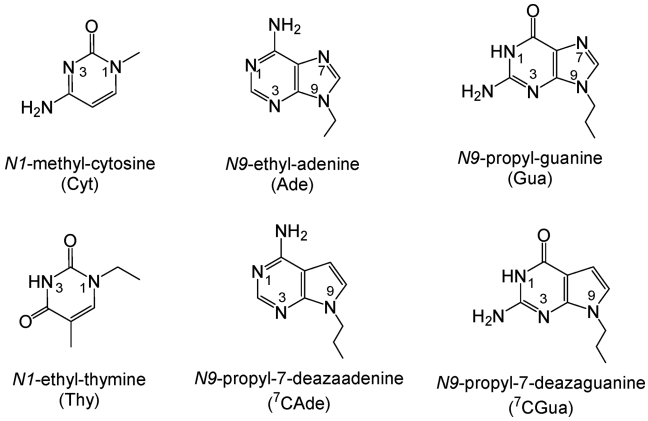

[a]For easy reading, the labels of the modified nucleobases avoid any reference to their alkyl functionalization.[57]

the Experimental Section). In all cases except for the Thy and ^{7C}**Gua** nucleobases, single crystals were formed after a few days and were characterized by X-ray diffraction as [Cu(mcheld)-(*N*3-Cyt)(H_2O)]·3H_2O (**1Cu_Cyt**), [Cu(mcheld)(*N*7-Ade)-(H_2O)$_2$]·2H_2O (**1Cu_Ade**), [Cu(mcheld)(*N*7-Gua)(H_2O)] (**1Cu_Gua**) and [Cu(mcheld)(*N1*-^{7C}Ade)(H_2O)]·H_2O (**1Cu_^{7C}Ade**).

The complex **1Cu_Cyt** crystallizes in the triclinic space group $P\bar{1}$ (Table S1). The asymmetric unit consists of one metal ion, one mcheld ligand, one Cyt nucleoside, and four water molecules, all in general positions. The copper(II) ion is six-coordinated and adopts a distorted-octahedral geometry. The mcheld ligand shows the μ,κ^3-N10,O2,O4 coordination mode (Figure 1-a) (Cu−N10 1.893(3) Å, Cu−O2 1.997(2) Å, Cu−O4 2.027(2) Å), occupying three equatorial positions, while the Cyt ligand shows the μ,κ^2-N3,O21 coordination mode (Figure 1a) (Cu−N3 1.956(3) Å, Cu−O21 2.711(3) Å), completing the equatorial plane with the pyrimidine nitrogen atom N3 and locating the ketonic oxygen atom O21, with a loose interaction, at one of the axial positions. One water molecule completes the coordination sphere (Cu−O1w 2.407(2) Å) at the remaining axial position, opposite to O21. Again, the longer axial Cu−O distances are reasonably the result of the Jahn−Teller effect. An intramolecular hydrogen bond is found between the coordinated water molecule O1w and the nitrogen atom N4 of the Cyt amino group (Figure 1a) (N4···O1w 2.822(2) Å). Intermolecular hydrogen bonds[56] are present between N4 and one non-coordinated water molecule (N4···O2w 2.863(4) Å) and among noncoordinated water molecules (O3w···O2w 2.821(5) Å, 2.826(3) Å, O3w···O3w 2.796(5) Å), as well as between water molecules and coordinated and dangling oxygen atoms of the carboxylate groups of mcheld (O4w···O2 2.886(4) Å, O4w···O4 2.866(4) Å, O1w···O5 2.775(4) and 2.841(4) Å). Overall, all the hydrogen-bond donor and acceptor atoms, from both mcheld and the Cyt moiety, are involved in hydrogen bonds (Figure 1b). The O1w···O5 interactions define a graph set motif of the type $R^2_4(8)$ (Figure S3).[50] In addition, each O2w···O3w···O3w···O2w segment (Figure 1b), running along the [001] crystallographic direction and lying on an inversion center, connects six [Cu(mcheld)(*N*3-Cyt)-(H_2O)] complexes. The crystal structure of **1Cu_Cyt** is

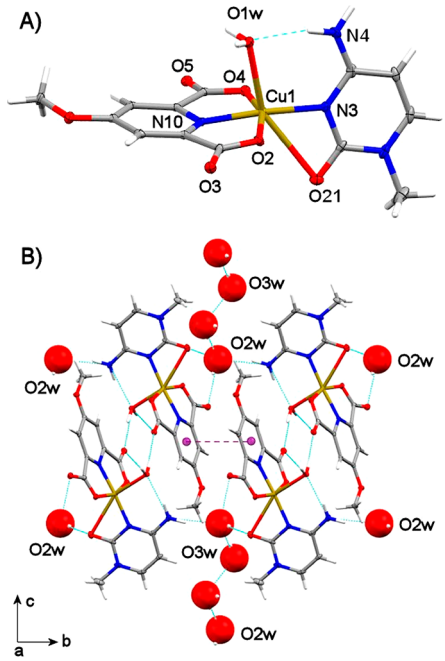

Figure 1. (a) Molecular structure of the complex [Cu(mcheld)(*N*3-Cyt)(H_2O)]·3H_2O (**1Cu_Cyt**) with thermal ellipsoids set at the 30% probability level. (b) Portion of the crystal structure of **1Cu_Cyt**, showing pairs of **1Cu_Cyt** complexes connected by hydrogen bonds (dashed cyan lines) and $\pi-\pi$ interactions (dashed purple line). The uncoordinated water molecules O4w (and the corresponding hydrogen bonds) have been omitted for clarity. The O2w and O3w noncoordinated water molecules have been represented as space-filling spheres.

further stabilized by the formation of $\pi-\pi$ interactions (distance between the centroids 3.596(2) Å, α = 0°, $\beta = \gamma$ = 27.25°) between the pyridine rings of mcheld (Figure 1b). The angle between the rms planes of Cyt and the [Cu(mcheld)] fragment is 77.64(11)°, highlighting the high deviation from coplanarity of the two ligands, likely enforced by the coordination of N3 and O21 to the same metal center.

The complex [Cu(mcheld)(*N*7-Ade)(H_2O)$_2$]·2H_2O (**1Cu_Ade**) crystallizes in the monoclinic space group $P2_1/n$ (Table S1). The asymmetric unit features one copper(II) ion, one mcheld ligand, one Ade nucleoside, and four water molecules, all in general positions. The copper(II) ion is six-coordinated in a distorted-octahedral geometry. The ligand mcheld shows the μ,κ^3-N10,O2,O4 coordination mode (Figure 2) (Cu−N10 1.953(4) Å, Cu−O2 2.229(3) Å, Cu−O4 2.310(4) Å), occupying three meridional positions within the octahedron. Ade is coordinated to the copper(II) ion through

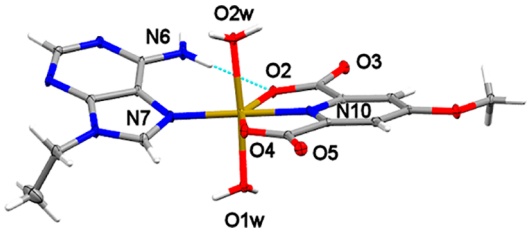

Figure 2. Molecular structure of the complex [Cu(mcheld)(*N*7-Ade)(H_2O)$_2$]·2H_2O (**1Cu_Ade**) with thermal ellipsoids set at the 30% probability level. The intramolecular hydrogen bond is depicted as a cyan dashed line.

https://dx.doi.org/10.1021/acs.inorgchem.0c01210
Inorg. Chem. 2020, 59, 9325−9338

N7 (Cu−N7 1.960(4) Å), occupying the remaining meridional position. Two water molecules occupy the axial positions (Cu−O1w 2.032(3) Å, Cu−O2w 2.072(4) Å) (Figure 2). The observed *N7*-Ade coordination mode is reinforced by an intramolecular hydrogen bond, involving the Ade N6 exocyclic amino group as a donor and one carboxylate group of mcheld as an acceptor (N6···O2 2.846(6) Å) (Figure 2). This molecular recognition pattern has been previously observed in related aromatic amine analogues[27,51,52] and reasonably influences the low value of the angle between the rms planes of mcheld and the nucleobase (23.98(12)°).

The crystal structure is further stabilized by intermolecular hydrogen bonds[56] involving coordinated and uncoordinated water molecules, the aminic nitrogen atom N6 of Ade, and the carboxylate groups of mcheld (N6···O5 2.964(5) Å, O1w···O3 2.678(4) Å, O1w···O5 2.743(5) Å, O2w···O4w 2.749(4) Å, O2w···N3 2.819(6) Å, O3w···N1 2.834(5) Å, O3w···O4w 2.736(5) Å, O4w···O3 2.814(5) Å) (Figure 3). Interestingly,

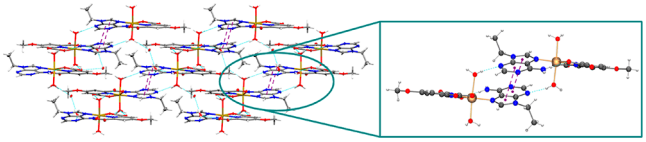

Figure 3. Portion of the crystal structure of **1Cu_Ade**. The hydrogen bonds (dashed cyan lines) involving the coordinated water molecules O2w lead to the formation of 1D double-strand motifs running along [001]. These motifs are connected by additional intermolecular $\pi-\pi$ interactions (purple lines), contributing to the formation of 2D supramolecular layers (a detail of the antiparallel $\pi-\pi$ interactions is provided in the inset).

upon consideration of the hydrogen bonds involving the coordinated water molecule O2w, a 1D double-strand motif running along the [001] direction can be envisaged (Figure 3). The strands interact through antiparallel $\pi-\pi$ stacking interactions between the five- and six-membered rings of Ade (distance between the centroids 3.552(3) Å, α = 2.30°, β = 19.93°, γ = 22.26°) (Figure 3 and Figure S4). Further hydrogen bond interactions define a 3D supramolecular network, in which two graphs set motifs of the kinds $R^3_4(10)$ and $R^3_2(10)$ can be identified (Figure S5).

The complex **1Cu_Gua** crystallizes in the monoclinic space group *Cc* (Table S1). The asymmetric unit consists of one copper(II) ion, one mcheld ligand, one Gua nucleoside, and one water molecule, all in general positions. The copper(II) ion adopts a distorted-square-pyramidal geometry (τ = 0.20)[45] (Figure 4). The mcheld ligand shows the μ,κ^3-N10,O2,O4 coordination mode (Cu−N10 1.908(4) Å, Cu−O2 2.061(4) Å, Cu−O4 2.046(4) Å), occupying three basal positions of the pyramid. The nucleobase Gua is coordinated to the copper(II) ion through N7 (Cu−N7 1.979(4) Å), occupying the fourth basal position. The apical position is occupied by a water molecule (Cu−O1w 2.155(4) Å). An intramolecular hydrogen bond is present between the water molecule and the keto group oxygen atom O61 of the nucleobase (Figure 4) (O1w···O61 2.698(5) Å). Moreover, intermolecular hydrogen bonds[56] are observed between the water molecule and the carboxylic atom O4 of mcheld (O1w···O4 2.746(6) Å), which leads to the formation of a 1D supramolecular chain of collinear metal ions 5.3 Å apart running along [010] (Figure S6). Hydrogen bonds are also present between the guanine N2 amino group and the carboxylate O5 atom of mcheld and between the

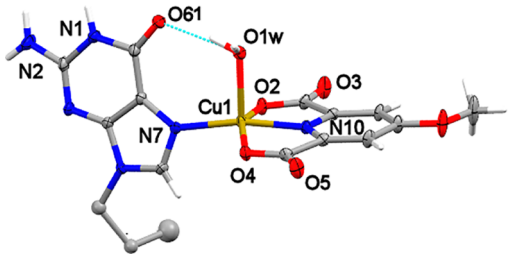

Figure 4. Molecular structure of [Cu(mcheld)(*N7*-Gua)(H_2O)] (**1Cu_Gua**) with thermal ellipsoids set at the 30% probability level. The intramolecular hydrogen bond interaction is highlighted by a cyan dashed line. For clarity, an ordered model has been adopted for the Gua propylic residue.

guanine endocyclic N1 nitrogen atom and the carboxylate O3 atom of mcheld (N2···O5 2.988(7) Å, N1···O3 2.827(7) Å) (Figure S7). Overall, a 3D network of intermolecular hydrogens bond is formed. The [Cu(mcheld)] fragment and the Gua moiety are not coplanar, with an angle between their rms planes of 78.94(10)°. This non-negligible deviation from planarity can be due to the repulsive interactions that take place between the Gua keto group and the mcheld carboxylate groups, which also allows for the formation of the intramolecular hydrogen bond. No $\pi-\pi$ stacking interactions are observed in the crystal structure.

The interaction of complex **1Cu** with Ade and Gua derivatives occurs via the Hoogsteen-position N7 atom, as is evidenced by the complexes **1Cu_Ade** and **1Cu_Gua**, respectively. This metal−nucleoside binding mode is expected, since the N7 position is usually preferred by metal ions that interact with purine nucleobases/nucleosides, especially guanine.[53] The fact that no interaction was observed via the Watson−Crick position (the N1 atom) prompted us to use a different strategy to evaluate this alternative binding mode that could also occur when Cheld-Cu complexes are introduced in a DNA molecule. Thus, 7-deazapurine analogues were employed, namely *N9*-propyl-7-deazaadenine (**^{7C}Ade**) and *N9*-propyl-7-deazaguanine (**^{7C}Gua**), and their interactions toward **1Cu** were evaluated. This strategy has been already proven to be successful to study the interactions of metal ions toward Watson−Crick positions.[11,12]

The complex **1Cu_^{7C}Ade** was obtained upon reaction of **1Cu** with **^{7C}Ade** in water. This complex crystallizes in the triclinic space group $P\bar{1}$ (Table S1). The asymmetric unit contains one copper(II) ion, one mcheld ligand, one **^{7C}Ade** nucleoside, and one water molecule, all in general positions. The copper(II) ion shows a distorted-square-pyramidal coordination (τ = 0.10)[45] (Figure 5). The mcheld ligand shows the μ,κ^3-N10,O2,O4 coordination mode (Cu−N10 1.922(3) Å, Cu−O4 2.128(2) Å, Cu−O2 2.038(2) Å), occupying three basal positions. In this case, the nucleoside **^{7C}Ade** is coordinated to the copper(II) ion through the Watson−Crick position N1, occupying the fourth basal position of the pyramid (Cu−N1 1.974(3) Å) (Figure 5). The apical position is occupied by a water molecule (Cu−O1w 2.210(2) Å) (Figure 5).

The mcheld ligand and the **^{7C}Ade** nucleoside are not coplanar, with an angle between their rms planes of 45.47(7)°, considerably larger than the angle observed when the [Cu(mcheld)] fragment binds via the Ade-N7 atom (vide supra). Intra- and intermolecular hydrogen bonds are present between the **^{7C}Ade**-N6 amino protons and the carboxylate O2

https://dx.doi.org/10.1021/acs.inorgchem.0c01210
Inorg. Chem. 2020, 59, 9325−9338

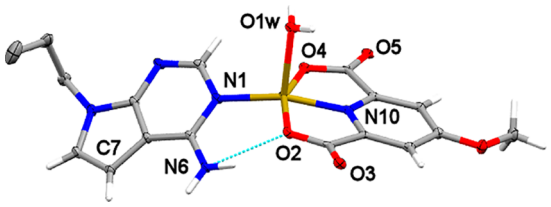

Figure 5. Molecular structure of the complex [Cu(mcheld)-(*N1*-^{7C}**Ade**)(H_2O)]·H_2O (**1Cu_^{7C}Ade**) with thermal ellipsoids set at the 30% probability level. The intramolecular hydrogen bond is highlighted by a dashed cyan line. The uncoordinated water molecule (and the corresponding hydrogen bonds) has been omitted for clarity. An ordered model has been adopted for the ^{7C}**Ade** propylic residue.

and O3 atoms of the mcheld ligand (N6···O2 2.768(4) Å and N6···O3 2.960(3) Å, respectively). Also, the water molecule O1w forms intermolecular hydrogen bonds[56] with the donor atoms of two different adjacent complexes (O1w···O4 2.790(4) Å, O1w···O5 2.717(3) Å, O2w···N3 2.956(4) Å), leading to a staircase-like 3D structure (Figure 6). No $\pi-\pi$ stacking interactions are present.

Interestingly, no complexes were either isolated or detected in solution when **1Cu** was reacted with thymidine and 7-deazaguanine derivatives (Scheme 2). This is probably due to the experimental conditions adopted. Unfortunately, although several attempts were performed at higher pH (9.5) to fully deprotonate such nucleosides, no complexes were isolated and further efforts still need to be done in this regard.

CD Spectroscopy Interaction Studies between Complex 1Cu and Single-Stranded DNA Homopolymers. The interaction of **1Cu** toward single-stranded DNA (ss-DNA) molecules was studied in an effort to evaluate the possible formation of a contiguous array of **1Cu_nucleobase** base pairs. To this aim, we used circular dichroism (CD) to unveil the interactions, at the oligomer level, between **1Cu** and different synthetic ss-DNA homopolymers containing the nucleoside analogues studied herein: namely, $d(Ade)_{15}$, $d(^{7C}Ade)_{15}$, $d(Cyt)_{15}$, and $d(Gua)_{10}$. The **1Cu** complex is CD inactive, and its UV−vis absorbance spectrum shows a broad band in the range 240−280 nm. Therefore, any induced circular dichroism (ICD) signal caused by the interaction of **1Cu** with the DNA homopolymers should be developed in this region. Unfortunately, in all cases, the addition of **1Cu** did not bring about significant changes in the CD spectra (Figure S8), thus indicating that the DNA helix conformation is not significantly altered. Therefore, nothing but weak interactions between **1Cu** and the ss-DNA homopolymers can be expected in solution. This is in contrast with the reported formation of individual mcheld-Cu-nucleobase base pair mismatches within double-stranded DNA scaffolds.[4] In that case, the copper(II) complex was covalently attached to the backbone of the DNA molecule and only one mismatch was introduced within the helix. On the other hand, in our study, the **1Cu** fragments are unrestricted in solution and the Cu···N(nucleoside) interaction does not seem to be strong enough to yield a Cu(II)-mediated base pair in solution. This fact, together with the hindering effect of several copper(II) ions close to each other, reasonably prevents the formation of stable Cu-ss-DNA hybrid systems in solution.

***Ab Initio* Computational Studies: Structural Features of 1Cu_nucleoside Pairs inside DNA Molecules.** As was mentioned above, the binding of complex **1Cu** toward canonical nucleosides has been previously reported in solution at the oligomer level in double-stranded DNA (except for thymidine),[4] while the crystal and molecular structures of the resulting **1Cu_nucleoside** monomers have been determined in this work. These results prompted us to evaluate the structural organization of **1Cu_nucleoside** pairs inside DNA double-helix structures and compare the structural features derived therefrom with those of the monomers described herein, as we believe that the DNA structure should have an important influence on the arrangement of these copper−base pairs. Furthermore, we aimed at evaluating the effect of Cu(II)-mediated nucleobase formation on the DNA structure that contains it.

The study of a DNA structure, in the solid state or solution, can be very difficult and expensive due to the difficulty in obtaining single crystals suitable for X-ray diffraction measurements or powdered batches in enough quantity to accomplish nuclear magnetic resonance studies (in the present case the latter studies are made even more difficult by the presence of the paramagnetic Cu(II) ions). More affordable spectroscopic or spectrometric studies (for instance, UV−vis absorption and fluorescence spectroscopy, CD, ESI-MS, MALDI-TOF) do not provide information on the three-dimensional structure. For this reason, theoretical computational studies can be a very important tool.

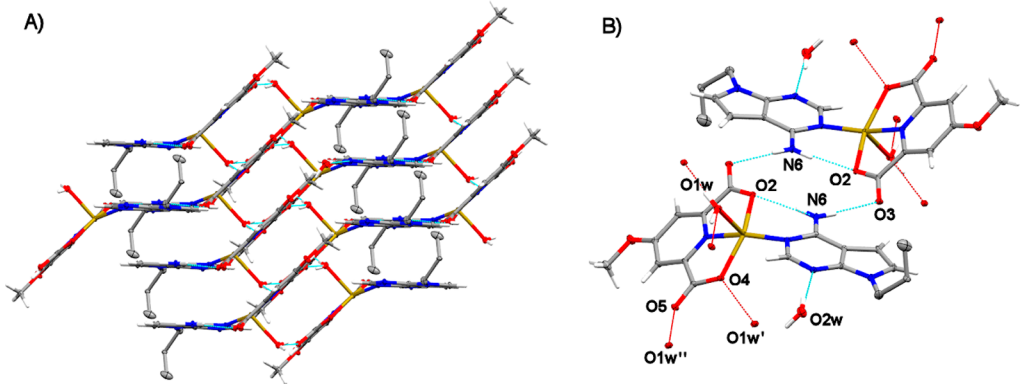

Figure 6. (A) In the crystal structure of **1Cu_^{7C}Ade**, hydrogen bonds (dashed cyan lines) involving the coordinated water molecule O1w and the exocyclic ^{7C}**Ade** amino group lead to the formation of staircase motifs. (B) Detail of the symmetry-related hydrogen bond interactions present in each "step" of the staircase. Red dotted lines represent hanging contacts.

https://dx.doi.org/10.1021/acs.inorgchem.0c01210
Inorg. Chem. 2020, 59, 9325−9338

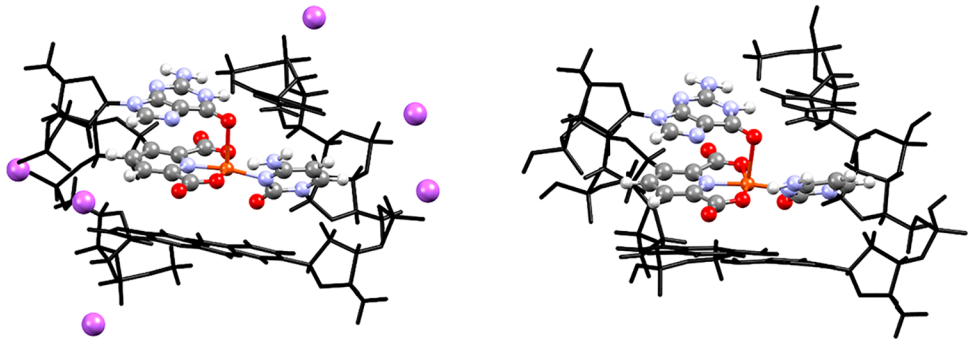

Figure 7. *Ab initio* HF-3c optimized geometries for the structures **DNA_3-Na** (left) and **DNA_3-H** (right) hosting the **1Cu_Cyt** complex.

Table 1. Comparison of the Relevant Bond Distances (Å) and Dihedral Angles (deg) of the 1Cu_Cyt Base Pair in the DNA_3 Optimized Models with the Experimental Values[a]

	exptl **1Cu_Cyt**	**DNA_3-Na**[b]	**DNA_3-H**[c]	**DNA_3-H-SE**[d]
Cu−N10	1.893	1.902 (0.009)	1.924 (0.031)	1.966 (0.073)
Cu−O2	1.997	1.900 (−0.097)	1.908 (−0.089)	1.923 (−0.074)
Cu−O4	2.027	1.900 (−0.127)	1.9 (−0.127)	1.916 (−0.111)
Cu−O_{axial}	2.407	2.527 (0.120)	2.504 (0.097)	2.488 (0.081)
Cu−N3	1.956	1.939 (−0.017)	1.965 (0.009)	1.977 (0.021)
Cu−O21	2.711	2.844 (0.133)	2.957 (0.246)	2.948 (0.237)
interplanar angle	77.7	47.6 (−30.1)	36.6 (−41.1)	34.9 (−42.8)
$C1'_{Gua}\cdots C1'_{Cyt}$		10.509	10.656	10.668
$C1'_{1Cu}\cdots C1'_{Cyt}$		8.759	9.284	9.566
$C1'_{Gua}\cdots C1'_{Cyt}$		10.760	10.682	10.688

[a]Deviations with respect to the latter are shown in parentheses. [b]Na indicates the use of sodium(I) as a cation. [c]H indicates the use of a proton as a cation. [d]SE indicates that the "solvent effect" has been included in the calculation.

We have employed computational calculations to study the structure of a 10-mer and a 15-mer DNA duplex model containing one Cu(II)-mediated base pair covalently attached to the DNA structure. Although they could be considered simple, these models enable us to study a realistic structure. Within the available theoretical models, molecular mechanics is not a valid method in the presence of metal ions such as Cu(II), while semiempirical models, although parametrized, can result in significant errors in the estimation of bond distances and angles.

Therefore, we strongly believe that the most useful methods to approach a DNA molecule of ca. 1000 atoms and containing metal ions are the *ab initio* and QMM methodologies. The latter approach, though faster, has the problem of validation. In our case, we do not have a reliable starting DNA structure to be validated. Thus, we decided not to use an approach that could lead to artifacts but rather to carry out a theoretical−computational structural study using the *ab initio* HF-3c method for DNA molecules holding the **1Cu_Cyt** or **1Cu_Gua** base pair located in the middle of the double helix. We have selected these Cu(II)−base pairs, as they exhibited the longest deviation from coplanarity between the [Cu(mcheld)] fragment and the Cyt or Gua bases in their crystal structure (see Synthesis and Crystal Structure of mcheld-Cu-Nucleoside Complexes), and thus they will potentially have a greater effect on the DNA double-helix conformation.

To this purpose, we have followed a bottom-up strategy, starting with the study of the **1Cu_Cyt** complex, followed by the study of a 3-mer DNA molecule containing the **1Cu_Cyt** base pair in the center of the structure, and finally performing calculations for 10-mer and 15-mer DNA molecules containing the **1Cu_Cyt** or **1Cu_Gua** complexes. To the best of our knowledge, this is the first time that a duplex DNA molecule containing metal-mediated base pairs has been studied at this computational level.

Single Model Complex. Initially, we carried out a theoretical study of the **1Cu_Cyt** molecular structure, starting from the experimentally determined one, to validate the theoretical *ab initio* HF-3c method employed in our following studies. After this preliminary study, we compared the computational results (**1Cu_Cyt-S**) with the experimental results, giving special attention to the interaction of the Cyt base with the copper(II) ion. Subsequently, we performed additional studies taking into account solvent effects (**1Cu_Cyt-SE**), using water as the solvent, and removing the coordinated water molecule (**1Cu_Cyt-NW**) to evaluate the consequence of the absence of the sixth coordination position observed experimentally.

For **1Cu_Cyt-S**, the results show a good agreement among the calculated and observed Cu−O and Cu−N distances (Table S2), with the greatest deviations observed for the Cu−O2 and Cu−O4 distances and for the angle between the [Cu(mcheld)] fragment and Cyt base (by 10°; see Figure S9). When the calculations were repeated with the solvent effects (**1Cu_Cyt-SE**) or without the coordinated water molecule (**1Cu_Cyt-NW**) taken into account, the results were very similar, and no significant differences were observed.

Model Systems of Three Base Pairs. After validating the theoretical model of **1Cu_Cyt** with the experimental observations, we set out to study how the scaffolding of a DNA molecule would affect the conformation of the **1Cu_Cyt** base pair. In an effort to work with the simplest DNA model, we studied a DNA duplex structure comprising only three base

https://dx.doi.org/10.1021/acs.inorgchem.0c01210
Inorg. Chem. 2020, 59, 9325−9338

pairs (**DNA$_3$**), constructed with the sequences 5′-(G **1Cu** G)-3′ and 5′-(CCC)-3′. This **DNA$_3$** molecule represents a good starting point before studying larger DNA molecules (*vide infra*) because it takes into account the influence of the base pairs above and below the **1Cu_Cyt** base pair, which has been positioned in the middle.

For these calculations, the counteranions (namely the phosphate groups) were treated with either sodium cations (**DNA$_3$-Na**) or protons (**DNA$_3$-H**) and the results obtained with the two strategies were compared. We also evaluated the influence of the solvent effect on the latter model (**DNA$_3$-H-SE**).

In all cases, the copper(II) ion is five-coordinated in a square-pyramidal geometry. The mcheld ligand shows the μ,κ^3-N10,O2,O4 coordination mode, occupying three equatorial positions, while the Cyt ligand acts as a monodentate ligand via N3 coordination, completing the basal plane. Remarkably, the axial position of the copper(II) coordination sphere now involves a neighboring nucleotide, and the copper(II) ions bind the guanine-O6 atom (Figure 7). This situation is similar to that observed in the crystal structure of a related copper-mediated base pair in DNA.[20]

The results show that in all cases there is a good agreement among the experimental and calculated bond distances involving the copper(II) ions (Table 1). The greatest deviations are again observed for the Cu−O2 and Cu−O4 distances and the interplanar angle between the [Cu(mcheld)] fragment and the cytosine base. Both **DNA$_3$** models show a significantly lower interplanar angle in comparison to the complex alone, which can be explained as a result of the influence of the DNA scaffold: the presence of the base pairs above and below the **1Cu_Cyt** base pair reasonably limits the rotation around the Cu−N3 bond. In this regard, the best agreement was found with the **DNA$_3$-Na** model, which exhibits an interplanar angle closer to the observed angle.

The glyosidic C1′···C1′ distances between opposite nucleobases are within the range 10.5−10.8 Å observed for natural base pairs, while they are significantly smaller for the **1Cu_Cyt** base pair (<9.56 Å), especially in the **DNA$_3$-Na** model, which displays a distance of 8.76 Å.

Interestingly, the presence of the **1Cu_Cyt** complex seems to affect more the conformation of the strand that holds the **1Cu** metal fragment. This is highlighted by the shorter P···P distance (5.94 Å) of contiguous phosphate groups attached to the sugar unit of [Cu(mcheld)] vs the other P···P distances in the duplex (>6.39 Å). This is situation is more pronounced in the case of the **DNA$_3$-Na** model, where the phosphate groups are separated by only 4.2 Å and seem to be stabilized by two nearby sodium cations (Na···Na 3.766 Å) that bridge both phosphate groups (Na···O 2.068−2.132 Å) (Figure 8).

It is worth mentioning that, since a water molecule was found to be involved in the coordination sphere of copper(II) in the **1Cu_Cyt** complex, the **DNA$_3$-H** model was also studied in the presence of a water molecule placed near the metal ion. In this situation, the results also showed the formation of the Cu(II)−Gua(O6) bond (Figure S10).

Full DNA Model Systems. Finally, we performed a theoretical study for 15-mer (**DNA$_{15}$**) and 10-mer (**DNA$_{10}$**) duplexes containing the **1Cu_Cyt** and **1Cu_Gua** base pairs, respectively, in the middle of the double helixes. In an effort to reduce the influence of arbitrary DNA sequences surrounding the copper-mediated base pair, the model sequences have been designed to contain only guanosine and cytidine bases (Table 2).

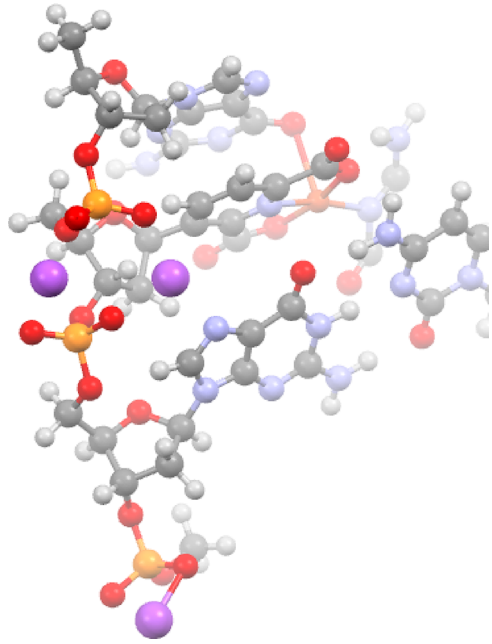

Figure 8. Close view of the HF-3c optimized geometry for **DNA$_3$-Na** showing the position of two sodium ions (purple) bridging contiguous phosphate groups.

Table 2. DNA Duplexes Employed in the *Ab Initio* Calculations

duplex	sequence
DNA$_{15}$	5′-(CCC CCC C **C** C CCC CCC)-3′
	3′-(GGG GGG G **1Cu** G GGG GGG)-5′
DNA$_{10}$	5′-(CCC C **1Cu** C CCC C)-3′
	3′-(GGG G **G** G GGG G)-5′

First, we studied the structure of the 15-mer duplex **DNA$_{15}$**, compensating the negative charge of the phosphate groups with the presence of sodium cations (**DNA$_{15}$-Na**). It is worth noting that this study required an extensive computational effort, as up to 28 sodium cations were considered in the *ab initio* calculations.

We also performed the same calculation using protons as counterions (**DNA$_{15}$-H**) to reduce the computational cost, and the results were compared to those obtained with **DNA$_{15}$-Na** to evaluate the consequences of this approach. Finally, we studied duplex **DNA$_{10}$** by treating the phosphate groups with protons (**DNA$_{10}$-H**). The solvent effect was not taken into account in any case, due to the great calculation effort that this would have required.

The optimized geometry of duplex **DNA$_{15}$-Na** contains 15 base pairs and completes an entire turn, holding a right-handed B-like conformation (Figure 9). The **1Cu_Cyt** base pair is placed at site 8, and copper(II) is six-coordinated and adopts a distorted-octahedral geometry, as seen for the **1Cu_Cyt** complex. The mcheld ligand shows the expected μ,κ^3-N10,O2,O4 coordination mode (Cu−N10 1.916 Å, Cu−O2 1.900 Å, Cu−O4 1.906 Å), occupying three basal positions. However, in contrast to the studied trimer **DNA$_3$-Na**, where the Cyt base acts as a monodentate ligand via N3 coordination, in duplex **DNA$_{15}$-Na** the Cyt base shows a μ,κ^2-N3,O21

https://dx.doi.org/10.1021/acs.inorgchem.0c01210
Inorg. Chem. 2020, 59, 9325−9338

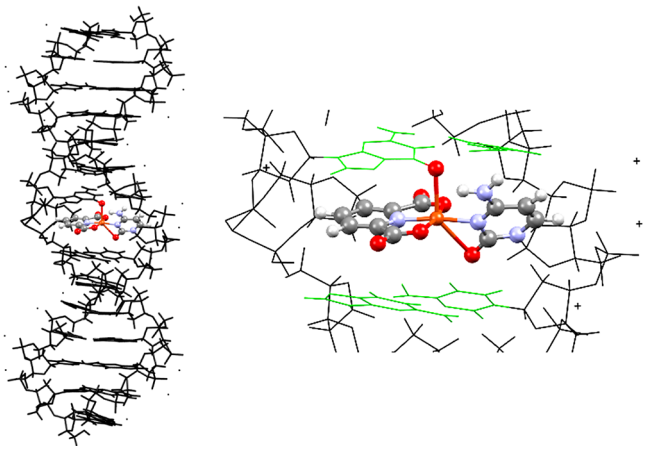

Figure 9. (left) The geometry-optimized duplex **DNA$_{15}$-Na**. (right) Closer view of the **1Cu_Cyt** base pair formed in the duplex structure showing the apical Cu−Gua-O6 and the Cu−Cyt-μ-N3,O21 bonds. Dots surrounding the double helix represent sodium cations which balance the negative charge of the phosphate DNA backbone. Color scheme: black, DNA structure different from the Cu(II)-mediated base pairs; green, neighboring nucleobases to **1Cu_Cyt** base pair.

coordination mode (Cu−N3 1.964, Cu−O21 2.703 Å), as seen in the X-ray crystal structure of the **1Cu_Cyt** complex (Table 3).

The axial position of the copper(II) coordination sphere involves a neighboring nucleotide: i.e., the copper(II) ion binds a neighboring Gua-O6 atom (Cu−O6 2.444 Å). It should be noted that this distance is considerably shorter than the sum of the Cu/O van der Waals radii. This situation has been also observed for the **DNA$_3$-Na** model, which displays a longer distance (2.527 Å), as well as for the crystal structure of the copper-mediated Dipic-Py base pair in DNA (Dipic = pyridine-2,6-dicarboxylate; Py = pyridine), although in that case the Cu−O6 distance was considerably longer (3.1 Å).[24] The fact that our *ab initio* calculation reveals the formation of the Cu−O axial bond with an adjacent guanidine nucleoside, for both **DNA$_3$-Na** and **DNA$_{15}$-Na** models, as reported for the DNA crystal structure, constitutes a validation that supports our theoretical method to study these copper-mediated base pairs in DNA duplexes.

Interestingly, the optimized geometry of **DNA$_{15}$-Na** reveals a larger interplanar angle (54.43°) between the [Cu(mcheld)] fragment and the cytidine base in comparison to that observed in the **DNA$_3$-Na** model (43.63°). This evidence shows that our original assumptions were not entirely correct; larger DNA molecules are not necessarily more constrained. Indeed, the rotation around the Cu−N3 bond inside the helix is allowed, leading to arrangements far from coplanarity. As a consequence, the Cu−O21 distance in our optimized **DNA$_{15}$-Na** model is very similar to that observed in **1Cu_Cyt**, indicating that this interaction could also occur in a duplex structure. This unexpected result indicates that the adjacent base pairs are not the only ones that influence the organization of the **1Cu_Cyt** base pair, but instead, the overall structure of a large DNA molecule has an effect. This could also be explained by the fact that the energy required to rotate the Cu−N3 bond and diminish the deviation from planarity of the complex can be dampened by a higher number of slight deviations from the optimal bond geometry of the higher number of bonds present in larger DNA structures.

In the duplex **DNA$_{15}$-Na**, the C1′···C1′ distances between opposite 2′-deoxyriboses of natural base pairs vary in the range 10.5−10.7 Å, which is consistent with a standard B-form conformation. However, as foreseen by our previous **DNA$_3$** models, at the copper−base pairs level (site 8) the C1′···C1′ distance is considerably shorter (8.3 Å), causing a narrowing of the double helix. The distortion caused by the **1Cu_Cyt** base pair in the duplex structure is analogous to what was observed for **DNA$_3$-Na**. Actually, two sodium(I) cations are also very close to each other (Na···Na 3.741 Å) and bridge two contiguous phosphate groups (Na···O 2.093−2.128 Å). In addition, stacking interactions occur between the mcheld ligand and the contiguous guanosine base to which the copper(II) ions coordinate through O6 coordination. The rest of the DNA structure presents a characteristic B-form conformation, without other remarkable changes. Therefore, the presence of **1Cu_Cyt** appears to only distort neighboring base pairs and is suitable to be formed in a DNA structure without major disruption of the structure.

The structure of **DNA$_{15}$-H** is shown in Figure 10. The optimized copper(II) ion is in a five-coordinated square-pyramidal geometry. The mcheld ligand shows the expected μ,κ^3-N10,O2,O4 coordination mode (Cu−N10 1.927 Å, Cu−O2 1.910 Å, Cu−O4 1.901 Å), occupying three basal positions. However, in contrast to the molecular structures of **1Cu_Cyt** and **DNA$_{15}$-Na**, where the Cyt ligand shows a μ,κ^2-N3,O21 coordination mode (*vide supra*), in duplex **DNA$_{15}$-H** the Cyt base acts as a monodentate ligand via N3 coordination,

Table 3. Comparison of the Relevant Bond Distances (Å) and Dihedral Angles (deg) in the Crystal Structures of the 1Cu_Cyt Base Pair and the DNA$_3$-Na, DNA$_{15}$-Na and DNA$_{15}$-H Optimized Models[a]

	exptl **1Cu_Cyt**	**DNA$_3$-Na**[b]	**DNA$_{15}$-Na**	**DNA$_{15}$-H**[c]
Cu−N10	1.893	1.902 (0.009)	1.916 (0.023)	1.927 (0.034)
Cu−O2	1.997	1.900 (−0.097)	1.900 (−0.097)	1.910 (−0.087)
Cu−O4	2.027	1.900 (−0.127)	1.906 (−0.121)	1.901 (−0.126)
Cu−O$_{axial}$	2.407	2.527 (0.120)	2.444 (0.037)	2.470 (0.063)
Cu−N3	1.956	1.939 (−0.017)	1.964 (0.008)	1.965 (0.009)
Cu−O21	2.711	2.844 (0.133)	2.703 (−0.008)	2.968 (0.257)
interplanar angle	77.7	47.6 (−30.1)	54.4 (−23.3)	38.9 (−38.9)
C1′$_{Gua}$···C1′$_{Cyt}$		10.509	10.547	10.681
C1′$_{1Cu}$···C1′$_{Cyt}$		8.759	8.347	9.263
C1′$_{Gua}$···C1′$_{Cyt}$		10.760	10.694	10.624

[a]Deviations with respect to the observed crystal structure are shown in parentheses. [b]Na indicates the use of sodium(I) as a cation. [c]H indicates the use of a proton as a cation.

https://dx.doi.org/10.1021/acs.inorgchem.0c01210
Inorg. Chem. 2020, 59, 9325−9338

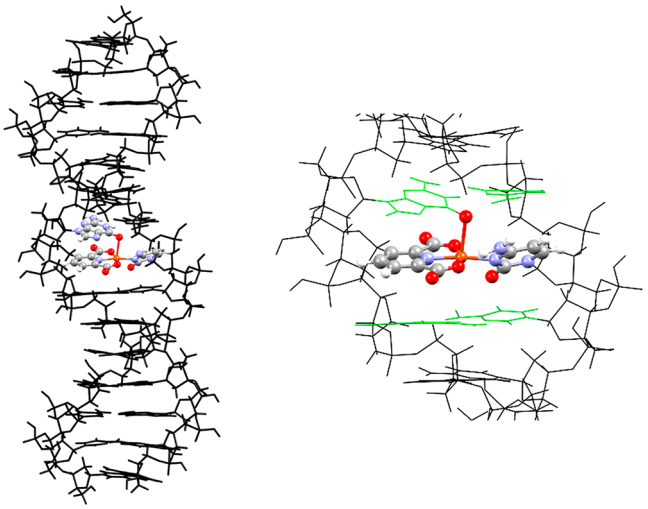

Figure 10. (left) The geometry-optimized duplex **DNA$_{15}$-H**. (right) Closer view of the **1Cu_Cyt** base pair formed in the duplex structure showing the Cu-Gua-O6 and Cu-Cyt-N3 bonds Color scheme: black, DNA structure different from the Cu(II)-mediated base pairs; green, neighboring nucleobases to **1Cu_Cyt** base pair.

completing the basal plane (Cu−N3 1.965 Å). This organization can be explained as a result of a smaller interplanar angle between the [Cu(mcheld)] fragment and the cytidine base (38.88°) and consequently a greater Cu−O21 distance (2.968 Å). The axial position of the copper(II) coordination sphere also involves a neighboring nucleotide: i.e., the copper(II) ion binds a neighboring Gua-O6 atom (Cu−O6 2.470 Å), as observed in **DNA$_{15}$-Na**. In this case, the C1′···C1′ distance between opposite 2′-deoxyriboses at the copper−base pairs level (site 8) is larger (9.2 Å), although the distance for natural base pairs remains within the expected 10.5−10.7 Å range. Importantly, the rest of the **DNA$_{15}$-H** structure does not show any major differences vs **DNA$_{15}$-Na**.

These results indicate that our *ab initio* calculations performed for the DNA molecules containing one **1Cu_Cyt** base pair can be successfully performed using sodium(I) ions or protons as counterions to compensate for the negative charge of the phosphate groups. The choice of one strategy or another will depend on the objective of the study. The **DNA$_{15}$-Na** model is more accurate by comparison with the observed molecular structure of **1Cu_Cyt**, at the expense of a considerably higher computational cost. Replacing Na^+ ions with protons (**DNA$_{15}$-H**) requires less demanding and more affordable computational resources. However, this model can lead to variations in the angles and bond distances of the **1Cu_Cyt** base pair, although the overall DNA structure is little affected. Therefore, these considerations must be taken into account depending on the aim of the calculation: namely, to study the overall DNA structure containing metal-mediated base pairs or to evaluate the arrangement of a specific base pair in the DNA structure. Although experimental structural data are required to evaluate the conformation in solution, namely high-resolution NMR data, our result indicates that the **1Cu-Cyt** base pair will exist inside the double helix with a large interplanar angle, as observed in the **DNA$_{15}$** models.

In an effort to assess the effect of the **1Cu_Gua** base pair in the DNA structure, we also performed a calculation using protons as counterions (**DNA$_{10}$-H**), as the computational cost was considerably lower (Figure S10). The **DNA$_{10}$-H** double helix contains 10 base pairs, holds a right-handed B-like form, and nearly completes a turn, with all the complementary cytidine and guanosine bases assembled via Watson−Crick hydrogen bonds along with stacking interactions. The [Cu(mcheld)] fragment is placed at site 5 (starting from the 5′-end), in the middle of the duplex, and binds guanosine 5 via the N7 atom, as observed in **1Cu_Gua** (*vide supra*). The copper(II) ion adopts a square-planar geometry, as previously described in related systems,[24] with no additional axial coordination observed. The mcheld ligand shows the expected μ,κ^3-N10,O2,O4 coordination mode, and the copper(II) ion is involved in shorter bonds (Cu−N10 1.925 Å, Cu−O2 1.884 Å, Cu−O4 1.903 Å) than in the crystal structure of **1Cu_Gua**. The guanosine moiety is coordinated to the copper(II) ion through N7 with a distance (Cu−N7 1.975 Å) very close to that present in the crystal structure. However, the spatial assembly of the units has considerably changed in comparison to the free **1Cu_Gua** monomer. In duplex **DNA$_{10}$-H**, the [Cu(mcheld)] fragment and the guanosine base self-assemble with a lower deviation from coplanarity, with an interplanar angle of 19.6°, instead of the 78.94(10)° angle observed in the crystal structure. Surprisingly, this arrangement appears to be possible despite the short distance observed between the guanosine keto group and the mcheld carboxylic atom (O61···O2 2.866 Å), which would be expected to generate a significant repulsion. This fact could be due to the strong influence that the overall duplex structure must have on the copper−base pair, indicating that the formation of the double helix may restrict the free rotation around the Cu−N7 bond, hampering the separation of the keto and carboxylic groups any further.

CONCLUSIONS

The formation of copper-mediated base pairs containing a pyridine-2,6-dicarboxylate derivative (mcheld) and model nucleosides (**Ade**, **Cyt**, **Gua**, and **^{7C}Ade**) was studied in the solid state and solution by means of single-crystal X-ray diffraction and CD spectroscopy, respectively. The former revealed the crystal and molecular structures of four mcheld-Cu-nucleoside systems, namely **1Cu_Cyt**, **1Cu_Ade**, **1Cu_^{7C}Ade**, and **1Cu_Gua**, which have been reported to occur individually in double-stranded DNA molecules.[4] Unfortunately, no single crystals suitable for X-ray diffraction could be isolated for the **1Cu_^{7C}Gua** compound. The versatility of these nucleoside analogues is evidenced in the case of adenine derivatives, where the coordination to the metal ion can be directed via either the Hoogsteen N7 position (as in **1Cu_Ade**), or the Watson−Crick N1 atom (as in **1Cu_^{7C}Ade**). Although the interaction metal−N1-Gua has not been observed in the present work, its formation cannot be ruled out; indeed, it is expected for the **1Cu_^{7C}Gua** complex and it has been previously reported for silver(I) ions.[54] The complex **1Cu_Cyt** demonstrates that the binding of **1Cu** could occur via both keto and amino groups simultaneously. The presence of a keto group in the nucleobase moiety induces a nearly perpendicular disposition of the [Cu(mcheld)] fragment vs the Gua or Cyt residues, as observed in **1Cu_Gua** and **1Cu_Cyt**, respectively, which could be attributed to the reciprocal repulsion of the keto and carboxylate groups. Interestingly, this high deviation from coplanarity between the [Cu(mcheld)] moiety and the nucleosides is not present in the **1Cu_Ade** and **1Cu_^{7C}Ade** derivatives, most likely due to the cooperation of the coordination bonds along with an

https://dx.doi.org/10.1021/acs.inorgchem.0c01210
Inorg. Chem. 2020, 59, 9325−9338

intramolecular hydrogen bond interaction involving the exocyclic amino group NH_2. These results are in agreement with the stabilization trend observed for the Cheld-Cu-nucleobase system inside DNA duplexes (adenine > cytosine > guanine),[4] since a lower deviation from coplanarity of the units can facilitate the formation of intermolecular $\pi-\pi$ interactions and intramolecular hydrogen bonds between adenine and Cheld.

Importantly, the *ab initio* calculations performed for duplexes **DNA_{15}** and **DNA_{10}**, which embrace the **1Cu_Cyt** and **1Cu_Gua** base pairs in the middle of the duplexes, respectively, revealed that these base pairs can be formed inside DNA duplexes without significant distortion of the natural base pair arrangement. As a matter of fact, the geometry-optimized structures for duplexes **DNA_{15}** and **DNA_{10}** show that the **1Cu_nucleoside** base pairs remain in good harmony with the rest of the canonical Watson−Crick base pairs. The *ab initio* methodologies also revealed that the phosphate groups can be treated with Na^+ ions or protons, depending on the purposes of the computational calculations. A better agreement among the **1Cu_Cyt** calculated and experimental bond distances was found for the **DNA_{15}-Na** model, using Na^+ ions as counterions. However, the calculation performed on the **DNA_{15}-H** model, using protons as counterions, revealed some small deviations for the relevant bond distances at the Cu(II) ion, but the overall DNA structure can be correctly studied using this approach.

These results demonstrate that the organization of Cu−nucleobase base pairs can be studied in the solid state and in the context of a double helix using *ab initio* methodologies to evaluate the potential effects derived from the DNA scaffold, which may drive both metal coordination and the supramolecular assembly. These results can be extended to other metal-mediated base pairs.

■ ASSOCIATED CONTENT

Supporting Information

The Supporting Information is available free of charge at https://pubs.acs.org/doi/10.1021/acs.inorgchem.0c01210.

> Crystallographic information and relevant X-ray diffraction experimental details, additional figures of the crystal structures, circular dichroism spectra, additional figures for *ab initio* optimized geometries, and Cartesian coordinates (Å) for geometry-optimized molecules (PDF)

Accession Codes

CCDC 1835231−1835235 contain the supplementary crystallographic data for this paper. These data can be obtained free of charge via www.ccdc.cam.ac.uk/data_request/cif, or by emailing data_request@ccdc.cam.ac.uk, or by contacting The Cambridge Crystallographic Data Centre, 12 Union Road, Cambridge CB2 1EZ, UK; fax: +44 1223 336033.

■ AUTHOR INFORMATION

Corresponding Author

Miguel A. Galindo − *Departamento de Química Inorgánica, Universidad de Granada, 18071 Granada, Spain;* orcid.org/0000-0003-4355-4313; Email: magalindo@ugr.es

Authors

Alicia Dominguez-Martin − *Departamento de Química Inorgánica, Universidad de Granada, 18071 Granada, Spain;* orcid.org/0000-0001-8669-6712

Simona Galli − *Dipartimento di Scienza e Alta Tecnologia, Università dell'Insubria, 22100 Como, Italy;* orcid.org/0000-0003-0335-5707

José A. Dobado − *Grupo de Modelización y Diseño Molecular, Departamento de Química Orgánica, Universidad de Granada, 18071 Granada, Spain*

Noelia Santamaría-Díaz − *Departamento de Química Inorgánica, Universidad de Granada, 18071 Granada, Spain*

Antonio Pérez-Romero − *Departamento de Química Inorgánica, Universidad de Granada, 18071 Granada, Spain*

Complete contact information is available at: https://pubs.acs.org/10.1021/acs.inorgchem.0c01210

Author Contributions

The manuscript was written through contributions of all authors. All authors have given approval.

Notes

The authors declare no competing financial interest.

■ ACKNOWLEDGMENTS

Financial support from the Spanish MINECO (CTQ2017-89311-P), FEDER/Junta de Andalucía-Consejería de Economía y Conocimiento/Proyecto (A-FQM-465-UGR18), Junta de Andalucía (FQM-2293, FQM-283, FQM-174), and Unidad de Excelencia de Química aplicada a Biomedicina y Medioambiente (UGR) are acknowledged. S.G. acknowledges Università dell'Insubria for partial funding. We also thank the "Centro de Servicios de Informática y Redes de Comunicaciones" (CSIRC) (UGRGrid), University of Granada, for providing computing time.

■ REFERENCES

(1) Jones, M. R.; Seeman, N. C.; Mirkin, C. A. Programmable Materials and the Nature of the DNA Bond. *Science* **2015**, *347*, 1260901.

(2) Rothemund, P. W. K. Folding DNA to Create Nanoscale Shapes and Patterns. *Nature* **2006**, *440*, 297−302.

(3) Wilner, O. I.; Willner, I. Functionalized DNA Nanostructures. *Chem. Rev.* **2012**, *112*, 2528−2556.

(4) Meggers, E.; Holland, P. L.; Tolman, W. B.; Romesberg, F. E.; Schultz, P. G. A Novel Copper-Mediated DNA Base Pair. *J. Am. Chem. Soc.* **2000**, *122*, 10714−10715.

(5) Jash, B.; Müller, J. Metal-Mediated Base Pairs: From Characterization to Application. *Chem. - Eur. J.* **2017**, *23*, 17166−17178.

(6) Tanaka, K.; Shionoya, M. Synthesis of a Novel Nucleoside for Alternative DNA Base Pairing through Metal Complexation. *J. Org. Chem.* **1999**, *64*, 5002−5003.

(7) Takezawa, Y.; Shionoya, M. Metal-Mediated DNA Base Pairing: Alternatives to Hydrogen-Bonded Watson−Crick Base Pairs. *Acc. Chem. Res.* **2012**, *45*, 2066−2076.

(8) Takezawa, Y.; Müller, J.; Shionoya, M. Artificial DNA Base Pairing Mediated by Diverse Metal Ions. *Chem. Lett.* **2017**, *46*, 622−633.

(9) Polonius, F.-A.; Müller, J. An Artificial Base Pair, Mediated by Hydrogen Bonding and Metal-Ion Binding. *Angew. Chem., Int. Ed.* **2007**, *46*, 5602−5604.

(10) Megger, D. A.; Fonseca-Guerra, C.; Hoffmann, J.; Brutschy, B.; Bickelhaupt, F. M.; Müller, J. Contiguous Metal-Mediated Base Pairs Comprising Two Ag(I) Ions. *Chem. - Eur. J.* **2011**, *17*, 6533−6544.

(11) Santamaría-Díaz, N.; Méndez-Arriaga, J. M.; Salas, J. M.; Galindo, M. A. Highly Stable Double-Stranded DNA Containing

Sequential Silver(I)-Mediated 7-Deazaadenine/Thymine Watson-Crick Base Pairs. *Angew. Chem., Int. Ed.* **2016**, *55*, 6170−6174.
(12) Méndez-Arriaga, J. M.; Maldonado, C. R.; Dobado, J. A.; Galindo, M. A. Silver(I)-Mediated Base Pairs in DNA Sequences Containing 7-Deazaguanine/Cytosine: Towards DNA with Entirely Metallated Watson-Crick Base Pairs. *Chem. - Eur. J.* **2018**, *24*, 4583−4589.
(13) Toomey, E.; Xu, J.; Vecchioni, S.; Rothschild, L.; Wind, S.; Fernandes, G. E. Comparison of Canonical versus Silver(I)-Mediated Base-Pairing on Single Molecule Conductance in Polycytosine DsDNA. *J. Phys. Chem. C* **2016**, *120*, 7804−7809.
(14) Jash, B.; Scharf, P.; Sandmann, N.; Fonseca Guerra, C.; Megger, D. A.; Müller, J. A Metal-Mediated Base Pair That Discriminates between the Canonical Pyrimidine Nucleobases. *Chem. Sci.* **2017**, *8*, 1337−1343.
(15) Al-Mahamad, L. L. G.; El-Zubir, O.; Smith, D. G.; Horrocks, B. R.; Houlton, A. A Coordination Polymer for the Site-Specific Integration of Semiconducting Sequences into DNA-Based Materials. *Nat. Commun.* **2017**, *8*, 720.
(16) Liu, S.; Clever, G. H.; Takezawa, Y.; Kaneko, M.; Tanaka, K.; Guo, X.; Shionoya, M. Direct Conductance Measurement of Individual Metallo-DNA Duplexes within Single-Molecule Break Junctions. *Angew. Chem., Int. Ed.* **2011**, *50*, 8886−8890.
(17) Xu, E.; Lv, Y.; Liu, J.; Gu, X.; Zhang, S. An Electrochemical Study Based on Thymine-Hg-Thymine DNA Base Pair Mediated Charge Transfer Processes. *RSC Adv.* **2015**, *5*, 49819−49823.
(18) Müller, J. Nucleic Acid Duplexes with Metal-Mediated Base Pairs and Their Structures. *Coord. Chem. Rev.* **2019**, *393*, 37−47.
(19) Fortino, M.; Marino, T.; Russo, N. Theoretical Study of Silver-Ion-Mediated Base Pairs: The Case of C-Ag-C and C-Ag-A Systems. *J. Phys. Chem. A* **2015**, *119*, 5153−5157.
(20) Li, G.; Liu, H.; Chen, X.; Zhang, L.; Bu, Y. Multi-Copper-Mediated DNA Base Pairs Acting as Suitable Building Blocks for the DNA-Based Nanowires. *J. Phys. Chem. C* **2011**, *115*, 2855−2864.
(21) Swasey, S. M.; Rosu, F.; Copp, S. M.; Gabelica, V.; Gwinn, E. G. Parallel Guanine Duplex and Cytosine Duplex DNA with Uninterrupted Spines of Ag I -Mediated Base Pairs. *J. Phys. Chem. Lett.* **2018**, *9*, 6605−6610.
(22) Schönrath, I.; Tsvetkov, V. B.; Zatsepin, T. S.; Aralov, A. V.; Müller, J. Silver(I)-Mediated Base Pairing in Parallel-Stranded DNA Involving the Luminescent Cytosine Analog 1,3-Diaza-2-Oxophenoxazine. *JBIC, J. Biol. Inorg. Chem.* **2019**, *24*, 693−702.
(23) Zimmermann, N.; Meggers, E.; Schultz, P. G. A Second-Generation Copper(II)-Mediated Metallo-DNA-Base Pair. *Bioorg. Chem.* **2004**, *32*, 13−25.
(24) Atwell, S.; Meggers, E.; Spraggon, G.; Schultz, P. G. Structure of a Copper-Mediated Base Pair in DNA. *J. Am. Chem. Soc.* **2001**, *123*, 12364−12367.
(25) Ghosh, S. K.; Ribas, J.; Bharadwaj, P. K. Metal-Organic Framework Structures of Cu(II) with Pyridine-2,6- Dicarboxylate and Different Spacers: Identification of a Metal Bound Acyclic Water Tetramer. *CrystEngComm* **2004**, *6*, 250−256.
(26) Das, B.; Baruah, J. B. Assembling of Copper(II) Dipicolinate Complexes. *Polyhedron* **2012**, *31*, 361−367.
(27) Del Pilar Brandi-Blanco, M.; Choquesillo-Lazarte, D.; Domínguez-Martín, A.; Matilla-Hernández, A.; González-Pérez, J. M.; Castiñeiras, A.; Niclós-Gutiérrez, J. Molecular Recognition Modes between Adenine or Adeniniun(1+) Ion and Binary M^{II}(Pdc) Chelates (M = Co-Zn; Pdc = Pyridine-2,6-Dicarboxylate(2-) Ion). *J. Inorg. Biochem.* **2013**, *127*, 211−219.
(28) Domínguez-Martín, A.; Choquesillo-Lazarte, D.; Dobado, J. A.; Vidal, I.; Lezama, L.; González-Pérez, J. M.; Castiñeiras, A.; Niclós-Gutiérrez, J. From 7-Azaindole to Adenine: Molecular Recognition Aspects on Mixed-Ligand Cu(II) Complexes with Deaza-Adenine Ligands. *Dalt. Trans.* **2013**, *42*, 6119−6130.
(29) Greco, E.; Aliev, A. E.; Lafitte, V. G. H.; Bala, K.; Duncan, D.; Pilon, L.; Golding, P.; Hailes, H. C. Cytosine Modules in Quadruple Hydrogen Bonded Arrays. *New J. Chem.* **2010**, *34*, 2634−2642.
(30) Nowick, J. S.; Chen, J. S.; Noronha, G. Molecular Recognition in Micelles: The Roles of Hydrogen Bonding and Hydrophobicity in Adenine-Thymine Base-Pairing in SDS Micelles. *J. Am. Chem. Soc.* **1993**, *115*, 7636−7644.
(31) Vermonden, T.; Branowska, D.; Marcelis, A. T. M.; Sudhölter, E. J. R. Synthesis of 4-Functionalized Terdendate Pyridine-Based Ligands. *Tetrahedron* **2003**, *59*, 5039−5045.
(32) *APEX3 Software,V2016.1*; Bruker AXS: Madison, WI, USA, 2016.
(33) Sheldrick, G. M. *SADABS 2016/2, Program for Empirical Absorption Correction of Area Detector Data*; University of Göttingen: Göttingen, Germany. 2016.
(34) Sheldrick, G. M. A Short History of SHELX. *Acta Crystallogr., Sect. A: Found. Crystallogr.* **2008**, *A64*, 112−122.
(35) (a) Hanwell, M. D.; Curtis, D. E.; Lonie, D. C.; Vandermeerschd, T.; Zurek, E.; Hutchison, G. R. Avogadro: An Advanced Semantic Chemical Editor, Visualization, and Analysis Platform. *J. Cheminf.* **2012**, *4*, 17. (b) *Avogadro: an open-source molecular builder and visualization tool. Version 1.XX*; http://avogadro.cc/.
(36) Neese, F. The ORCA Program System. *Wiley Interdiscip. Rev.: Comput. Mol. Sci.* **2012**, *2*, 73−78.
(37) Neese, F. Software Update: The ORCA Program System, Version 4.0. *Wiley Interdiscip. Rev.: Comput. Mol. Sci.* **2018**, *8*, e1327.
(38) Sure, R.; Grimme, S. Corrected Small Basis Set Hartree-Fock Method for Large Systems. *J. Comput. Chem.* **2013**, *34*, 1672−1685.
(39) Kruse, H.; Grimme, S. A Geometrical Correction for the Inter- and Intra-Molecular Basis Set Superposition Error in Hartree-Fock and Density Functional Theory Calculations for Large Systems. *J. Chem. Phys.* **2012**, *136*, 154101.
(40) Becke, A. D.; Johnson, E. R. A Density-Functional Model of the Dispersion Interaction. *J. Chem. Phys.* **2005**, *123*, 154101.
(41) Johnson, E. R.; Becke, A. D. A Post-Hartree−Fock Model of Intermolecular Interactions. *J. Chem. Phys.* **2005**, *123*, 024101.
(42) Johnson, E. R.; Becke, A. D. A Post-Hartree-Fock Model of Intermolecular Interactions: Inclusion of Higher-Order Corrections. *J. Chem. Phys.* **2006**, *124*, 174104.
(43) (a) Marenich, A. V.; Cramer, C. J.; Truhlar, D. G. Universal Solvation Model Based on Solute Electron Density and on a Continuum Model of the Solvent Defined by the Bulk Dielectric Constant and Atomic Surface Tensions. *J. Phys. Chem. B* **2009**, *113*, 6378−6396. (b) Tomasi, J.; Benedetta, M.; Cammi, R. Quatum Mechanical Continuum Solvation Models. *Chem. Rev.* **2005**, *105* (8), 2999−3094.
(44) Harnden, M. R.; Jarvest, R. L.; Bacon, T. H.; Boyd, M. R. Synthesis and Antiviral Activity of 9-[4-Hydroxy-3-(Hydroxymethyl)-but-l-Yl]Purines. *J. Med. Chem.* **1987**, *30*, 1636−1642.
(45) Addison, A. W.; Rao, T. N.; Reedijk, J.; Van Rijn, J.; Verschoor, G. C. Synthesis, Structure, and Spectroscopic Properties of Copper-(II) Compounds Containing Nitrogen-Sulphur Donor Ligands; the Crystal and Molecular Structure of Aqua[l,7-Bis(N-Methylbenzimidazol-2′-Yl)- 2,6-Dithiaheptane]Copper(II) Perchlorate. *J. Chem. Soc., Dalton Trans.* **1984**, *7*, 1349−1356.
(46) Hong-Ling, G.; Jian-Zhong, C. Hydrothermal Synthesis and Crystal Structures of Complex [Cu(CAM)(H_2O)$_2$]. *Chin. J. Inorg. Chem.* **2007**, *23*, 1072−1074.
(47) Janes, R.; Moore, E. A.; *Open University. Metal-Ligand Bonding*; Royal Society of Chemistry: London, 2004; pp 21−27.
(48) Mirzaei, M.; Eshtiagh-Hosseini, H.; Karrabi, Z.; Notash, B.; Bauzá, A.; Frontera, A.; Habibi, M.; Ardalani, M.; Shamsipur, M. Synthesis, Structure, Solution and DFT Studies of a Pyrazine-Bridged Binuclear Cu(II) Complex: On the Importance of Noncovalent Interactions in the Formation of Crystalline Network. *J. Mol. Struct.* **2015**, *1079*, 78−86.
(49) Vural, H.; Uçar, İ. A Mixed Experimental and Theoretical Study on Chelidamate Copper(II) Complex with 4-Methylpyrimidine. *J. Coord. Chem.* **2016**, *69*, 3010−3020.

https://dx.doi.org/10.1021/acs.inorgchem.0c01210
Inorg. Chem. 2020, 59, 9325−9338

(50) Grell, J.; Bernstein, J.; Tinhofer, G. Graph-Set Analysis of Hydrogen-Bond Patterns: Some Mathematical Concepts. *Acta Crystallogr., Sect. B: Struct. Sci.* **1999**, *B55*, 1030−1043.
(51) Yenikaya, C.; Büyükkidan, N.; Sari, M.; Keşli, R.; Ilkimen, H.; Bülbül, M.; Büyükgüngör, O. Synthesis, Characterization, and Biological Evaluation of Cu(II) Complexes with the Proton Transfer Salt of 2,6-Pyridinedicarboxylic Acid and 2-Amino-4-Methylpyridine. *J. Coord. Chem.* **2011**, *64*, 3353−3365.
(52) Yenikaya, C.; Poyraz, M.; Sarı, M.; Demirci, F.; İlkimen, H.; Büyükgüngör, O. Synthesis, Characterization and Biological Evaluation of a Novel Cu(II) Complex with the Mixed Ligands 2,6-Pyridinedicarboxylic Acid and 2-Aminopyridine. *Polyhedron* **2009**, *28*, 3526−3532.
(53) Lippert, B. Multiplicity of Metal Ion Binding Patterns to Nucleobases. *Coord. Chem. Rev.* **2000**, *200−202*, 487−516.
(54) Kondo, J.; Tada, Y.; Dairaku, T.; Hattori, Y.; Saneyoshi, H.; Ono, A.; Tanaka, Y. A Metallo-DNA Nanowire with Uninterrupted One-Dimensional Silver Array. *Nat. Chem.* **2017**, *9*, 956−960.
(55) For the sake of comprehension, mcheld numbering in **1Cu** follows that adopted in the mcheld-Cu-nucleobase base pairs.
(56) Hydrogen bonds with D···A distances larger than 3.0 Å have been omitted. The reader is referred to the CIF file.
(57) The difference in the length of the alkyl chain is merely due to the access to specific starting materials at the time of the synthesis.

https://dx.doi.org/10.1021/acs.inorgchem.0c01210
Inorg. Chem. 2020, 59, 9325−9338

SUPPORTING INFORMATION

A Comparative Structural Study of Metal-Mediated Base Pairs Formed Outside and Inside DNA Molecules

Alicia Dominguez-Martin,[1] Simona Galli,[2] José A. Dobado,[3] Noelia Santamaría-Díaz,[1] Antonio Pérez-Romero,[1] and Miguel A. Galindo[1,]*

[1] Departamento de Química Inorgánica, Universidad de Granada, Avd Fuentenueva s/n, 18071 Granada, Spain.

[2] Dipartimento di Scienza e Alta Tecnologia, Università dell'Insubria, via Valleggio 11, 22100 Como, Italy.

[3] Grupo de Modelización y Diseño Molecular, Departamento de Química Orgánica, Universidad de Granada, Avd Fuentenueva s/n, 18071 Granada, Spain.

Table of Contents

Table S1. Summary of crystallographic information and relevant X-ray diffraction experimental details. S3

Table S2. Comparison of the relevant bond distances and dihedral angles in the calculated and observed molecular structure of **1Cu_Cyt.** S10

Scheme S1. Synthesis of the 4-methoxypyridine-2,6-dicarboxylic acid (**mcheld**). S4

Figure S1. Molecular structure of [Cu(mcheld)(H_2O)$_2$], **1Cu** S4

Figure S2. Portion of the hydrogen bonding pattern observed in the crystal structure of [Cu(H_2O)$_2$(mcheld)], **1Cu** S5

Figure S3. The graph set motif in the crystal structure of [Cu(mcheld)(*N3*-Cyt)(H_2O)]·3H_2O,**1Cu_Cyt**. S6

Figure S4. Antiparallel π-π interaction observed in the crystal structure of [Cu(mcheld)(*N7*-Ade)], **1Cu_Ade**..... S6

Figure S5. Detail of the crystal structure of [Cu(mcheld)(*N7*-Ade)], **1Cu_Ade**. S7

Figure S6. Representation of portion of the 1D supramolecular chain in the crystal structure of [Cu(mcheld)(*N7*-Gua)], **1Cu_Gua** S8

Figure S7. Portion of the hydrogen bonding pattern observed in the crystal structure of [Cu(mcheld)(*N7*-Gua)], **1Cu_Gua**..... S9

Figure S8. CD spectra of single-stranded DNA molecules S10

Figure S9. Ab-initio HF-3c optimized geometries for **1Cu_Cyt-S** and **1Cu_Cyt-NW**. S11

Figure S10. Different views for the geometry-optimized duplex **DNA_{10}-H**. S11

Table S3. Cartesian coordinates (Å) for geometry-optimized (HF-3c, MINIX basis set) **1Cu_Cyt-S** S12

Table S4. Cartesian coordinates (Å) for geometry-optimized (HF-3c, MINIX basis set) **1Cu_Cyt-SE** S13

Table S5. Cartesian coordinates (Å) for geometry-optimized (HF-3c, MINIX basis set) duplex **1Cu_Cyt-NW**.....S14

Table S6. Cartesian coordinates (Å) for geometry-optimized (HF-3c, MINIX basis set) duplex **DNA_3-Na** S15

Table S7. Cartesian coordinates (Å) for geometry-optimized (HF-3c, MINIX basis set) duplex **DNA_3-H** S19

Table S8. Cartesian coordinates (Å) for geometry-optimized (HF-3c, MINIX basis set) duplex **DNA_3-H-SE** S23

Table S9. Cartesian coordinates (Å) for geometry-optimized (HF-3c, MINIX basis set) duplex DNA_{15}-Na S27

Table S10. Cartesian coordinates (Å) for geometry-optimized (HF-3c, MINIX basis set) duplex DNA_{15}-H S46

Table S11. Cartesian coordinates (Å) for geometry-optimized (HF-3c, MINIX basis set) duplex DNA_{10}-H S64

Table S1. Summary of crystallographic information and relevant X-ray diffraction experimental details for **1Cu**, **1Cu_Cyt**, **1Cu_Ade**, **1Cu_Gua** and **1Cu_^{7C}Ade**.

	1Cu	**1Cu_Cyt**	**1Cu_Ade**	**1Cu_Gua**	**1Cu_^{7C}Ade**
Formula	$C_8H_9CuNO_7$	$C_{13}H_{20}CuN_4O_{10}$	$C_{15}H_{22}CuN_6O_9$	$C_{16}H_{18}CuN_6O_7$	$C_{17}H_{21}CuN_5O_7$
MW [g/mol]	294.71	455.88	493.94	469.90	470.93
T [°C]	-173.5	-173.5	25	25	-173
Color, habit	n.a.	n.a.	Pale blue, prism	Blue, prism	n.a.
Dimensions [mm^3]	n.a.	n.a.	0.12×0.11×0.07	0.13×0.09×0.07	n.a.
Crystal system	Monoclinic	Triclinic	Monoclinic	Monoclinic	Triclinic
Space group	$P2_1/n$	P-1	$P2_1/n$	Cc	P-1
Z, Z'	4, 4	2, 2	4, 4	4, 4	2, 2
a [Å]	9.6792(16)	6.6005(17)	12.6963(3)	19.2898(15)	4.9903(3)
b [Å]	5.7689(7)	9.435(2)	10.2849(2)	5.2866(4)	13.8745(10)
c [Å]	18.198(4)	15.099(4)	15.9465(4)	17.8217(12)	13.9977(10)
α [°]	90	87.447(4)	90	90	91.593(3)
β [°]	91.279(11)	83.828(5)	109.768(2)	92.508(3)	92.468(3)
γ [°]	90	69.860(4)	90	90	99.690(3)
V [Å^3]	1015.9(3)	877.7(4)	1959.59(8)	1815.7(2)	954.14(11)
F(000)	596	470	1020	964	486
μ [cm^{-1}]	21.75(Mo Kα)	13.09(Mo Kα)	21.65(Cu Kα)	12.60 (Mo Kα)	20.96(Cu Kα)
ρ [g cm^{-3}]	1.9269(6)	1.7250(8)	1.6742(1)	1.7192(2)	1.6147(2)
θ range [°]	2.4<θ<27.5	1.3<θ<28.2	3.9<θ<66.6	3.0<θ<25.1	3.2<θ<66.7
	-12<h<12	-8<h<8	-15<h<13	-22<h<22	-5<h<5
h, k, l ranges	-7<k<6	-12<k<11	-12<k<9	-6<k<6	-16<k<16
	-23<l<23	-19<l<19	-17<l<18	-21<l<21	-16<l<16
Tot., indep., obs. [F_o>4σ(F_o)] refl.	7538, 2333, 2139	10167, 3925, 2990	13346, 3409, 2125	9279, 3205, 2290	12114, 3210, 2816
R_{int}, R	0.074, 0.074	0.080, 0.056	0.096, 0.090	0.049, 0.034	0.047, 0.052
Param., restr.	157, 0	262, 0	290, 0	263, 2	283, 0
Indep. refl. R1	0.043	0.075	0.113	0.037	0.054
Obs. refl. R1	0.039	0.051	0.057	0.032	0.048
wR2	0.102	0.111	0.148	0.077	0.143
GoF	1.068	1.022	1.047	1.059	1.071
Highest peak [e Å^{-3}]	0.59	0.56	0.73	0.53	0.69
Deepest hole [e Å^{-3}]	-0.50	-0.43	-0.74	-0.32	-0.57
CCDC number	1835231	1835232	1835233	1835234	1835235

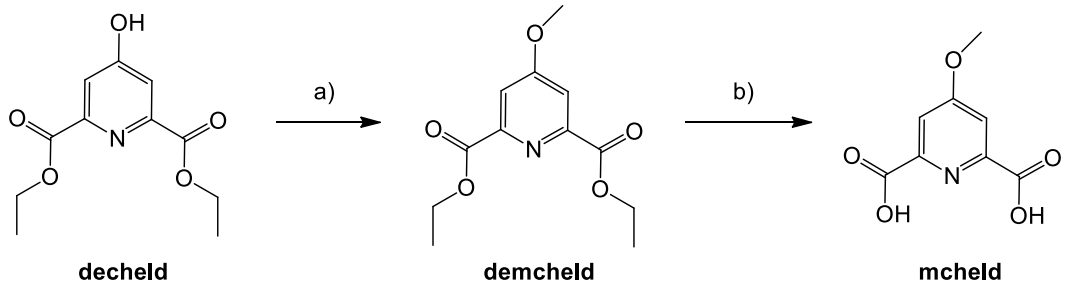

Scheme S1. Synthesis of the 4-methoxypyridine-2,6-dicarboxylic acid (mcheld). a) Sodium hydride, iodomethane, anhydrous *N,N*-dimethylformamide, 48 h. b) Sodium hydroxide (0.5 M), overnight.

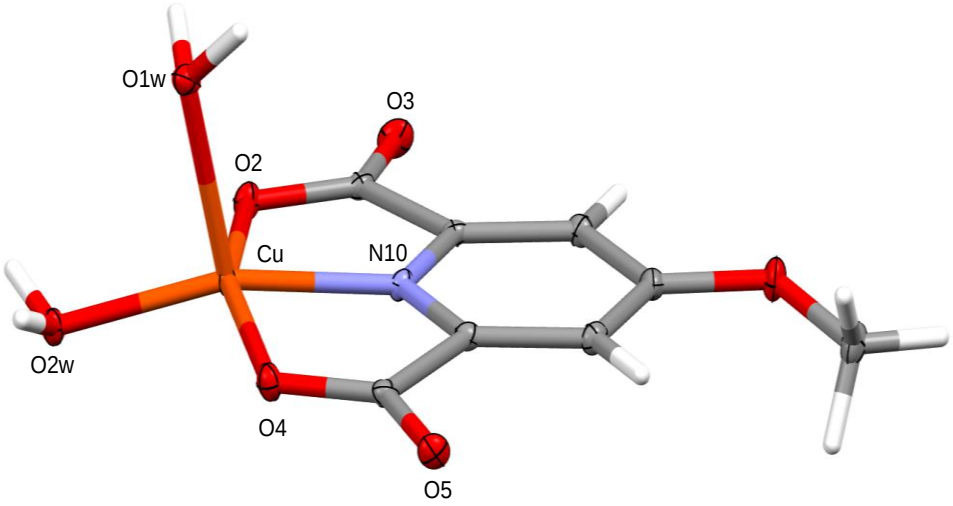

Figure S1. Molecular structure of [Cu(mcheld)(H_2O)$_2$], **1Cu**, with thermal ellipsoids set at 30% probability level. Atom color code: carbon, grey; hydrogen, light grey; copper, orange; nitrogen, blue; oxygen, red.

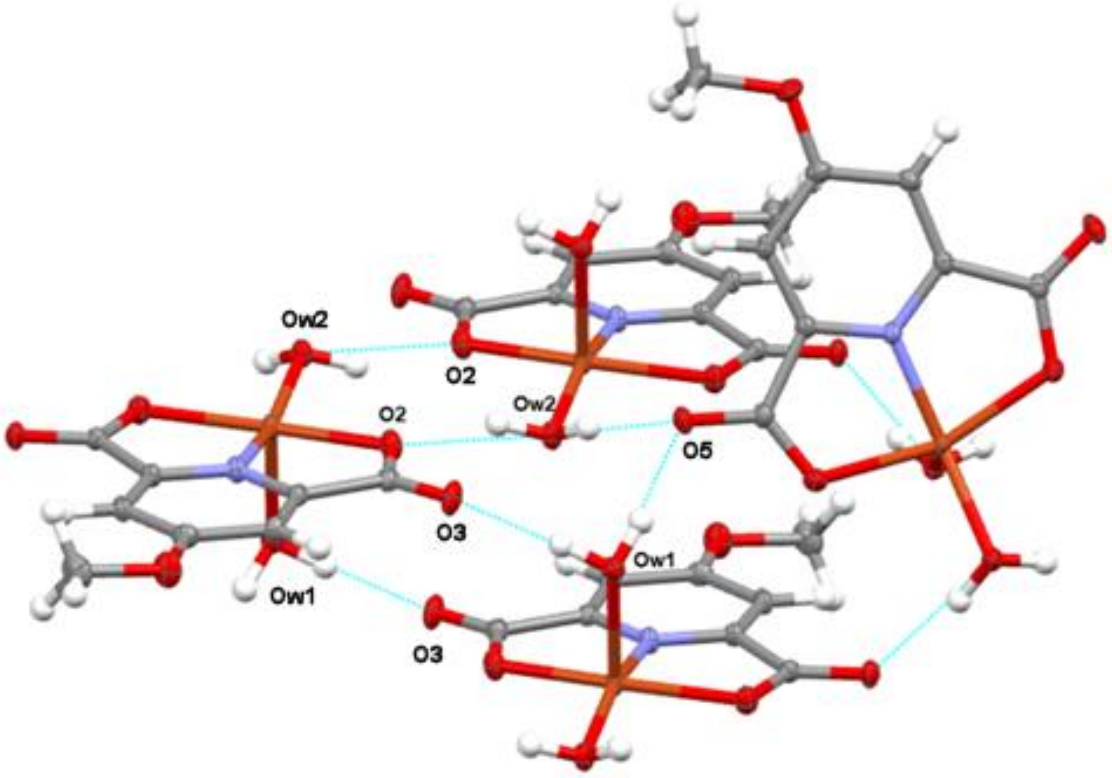

Figure S2. A portion of the hydrogen-bonding pattern observed in the crystal structure of [Cu(H_2O)$_2$(mcheld)], **1Cu,** with thermal ellipsoids set at 50% probability level. Atom color code: carbon, grey; hydrogen, light grey; copper, orange; nitrogen, blue; oxygen, red. The intermolecular hydrogen bond interactions are depicted with cyan dashed lines.

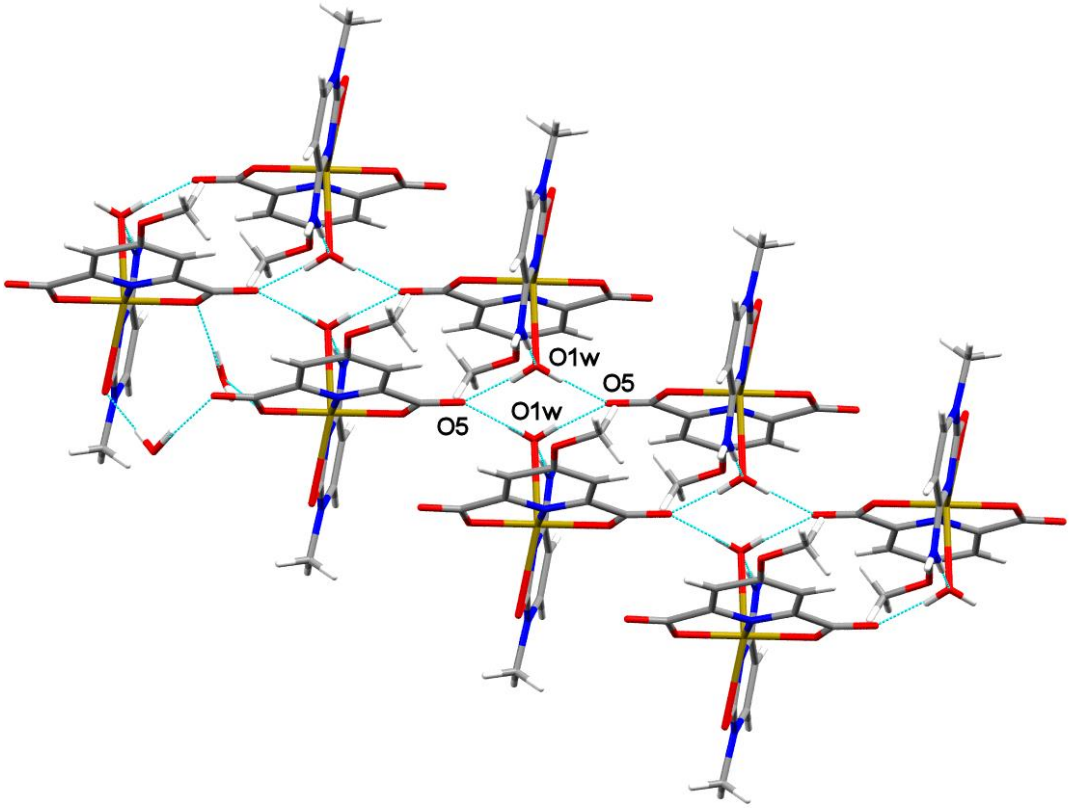

Figure S3. The graph set motif of the type $R_2^4(8)$ defined by the intermolecular hydrogen-bonding interactions (dashed cyan lines) involving O5 and O1w in the crystal structure of [Cu(mcheld)(*N3*-Cyt)(H_2O)]·3H_2O,**1Cu_Cyt.**

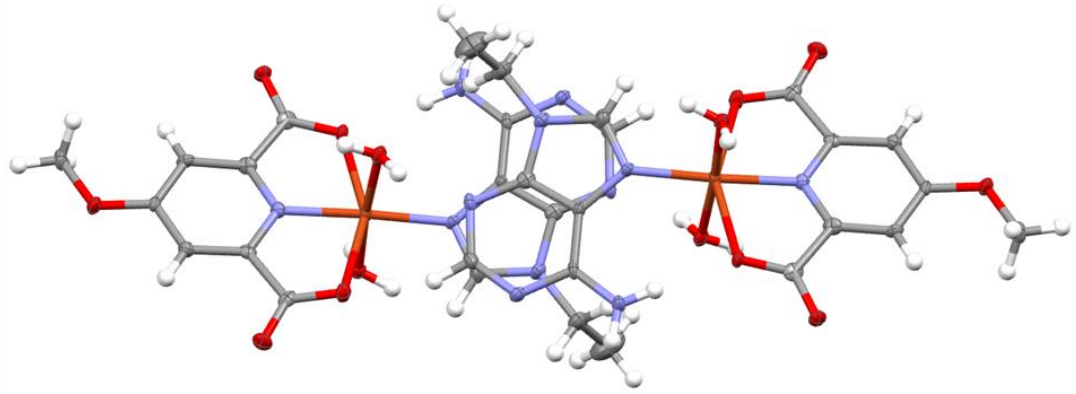

Figure S4. Overlap of the Ade moieties forming the antiparallel π-π interaction observed in the crystal structure of [Cu(mcheld)(*N7*-Ade)], **1Cu_Ade**, with thermal ellipsoids set at 50% probability level.

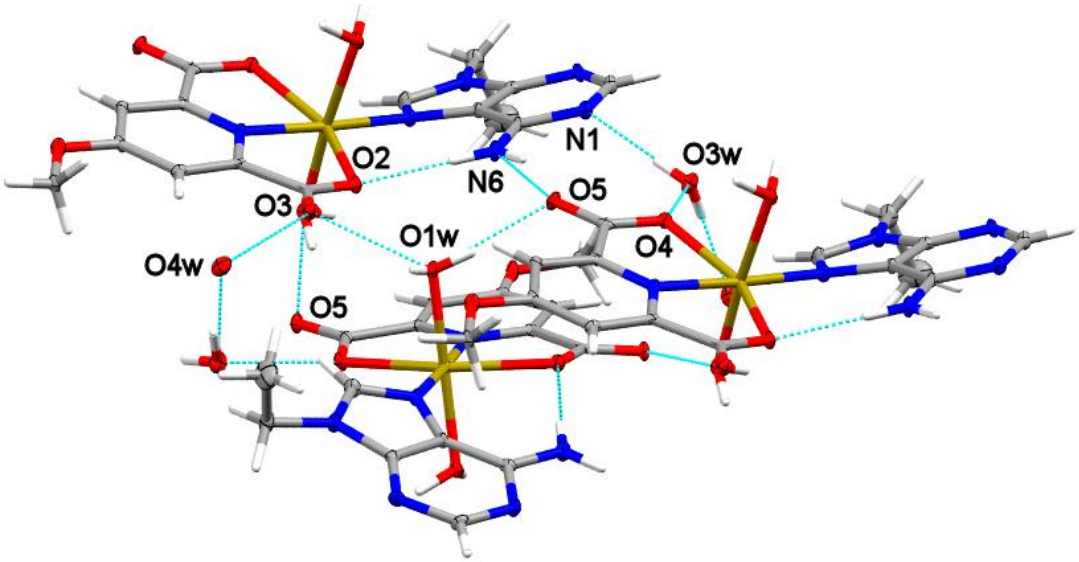

Figure S5. Detail of the graph set motifs $R^3_4(10)$ and $R^3_2(10)$ defined by the hydrogen bond interactions (cyan dashed lines) involving O2, O3, O1w, O5, N6 and N1, N6, O5, O4, O3w, respectively, in the crystal structure of [Cu(mcheld)(*N7*-Ade)], **1Cu_Ade**. Hanging contacts have been omitted for clarity.

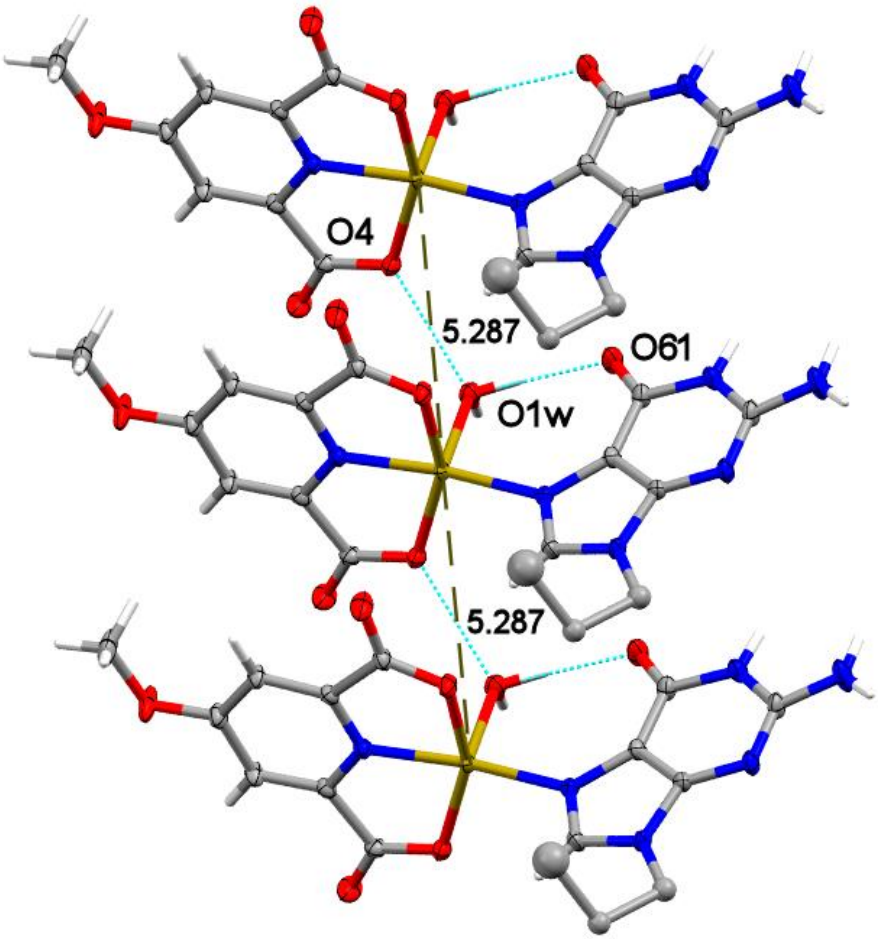

Figure S6. Representation of portion of the 1D supramolecular chain of collinear metal ions 5.287 Å apart (dashed black line) running along [010] in the crystal structure of [Cu(mcheld)(*N7*-Gua)], **1Cu_Gua.** The cyan dotted lines represent the hydrogen-bond interactions O1w···O61 (intramolecular) and O1w···O4 (intermolecular), bringing about the formation of the 1D chain. For clarity, an ordered model has been adopted for the Gua propyl moiety.

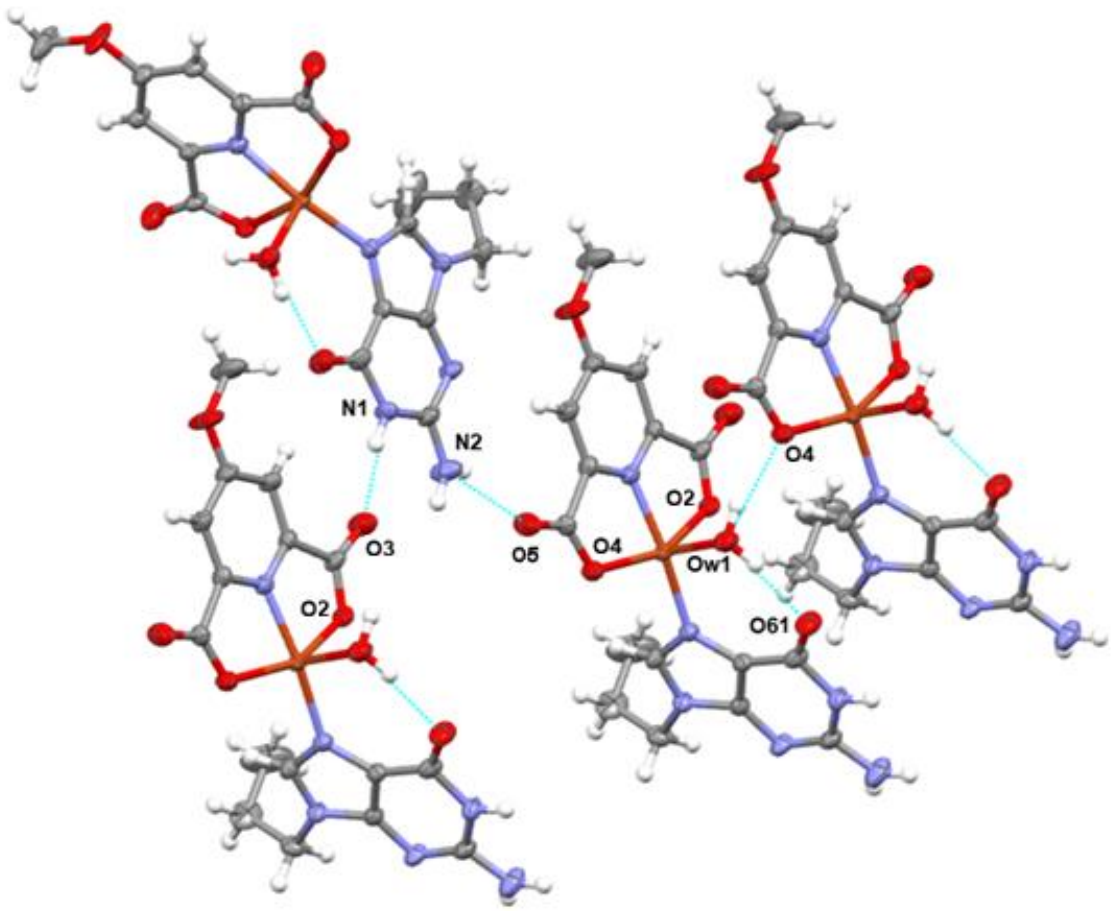

Figure S7. A portion of the hydrogen bonding pattern observed in the crystal structure of [Cu(mcheld)(*N7*-Gua)], **1Cu_Gua,** with thermal ellipsoids set at 50% probability level. Hydrogen bond interactions are depicted with cyan dotted lines.

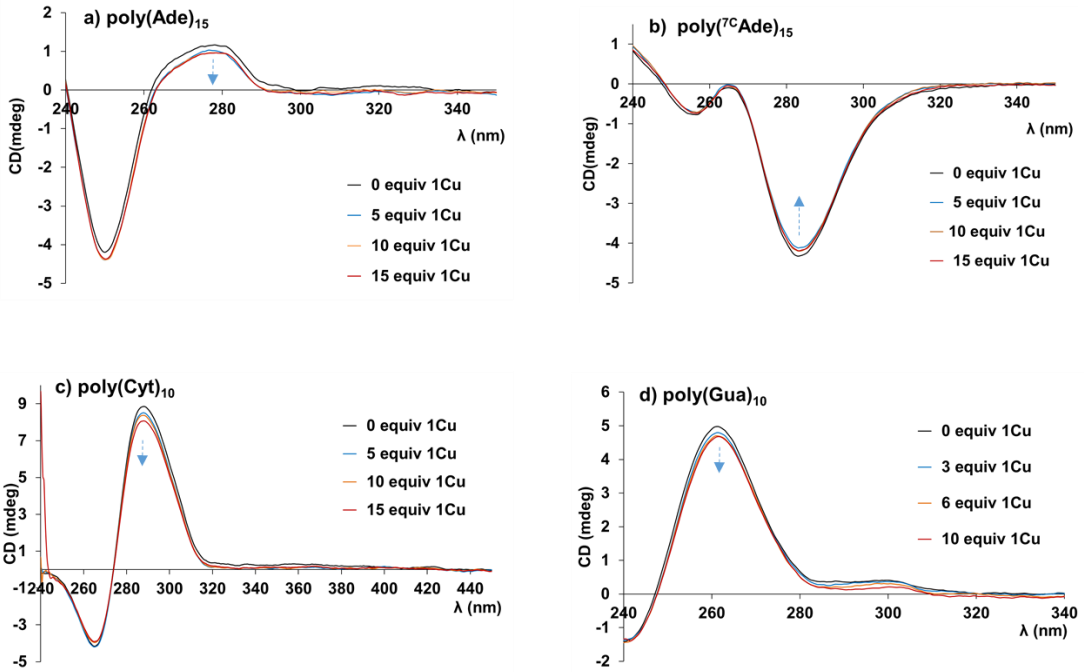

Figure S8. CD spectra of single-stranded DNA molecules: a) poly(Ade)$_{15}$, b) poly(^{7C}Ade)$_{15}$, c) poly(Cyt)$_{15}$ and d) poly(Gua)$_{10}$, in presence and absence of one equivalent of **1Cu** (*per* base). Conditions: 2 μM oligonucleotide, 0→30 μM **1Cu**, 100 mM $NaClO_4$ and 5 mM MOPS pH 6.8.

Table S2. Comparison of the relevant bond distances (Å) and dihedral angles (°) in the calculated and observed molecular structure of **1Cu_Cyt** (deviations with respect to the observed values are reported in brackets).

	Exp. 1Cu_Cyt	1Cu_Cyt-S	1Cu_Cyt-SE	1Cu_Cyt-NW
Cu-N10	1.893	1.917 (-0.024)	1.918 (-0.025)	1.904 (-0.011)
Cu-O2	1.997	1.94 (0.057)	1.919 (0.078)	1.893 (0.104)
Cu-O4	2.027	1.906 (0.121)	1.919 (0.108)	1.897 (0.130)
Cu-Ow	2.407	2.479 (-0.072)	-	-
Cu-N3	1.956	1.979 (-0.023)	1.955 (0.001)	1.983 (-0.027)
Cu-O21	2.711	2.573 (0.138)	2.538 (0.173)	2.55 (0.161)
Ligands dihedral angle	77.7	87.7 (-10)	88.5 (-10.8)	88.5 (-10.8)

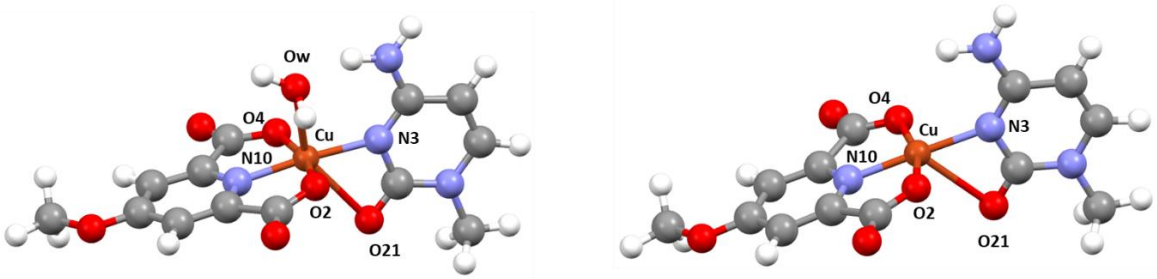

Figure S9. Ab-initio HF-3c optimized geometries for **1Cu_Cyt-S** (left) and **1Cu_Cyt-NW** (right).

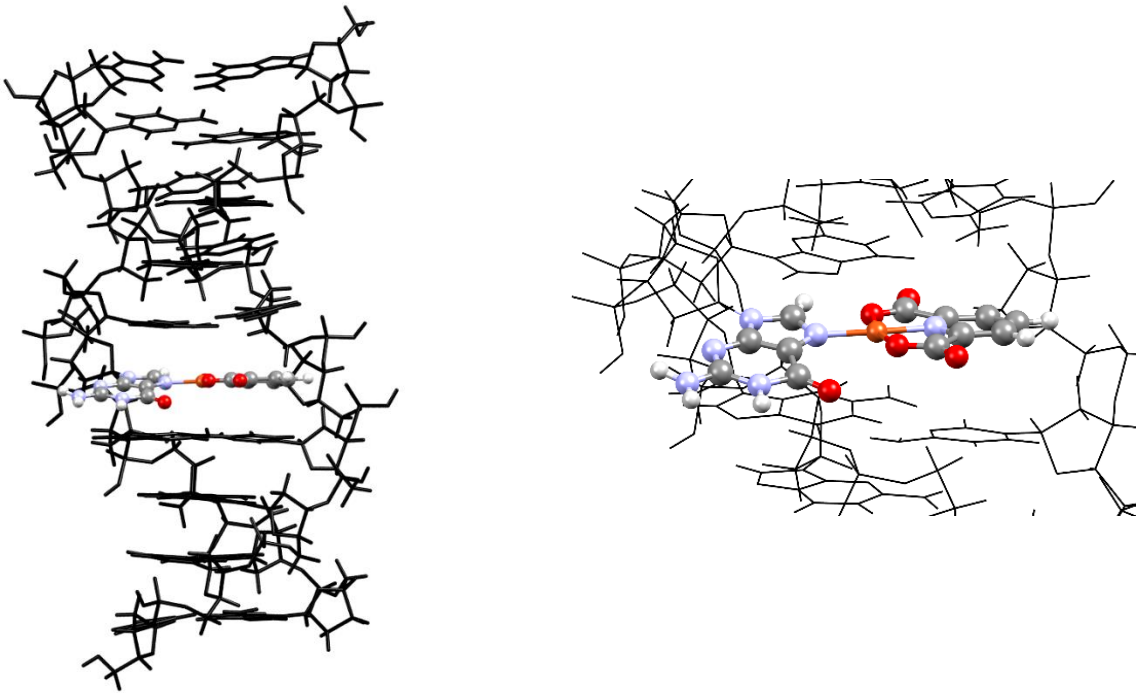

Figure S10. Left: view of the geometry-optimized duplex **DNA$_{10}$-H**. Right: a closer view of the **1Cu_Gua** base pair formed in the duplex structure.

Tentative tittle: Supramolecular DNA-Pd Hybrids Integrated With Conducting Polymers.

These results are included in Charpter 4 and will be submitted for publication

Received 00th January 20xx,
Accepted 00th January 20xx

DOI: 10.1039/x0xx00000x

Antonio Pérez-Romero, [a] Carmen López-Chamorro, [a] Fátima linares [b] and Miguel A. Galindo*

ss-DNA template have been employed to guide metal-mediated base pairs modified with polymeric fragments. The AFM confirms the formation of elongated and stretched DNA-based polymeric structures. Moreover, EFM experiments suggest the presence of donductivity properties within these structures.

Previously, we have reported the template-driven self-assembly of adenine single-stranded DNA (**dA_{15}**) and palladium complexes, which selectively bind to the Watson-Crick-Franklin (WCF) face of the nucleobases via metal-mediated base pairs.[1] ss-DNA serve as a guiding template for the arrangement of Pd^{II} complexes, resulting in the formation of a supramolecular structure that closely mimics a double-stranded DNA (ds-DNA). Here, Pd^{II} ions are organized into a one-dimensional array along the ss-DNA and the complexes are further stabilized through stacking interactions. It is widely recognized that DNA metallization is a crucial process to enhance its nanotechnological properties.[2] However, a highly popular approach to providing new properties has been centered around the use of polymers capable of growing along its structure.[3–7] Recently, our results have indicated the possibility of modifying palladium complexes with a 2-(2-thienyl)pyrrole (**Tp**) monomer. Typically, integrating **Tp** fragments into the nucleobase structure, and thus into a DNA strands, requires intricate synthetic processes.[8–12] However, here we present a mechanism to organized polymerizable **Tp** structures through a self-assembly process by metal-mediated base pairs interactions. The resulting polymer grows along the ss-DNA template, providing a highly conjugated structure that facilities the transport of charge along the polymer. **Tp** moiety can be polymerized under controlled conditions to obtain conductive polymers.[11,13–18]

The previous reported [Pd(Cheld)(CH_3CN)] (**Pd-Cheld**) metal complex was successfully modified, characterized and coordinated with $Pd(NO_3)_2$ to obtain [Pd(CheldTP)(DMSO)], (**Pd-CheldTP**) (Supp.Inf.SX). First, the interaction between **Pd-CheldTP** and the model nucleobase 9-ethyl-adenine (**eA**) was followed by H^1-RMN (400Mhz, $DMSO^{d6}$) (Sup.Inf.SX). Figure 1a display spectrum data for **[Pd(CheldTP)(eA)]** complex. As previously reported, singlets at 8.46, 8.39, 8.32 and 8.13 ppm corresponding to H2 and H8 of adenine, were observed. [8,11,12] These signals are consistent with the formation of two different structures that coexist in equilibrium as a consequence of the N1 and N7 coordinated isomers; **[Pd(CheldTP)(*N1*-eA)]** and **[Pd(CheldTP)(*N7*-eA)]**.[1] Furthermore, singlets at 8.53 and 8.52 ppm can be attributed to the NH_2 group of **eA**, and singlets at 7.33 and 7.31 ppm, which correspond to aromatics Ha_{py} and Hb_{py} protons isomers, are also observed.

Therefore, these results suggest that **[Pd(CheldTP)(eA)]** complex could also interact with oligonucleotide sequences containing adenosine to form a supramolecular system [{Pd(CheldTP)}$_{15}$(dA_{15})] (**dA_{15}-Pd-CheldTP**), where the **TP** units can be arranged according to the single-stranded oligonucleotide structure.

To study the interaction between **dA_{15}** and **Pd-CheldTP** a titration experiment followed by Circular Dichroism (CD) at pH6.8 was carried out (Supp.Inf.XX). The spectra of free **dA_{15}** showed both negative and positive bands in the range of 245-300 nm, where DNA typically absorbs. Upon the controlled addition of **Pd-CheldTP**, distinct Cotton effects were observed along with induced circular dichroism (ICD) bands appearing in the region above 300 nm, where **Pd-CheldTP** absorb (Sp.Inf.XX). Specifically, an intense negative band at 307 nm and a small broad positive band between 350 and 400 nm emerged, accompanied by a decrease in the **dA_{15}** band as Pd^{II} complex was added. These ICD bands illustrate the interaction between the **Pd-CheldTP** fragment and **dA_{15}**. Importantly, upon introducing the Pd^{II} complex, the presence of the ascending band at 275 nm remains, albeit with a shift towards negative ellipticity values. These findings, together with studies using isolated adenine derivatives described above, suggest that **Pd-CheldTP** units are organized along the single strand of DNA by binding to adenine bases via N1, and the system retains a helical structure, suggesting the formation of the supramolecular hybrid **dA_{15}-Pd-CheldTP**. To confirm these facts, a similar CD titration

[a] *Departamento de Química Inorgánica. Unidad de Excelencia Química Aplicada a Biomedicina y Medioambiente, Universidad de Granada. Avda Fuentenueva s/n, 18071 Granada (Spain)*
[b] *Address here.*
† Footnotes relating to the title and/or authors should appear here.
Electronic Supplementary Information (ESI) available: [details of any supplementary information available should be included here]. See DOI: 10.1039/x0xx00000x

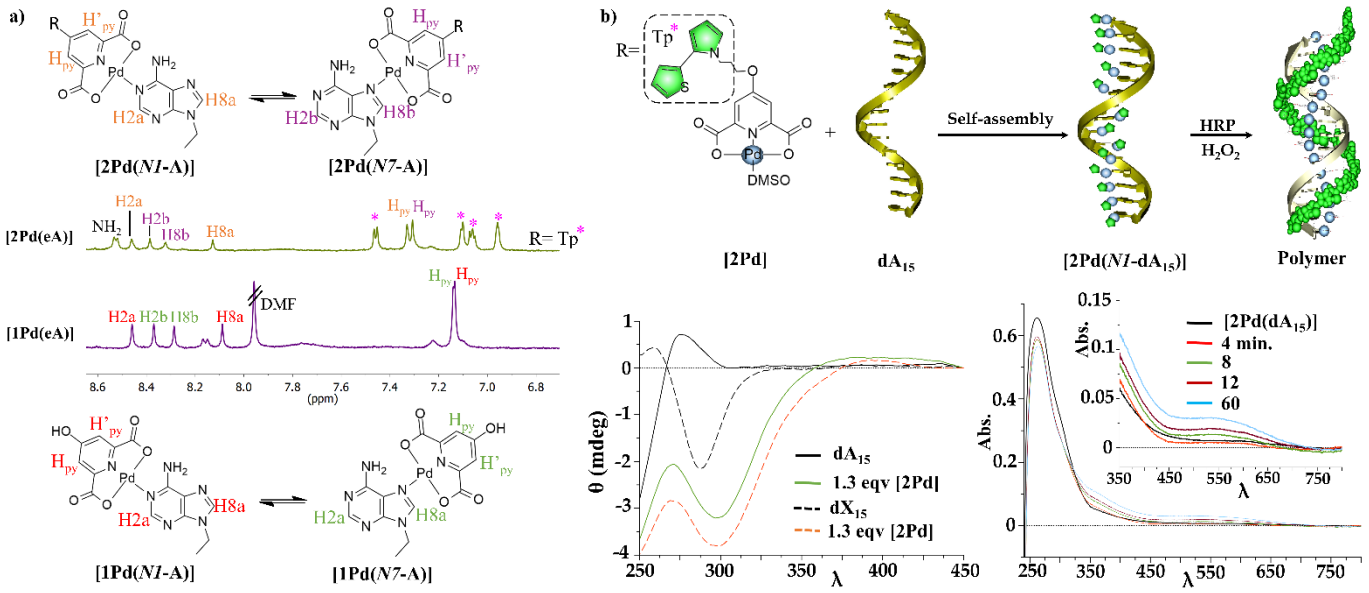

Figure 1: a) ^{1}H-RMN (400 Mhz, DMSO^{d6}) for the interaction studies between the free modified **eA**, **Pd-CheId** and **Pd-CheIdTP** complexes to obtain **[Pd(CheId)(eA)]** (bottom MNR) and **[Pd(CheIdTP)(eA)]** (top MNR) structures. In both cases, isomers structures via Pd-*N1*(A) and Pd-*N7*(A) were observed. R2 code refers to **Tp** moiety (pink asterisk). b) Schematic reaction between **Pd-CheIdTP** complex and **dA$_{15}$** to obtain the hybrid **[Pd(CheIdTP)(dA$_{15}$)]** followed by CD and the polymerization process followed by UV-Vis. For clarity, a code for PdII complexes is used, (**1Pd**) = **Pd-CheId** and (**2Pd**) =**Pd-CheIdTP**.

experiment was conducted using a reference oligonucleotide comprising 7-deazaadenosine (**dX$_{15}$**), therefore restricting the binding of the Pd^{II} fragment towards the N1-atom at WCF face of adenine. In this instance, a CH group replaces the N7 atom in adenine, promoting exclusive interaction with the **Pd-CheIdTP** fragment via N1 atom to obtain **[Pd(CheIdTP)(*N1*-dX$_{15}$)].** Figure 1b (left) show the CD spectra for both ss-DNA experiments when 1.3 equivalents of **Pd-CheIdTP** were added. The CD spectra for free **dA$_{15}$** and **dX$_{15}$**, shows a positive and negative band, in the range of 275-300 nm, respectively. However, in the presence of **Pd-CheIdTP**, comparable spectra are observed. The CD spectra exhibited a similar interaction pattern, with the appearance of ICD band in the region above 300 nm. Both systems exhibit a similar interaction, resembling the formation of a helix structure and confirming the binding of the **Pd-CheIdTP** fragment via N1-adenine position. Analogous control CD experiments were conducted to rule out the interactions of **dA$_{15}$** with free **CheIdTp** ligand or $Pd(NO_3)_2$, revealing different outcomes compared to those previously discussed. (Supp.Inf.XX).

The CD data obtained for **dA$_{15}$-Pd-CheIdTP** hybrids at pH6.8 provided the possibility to design an analogous experiment to investigate the polymerization process of TP fragments. To initiate the polymerization process, a pH4.5 and an oxidizing environment were required.[11] The polymerization reaction for **dA$_{15}$-Pd-CheIdTP** was initially monitored using UV-vis spectroscopy and performed following the procedure outlined in the previous CD experiment (Supp.Inf.XX). To initiate the polymerization process, a pH 4.5 and oxidizing environment were required. To achieve this, nitric acid (0.5M) was added to adjust pH from 6.8 to 4.5. Subsequently, ABTS (10 µM), HRP (1mg/mL) and H2O2 (15%v/v) were added into the solution. For **dA15-Pd-CheIdTP**, UV-Vis exhibit an intense peak at 266 nm, characteristic of **dA$_{15}$**, alongside a shoulder band centred at approximately 350 nm, corresponding to the absorption of the **Pd-CheIdTP** fragment, which participates in the formation of the Pd-mediated base pairs. Upon the addition of polymerization reactants, a new broad absorption band emerged within the range of 450 – 700 nm, and its intensity increased over time. This finding is agreeing with the formation of **(TP)**$_n$ polymers, thus indicating the occurrence of polymerization events.[8,12,15] Notably, no absorption bands were registered in the region above 700 nm. In addition, the absorption band for **dA$_{15}$** shows minimal changes, thus suggesting non-significant alteration of the oligonucleotide strand. These results suggest the formation of polymer strands,

likely influenced by the organized arrangement of **TP** moieties along the ss-DNA via metal-mediated base pairs, leading to the Polymerized system **dA15-Pd-CheldTP^{polym}**. Additionally, a control experiment was also performed using a solution containing **dA$_{15}$** in the presence of **CheldTP**, excluding the Pd^{II} ions (Supp.Inf.XX). UV-Vis reveals a significant change in the spectra when Pd^{II} is omitted. Here, the intensity of the absorption band at 500-600 nm increased more rapidly, and the maximum for **dA$_{15}$** underwent several changes. These results suggest the formation of the polymer without structural control, facilitating polymerization around the ss-DNA structure and resulting in a significant conformational change of the DNA geometry. This interaction can be attributed to spontaneous electrostatic interactions between the cationic polymer and the anionic ss-DNA strand [19]

A CD was carried out to gain more insight into how polymerization process could affect the geometrical disposition of **dA$_{15}$-Pd-CheldTP** hybrids (Supp.Inf.XX). Following pH adjustment to 4.5, the CD curve maintained its profile with two ascending bands at 264 and 400 nm, and a descending band at 307 nm. Subsequently, the sample underwent polymerization upon adding the reactants (HRP/H2O2/ABTS) and the corresponding CD was measured at different stages of the polymerization process. The CD spectra before and after polymerization display comparable profiles, with a slight increase in ellipticity observed post-polymerization. Additionally, the broadband within 350-450nm seems to disappear and leads to the suppression of the initial ICD band before polymerization, which is related to the absorbance changes of the polymer in this region.

The results obtained from UV-Vis and CD spectroscopy indicate that the helix's conformation does not significant alter upon polymerization of the **TP** units, suggesting a match between the polymer structure and the helicity of the single strand. To further evaluate this structural aspect, computational studies for the polymerized **dA$_{15}$-Pd-CheldTP^{polym}** system were conducted (Supp.Inf.XX). In this regard, its optimized geometry was calculated employing Hartee-Fock (HF) methodologies. The optimized geometry structure unveils a double-helix configuration that accommodates the polymer. One strand is formed by a **dA$_{15}$** and the other strand comprises **Pd-CheldTP^{polym}** units. The supramolecular structure is formed by continuous Pd-mediated base pairs with the **Pd-CheldTP** fragment binding at the N1-adenine position and also stacked along the ss-DNA. Computational calculations shows that the polymer nicely follows the helicity of the DNA strand and fits within the structure dimension without alteration of the Pd-base pairs.

Once demonstrated the possibility of obtaining **dA$_{15}$-Pd-CheldTP^{polym}** hybrid systems scanning probe microscopy, particularly Atomic Force Microscopy (AFM) and Electronic Force Microscopy (EFM) were conducted.[20–25] However, the previously studied **dA$_{15}$** strand and the subsequent **dA$_{15}$-Pd-CheldTP^{polym}** hybrid may prove too short for microscopy studies. To address the challenge of working with strands that were too short for surface characterization, poly(adenylic) acid, **poly(A)**, with a variable length between 2.100 and 10.000 nucleotides, was employed to create longer [Pd(CheldTP)(polyA)] structures (**poly(A)-Pd-CheldTP^{polym}**). Two surfaces, mica and SiO_2, were employed to study different characteristics of the poly(A)-Pd systems.

First, mica surface was initially employed and functionalized with APTES (0.1%)[24] to deposit samples of free **poly(A)**, supramolecular **poly(A)-Pd-CheId** system, non-polymerized **poly(A)-Pd-CheldTP** and polymerized **poly(A)-Pd-CheldTP^{polym}**. The structural images for each sample are shown in Figure 2.b. The results indicate that, in general, the absence of the **Pd-CheId** complex resulted in aggregation, with rounded structures observed for **poly(A)**. This observation corresponds to the inherent tendency of single-stranded RNA molecules to adopt complex structures, often leading to globular aggregation. In contrast, when **Pd-CheId** is present in the sample, the images show elongated and stretched strands, with widths ranging between 10-20 nm and heights of around 1nm, forming a densely interconnected network, in agreement with the formation of **poly(A)-PdCheId** structures. This transformation can be attributed to the disruption of hydrogen bond formation within **poly(A)** strands due to the formation of Pd-mediated base pairs, thus preventing aggregation. The images registered for **poly(A)-Pd-CheldTP** system also revealed elongated structures, but in this case, resulting in a more distinct interconnected network with strands showing a width between 10-20 nm and height around 2 nm. Finally, the polymerized **poly(A)-Pd-CheldTP^{polym}** sample exhibited an intricate, densely interconnection network between strands of broad nodes, that can be related to the polymerization process. In this sample, the width and height of the strands exceeded that of any other case, with widths ranging from 30-40 nm and heights around 3nm. Consequently, it can be concluded that forming Pd-mediated base pairs promotes the development of more extended and interconnected structures. Still, more detailed studies are needed to fully understand cross-polymerization events between **poly(A)** molecules. This could explain the presence of more connected and broader nodes in **poly(A)-Pd-CheldTPpolym** structures.

After investigating the formation of supramolecular **poly(A)-Pd-CheldTPpolym** hybrids by AFM, their electrical properties were studied. As mentioned above, polymers derived from **TP** have been demonstrated to be effective in creating electrically conductive structures.[9,26] To study the electrical properties of

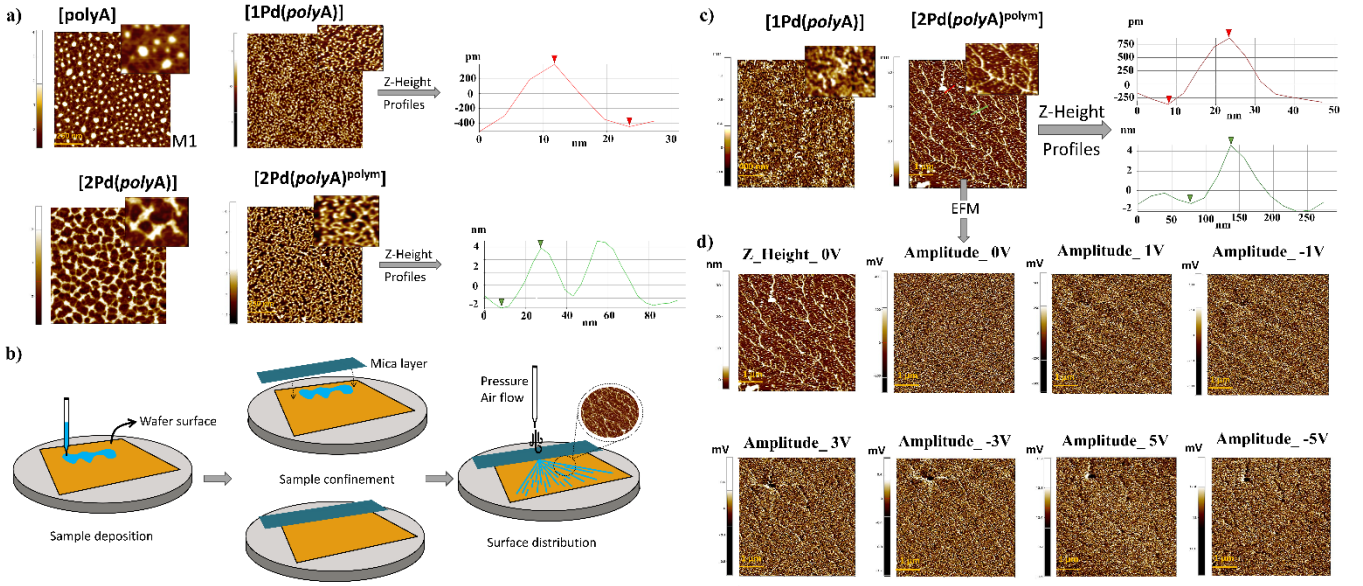

Figure 2: a) AFM and Z-Height profiles for samples in a mica wafer. b) Schematic representation of sample deposition over silicon surface. 10-15 µL sample was added onto a wafer surface and covered with a mica layer. Then, a pressure flow air facilitates the dispersion of the sample along the surface. The orange square represents the chosen mica or SiO_2 surface, and the blue one a mia layer. c) AFM, Z-Height profile, and d) EFM (0 to ±5 V) for samples in SiO_2 wafer.

poly(A)-Pd-CheldTP supramolecular hybrids, SiO_2 surfaces were chosen and properly functionalized.[10,27,28] SiO_2 wafers are commonly employed for this task and have been evaluated as proper candidates for electrical studies.[29] Figure 2a shows a schematic representation of the protocol to deposit the sample on SiO_2. Subsequently, the samples were studied using AFM and EFM.

As observed in the AFM experiments using SiO_2, free poly(A) strands tend to form granular structures (Figure 2b, top). As expected by the non-conducting nature of these structures, the corresponding electrical signal amplitude and phase acquired by EFM (from -5V to 5V) did not display any charge distribution over the sample. The images recorded for **poly(A)-Pd-Cheld** structures exhibited an irregular strand organization, with multiple overlapping layers and poor strand stretching with structures ranging from 20 to 40 nm (Supp.Inf.XX). These results are different from those conducted on mica for **poly(A)-Pd-Cheld** hybrid. Unfortunately, all attempts to obtain images showing stretched p**oly(A)-Pd-Cheld** strands on SiO_2 were unsuccessful. Nonetheless, EFM measurements were conducted for these **poly(A)-Pd-Cheld** irregular structures and no electrical signal amplitude or phase was observed. These results also indicate that the presence of **Pd-Cheld** does not lead to noticeable changes in the conductive characteristic of this material.

AFM experiments were them conducted for **poly(A)-Pd-CheldTP** on SiO_2 (Supp.Inf.XX), revealing granular and slightly elongated structures with widths ranging from 50 to 100 nm. Unfortunately, no stretched structures were observed. Nevertheless, EFM was conducted on the deposited material, and as expected, no electrical signal amplitude or phase was detected. This behaviour is consistent with the above findings, as neither the presence of **Pd-Cheld** nor Pd-CheldTP monomers change the conductive characteristic of **poly(A)-Pd-CheldTP** hybrids. Finally, the AFM studies performed on polymerized **poly(A)-Pd-CheldTP^{polym}** samples yielded promising results. Figure 2b displays the initial AFM topography on SiO_2 studies, showing stretched and continuous structures with intercalated small nodes along the structures. Graphics for Z-height profiles present a cross-section of the structures (Figure 42b, right), revealing that the heights range between 1nm for thinner structures and 4 nm for wider structures. These results suggest that the formation of isolated polymer stranded (Z_Height ≈ 1 nm) is accompanied by the deposition of several ones (Z_Height ≈ 4 nm), although possible cross-polymerization processes leading to wider and more complex structures cannot be ruled out. On the other hand, the width for **poly(A)-Pd-CheldTP^{polym}** structures ranges from 100 to 200 nm, in contrast with the 50 to 100 nm found for **poly(A)-Pd-CheldTP**. The significant difference in thickness between both samples suggests a better elongation when the polymer is formed, and probably, two or more strands should adhere together over the silicon oxide surface.

Moreover, a comparison of AFM topography between mica and SiO_2 surfaces for **poly(A)-Pd-CheldTP^{polym}**, shows that the silicon surface facilitates the stretching of the strands and the formation of single layers. It is worth mentioning that the depositions of these samples proved to be challenging and required tedious and meticulous procedures to yield reproducible data.

Subsequently, the conducting characteristics of **poly(A)-Pd-CheldTP^{polym}** structures were investigated by EFM measurements. The corresponding electrical signal amplitude and phase acquired at different voltages (-5V to 5V) are presented in Figure 2b, bottom. The amplitude signals indicate that the charge distribution in the sample follows the topography observed by AFM, where a multitude of structures were visualized between -3 and 3 V, following the topographic signal. Graphics for Z-µV profiles present a cross-section for the amplitude signal (Figure 2b, right), and a comparison of Z-µV profiles for the same cross-section (red line or green line) at 1V and 3V are presented. In all the experiences, Z-µV profiles exhibit values ranging from 400 to 600 µV and a width of 200 nm, indicating the existence of charge conduction in this case.

Comparing these results with EFM experiments for **poly(A)**, **poly(A)-Pd-CheId** and **poly(A)-Pd-CheldTP^{polym}**, only for samples containing polymerized **TP** structures along the ss-DNA template, electrostatics properties were observed. Overall, the results obtained in this research provide initial evidence suggesting that **polyA-Pd-CheldTP^{polym}** structures can be conductive. However, it is important to clarify that while these supramolecular structures have exhibited EFM signals, this does not necessarily imply intrinsic conductivity. Complementary studies, such as conductive AFM (c-AFM) experiments, would be necessary to study the electrical conductivity of these systems more deeply. In this regard, Houlton and co-workers have made significant advances in studying DNA-based material using c-AFM measurements, demonstrating that polymers derived from thiophene/pyrrole systems deposited on DNA molecules can act as conducting material. [7,30–32]

Conclusions

A strategy to obtain metal-DNA hybrids with potential nanotechnological properties has been presented. Initially, the characterization of the **[Pd(CheldTP)(DMSO)]** complex was described. Subsequently, interaction studies between **Pd-CheldTP** and the model nucleobase 9-ethyl-adenine (**eA**) confirmed the formation of the **[Pd(CheldTP)(eA)]** complex, serving as a preliminary step toward the formation of supramolecular DNA-Pd hybrids that incorporate the **TP** unit.

Following previously repoted methodologies, the formation of the supramolecular [{**Pd(CheldTP}$_{15}$)(dA15)]** hybrid was confirmed. This structure resembles a helix due to the binding of the **Pd-CheldTP** fragment via ***N1***-adenine position, with one strand formed by **dA$_{15}$** and the other one by **Pd-CheldTP** complexes. Furthermore, the organization of **TP** monomers along the ss-DNA template makes them suitable for further reactions. The subsequent polymerization of these monomers was studied by UV-Vis, CD, and computational studies, confirming that the conformation of the nucleic acid helix does not significantly alter upon polymerization of the **TP** units.

Finally, preliminary investigations were conducted to determine the potential conductive properties of the polymeric structures, [[{**Pd(CheldTP}$_{15}$)(dA$_{15}$)]^{polym},** using EFM. While these results suggest that the supramolecular structures exhibit charge distribution, they do definitively confirm conductivity. More profound studies in this regard need to be conducted due to the difficulty in obtaining reproducible samples with stretched polymeric structures suitable for c-AFM.

Author Contributions

We strongly encourage authors to include author contributions and recommend using CRediT for standardised contribution descriptions. Please refer to our general author guidelines for more information about authorship. Please remove the "**Author Contributions**" heading for articles submitted to *Chemical Communications*.

Conflicts of interest

In accordance with our policy on Conflicts of interest please ensure that a conflicts of interest statement is included in your manuscript here. Please note that this statement is required for all submitted manuscripts. If no conflicts exist, please state that "There are no conflicts to declare".

Notes and references

1 A. Pérez-Romero, A. Domínguez-Martín, S. Galli, N. Santamaría-Díaz, O. Palacios, J. A. Dobado, M. Nyman and M. A. Galindo, *Angew. Chem. Int. Ed*, 2021, **133**, 10177–10182.

2 Z. Chen, C. Liu, F. Cao, J. Ren and X. Qu, *Chem Soc Rev*, 2018, **47**, 4017–4072.

3 P. Nickels, W. U. Dittmer, S. Beyer, J. P. Kotthaus and F. C. Simmel, *Nanotechnology*, 2004, **15**, 1524–1529.

4 R. Nagarajan, W. Liu, J. Kumar, S. K. Tripathy, F. F. Bruno and L. A. Samuelson, *Macromolecules*, 2001, **34**, 3921–3927.

5 R. Hassanien, M. Al-Hinai, S. A. Farha Al-Said, R. Little, L. Šiller, N. G. Wright, A. Houlton and B. R. Horrocks, *ACS Nano*, 2010, **4**, 2149–2159.

6 S. Pruneanu, S. A. F. Al-Said, L. Dong, T. A. Hollis, M. A. Galindo, N. G. Wright, A. Houlton and B. R. Horrocks, *Adv Funct Mater*, 2008, **18**, 2444–2454.

7 L. Dong, T. Hollis, S. Fishwick, B. A. Connolly, N. G. Wright, B. R. Horrocks and A. Houlton, *Chem. Eur. J.*, 2007, **13**, 822–828.

8 W. Chen, G. Güler, E. Kuruvilla, G. B. Schuster, H.-C. Chiu and E. Riedo, *Macromolecules*, 2010, **43**, 4032–4040.

9 S. M. D. Watson, A. R. Pike, J. Pate, A. Houlton and B. R. Horrocks, *Nanoscale*, 2014, **6**, 4027–4037.

10 S. M. D. Watson, J. H. Hedley, M. A. Galindo, S. A. F. Al-Said, N. G. Wright, B. A. Connolly, B. R. Horrocks and A. Houlton, *Chem. Eur. J.*, 2012, **18**, 12008–12019.

11 W. Chen and G. B. Schuster, *J Am Chem Soc*, 2013, **135**, 4438–4449.

12 W. Chen and G. B. Schuster, *J Am Chem Soc*, 2012, **134**, 840–843.

13 H.-K. Song and G. T. R. Palmore, *J Phys Chem B*, 2005, **109**, 19278–19287.

14 H.-K. Song and G. T. R. Palmore, *Adv. Mater.*, 2006, **18**, 1764–1768.

15 W. Chen and G. B. Schuster, *Org. Biomol. Chem.*, 2013, **11**, 35–40.

16 R. Santucci, E. Laurenti, F. Sinibaldi and R. P. Ferrari, *Biochimica et Biophysica Acta (BBA) - Protein Structure and Molecular Enzymology*, 2002, **1596**, 225–233.

17 A. M. Azevedo, D. M. F. Prazeres, J. M. S. Cabral and L. P. Fonseca, *J Mol Catal B Enzym*, 2001, **15**, 147–153.

18 B. Datta, G. B. Schuster, A. McCook, S. C. Harvey and K. Zakrzewska, *J Am Chem Soc*, 2006, **128**, 14428–14429.

19 S. M. D. Watson, M. A. Galindo, B. R. Horrocks and A. Houlton, *J Am Chem Soc*, 2014, **136**, 6649–6655.

20 H. G. Hansma, I. Revenko, K. Kim and D. E. Laney, *Nucleic Acids Res*, 1996, **24**, 713–720.

21 C. Ke, A. Loksztejn, Y. Jiang, M. Kim, M. Humeniuk, M. Rabbi and P. E. Marszalek, *Biophys J*, 2009, **96**, 2918–2925.
22 N. Crampton, W. A. Bonass, J. Kirkham and N. H. Thomson, *Langmuir*, 2005, **21**, 7884–7891.
23 L. S. Shlyakhtenko, A. A. Gall, A. Filonov, Z. Cerovac, A. Lushnikov and Y. L. Lyubchenko, *Ultramicroscopy*, 2003, **97**, 279–287.
24 A. Japaridze, D. Vobornik, E. Lipiec, A. Cerreta, J. Szczerbinski, R. Zenobi and G. Dietler, *Macromolecules*, 2016, **49**, 643–652.
25 A. Y. Lushnikov, A. Bogdanov and Y. L. Lyubchenko, *J.B.C.*, 2003, **278**, 43130–43134.
26 G. G. Abashev, A. Y. Bushueva and E. V. Shklyaeva, *Chem Heterocycl Compd (N Y)*, 2011, **47**, 130–154.
27 G. Soliveri, V. Pifferi, R. Annunziata, L. Rimoldi, V. Aina, G. Cerrato, L. Falciola, G. Cappelletti and D. Meroni, *J.Phys. Chem.*, 2015, **119**, 15390–15400.
28 E. L. Sciuto, C. Bongiorno, A. Scandurra, S. Petralia, T. Cosentino, S. Conoci, F. Sinatra and S. Libertino, *Chemosensors*, 2018, **6**, 59.
29 J. Castellon, D. El Khoury and R. Arinero, *Int J Nanosci*, 2019, **18**, 1940038.
30 S. M. D. Watson, A. R. Pike, J. Pate, A. Houlton and B. R. Horrocks, *Nanoscale*, 2014, **6**, 4027–4037.
31 A. Houlton, A. R. Pike, M. Angel Galindo and B. R. Horrocks, *Chem. Comm.*, 2009, 1797.
32 S. M. D. Watson, A. R. Pike, J. Pate, A. Houlton and B. R. Horrocks, *Nanoscale*, 2014, **6**, 4027–4037.